LEWIS

NASA Conference Publication 10010

Nonlinear Constitutive Relations for High Temperature Applications–1986

(NASA-CP-10010) NONLINEAR CONSTITUTIVE
RELATIONS FOR HIGH TEMPERATURE APPLICATIONS,
1986 (NASA) 482 p CSCL 20K
N88-21498
--THRU--
N88-21527
Unclas
G3/39 0136196

Proceedings of a symposium held at
the University of Akron
Akron, Ohio
June 11-13, 1986

NASA Conference Publication 10010

Nonlinear Constitutive Relations for High Temperature Applications–1986

Proceedings of a symposium sponsored by
the University of Akron and NASA Lewis Research Center
held at the University of Akron
Akron, Ohio
June 11-13, 1986

NASA
National Aeronautics and
Space Administration

Scientific and Technical
Information Branch

1988

PREFACE

The Third Symposium on Nonlinear Constitutive Relations for High Temperature Applications, sponsored jointly by the NASA Lewis Research Center, Cleveland, Ohio, and The University of Akron was held at The University of Akron, Akron, Ohio, June 11-13, 1986. Over one-hundred participants and attendees representing government agencies, universities, and industry were in attendance. The purposes of the symposium were (1) to review the state-of-the art in nonlinear constitutive modeling of high-temperature materials, (2) to document and disseminate the research progress and new technology developed to date and (3) to identify needs for future research and development in the areas of constitutive modeling, life prediction, and structural analysis applications.

One of the specific goals of NASA is to foster technological development of analytical/experimental methodologies for improved design of gas turbine engine structures as well as advanced aerospace propulsion engine structures, including hypersonic vehicle and reusable space propulsion engine structures. To support these technologies, there is considerable development work yet needed in the area of nonlinear constitutive relations for high-temperature applications. This has become an increasingly critical need in light of recent advances in high-temperature materials technology (including single crystal and directionally solidified superalloys, metal matrix composites, and ceramic matrix composites) in response to new demands on material performance. NASA Lewis, in cooperation with industry, universities, and other government agencies, is supporting this new technology development; some of which is reported in this symposium publication. The symposium served not only to foster this technological development, but also to serve as a forum for all industries with a commonality in technology interests. The common interests addressed were development of nonlinear constitutive models/experiments (including life prediction models for advanced materials), their implementation into structural analysis codes, and their application to analyze advanced structures at elevated temperatures.

The symposium was organized into the following five sessions:

I. Constitutive Modeling
II. Damage and Life Prediction Modeling
III. Experimental Techniques
IV. Numerical Methods and Computation
V. Structural Applications

There were a total of twenty-nine papers presented. The papers and authors are grouped by session in the Contents.

The symposium co-chairmen wish to thank the session chairmen; distinguished invited lecturers, Professor E.T. Onat from Yale University, Professor F.A. Leckie from the University of California at Santa Barbara, and Professor A.R.S. Ponter from the University of Leicester, England; and authors whose efforts contributed greatly to the technical excellence of the symposium.

PRECEDING PAGE BLANK NOT FILMED

We are also grateful to Mr. Marvin Phillips and the Continuing Education Office at the University of Akron, for their help and superb handling of the logistics of the symposium.

Symposium Co-chairmen:

NASA Lewis Research Center	The University of Akron
R.L. Thompson	T.Y. Chang
G.R. Halford	D.N. Robinson
	J.R. Ellis

CONTENTS

Page

Preface iii

SESSION I - CONSTITUTIVE MODELING
Co-Chairmen: E.T. Onat, Yale University
D.J. Gauntner, NASA Lewis Research Center

THE VISCOPLASTICITY THEORY BASED ON OVERSTRESS APPLIED TO THE MODELING OF A NICKEL BASE SUPERALLOY AT 815 °C
E. Krempl, H. Lu, and D. Yao, Rensselaer Polytechnic Institute . . . 1

A VISCOPLASTIC CONSTITUTIVE THEORY FOR METAL MATRIX COMPOSITES AT HIGH TEMPERATURE
D.N. Robinson, S.F. Duffy, and J.R. Ellis,
The University of Akron 7

DEVELOPMENT OF A UNIFIED CONSTITUTIVE MODEL FOR AN ISOTROPIC NICKEL BASE SUPERALLOY RENE' 80
V.G. Ramaswamy, R.H. Van Stone, J.H. Laflen, and D.C. Stouffer,
General Electric Company 27

MODELING THE VISCOPLASTIC BEHAVIOR OF INCONEL 718 AT 1200 °F
M.S. Abdel-Kader, J. Eftis, and D.L. Jones,
The George Washington University 37

AN INTERNAL VARIABLE CONSTITUTIVE MODEL FOR THE LARGE DEFORMATION OF METALS AT HIGH TEMPERATURES
S. Brown and L. Anand, Massachusetts Institute of Technology 69

PRESSURE INDUCED AGEING OF POLYMERS
I. Emri, University of Ljubljana, Yugoslavia; W.G. Knauss,
California Institute of Technology 77

A SIMPLIFIED ORTHOTROPIC FORMULATION OF THE VISCOPLASTICITY THEORY BASED ON OVERSTRESS
M. Sutcu, General Electric Corporate R&D Center; E. Krempl,
Rensselaer Polytechnic Institute 89

CONSTITUTIVE MODELING AND THERMOVISCOPLASTICITY
R.B. Hetnarski and H. Ghoneim, Rochester Institute of Technology;
D.B. Paul, Wright Patterson Air Force Base 97

SESSION II - DAMAGE AND LIFE PREDICTION MODELING
Co-Chairmen: F.A. Leckie, University of Illinois
G.R. Halford, NASA Lewis Research Center

APPLICATIONS OF ELASTIC-VISCOPLASTIC CONSTITUTIVE MODELS IN DYNAMIC ANALYSES OF CRACK RUN-ARREST EVENTS
B.R. Bass, C.E. Pugh, and R.W. Swindeman,
Oak Ridge National Laboratory 109

A THEORY OF VISCOPLASTICITY ACCOUNTING FOR INTERNAL DAMAGE
A.D. Freed, NASA Lewis Research Center;
D.N. Robinson, The University of Akron 119

CREEP RUPTURE ANALYSIS OF A BEAM RESTING ON HIGH TEMPERATURE FOUNDATION
R.J. Gu, Oakland University; F.A. Cozzarelli,
State University of New York at Buffalo 137

A CONSTITUTIVE MODEL WITH DAMAGE FOR HIGH TEMPERATURE SUPERALLOYS
J.A. Sherwood and D.C. Stouffer, University of Cincinnati 187

EVALUATION OF STRUCTURAL ANALYSIS METHODS FOR LIFE PREDICTION
A. Kaufman and M. Tong, Sverdrup Technology, Inc; J.F. Saltsman
and G.R. Halford, NASA Lewis Research Center 201

SESSION III - EXPERIMENTAL TECHNIQUES
Co-Chairmen: H. Stamm, KFK/Karlsruhe, West Germany
M.S. Hirschberg, NASA Lewis Research Center

DATA REQUIREMENTS TO MODEL CREEP IN 9CR-1MO-V STEEL
R.W. Swindeman, Oak Ridge National Laboratory 217

CONTROLLED-STRAIN RATE TESTS AT VERY LOW STRAIN RATES OF 2618 ALUMINUM AT 200 °C
J.L. Ding and S.R. Lee, Washington State University 225

CYCLIC UNIAXIAL AND BIAXIAL HARDENING OF TYPE 304 STAINLESS STEEL MODELED BY THE VISCOPLASTICITY THEORY BASED ON OVERSTRESS
D. Yao and E. Krempl, Rensselaer Polytechnic Institute 239

SOME IMPLICATIONS FOR CYCLIC PLASTIC AND VISCOPLASTIC EQUATIONS BASED ON NONPROPORTIONAL LOADING EXPERIMENTS
D.L. McDowell, J.Moosbrugger and M. Doumi, Georgia Institue of
Technology; E.H. Jordan, University of Connecticut 247

AN EXPERIMENTAL COMPARISON OF SEVERAL CURRENT VISCOPLASTIC CONSTITUTIVE MODELS AT ELEVATED TEMPERATURE
G.H. James, P.K. Imbrie, P.S. Hill, D.H, Allen, and W.E. Haisler,
Texas A&M University 253

THE EFFECTS OF TEMPERATURE AND STRAIN RATE ON THE YIELDING BEHAVIOR OF THE SINGLE CRYSTAL SUPERALLOY PWA 1480
W.W. Milligan and S.D. Antolovich, Georgia Institute of Technology . 291

A UNIFIED CREEP-PLASTICITY MODEL SUITABLE FOR THERMO-MECHANICAL LOADING
D. Slavik and H. Sehitoglu, University of Illinois
at Urbana-Champaign 295

SESSION IV - NUMERICAL METHODS AND COMPUTATION
Chairman: T. Nicholas, Wright Patterson Air Force Base

ON THE GLOBAL/LOCAL TIME INCREMENTING FOR VISCOPLASTIC ANALYSIS
A.F. Saleeb, T.Y. Chang, and J.Y. Chen, The University of Akron . . . 307

AN AUTOMATED PROCEDURE FOR MATERIAL PARAMETER EVALUATION FOR VISCOPLASTICITY CONSTITUTIVE MODELS
P.K. Imbrie, G.H. James, P.S. Hill, D.H. Allen, and W.E. Haisler, Texas A&M University 317

A CONSTITUTIVE MATERIAL MODEL FOR NONLINEAR FINITE ELEMENT STRUCTURAL ANALYSIS USING AN ITERATIVE MATRIX APPROACH
H.A. Koening, Universiy of Connecticut; K.S. Chan, Southwest Research Institute; B.N. Cassenti, United Technologies Research Center; R.M. Weber, Pratt & Whitney 353

SESSION V - Structural Applications
Chairman: A.R.S. Ponter, University of Leicester, England

NONLINEAR STRUCTURAL ANALYSIS OF A TURBINE AIRFOIL USING THE WALKER VISCOPLASTIC MATERIAL MODEL FOR B1900 + Hf
T.G. Meyer, J.T. Hill, and R.M. Weber, Pratt & Whitney 359

UNIFIED CONSTITUTIVE MODELS FOR HIGH-TEMPERATURE STRUCTURAL APPLICATIONS
U.S. Lindholm and K.S. Chan, Southwest Research Institute; S.R. Bodner, Technion-Israel Institute of Technology; R.M. Weber, Pratt & Whitney; K.P. Walker, Engineering Scientific Software, Inc. 371

CONSTITUTIVE RESPONSE OF RENE 80 UNDER THERMAL MECHANICAL LOADS
K.S. Kim, T.S. Cook, and R.L. McKnight, General Electric Company . . 395

A CONSTITUTIVE MODEL FOR AN OVERLAY COATING
D.M. Nissley and G.A. Swanson, Pratt & Whitney 419

NON-ISOTHERMAL ELASTOVISCOPLASTIC ANALYSIS OF PLANAR CURVED BEAMS
G.J. Simitsis, R.L. Carlson, and R. Riff, Georgia Institute of Technology 437

EFFECTS OF STATE RECOVERY ON CREEP BUCKLING UNDER VARIABLE LOADING
D.N. Robinson and S.M. Arnold, The University of Akron 461

N88
21499
UNCLAS

N88-21499

THE VISCOPLASTICITY THEORY BASED ON OVERSTRESS APPLIED TO THE MODELING OF A NICKEL BASE SUPERALLOY AT 815°C

E. Krempl, H. Lu and D. Yao
Department of Mechanical Engineering,
Aeronautical Engineering and Mechanics
Rensselaer Polytechnic Institute
Troy, NY 12180-3590

Short-term strain rate change, creep and relaxation tests were performed in an MTS computer-controlled servohydraulic testing machine. Aging and recovery were found to be insignificant for test times not exceeding thirty hours. The material functions and constants of the theory were identified from results of strain rate change tests. Numerical integration of the theory for relaxation and creep tests showed good predictive capabilities of the viscoplasticity theory based on overstress.

Introduction

Advanced materials are being developed for use in high temperature gas turbine applications. To fully utilize the capability of these new materials their deformation properties and their creep and fatigue fracture characteristics must be determined by suitable experiments. The experimental findings must be analyzed, idealized and translated into constitutive equations for use in stress analysis and life prediction. Only when these ingredients together with appropriate computational tools are available can durability analysis be performed in the design stage long before a component is being built. This paper contributes to the design methodology and reports on an experimental investigation of the deformation behavior of a nickel-base superalloy at 815°C and on its mathematical modeling using the viscoplasticity theory based on overstress.

Testing Method and Test Materials

All tests were performed in an MTS axial-torsion servohydraulic mechanical testing machine with an MTS 463 Data/Control processor for computer control. An MTS clamshell furnace was used to heat the specimens. Strain measurement on the gage section was done with an MTS high-temperature uniaxial extensometer. Strain and load controlled tests were performed at 815°C. Separate tests checked on the extensometer calibration (at room temperature) and on the uniformity of the temperature along the gage length. For the duration of the tests the temperature of the gage section stayed within 2°C of the nominal temperature.

The nickel-base superalloy test material was donated by AVCO Lycoming and was delivered in the form of 19 mm coupons. The machined specimens had a gage section diameter of about 6.5 mm. They were tested in the as-received condition at 815°C.

Experimental Results

Effects of strain rate

Figure 1 shows the results of three tests: two were subjected to continuous straining at 10^{-4} and 10^{-6} s^{-1}, respectively; the other to a sequential decrease in strain rates. The significant influence of strain rate is evident. These and other strain rate change tests revealed no discernible strain rate history effect. The strain rate change tests in Fig. 1 and others indicate that there is a unique stress level associated with each strain rate which will be reached after a transient period irrespective of the prior history. The stress levels were determined from the tests and are listed in Table 1 together with the stress level differences relative to the stress corresponding to 10^{-4} s^{-1}.

The tests in Fig. 1 show good reproducibility which was also found with others. An exception is the stress level at 10^{-6} s^{-1} for specimens #12 and #15. At 1.1 percent strain, specimen 15 suffered a temperature variation of about 4°C which may have caused the drop-off at point A. The filled triangle indicates the stress level at 10^{-7} s^{-1} found in other experiments. Premature cracking is probably the cause for the decrease in stress level of specimen #7 before unloading started.

Aging and recovery

To ascertain whether these phenomena have a significant influence on the deformation behavior two specimens were subjected to a 3 and 33 hours hold period, respectively, at zero load after loading to 1 percent strain and subsequent unloading had been accomplished. It is seen from Fig. 2 that the stress-strain curves before and after the rest period are within the normal scatter of the test results. This can be easily ascertained by comparing the responses of the two specimens and the results of Figs. 1 and 2.

The tests show therefore that recovery and aging are insignificant for this material for times less than 33 hours at 815°C. This result was very surprising to the authors.

Modeling. The Viscoplasticity Theory Based on Overstress (VBO)

The model and its material functions

In the present version of VBO recovery and aging are not included. In the uniaxial state of stress the theory consists of two coupled, nonlinear, ordinary differential equations which contain two positive, decreasing material functions; the viscosity function k controls the rate dependence and the shape function ψ influences the shape of the knee of the stress-strain curve. In addition, the elastic modulus E, the tangent modulus E_t and the asymptotic value A of the equilibrium stress g enter into the theory. The equilibrium stress is attained in the limit as rates approach zero. The difference $\sigma - g = x$ between the stress σ and g is called the overstress and k and ψ are only functions of x. The equations are

$$d\epsilon/dt = d\epsilon^{el}/dt + d\epsilon^{in}/dt = d\sigma/dt/E + (\sigma-g)/(Ek[x]) \tag{1}$$

$$dg/dt = \psi[x]d\epsilon/dt - (g-E_t\epsilon)(\psi[x]-E_t)|d\epsilon^{in}/dt|/A \tag{2}$$

where square brackets following a symbol denote "function of." Under constant strain rate loading, the system of equations permits asymptotic solutions given by

$$\{d\sigma/d\epsilon\} = \{dg/d\epsilon\} = E_t \tag{3}$$

$$\{x\} = (E-E_t)\ k[\{x\}]d\epsilon/dt \tag{4}$$

$$\{g-E_t\epsilon\} = A\ d\epsilon/dt/|d\epsilon^{in}/dt| \tag{5}$$

where braces denote asymptotic values. Details of the theory are found in [1,2].

The asymptotic solutions are algebraic equations and are used in identifying the material constants and functions. The procedure exploits (4) to compute the stress level differences at different strain rates so that the data of Table 1 can be used. Details can be found in [3]. The g-curve is obtained by extrapolation and a nonlinear least square analysis is performed to determine the constants of the shape function. The material functions and constants obtained by this method are given in Table 2.

Predictions of the theory

With the material constants determined from strain rate change tests, the theory was applied to predict the outcome of relaxation and creep tests. Figure 3 shows the results of a strain rate change test followed by relaxation tests of 1024 s duration. The triangles represent experimental results; the continuous line, the predictions of the theory as obtained by integrating (1) and (2) numerically using the IMSL routine DGEAR. The prediction for incremental creep tests is depicted in Fig. 4. The creep periods last 700 s except at the highest stress level where creep was terminated after 300 s. The experimental results are again given as triangles.

The discrepancy between predictions and experiment in Fig. 3 is mainly due to an overprediction of relaxation in the first relaxation period aa'. If allowance is made for this difference and the theoretical curves are translated upwards so that they coincide at the end of the first relaxation period, the subsequent predictions are very reasonable. A similar observation holds for the stress vs time relaxation curves.

It is seen that both the theory and the experiment do not show creep at stress levels a and b in Fig. 4. At the next two stress levels the theory underpredicts the creep strain but overpredicts it at stress levels e and f.

The fitting of the material functions was only done once on the basis of the strain rate change test results. Both the creep and the relaxation experiments suggest that the theory overpredicts at high inelastic strain rates. Since underprediction is observed at the small stress levels in Fig. 4, it is reasonable to assume that an optimization of the material functions is possible so as to improve the predictions. This optimization and other tests are planned for the future.

Acknowledgment

This investigation was made possible by a grant from AVCO Lycoming. Dr. Sait Aksoy provided liaison and helpful suggestions.

References

[1] Krempl, E., J. J. McMahon and D. Yao, "Viscoplasticity Theory Based on Overstress with a Differential Growth Law for the Equilibrium Stress," in print *Mechanics of Materials*.

[2] Yao, D., and E. Krempl, "Viscoplasticity Based on Overstress. The Prediction of Monotonic and Cyclic Proportional and Nonproportional Loading Paths of an Aluminum Alloy," *Int. J. of Plasticity, 1*, 259-274 (1985).

[3] Krempl, E., H. Lu and D. Yao, Rensselaer Polytechnic Institute Report MML 85-4, November 1985.

TABLE 1

Averaged Flow Stress Levels and Stress Level Differences for C101 at 815°C

Strain Rate s^{-1}	Stress Level at 1.2% MPa	Stress Level Difference MPa
10^{-3}	966	132
10^{-4}	834	0
10^{-5}	721	-113
10^{-6}	638.4	-195.6
10^{-7}	554.4	-279.6

TABLE 2

THE DETERMINED MATERIAL CONSTANTS AND FUNCTIONS

Material Constants

$E = 156620$ MPa

$E_t = 267$ MPa

$A = 421.7$ MPa

Viscosity Function

$$k[x] = k_1\left(1 + \frac{|x|}{k_2}\right)^{-k_3}$$

$k_1 = 3150000$ s

$k_2 = 186$ MPa

$k_3 = 9.96$

Shape Modulus

$$\psi[x] = c_1 + (c_2 - c_1)\exp(-c_3|x|)$$

c_1, c_2 and x in units of MPa;

$c_1 = 62500$, $c_2 = 150000$

c_3 in units of MPa^{-1};

$c_3 = 0.0387$

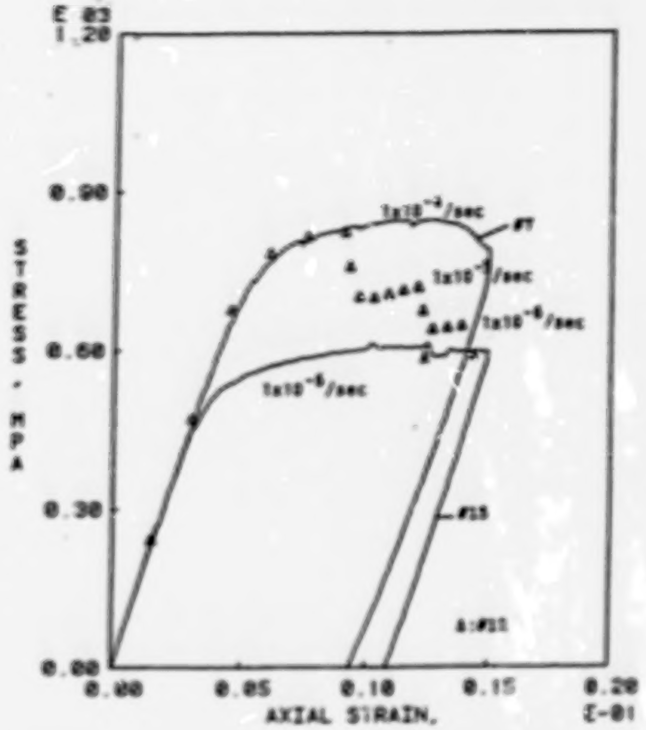

Figure 1. Stress-strain curves of constant strain-rate test (solid lines) and strain-rate change tests (triangles). Filled triangle denotes the approximate stress level at 1x10^{-7} per second.

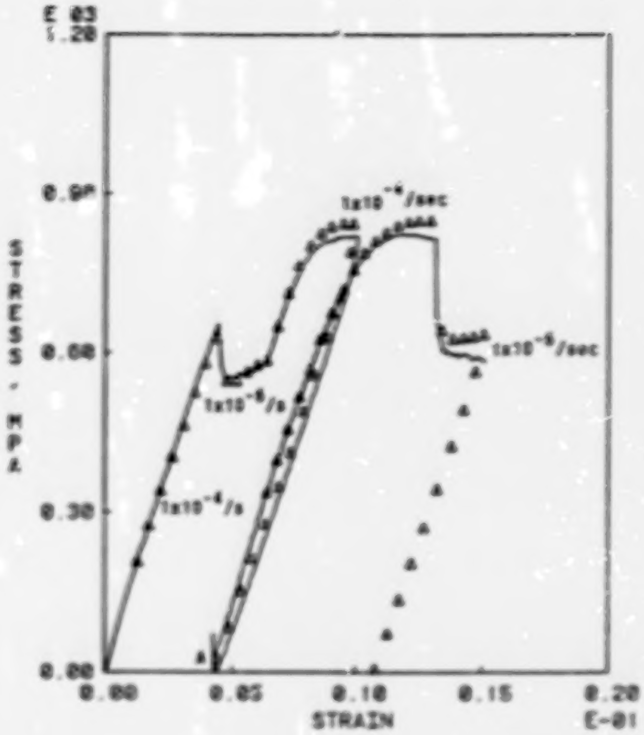

Figure 2. Stress-strain curves of specimens #8(–) and #10(Δ). Hold periods of 3 and 33 hrs at A.

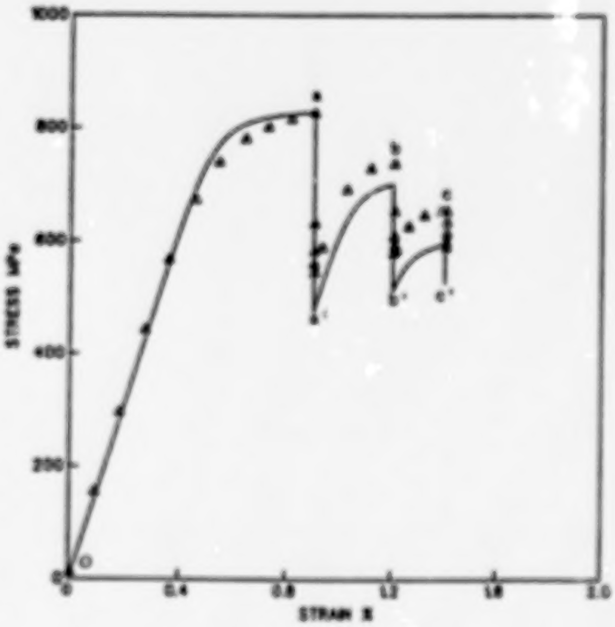

Figure 3. Prediction of strain-rate change and relaxation tests. Triangles represent experimental results. Strain-rate history: oa 10^{-7}, aa' 0, a'b 10^{-5}, bb' 0, b'c 10^{-4}, cc' 0. All values are given in units of s^{-1}. Relaxation time = 1024 s.

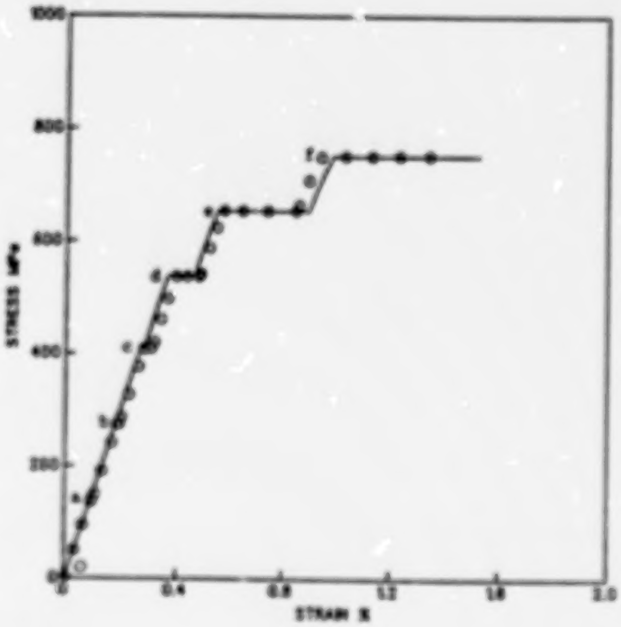

Figure 4. Incremental creep tests at various stress levels. Between creep periods the stress rate is 2.8 MPa/s. Almost no creep is observed at the two stress levels below 300 MPa. Creep periods are 700 s except at level 4. Circles represent experimental points.

N88
21500
UNCLAS

N88-21500

A VISCOPLASTIC CONSTITUTIVE THEORY FOR METAL MATRIX COMPOSITES AT HIGH TEMPERATURE

David N. Robinson*
The University of Akron
Akron, Ohio 44325

Stephen F. Duffy*
Cleveland State University
Cleveland, Ohio 44115

John R. Ellis†
The University of Akron
Akron, Ohio 44325

SUMMARY

A viscoplastic constitutive theory is presented for representing the high-temperature deformation behavior of metal matrix composites. The point of view taken is one of a continuum wherein the composite is considered a material in its own right, with its own properties that can be determined for the composite as a whole. It is presumed that a single preferential (fiber) direction is identifiable at each material point (continuum element), thereby admitting the idealization of local transverse isotropy. A key ingredient in this work is the specification of an experimental program for the complete determination of the material functions and parameters for characterizing a particular metal matrix composite. The parameters relating to the strength of anistropy can be determined through tension and torsion tests on longitudinally and circumferentially reinforced thin-walled tubes. Fundamental aspects of the theory are explored through a geometric interpretation of some basic features analogous to those of the classical theory of plasticity.

E-3956-2

INTRODUCTION

Structural alloys used in high-temperature applications exhibit complex thermomechanical behavior that is inherently time-dependent and hereditary, in the sense that current behavior depends not only on current conditions but also on thermomechanical history. Considerable attention is being focused now on metal matrix composite materials that possess strong directional characteristics. In high-temperature applications these materials exhibit all the complexities of conventional alloys (e.g., creep, relaxation, recovery, rate sensitivity, etc.), and in addition, their strong initial anistropy adds further complexities.

Here, we present a continuum theory to represent the high-temperature, time-dependent, hereditary deformation behavior of materials that are initially

---

*NASA Lewis Resident Research Associate.
†Now at NASA Lewis.

PRECEDING PAGE BLANK NOT FILMED

transversely isotropic. The theory is intended to apply to materials, particularly metallic composites, that can be idealized as psuedohomogeneous continua with locally definable directional characteristics.

The composite material is viewed as a material in its own right, with its own properties that can be measured and specified for the composite as a whole. Experiments for this purpose are outlined in detail in the fourth section of the paper. This view is intended to satisfy the structural analyst or design engineer who needs reasonably simple continuum methods of structural analysis to predict deformation behavior in complex multiaxial situations, particularly at high temperature where material response is enormously complex. Indeed, the prediction of component lifetime depends critically on the accurate prediction of deformation behavior.

The alternative approach is concerned with detailed interactions of the constituents of the composite: fabrication, bonding, and the relation of the properties of the composite to the individual properties of the fiber and matrix. Clearly, such problems are of great importance, and the two approaches mentioned are not mutually exclusive. Here, however, the continuum point of view will be emphasized. This is done in the same spirit that the theories of elasticity, plasticity, viscoelasticity, and others are formulated; on the basis of macroscopic observations, without direct consideration of the details of intermolecular, intergranular or interdislocation interactions. Of course, this is not to imply that qualitative (and quantitative) understanding of behavior on the microscale should not strongly influence the formulation and structure of phenomenological theories.

The authors are hopeful this research will complement other ongoing efforts at NASA Lewis Research Center relating to the high-temperature behavior of metal matrix composites (refs. 1 to 5). Parts of the present work (believed essential in representing the time-dependent, hereditary behavior of metals) may prove helpful in extending the micromechanics equations for the thermal and mechanical behavior of composites (refs. 1 and 2) to include some important viscoplastic features.

STATEMENT OF THE THEORY

This work is an extension of that by Robinson (ref. 6) and includes the former work as a special case. In reference 6, three material parameters over and above those necessary for representing isotropic viscoplastic behavior were necessary to account for transverse isotropy. Here, four parameters have to be specified (fig. 1). The additional parameter arises from a less restrictive set of assumptions made in the theoretical development. Definition of the additional parameter leads to more testing to characterize a particular material but, at the same time, offers the distinct advantage of greater flexibility in correlating predictions with experimental data.

As in reference 6, the starting point is the assumed existence of a dissipation potential function (refs. 7 to 9); that is

$$\Omega = \Omega\,(\sigma_{ij},\alpha_{ij},T) \tag{1}$$

with the generalized normality structure

$$\dot{\varepsilon}_{ij} = \frac{\partial\Omega}{\partial\sigma_{ij}} \tag{2}$$

$$\frac{-\dot{\alpha}_{ij}}{h(\alpha_{kl})} = \frac{\partial\Omega}{\partial\alpha_{ij}} \tag{3}$$

Here, σ_{ij} and α_{ij} denote the components of the applied and internal stress tensors, respectively, $\dot{\varepsilon}_{ij}$ denotes the components of the inelastic strain rate tensor, h is a scalar function of the internal stress, and T is the temperature. Although Ω is shown as a function of temperature, only isothermal deformations will be considered in the following development. Extension to nonisothermal conditions follows as in reference 10.

In the fully isotropic case, the stress dependence of Ω enters only through the principal invariants of the deviatoric applied and internal stresses (ref. 10). For transverse isotropy, Ω must depend additionally on the local preferential (fiber) direction denoted by the components of a unit vector d_i (or, as the sense of d_i is immaterial, on the components of a symmetric directional tensor $d_i d_j$). Form invariance (objectivity) of Ω requires that it depend only on invariants of the applied and internal stresses, the directional tensor, and certain products of these tensors (ref. 11).

A subset of the irreducible set of invariants for form invariance (integrity basis) is used (ref. 11)

$$I_1 = \frac{1}{2}\Sigma_{ij}\Sigma_{ji} \tag{4}$$

$$I_2 = d_i d_j \Sigma_{jk}\Sigma_{ki} - 4I_3^2 \tag{5}$$

$$I_3 = \frac{1}{2} d_i d_j \Sigma_{ji} \tag{6}$$

where Σ_{ij} denotes the components of the effective stress, that is, the difference of the deviatoric applied and internal stresses. I_1 relates, as in the isotropic case, to the effective octahedral shear stress, I_2 relates to the shear component of the effective traction on the plane of isotropy (plane normal to d_i), and I_3 corresponds to the normal component of the effective traction along d_i.

Taking Ω to be dependent on the appropriate invariants and using equations (2) and (3), the flow law becomes

$$\dot{\epsilon}_{ij} = f(F)\left\{\Sigma_{ij} - \left(\frac{\eta^2 - 1}{\eta^2}\right)\left(d_k d_i \Sigma_{jk} + d_j d_k \Sigma_{ki} - 4I_3 d_i d_j\right) - 4I_3\left(\frac{\omega^2 - 1}{4\omega^2 - 1}\right)\left(3d_i d_j - \delta_{ij}\right)\right\} \qquad (7)$$

and the evolutionary law becomes

$$\dot{a}_{ij} = \frac{H}{G^{\beta}}\dot{\epsilon}_{ij} - RG^{m-\beta}\left\{a_{ij} - \left(\frac{\eta^2 - 1}{\eta^2}\right)\left(d_k d_i a_{jk} + d_j d_k a_{ki} - 4I_3' d_i d_j\right) - 4I_3'\left(\frac{\omega^2 - 1}{4\omega^2 - 1}\right)\left(3d_i d_j - \delta_{ij}\right)\right\} \qquad (8)$$

with

$$F = \frac{1}{K_T^2}\left\{I_1 - \left(\frac{\eta^2 - 1}{\eta^2}\right)I_2 - \left(\frac{12(\omega^2 - 1)}{4\omega^2 - 1}\, I_3^2\right) - 1\right\} \qquad (9)$$

and

$$G = \frac{1}{K_T^2}\left\{I_1' - \left(\frac{\eta^2 - 1}{\eta^2}\right)I_2' - \left(\frac{12(\omega^2 - 1)}{4\omega^2 - 1}\right)(I_3')^2\right\} \qquad (10)$$

The function $f(F)$ and the material parameters m, β, R, H, and K_T are associated with the viscoplastic response (ref. 10); the components of the unit vector d_i (specified in terms of two Euler angles), ω, and η, are the four parameters associated with the direction and strength of transverse isotropy (fig. 1). I_1', I_2', I_3' are invariants of the deviatoric internal stress a_{ij}, similar in form to equations (4) to (6). Note that with $\omega = \eta = 1$ equations (7) to (10) reduce to the isotropic forms reported in reference 10. The details of the derivation of equations (7) to (10) are left to the references 6, 10, and 11.

For a particular composite material the parameters ω and η, designating the strength of anisotropy, depend on the individual constituent materials (fiber and matrix) and their volume ratio. Different volume ratios involving the same constituents are considered different materials. In extending the present theory to arbitrarily large deformations, the local volume ratio may change in the course of deformation (as does the local density in an isotropic material); in which case evolutionary laws for ω and η must be specified. Also, for large deformations and/or rotations, the preferential direction d_i may convect with the material thereby resulting in increasing anisotropic inhomogeneity. At this time, large deformations and rotations are not considered.

SOME FUNDAMENTAL IMPLICATIONS OF THE THEORY

As in earlier works (refs. 6 and 10) F plays the role of a Bingham-Prager threshold stress function; inelastic response occurs only for $F > 0$. The surface $F = 0$ in the stress space encloses stress states that produce elastic behavior only. Figure 2 shows a typical projection of $F = 0$ on the $\sigma_{11} - \sigma_{22}$ plane for full isotropy ($\omega = \eta = 1$) and the virgin state ($a_{ij} = 0$). An infinite family of surfaces F = constant is associated with each inelastic state. The direction of the inelastic strain rate vector at each stress point on a given surface is directed normal to the surface. The existence of these surfaces and the concept of normality has been demonstrated experimentally for the isotropic case in reference 12.

Figure 3 shows the corresponding projection of $F = 0$ on the $\sigma_{11} - \sigma_{22}$ plane for the transversely isotropic case with $\omega = \eta = 2$. For each curve shown, the preferential direction is taken to lie in the X_1, X_2 physical plane with a specified angle φ relative to the X_1 axis. These curves, as in figure 2, correspond to the virgin state. The shape and orientation of the surfaces $F = 0$ (and all surfaces F = constant) now depend on the local preferential direction d_i. Note, for instance, that for $\varphi = 0$, the intercept on the σ_{11} axis is the threshold stress Y_L, (figs. 1 and 3), the intercept on the σ_{22} axis is Y_T, and $\omega = (Y_L/Y_T) = 2$.

As an interesting and illustrative example, consider the stress path $\sigma_{11} = 2\sigma_{22}$ that is denoted as a dotted line in figures 2 and 3. This is equivalent to the stress state in a thin-walled tube with closed ends under internal pressure, where σ_{11} is the circumferential or hoop stress and σ_{22} the axial stress. With increasing pressure, the stress point eventually reaches the surface $F = 0$ and the tube begins to deform inelastically. In figure 2, corresponding to the isotropic tube, inelastic deformation occurs as indicated by the strain rate vector shown. Normality dictates that the axial strain rate $\dot{\epsilon}_{22}$ is zero, that is, the tube incurs no inelastic change in length. Contrast this behavior with that of figure 3 with $\varphi = 0$. This case represents a circumferentially reinforced tube with a threshold stress in the circumferential direction that is twice that of the axial direction. As $F = 0$ is reached and inelasticity begins to occur, the (normal) strain rate vector has a relatively large axial component $\dot{\epsilon}_{22}$. The thin tube now experiences inelastic axial extension. Thus the mode of inelastic deformation has changed qualitatively with reinforcement. Similar observations are well documented for time-independent reinforced structures (ref. 13).

EXPERIMENTAL DETERMINATION OF MATERIAL PARAMETERS

Two types of specimens are presumed to be available: thin-walled composite tubes that are longitudinally reinforced (having a single fiber direction oriented axially) and those that are circumferentially reinforced (circumferential fiber orientation). Each type of tube will be loaded either in pure torsion or in pure tension. Although not discussed here, combined tension and torsion experiments can be used as verification tests to assess the correctness of the multiaxial theory (ref. 12). As is well known, the thin-walled tube is an ideal specimen for the development of constitutive relationships in that it provides a nearly homogeneous and uniform region of stress and strain, and is statically determinate.

Those parameters relating to the strength of anisotropy, ω and η, and the threshold strength $Y_L(\equiv K_T(4\omega^2 - 1)^{1/2})$ are determined through probing tests. These tests are designed to determine the inelastic strain rate for a given stress in the neighborhood of a constant inelastic state, here the initial (virgin) state of the material. Indeed, it is the degree of initial transverse isotropy that is of interest in this study. The probing test, conducted properly, furnishes the desired information without significantly changing the state.

The material function $f(F)$ and the parameters m, β, R, and H relating to the viscoplastic properties of the composite are obtained from a combination of the probing tests and creep tests conducted on longitudinally-reinforced tubes (or bars). Alternately, in place of the latter tests, one could use torsion tests on circumferentially reinforced tubes as outlined in reference 11. The present choice of basing the viscoplastic parameters on uniaxial creep tests of axially reinforced tubes is motivated by (1) the relative ease of fabricating longitudinally reinforced tubular specimens over those reinforced circumferentially and (2) the advantage of characterizing directly the inelastic response in the critical fiber direction. In the case of extreme reinforcement (e.g., a relatively high volume ratio of very strong fibers that remain essentially elastic), composite structures are known to be "shear limited" (ref. 12), and their inelastic behavior is governed largely by the shear response of the matrix. Under these conditions it may be advantageous to determine the viscoplastic parameters through the torsional creep tests on circumferentially reinforced tubes discussed in reference 11.

First, consider a probing test on a longitudinal tube. Pure torsion and pure tension probes are schematically illustrated as the respective paths o-a and o-b in the σ-τ stress space of figure 4(a). Data from such tests take the form of a sequence of stress and inelastic strain rate pairs, $(\tau,\dot{\gamma})$ along o-a and $(\sigma,\dot{\epsilon})$ along o-b. These data can be conveniently plotted as the solid curves σ versus $\dot{\epsilon}$ and τ versus $\dot{\gamma}$ in figure 5. Extrapolation of the σ versus $\dot{\epsilon}$ curve in figure 5 to the $\dot{\epsilon} = 0$ axis furnishes the longitudinal threshold stress Y_L.

Specialization of equations (9) and (7) for the path o-a in figure 4(a) results in

$$F = \frac{\tau^2}{\eta^2 K_T^2} - 1 \tag{11}$$

and

$$2\dot{\epsilon}_{12} = \dot{\gamma} = f(F)\,\frac{2\tau}{\eta^2} \tag{12}$$

in which $\tau(\equiv\sigma_{12})$ is the applied shear stress. The corresponding equations for path o-b are

$$F = \frac{\sigma^2}{(4\omega^2 - 1)K_T^2} - 1 \tag{13}$$

and

$$\dot{\epsilon}_{11} = \dot{\epsilon} = f(F)\,\frac{2\sigma}{4\omega^2 - 1} \tag{14}$$

where $\sigma(\equiv\sigma_{11})$ is the applied normal stress. Now for F = constant (Ω = constant), equations (11) and (13) give

$$\frac{\sigma}{\tau} = \left(\frac{4\omega^2 - 1}{\eta^2}\right)^{1/2} \tag{15}$$

while equations (12) and (14) combine to give

$$\frac{\dot{\gamma}}{\dot{\epsilon}} = \left(\frac{4\omega^2 - 1}{\eta^2}\right)\frac{\tau}{\sigma} = \frac{\sigma}{\tau} \tag{16}$$

or

$$\sigma\dot{\epsilon} = \tau\dot{\gamma} \tag{17}$$

Thus, in figure 4(a) points $(\tau,\dot{\gamma})$ along o-a and $(\sigma,\dot{\epsilon})$ along o-b, having the same dissipation rate, lie on a common F = constant (Ω = constant) curve; for example, the particular points $(\tau_A,\dot{\gamma}_A)$ and $(\sigma_A,\dot{\epsilon}_A)$ in figure 4(b).

Pairs of points in the plot of figure (5) that lie on an F = constant locus are related geometrically such that areas $\sigma_A\dot{\epsilon}_A$ and $\tau_A\dot{\gamma}_A$ are equal. Several such pairs can be matched up giving an average value of the ratio

$$\frac{\sigma}{\tau} = \left(\frac{\sigma}{\tau}\right)_L \tag{18}$$

Thus, from equation (15)

$$\left(\frac{4\omega^2 - 1}{\eta^2}\right)^{1/2} = \left(\frac{\sigma}{\tau}\right)_L \tag{19}$$

Probing tests on circumferentially reinforced tubes produce results entirely analogous to those discussed above for longitudinally reinforced tubes; counterparts of figures 4(a), 4(b), and 5 can be constructed.

The governing equations corresponding to the pure torsional loading of the circumferential tube are identical to equations (11) and (12). The equations relating to pure tension of the circumferential tube are

$$F = \frac{\sigma^2\omega^2}{(4\omega^2 - 1)K_T^2} - 1 \tag{20}$$

and

$$\dot{\epsilon}_{11} = \dot{\epsilon} = f(F)\,\frac{2\sigma}{4\omega^2 - 1}\,\omega^2 \tag{21}$$

As before, for F = constant (Ω = constant), equations (11) and (20) combine to give

$$\frac{\sigma}{\tau} = \left(\frac{4\omega^2 - 1}{\eta^2\omega^2}\right)^{1/2} \tag{22}$$

whereas equations (12) and (21) give

$$\frac{\dot{\gamma}}{\dot{\epsilon}} = \left(\frac{4\omega^2 - 1}{\eta^2\omega^2}\right)\frac{\tau}{\sigma} = \frac{\sigma}{\tau} \tag{23}$$

or

$$\sigma\dot{\epsilon} = \tau\dot{\gamma} \tag{24}$$

Again, in figure 4(a) points $(\tau,\dot{\gamma})$ along o-a and $(\sigma,\dot{\epsilon})$ along o-b, with equal dissipation rates, fall on a common F = constant curve (fig. 4(b)). Similarly, matching pairs of points corresponding to F = constant curves and averaging gives

$$\left(\frac{4\omega^2 - 1}{\omega^2\eta^2}\right)^{1/2} = \left(\frac{\sigma}{\tau}\right)_C \tag{25}$$

Making use of equation (19), from tests on longitudinally reinforced tubes, and equation (25), from circumferentially reinforced tubes, results in

$$\omega = \frac{\left(\frac{\sigma}{\tau}\right)_L}{\left(\frac{\sigma}{\tau}\right)_G} \tag{26}$$

and

$$\eta = \frac{(4\omega^2 - 1)^{1/2}}{\left(\frac{\sigma}{\tau}\right)_L} \tag{27}$$

thereby completely characterizing the strength of initial anisotropy. Recall that the longitudinal threshold stress $Y_L(\equiv K_T(4\omega^2 - 1)^{1/2})$ is also known.

Turn now to the determination of the remaining viscoplastic material parameters. As indicated earlier, although several options are open in this regard (including torsional tests on circumferentially strengthened tubes as in ref. 11), the choice here is to consider uniaxial creep tests on longitudinally reinforced thin-walled tubes. This is in addition to the probing tests on longitudinal tubes already discussed. Typical results of uniaxial creep tests are illustrated in figure 6.

According to the present theory, the governing equations for the considered creep conditions are

$$F = \frac{(\sigma - s)^2}{Y_L^2} - 1 \tag{28}$$

$$G = \frac{s^2}{Y_L^2} \tag{29}$$

$$\dot{\epsilon} = \frac{1}{\mu(4\omega^2 - 1)} F^n(\sigma - s) \tag{30}$$

and

$$\dot{s} = \left(\frac{\hat{H}}{s^{\hat{\beta}}}\right)\dot{\epsilon} - \hat{R}s^{\hat{m}-\hat{\beta}+1} \tag{31}$$

where

$$\left.\begin{aligned} f(F) &= \frac{F^n}{2\mu} \\ \hat{H} &= \frac{3HY_L^{2\beta}}{2} \\ \hat{R} &= \frac{3R}{(4\omega^2 - 1)Y_L^{2(m-\beta)}} \\ \hat{\beta} &= 2\beta \\ \hat{m} &= 2m \end{aligned}\right\} \tag{32}$$

Here, $\dot{\epsilon}(\equiv\dot{\epsilon}_{11})$ is the axial component of inelastic strain rate, and $s(\equiv\alpha_{11})$ is the uniaxial component of the internal state variable α_{11}. The first of equations (32) indicates that the function $f(F)$ has been specialized as a power function characterized by the constants μ and n.

Note for future reference that for $F \gg 0$, equation (30), the flow law, can be approximated as

$$\dot{\varepsilon} = B(\sigma - s)^{2n+1} \tag{33}$$

where

$$B = \frac{1}{\mu(4\omega^2 - 1)Y_L^{2n}} \tag{34}$$

Also, during the early part of primary (transient) creep where s is small (fig. 6), the evolutionary law equation (31) can be approximated as

$$\dot{s} \approx \left(\frac{\hat{H}}{s^{\hat{\beta}}}\right)\dot{\varepsilon} \tag{35}$$

The initial creep rate following abrupt application of the stress σ (fig. 6), is expressed by equation (33) with $s = 0$. That is

$$\dot{\varepsilon} = B\sigma^{2n+1} \tag{36}$$

Information for determining B and n can be obtained directly from the initial creep rates as illustrated in figure 6, or alternatively, and more accurately, from the data generated from the probing tests already considered; the σ versus $\dot{\varepsilon}$ data illustrated in figure 5. By assuming these data correlate with equation (36), a plot of $\log(\dot{\varepsilon})$ versus $\log(\sigma)$ provides both n and B directly (fig. 7). If correlation with equation (36) is not satisfactory a different function $f(F)$ may have to be considered in the first of equations (32). In this study, it is assumed that the power law form is appropriate (as has been found for several isotropic alloys) and that n and B can be determined. With n, B, ω, and Y_L known, μ is then determined from equation (34).

Now focus attention on steady state creep information (fig. 6). At steady state $\dot{s} = 0$, so from equation (31)

$$\dot{\varepsilon}_s = \left(\frac{\hat{R}}{\hat{H}}\right) s_s^{\hat{m}+1} \tag{37}$$

Steady state creep data provides the pairs $(\sigma, \dot{\varepsilon}_s)$ but with ω, μ, Y_L, and n known, equation (30) allows s_s (the steady state internal stress) to be calculated for each pair, thus giving the data pairs $(\dot{\varepsilon}_s, s_s)$. Plotting $\log(\dot{\varepsilon}_s)$ versus $\log(s_s)$ provides values of $(\hat{R}/\hat{H})$ and $\hat{m}$ directly as indicated by the logarithmic form of equation (37) and figure 8. The last of equations (32) provides the exponent m.

Attention is now turned to the primary creep stage of the creep tests. As indicated in equation (35), the evolution of s in the early stages of primary creep is governed by

$$\dot{s} = \left(\frac{\hat{H}}{s^{\hat{\beta}}}\right)\dot{\epsilon} \tag{38}$$

Eliminating time and integrating

$$\int_{s=0}^{s} s^{\hat{\beta}}\, ds = \int_{0}^{\epsilon} \hat{H}\, d\epsilon \tag{39}$$

results in

$$\frac{s^{\hat{\beta}+1}}{(\beta + 1)} = \hat{H}\epsilon \tag{40}$$

or in transposed logarithmic form

$$\log(\epsilon) = (\hat{\beta} + 1)\log(s) + \log\left(\frac{1}{\hat{H}(\hat{\beta} + 1)}\right) \tag{41}$$

Now using equation (33) to solve for s yields,

$$s = \sigma - \left(\frac{\dot{\epsilon}}{B}\right)^{1/2n+1} \tag{42}$$

and substituting this result into equation (41) gives

$$\log(\epsilon) = (\hat{\beta} + 1)\log\left\{\sigma - \left(\frac{\dot{\epsilon}}{B}\right)^{1/2n+1}\right\} + \log\left(\frac{1}{\hat{H}(\hat{\beta} + 1)}\right) \tag{43}$$

Early primary creep data provides the data triplets $(\sigma,\epsilon,\dot{\epsilon})$ at each time. With B and n known, these data can be plotted (fig. 9) in the form of equation (43) yielding $\hat{H}(\hat{\beta} + 1)$ and $(\hat{\beta} + 1)$. Using equations (32), β and H can then be determined. Since $\hat{R}/\hat{H}$ is known from steady state creep data, individual values for $\hat{R}$ and $\hat{H}$ can then be found. Further, by making use of the second and third of equations (32), the parameters R and H then are known. Finally, the viscoplastic parameters $Y_L(\equiv K_T(4\omega^2 - 1)^{1/2})$, μ, n, m, β, R, and H are completely determined, as are the measures of the strength of transverse isotropy, ω and η.

SUMMARY AND CONCLUSIONS

A constitutive theory is presented to represent the high-temperature, time-dependent, hereditary behavior of materials that can be idealized as initially transversely isotropic. In particular, the theory is applicable to metal matrix composite materials at elevated temperature where their mechanical behavior includes significant viscoplasticity (e.g., creep, relaxation, thermal recovery, etc.) and, at the same time these materials are strongly directional. It is presumed that a single preferential (fiber) direction is identifiable at each material point thereby admitting the idealization of local transverse isotropy. Although not addressed here, the theory can be extended, at the expense of some additional complexity, to account for two (or more) identifiable preferential directions at each material point.

The composite is viewed as a continuum in its own right; and detailed interactive effects of the constituents are not accounted for directly. Of course, this precludes predictions of detailed phenomena such as failure by debonding, delamination, and so forth. However, the result is a reasonably simple multiaxial constitutive theory that is easily implemented into structural analysis codes for predicting the deformation response of structures subjected to complex thermomechanical loading histories. Because the response in the presence of material anisotropy is often highly nonintuitive, this theory provides a valuable tool for the design engineer.

Some fundamental aspects of the theory are explored through geometric interpretation of some basic features analogous to those of time-independent plasticity theory. Convexity of the dissipation potential surfaces (F = constant or Ω = constant) is demonstrated, and the shape of the surfaces is shown to be dependent on the strength and orientation of anisotropy. An example involving the response of a thin-walled tube under internal pressure demonstrates the qualitative changes in the inelastic deformation mode that can result from directional strengthening (anisotropy).

A key ingredient in the present work is the specification of an experimental procedure for the complete determination of the material parameters for a particular metal matrix composite. The parameters relating to the strength of anisotropy are determined through probing experiments on thin-walled tubes of two kinds; circumferentially reinforced (a single fiber direction oriented circumferentially) and longitudinally reinforced (axial fiber direction). The tubes are loaded in both tension and torsion. The parameters relating to the viscoplastic properties of the composite are determined primarily through uniaxial creep tests conducted on longitudinally reinforced tubes. Alternately, as discussed, one could use pure torsion tests on circumferentially reinforced tubes in place of the uniaxial creep tests. Additional tests are suggested in order to assess the correctness and accuracy of the theory.

REFERENCES

1. Chamis, C.C.: Simplified Composite Micromechanics Equations for Hygral, Thermal and Mechanical Properties. SAMPE Q., vol. 15, no. 3, Apr. 1984, pp. 14-23.

2. Chamis, C.C.; and Hopkins, D.A.: Thermoviscoplastic Nonlinear Constitutive Relationships for Structural Analysis of High Temperature Metal Matrix Composites. NASA TM-87291, 1985.

3. Petrasek, D.W.; and Signorelli, R.A.: Tungsten Fiber Reinforced Superalloys - A Status Review. Ceram. Eng. Sci. Proc., vol. 2, nos. 7-8, 1981, pp. 739-786.

4. Westfall, L.J., et al.: Preliminary Feasibility Studies of Tungsten/Niobium Composites for Advanced Space Power Systems Applications. NASA TM-87248, 1986.

5. McDanels, D.L.; Serafini, T.T.; and DiCarlo, J.A.: Polymer, Metal, and Ceramic Matrix Composites for Advanced Aircraft Engine Applications. NASA TM-87132, 1985.

6. Robinson, D.N.: Constitutive Relationships for Anisotropic High-Temperature Alloys. Nucl. Eng. Des., vol. 83, no. 3, 1984, pp. 389-396.

7. Rice, J.R.: On the Structure of Stress-Strain Relations for Time-Dependent Plastic Deformations in Metals. J. Appl. Mech. vol. 37, no. 3, Sept. 1970, pp. 728-737.

8. Ponter, A.R.S.; and Leckie, F.A.: Constitutive Relationships for Time Dependent Deformation of Metals. J. Eng. Mater. Technol., vol. 98, no. 1, Jan. 1976, pp. 47-51.

9. Ponter, A.R.S.: Convexity and Associated Continuum Properties of a Class of Constitutive Relationships. J. Mec., vol. 15, no. 4, 1976, pp. 527-542.

10. Robinson, D.N.: A Unified Creep-Plasticity Model for Structural Metals at High Temperature. ORNL/TM-5969, 1978.

11. Duffy, S.: A Viscoplastic Constitutive Theory for Transversely Isotropic Metal Alloys. Ph.D. Dissertation, University of Akron, 1986.

12. Lance, R.H.; and Robinson, D.N.: Limit Analysis of Ductile Fiber Reinforced Structures. J. Eng. Mech. Div. Am. Soc. Civ. Eng., vol. 98, no. EM1, Feb. 1972, pp. 195-209.

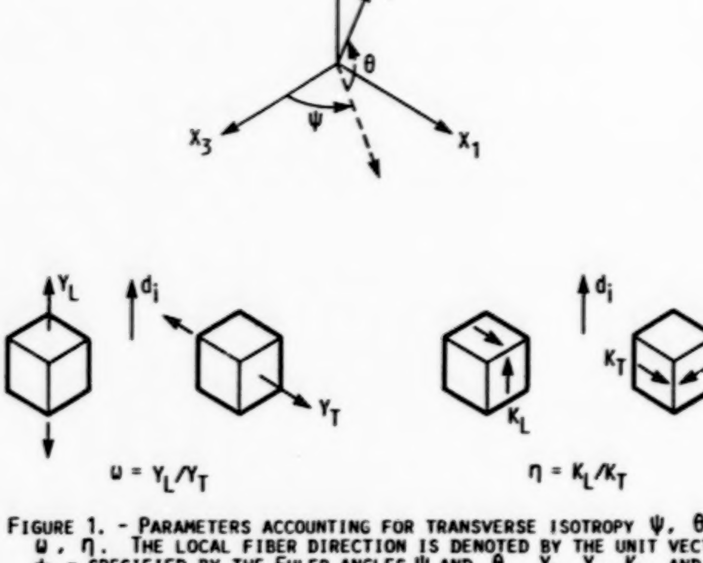
X_2
d_i
θ
X_3
ψ
X_1
Y_L
d_i
Y_T
d_i
K_L
K_T
$\omega = Y_L/Y_T$
$\eta = K_L/K_T$

FIGURE 1. - PARAMETERS ACCOUNTING FOR TRANSVERSE ISOTROPY ψ, θ, ω, η. THE LOCAL FIBER DIRECTION IS DENOTED BY THE UNIT VECTOR d_i - SPECIFIED BY THE EULER ANGLES ψ AND θ. Y_L, Y_T, K_L, AND K_T ARE THRESHOLD STRESSES AS INDICATED. DEFINITIONS OF THE PARAMETERS ω AND η ARE GIVEN.

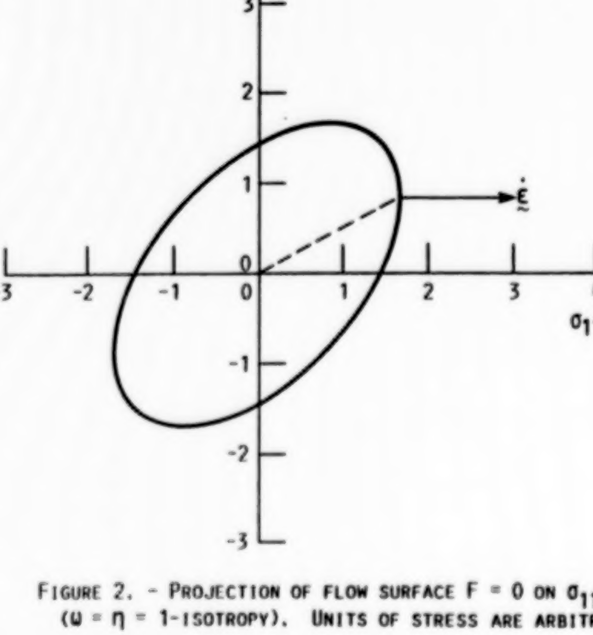

FIGURE 2. - PROJECTION OF FLOW SURFACE F = 0 ON σ_{11}-σ_{22} PLANE ($\omega = \eta = 1$-ISOTROPY). UNITS OF STRESS ARE ARBITRARY.

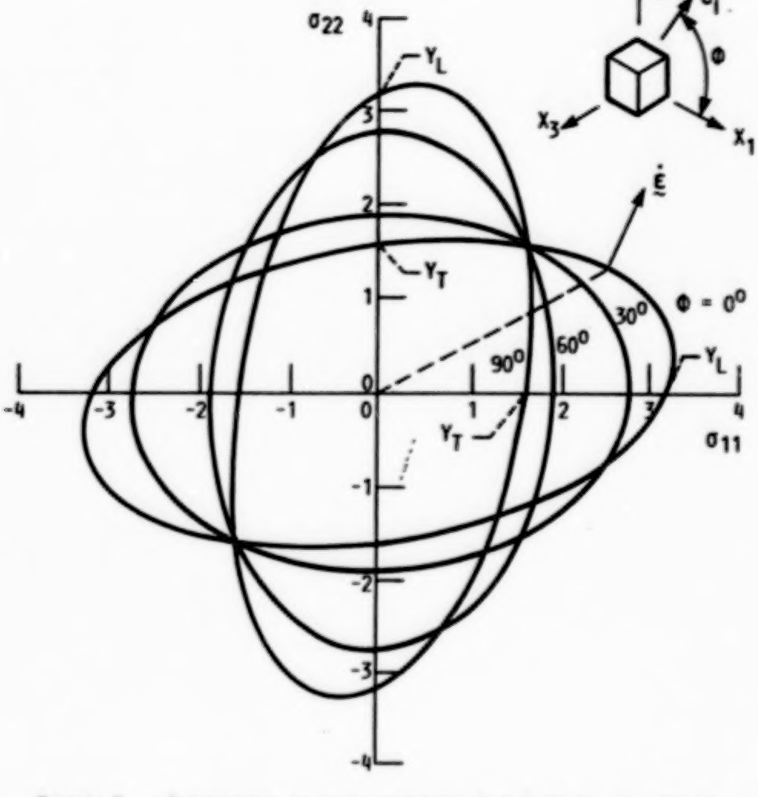

Figure 3. - Projection of flow surfaces $F = 0$ on σ_{11}-σ_{22} plane ($\omega = \eta = 2$). Units of stress are arbitrary.

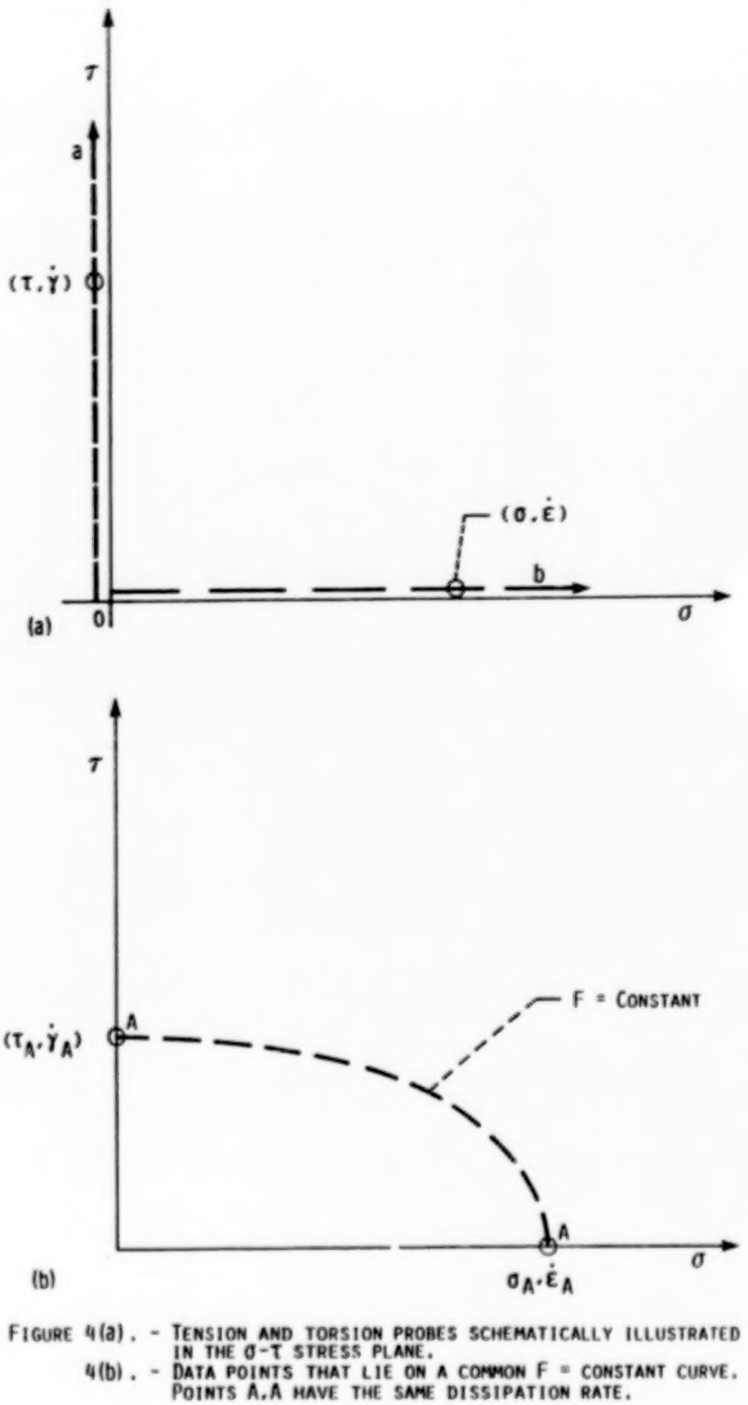
τ
a
(τ, $\dot{\gamma}$)
(σ, $\dot{\varepsilon}$)
b
(a)
0
σ
τ
F = Constant
A
(τ_A, $\dot{\gamma}_A$)
A
(b)
σ_A, $\dot{\varepsilon}_A$
σ

Figure 4(a). - Tension and torsion probes schematically illustrated in the σ-τ stress plane.
4(b). - Data points that lie on a common F = constant curve. Points A,A have the same dissipation rate.

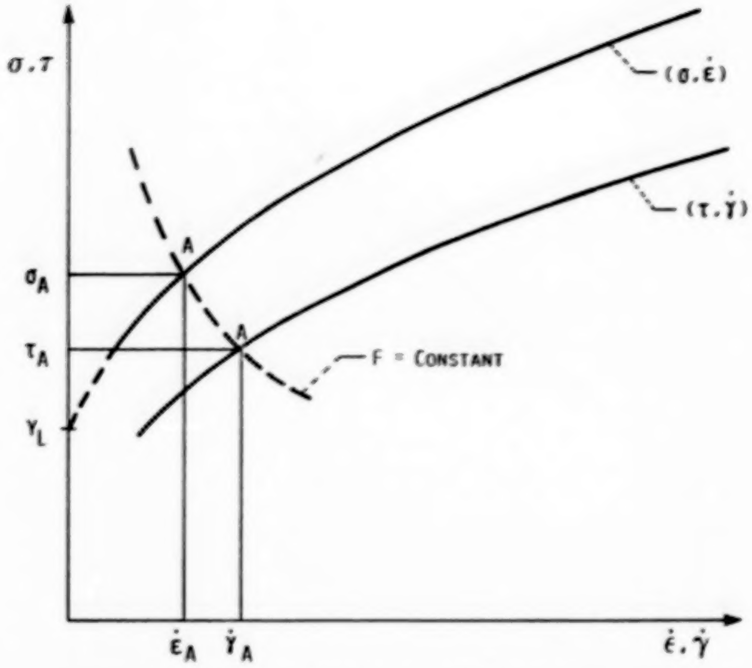
σ,τ
$(\sigma,\dot{\epsilon})$
$(\tau,\dot{\gamma})$
A
A
σ_A
τ_A
Y_L
F = CONSTANT
$\dot{\epsilon}_A$
$\dot{\gamma}_A$
$\dot{\epsilon},\dot{\gamma}$

FIGURE 5. - STRESS AND INELASTIC STRAIN RATE PAIRS FROM TORSION AND TENSION PROBE DATA ON A LONGITUDINALLY REINFORCED TUBE.

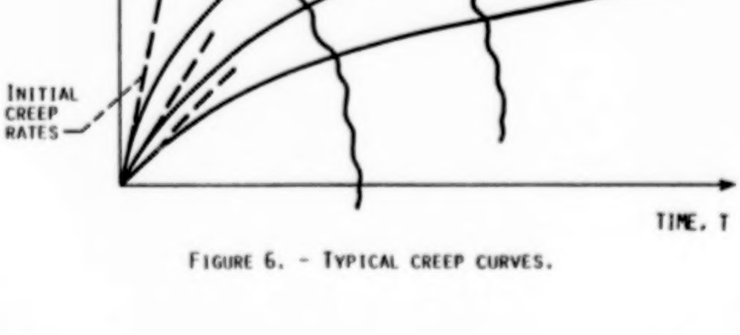
ϵ
"EARLY" PRIMARY CREEP
σ_3
σ_2
STEADY STATE CREEP
σ_1
INITIAL CREEP RATES
TIME, T

FIGURE 6. - TYPICAL CREEP CURVES.

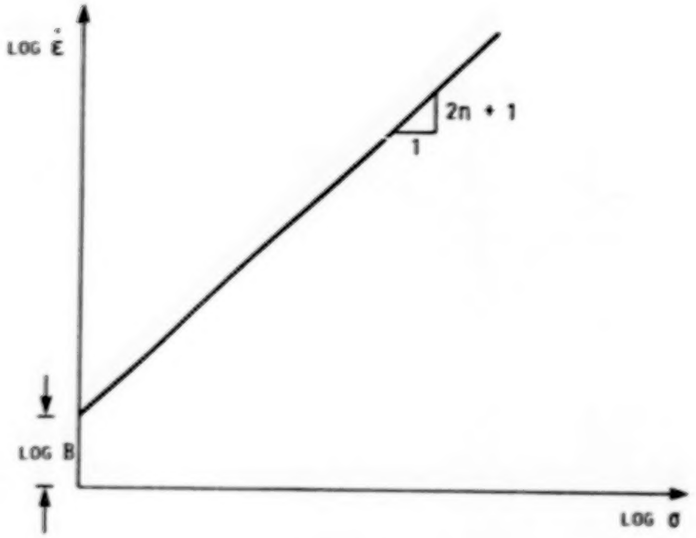

FIGURE 7. - DETERMINATION OF B AND n.

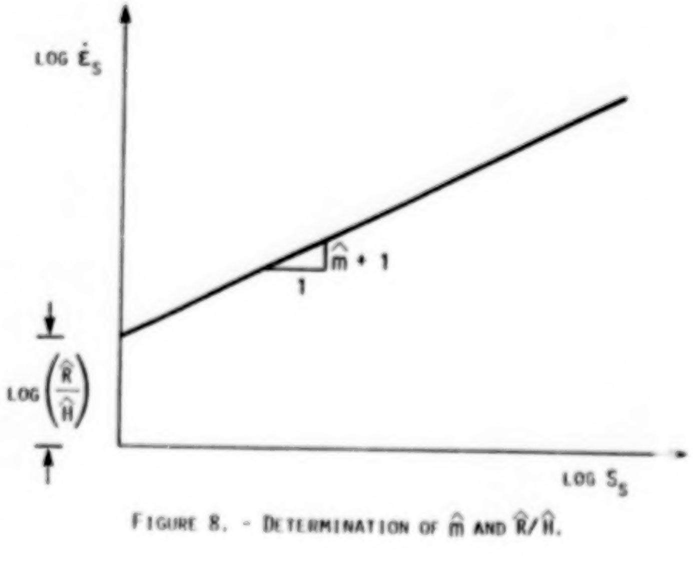

FIGURE 8. - DETERMINATION OF $\hat{m}$ AND $\hat{R}/\hat{H}$.

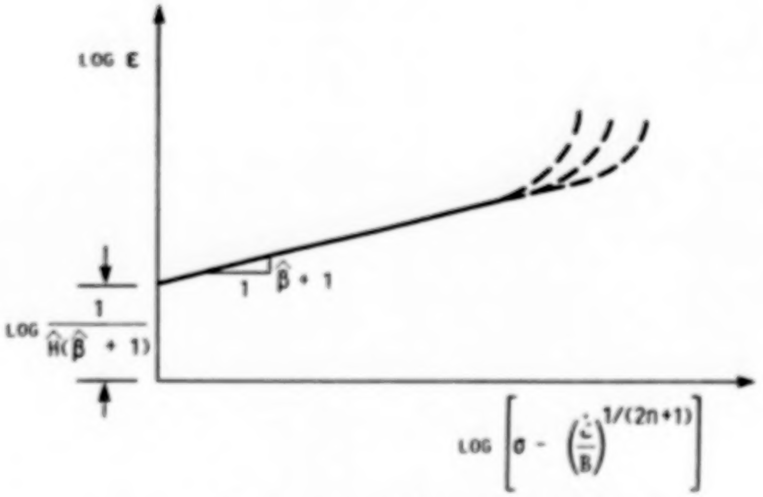
LOG ε
$\hat{\beta} + 1$
1
$\log \frac{1}{\hat{H}(\hat{\beta} + 1)}$
$\log \left[\sigma - \left(\frac{\dot{\epsilon}}{B} \right)^{1/(2n+1)} \right]$

FIGURE 9. - DETERMINATION OF $(\hat{\beta} + 1)$ AND $1/\hat{H}(\hat{\beta} + 1)$.

N88
21501
UNCLAS

N88-21501

DEVELOPMENT OF A UNIFIED CONSTITUTIVE MODEL FOR AN ISOTROPIC NICKEL BASE SUPERALLOY RENÉ 80

V.G. Ramaswamy, R.H. Van Stone, J.H. Laflen
General Electric Company
Cincinnati, Ohio 45215

D.C. Stouffer
University of Cincinnati
Cincinnati, Ohio 45221

Accurate analysis of stress-strain behavior is of critical importance in the evaluation of life capabilities of hot section turbine engine components such as turbine blades and vanes. The constitutive equations used in the finite element analysis of such components must be capable of modeling a variety of complex behavior exhibited at high temperatures by cast superalloys. The classical separation of plasticity and creep employed in most of the finite element codes in use today is known to be deficient in modeling elevated temperature time dependent phenomena. Rate dependent, unified constitutive theories can overcome many of these difficulties. A new unified constitutive theory was developed to model the high temperature, time dependent behavior of Rene' 80 which is a cast turbine blade and vane nickel base superalloy. Considerations in model development included the cyclic softening behavior of Rene' 80, rate independence at lower temperatures and the development of a new model for static recovery.

EXPERIMENTAL PROGRAM

The constitutive behavior of Rene' 80 under a multitude of conditions was experimentally determined.The test specimens, experimental temperatures, strain ranges, strain ratios, hold times, and strain rates were established through an evaluation of the operating conditions in commercial jet engines. In performing the experiments, the approach was to evaluate a series of transient and steady state conditions in each test by using a block cycling method. By using several combinations of strain range blocks in different sequences in a single experiment all combinations of transient effects could be interrogated. The block length was selected to produce cyclically stable hysteresis loops by the end of each block. The experimental results of each test were automatically saved in digitized form in real time by using a data acquisition device. These final data files could then be used in plotting data or determining constants in constitutive theories.

PRECEDING PAGE BLANK NOT FILMED

THEORY DEVELOPMENT

Following a detailed review, the Bodner model [1] and a generic back stress/drag stress model [2] were selected for further detailed evaluations with the Rene' 80 data. Many of the results from that study have been presented previously [2]. It was found that neither model was adequate for predicting the response characteristics of Rene' 80 at 1800F. Consequently a new theory was developed which combined the Bodner exponential flow law with a back stress formulation. It was found to be necessary to modify the evolution equations for the back stress to account for static recovery effects and to account for effects in the small inelastic strain regime. When these factors were included the final set of equations could be written as:

$$\dot{\varepsilon}_{ij}{}^{I} = D \exp\left[-\frac{A}{2} \left(\frac{Z^2}{3K_2} \right)^n \frac{(S_{ij} - \Omega_{ij})}{\sqrt{K_2}} \right] \tag{1}$$

$$K_2 = 1/2\, (S_{ij} - \Omega_{ij})\ (S_{ij} - \Omega_{ij}) \tag{2}$$

$$\Omega_{ij} = \frac{G}{E} S_{ij} + \left(1 - \frac{G}{E}\right) \Omega_{ij}{}^{I} \tag{3}$$

$$\dot{\Omega}_{ij}{}^{I} = f_1 \dot{\varepsilon}_{ij}{}^{I} - \frac{f_1}{\Omega_s} \Omega_{ij} \dot{R} \tag{4}$$

$$\dot{Z} = m(Z_1 - Z)\, \dot{W}^{I} \tag{5}$$

$$\dot{\Omega}_s = -B(\sigma_e/\sigma_0)^r\ (\Omega_s - \Omega_{sat}) \tag{6}$$

where

$$\dot{R} = \sqrt{\frac{2}{3} \dot{\varepsilon}_{ij}^{I} \dot{\varepsilon}_{ij}^{I}}\,, \quad \Omega_s(0) = \Omega_{max},\ \Omega_{ij}{}^{I}(0) = 0,\ Z(0) = Z_0$$

The procedures for determining the constants in these equations have been reported previously in [2,3]. Basically it involves the determination of most of the constants through the use of the monotonic, strain rate dependent, stress-strain curves; only the saturated value of the drag stress, Z1, and the rate of softening parameter, m, are determined from cyclic tests. The accuracy of these equations. has been verified very extensively through comparisons with a wide variety of experimental data . Figures 1 and 2 show the correlation of the monotonic stress-strain data at 1400F through 1800F, respectively. That the theory is capable of predicting strain rate dependent as well as rate independent behavior is clear.

Figure 3(a) shows a comparison with the first two cycles of a compressive mean strain test, while Figure 3(b) shows a comparison with the saturated hysteresis loop of this test. It has been seen that the theory can also predict the stress relaxation behavior at high and low temperatures. At 1400F Rene'80 exhibits stress relaxation, but no strain rate dependence. Creep capability comparisons are shown in Figures 4 and 5. These predictions depend strongly on the form of the static recovery term. Note that the form that is used in the current theory is much different than those used in other unified approaches.

Multiaxial capability verifications are shown in Figures 6,7 and 8. Figures 6 (a) and (b) show the axial and shear responses, respectively, for a combined tension/torsion (in-phase) test. Figure 7 shows the experimental results and theory predictions from a special nonproportional test where segments of proportional cycles were used . Comparisons of results from the first segment (cycle 5), and the last segment (cycle 32) of this nonproportional loading experiment are shown. That the predictions are accurate illustrates that the theory is good for such conditions without considering the additional hardening that has been found in some other materials. Figures 8 shows that the new theory can predict 90 deg. out-of-phase tension/torsion experimental results with good accuracy.

Figures 9 and 10 show two predictions of the theory with test data from combined temperature and strain cycling tests. The predictions are shown to be reasonable considering that the model development was based only on isothermal test data.

SUMMARY

A new multiaxial constitutive model which can represent the complex nonlinear high temperature behavior of Rene' 80 has been developed. The model was extensively verified based on experimental data at several temperatures. The TMF and nonproportional cyclic modeling capabilities of the model were demonstrated.

REFERENCES

1. Bodner, S.R. and Partom, Y., "Constitutive Equations for Elastic-Viscoplastic Strain Hardening Materials", ASME Journal of Applied Mechanics, 42, 1975.

2. Ramaswamy, V.G., Van Stone, R.H., Dame, L.T., and Laflen, J.H., "Constitutive Modeling for Isotropic Materials," NASA Conference Publication 2339, October 1984.

3. Ramaswamy, V.G., Van Stone, R.H., Dame, L.T., and Laflen, J.H., "Constitutive Modeling for Isotropic Materials", Annual Report, NASA CR17485, March 1985.

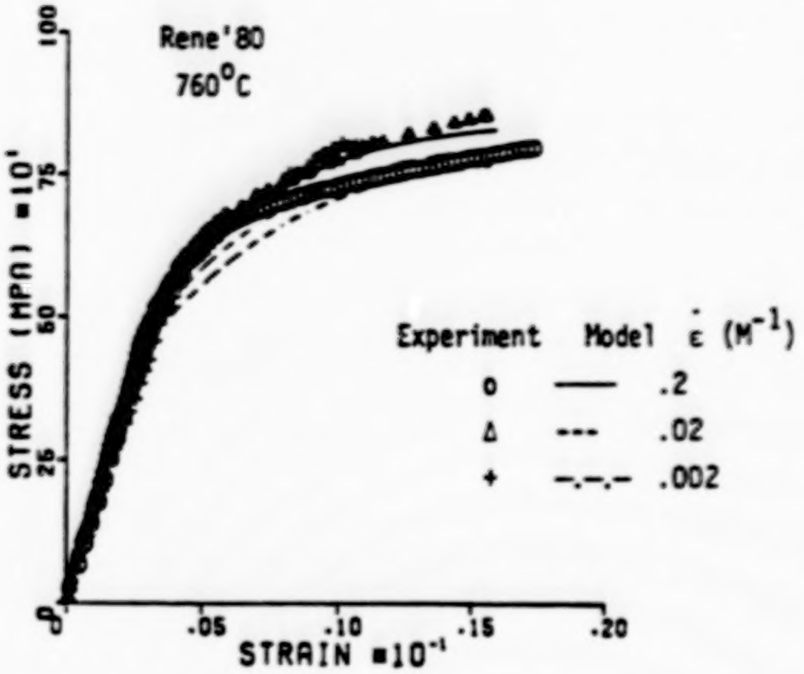

Figure 1 Monotonic Tensile Response of Rene'80 at 760°C

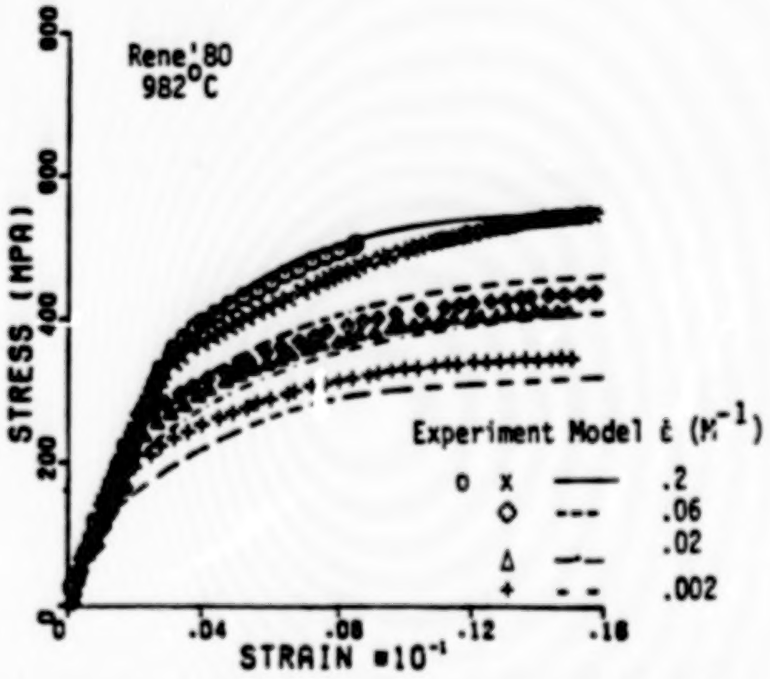

Figure 2 Monotonic Tensile Response of Rene'80 at 982°C

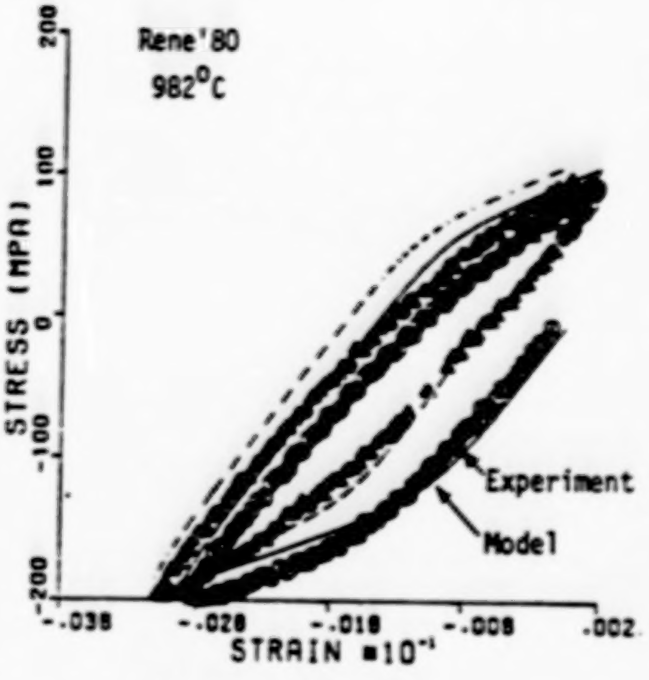

(a) First Two Cycles

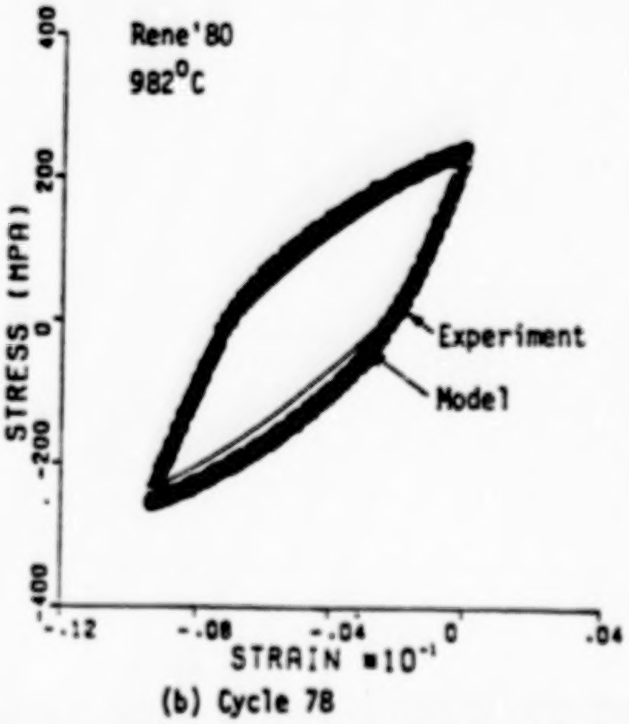

(b) Cycle 78

Figure 5 Cyclic Response of Rene'80 with Mean Strain

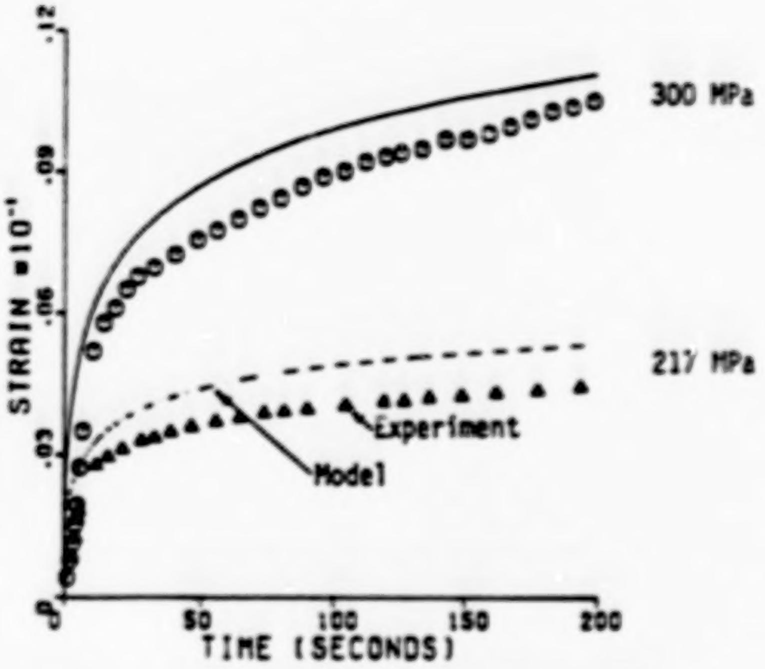

Figure 4. Creep Response of Rene'80 at 982°C

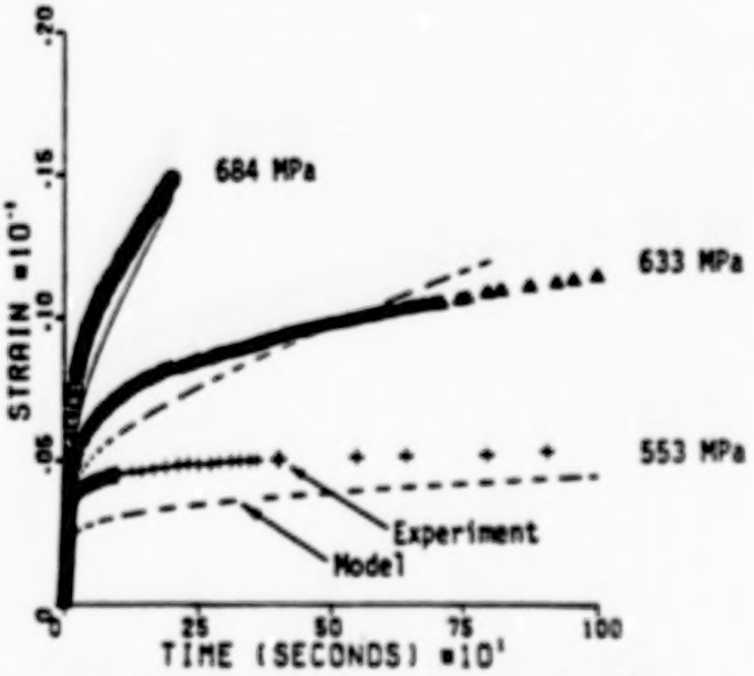

Figure 5 Creep Response of Rene'80 at 760°C

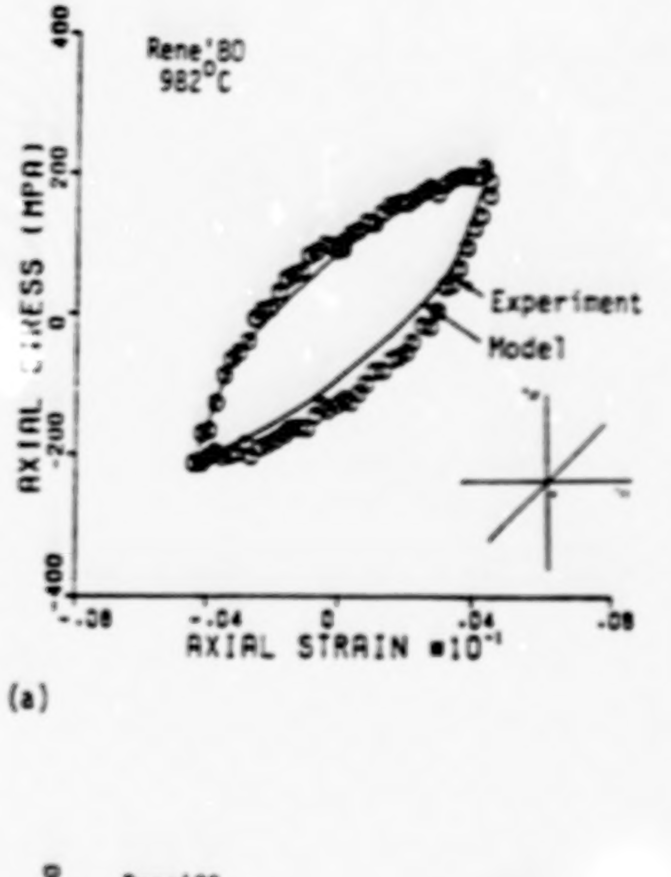

Figure 6 In phase Tension Torsion Cyclic Response of Rene'80 at 982°C, .002M^{-1}

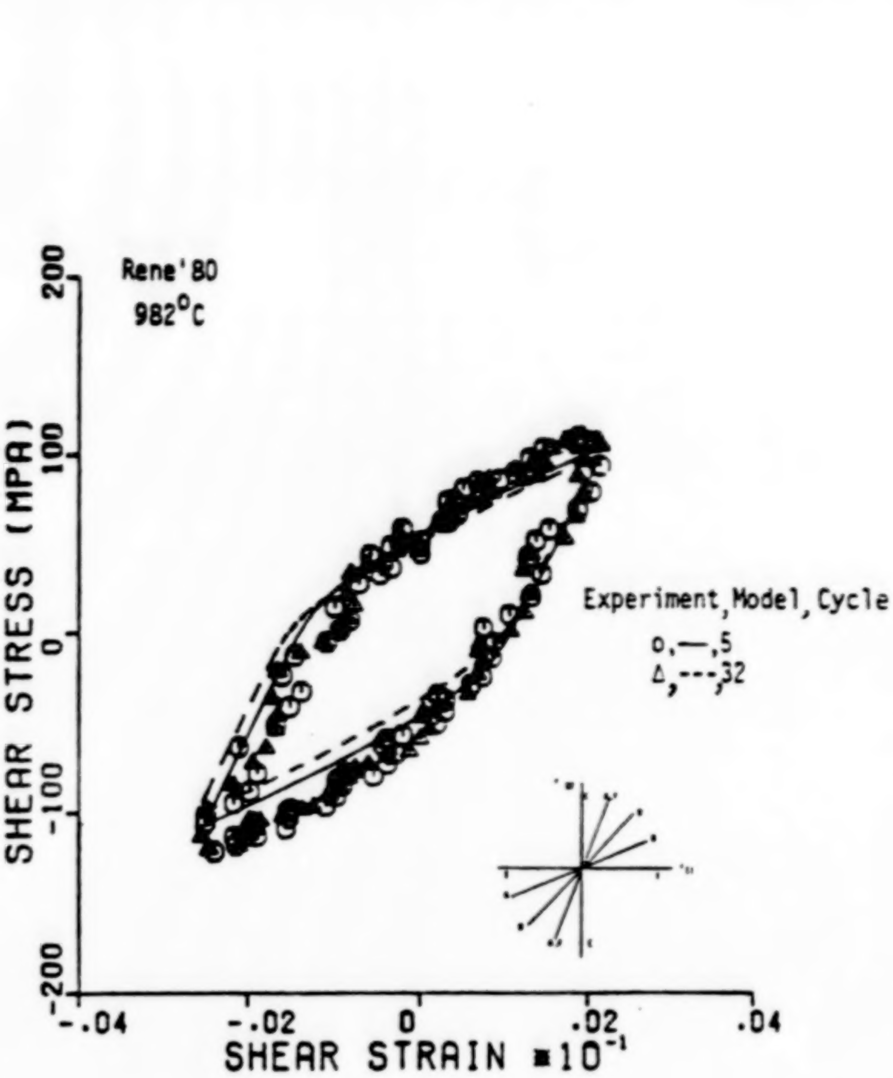

Figure 7 Comparison of Rene'80 Response Before and After Non proportional loading (Paths A,F)

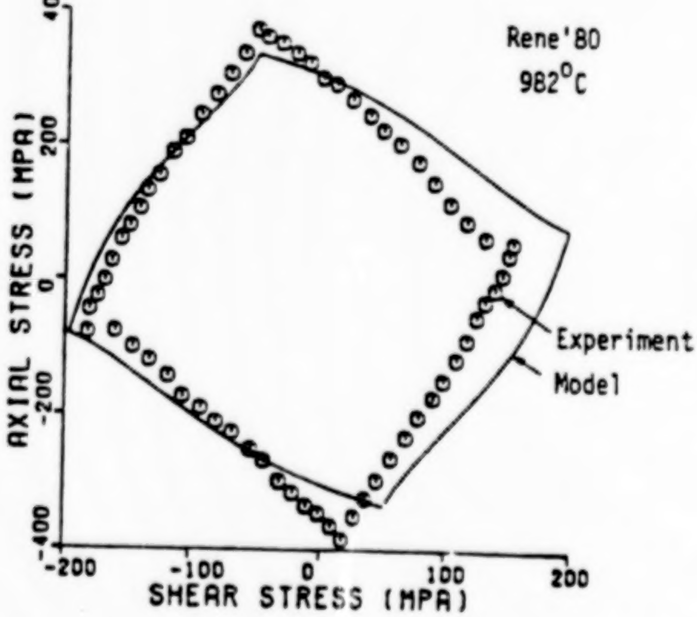

Figure 8 Rene'80 Response to 90° Out of Phase Tension/Torsion Cyclic Loading

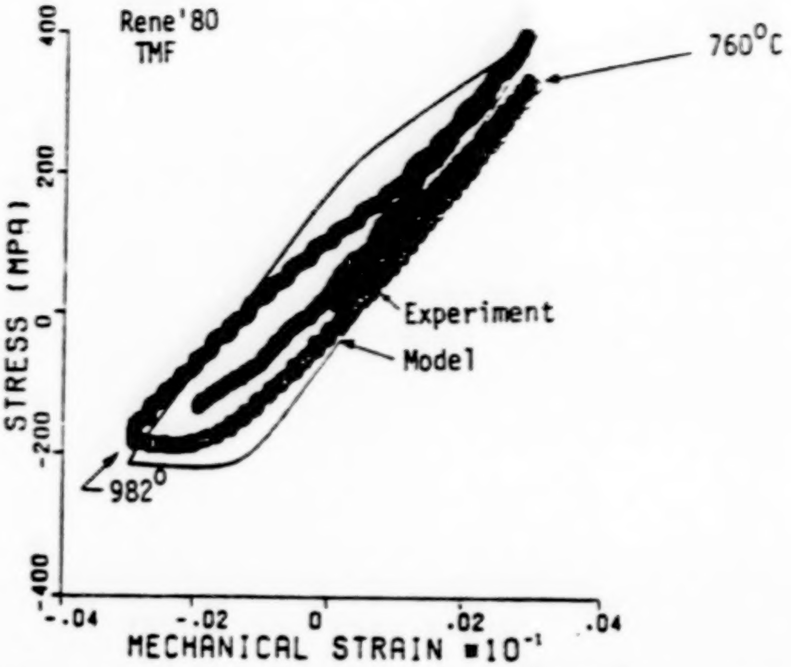

Figure 9 Rene'80 TMF Response (760°C-982°C Out of Phase)

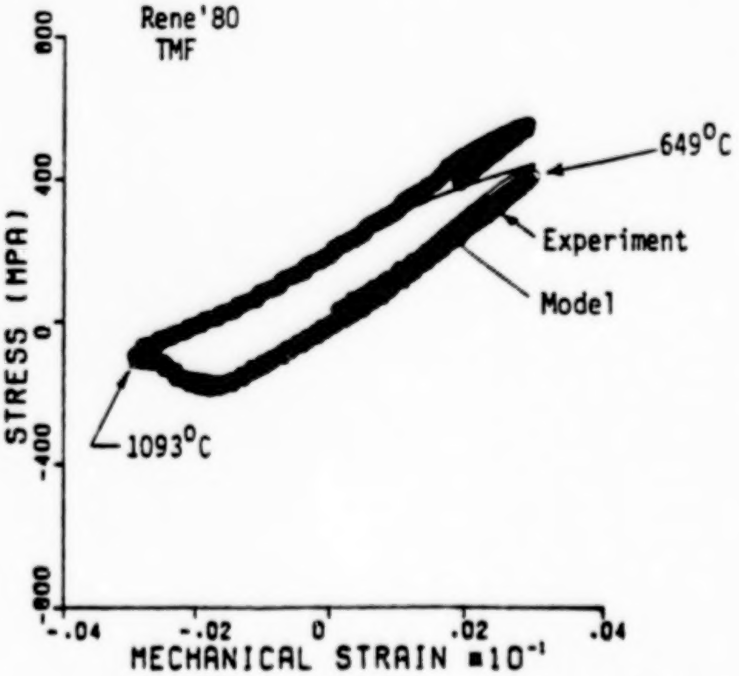

Figure 10 Rene'80 TMF Response (649°C-1093°C Out of Phase)

N88

21502

UNCLAS

N88-21502

MODELING THE VISCOPLASTIC BEHAVIOR OF INCONEL 718 AT 1200°F

M.S. Abdel-Kader[†], J. Eftis, and D.L. Jones
School of Engineering and Applied Science
The George Washington University
Washington, D.C. 20052

Inconel 718 is a nickle-based superalloy that possesses several outstanding elevated-temperature mechanical properties. It has been widely used for the manufacture of critical compressor and turbine engine components requiring relatively long service lives. A large number of tests, including tensile, creep, fatigue, and creep-fatigue have been performed to characterize the mechanical properties of Inconel 718 at 1200°F, the operating temperature for turbine blades. In addition, a few attempts have been made to model the behavior of Inconel 718 at 1200°F using viscoplastic theories.

The Chaboche theory of viscoplasticity can model a wide variety of mechanical behavior, including monotonic, sustained, and cyclic responses of homogeneous, initially-isotropic, strain-hardening (or softening) materials. It has been successfully used to model the viscoplastic behavior of several structural materials of practical importance. This paper shows how the Chaboche theory can be used to model the viscoplastic behavior of Inconel 718 at 1200°F. First, an algorithm has been developed to systematically determine the material parameters of the Chaboche theory from uniaxial tensile, creep, and cyclic data. The algorithm, however, is general and can be used in conjunction with similar high-temperature materials. A sensitivity study was then performed and an 'optimal' set of Chaboche's parameters was obtained. This study has also indicated the role of each parameter in modeling the response to different loading conditions. Based on the 'optimal' set of material parameters, uniaxial tensile, creep, and cyclic behavior has been predicted. The results were compared to available experimental data and the agreement was found to be good. Moreover, predicted behavior of Inconel 718 at 1200°F under a variety of additional loading conditions has been examined and relevant conclusions were drawn.

I. INTRODUCTION

For high temperature applications, such as those encountered in the nuclear and aerospace industries, severe demands are generally placed on candidate structural materials. These demands have led to the development of a new class of structural materials called superalloys having considerably improved elevated-temperature mechanical properties. One such material is Inconel 718, which possesses several excellent properties such

---

[†] On leave from The Military Technical College, Cairo, Egypt.

PRECEDING PAGE BLANK NOT FILMED

as creep-rupture strength, high-cycle fatigue strength, oxidation resistance, and long time stability [1-3]. These properties are, for the most part, due to the susceptibility of this material to precipitation hardening and strengthening caused by coherent gamma prime precipitates. These properties can be obtained by two different solution annealing and aging procedures. A comparative study of the effects of both types of heat treatment procedures on the tensile and fatigue behavior of Inconel 718 from room temperature to 1200°F has been presented in Ref. [2]. It was concluded that Inconel 718 subjected to the so called 'standard heat treatment' exhibits higher resistance to stress rupture and fatigue. Therefore, Inconel 718 in this condition is widely used in current production of gas turbine engine components requiring relatively long service lives and operating normally at high temperatures [1,4].

A large number of uniaxial monotonic, sustained, and cyclic tests have been performed to obtain the mechanical properties of Inconel 718 at 1200°F [1-9]. However, only a few of these tests address the strain-rate sensitivity, with the result that no significant strain rate sensitivity could be observed for $\dot{\epsilon} > 5 \times 10^{-5}$ sec^{-1}. At lower strain rates, tensile and cyclic data were too limited to establish the rate sensitivity of this material, although existing creep data do suggest the existence of some rate sensitivity.

Domas, et al [4] have shown that the tensile and stabilized cyclic stress-inelastic strain curves for Inconel 718 at 1200°F can be described by the Ramberg-Osgood form

$$\sigma = K^{*} (\epsilon'')^{n^{*}}, \tag{1}$$

where σ and ϵ'' are the tensile stress and inelastic strain (or the stress at the tensile tip of the stabilized hysteresis loop and the corresponding inelastic strain amplitude), respectively, and K^{*} and n^{*} are material parameters that depend on the heat treatment and strain rate. Values of K^{*} and n^{*} for Inconel 718 (standard heat treatment) at 1200°F and for different tensile and cyclic strain rates are listed in Table 1. The first five sets of values were determined by Domas, et al [4], whereas the remaining values were determined within a larger study [10], part of which is the present work. Available experimental data on the cyclic behavior of Inconel 718 at 1200°F have also indicated that this material cyclically softens for approximately 10-20% of its fatigue life, followed by a period of near-stabilization when damage mechanisms are activated. For convenience the values of σ and $\dot{\epsilon}$ used to evaluate the cyclic material parameters in Table 1 were those at $N_f/2$, where N_f is the fatigue life.

Inconel 718 at 1200°F displays classical creep response (primary, secondary, and tertiary creep stages). The time to the onset of tertiary creep is normally about 0.5 t_r, where t_r is the rupture life [11]. For Inconel 718, however, the region of increasing creep rates following steady state creep commences at about 0.3 t_r [3]. This suggests that the initiation of increasing creep rates may be due to softening and is not necessarily a manifestation of the instability associated with tertiary creep [3,6]. Thus, from a unified viscoplastic theory view-point, some provision for softening (or increasing creep rates) must be incorporated into the theory. Booker [3,6] has developed a creep model in the form

$$\epsilon_n = \mathrm{EXP}\,[1.75(t_n - 1)] \cdot t_n^{0.2}\,, \qquad 0 < t_n < 1, \tag{2}$$

which describes the salient features of the creep behavior of Inconel 718 at 1200°F. In Eq. (2), $\epsilon_n = \epsilon/\epsilon_{tr}$ is the normalized creep strain, $t_n = t/t_{tr}$ is the normalized time; provided that ϵ_{tr} and t_{tr} are the strain and time to tertiary creep given empirically by

$$t_{tr} = 0.392\ t_r^{1.04}\,, \tag{3}$$

$$\epsilon_{tr} = 0.2 + 1.16\ t^{-0.14}\,. \tag{4}$$

The time to failure, t_r, is given by

$$\log t_r = 163.92 + 23924/T - 226.92 \log \sigma_h$$
$$+ 94.196\ (\log \sigma)^2 - 13.215\ (\log \sigma)^3, \tag{5}$$

where T is the temperature in ^{o}K and σ_h is the hold stress in MPa. In Eqs. (2) thru (5), time is given in hours and strain in percent.

A few attempts have been made to model the behavior of Inconel 718 at 1200°F using unified viscoplastic theories, e.g., [7,8]. In this paper, the Chaboche yield-based theory of viscoplasticity [12,13] is used for the same purpose. This theory can model a wide variety of rate-dependent inelastic mechanical behavior, including monotonic, sustained, and cyclic responses. It also models isotropic and kinematic strain hardening, including cyclic hardening (or softening) and the multidimensional Bauschinger effect. This theory has been employed to model the mechanical response of Inconel 100 [12,14], type 316 stainless steel [15,16], and Ti-6Al-4V alloy [17,18]. However, the theory does not account for the rate dependence of initial yield, which limits its use to materials that do not exhibit such behavior within the loading rates of interest. In a previous paper [19], the authors have shown how rate dependency of initial yielding can be incorporated into the Chaboche theory, without changing its general structure. The principal objective of the current paper is to show how the extended theory can be used to model the mechanical behavior of Inconel 718 at 1200°F. A major part of this effort has been devoted to developing a systematic algorithm for the determination of the Chaboche material parameters from available uniaxial test data. The need for a systematic procedure for determining the material parameters of a viscoplastic theory from the results of standard mechanical tests has been addressed [17,21].

A sensitivity study was then undertaken to explore the effects of introducing small changes in the Chaboche material parameters on different predictions and to obtain an 'optimal' set of the material parameters that globally improves the predicted behavior. The 'optimal' set was then incorporated into the Chaboche set of differential equations; and uniaxial tensile, creep, and cyclic responses were predicted and compared to available experimental data. In addition, strain-rate and strain-rate-history effects, creep, stress relaxation, and the load-unload-reload effects were predicted and examined.

II. CONSTITUTIVE EQUATIONS

In the present paper, the one-dimensional form of the Chaboche theory is presented and used; the three-dimensional form of the theory can be found elsewhere [12,13]. A basic assumption of the theory is the decomposition of the rate of deformation into rate-independent elastic and rate-dependent inelastic components. For infinitesimal deformations, the strain rate, $\dot{\epsilon}$, approximates the rate of deformation, or

$$\dot{\epsilon} = \dot{\epsilon}' + \dot{\epsilon}'' \; . \tag{6}$$

The linear elastic strain rate, $\dot{\epsilon}'$, is obtained from the time derivative of Hooke's law, that is,

$$\dot{\epsilon}' = \dot{\sigma}/E \tag{7}$$

where σ is the stress and E is Young's modulus. The nonlinear inelastic strain rate, $\dot{\epsilon}''$, is based on the normality hypothesis and has the form

$$\dot{\epsilon}'' = \begin{cases} \left(\frac{F}{K}\right)^n \; Sg(\sigma - Y), & F > 0, \\ 0, & F \leq 0, \end{cases} \tag{8}$$

where K and n are material parameters. F is the von Mises yield function given by

$$F(\sigma, Y, p) = |\sigma - Y| - R(p), \tag{9}$$

where Y is the kinematic hardening variable, p is the cumulative inelastic strain defined in terms of the inelastic strain rate by

$$p = \int_0^t |\dot{\epsilon}''| \, d\tau, \tag{10}$$

and R is the isotropic hardening variable associated with p. Note that in Chaboche's theory, as in most of the viscoplastic theories, two variables, Y and p, are employed to model hardening. Note also that F represents the overstress, whose positive values signify the initiation of inelastic deformations [c.f. Eq. (8)].

The evolution of the kinematic hardening variable is given by

$$\dot{Y} = c(a\dot{\epsilon}'' - Y\dot{p}) - \gamma|Y|^{m}\, Sg(Y), \tag{11}$$

where c,a,γ, and m are material parameters. The first term on the right hand side of Eq. (11) is the nonlinear Armstrong-Frederick modification of Prager's linear kinematic hardening rule, which is appropriate for cyclic loading. The second term models softening effects such as reduced hardening rate, secondary creep, and stress relaxation typically associated with elevated temperatures. Equation (11) provides an effective tool by which anisotropic hardening (Bauschinger effect) and creep/relaxation effects can be appropriately modeled and represents one of the principal advantages of the Chaboche theory. In its modified form [19], the isotropic hardening variable, R, depends on the cumulative inelastic strain, p, and the total strain rate, $\dot{\epsilon}$, rather than on p alone, as postulated in the original theory. The dependence of R on $\dot{\epsilon}$ is assumed to be limited to its initial value, R_o, that is,

$$R(p,\dot{\epsilon}) = q + [R_o(\dot{\epsilon}) - q]\, e^{-bp}, \tag{12}$$

where b and q are material parameters and R_o is the rate-dependent initial yield strength.

III. DETERMINATION OF THE CHABOCHE MATERIAL PARAMETERS

In its modified form, the Chaboche theory incorporates eight viscoplastic material parameters and the rate-dependent initial yield strength [c.f. Eqs. (8), (11), and (12)], which are generally temperature-dependent. It is now shown how these parameters as well as the function $R_o(\dot{\epsilon})$ were determined from available experimental data of Inconel 718 at 1200°F. Some approximations and assumptions had to be made; these will be discussed as they are introduced.

Determination of a and c

The Chaboche flow law given by Eqs. (8) and (9), upon inversion, takes the form

$$\sigma = Y + R + K(\dot{\epsilon}'')^{1/n} \quad . \tag{13}$$

At relatively high strain rates, the recovery term in Eq. (11) can be neglected, thereby allowing it to be integrated as

$$Y = sa + (Y_o - sa)\, e^{-sc(\epsilon'' - \epsilon''_o)} \quad , \tag{14}$$

where

$$s = Sg(\dot{\epsilon}'') = \begin{cases} +1, & \dot{\epsilon}'' > 0, \\ -1, & \dot{\epsilon}'' < 0, \end{cases} \tag{15}$$

and Y_o and ϵ''_o are the initial values of Y and ϵ''.

For the stabilized cycle of a strain-controlled cyclic test, R assumes its saturation value q [c.f Eq. (12)], whereas Y alternates between two extreme values, Y_{max} and $Y_{min} = - Y_{max}$. It can be shown that [10,12]

$$Y_{max} = a(1 - e^{-c\Delta\epsilon''})/(1 + e^{-c\Delta\epsilon''}) = a \tanh(c\epsilon''_a) \quad , \tag{16}$$

where $\epsilon''_a = \Delta\epsilon''/2$ is the stabilized inelastic strain amplitude. Hence, if a series of stain-controlled cyclic tests are performed until stabilization has occurred, a cyclic stress-strain curve can be established through the tensile peaks of these stabilized hysteresis loops. Such a curve, within the context of Chaboche's theory, can be represented by use of Eqs. (13) and (16) as

$$\sigma = a \tanh(c\epsilon''_a) + q + K(\dot{\epsilon}'')^{1/n} \quad , \tag{17}$$

which, when differentiated with respect to ϵ''_a, yields

$$d\sigma/d\epsilon''_a = a\, c\, \mathrm{sech}^2(c\epsilon''_a) \quad . \tag{18}$$

An alternative form for Eq. (18) can also be obtained by differentiating Eq. (1), i.e.,

$$d\sigma/d\epsilon_a^* = n^*K^*(\epsilon_a^*)^{n^*-1} \; . \tag{19}$$

Since values of K^* and n^* are available (c.f. Table 1), Eq. (19) can be used to generate values of $f_i = d\sigma/d\epsilon_a^*$ for $(\epsilon_a^*)_i$, $i=1,2,\ldots,n$. These values can be used to evaluate a and c in Eq. (18). This is, in fact, a nonlinear regression analysis problem. Draper and Smith [22] have shown how such a problem can be solved based on the least squares technique. A computer program based on their analysis has been developed and used to find the values of a and c listed in Table 1. The first and seventh sets are considerably different from the remaining values. Therefore, these two sets were excluded and mean values of a and c were calculated for the remaining sets as

$$a = 31.40 \text{ KSI}, \qquad c = 349.5 \; . \tag{20}$$

Determination of K and n

Since the material parameters K and n characterize the rate dependency of the material response, they were evaluated from tensile data at different strain rates. Two tensile stress-strain curves may be adequate for this purpose. Figure 1 illustrates two stress-strain curves at strain rates of $\dot\epsilon_1$ and $\dot\epsilon_2$, where $\dot\epsilon_2 > \dot\epsilon_1$. If it is assumed that these rates are sufficiently high and close together, then Eq. (14) holds for Y, and R_o can be considered the same for both cases. Thus,

$$Y_{a_1} = Y_{a_2} \;,\quad Y_{b_1} = Y_{b_2} \;,\quad R_{a_1} = R_{a_2} \;,\quad R_{b_1} = R_{b_2} \;. \tag{21}$$

where a_1, a_2, b_1, and b_2 are shown in Fig. 2.

From Eqs. (13) and (21), the stress differential may be written as

$$\Delta\sigma_a = \sigma_{a_2} - \sigma_{a_1} = K\left[(\dot\epsilon^*_{a_2})^{1/n} - (\dot\epsilon^*_{a_1})^{1/n}\right]. \tag{22}$$

which relates the difference in stress levels to the corresponding inelastic strain rates at specific inelastic strain values. It is necessary, therefore, to evaluate the inelastic strain rate at different points on both curves using the equation

$$\dot{\epsilon}'' = \dot{\epsilon} - \dot{\epsilon}' = \dot{\epsilon} - \dot{\sigma}/E = \dot{\epsilon} - \dot{\epsilon}(\frac{d\sigma}{d\epsilon})/E = \dot{\epsilon}(1 - E^*/E), \qquad (23)$$

where $E^* = d\sigma/d\epsilon$ is the instantaneous slope of the stress-strain curve. Equation (1), along with the integrated form of Eq. (6), can be employed to obtain the relation

$$\frac{d\epsilon}{d\sigma} = \frac{1}{E} + \frac{1}{n^*K^*}\left(\frac{\sigma}{k^*}\right)^{\frac{1}{n^*} - 1} . \qquad (24)$$

Note that the inverse of this equation is E^*. Therefore, Eqs. (23) and (24) can be used to calculate values of $\dot{\epsilon}''_{a_1}$ and $\dot{\epsilon}''_{a_2}$ in Eq. (22), and $\Delta\sigma_a$ can be obtained by applying Eq. (1) independently to curve 1 and curve 2 of Fig. 1. Then, K and n in Eq. (22) are evaluated using a nonlinear regression procedure similar to that used in evaluating a and c. The tensile data of Table 1 were used for this purpose, and the following values of n and K were obtained

$$n = 5.12, \qquad K = 154.4 \text{ KSI} \sqrt[n]{\text{sec}} . \qquad (25)$$

Determination of b and q

Once a, c, n, and K have been obtained, b and q can be determined from the results of one strain-controlled cyclic test, such as that reported in Refs. [7,9] at $|\dot{\epsilon}| = 2.667\text{x}10^{-3}\ \text{sec}^{-1}$ and $\epsilon = \pm 1\%$. At the tensile tip of a hysteresis loop, Eqs. (13) and (16) can be combined and solved for R as

$$R = \sigma - a \tanh(c\epsilon''_a) - K(\dot{\epsilon}'')^{1/n}, \qquad (26)$$

and p can be calculated from

$$p_n = \epsilon''_1/2 + 2\sum_{i=2}^{n} \Delta\epsilon''_i , \qquad (27)$$

where n represents the n-th cycle and $\Delta\epsilon_i^*$ represents the inelastic strain range at the i-th cycle. Equations (26) and (27) were then used to calculate R and p values from the strain-controlled test discussed above, with the results given in Table 2. In these calculations the overstress, $K(\dot{\epsilon}^*)^{1/n}$, was assumed to be constant, since the slopes of the loops at their peaks were relatively constant. The value of $\dot{\epsilon}^*$ was calculated from Eq. (23) to be 2.465×10^{-3} sec^{-1}, from which the overstress was determined to be 47.73 KSI. Since the available results did not include records of all hysteresis loops, it was assumed that a missing loop had the same value of $\Delta\epsilon^*$ as the first preceding available loop. Table 2 shows that R had essentially saturated by the 32nd cycle. The corresponding value of R was, therefore, taken to be the saturation value, i.e.,

$$q = 18.63 \text{ KSI} \quad . \tag{28}$$

A value for b was then determined from the slope of the line

$$\ln(R-q) = \ln(R_o-q) - bp, \tag{29}$$

to be

$$b = 4.679 \quad . \tag{30}$$

Determination of R_o

In a previous paper [19], the authors have shown how the Chaboche theory can be modified to account for the rate-dependent initial yield response and permit prediction of creep behavior at low stress levels. In effect, the function $R_o(\dot{\epsilon})$ in Eq. (12) had to be evaluated. Based on the analogy between tensile and creep responses [23] and the creep data base of Ref. [8], a form for $R_o(\dot{\epsilon})$ was selected as

$$R_o = R_{oo} \left\{1 + \ln\left\{1 + \text{EXP}\left[\sum_{i=0}^{3} \alpha_i (\ln\dot{\epsilon})^i\right]\right\}\right\} , \tag{31}$$

where $R_{oo}=q=18.63$ KSI, $\alpha_o=25.56$, $\alpha_1=-4.551$, $\alpha_2=-0.3360$, and $\alpha_3=-0.8375 \times 10^{-2}$, as shown in Ref. [19].

Booker's creep model [c.f. Eqs. (2-5)] was used to evaluate the strain at the initiation of steady-state creep needed for these calculations. This was achieved by differentiating Eq. (2) twice with respect to time, equating to zero, solving for t_n, and then substituting back into Eq. (2) to obtain the required strain values.

Determination of m and γ

It has been shown in Ref. [17] that hardening is mostly kinematic during primary creep, because of the relatively high value of the ratio of the hardening exponents c and b [c.f. Eqs. (12) and (13)], and because of the small amount of inelastic strains that are likely to have accumulated. Therefore, it can be assumed that $R = R_o$ = constant at the attainment of steady-state creep. During secondary creep, $\dot{\epsilon} = \dot{\epsilon}''$ = constant, and the time derivative of Eq. (13) reduces to

$$\dot{Y} = c(a-Y)\,\dot{\epsilon}_{ss} - \gamma\, Y^{m} = 0, \tag{32}$$

where $\dot{\epsilon}_{ss}$ is the steady-state creep rate. Equation (32) can also be written as

$$\ln[c(a-Y)\,\dot{\epsilon}_{ss}] = m \ln Y + \ln\gamma, \tag{33}$$

which represents a straight line whose slope is m and intercept is ln γ. In this equation, Y can be calculated from Eq. (13) with $R = R_o$. The data of Ref. [8] for small creep stresses, where the recovery effects are significant, were used to evaluate γ and m as

$$\gamma = 0.4\text{x}10^{-10} \quad , \qquad\qquad m = 6.942 \;\cdot \tag{34}$$

To conclude, a procedure has been developed to evaluate the material parameters of the modified Chaboche theory of viscoplasticity from uniaxial tensile, creep, and cyclic test data. Since these tests were not specifically designed for the purpose of determining the Chaboche parameters, the procedure employed herein to determine these parameters is not unique, but appropriate for the kind of data available. However, the procedure is general and can be employed to determine the Chaboche parameters for any similar material. Values of the parameters are listed in Table 3. Based on these values, predictions of a tensile test at $\dot{\epsilon} = 1.333\mathrm{x}10^{-5}\mathrm{sec}^{-1}$, a creep test at 130 KSI, and a strain-controlled, fully-reversed cyclic test at $|\dot{\epsilon}| = 4\mathrm{x}10^{-5}\mathrm{sec}^{-1}$ and $\Delta\epsilon = 2\%$ are shown in Figs. 2 to 4, respectively, along with available experimental data for comparison.

IV. SENSITIVITY STUDY

Although the predicted and actual responses are in reasonable agreement, it was anticipated that better agreement could be achieved by modifying the parameter values. Therefore, a parametric study was undertaken to explore the sensitivity of each of the parameters to the overall predicted behavior of Inconel 718 at 1200°F, and thus lead to the determination of an 'optimal' modeling of overall material response. To perform such a multi-parameter optimization, it is necessary to have a complete and accurate set of experimental results of specific base-line tests. These tests should be chosen in such a way that all aspects of material behavior to be modeled by the theory are represented in the test data. Such a data set is not available for Inconel 718 at 1200°F, partly because of the expense of such testing, but also because existing test data were not acquired for the purpose of evaluating Chaboche's model. Therefore, it has been necessary to work with available data sets that are not adequate for the present purpose.

With this in mind, the data base of Ref. [8], which consists of tensile and creep test results only was employed to perform the parametric study. Then this data base was enlarged by including cyclic data from Ref. [4]. The first step of the parametric study consisted of varying the parameters, one at a time, by ±7% of the value listed in Table 3, predicting the corresponding material responses, and comparing these predictions with the selected data base. Because of space limitations, only representative samples of the results of this step are shown in Tables 4 to 6 , along with corresponding experimental data. A thorough examination of the results of this step of the parameteric study has led to the following observations:

(a) Some parameters have stronger effects on material behavior than others, in decreasing order, R_o, n, k, and m have the strongest effects.

(b) Whereas a material parameter or a subset of the parameters has a strong effect on a certain facet of material behavior, it does not necessarily have the same effect on a different aspect of material behavior. For instance, R_o had a strong effect on the creep behavior; however, it had less effect on the tensile and cyclic behavior.

(c) Creep response seems to be the most sensitive to changes in parameter values. For instance, changing R_o by ±7% results in approximately one order-of-magnitude change in the minimum creep rate value.

(d) Increases in b, γ, and m increase the minimum creep rate and the inelastic strain range, and decrease the saturation stress, whereas the other remaining parameters have the opposite influence.

Based on these observations, it was decided to extend the parametric study for the parameters that strongly affect the material behavior by reducing the amount of change from ±7% to ±3.5% for n, K, and m and to ±5.25, 3.5, and 1.75% for R_o, since it seemed to be the most influential. Representative results of these changes are also included in Tables 4 to 6. These results support the previous observations in that they confirm that the overall material behavior is most sensitive to variations of R_o. For example, a change of ±1.75% in R_o changes the minimum creep rate by about 50 to 100%. Thus, the results of the current parametric study verify that the modification introduced to Chaboche's theory, i.e., considering R_o to be a function of the strain rate, is of critical importance for improving the accuracy of this theory.

Although the results of this parametric study have shown that the cyclic material response (first cycle $\Delta\sigma$ and $\Delta\epsilon''$) is not strongly affected by small changes in b and q, the influence of these parameters is best exhibited by studying the complete cyclic behavior and not just the first cycle. Unfortunately, the only cyclic test available for this material is the one previously used to determine values of b and q. This test was conducted at $|\dot{\epsilon}| = 2.667\times10^{-3}$ sec^{-1}, a value which is well above the limit of rate sensitivity for Inconel 718 at 1200°F - estimated to be about 4×10^{-5} sec^{-1}. Thus the results of such a test should not be used to determine the material parameters. Problems also arise in attempting to use Chaboche's theory to predict a rate-insensitive response, since it is basically a rate-dependent plasticity theory. This problem was demonstrated by predicting the cyclic behavior at $|\dot{\epsilon}| = 2.667\text{x}10^{-3}\ \text{sec}^{-1}$ and $\epsilon = \pm 1\%$ for the first several cycles. The results showed that the stress was initially overestimated and the inelastic strain was underestimated. Also, the predicted cycles softened at a higher rate than actually observed, which suggests that b and q must be re-evaluated.

To best accomplish such a task, the hysteresis loops from a cyclic test at $|\dot{\epsilon}| \leq 4\text{x}10^{-5}\ \text{sec}^{-1}$ are needed. Such data, however, are not available*, and it was hypothesized by virtue of the material rate insensitivity for $\dot{\epsilon} > 4\text{x}10^{-5}\ \text{sec}^{-1}$ that the results of a cyclic test at $|\dot{\epsilon}| = 2.667\text{x}10^{-3}\ \text{sec}^{-1}$ are essentially the same as a test at $|\dot{\epsilon}| = 4\text{x}10^{-5}\ \text{sec}^{-1}$. In effect, values of R have been recalculated and the new estimates of the material parameters b and q were found to be

$$b = 3.75, \qquad q = 50\ \text{KSI}\ . \tag{35}$$

It was also found that by rounding off the values of a, c, K, m, and n, i.e.,

$$a \rightarrow 30\ \text{KSI},\ c \rightarrow 350,\ K \rightarrow 155\ \text{KSI}\sqrt[n]{\text{sec}},\ m \rightarrow 7,\ n \rightarrow 5.1, \tag{36}$$

insignificant effects on the predicted behavior were observed. Therefore, these values will be considered in the remainder of this work to be the 'optimal' values.

The final step in the optimization procedure was to change the form for $R_o(\dot{\epsilon})$ such that the best possible agreement could be obtained between experimental and predicted behavior. First the values of R_o that gave best prediction of overall behavior were determined and are shown in Ref. [19]. Then, an improved expression for R_o was established as

$$R_o = R_{oo}\left\{1 + \ln\left\{1 + \text{EXP}\left[\sum_{i=0}^{5} \beta_i(\ln\dot{\epsilon})^i\right]\right\}\right\}\ , \tag{37}$$

where $R_{oo} = q = 50$ KSI, $\beta_o = 48.88$, $\beta_1 = 18.30$, $\beta_2 = 2.767$, $\beta_3 = 0.2082$, $\beta_4 = 0.7813\text{x}10^{-2}$, and $\beta_5 = 0.1174\text{x}10^{-3}$.

---

*Contacts were made with ORNL to obtain the cyclic data from the tests reported in Refs. [2,5] but it was indicated that they were not available.

The revised material parameters of the extended Chaboche theory are listed in Table 3, and were employed to improve the material response predictions in Figs. 2 to 4.

IV. PREDICTIVE CAPABILITIES

The Chaboche theory has been employed to predict a wide range of additional mechanical behavior of Inconel 718 at 1200°F, including: strain-rate and strain-rate-history effects, creep and relaxation behavior, load-unload-reload behavior under strain or stress control, and strain-controlled, fully-reversed cyclic behavior.

Strain-Rate and Strain-Rate-History Effects

Three different strain rates; namely, $\dot{\epsilon}_1 = 5\text{x}10^{-5}\text{sec}^{-1}$, $\dot{\epsilon}_2 = 5\text{x}10^{-7}\text{sec}^{-1}$, $\dot{\epsilon}_3 = 5\text{x}10^{-9}\text{sec}^{-1}$, have been arbitrarily considered in studying the strain-rate effect. The stress-strain curves at these rates are shown in Fig. 5, which shows a rate dependency of initial yield that could not be predicted by the original Chaboche theory. This figure shows that the extended Chaboche theory predicts a pronounced strain rate effect for the strain rates considered. It is also noted that the stress-strain curves tend to be closer to each other as $\dot{\epsilon}$ increases. This behavior is consistent with the experiments, which have shown that an asymptotic behavior can eventually be reached.

A similar stress rate effect was predicted for three stress rates, obtained by multiplying the aforementioned strain rates by Young's modulus, as shown in Fig. 5. It is seen that the stress-controlled response overrides the strain-controlled response, the difference being attributed to the stress-strain nonlinearity of the constitutive equations.

The response of viscoplastic materials is significantly influenced by their strain rate history [24,26]. Perhaps the most useful and widely used experiment developed to study this behavior is the incremental (jump) test, where a specimen is first prestrained at one strain rate and then the strain rate is abruptly changed to another value. A material is said to exhibit a strain-rate-history effect if the jump (interrupted) and monotomic (pure) responses remain distinct after significant strains have been imposed [21].

Let the constant strain rates before and after a jump be denoted $\dot{\epsilon}_1$ and $\dot{\epsilon}_2$, respectively, and let $\delta = \dot{\epsilon}_2/\dot{\epsilon}_1$; where $\delta > 1$ indicates a strain rate increase, $0 < \delta < 1$ corresponds to a strain rate decrease with increasing strain, and $\delta < 0$ implies strain rate reversal (unloading), Fig. 6. It can be shown that [27]

$$E_2^* = E - \frac{1}{\delta}(E - E_1^*) \; , \tag{38}$$

where E_2^* and E_1^* are the slopes of the stress-strain curve immediately before and after the strain rate jump is imposed. If it is further assumed that $E_1^* \ll E$, it follows that $E_2^* \approx E$ for $\delta \gg 1$. In other words, the initial response after the strain rate increment is imposed is elastic, as experiments show. In case of stress-rate jumps, the analogue of Eq. (38) is

$$E_2^* = E \left[1 + \frac{1}{\gamma}\left(\frac{E}{E_1^*} - 1\right)\right]^{-1} \; , \tag{39}$$

where $\gamma = \dot{\sigma}_2/\dot{\sigma}_1$ is the ratio of the stress rates [27].

Figure 7 shows the predicted monotonic responses at $\dot{\epsilon}_1 = 10^{-6}$ sec^{-1} and $\dot{\epsilon}_2 = 5\text{x}10^{-5}$ sec^{-1} as well as the corresponding interrupted responses for $\delta = 50$ (low-to-high strain rate) and $\delta = 0.02$ (high-to-low strain rate) after a prestrain of 0.75%.

For tensile loading, the saturation stress can be reached when each of the terms on the right hand side of Eq. (13) saturates. Numerical exercises with the Chaboche theory, however, have shown that R does not change substantially when small deformations, such as those produced during a tensile test, are considered, i.e., $R \approx R_o$. Thus, the hardening process is essentially kinematic, and, in the presence of recovery, the saturation value of Y is smaller than a and can be determined by solving Eq. (32). This equation shows that the saturation value of Y is solely dependent on the strain rate and is, therefore, strain-rate-history independent. The difference observed in predicted monotonic and interrupted behavior is, thus caused by different values of $R = R_o$ in the monotonic and jump tests. Since R_o increases with $\dot{\epsilon}$, the jump response lies below the uninterrupted response for $\delta > 1$, i.e., the theory predicts a strain rate history effect typical of FCC materials [26]. Due to its treatment of R_o as a constant, the original Chaboche theory cannot predict strain-rate-history effects.

Prediction of the creep behavior of Inconel 718 at $\sigma_h = 140$ KSI, for load application rates of $\dot{\sigma}_1 = 20$ KSI/sec and $\dot{\sigma}_2 = 0.20$ KSI/sec, are presented in Fig. 8. In each case, the response from the moment of loading until the stress reached its hold value was predicted as well as the response for an additional 300 sec, with only the creep strains shown in Fig. 8. It was found that the creep strain corresponding to the higher stress rate overrides that corresponding to the lower rate. However, the total strain (not shown in Fig. 8) in the latter case was greater. This was expected, since at the lower stress rate, yielding initiated at a stress value much lower than $\sigma_h = 140$ KSI and by the time the stress value reached the hold value substantial hardening had already taken place. Thus, the material was capable of sustaining further deformations only at lower rates. These results suggest the importance of specifying the rate of load application, in addition to the hold stress, when reporting creep data.

When steady-state creep is reached, Eq. (13) yields upon differentiation with respect to time

$$\dot{Y} - \dot{R} = 0 , \qquad \text{or} \qquad \dot{Y} = -\dot{R} \cdot \tag{40}$$

For tensile creep, $\dot{Y}$ is positive, and Eq. $(40)_b$ is valid only if $\dot{R}$ is negative, i.e., when the material undergoes isotropic softening. Numerical solutions have shown that Inconel 718 at 1200°F starts to harden kinematically and soften isotropically with the initiation of creep deformations, with the rate of hardening being higher than the softening rate. However, a point is eventually reached where both rates are equal in magnitude. At this point Eq. $(40)_b$ is satisfied and thereafter softening begins to dominate, thus allowing for increasing strain rates, as Fig. 9 depicts for creep at 125 KSI. As mentioned earlier, there is experimental evidence that the increasing creep rates, at least in early stages, are not a manifestation of instability or impending failure [3,6]. Therefore, it is concluded that the Chaboche theory can predict realistic creep behavior, including increasing creep rates following steady-state creep, caused by material softening.

Relaxation Behavior

In a stress relaxation situation, Eqs. (6) and (7) give

$$\dot{\sigma} = -E\dot{\epsilon}'' \ . \qquad (41)$$

If the stress relaxes from a positive value, $\dot{\epsilon}''$ is initially positive and $\dot{\sigma}$ is, therefore, negative. Experimental data on metals and alloys show that the stress normally relaxes at a decreasing rate until a steady state is eventually reached when $\dot{\sigma} = 0$, i.e., when

$$\sigma = Y + R \ . \qquad (42)$$

To examine the stress relaxation prediction of the Chaboche theory, a loading history was chosen, which consisted of straining at a rate of 5×10^{-5} $\sec^{-1}$ to 1% strain. The strain was then held at this value for 50 minutes. The results are shown in fig. 10, and are consistent with the above discussion.

Load-Unload-Reload Behavior

A reversal in strain (stress) corresponds to an instantaneous jump in $\dot{\epsilon}(\dot{\sigma})$ with $\delta(\gamma) < 0$. Three different cases can be distinguished (c.f. Fig.6): (a) $\delta(\gamma) = -1$, which corresponds to a reversal with constant strain (stress) rate magnitude, (b) $\delta(\gamma) << -1$, which represents a large increase in the strain (stress) rate magnitude, and (c) $1/\delta(\gamma) << -1$, which represents a large decrease in strain (stress) rate magnitude upon unloading.

The loading-unloading behavior of Inconel 718 at 1200°F is now studied under strain (stress) control in a fashion similar to that of Ref. [28]. For strain control, a loading rate of $\dot{\epsilon}_o = 5 \times 10^{-7}$ $\sec^{-1}$ was arbitrarily selected, along with unloading rates of $\dot{\epsilon}_1 = -5 \times 10^{-5}$ $\sec^{-1}$ ($\delta_1 = -10^2 << -1$), $\dot{\epsilon}_2 = -5 \times 10^{-7}$ $\sec^{-1}$ ($\delta_2 = -1$), $\dot{\epsilon}_3 = -5 \times 10^{-9}$ $\sec^{-1}$ ($\delta_3 = -10^{-2}$, or $1/\delta_3 = -10^2 << -1$). In each case, unloading was initiated after a strain of 0.75% was reached, where $E_1^* \ll 1$, as was assumed in deriving Eq. (38). The results are shown in Fig. 11, where it is seen that the initial unloading behavior is inelastic and is sensitive to δ. For a large increase in the strain rate magnitude at reversal, the terms with $1/\delta$ in Eq. (38) are negligible and $E_2^* \approx E$, i.e., the initial unloading response is elastic, which is in agreeement with the predicted behavior shown in Fig. 11 for $\delta_1 = -10^{-2}$. For $\delta_2 = -1$, Eq. (38) gives $E_2^* = 2E$, which means that the initial unloading response is inelastic. Figure 11 however, shows that the slope very rapidly approximated E as the stress decreased. For large decreases in strain rate magnitudes at reversal, the terms with $1/\delta$ dominate and $E_2^* \approx E/|\delta|$. Therefore, significant inelastic unloading response with a very large positive slope was predicted, resulting in near-vertical decay of the stress at the start of unloading. The inelastic strain increased when $\delta_3 = -10^{-2}$ was imposed, and can be thought of as stress relaxation, since the stress decreases at almost constant strain.

For stress control, the stress rates were obtained by multiplying the prior strain rates by E. In each case, the loading period was adjusted so that a strain of 1% was obtained before unloading was started. The results are shown in Fig. 12. For $\gamma \ll -1$, Eq. (39) yields a value of $E_2^* = E$, i.e., the initial unloading response is elastic, as Fig. 12 depicts for $\gamma_1 = -10^2$. For $\gamma_2 = -1$, the initial slope upon unloading can be found from Eq. (45) to be $E_2^* = -E_1^*$, i.e., the initial unloading response is inelastic with a negative slope that is equal in magnitude to the slope before unloading. As the stress decreases, however, the unloading response approaches a linear shape typical of elastic unloading, as shown in Fig. 12. For $1/\gamma \ll -1$, Eq. (39) reduces to $E_2^* = -|\gamma| E_1^*$. Consequently, the initial unloading slope is negative and much smaller in magnitude than the slope before unloading. The theory, therefore, predicts significant inelastic unloading behavior with small decreases in stress and very large increases in inelastic strain, as shown in Fig. 12, for $\gamma_3 = -10^{-2}$. This latter case is analogous to a creep test, where the stress is held almost constant while the strain increases substantially.

The analysis was further expanded by studying the effect of unloading rate on subsequent reloading behavior. Two cases were considered: (a) loading, unloading, and reloading at $|\dot{\epsilon}| = 5\text{x}10^{-5}\text{sec}^{-1}$, and (b) loading and reloading at $\dot{\epsilon}_1$ and unloading at $\dot{\epsilon}_2 = -5\text{x}10^{-7}\text{sec}^{-1}$. In each case, loading was applied until a strain of 0.75% was reached, unloading was initiated and maintained to a strain of 0.45%, and finally loading was continued to a strain of 1.0%. The results are shown in Fig. 13 for both cases. In the first case ($\delta = -1$ at unloading), the initial slope upon unloading is positive and twice the elastic response, i.e., the initial response is inelastic. However, it rapidly approximates the linear elastic response and, therefore, the reloading response immediately approaches the monotonic response at the loading rate. In the second case ($\delta = -10^{-2}$ at unloading), however, significant inelastic deformations occurred upon unloading and the consequent reloading response at $\dot{\epsilon}_1$ was considerably different from the monotonic response at the same rate. Note that differences in reloading behavior in the two cases are due essentially to the amount of inelastic deformations that occurred upon unloading. It is possible to conclude, therefore, that the Chaboche theory is capable of simulating a history-dependent reloading response that memorizes rate-dependent prior deformations.

Cyclic Softening

As mentioned earlier, Inconel 718 at 1200°F undergoes cyclic softening for approximately 10-20 % of its fatigue life. In Chaboche's theory, cyclic softening is modeled by the isotropic hardening variable R, with its saturation value q smaller than its initial value R_o. The first few hysteresis loops of a strain-controlled, fully-reversed cyclic test at $|\dot{\epsilon}| = 4\text{x}10^{-5}\ \text{sec}^{-1}$ and $\Delta\epsilon = 2\%$ were predicted and are shown in Fig. 14. In this figure, cyclic softening is manifested by a continuous decrease in the stress range and a corresponding increase in the inelastic strain range with cycling.

V. CONCLUSIONS

The modified Chaboche theory of viscoplasticity has been employed to model the viscoplastic behavior of Inconel 718 at 1200°F. A procedure has been developed and used for the determination of the material parameters of this theory from available uniaxial experimental data of standard mechanical tests. The procedure for determining the parameters is not unique, but is considered appropriate for the available data, which were not adequate for the purpose of evaluating the Chaboche material parameters.

The sensitivity study undertaken herein has resulted in an 'optimal' set of material parameters, which gave better overall agreement between theory and prediction. The study has also emphasized the influence of each material parameter on different aspects of material behavior.

The predictive capabilities of the theory have been demonstrated for a variety of uniaxial loading conditions. The lack of adequate data base, however, precludes drawing detailed conclusions about the accuracy of the predicted behavior. Nonetheless, the Chaboche theory appears to offer a considerable promise for successfully modeling viscoplastic material behavior.

ACKNOWLEDGMENT - The authors thank Dr. T. Nicholas of the AFWAL Materials Laboratory, Wright-Patterson Air Force Base, for his technical assistance in providing experimental data for Inconel 718 at 1200°F.

VI. REFERENCES

1. Barker, J.F., Ross, E.W., and Radavich, J.F., "Long Time Stability of INCONEL 718," Journal of Metals, pp. 31-41, January 1970.

2. Brinkman, C.R., and Korth, G.E., "Strain Fatigue and Tensile Behavior of Inconel 718 from Room Temperature to 650°C," Journal of Testing and Evaluation, JTEVA, Vol. 2, No. 4, pp. 249-259, 1984.

3. Booker, M.K., "An Interim Analytical Representation of the Creep Strain-Time Behavior of Commercially Heat Treated Alloy 718," ORNL/TM 6232, 1978.

4. Domas, P.A., Sharpe, W.N., Ward, M., and Yau, J., "Benchmark Notch Test for Life Prediction," Technical Report Submitted to NASA under contract NAS3-22522, 1982.

5. Korth, G.E., and Smolik, G.R., "Status Report of Physical and Mechanical Test Data of Alloy 718," TREE 1254, 1978.

6. Booker, M.K., "Progress Toward Analytical Description of the Creep Strain-Time Behavior of Engineering Alloys," CONF 800907-2, 1980.

7. Wilson, D.A., and Walker, K.P., "Constitutive Modeling of Engine Materials," AFWAL-TR-84-4073, 1984.

8. Beaman, R.L., "The Determination of the Bodner Material Coefficients for IN 718 and Their Effects on Cyclic Loading," M.S. Thesis, Air Force Institute of Tehcnology, 1984.

9. Nicholas, T., Private Communication.

10. Abdel-Kader, M.S., "A Comparative Study of the Chaboche and Bodner Theories of Viscoplasticity for High Temperature Applications," D.Sc. Dissertation, The George Washington University, Washignton, D.C., 1986.

11. Booker, M.K., and Sikka, V.K., "A Study of Tertiary Creep Instability in Several Elevated-Temperature Structural Materials," Thechnical Report Submitted to the Division of Reactor Research and Technology, U.S. Department of Energy under Contract W-7405-eng-26, 1979.

12. Chaboche, J.L., "Viscoplastic Constitutive Equations for the Description of Cyclic and Anistotropic Behavior of Metals," Bulletin De L'Academie Polanaise des Sciences, Vol. 25, No. 33, 1977.

13. Chaboche, J.L., and Rousselier, G., "On the Plastic and Viscoplastic Constitutive Equations - Part I: Rules Developed With Internal Variable Concept," J. Pressure Vessel Tech., Vol. 105, pp. 153-158, 1983.

14. Chaboche, J.L., "Thermodynamic and Phenomenological Description of Cyclic Viscoplasticity With Damage," Translation of Publication No. 1978-3 of the Office National d'Etudes et de Researches Aerospatiales, France, by the European Space Agency Technical Translation Service, Publication No. ESA-TT-548, 1979.

15. Chaboche, J.L., et al, "Modelization of the Strain Memory Effects on the Cyclic Hardening of 316 Stainless Steel," in Fifth Int. Conference on Structural Mechanics in Reactor Technology, Berlin, W. Germany, 1979.

16. Chaboche, J.L., and Rousselier, G., "On the Plastic and Viscoplastic Constitutive Equations - Part II: Application of Internal Variable Concepts to the 316 Stainless Steel," J. Pressure Vessel Tech., Vol. 105, pp. 159-164, 1983.

17. Eftis, J., and Jones, D.L., "Life Prediction for a Structural Material Under Cyclic Loads With Hold Times Using a Viscoplastic Constitutive Model," Final Technical Report, Air Force Office of Scientific Research, Washington, D.C., U.S.A., 1983.

18. Chiu, S.S., Eftis, J., and Jones, D.L., "Application of Cyclic Viscoplastic Theory to Low Cycle Fatigue Life Prediction of Ti-6Al-4V," Proc. NUMETA' 85 Conference, Swansea, U.K., 7-11 January, 1985.

19. Abdel-Kader, M.S., Eftis, J., Jones, D.L., "An Extension of the Chaboche Theory of Viscoplasticity to Account for Rate-Dependent Initial Yield," SECTAM XIII, Columbia, South Carolina, 1986.

20. Eftis, J., and Jones, D.L., "Evaluation and Development of Constitutive Relations for Inelastic Behavior," Final Technical Report, Air Force Office of Scientific Research, Washington, D.C., U.S.A., 1983.

21. Haisler, W.E., and Imbire, P.K., "Numerical Considerations in the Development and Implementation of Constitutive Models," NASA Second Symposium on Nonlinear Constitutive Relations for High Temperature Applications," NASA Lewis Research Center, Clev., Ohio, 1984.

22. Draper, N.R., and Smith, H., "Applied Regression Analysis," J. Wiley, pp. 263-304, 1966.

23. Stouffer, D.C., "A Constitutive Representation for IN 100," Technical Report AFWAL-TR-81-4039, 1981.

24. Lindholm, U.S., "Some Experiments With Split Hopkinson Pressure Bar," J. Mech. Phys. Solids, Vol. 12, pp. 317-335, 1964.

25. Eleiche, A.M., and Campbell, J.K., "The Influence of Strain Rate History and Temperature on the Shear Strength of Copper, Titanium, and Mild Steel, "Technical Report AFML-TR-76-90, 1976.

26. Duffy, J., "Strain Rate History Effects and Dislocation Substructure at High Strain Rates," in Mechanical Behavior Under High Stress and Ultrahigh Loading Rates, Ed. by J. Mescall and V. Weiss, Plenum Publishing Corporation, 1983.

27. Cernocky, E.P., "An Examination of Four Viscoplastic Constitutive Theories in Uniaxial Monotonic Loading," Int. J. Solids Structures, Vol. 18, No. 11, pp. 989-1005, 1982.

28. Cernocky, E.P., "Comparison of the Unloading and Reversed Loading Behavior of Three Viscoplastic Constitutive Theories," Int. J. Nonlinear Mechanics, Vol. 17, No. 4, pp. 255-266, 1982.

Table 1: Values of K^*, n^*, a, and c for Inconel 718 at 1200°F

Ser. No.	Ref.	Test	Strain Rate, Sec^{-1}	No. of Data Points	K^* KSI	n^*	a KSI	c
1	4	cyclic	8.333×10^{-4}	4	202.3	0.1080	24.46	364.4
2	4	cyclic	3.333×10^{-3}	3	188.7	0.1100	31.81	347.0
3	4	cyclic	1.667×10^{-2}	4	156.6	0.0920	33.86	349.0
4	5	cyclic	4.000×10^{-3}	12	188.2	0.1078	31.49	349.1
5	2	cyclic	4.000×10^{-3}	37	172.2	0.1017	28.13	355.0
6	2,5	cyclic	4.000×10^{-3}†	49	187.9	0.1096	31.64	347.5
7	9	cyclic	2.667×10^{-3}†	3	214.9	0.1562	39.97	301.5
8	4	tensile	1.670×10^{-4}		166.9	0.0540	----	----
9	4	tensile	3.330×10^{-5}		210.0	0.0630	----	----

†Some tests were performed at $\dot{\epsilon} = 10^{-4}\ sec^{-1}$ and $10^{-5} sec^{-1}$

Table 2: Calculation of R and p for the determination of b and q

Cycle No.	σ KSI	ϵ''_a† %	p	Y KSI	R KSI
1	115.0	0.530	0.0265	28.57	39.04
4	109.8	0.546	0.0907	28.71	33.32
8	105.4	0.561	0.1568	28.84	28.83
12	102.4	0.561	0.2247	28.95	25.72
16	101.0	0.588	0.2942	29.04	24.25
20	99.42	0.588	0.3648	29.04	22.66
24	98.43	0.588	0.4354	29.04	21.67
28	97.43	0.588	0.5059	29.04	20.67
32	95.44	0.591	0.5766	29.06	18.66
36	95.44	0.596	0.6477	29.09	18.63
40	95.44	0.596	0.7192	29.09	18.63

†Inelastic strain amplitude, $\Delta\epsilon''/2$

Table 3: Material parameters of Chaboche's theory, Inconel 718 at 1200°F

Parameter	Description	Initial Value	Optimal Value
E	Young's modulus	24.73×10^{-3}	$24.73\text{X}10^{-3}$
ν	Poisson's ratio	0.3356	0.3356
a	Saturation value of kinematic hardening variable	31.40	30.00
c	Kinematic hardening exponent	349.5	350.0
γ	Coefficient of recovery	0.4×10^{-10}	0.4×10^{-10}
m	Recovery exponent	6.942	7.000
K	Overstress parameter	$154.4\ \text{KSI}\sqrt[n]{\text{sec}}$	$155.0\ \text{KSI}\sqrt[n]{\text{sec}}$
n	Strain rate sensitivity parameter	5.120	5.100
q	Saturation value of isotropic hardening variable	18.62 KSI	50.00 KSI
b	Isotropic hardening exponent	4.679	3.75
R_o	Initial, rate-dependent value of isotropic hardening	Eq.(31)	Eq.(37)

Table 4: Effect of changing n by ±(3.5, 7.0)% on tensile behavior, Inconel 718 at 1200°F

Strain Rate, Sec^{-1}	Saturation Stress, KSI					
	Exper.	Predictions				
		0.930n	0.965n	n	1.035n	1.70n
1.1×10^{-6}	134	128.28	129.20	130.18	131.12	132.33
1.3×10^{-5}	142	143.57	144.85	146.23	147.62	148.90

Table 5: Effect of changing R_o by $\pm$(1.75, 3.5, 5.25, 7.0)% on creep behavior, Inconel 718 at 1200°F

Hold Stress KSI	Minimum Creep Rate, Sec^{-1}									
	Exper.	Predictions								
		$0.930R_o$	$0.9475R_o$	$0.965R_o$	$0.985R_o$	R_o	$1.0175R_o$	$1.035R_o$	$1.0525R_o$	$1.070R_o$
80	4.0×10^{-9}	4.519×10^{-8}	2.668×10^{-8}	1.503×10^{-8}	8.038×10^{-9}	3.991×10^{-9}	1.853×10^{-9}	9.831×10^{-10}	7.119×10^{-10}	7.004×10^{-10}
100	1.6×10^{-8}	4.250×10^{-7}	2.706×10^{-7}	1.660×10^{-7}	9.828×10^{-8}	5.533×10^{-8}	2.944×10^{-8}	1.470×10^{-8}	7.518×10^{-9}	1.209×10^{-8}
110	3.0×10^{-8}	5.519×10^{-7}	3.374×10^{-7}	1.984×10^{-7}	1.113×10^{-7}	5.898×10^{-8}	2.917×10^{-8}	1.325×10^{-8}	9.232×10^{-9}	9.048×10^{-9}
120	1.5×10^{-7}	1.141×10^{-6}	7.052×10^{-7}	4.200×10^{-7}	2.394×10^{-7}	1.295×10^{-7}	6.591×10^{-8}	3.441×10^{-8}	2.245×10^{-8}	2.806×10^{-8}
125	3.5×10^{-7}	2.253×10^{-6}	1.439×10^{-6}	8.931×10^{-7}	5.331×10^{-7}	3.058×10^{-7}	1.667×10^{-7}	8.627×10^{-8}	4.955×10^{-8}	6.433×10^{-8}
130	8.3×10^{-7}	5.119×10^{-6}	3.418×10^{-6}	2.228×10^{-6}	1.413×10^{-6}	8.674×10^{-7}	5.127×10^{-7}	2.898×10^{-7}	1.584×10^{-7}	1.171×10^{-7}
135	5.5×10^{-6}	1.139×10^{-5}	7.863×10^{-6}	5.345×10^{-6}	3.558×10^{-6}	2.311×10^{-6}	1.459×10^{-6}	8.916×10^{-7}	5.244×10^{-7}	3.804×10^{-7}
140	7.0×10^{-6}	2.129×10^{-5}	1.509×10^{-5}	1.051×10^{-5}	7.198×10^{-6}	4.834×10^{-6}	3.172×10^{-6}	2.023×10^{-6}	1.254×10^{-6}	1.126×10^{-6}

Table 6: Effect of changing material parameters by values ranging from ±1.75% to ±7.0% on cyclic behavior[1], Inconel 718 at 1200°F

Parameter	0.930P[2]		0.9475P		0.9650P		0.9825P		P		1.0175P		1.0350P		1.0525P		1.070P	
	$\Delta\sigma_1$ KSI	$\Delta\epsilon_1^*$ %	$\Delta\sigma_1$ KSI	$\Delta\epsilon_1^*$ %	$\Delta\sigma_1$ KSI	$\Delta\epsilon_1^*$ %	$\Delta\sigma_1$ KSI	$\Delta\epsilon_1^*$ %	$\Delta\sigma_1$ KSI	$\Delta\epsilon_1^*$ %	$\Delta\sigma_1$ KSI	$\Delta\epsilon_1^*$ %	$\Delta\sigma_1$ KSI	$\Delta\epsilon_1^*$ %	$\Delta\sigma_1$ kSI	$\Delta\epsilon_1^*$ %	$\Delta\sigma_1$ kSI	$\Delta\epsilon_1^*$ %
a	307.5	0.753	...	...	...	...	...	...	309.6	0.745	...	...	...	...	...	...	311.5	0.737
c	308.6	0.749	...	...	...	...	...	...	"	"	...	...	...	...	...	...	310.4	0.742
γ	309.7	0.744	...	...	...	...	...	...	"	"	...	...	...	...	...	...	309.4	0.747
m	312.0	0.735	...	...	311.0	0.739	...	...	"	"	...	...	307.7	0.753	...	...	305.7	0.761
K	306.7	0.758	...	...	308.2	0.751	...	...	"	"	...	...	311.1	0.740	...	...	312.4	0.733
n	303.9	0.768	...	...	306.7	0.757	...	...	"	"	...	...	312.4	0.734	...	...	315.2	0.722
b	310.0	0.743	...	...	...	...	...	...	"	"	...	...	...	...	...	...	309.2	0.747
q	309.5	0.745	...	...	...	...	...	...	"	"	...	...	...	...	...	...	309.7	0.745
R_o[3]	294.3	0.808	298.2	0.793	302.0	0.777	305.8	0.761	"	"	313.4	0.730	317.2	0.714	320.9	0.699	324.7	0.689

---

[1] Experimental values : $\Delta\sigma_1$ = 285 KSI, $\Delta\epsilon_1^*$ = 0.83%.
[2] P refers to any of Chaboche's parameters.
[3] R_o = 115.5 KSI for $\dot{\epsilon} = 4 \times 10^{-6}$ sec^{-1}, Eq. (31).

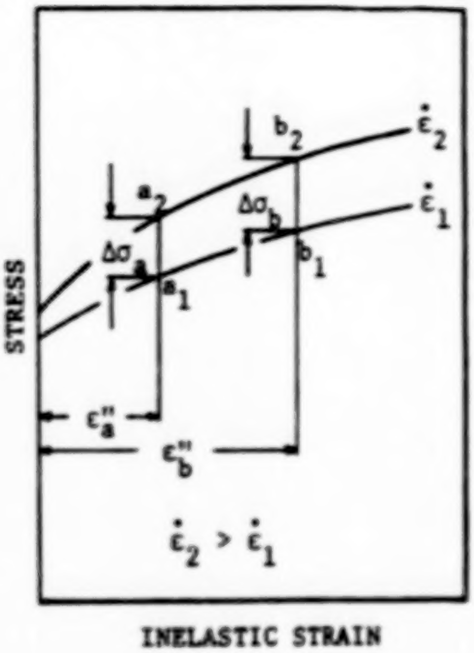
b_2
$\dot{\varepsilon}_2$
a_2
$\Delta\sigma_b$
$\dot{\varepsilon}_1$
$\Delta\sigma_a$
b_1
a_1
STRESS
ε''_a
ε''_b
$\dot{\varepsilon}_2 > \dot{\varepsilon}_1$
INELASTIC STRAIN

Fig. 1. Illustration of two stress-inelastic strain curves at different strain rates.

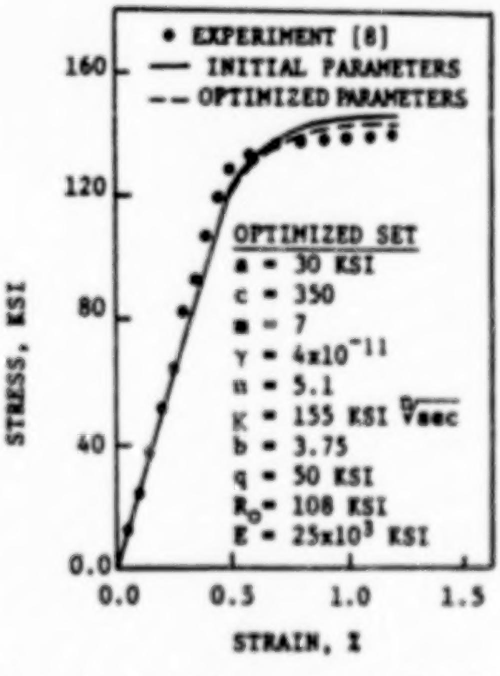

Fig. 2. Comparison of experimental and predicted monotonic response at $\dot{\varepsilon} = 1.333\times10^{-5}\,\mathrm{sec}^{-1}$.

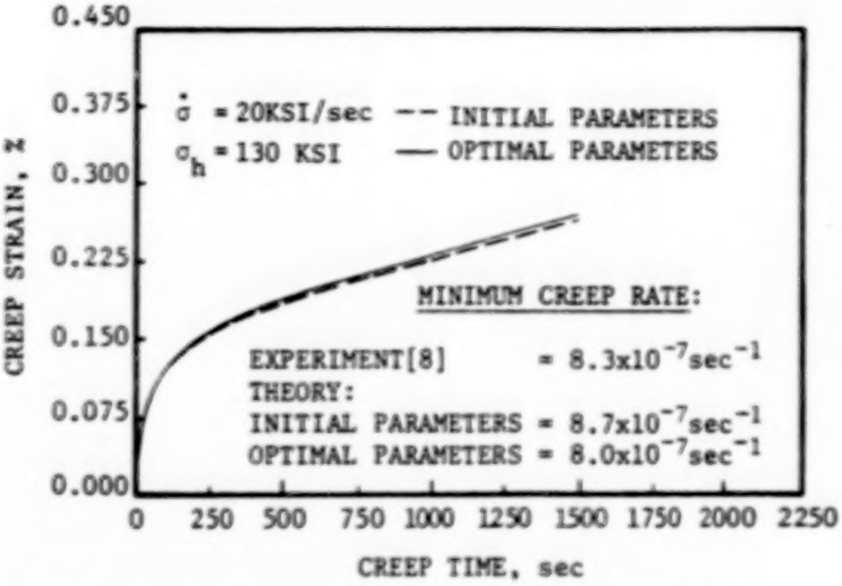

Fig. 3. Predicted creep response at $\sigma_h = 130$ KSI; only experimental steady state is available.

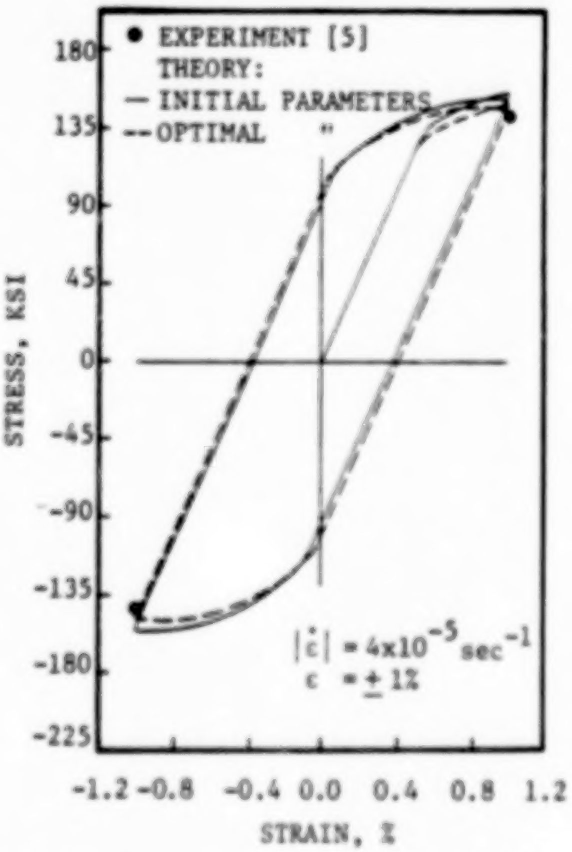

Fig. 4. Predicted cyclic response at $|\dot{\epsilon}| = 4\times10^{-5}$sec^{-1} and $\epsilon = \pm 1\%$; only experimental peak stresses are available.

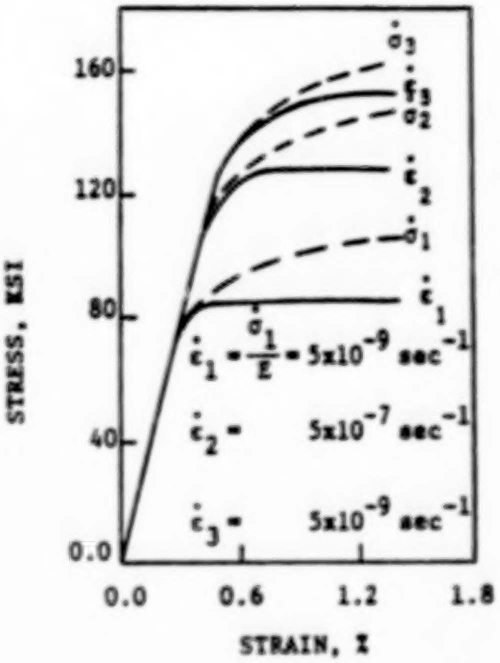

Fig. 5. Predicted stress-strain response at different strain and stress rate.

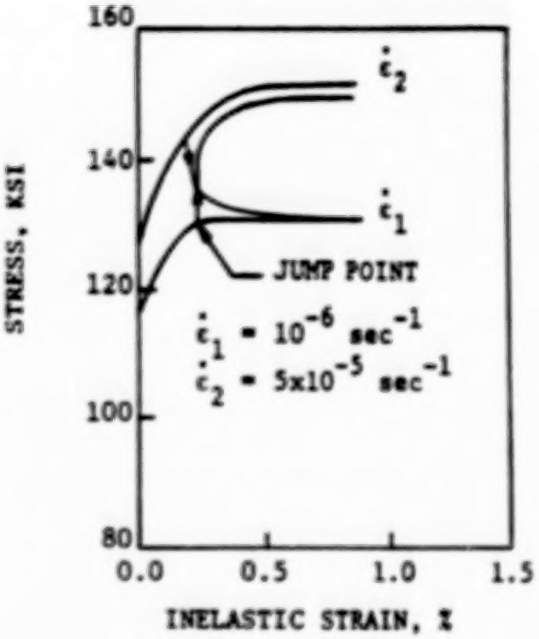

Fig. 7. Predicted monotonic and interruped responses at different strain rates.

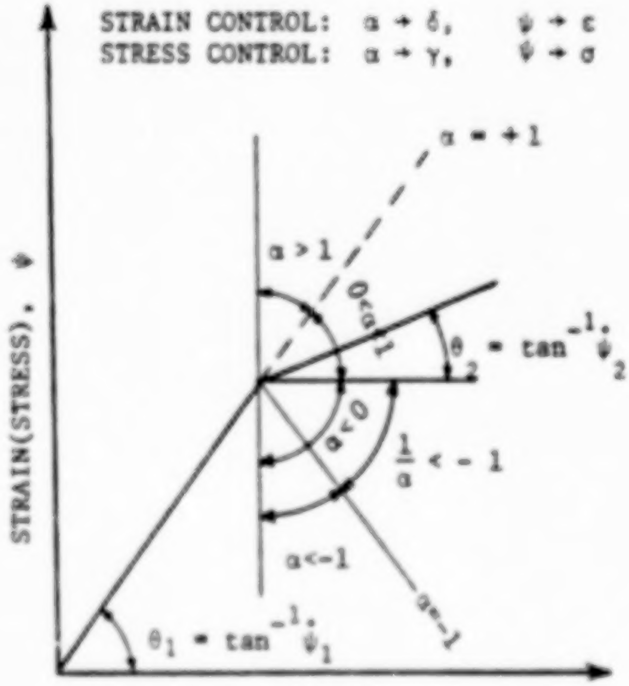

STRAIN CONTROL: $\alpha \rightarrow \delta$, $\psi \rightarrow \varepsilon$
STRESS CONTROL: $\alpha \rightarrow \gamma$, $\psi \rightarrow \sigma$
$\alpha = +1$
$\alpha > 1$
$0<\alpha<1$
$\theta_2 = \tan^{-1}\dot{\psi}_2$
$\alpha < 0$
$\frac{1}{\alpha} < -1$
$\alpha<-1$
$\alpha=-1$
$\theta_1 = \tan^{-1}\dot{\psi}_1$
STRAIN(STRESS), ψ
TIME

Fig. 6. Illustration of strain (stress) rate changes.

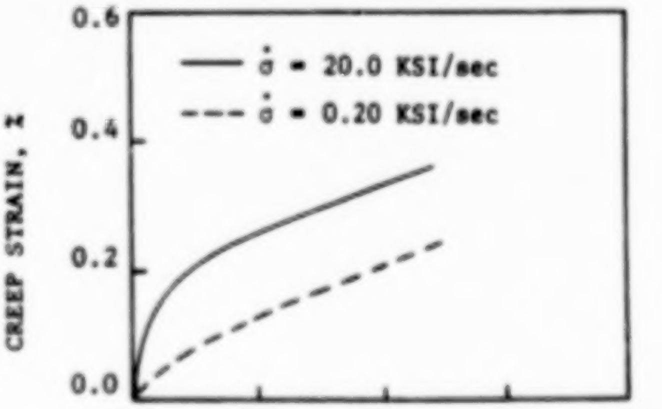

Fig. 8. Predicted creep response at $\sigma_h = 140$ KSI for different loading rates.

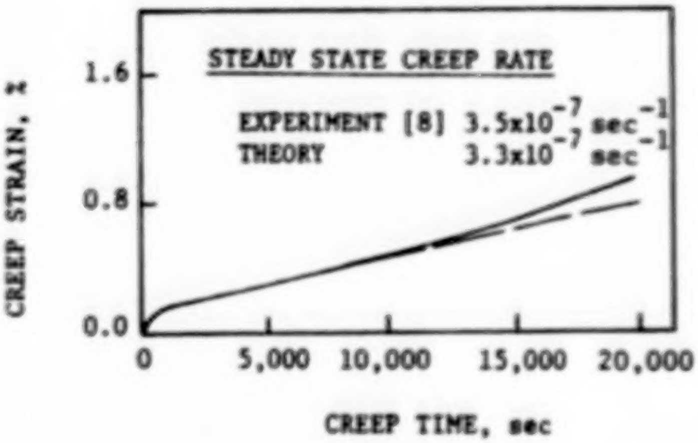

Fig. 9. Predicted creep response at σ_h = 125 KSI and $\dot{\sigma}$ = 20 KSI/sec.

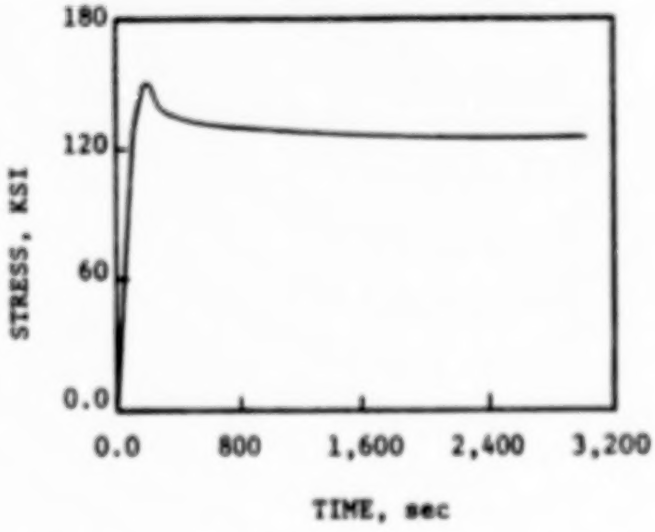

Fig. 10. Predicted relaxation response at ε = 1%

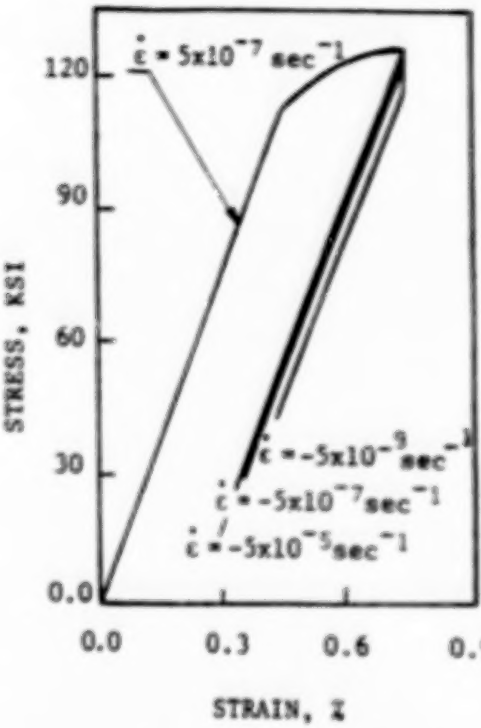

Fig. 11. Predicted load-unload response at different unloading strain rates.

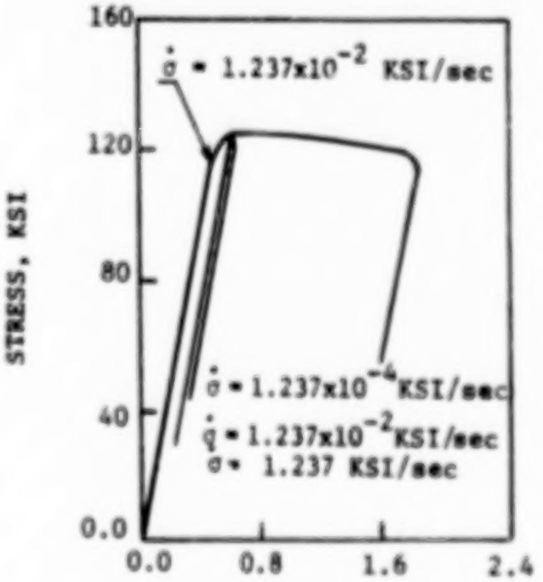

Fig. 12. Predicted load-unload response at different unloading stress rates.

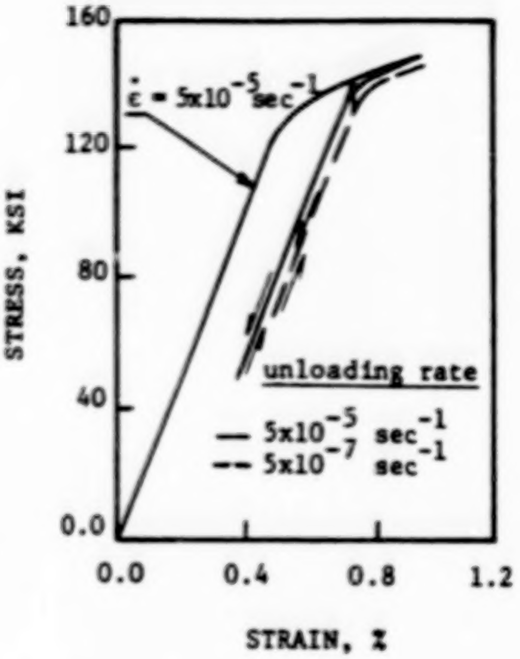

Fig. 13. Predicted load-unload-reload response at different unloading strain rates.

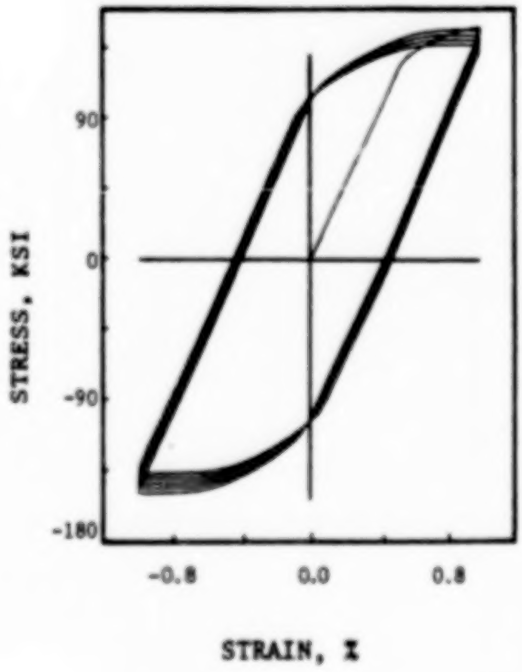

Fig. 14. Predicted cyclic response at $|\dot{\varepsilon}| = 4x10^{-5} sec^{-1}$ and $\varepsilon = \pm 1\%$.

N88
21503
UNCLAS

N88-21503

An Internal Variable Constitutive Model for the Large Deformation of Metals at High Temperatures

Stuart Brown and Lallit Anand
Massachusetts Institute of Technology
Cambridge, Massachusetts

Elevated temperature deformation processing, "hot working," is central to the production of more than 80% of all metal products. The advent of large deformation finite element methodologies is beginning to permit the numerical simulation of hot working processes whose design until recently has been based on prior industrial experience. Proper application of such finite element techniques requires realistic constitutive equations which more accurately model material behavior during hot working.

The constitutive equations should satisfy several requirements. First, the equations should be able to model large, three dimensional deformations. Second, the model should encompass the range of hot working conditions, which includes strain rates ranging from 10^{-3} to 10^{1} sec^{-1} or greater, homologous temperatures from .5 to .9, and interrupted deformation histories. Third, determination of parameters associated with the model should be straightforward and require a minimum of materials testing. Fourth, the model should provide a means of representing material microstructural state and its evolution during deformation. Finally, the model should be formulated with due consideration of issues regarding their numerical implementation in finite element programs.

A simple constitutive model for hot working which satisfies most of these requirements is the single-scalar internal variable model for isotropic thermo-elasto-viscoplasticity proposed by Anand [1985,1982]. In the next section we recall this constitutive model. The specific scalar functions for the equivalent plastic strain rate and the evolution equation for the internal variable presented here are slight modifications of those proposed by Anand [1982]. These modified functions are better able to represent high temperature material behavior. Following this presentation of the constitutive equations we briefly describe our monotonic constant true strain rate and strain rate jump compression experiments on a 2% silicon iron. The material parameters appearing in the constitutive model can be determined from the stress-strain curves resulting from such experiments. The model is implemented in the general purpose finite element program ABAQUS [Hibbitt, et.al., 1984]. Finally, using this program, the predictive capabilities of the model are evaluated for some simple deformation histories.

Constitutive Model

(a) Stress-strain-temperature rate relation:

$$\bar{\mathbf{T}}^{\nabla} = \mathcal{L}[\mathbf{D} - \mathbf{D}^p] - \mathbf{\Pi}\dot{\theta}, \tag{1}$$

where with $\mathbf{T}$ denoting the Cauchy stress and $\mathbf{F}$ denoting the deformation gradient,

$\bar{\mathbf{T}} \equiv (det\,\mathbf{F})\mathbf{T}$	Kirchhoff stress;
$\bar{\mathbf{T}}^{\nabla} \equiv \dot{\bar{\mathbf{T}}} - \mathbf{W}\bar{\mathbf{T}} + \bar{\mathbf{T}}\mathbf{W}$	Jaumann derivative of Kirchhoff stress;
$\mathcal{L} = 2\mu\mathcal{I} + [\kappa - (2/3)\mu]\mathbf{1} \otimes \mathbf{1}$	Elasticity tensor;
$\mu = \hat{\mu}(\theta), \quad \kappa = \hat{k}(\theta)$	Shear and bulk moduli;
$\mathbf{\Pi} = (3\kappa\alpha)\mathbf{1}$	Stress temperature tensor;
α	Coefficient of thermal expansion;
$\mathbf{D} = \mathrm{sym}\ \dot{\mathbf{F}}\mathbf{F}^{-1}$	Stretching tensor;
$\mathbf{W} = \mathrm{skew}\,\dot{\mathbf{F}}\mathbf{F}^{-1}$	Spin tensor;
θ	Absolute temperature.

(b) Flow rule:

The constitutive equation for $\mathbf{D}^p$ is:

$$\mathbf{D}^p = \dot{\bar{\epsilon}}^p \left(\frac{3}{2}\frac{\bar{\mathbf{T}}'}{\bar{\sigma}}\right), \tag{2}$$

where

$\dot{\bar{\epsilon}}^p = f(\bar{\sigma}, \theta, s) > 0, \quad \bar{\sigma} < s$	equivalent plastic tensile strain rate,
$\bar{\sigma} = \sqrt{(3/2)\bar{\mathbf{T}}' \cdot \bar{\mathbf{T}}'}$	equivalent tensile stress,

and s is a scalar internal variable with the dimension of stress. We call it the deformation resistance which may be associated with a microstructural characteristic such as dislocation density.

(c) Evolution equation:

The deformation resistance s is assumed to evolve according to:

$$\dot{s} = h(\bar{\sigma}, \theta, s)\dot{\bar{\epsilon}}^p - \dot{r}(\theta, s),$$

where h represents strain hardening (with dynamic recovery) and $\dot{r}$ represents static recovery.

The major task in completing the constitutive model involves a specification of the rate equation f above and the evolution equation for the internal variable s. We propose the following model:

$$\dot{\bar{\epsilon}}^p = A \exp\left(-\frac{Q}{k\theta}\right)\left[\sinh\left(\xi\frac{\bar{\sigma}}{s}\right)\right]^{1/m}, \quad \bar{\sigma} < s, \tag{3}$$

$$\dot{s} = h_0[< 1 - (s/s^*) >]^a, \quad a \geq 1, \tag{4}$$

with

$$s^* = \tilde{s}\left[\frac{\dot{\bar{\epsilon}}^p}{A}\exp\left(\frac{Q}{k\theta}\right)\right]^n. \tag{5}$$

In this model the material parameters are $A, Q, \xi, m, h_0, a, \tilde{s},$ and n, and k is Boltzmann's constant.

The static recovery function $\dot{r}$ in this model is set equal to zero. Accordingly, these equations are unable to model recovery during hold periods between high rate deformation passes or during very slow deformation processing.

Compression Experiments on a 2% Silicon Iron

Isothermal hot-compression tests have been performed to evaluate the material constants associated in the above model. A 2% silicon iron was selected since it does not dynamically recrystallize and since it does not experience a change in crystal structure upon quenching from elevated temperature deformation. Tests were performed on a high temperature materials test system consisting of a vacuum furnace mounted in a servo-hydraulic test machine. An analog function generator was used to produce constant true strain rates and strain rate jumps. Data was collected on a microcomputer data acquisition system.

The test specimens were circular cylinders with a height-to-diameter ratio 1.5. Shallow, concentric, circular grooves were machined into the ends of each specimen to hold a high temperature lubricant. Lubricants were mixtures of powdered glass and boron nitride powder. Homogeneous compression to a true strain of approximately -1.0 was achievable on a routine basis.

Two sets of experiments were performed: isothermal, constant true strain rate tests and strain rate jump tests. The constant true strain rate tests were performed for a range of temperatures from 800 to 1200 degrees Celsius, and a range of strain rates from 10^{-3} to 10^{0} per second. Figure 1 provides a representative subset of these tests for a given temperature at varying true strain rates. Strain rate jump tests were performed to provide means of evaluating strain rate dependence *at a given internal state*, because such a test instantaneously decouples the strain rate equation (3) from the evolution equation for the internal variable (4). Figure 2 shows a representative series of jump tests at a constant temperature. The stress/strain data following the jump in strain rate also provides data for an independent comparison of the constitutive model predictions and actual material response.

Material Constant Determination and Model Evaluation

Material constants for the model represented by equations (3) to (5) have been determined using data obtained from the constant true strain rate and strain rate jump tests. The equations have been incorporated using procedures outlined by Anand [1986] via a user-material interface in the finite element program ABAQUS. Stress-strain curves have been calculated using ABAQUS for conditions representative of the experiments on the silicon iron. The calculated curves are compared with the experimental data in Figures 3 and 4. The agreement between the theory and experiment is excellent.

Several test specimen geometries have also been evaluated which produce a gradient of internal microstructure within a single deformed specimen. These specimens have been deformed at temperature and then quenched. Different measures of microstructure, such as microhardness and etchpit density, have been compared with the variation in the internal variable predicted by the constitutive model.

References

1982 Anand, L., "Constitutive Equations for the Rate-Dependent Deformation of Metals at Elevated Temperatures," Journal of Engineering Materials and Technology, 104, January, 1982, pp. 12-17.

1984 H. D. Hibbitt, ABAQUS/EPGEN, "A General Purpose Finite Element Code with Emphasis on Non-Linear Applications," Nuclear Engineering and Design 77, 1984, pp 271-297. Also: ABAQUS manuals by Hibbitt, Karlsson, and Sorensen, Inc., Providence, R.I. (1984).

1985 Anand, L.,"Constitutive Equations for the Hot Working of Metals," International Journal of Plasticity, 1, 1985, pp. 213-231.

1986 Anand,L., Lush, A., Briceno, M., and Parks, D., "A Time-Integration Procedure for a Set of Internal Variable Type Elasto-Viscoplastic Constitutive Equations," Journal of Computers and Structures, forthcoming.

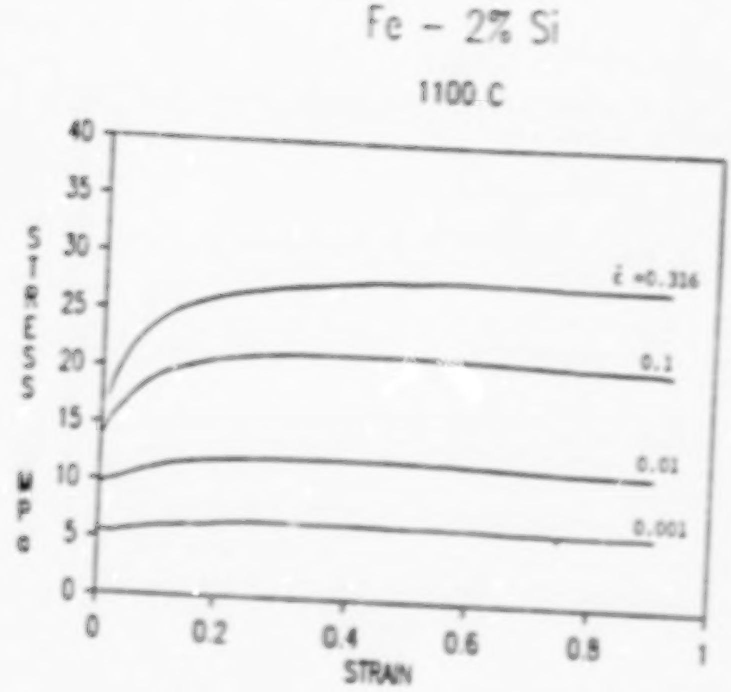

FIGURE 1. Constant True Strain Rate Tests

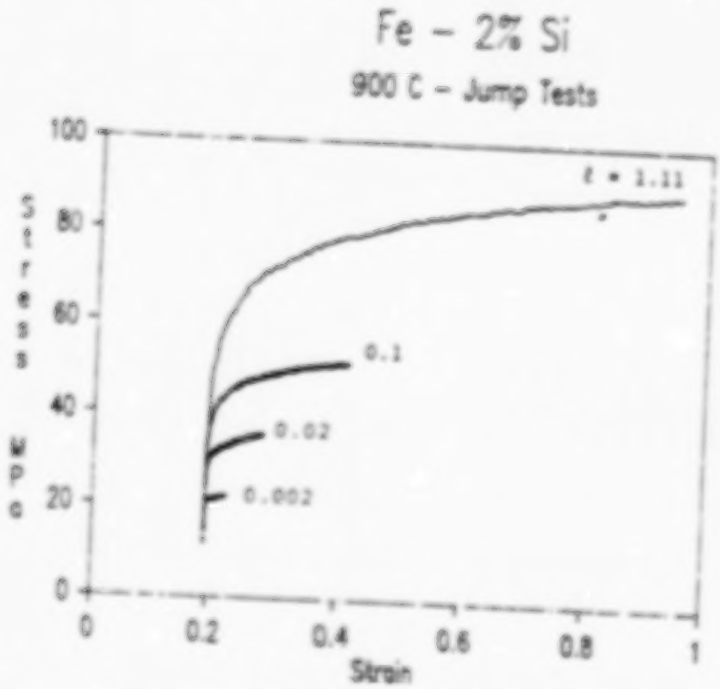

FIGURE 2. Strain Rate Jump Tests from the Same Initial Conditions. (Initial Strain Rate = 2×10^{-4} sec^{-1})

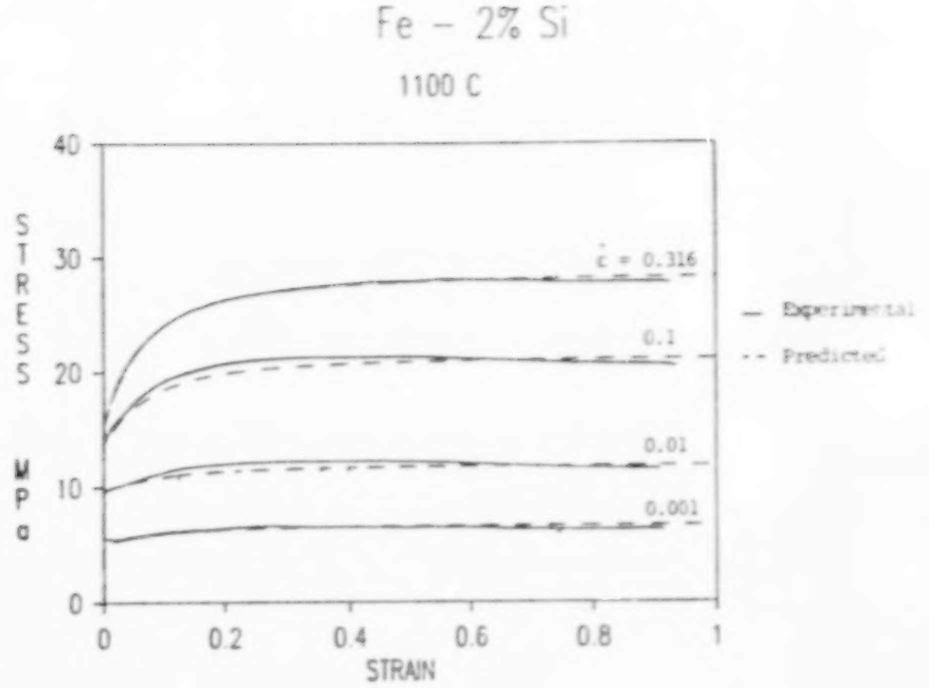

FIGURE 3. Predicted Stress/Strain Curves versus Experimental Data

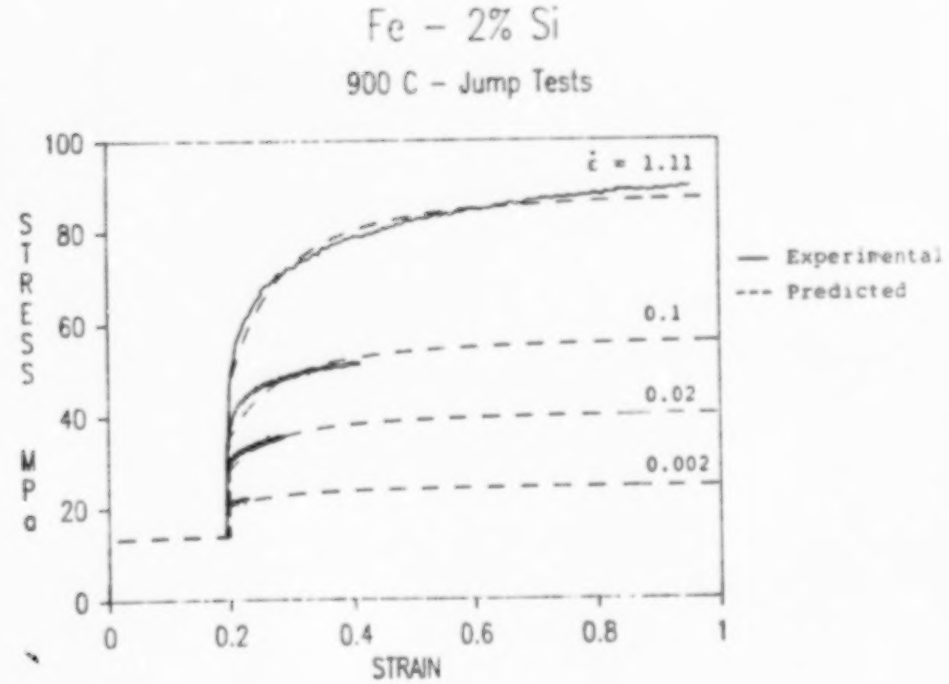

FIGURE 4. Predicted Strain Rate Jump Test, Stress/Strain Curves versus Experimental Data.

N88
21504
UNCLAS

N88-21504

PRESSURE INDUCED AGEING OF POLYMERS

I. Emri
Assistant Professor
Department of Mechanical Engineering
University of Ljubljana, Yugoslavia

W.G. Knauss
Professor of Aeronautics and Applied Mechanics
Graduate Aeronautical Laboratories
California Institute of Technology
Pasadena, California, U.S.A.

The nonlinearly viscoelastic response of an amorphous homopolymer is considered under aspect of time dependent free volume behavior. In contrast to linearly viscoelastic solids, this model couples shear and volume deformation through a shift function which influences the rate of molecular relaxation or creep. Sample computations produce all those qualitative features one observes normally in uniaxial tension including the rate dependent formation of a yield point as a consequence of the history of an imposed pressure.

I. INTRODUCTION

It is a well known fact that polymers change their physical response characteristics in a very significant manner when they are cooled or heated, and especially so when the temperature change spans the glass transition range. This behavior is exemplified, perhaps, most clearly in terms of mechanical relaxation or creep phenomena, though it is equally evident in optical, electrical and masstransport characteristics. These macroscopically observable phenomena are manifestations of the motion of segments of molecule chains relative to each other. This motion is controlled by both the thermal activation of the molecule segments and by the space available to these segments to move. This space is often associated with the concept of "free volume" and has a highly non-linear effect on the segment mobility in the sense that a change has a roughly exponential effect on the rate of segment motion. Thus small changes in free volume will produce very large changes in the mobility of molecule segments, and thus in the physical characterstics of the material.

The change in free volume has been most often connected with thermal changes where it has been associated with time-temperature trade-off in material characterization. However, volume changes arise not only from temperature alterations but also from the absorption of solvents and from mechanical stresses. The latter effect has been studied mostly in the context of the influence of pressure on the glass transition temperature.

Volume changes in polymers can occur over considerably long time scales, and it is a characteristic of these materials that the approach to equilibrium conditions occurs under ever decreasing rates of change. Thus equilibrium behavior of polymers is often only approached but not reached, in particular at temperatures below the glass transition

PRECEDING PAGE BLANK NOT FILMED

range. Thus Struik [1][1] has observed that creep (or relaxation) behavior of polymers below the glass transition keeps changing for some time after the material has been quenched to the "rigid" state. This change is first rather rapid after quenching and slows down with time to a steady behavior and occurs at a rate that is consistent with the decreasing free volume as it adjusts slowly to equilibrium conditions. The idea here is, that the quenching process ellicits a delayed volume consolidation which entails a lower and lower rate of molecular mobility.

While there seems to be little question regarding the qualitative correctness of these concepts, there is still considerable discussion with respect to the analytical representation or description of these processes. A particular stumbling block in this context seems to be our lack of understanding or experimental assessment of how the free volume approaches equilibrium conditions. On the one hand one finds that the appropriate experiments demand a very high degree of accuracy in volume measurements over long periods of time under extremely well controlled environmental conditions, while, on the other hand one needs to model and represent this behavior analytically in order to ascertain whether the postulated, physics-based model conforms to the measurements. Neither propositions are accomplished easily.

In this paper we shall be concerned with the mechanical behavior of polymers which undergo densification (vitrification) while simultaneously subjected to mechanical straining. In view of several unresolved issues with respect to representing the time-dependent effects of the quenching process we confine ourselves for now to vitrification resulting from the imposition of pressure. The work is almost exclusively computational in nature, based on the experimentally determined uniaxial relaxation behavior which corresponds to that of Solithane 113 (50/50 composition [2]), a polyurethane elastomer manufactured by the Thiokol Chemical Company in Trenton, N.J. The computations were motivated by high pressure experiments on the same material by K. Pae et alii [3], who appear to have used a somewhat differently formulated or processed version of the same material, which did not allow a point by point comparison. We offer these computations, therefore, as an indication of what the effect of time-dependent volume consolidation is on the subsequent mechanical behavior of the polymer. These results are in qualitative agreement with Pae's experiments.

2. THE MOLECULAR MECHANICS VIEW

In order to relate the following developments to the proper view of molecular mechanics it is appropriate to give consideration to how the molecular motion is related to the material properties when linearly viscoelatic behavior is involved and when the stress state induces non-linearly viscoelastic response. We start with the proposition that molecular conformations of the molecule chains and the interdependent motion of their segments give rise to the macroscopically observed time-dependent behavior. Short-time response derives from near-range interactions while the long-time behavior is governed by long-range interactions with a spectral distribution spanning the whole range of time dependence. As long as the macroscopic deformation gradients (strains) are so small that the molecular topology is not disturbed greatly, (not rubber-like

---

[1] Numbers in brackets refer to references at the end of the paper.

deformations), one can argue that the molecular interactions as characterized by the spectral distribution functions of relaxation or creep remain essentially unchanged. Stating this assumption is an alternate way of saying that molecule segments move according to the local constraints offered by neighboring molecules; their rate of motion is governed by their mutual proximity but the type of motion such as slippage or rotation are not affected strongly. Thus one expects that the distribution functions appropriate for infinitesimal deformations, i.e. linear viscoelasticity, apply. Specifically, we assume that this understanding holds for both viscoelastic response in shear and volume deformation.

One must admit that our knowledge of molecular motion under a variety of deformation gradients is rather limited. Thus it is sometimes suggested, in particular in connection with thermal changes below the glass transition temperature, that certain types of molecular motions cease to occur the lower the temperature becomes. In terms of a phenomenological description such changes would entail changes in the spectral distribution functions. However, in order to investigate such potential changes it is necessary to develop improved descriptions of constitutive behavior, and it is just that purpose we have in mind in this contribution. Thus we feel entitled to assume at this stage of development that the spectral functions remain unchanged and leave the examination of deviations from this assumption to future experimental and analytical scrutiny.

We limit ourselves in this inital investigation to materials which are thermorheologically simple. This restriction is assumed primarily because we do not understand very well the reason for the breakdown of thermorheological simplicity from a molecular point of view, though we surmise that the breakdown results from the mechanical interaction of domains of multiple phases of different constituents in the case of thermorheologically non-simple materials. In the latter context it would be necessary to apply the considerations outlined below to each constituent in the (molecular) composite but with the constraint of mechanically compatible interactions imposed.

Some aspects of this work have been presented in an earlier publication [4] where the purely mechanical response as well as the effect of certain thermal histories were considered from a unified point of view besides the pressure-ageing. While we shall deal here only with the latter topic, we shall next discuss the complete set of constitutive equations which apply to the former set of conditions and then specialize them to the problem of pressure-ageing.

3. GENERAL EQUATIONS

In adhering to the assumptions stated towards the end of the previous section we choose the material description to be governed by the functions of linear viscoelasticity, except that the time-temperature shift function of thermorheologically simple solids is a more general function of the time-dependent and thus instantaneous volume change, regardless of whether the volume change is induced thermally, mechanically or by solvent swelling. This shift function ϕ is considered to be a functional of the temperature T, of the solvent concentration c and of the mechanically induced dilatation θ, that is

$$\phi = \phi\{T,c,\theta\} \tag{1}$$

where curly brackets denote that ϕ is a functional of T,c, and θ. Doolittle [5] expressed this factor through the free volume by

$$\log\phi = \frac{b}{2.3}\left(\frac{1}{f} - \frac{1}{f_o}\right) \tag{2}$$

where f is the fractional free volume defined in terms of the total volume V of the solid and the free volume V_f as

$$f = \frac{V_f}{V} \tag{3}$$

and f_o denotes the fractional free volume at some reference temperature. We consider the free volume to depend on the temperature history and on the strain history, as well as on the history of swelling. We assume that at any instant in time the variable f is a linear functional of the temperature, solvent and of the dilatational stress component.

Linearly viscoelastic volume behavior requires that the dilatation θ is related to the first stress invariant τ_{kk} through

$$\theta(t) = \frac{1}{3}M(t) * d\tau_{kk} \tag{4}$$

where M(t) represents the bulk creep compliance and the star notation indicates Stieltjes convolution; this statement is true within the context of the present discussion provided the volume change is so small that the creep function M(t) is not affected. Similarly, we define a volume creep function for thermal expansion $\alpha(t)$ such that under a sufficiently small thermal excursion history (small volume change) the volume change is given by [4].

$$\Delta V_T = V_o{\cdot}\alpha(t) * dT \tag{5}$$

where V_o is a Reference volume. Let us leave the question as to whether the time scale of $\alpha(t)$ needs to be "temperature-reduced" moot for the moment. Finally, we would postulate a solvent related volume creep function $\gamma(t)$ which by analogy with (4) and (5) yields volume changes under a hypothetical instantaneous change in concentration "c" to

$$\Delta V_c = V_o{\cdot}\gamma(t) * dc \tag{6}$$

With the definitions (4),(5), and (6) in mind and the assumption of a linear dependence of the space for molecular motion on the volume change we write the contribution to this motion space f as

$$f = f_o + A.\alpha(t)*dT + B.M(t)*d\tau_{kk} + c.\gamma(t)*dc \tag{7}$$

where the constants A,B, and c need to be generally determined experimentally. They may possibly all have the same value.

Substitution of (7) into the Doolittle equation (2) renders for the instantaneous shift factor

$$\log\phi = \frac{b}{2.3 f_o}\,\frac{A.\alpha(t)*dT + B.M(t)*d\tau_{kk} + c.\gamma(t)*dc}{f_o + A.\alpha(t)*dT + B.M(t)*d\tau_{kk} + c.\gamma(t)*dc} \tag{8}$$

Note that if $\alpha = const$ and $\tau_{kk}=0$, $c=0$ this expression reduces to the standard Doolittle equation and thus to the WLF equation. In the present case this shift factor is a function of the volume history through the functionals of dilatation, temperature and solvent concentration. More specifically these latter functionals involve also the history of $\phi(t)$; for example, $\alpha*dT$ depends on the history of $\phi(t)$. Equation (8) is thus an implicit relation for ϕ.

The shift factor modifies the (material-internal) rate with which viscoelastic functions change. If an environmental change causes a constant change in the volume components, then ϕ multiplies the relaxation or retardation time in the material functions. We now assert that in general the argument in the creep functions $\alpha(t)$, $\gamma(t)$ and M(t) must be "reduced" by the instantaneous shift factor, where the shift function ϕ is itself a function of the environmental histories.

Lee suggested that the "standard" time-temperature shifting, demonstrated for time-independent temperatures, be valid instantaneously under transient thermal conditions [6,7]. We shall assume similarly that the shift relation (8) for ϕ is valid instantaneously while incorporating the effect of mechanically and solvent induced volume change. We have thus for a reduced time for the material behavior

$$dt' = \frac{dt}{\phi(t)} \quad or \quad t'(t) = \int_o^t \frac{du}{\phi\{T(u),c(u),\theta(u)\}} \tag{9}$$

Let τ_{ij} and ϵ_{ij} denote, respectively, the components of the Cauchy stress and of the (small) strain. In terms of the deviatoric stresses S_{ij} and deviatoric strains e_{ij} the stress-strain relations are (the summation convention for repeated indices applies)

$$S_{ij} = 2\int_{-\infty}^{t} \mu[t'(t) - \xi'(\xi)]\frac{\partial e_{ij}(\xi)}{\partial\xi}\, d\xi \tag{10a}$$

$$\tau_{kk} = 3\int_{-\infty}^{t} K[t'(t) - \xi'(\xi)]\frac{\partial\theta(\xi)}{\partial\xi}\, d\xi\,, \quad K*M = t \tag{10b}$$

$$t'(t) - \xi'(\xi) = \int_{\xi}^{t} \frac{du}{\phi\{T(u),c(u),\theta(u)\}} \tag{9a}$$

along with (8) for $\phi(t)$[2]

Equations (8), (9), and (10) are coupled and implicit relations for the stress history if, e.g., the strain history is prescribed at a material point[3] in dependence on the presumably known thermal and solvent history. Alternately, if the stress and environmental histories are prescribed - in particular when the stress is zero - these equations are implicit relations for the time-dependent volume change ϵ_{kk}.

4. EFFECT OF PRESSURE HISTORY ON UNIAXIAL DEFORMATION BEHAVIOR

In this section we are interested in demonstrating the profound effect which the simple concept of time-dependent volume change has on viscoelastic behavior when such volume change is allowed to affect the time-shift phenomenon. Struik's experiments revealed a time-dependent drift of properties toward an equilibrium behavior after initial quenching. Because no chemical changes were involved this change process was termed "physical ageing." Similar to the experiments on physical ageing by Struik [1] time dependent volume compaction under pressure changes the viscoelastic response of the material, tending to "push" the solid "towards glassy behavior" and we may then speak of an ageing process induced by pressurization. On the other hand, the imposition of a tensile stress causes an opposing trend. Let us consider uniaxial deformation histories with constant rate of straining and consider the response under two types of pressure histories: In one case let the pressure be applied just prior to or with the start of uniaxial straining; in the other case let straining start at various times after the pressure has been imposed. In this latter case the effect of time dependent volume consolidation (ageing) on the time scale of non-linearly viscoelastic will become apparent. Let us turn first to the case of

a) Simultaneous Pressurization and Straining.

We assume the temperature to remain constant[4] throughout these strain histories and consider a sudden step pressure P applied at time t=0 while a constant strain rate history $\dot{\epsilon}_o = const$ is imposed simultaneously. Thus,

$$\sigma_{kk} = 3.P.h(t) \tag{11}$$

and

$$\epsilon_{11} = \dot{\epsilon}_o.t, \qquad t \geq 0 \tag{12}$$

Let E(t) be the relaxation modulus for (infinitesimal) uniaxial deformation as shown in Figure 1 and represented by a Dirichlet series

$$E(t) = E_o + \sum_{n=1}^{18} E_n e^{-t/\tau_n} \tag{13}$$

---

[2] Note that with the present notation $\epsilon_{kk}(t)=\theta(t)+\alpha(t)\cdot\Delta T+\gamma(t)\cdot\Delta c$.

[3] We choose not to address here the wider problem of thermal and solvent *diffusion* and their interaction with the state of stress or its field.

[4] Actually pressurization produces in general also a temperature rise, which we neglect in these illustrations.

where the E_n and τ_n are given in Table I. These coefficients were determined in a collocation procedure based on the data in Figure 1.

Table I.
$E_e = 26.613$ [bar]

n	E_n [bar]	τ_n [min]	
1	677.827	1	10^{-8}
2	8.527	3.162	10^{-8}
3	545.344	1	10^{-7}
4	876.463	3.162	10^{-7}
5	564.947	1	10^{-6}
6	584.252	3.162	10^{-6}
7	340.672	1	10^{-5}
8	286.495	3.162	10^{-5}
9	262.926	1	10^{-4}
10	120.850	3.162	10^{-4}
11	22.663	1	10^{-3}
12	28.793	3.162	10^{-3}
13	5.446	1	10^{-2}
14	3.076	3.162	10^{-2}
15	1.561	1	10^{-1}
16	0.253	3.162	10^{-1}
17	0	1	
18	0.072	3.1622	

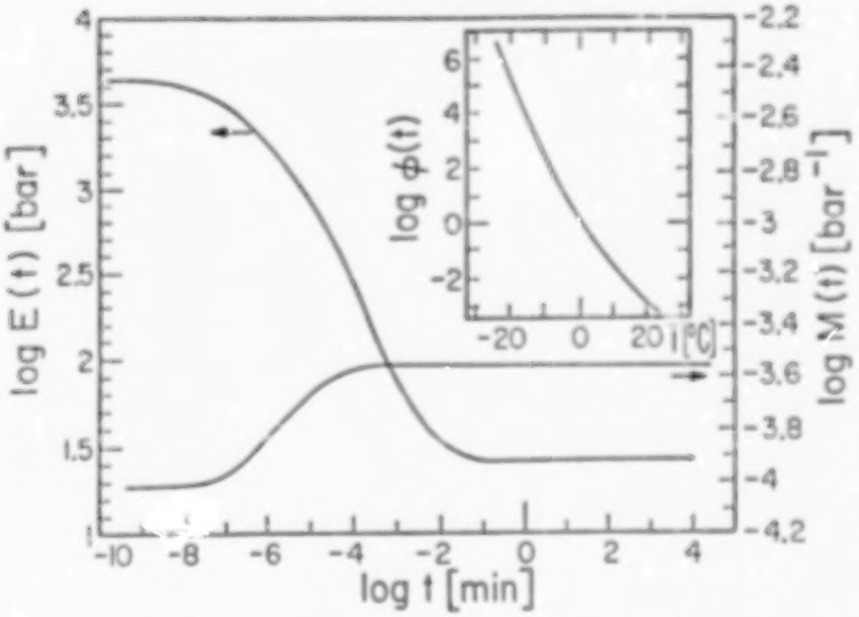

Figure 1. Relaxation modulus for uniaxial state of stress. Bulk creep compliance and thermal shift factor used for pressure related computations on Solithane 113 (50/50).

Further, let M be the corresponding bulk creep compliance similarly represented by

$$M(t) = M_e + \sum_{n=1}^{9} M_n(1 - e^{-t/\lambda_n}) \tag{14}$$

which is also indicated in Figure 1, the coefficients M_n and λ_n being listed in Table II. In view of the fact that we are concerned in this section with qualitative results we estimated the coefficients M_i from data offered by Pae [3] through collocation.

Table II.
$M_e = 9.1811\ 10^{-5}\ [bar^{-1}]$

n	M_n [bar^{-1}]	λ_n [min]	
1	$5.619\ 10^{-7}$	3.162	10^{-8}
2	$17.826\ 10^{-8}$	1	10^{-7}
3	$0.294\ 10^{-4}$	3.162	10^{-7}
4	$0.192\ 10^{-4}$	1	10^{-6}
5	$0.415\ 10^{-6}$	3.162	10^{-6}
6	$0.343\ 10^{-6}$	1	10^{-5}
7	$0.401\ 10^{-5}$	3.162	10^{-5}
8	$8.468\ 10^{-6}$	1	10^{-4}
9	$10.351\ 10^{-6}$	3.162	10^{-4}

If τ_{11} and ϵ_{11} are the increments of stress and strain from the pressure and the volume strain the stress strain relations are then

$$\tau_{11}(t) = \int_0^t E[t'(t) - \xi'(\xi)]\, \frac{d\epsilon_{11}(\xi)}{d\xi}$$

$$= \dot{\epsilon}_o \int_0^t E[t'(t) - \xi'(\xi)]\, d\xi \tag{15a}$$

$$\theta(t) = \int_0^t M[t'(t) - \xi'(\xi)]\, \frac{d}{d\xi}\, [P(\xi) + \frac{1}{3}\, \tau_{11}(\xi)]\, d\xi \tag{15b}$$

where, again

$$t'(t) = \int_0^t \frac{du}{\phi[T,O,\theta(u)]} \quad \text{and} \quad \xi'(\xi) = \int_0^\xi \frac{du}{\phi[T,O,\theta(u)]} \tag{16}$$

$$\ln\phi(T,O,\theta) = -\frac{b(T)}{f_o(T)}\, \frac{B.\theta(t)}{f_o(T)+B.\theta(t)} \tag{17}$$

In these computations we used B=1 because we do not know K(t) or M(t) closely. The properties in Figure 1 are defined for 0°C. To make use of these at different temperatures we shift the functions according to the shift factor inset in that figure. However, the parameters b(T) and $f_o(T)$ in (17) must be adjusted to the appropriate temperature [8]. It remains to evaluate equations 15-17 numerically.

In Figure 2 we show for reference purposes the non-linear response at $-20°C$, 2°C below the glass transition, under zero imposed pressure as the uniaxial strain rate is varied. One notices the appearance of a yield phenomenon, with the yield stress and yield strain increasing with the strain rate.

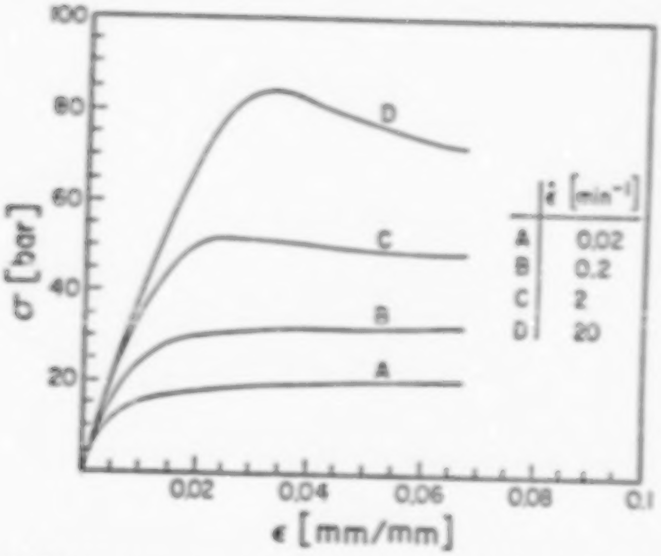

Figure 2. Uniaxial Stress response to constant strain rates for atmospheric pressure and for properties shown in Figure 1.

In terms of the present physical model the appearance of the yield phenomenon has the following explanation. The imposition of a pressure causes a decrease in the (free) volume and thus a vitrification of the solid. However, the imposition of a tensile stress counteracts this vitrification process and produces, with increasing strain (stress) an increase in the rate of molecular relaxation through a change in the time-shift function. Whether one achieves a yield phenomenon or not depends on the competition between the pressure-induced solidification and the tension-induced volume increase. Once the two rates roughly balance each other the stress reaches a plateau such as seems to be approximately the case for curve "B" in Figure 2 . For higher strain rates the tension-induced volume increase occurs faster than the solidification due to the imposition of the pressure thus leading to a relaxation process which overpowers the stress increase due to straining. We shall see that this phenomenon occurs again later in an even more pronounced fashion depending on the past vitrification history of the material.

Figure 3a illustrates the effect of increasing the pressure while keeping the temperature constant just below the glass transition ($-20°C$) and for a fixed strain rate of $\dot{\epsilon}=20\text{min}^{-1}$. Note again the occurance of the yield phenomenon, with the yield stress increasing with pressure. This observation merely substantiates the fact that a higher environmental pressure requires a higher tension in order to overcome the pressure-induced vitrification process. However, the yield phenomenon appears to depend also on the fact that the volume change induced by the uniaxial straining lags behind the strain due to the viscoelastic volume response. This statement becomes evident when one looks at the identical strain and pressure histories but at a temperature well above the glass transition temperature. Thus, Figure 3b shows results for the same pressure and strain histories as Figure 3a, but about 12 degrees above the glass temperature. Here one notes the absence of the yield behavior because first, the temperature is so high that pressure-induced volume decrease occurs almost instantaneously, and second, the volume change produced by the uniaxial straining is very much in phase with the strain so that any relaxation process occurs simultaneously with the straining rather than being delayed viscoelastically.

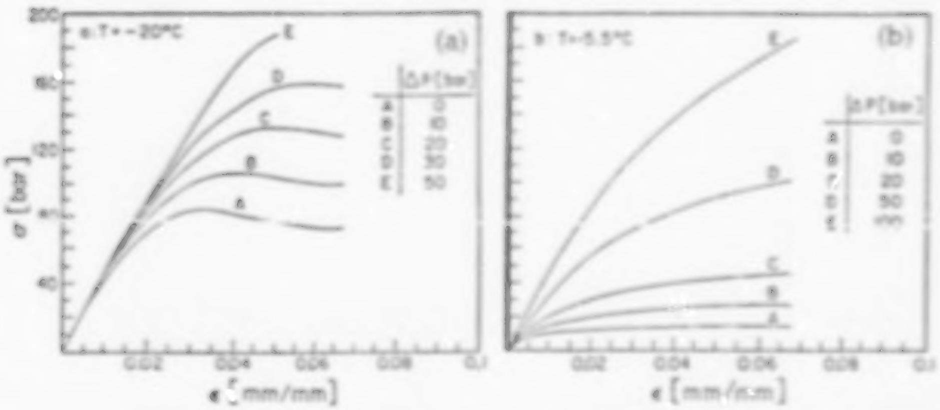

Figure 3. Simultaneous pressure application and imposition of strain rate of $\dot{\epsilon}=20\,\mathrm{min}^{-1}$. a: $T=-20°C$; b: $T=-5.5°C$.

b) Pressure Ageing

Consider next the effect of imposing pressure on the material at time t=0 and subjecting it to straining after different times t_1 have passed. The equations governing this history are similar to (14) and are given by

$$\tau_{11}(t) = \dot{\epsilon}_o h(t-t_1)\int_{t_1}^{t} E[t'(t)-\xi(\xi)]d\xi \tag{18a}$$

$$\theta(t) = P.M[t'(t)] + h(t-t_1)\frac{1}{3}\int_{t_1}^{t} M[t'(t)-\xi(\xi)]\frac{d\tau_{11}(\xi)}{d\xi}d\xi \tag{18b}$$

where $t'(t)$ and $\xi(t)$ are still given by (16) and (17).

Solutions to these equations for several situations are given in Figures 4a to 4d. Several features stand out and deserve attention: The effect of the time dependent consolidation process is clearly evident in that longer times between pressurization and straining gives rise to markedly stiffer material response and an increase in yield stress with this ageing time as noted in reference 3. Again, the competitive effect of pressure-induced consolidation with the tension-induced volume increase is very evident as in the cases considered in Figures 3a and b, except that the effect is more pronounced because with increased ageing time the consolidation can progress more completely and thus give rise to more pronounced relaxation upon reaching a sufficiently high tension-induced dilatation. Finally, Figure 4c illustrates again the behavior at about 12 degrees above the glass transition; one notes again that at this elevated temperature the adjustment of the (free) volume to equilibrium conditions occurs very rapidly so that the tension-induced volume change is very much in phase with the strain. As a consequence the time-dependence of the bulk deformation barely enters the considerations and the stress-strain curves for the material "aged" to varying degrees are virtually indistinguishable. Clearly, Figures 4a-c illustrate the importance of the time-dependent volume behavior of polymers in their non-linear mechanical characteristics.

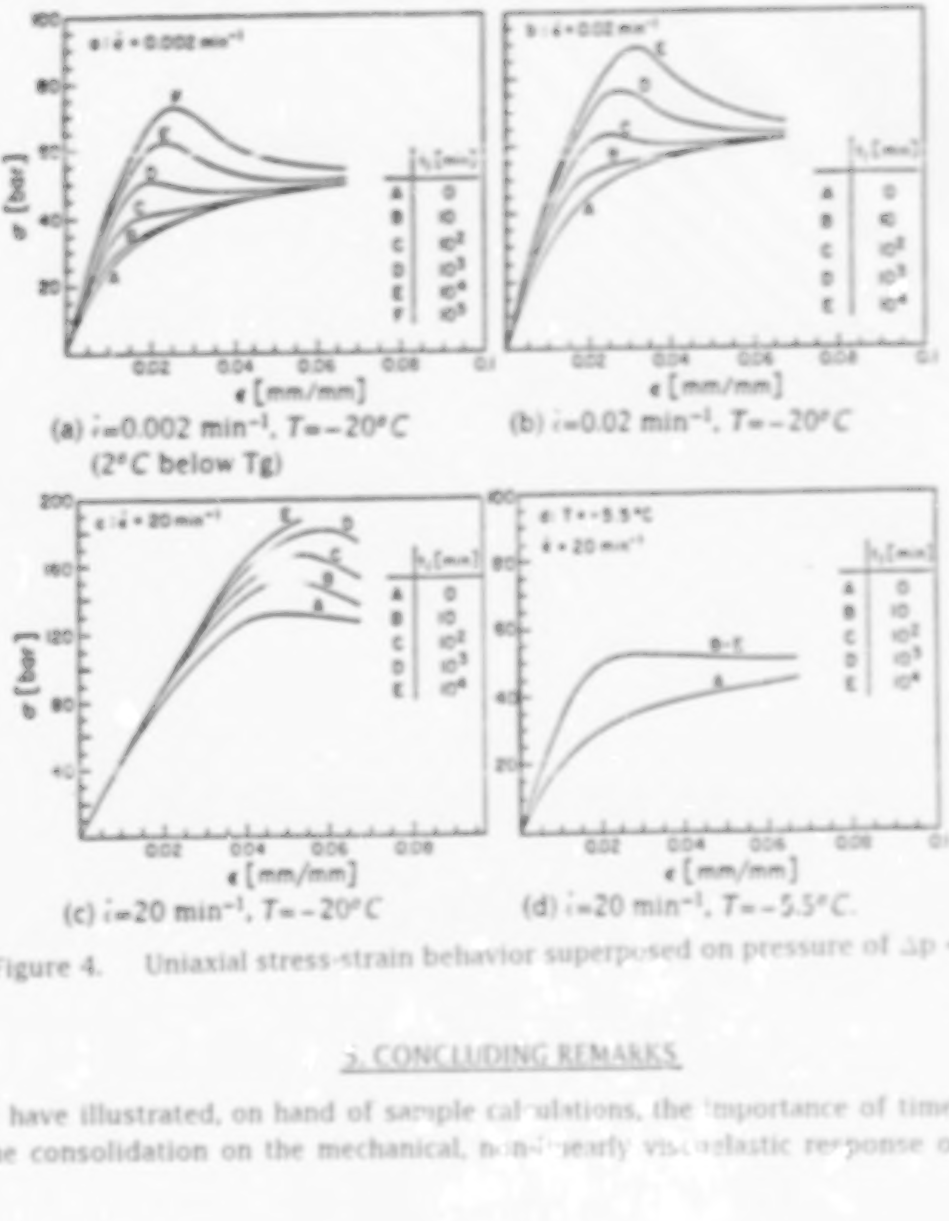

(a) $\dot{\epsilon}$=0.002 min^{-1}, T=−20°C
(2°C below Tg)

(b) $\dot{\epsilon}$=0.02 min^{-1}, T=−20°C

(c) $\dot{\epsilon}$=20 min^{-1}, T=−20°C

(d) $\dot{\epsilon}$=20 min^{-1}, T=−5.5°C.

Figure 4. Uniaxial stress-strain behavior superposed on pressure of Δp = 20 bar.

5. CONCLUDING REMARKS

We have illustrated, on hand of sample calculations, the importance of time-dependent volume consolidation on the mechanical, non-linearly viscoelastic response of polymers.

The temperature and deformation rates play an important part in this behavior, in large measure because these variables determine the rate of change of the (free) volume.

We point out in closing this presentation that the non-linear effects considerered here derive only from the single physical phenomenon of molecular motion and do not incorporate such macroscopic physical phenomena as crazing or fracturing, both of which effects give rise to (additional) non-linear "consitutive" behavior. The presently discussed behavior is, however, a precursor to the latter physical phenomena and can hardly be neglected in their time-dependent description. Thus one would expect that the "molecular" yielding exemplified here is the reason why zones of mechanic[illegible] unstable material behavior develop in materials around zones of stress concentration, which zones develop possibly into craze zones.

6. REFERENCES

1. Struik, L.C.E., - *Physical Ageing in Amorphous Polymers and Other Materials*, Elsevier Sci. Pub. Co., Amsterdam, 1978.
2. Muller, H.K., Knauss, W.G., - The Mechanical Characterization of Solithane 113 in the Swollen and Unswollen State, GALCIT SM Report 67-8, CHECIT PL 68-2, California Institute of Technology, Pasadena, California, U.S.A.
3. Pae, K.D., Kijayan, K., Tang, C.L., - Ageing Time Dependence of Mechanical Properties of Elastomeric Glasses at High Pressure. Personal communication in the form of an undated report draft.
4. Knauss, W.G., Emri, I. - Volume Change and the Non-Linearly Thermo-Viscoelastic Constitution of Polymers, GALCIT SM Report 85-26; to appear in Polymer Engineering and Science, edited by A. Yee, 1987.
5. Doolittle, A.K., - Studies in Newtonian Flow. II. The Dependence of the Viscosity of Liquids on Free-Space, J. Appl. Phys., *22*, 12, p. 1471, 1951.
6. Lee, E.H., Rogers, T.G., - Solution of Viscoelastic Stress Analysis Problems Using Measured Creep or Relaxation Functions, J. Appl. Mech., *30*, 1, p. 127, 1963.
7. Morland, L.W., Lee, E.H. - Stress Analysis for Linear Viscoelastic Materials with Temperature Variation, Trans. Soc. Rheol., *IV, p. 233, 1960.*
8. Schwarzl, F.R., Zahradnik, F. - The Time Temperature Position of the Glass-Rubber Transition of Amorphous Polymers and the Free Volume, Rheologica Acta, *19*, 2, p. 137, 1980.

N88
21505
UNCLAS

N88-21505

A SIMPLIFIED ORTHOTROPIC FORMULATION OF THE VISCOPLASTICITY THEORY BASED ON OVERSTRESS

M. Sutcu[1] and E. Krempl
Department of Mechanical Engineering,
Aeronautical Engineering and Mechanics
Rensselaer Polytechnic Institute
Troy, NY 12180-3590

An orthotropic, small strain viscoplasticity theory based on overstress is presented. In each preferred direction the stress is composed of time (rate)-independent (or plastic) and viscous (or rate-dependent) contributions. Tension-compression asymmetry can depend on direction and is included in the model. Upon a proper choice of a material constant one preferred direction can exhibit linear elastic response while the other two deform in a viscoplastic manner.

INTRODUCTION

Recently directionally solidified alloys, nickel base single crystal superalloys and other anisotropic metallic composites have attracted interest for use in gas turbines and other high temperature applications. The usual high temperature phenomena such as creep, relaxation, rate sensitivity, recovery and aging found in nearly isotropic materials are also present in these materials. However, all these properties are now dependent on direction.

For the prediction of life of components made of anisotropic materials and operating at elevated temperature the deformation behavior must be known in addition to anisotropic damage accumulation laws. It is the purpose of this paper to introduce an orthotropic version of the viscoplasticity theory based on overstress (VBO), (the transversely isotropic case can be recovered as a specialization). The uniaxial and the isotropic version of VBO were introduced previously [1,2]. The theory is of the unified type (plasticity and creep are not represented by separate constitutive equations) and does not employ the concepts of a yield surface and associated loading and unloading conditions. In the present form of the theory aging and recovery are not accounted for but can be added if need arises.

---

[1] Now with General Electric Corporate R & D Center, Schenectady, NY.

+ C.Q

The orthotropic formulation was derived with the help of tensor function representation theorems [3] and the uniaxial version of the VBO. Simplicity was a goal as long as it was consistent with the necessity of modeling key material phenomena. The tensor function approach is not restricted to the orthotropic case and can be applied to other material symmetries as well.

UNIAXIAL PROPERTIES OF VBO INCLUDING ASYMPTOTIC SOLUTIONS

In the formulation of VBO special consideration was given to the modeling of elastic regions in addition to the usual time-dependent properties [1]. A useful property of the system of nonlinear differential equations is the existence of asymptotic solutions which are algebraic expressions. They apply mathematically at infinite time in a constant strain rate or creep, or relaxation test. However, it is our experience that these asymptotic solutions can be used with confidence when plastic flow is fully developed in a tensile test [1,4].

A schematic of the properties of the model in a tensile test is given in Fig.1. The evolution of the stress σ, the equilibrium stress g (which is reached when all rates approach zero) and of the quantity $f = E_t \epsilon$ are shown. It is introduced for modeling a nonzero slope E_t in the plastic region even when the asymptotic solutions are attained. The asymptotic values are indicated by { } in Fig.1. It is seen that the stress consists of $\{\sigma - g\}$, the time-independent or viscous contribution, of $\{g - f\}$ which represents the time-independent or plastic part and of the portion which grows linearly with ϵ; it is termed the hardening contribution. It is zero when the tangent modulus E_t is set to zero, see [1,2] for further details. In a neighborhood of the origin, σ and g almost coincide and nearly elastic behavior is represented.

In the formulation of the anisotropic version of VBO the elastic properties can depend on direction. In addition, it was felt necessary to have separate directional properties for the viscous, the plastic and the hardening contributions to the stress. (It is important to note that the theory does not separately formulate plastic and time-dependent constitutive equations. However, the asymptotic solutions of the theory permit such a distinction.) The reason for this distinction lies in the realization that different material constituents may be used in different directions (example; directionally solidified alloys) or that the microstructure may develop an orientation dependence. Moreover, fibers with predominantly elastic behavior may run in one direction and the viscoplastic matrix may control the behavior in other directions.

AN ORTHOTROPIC VISCOPLASTICITY THEORY BASED ON OVERSTRESS

In [6] a fully invariant theory is developed with arbitrary orientation of the principal material axes relative to the coordinate system used in the representation of the tensors. Presently we assume that the coordinate system in which the tensor components are given coincides with the material axes. Vector notation is used with

$$\sigma_{11}=\sigma_1\,,\quad \sigma_{22}=\sigma_2\,,\quad \sigma_{33}=\sigma_3\,,\quad \sigma_{23}=\sigma_4\,,\quad \sigma_{13}=\sigma_5 \quad\text{and}\quad \sigma_{12}=\sigma_6 \tag{1}$$

and with a similar convention for the small strain ϵ except that engineering shear strains are used for the vector components ϵ_4 through ϵ_6.

The evolution of the stress is governed by

$$d\underset{\sim}{\sigma}/dt = \underset{\sim}{C}[d\underset{\sim}{\epsilon}/dt - d\underset{\sim}{\epsilon}^{in}/dt] \tag{2}$$

where C is the matrix of elastic constants. The inverse of $\underset{\sim}{C}$, $\underset{\sim}{C}^{-1}$ is given by, see [5]

$$\underset{\sim}{C}^{-1} = \begin{bmatrix} 1/E_1 & -\nu_{21}/E_2 & -\nu_{31}/E_3 & 0 & 0 & 0 \\ & 1/E_2 & -\nu_{32}/E_3 & 0 & 0 & 0 \\ & & 1/E_3 & 0 & 0 & 0 \\ \text{Symmetric} & & & 1/G_{23} & 0 & 0 \\ & & & & 1/G_{13} & 0 \\ & & & & & 1/G_{12} \end{bmatrix} \tag{3}$$

The inelastic strain rate $d\underset{\sim}{\epsilon}^{in}/dt$ is represented by

$$d\underset{\sim}{\epsilon}^{in}/dt = K[\Gamma]\,\underset{\approx}{R}\underset{\sim}{x} \tag{4}$$

where the positive function $K[\Gamma]$ is a repository of viscous effects ($K[\Gamma] = 1/(Ek[\Gamma])$ where $k[\Gamma]$ is the viscosity function used in [1]). The dimensionless components of the matrix $\underset{\sim}{R}$ are called the inelastic lateral ratios. The invariant Γ is defined as

$$\Gamma = (\underset{\sim}{x}^T \underset{\approx}{V}\underset{\approx}{V}\underset{\sim}{x})^{1/2} + \underset{\sim}{a}^T \underset{\approx}{V}\underset{\sim}{x} \tag{5}$$

with $\underset{\sim}{a}^T = [a_1\; a_2\; a_3\; 0\; 0\; 0]$, where the dimensionless components a_i are zero when the viscous effects are the same in tension and compression.

$\underset{\sim}{V}$ is the matrix of the viscous lateral ratios. The overstress is $\underset{\sim}{x} = \underset{\sim}{\sigma} - \underset{\sim}{g}$. The equilibrium stress evolves according to

$$d\underset{\sim}{g}/dt = \psi[\Gamma]\underset{\sim}{B}[\Gamma](d\underset{\sim}{\varepsilon}/dt - \theta^2 d\underset{\sim}{\varepsilon}^{in}/dt) \tag{6}$$

This growth law is very similar to the one used in [1,2]. The invariant θ is given by

$$\theta = \Big((\underset{\sim}{g}^T\underset{\sim}{S}\,\underset{\sim}{S}\,\underset{\sim}{g})^{1/2} + \underset{\sim}{b}^T\underset{\sim}{S}\,\underset{\sim}{g}\Big)/A \tag{7}$$

with $\underset{\sim}{b}^T = [b_1\ b_2\ b_3\ 0\ 0\ 0]$. The dimensionless components b_i are zero when the plastic effects in tension and compression are equal. The analysis of the asymptotic behavior of the uniaxial equivalent of (6) in [1] shows that $\{g - f\}$ in Fig.1 equals the constant A which has the dimension of stress. The dimensionless components of the matrix $\underset{\sim}{S}$ are the plastic lateral ratios. The dimensionless components of $\underset{\sim}{B}$ are called shape ratios and are initially equal to the components of $E_1\underset{\sim}{C}^{-1}$, called the elastic ratios. The positive, decreasing shape function $\psi[\Gamma]$ has the dimension of stress with $\psi[0]$ slightly less than the elastic modulus E_1, see [1]. For simplicity the tangent modulus E_t was set equal to zero so that f in Fig.1 is zero and all the stress-strain curves become ultimately horizontal.

Due to orthotropy, the matrices $\underset{\sim}{R}$, $\underset{\sim}{V}$, $\underset{\sim}{S}$ and $\underset{\sim}{B}$ all have the same representation as the matrix $\underset{\sim}{C}^{-1}$ in (3) and have therefore nine independent components. The components of each matrix can be selected independently to model the observed directional dependence of the various material properties.

The initial elastic properties are controlled by $\underset{\sim}{C}$ as in the case of elasticity. The evolution of the inelastic strain rates are influenced by $\underset{\sim}{R}$ and $\underset{\sim}{V}$. They also contribute to the asymptotic overstress $\{\underset{\sim}{x}\}$, see Fig.1, given by

$$\{\underset{\sim}{x}\} = \underset{\sim}{R}^{-1}\, d\underset{\sim}{\varepsilon}/dt/K[\{\Gamma\}] \tag{8}$$

The asymptotic time-independent or plastic contribution to the stress is controlled by the invariant θ through

$$\{\theta\}^2 = 1 \tag{9}$$

and it is seen from (7) that the directional properties are controlled by $\underset{\sim}{S}$ alone.

Detailed analysis in [6] shows that the matrix $\underset{\sim}{B}$ together with the shape function $\psi[\Gamma]$ controls the "knee" of the stress-strain curves in different directions.

A simplified version which has been shown to be useful [6] is to set $\underset{\sim}{R} = \underset{\sim}{B}^{-1} = E_1\underset{\sim}{C}^{-1}$ and to choose $\underset{\sim}{S}$ and $\underset{\sim}{V}$ independently. This choice permits the independent adjustment of the viscous and plastic asymptotic contributions to the stress. Within this choice it is possible to model

i) purely elastic behavior under a hydrostatic state of stress,

ii) linear elastic behavior in any of the preferred directions while the other directions behave in a viscoplastic manner.

This last property is very useful for modeling fiber reinforced materials. It should also be stressed that the theory permits the modeling of tension/compression asymmetry which depends on direction through the dimensionless vectors $\underset{\sim}{a}$ and $\underset{\sim}{b}$.

The capabilities of the theory are demonstrated in Figs.2 through 4. They depict the response of a transversely isotropic material to a constant strain rate tensile test in the 1- and 3-directions, respectively. In Fig.2 $\underset{\sim}{R} = \underset{\sim}{S} = \underset{\sim}{V} = \underset{\sim}{B}^{-1} = E_1\underset{\sim}{C}^{-1}$ and the evolution of the stress and of the equilibrium stress are governed by the values of $\underset{\sim}{C}^{-1}$. It is seen that the elastic modulus, the stress and the overstress in the 3-direction are always larger than in the 1-direction. When S_{33} and V_{33} are set equal to zero (all other quantities are the same as in Fig.2) the response in the 3-direction is nearly linear elastic whereas that in the 1-direction is unaffected, see Fig.3. When S_{33} is set equal to 0.5 (instead of 50/35 used in Fig.2; all other quantities are unchanged from Fig.2) the curves of Fig.4 result. This choice will increase $\{g_{03}\}$, the plastic or time independent part of the stress, but will leave the overstress, the viscous contribution to the stress, unchanged. Due to the nature of the constants the equilibrium solution has not been attained within the limits of the graph in Fig.4.

The above represents only part of the capabilities of the theory developed in [6]. It includes an incompressible inelastic, deviatoric formulation. Further developments are given in [7]. The theory needs to be applied to real anisotropic materials so that the material functions and constants can be identified and the usefulness of the theory be demonstrated.

ACKNOWLEDGEMENTS

This work was initially supported by NASA under Grant NAG3-262. Support of Rensselaer Polytechnic Institute enabled the completion of the task. The second author acknowledges the support of the National Science Foundation.

REFERENCES

1. Krempl, E., J.J. McMahon and D. Yao, "Viscoplasticity Theory Based on Overstress with a Differential Growth Law for the Equilibrium Stress," in print, Mechanics of Materials.

2. Yao, D. and E. Krempl, "Viscoplasticity Based on Overstress. The Prediction of Monotonic and Cyclic Proportional and Nonproportional Loading Paths of an Aluminum Alloy," Int. J. of Plasticity, 1, 259-274 (1985).

3. Boehler, J.P., "A Simple Derivation of Nonpolynomial Constitutive Equations in Some Cases of Anisotropy," ZAMM, 59, 157-167 (1979).

4. Krempl, E., "The Role of Servocontrolled Testing in the Development of the Theory of Viscoplasticity Based on Total Strain and Overstress," Mechanical Testing for Deformation Model Development, ASTM STP 765. R.W. Rohde and J.C. Swearengen, American Society for Testing and Materials, 1982, pp.5-28.

5. Jones, R.M., Mechanics of Composite Materials, McGraw-Hill Book Co., Washington, DC, 1975.

6. Sutcu, M., An Orthotropic Formulation of the Viscoplasticity Theory Based on Overstress, Ph.D. Thesis, Rensselaer Polytechnic Institute, December 1985.

7. Sutcu, M. and E. Krempl, "A Simplified Orthotropic Formulation of the Viscoplasticity Theory Based on Overstress," Transactions of the Third Army Conference on Applied Mathematics and Computing, ARO Report 86-1, 307-337, 1986.

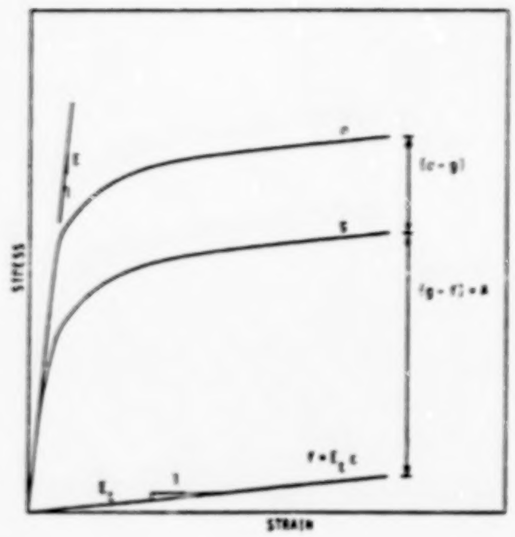

Figure 1. Schematic showing the viscous $(\sigma - g)$, plastic $(g - f)$ asymptotic contributions to the stress. The hardening contribution $f = E_t\varepsilon$ is also shown. In this paper $E_t = 0$.

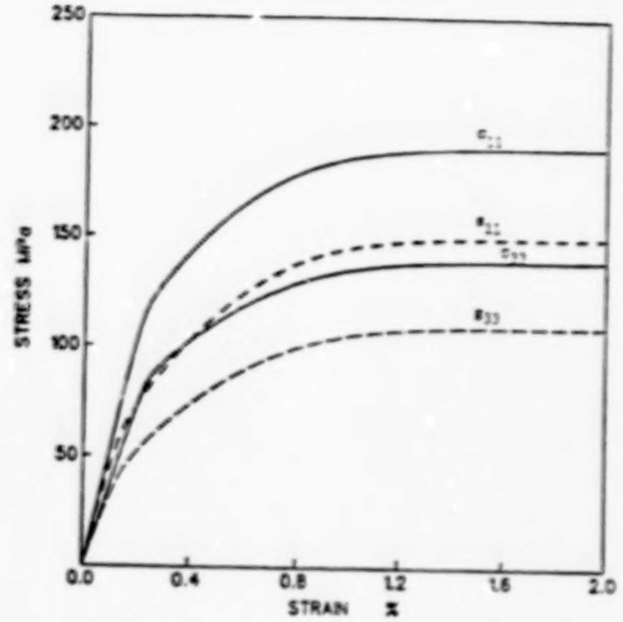

Figure 2. Uniaxial tensile tests in the 1- and 3-directions, respectively. Strain rate is 10^{-4} s^{-1}. $\underline{R} = \underline{S} = \underline{V} = \underline{B}^{-1} = E_1\underline{C}^{-1}$.

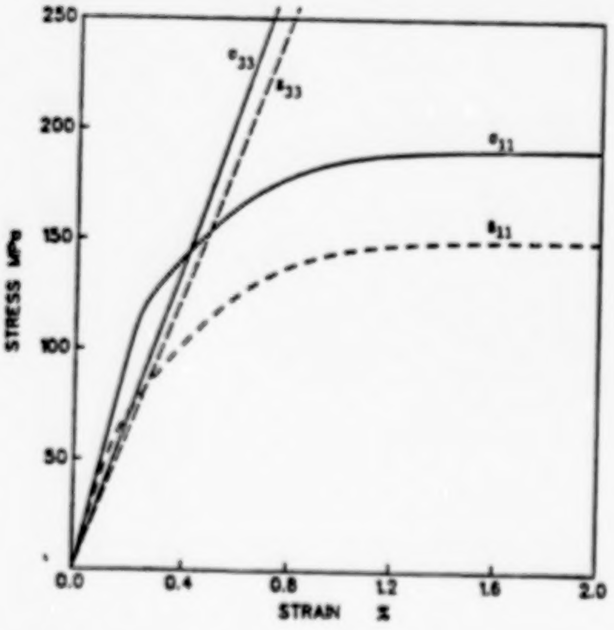

Figure 3. Same as Fig. 2 except that $S_{33} = V_{33} = 0$. Nearly linear elastic response in the 3-direction results. The response in the 1-direction is unaltered.

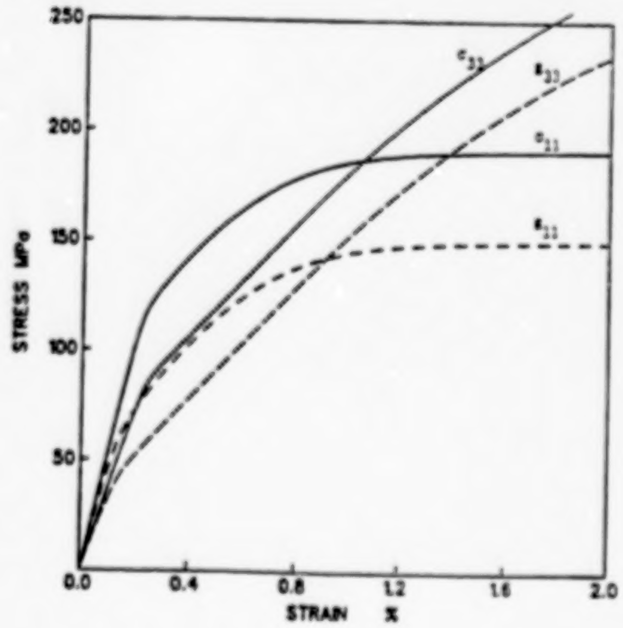

Figure 4. Same as Fig. 2 except that $S_{33} = 0.5$ instead of 50/35 used in Fig. 2. As a consequence (g_{33}) is increased without changing $(\sigma_{33} - g_{33})$. The response in the 1-direction is unaltered.

N88
21506
UNCLAS

N88-21506

CONSTITUTIVE MODELING AND THERMOVISCOPLASTICITY

Richard B. Hetnarski and Hany Ghoneim
Rochester Institute of Technology
Rochester, New York 14623

Donald B. Paul
Air Force Wright Aeronautical Laboratories
Wright Patterson Air Force Base, Ohio 45433

Constitutive Modeling and Thermoviscoplasticity

Development and solution of coupled thermomechanical equations at elevated temperature and/or high strain rates are discussed. Three main considerations are presented: development of the coupled thermomechanical equations by means of the rational theory of thermodynamics, development of a thermoviscoplastic constitutive equation which is congruous with the developed coupled equations, and the applicability of the developed equations to the treatment by the finite element method.

PRECEDING PAGE BLANK NOT FILMED

Introduction

It is well established that finite deformations of a solid body particularly at elevated temperature and/or high strain rates represent coupled thermomechanical processes, which require the simultaneous solution of the coupled balance of momenta and energy equations. A proper development and solution of such thermomechanical problems requires: 1) adoption of the rational theory of thermodynamics, 2) a comprehensive viscoplastic constitutive equation which accounts for the strain rate, temperature and hardening effects, and 3) compatibility with the available numerical tools, particularly the finite element method. These requirements taken together have not been used extensively by researchers in dealing with the coupled thermomechanical problems. However, because of the need for stringent accuracy when solving practical thermomechanical problems such as in rockets and in nuclear reactors, the importance of these requirements is being recognized. Inoue and Nagaki [1] and Allen [2] developed coupled thermomechanical equations with limited applications to one dimensional problems. Ghoneim [3] presented a coupled equations, without hardening effects, and applied them to a two dimensional axisymmetric problem of compression of a constrained-ends cylinder. Lehmann [4] presented a comprehensive analysis of the development of the coupled equations with application to the necking problem in a specimen subjected to the tensile test. However, a more realistic constitutive law which includes strain rate and temperature effects is needed.

In this paper development and solution of the coupled thermomechanical problems is considered, based on the three requirements listed earlier: The coupled thermomechanical equations are developed on the basis of the rational theory of thermodynamics; a viscoplastic constitute equation which accounts for the temperature, strain rate, and hardening effect is proposed; and the computability of the developed coupled thermomechanical equation with the finite element method is discussed.

Development of the Coupled Thermomechanical Equations

We assume that the state of a material point is completely determined by the knowledge of the elastic strain tensor $\underline{E}^e$, the inelastic strain tensor $\underline{E}^I$, the absolute temperature T, the temperature gradient $\underline{\nabla} T$, and a set of internal state variables $\underline{\alpha}^i$, $i = 1, \ldots, p$. Consequently, the following constitutive relations may be postulated:

$$\underline{S} = \underline{S}\,(\,\underline{E}^e, \underline{E}^I, T, \underline{\nabla T}, \underline{\alpha}^i\,) \tag{1.1}$$

$$\psi = \psi\,(\,\underline{E}^e, \underline{E}^I, T, \underline{\nabla T}, \underline{\alpha}^i\,) \tag{1.2}$$

$$s = s\,(\,\underline{E}^e, \underline{E}^I, T, \underline{\nabla T}, \underline{\alpha}^i\,) \tag{1.3}$$

$$\underline{q} = \underline{q}\,(\,\underline{E}^e, \underline{E}^I, T, \underline{\nabla T}, \underline{\alpha}^i\,) \tag{1.4}$$

$$\dot{\underline{E}}^I = \underline{g}_1\,(\,\underline{E}^e, \underline{E}^I, T, \underline{\nabla T}, \underline{\alpha}^i\,) \tag{1.5}$$

and

$$\dot{\underline{\alpha}}^i = \underline{g}_2\,(\,\underline{E}^e, \underline{E}^I, T, \underline{\nabla T}, \underline{\alpha}^i\,) \tag{1.6}$$

where $\underline{S}$ is the second Piola-Kirchhoff stress tensor, ψ stands for the Helmholtz free energy, s means the specific entropy, and q is the heat flux per unit area.

Upon invoking the axiom of admissibility (i.e., the compatibility of the assumed constitutive relations with the fundamental equations of mechanics) and when adopting the separabilty of the total Green-Lagrange strain energy

$$\underline{E} = \underline{E}^e + \underline{E}^I + \underline{\gamma} T$$

where $\underline{\gamma}$ is the coefficient of the thermal expansion tensor, it follows:

$$1)\quad \psi = \psi\,(\underline{E}^{e}, \underline{E}^{I}, T, \underline{\alpha}^{i})$$

$$s = \frac{\partial\psi}{\partial\underline{E}^{e}} : \underline{\gamma} - \frac{\partial\psi}{\partial T} = s\;(\underline{E}^{e}, \underline{E}^{I}, T, \underline{\alpha}^{i})$$

$$\underline{S} = \rho\,\frac{\partial\psi}{\partial\underline{E}^{e}} = \underline{S}\;(\underline{E}^{e}, \underline{E}^{I}, T, \underline{\alpha}^{i})$$

$$2)\quad \rho\,\Big(\frac{\partial\psi}{\partial\underline{E}^{I}} : \dot{\underline{E}}^{I} + \frac{\partial\psi}{\partial\underline{\alpha}} : \dot{\underline{\alpha}} + \dot{s}T\Big) = \underline{S} : \dot{\underline{E}}^{I} - \underline{\nabla}\cdot\underline{q} \qquad \ldots(2)$$

$$\text{and } 3)\quad \Big(\underline{S} - \rho\,\frac{\partial\psi}{\partial\underline{E}^{e}}\Big) : \dot{\underline{E}}^{I} + \rho\,\frac{\partial\psi}{\partial\underline{\alpha}} : \dot{\underline{\alpha}} - \underline{q}\,\frac{\underline{\nabla\theta}}{\theta} \geq 0 \qquad \ldots(3)$$

At this stage, we may postulate

$$\rho\psi = \rho\psi_0 + \tfrac{1}{2}\,\underline{E}^{e} : D^{4} : \underline{E}^{e} + \rho\,c_v\,T\,(1 - \ln T) + \underline{\beta} : \underline{\alpha} \qquad \ldots(4)$$

where D^4 is the fourth order elasticity tensor, ρ is the density at the reference configuration, and c_v stands for the specific heat at constant deformation. The tensor $\underline{\beta}$ is the material property tensor. Substituting (4) and the Fourier's law, $\underline{q} = -k\underline{\nabla}T$ into equations (2) and (3), we obtain

$$-k\nabla^2 T + \rho c_v \dot{T} = -\rho(\underline{\gamma} : D^4 : \dot{E}^{e})\,T + \underline{S} : \dot{\underline{E}}^{I} - \rho\,\underline{\beta} : \dot{\underline{\alpha}} \qquad \ldots(5)$$

and

$$\underline{S} : \dot{\underline{E}}^{I} + \rho\,\underline{\beta} : \dot{\underline{\alpha}} + k\,\frac{(\nabla T)^2}{T} \geq 0$$

Equation (5) is the coupled heat equation which together with the balance of linear momentum equation constitutes the set of coupled thermomechanical equations. It might be worth pointing out that the right-hand side of the equation (5) represents the mechanical energy generation; the first term stands for the reversible part, the second for the dissipated irreversible part, and the third for the stored irreversible part due to microstructural effects.

The Viscoplactic Constitutive Equation

Solution of the coupled thermomechanical equations requires closed-form expressions for (1.5) and (1.6). These may be taken from any of the state variable theories [5-8]. Inhere, a constitutive equation which may be regarded as a modification of th Bodner-Partom's power law is proposed. The proposed equations are thought to be simple, lucid, and consequently very practical. As in the case of the internal state variables theory, the proposed constitutive equations utilize two state variables: a kinematic hardening state variable which accounts for the "rest" stress, and an isotropic hardening state variable which accounts for the "drag" stress. Only the isotropic hardening state variable will be considered in this paper.

After adopting the flow rule, we can show that

$$\dot{\underline{\underline{E}}}^{I} = \gamma_{\circ} \left(\frac{\tau^{E}}{Y} \right)^{n} \frac{\underline{\underline{S}}'}{\tau^{E}} \qquad \ldots(6)$$

where τ^{E} is the effective stress $\left(\tau^{E} = \sqrt{\frac{3}{2} S'_{ij} S'_{ij}} \right)$, $\underline{\underline{S}}'$ is the deviatoric stress tensor, n is a strain rate sensitivity parameter, and Y is the isotropic hardening state variable which is equivalent to the dynamic yield stress [8]. In general, Y is a functional of the history of deformation or any related quantity such as the viscoplastic work W^{P}. If the convolution form of Stieltjes integral is adopted for such functional

$$Y = \int_{0}^{t} e^{-\tau/\tau_{0}} W^{p} (t - \tau) \, d\tau$$

where t is the time and τ_{0} stands for the relaxation time constant, and when the 3-parameter element model is considered, we get

$$\dot{Y} + aY = H_{1} \dot{W}^{p} + H_{2} \sqrt{W^{p}} \qquad \ldots(7)$$

where a, H_1 , and H_2 are material constants.

In order to incorporate the temperature effects into the evolution equations (6) and (7), Y is expressed as a function of temperature. Since in the proposed constitutive equations Y can be viewed as the equivalent dynamic yield stress, the function may be constructed from experimental data of the yield stress versus temperature. A possible form of this function is

$$Y = Y_o \left(\frac{Tc - T}{Tc - To}\right) \qquad \ldots(8)$$

where T_c is a constant, T_o is a reference temperature, and Y_o is the value of the yield stress at T_o. In addition, from the observation of the variation of the plastic flow with temperature, we have $\dot{\underline{\underline{E}}}^I$ proportional to exp (-Q/RT),

$$\dot{\underline{\underline{E}}} \sim \exp(-Q/RT) \qquad (9)$$

where Q is the activation energy (assumed constant), and R is the universal gas constant. From equations (6), (8) and (9) it follows that n must be a function of T,

$$n = \frac{Q}{R}\left(\frac{T-To}{ToT}\right) / \ln\left(\frac{Tc-To}{Tc-T}\right) \qquad \ldots(10)$$

The proposed viscoplastic constitutive equations (equations (6) and (7) subjected to (8) and (10)) are examined by conducting a series of one-dimensional uniaxial numerical calculations. Samples of the results are given in Figures 1-4. Figures 1 and 2 display the tensile stress-strain results at different strain rates and temperature. Strain rate history effects are demonstrated by a jump test in Figure 3. Cyclic test results, Figure 4, depict the cyclic hardening effects. Qualitatively speaking, results demonstrate the capability of the proposed viscoplastic constitutive equations in generating some of the important characteristics of a class of viscoplastic materials. A quantitative investigation of the constitutive equations is to be conducted experimentally for some viscoplastic materials in a future work.

Finite Element Implementation

Compatibility of the developed coupled thermomechanical equations is demonstrated for the case of quasistatic infinitesimal deformation with no body force and no heat generation, i.e.,

$$\underline{\nabla} \cdot \underline{\sigma} = 0 \qquad \ldots(11)$$

$$-k\nabla^2 T + \rho c_v \dot{T} = \underline{\sigma} \cdot \underline{\dot{\varepsilon}}^p - \left(\frac{E}{1-2\nu}\right) \dot{\varepsilon}_v T - \rho \beta \dot{Y} \qquad \ldots(12)$$

where $\underline{\sigma} = [D] \left(\underline{\varepsilon} - \underline{\varepsilon}^{vp} - \gamma T \underline{\delta}\right)$

and $\underline{\varepsilon}^{vp} = \gamma_0 \left(\frac{\tau^E}{Y}\right) \frac{\sigma^1}{\tau^E}$

γ_0 is a scalara constant, ρ is the density, $\underline{\delta}$ stands for the Kronecker symbol, $\underline{\sigma}$ and $\underline{\varepsilon}$ are the stress and strain tensors, respectively, expressed in vector form, $\underline{\sigma}^1$ and $\underline{\varepsilon}^{vp}$ the corresponding deviatoric stress and viscoplastic strain vectors, respectively, ε_v is the dilatation, and [D] is the elastic matrix.

When adopting the Galerkin finite element method, (11) and (12) become, respectively,

$$[K1]\, \underline{\dot{U}} + [C1]\, \underline{\dot{T}} = \underline{R} + \underline{F_1} \qquad \ldots(13)$$

$$[C2]\, \underline{\dot{T}} + [K2]\, \underline{T} = \underline{Q} + \underline{F_2} \qquad \ldots(14)$$

where $\underline{U}$, $\underline{T}$, $\underline{R}$, and $\underline{Q}$ are the nodal displacement, the nodal temperature, the nodal force, and the thermal convection load vectors, respectively, $\underline{F_1}$ is a vector which accounts for the viscoplastic effects of the balance of momentum equation, and $\underline{F}_2$ is a vector which accounts for the mechanical heat generation. Also, [K1], [K2], [C1], and [C2] are, respectively, the stiffness, conductivity, coupling, and consistency matrices. The differential equations (13) and (14) can be solved by using the general "θ" method in conjunction with the fixed point iteration method for the solution of the ensuing nonlinear algebraic equations. Results of tensile and compression loading of a constrained-ends cylinder for a constant Y can be found in [8].

The extension of this work to incorporate hardening and temperature effects and solving other practical problems is being undertaken.

References

1) T. Inoue, and S. Nagaki, "A Constitutive Modeling of Thermoviscoelastic-Plastic Materials," Journal of Thermal Stresses, Vol. 1, pp.53-61, 1978.

2) D.H. Allen, "A Prediction of Heat Generation in a Thermoviscoelastic Uniaxial Bar," International Journal of Solids and Structures, Vol. 21, pp. 325-343, 1985.

3) H. Ghoneim, and S. Matsuoka, "Thermoviscoplasticity by Finite Element: Tension and Compression Test," Report No. 311201-0199, AT&T Bell Laboratories, Murray Hill, N.J. 1985.

4) Th. Lehmann, and U. Blix, "On the Influence of the Coupling of Thermal and Mechanical Processes in the Necking Problem in Uniaxial Tension," Journal of Thermal Stresses, Vol. 8, pp. 153-165, 1985.

5) A.K. Miller, "An Inelastic Constitutive Model for Monotonic, Cyclic, and Creep Deformation," ASME Journal of Engineering Materials and Technology, Vol. 98, pp. 97-113, 1976.

6) E.W. Hart, "Constitutive Equations for the Nonelastic Deformation of Metals," ASME Journal of Engineering Materials and Technology, Vol. 98, pp. 193-202, 1976.

7) S.R. Bodner, I. Partom, and Y. Partom, "Uniaxial Cyclic Loading of Elastic-Viscoplastic Materials," ASME Journal of Applied Mechanics, Vol. 46, pp. 805-810, 1979.

8) H. Ghoneim, S. Matsuoka, and Y. Chen, "Viscoplastic Modeling with Strain Rate History Dependency," ASME Journal of Applied Mechanics, Vol. 50, pp. 465-468, 1983.

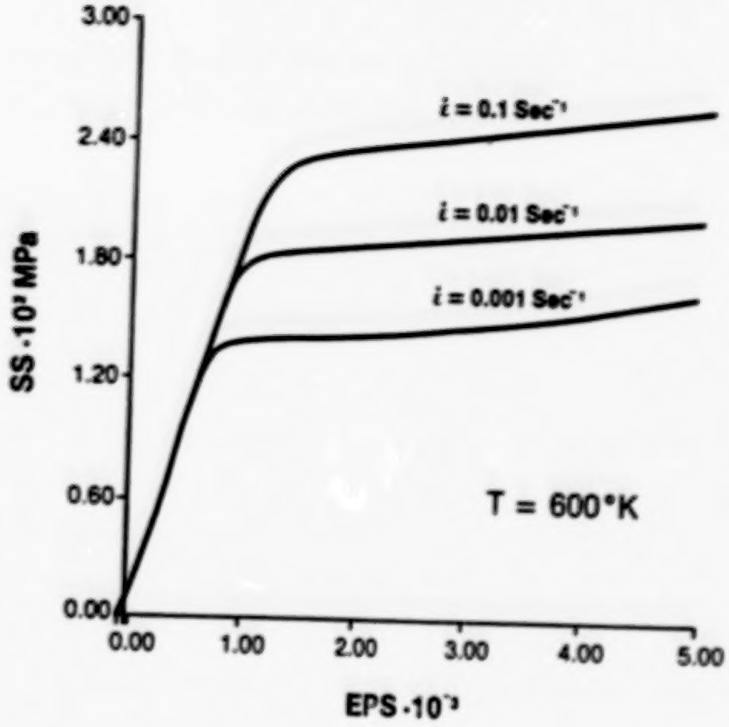
3.00
2.40
1.80
1.20
0.60
0.00
$SS \cdot 10^3$ MPa
$\dot{\epsilon} = 0.1\ \mathrm{Sec}^{-1}$
$\dot{\epsilon} = 0.01\ \mathrm{Sec}^{-1}$
$\dot{\epsilon} = 0.001\ \mathrm{Sec}^{-1}$
T = 600°K
0.00
1.00
2.00
3.00
4.00
5.00
$EPS \cdot 10^{-3}$

Fig. 1

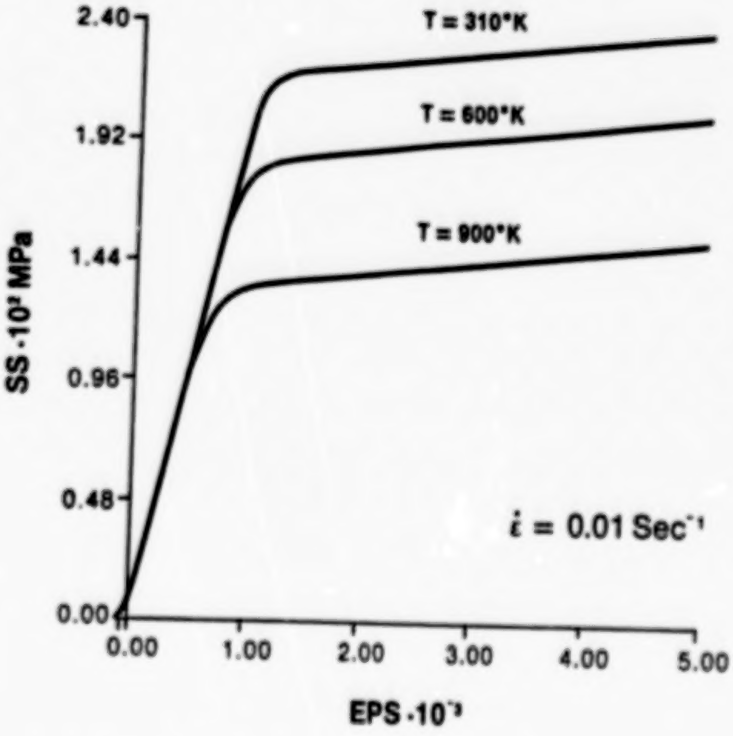
2.40
1.92
1.44
0.96
0.48
0.00
$SS \cdot 10^3$ MPa
T = 310°K
T = 600°K
T = 900°K
$\dot{\epsilon} = 0.01\ \mathrm{Sec}^{-1}$
0.00
1.00
2.00
3.00
4.00
5.00
$EPS \cdot 10^{-3}$

Fig. 2

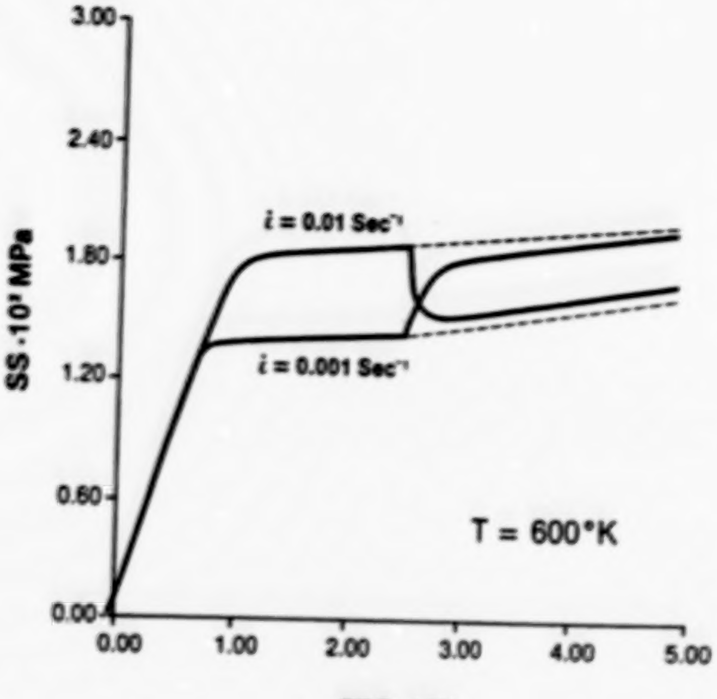
3.00
2.40
1.80
1.20
0.60
0.00
SS·10^2 MPa
$\dot{\varepsilon}$ = 0.01 Sec^{-1}
$\dot{\varepsilon}$ = 0.001 Sec^{-1}
T = 600°K
0.00
1.00
2.00
3.00
4.00
5.00
EPS·10^{-2}

Fig. 3

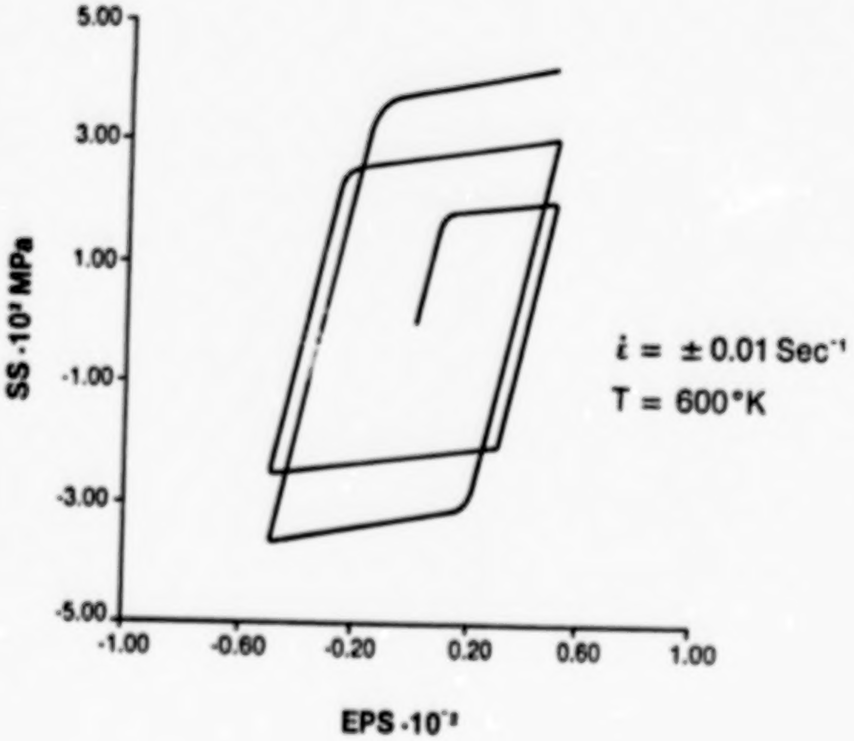
5.00
3.00
1.00
-1.00
-3.00
-5.00
SS·10^2 MPa
$\dot{\varepsilon}$ = ± 0.01 Sec^{-1}
T = 600°K
-1.00
-0.60
-0.20
0.20
0.60
1.00
EPS·10^{-2}

Fig. 4

N88
21507
UNCLAS

N88-21507

APPLICATIONS OF ELASTIC-VISCOPLASTIC CONSTITUTIVE MODELS IN DYNAMIC ANALYSES OF CRACK RUN-ARREST EVENTS*

B. R. Bass, C. E. Pugh, R. W. Swindeman
Heavy-Section Steel Technology Program
Oak Ridge National Laboratory
P. O. Box Y
Oak Ridge, Tennessee 37831

Unified constitutive theories attempt to treat different manifestations of time-dependent inelastic behavior, such as creep, stress relaxation, and plastic flow, by a single kinematic equation and a discrete set of state variables. The motivation for developing such theories has, over the last fifteen years, come mostly from interest in high-temperature applications. High temperature refers to the range where observable creep deformations occur over long periods of time when the stress levels are near the engineering yield stress. There are, however, rapid loading situations at lower temperatures where rate effects can become equally important. One such situation is the representation of rapid crack propagation events in ductile structural alloys. Ductile here means that the material is at a temperature above that where cleavage (brittle) fracture characteristics cease to be

---

*Research sponsored by the Office of Nuclear Regulatory Research. U.S. Nuclear Regulatory Commission under Interagency Agreements 40-551-75 and 40-552-75 with the U.S. Department of Energy under Contract DE-AC05-84OR21400 with Martin Marietta Energy Systems, Inc.

By acceptance of this article, the publisher or recipient acknowledges the U.S. Government's right to retain a nonexclusive, royalty-free license in and to any copyright covering the article.

PRECEDING PAGE BLANK NOT FILMED

present. The temperature for transition from brittle to ductile fracture may be well below the classical creep regime, for example, about 50 to 100°C for some nuclear grade structural steels. This paper examines the role that viscoplasticity may play in the prediction of crack run/arrest behavior in such ductile steels.

The growing interest in the viscoplastic aspect of fracture behavior is reflected by several recent studies[1,2] in the literature which emphasize the importance of including combined plastic and strain-rate effects in constitutive relations. Accordingly, in concert with subcontracting groups, the Heavy-Section Steel Technology (HSST) Program at the Oak Ridge National Laboratory (ORNL) is supporting research efforts to develop viscoplastic-dynamic finite element analysis techniques for high strain-rate fracture analyses and to validate their utility through the analysis of carefully performed crack-arrest experiments. In particular, these analysis capabilities are expected to give an improved basis for assessing the dynamic fracture behavior of large (1 × 1 × 0.1 m) plate crack-arrest specimens currently being tested by the National Bureau of Standards as part of the HSST program.

In the studies being conducted at ORNL, various viscoplastic constitutive models and several nonlinear fracture criteria are being installed in the ADINA general purpose finite element computer program, and the combined predictive capabilities are being evaluated through applications to the HSST wide-plate experiments. The first two constitutive models selected for installation in ADINA were a variation of the Perzyna[3] elastic-viscoplastic model with linear strain hardening and the Bodner-Partom[4] viscoplastic model with strain hardening. Other models being examined include those due to Robinson-Pugh[5], and Hart.[6] The fracture criteria being examined for use with nonlinear analyses include several path-independent integrals that were formulated by different researchers (e.g., Atluri,[7] Kishimoto[8]) to remove limitations on the original J-integral of Rice. Some of these integrals represent slight modifications of the J-integral, while others have a different theoretical basis.

This paper describes applications of these nonlinear techniques to the first series of six HSST wide-plate crack-arrest tests that have been performed. These experiments include crack initiations at low temperatures and relatively long (20 cm) cleavage propagation phases which are terminated by arrest in high-temperature regions. Crack arrests are then followed by ductile tearing events. Consequently, the crack-front regions in these tests are exposed to wide ranges of strain rates and temperatures.

The viscoplastic formulations installed in ADINA at ORNL can be expressed in vector form at time t as

$$ {}^{t}\dot{\varepsilon}^{vp} = {}^{t}\Phi \, D \, {}^{t}\sigma \tag{1} $$

where $\dot{e}^{vp}$ is the viscoplastic strain rate, σ is the stress tensor, and D is the deviatoric stress operator matrix. The implementation of the Bodner-Partom[4] model in ADINA is based on the formulation described by Kanninen, et al.[9] for which Φ is defined by

$$ \Phi = \frac{D_0}{(J_2)^{1/2}} \exp\left[-\left(\frac{1}{2}\right)\left(\frac{Z^2}{3\ J_2}\right)^n\right] \tag{2} $$

where the hardening parameter Z has the form

$$Z = Z_1 + (Z_0 - Z_1) \exp (-m W_p) \quad (3)$$

and where Z_0, Z_1, n, m, D_0 = prescribed material constants,

W_p = accumulated plastic work, and

J_2 = second invariant of deviatoric stress.

In Ref. 9, temperature dependence of the material properties is taken into account primarily through the relations

$$n = \frac{175}{T} + 1.35 \quad \text{and} \quad Z_0 = \frac{2.44 \times 10^4}{T} + 1084 \text{ (MPa)} , \quad (4)$$

where temperature T is in deg K. Values for the remaining material constants are given by m = .061 (1/MPa), $D_0 = 10^6$, and Z_1 = 1550 MPa.

The Bodner-Partom model described above has been applied to the analysis of the fifth HSST wide-plate crack-arrest test, WP-1.5. Figure 1 shows the single-edge-notched plate specimen (1 × 1 × 0.1 m) that was cooled on the notched edge and heated on the other edge to give a linear temperature gradient (T_{min} = -83.3°C, T_{max} = 183.3°C) along the plane of crack propagation. Upon initiating propagation of the crack in cleavage, arrest was intended to occur in the higher-temperature ductile region of the specimen. The specimen had an initial crack depth-to-plate width ratio (a/w) of 0.2. Each surface was side-grooved to a depth equal to 12.5% of the plate thickness. The specimen was welded to pull-plates which have a pin-to-pin length of 9.6 m to minimize stress wave effects. Drop weight and Charpy test data indicate that RT_{NDT} = -23°C for this material. Information on material properties of the wide-plate material are described in Ref. 10.

The specimen was instrumented with thermocouples, strain gages, and crack-opening-displacement gages. A series of eleven thermocouples and sixteen strain gages were located about 65 mm above the crack plane across the plate to record temperature and strain as functions of time and crack position.

The two-dimensional (2-D) finite element model used in the analysis consisted of 1833 nodes and 567 eight-noded isoparametric elements. The measured fracture load of F_{in} = 11.03 MN was applied at the top of the load-pin hole to determine the load point displacement. For the dynamic analysis, the load point was fixed at the displacement value of the initiation load and the time step was set at $\Delta t = 1$ μs in the implicit Newmark scheme for the time integration. The estimate of crack position vs. time in Fig. 2 was constructed from strain-gage data and was used as input for a generation mode dynamic analysis. Figure 2 shows the measured first crack arrest at $a_{fm_1} = 0.52$ m which occurred at time $t = 0.723$ ms after crack initiation. Figure 3 shows contour plots of the effective viscoplastic strain at times $t = 0.7$ ms and $t = 2.9$ ms, respectively. The time histories of the Atluri and the Kishimoto path-independent integrals are depicted in Fig. 4. The results are expressed in terms of a pseudo-K_I value for purposes of comparison with elastodynamic values. The values at crack arrest were determined to be $K_I = 208$ MPa$\sqrt{m}$ (Atluri) and $K_I = 174$ MPa$\sqrt{m}$ (Kishimoto).

Computed results from the viscoplastic analysis are compared with measured data for crack-line strain-time response and with elastodynamic analyses of the same crack run-arrest event. Work is currently under way to determine material constants for the Perzyna model that can be applied to wide-plate analysis. Results of this effort will permit comparisons between the Perzyna and the Bodner-Parton models for the wide-plate material in the temperature and strain-rate regions of interest to the HSST program.

References

1. B. Brickstad, "A Viscoplastic Analysis of Rapid Crack Propagation Experiments in Steel," *J. Mech. Phys. Solids* 31, 307-27 (1983).
2. R. Hoff, C. A. Rubin, and G. T. Hahn, *Strain-Rate Dependence of the Deformation at the Tip of a Stationary Crack*, STP 868, American Society for Testing and Materials, 409-430 (1985).
3. P. Perzyna, "Fundamental Problems in Visco-Plasticity," pp. 244-368 in *Recent Advances in Applied Mechanics*, Academic Press, New York, 1966.
4. S. R. Bodner and Y. Parton, "Constitutive Equations for Elastic Viscoplastic Strain Hardening Materials," *J. Appl. Mech.* 42, 385 (1975).
5. C. E. Pugh and D. N. Robinson, "Some Trends in Constitutive Equation Model Development for High-Temperature Behavior of Fast-Reactor Structural Alloys," *Journal of Nuclear Engineering and Design*, Vol. 48, 1978, pp. 269-276.
6. E. W. Hart, "Constitutive Relations for the Nonelastic Deformation of Metals," *Journal of Engineering Materials and Technology, Transactions of the ASME*, Vol. 98, July 1976, pp. 193-202.
7. S. N. Atluri, "Path-Independent Integrals in Finite Elasticity and Inelasticity with Body Forces, Inertia and Arbitrary Crack Face Conditions," *Engineering Fracture Mechanics*, Vol. 16, 1982, p. 341-364.
8. K. Kishimoto, S. Aoki, and M. Sakata, "On the Path-Independent Integral - J," *Engineering Fracture Mechanics*, Vol. 13, 1980, pp. 841-850.
9. M. F. Kanninen et al., "Elastodynamic and Viscoplastic-Dynamic Fracture-Mechanics Analysis," pp. 18-28 in *Heavy-Section Steel Technology Program Semiann. Prog. Rep. for April-September 1985*, NUREG/CR-4219, Vol. 2 (ORNL/TM-9593/V2), Martin Marietta Energy Systems, Inc., Oak Ridge National Laboratory.
10. B. R. Bass, C. E. Pugh, and H. K. Stamm, "Dynamic Analysis of a Crack Run-Arrest Experiment in a Nonisothermal Plate," *Pressure Vessel Components Design and Analysis*, Vol. 4, ASME PVP Vol. 98-2 (1985) 175-184.

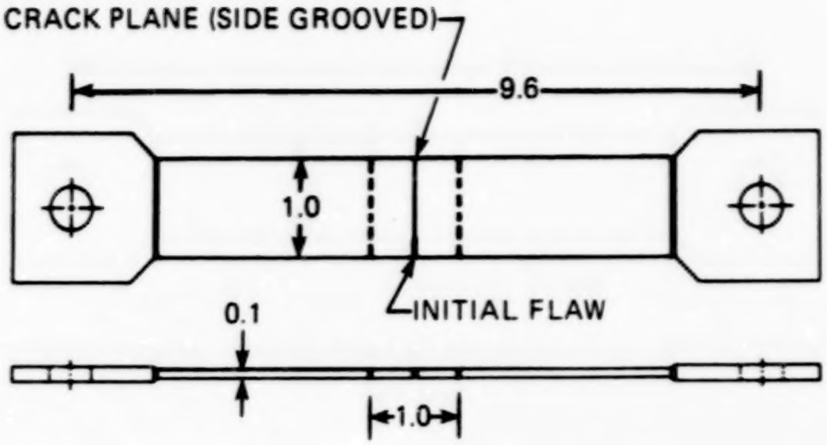
CRACK PLANE (SIDE GROOVED)
9.6
1.0
INITIAL FLAW
0.1
1.0

Fig. 1. Wide-plate crack-arrest specimen and pull-plate assembly.

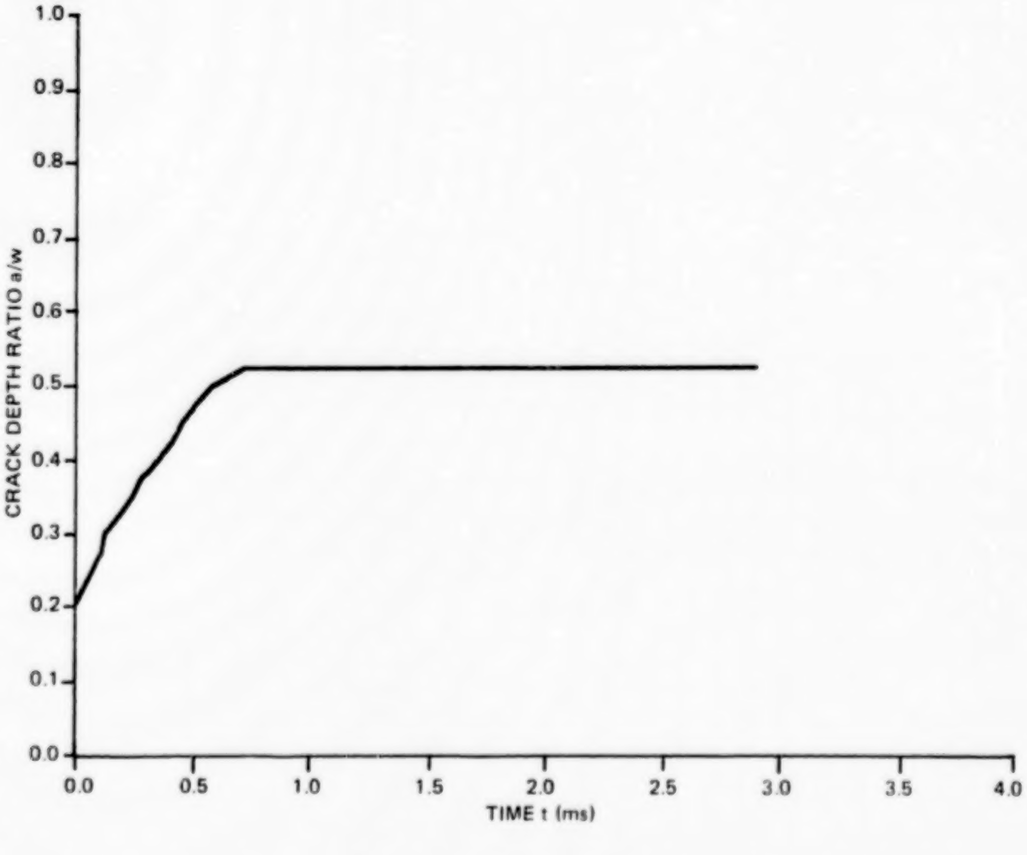

Fig. 2. Crack depth history derived from strain gage data for wide-plate test WP-1.5.

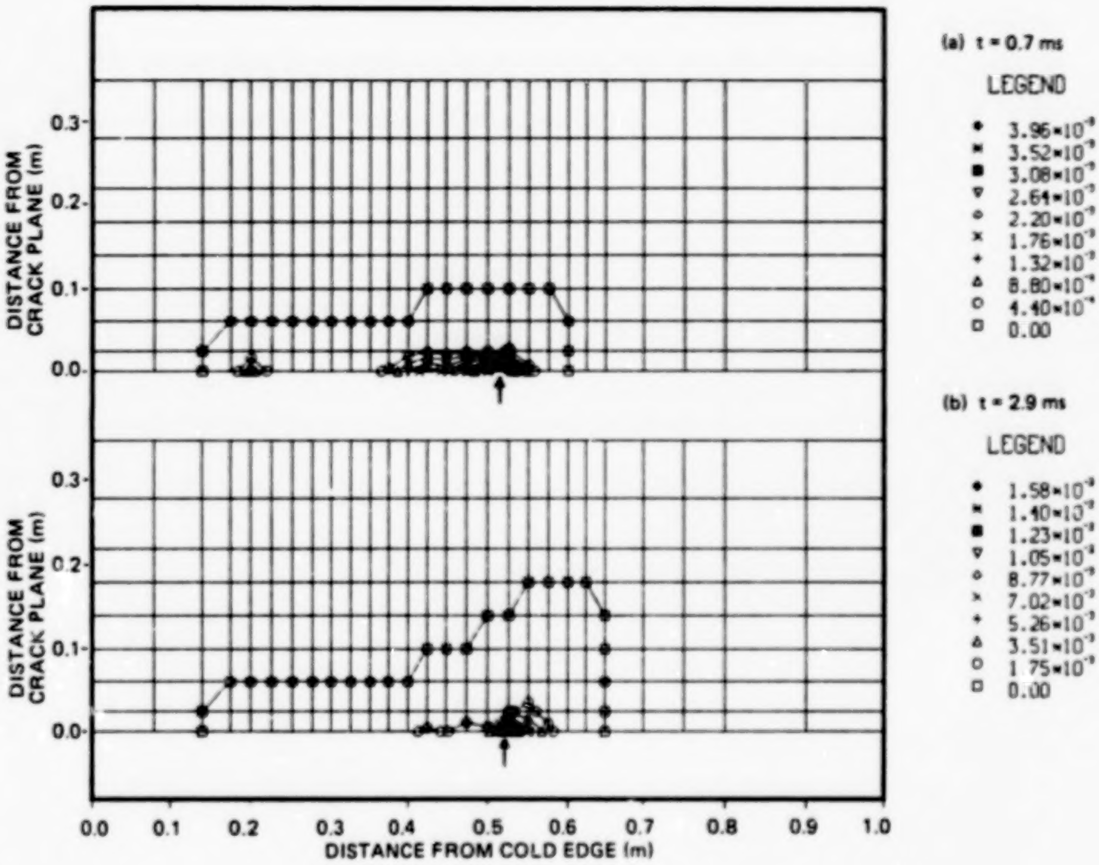

Fig. 3. Contour plots of effective viscoplastic strain at times t = 0.7 ms and t = 2.9 ms from generation mode analysis of wide-plate test WP-1.5.

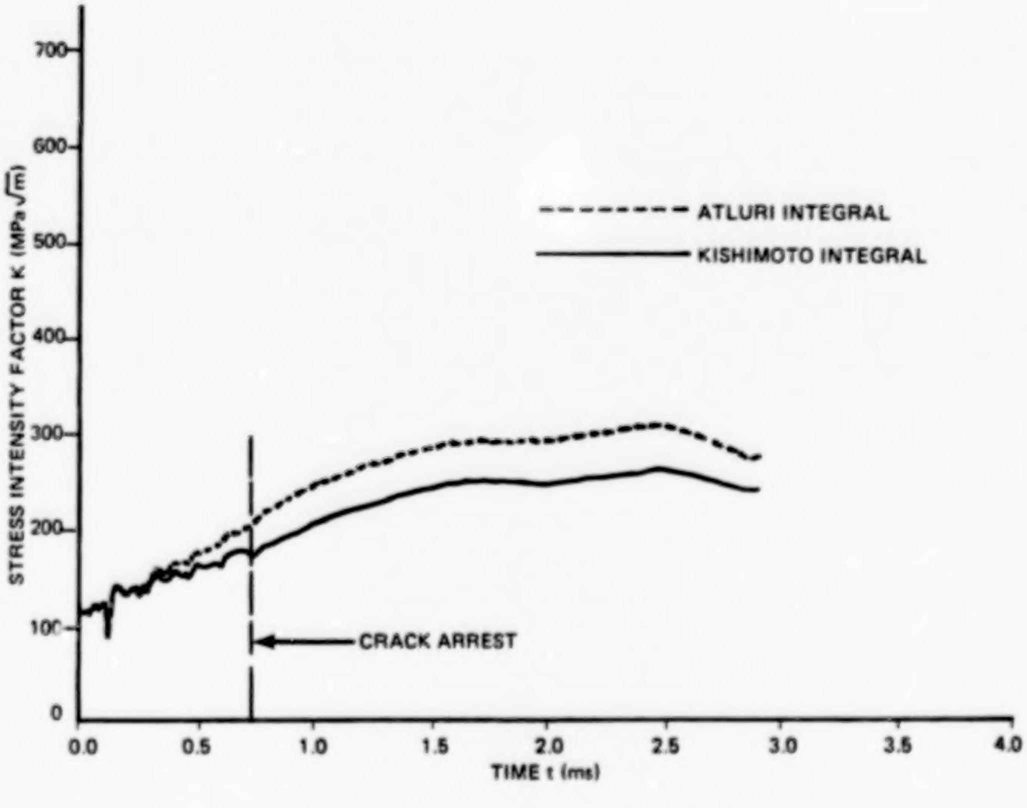

Fig. 4. Amplitude of pseudo-stress-intensity-factor versus time from two path-independent integrals for wide-plate test WP-1.5.

N88
21508
UNCLAS

N88-21508

A THEORY OF VISCOPLASTICITY ACCOUNTING FOR INTERNAL DAMAGE

A.D. Freed
NASA Lewis Research Center
Cleveland, Ohio 44135

D.N. Robinson*
The University of Akron
Akron, Ohio 44325

E-3956-10

A constitutive theory for use in structural and durability analyses of high-temperature isotropic alloys is presented. Constitutive equations based upon a potential function are determined from conditions of stability and physical considerations. The theory is self-consistent; terms are not added in an ad hoc manner. It extends a proven viscoplastic model by introducing the Kachanov-Rabotnov concept of net stress. Material degradation and inelastic deformation are unified; they evolve simultaneously and interactively. Both isotropic hardening and material degradation evolve with dissipated work which is the sum of inelastic work and internal work. Internal work is a continuum measure of the stored free energy resulting from inelastic deformation.

INTRODUCTION

The nucleation, growth and coalescence of voids and microcracks are physical phenomena that degrade a material's continuity. This degradation results in a loss of strength, and is the eventual cause of failure. Continuous damage mechanics applies whenever the distribution of defects does not include one or more dominating macroscopic cracks; otherwise, fracture mechanics applies. The subject of this paper falls under the topic of continuous damage mechanics; applications to fracture mechanics are not discussed.

A constitutive theory applicable to structural and durability analyses of high-temperature isotropic alloys is developed. A set of constitutive equations based on a single potential function is determined from stability conditions and physical considerations. A specific potential function from a proven viscoplastic theory is extended to account for internal damage by introducing the Kachanov - Rabotnov (refs. 1 and 2) concept of a net stress. Internal damage and inelastic deformation are unified in this approach; they evolve simultaneously and interactively. The theory is self-consistent in that it is derived from a potential function; terms are not added in an ad hoc manner. Other viscoplastic theories that incorporate continuous damage mechanics have been proposed. The evolutionary equations for material degradation in the theories of Chaboche (ref. 3), Bodner (ref. 4), and Walker and Wilson (ref. 5) are phenomonologically determined, whereas, the Perzyna theory (ref. 6) is micromechanistically based. In this paper the evolutionary equation for material degradation is derived from a potential function.

---

*NASA Lewis Resident Research Associate.

PRECEDING PAGE BLANK NOT FILMED

Continuous damage mechanics deals with, an infinitesimal volume element of material (called a particle), whose dimensions are large enough to contain many material defects, yet small enough to be treated as a mathematical point in a continuum sense. Consider a face on such an element whose unit normal is given by n_i.[1] Let A denote its surface area in a flawless (or undamaged) state, and let A' denote its net surface area in the presence of material defects (or in a damaged state); thus $A' \leq A$. The internal damage associated with this particle, and in the direction of this unit normal, is defined by

$$\omega = \frac{A - A'}{A} \tag{1}$$

which is bounded by the interval $0 \leq \omega < 1$ where $\omega = 0$ in an undamaged state. Whenever the orientations of material defects have preferred directions, damage becomes a function of these directions resulting in an entity of tensorial nature (refs. 7 to 9); otherwise, damage is isotropic and can be represented by a scalar. In this paper, damage is taken to be isotropic as a simplifying assumption. Kachanov (ref. 1) calls the quantity $\psi = 1 - \omega$ the continuity of the material.

Consider once again a face on an infinitesimal material volume element. In an undamaged state, traction is the ratio of the force transmitted through the surface F_i to the surface area A. It is related to the unit normal n_i by a homogeneous linear operator σ_{ij} called the applied (or Cauchy) stress, that is[2]

$$\frac{F_i}{A} = \sigma_{ij} n_j \tag{2}$$

In a damaged state, traction becomes the ratio of the force transmitted through the surface F_i to the net surface area A'. It is related to the unit normal n_i by a homogeneous linear operator σ'_{ij} called the net (or Kachanov-Rabotnov) stress; thus

$$\frac{F_i}{A'} = \sigma'_{ij} n_j \tag{3}$$

Combining equations (1) to (3) results in

$$\sigma'_{ij} = \frac{\sigma_{ij}}{(1 - \omega)} \tag{4}$$

which relates the net stress to the applied stress.

Like the classical theories of creep and plasticity, strain ϵ_{ij} is given by the sum

---

[1] All scalar, vector and tensor fields are defined at particles whose spatial coordinates are x_i at the instant t in a Cartesian reference frame.

[2] Repeated indices are summed over in the usual manner.

$$\varepsilon_{ij} = \varepsilon_{ij}^{e} + \varepsilon_{ij}^{p} \tag{5}$$

where ε_{ij}^{e} is the elastic strain and ε_{ij}^{p} is the inelastic (or plastic) strain. From a thermodynamic viewpoint, the elastic change in strain is the reversible portion of a change in strain, while the inelastic change in strain is the irreversible portion of that change in strain. Small displacements and rotations are assumed.

The elastic response of polycrystalline metals is given by the relationship

$$\varepsilon_{ij}^{e} = \frac{(1 + \nu)\sigma_{ij} - \nu\sigma_{kk}\delta_{ij} + \alpha\ \Delta T\ \delta_{ij}}{E(1 - \omega)} \tag{6}$$

where ν is the Poisson ration, α is the mean coefficient of thermal expansion, ΔT is the temperature change and δ_{ij} is Kronecker's delta. Since E is Young's modulus in an undamaged state, and $E' = E(1 - \omega)$ can be considered as Young's modulus in a damaged state, we obtain the following expression:

$$\omega = \frac{(E - E')}{E} \tag{7}$$

This is a useful measure of internal damage, because it can be readily determined by experiment (ref. 10).

CONSTITUTIVE THEORY

Much of the essential structure in the classical theory of plasticity derives, not so much from thermodynamic concepts, but from concepts of material stability as described by Drucker (ref. 11). A single postulate of stability is sufficient to unify the description of inelastic behavior of time-independent materials under isothermal conditions. A dual postulate of stability has been applied by Ponter (ref. 12) to time-dependent materials whose hereditary behavior can be represented in terms of internal state variables ξ_α $(\alpha = 1,2,\ldots,n)$ and their conjugate thermodynamic forces f_α. In that work, small isothermal changes in stress at constant internal state are assumed to obey the inequality

$$d\sigma_{ij}\ d\dot{\varepsilon}_{ji}^{p} \geq 0 \tag{8}$$

where f_α and T are constant; whereas small isothermal changes in internal state at constant stress are assumed to satisfy the inequality

$$df_\alpha\ d\dot{\xi}_\alpha \geq 0 \tag{9}$$

where σ_{ij} and T are constant. In contrast, a thermodynamic counterpart to the second-order inequality in equation (9) is the restriction of positive internal dissipation

$$f_\alpha \dot{\xi}_\alpha \geq 0 \tag{10}$$

which is derived from the second law.

Since changes in inelastic strain rate and internal variable rates are path independent in the complete state space, the inequalities in equations (8) and (9) can be integrated along a straight-line path between two arbitrary states $(\sigma^1_{ij}, f^1_\alpha, T)$ and $(\sigma^2_{ij}, f^2_\alpha, T)$ resulting in the following inequality:

$$\left(\sigma^2_{ij} - \sigma^1_{ij}\right)\left(\dot{\epsilon}^{p2}_{ji} - \dot{\epsilon}^{p1}_{ji}\right) + \left(f^2_\alpha - f^1_\alpha\right)\left(\dot{\xi}^2_\alpha - \dot{\xi}^1_\alpha\right) \geq 0 \tag{11}$$

Along a constant stress path (i.e. under conditions of creep) only the last term in this inequality remains, and we can easily show that a sufficient condition for its satisfaction is

$$\dot{\xi}_\alpha = \frac{\partial \Omega}{\partial f_\alpha} \tag{12}$$

where $\Omega(\sigma_{ij}, f_\alpha, T)$ is convex and positive definite in σ_{ij}, f_α. Here we assumed that equation (12) is not constrained just to constant stress conditions, but is valid in general. Rice (ref. 13), Martin (ref. 14), and others have shown, using thermodynamic arguments, that if the kinetic (or evolutionary) law can be expressed as equation (12), then the flow law given by

$$\dot{\epsilon}^p_{ij} = \frac{\partial \Omega}{\partial \sigma_{ij}} \tag{13}$$

is a derived result.

The criteria for stability and the resulting kinetic and flow laws lead to a vital theorem (ref. 12):

> "The stress and state histories are uniquely defined for time $t > t_0$ by the initial conditions at $t = t_0$ and the loading history."

The existence of this theorem is essential if this is to be a meaningful constitutive theory for use in structural analyses.

Following the lead of Ponter and Leckie (ref. 15) and Ponter (ref. 12), we adopted an additional constitutive assumption, that is

$$\frac{\dot{f}_\alpha}{h(f_\alpha)} = -\dot{\xi}_\alpha = -\frac{\partial \Omega}{\partial f_\alpha} \tag{14}$$

in which h is a hardening function of the internal force f_α. The physical origin of equation (14) in describing the local response of a crystallographic slip system, and the limitations that result in transferring from a local format to a global one, are discussed by Ponter and Leckie. An additional motive for adopting equation (14) comes from considering conditions in the neighborhood of a stress free state, as depicted in figure 1. In particular, for a "J_2-type" material (considered in the following section), the surface ($\Omega(0,f_\alpha,T)$ = constant) is a sphere of radius $|f_\alpha|$ in thermodynamic force space. The gradient vector $\partial\Omega/\partial f_\alpha$ at each point on the surface where Ω = constant is directed along the outward normal. By considering the constitutive assumption $\dot{f}_\alpha/h = -\dot{\xi}_\alpha$, the thermodynamic restriction in equation (10) can be expressed as $f_\alpha \dot{f}_\alpha/h \leq 0$, which for positive h constrains the vector $\dot{f}_\alpha/h$ to be contained within a half-sphere in thermodynamic force space. (See fig. 1.) The Ponter-Leckie constitutive assumption equation (14) selects the direction of $\dot{f}_\alpha/h$ so that its projection on f_α is a maximum; that is, the Ponter-Leckie constitutive assumption ensures that state recovery occurs under maximum internal dissipation in the neighborhood of a stress free state.

The extended normality structure expressed in equations (13) and (14) provides the basis for the present development. Moreover, this structure is assumed to hold under nonisothermal conditions.

A SPECIAL POTENTIAL FUNCTION

The governing differential equations of a theory of viscoplasticity that accounts for internal damage are taken to be associated with the normality structure of a potential function Ω as discussed in the previous section. The independent arguments of this potential function are the applied stress σ_{ij}, an internal stress β_{ij}, a threshold strength Z, the damage ω, and the temperature T; thus, $\Omega(\sigma_{ij},\beta_{ij},Z,\omega)$, where the temperature dependence is implicit. From a thermodynamic viewpoint, the internal stress and the threshold strength are averaged thermodynamic forces, and damage is an averaged internal variable (or thermodynamic displacement). The internal stress and threshold strength are associated with kinematic and isotropic hardening behaviors, whereas damage is associated with material degradation.

Moderate states of hydrostatic pressure have virtually no influence on the inelastic response of metals.[3] The stress dependence of Ω can therefore be expressed in terms of the deviatoric applied stress

$$S_{ij} = \sigma_{ij} - \frac{1}{3}\sigma_{kk}\delta_{ij} \tag{15}$$

and the deviatoric internal stress

$$B_{ij} = \beta_{ij} - \frac{1}{3}\beta_{kk}\delta_{ij} \tag{16}$$

---

[3] Moderate states of hydrostatic pressure have a strong influence on the formation and growth of material defects and, therefore, on the damage. This effect, however, is accounted for in the degradation function, not in the potential function.

where their difference

$$\Sigma_{ij} = S_{ij} - B_{ij} \tag{17}$$

is the effective stress associated with inelastic deformation. Under conditions of full isotropy, the invariants

$$\begin{aligned} I_2 &= \frac{1}{2} B_{ij}B_{ji} \\ I_3 &= \frac{1}{3} B_{ij}B_{jk}B_{ki} \end{aligned} \tag{18}$$

and

$$\begin{aligned} J_2 &= \frac{1}{2} \Sigma_{ij}\Sigma_{ji} \\ J_3 &= \frac{1}{3} \Sigma_{ij}\Sigma_{jk}\Sigma_{ki} \end{aligned} \tag{19}$$

provide a complete description of the stress dependence of Ω.

For the chosen potential function, the flow law is

$$\dot{\epsilon}^{p}_{ij} = \frac{\partial\Omega}{\partial\sigma_{ij}} \tag{20}$$

and the evolutionary laws are taken to be

$$\frac{\dot{B}_{ij}}{2h_b} = - \frac{\partial\Omega}{\partial B_{ij}} \tag{21}$$

$$\frac{\dot{Z}}{h_z} = - \frac{\partial\Omega}{\partial Z} \tag{22}$$

and

$$\frac{\dot{\omega}}{D} = \frac{\partial\Omega}{\partial\omega} \tag{23}$$

in accordance with the results of the previous section. Here h_b and h_z are the hardening functions for the internal stress and the threshold strength, and D is a degradation function. Equation (20) is the flow law of Rice (ref. 13). Equations (21) and (22) are the evolutionary laws of Ponter and Leckie (ref. 15) and equation (23) is the proposed evolutionary law for damage.

Since damage is an internal variable, whereas internal stress and threshold strength are thermodynamic forces, the sign for equation (23) is different from that for equations (21) and (22). The reason for this difference is a Legendre transformation, like those used in equilibrium thermodynamics. These equations form the foundation for a theory of viscoplasticity that incorporates internal damage. A specific model is obtained by choosing a particular form for the potential function.

The potential function considered for this model is

$$\Omega = \int K^2 \frac{1}{2\mu} f(F)\, dF + \int K^2 g(G)\, dG + \int z(Z)\, dZ \tag{24}$$

where the stress dependence enters through the functions $F(\Sigma_{ij})$ and $G(B_{ij})$. This extends the function used by Robinson (ref. 16) to include isotropic effects. The fact that equation (24) is a sum of integrals is consistent with Rice's formulation (ref. 13). In his definition of the potential function, each integrand denotes the rate of change of a thermodynamic displacement (or internal variable), which is integrated with respect to its conjugate thermodynamic force.

In the spirit of von Mises (ref. 17), the stress dependence of F and G relies only on the second invariants; in particular,[4]

$$F = \frac{J_2}{K^2} - 1 \tag{25}$$

and

$$G = \frac{I_2}{K^2} \tag{26}$$

Equation (25) is a Bingham-Prager (refs. 18 and 19) yield condition with K denoting the yield strength in shear. Inelastic strain only occurs when $F > 0$; an elastic domain is defined by the inequality $F \leq 0$. The boundary between these two regions, $F = 0$, is a sphere in deviatoric stress space; it is the threshold or quasi-static yield surface. The origin of this sphere is at B_{ij}, and its radius is K. The inelastic domain, at a fixed inelastic state, consists of a nested family of spherical surfaces in deviatoric stress space; each is a surface of constant F, and thus of constant Ω. Viscoplasticity differs from classical plasticity in that stress states that lie outside the quasi-static yield surface are admissible; they are not admissible in classical plasticity.

---

[4] Many theories of viscoplasticity take $F = J_2/K^2$ instead of equation (25); thus, there is no elastic domain. The only influence that this choice for F would have on the resulting theory is that the inequality would be removed from the flow function.

If the stress dependence of F and G is to be a net stress dependence in the sense of Kachanov (ref. 1) and Rabotnov (ref. 2), then K must be a linear homogeneous function of damage,

$$K = \kappa(Z)(1 - \omega) \tag{27}$$

where κ is the quasi-static yield strength in shear. Although damage, by definition, influences the state of stress, this influence is manifested by a reduction in strength as exemplified in equations (7) and (27). In equation (27) the reduction in strength due to material degradation competes with the process of hardening which enhances strength.

Given the potential function (eq. (24)), the flow law of equation (20) becomes Prager's flow equation (ref. 20),

$$2\mu \, \dot{\varepsilon}^{p}_{ij} = f(F)\Sigma_{ij} \tag{28}$$

where μ is the viscosity and f is the flow function. (This is derived in the appendix.) The Bingham-Prager yield condition (eq. (25)), constrains the flow function so that it is zero in the elastic domain. Coaxiality between the effective stress and the inelastic strain rate is implied in equation (28). Stability (in the sense of eq. (8)) constrains the flow function f(F) to be nondecreasing with increasing values of F. Most theories of viscoplasticity use the general form of this flow equation.

Given the potential function (eq. (24)) the evolutionary law for internal stress (eq. (21)), becomes a Bailey-Orowan type relationship (refs. 21 and 22), that is

$$\dot{B}_{ij} = 2h_b(G)\dot{\varepsilon}^{p}_{ij} - r_b(G)B_{ij} \tag{29}$$

where h_b and r_b are the kinematic functions for hardening and thermal recovery. (Equation (29) is derived in the appendix.) The first term in this equation, for constant h_b, is Prager's rule for kinematic hardening (ref. 20). To model dynamic recovery of the internal stress, Robinson (refs. 23 and 24) presents a kinematic hardening function that exhibits an analytical discontinuity whenever there is a reversal in stress.

The second term in equation (29) accounts for the thermal recovery of the internal stress state. This is an anelastic response since it continues until the internal stress has relaxed to zero, regardless of whether the current deformation state is elastic or inelastic.

The experimental results of Mitra and McLean (ref. 25) verify the Bailey-Orowan hypothesis that inelastic deformation occurs as a result of two competing mechanisms: a hardening process that progresses with inelastic deformation, and a thermal recovery process that progresses with time. Whenever these two mechanisms balance such that $\dot{B}_{ij} = 0$, the internal stress is in a steady state. Stability (in the sense of eq. (9)) constrains the function $g(G) = r_b(G)/2h_b(G)$ to be nondecreasing with increasing values of G.

The general form of this evolutionary equation for the internal stress is used in many viscoplastic models.

Data from metals that strain-age indicate that the evolution of the quasi-static yield strength (defined in eq. (27)) depends on the history of thermomechanical loading (ref. 26). These data suggest an evolution such that

$$\dot{\kappa} = \Gamma\dot{Z} - \theta(Z)\dot{T} \tag{30}$$

where the parameter Γ reflects the temperature dependence of the quasi-static yield strength in an annealed state, and the function θ represents the change in quasi-static yield strength resulting from a change in temperature. The evolution of the quasi-static yield strength given by equation (30) is path independent whenever the following equation is satisfied:

$$\theta(Z) = -Z\,\frac{d\Gamma}{dT} \tag{31}$$

If equation (30) is to be self-consistent, then $\dot{\kappa}$ must be path independent in the annealed state; therefore

$$\theta(Z_a) = -Z_a\,\frac{d\Gamma}{dT} \tag{32}$$

where $0 < Z_a \leq Z$. This constraint must always be satisfied; it is like an initial condition for the functional dependence of θ.

Given the potential function (eq. (24)) and the equation of evolution for the quasi-static yield strength (eq. (30)), the evolutionary law for the threshold strength (eq. (22)) becomes a Bailey-Orowan type relationship (refs. 21 and 22),

$$Z = h_Z(Z)\left(\Gamma - \int_0^t \frac{\partial\theta}{\partial Z}\dot{T}\,dt\right)\frac{\dot{W}}{\kappa} - r_Z(Z) \tag{33}$$

where

$$\dot{W} = \sigma_{ij}\dot{\epsilon}^p_{ji} - \frac{\beta_{ij}\dot{B}_{ji}}{2h_b}\,(G) \tag{34}$$

and h_Z and r_Z are the isotropic functions for hardening and thermal recovery. (These equations are derived in the appendix.) Equation (33) implies that the path of thermomechanical loading influences the rate of isotropic hardening; under isothermal conditions it reduces to

$$\dot{Z} = \frac{h_Z(Z)\dot{W}}{Z} - r_Z(Z) \tag{35}$$

The first term in equations (33) and (35) implies that isotropic hardening progresses with dissipated work. This dissipated work, as defined in equation (34), is the sum of the inelastic work and internal work.[5] The internal work can be thought of as a continuum measure of the free energy stored in the material that arises from inelastic deformation. With the exception of the viscoplastic model of Bodner and Partom (ref. 27) (where kinematic hardening is not present, and isotropic hardening evolves with inelastic work), all viscoplastic models that incorporate isotropic hardening, to the best of our knowledge, assume that this process progresses with inelastic path length $\int(\dot\epsilon^p_{ij}\dot\epsilon^p_{ji})^{1/2}\,dt$. This is an assumption that our theoretical derivation does not support.

The second term in equations (33) and (35) accounts for the anelastic thermal recovery (or annealing) of the threshold strength. This function must be constrained so that recovery terminates when the annealed value of threshold strength is obtained. Stability (in the sense of eq. (9)) constrains the function $z(Z) = r_Z(Z)/h_Z(Z)$ to be nondecreasing with increasing values of Z.

Given the potential function (eq. (24)), the evolutionary law for damage (eq. (23)) becomes

$$\omega = D(\omega)\frac{\dot W}{1 - \omega} \tag{36}$$

where D is the degradation function. (Equation (36) is derived in the appendix.)

Since materials do not degrade in states of sufficient hydrostatic compression, in general the degradation function ought to switch off the evolution of internal damage when a critical state of hydrostatic compression is reached. Equation (36) implies that damage evolves with dissipated work, as defined in equation (34). Hereditary effects are included through the dependence of dissipated work on inelastic strain and internal stress; thus, equation (36) has the potential to account for time-dependent effects in a natural way. Stability (in the sense of eq. (9)) is satisfied if $D(\omega)$ does not increase with increasing values of ω; but this is not observed. Initially the dissipation function is virtually a constant, and the material response is stable for all practical purposes. However, near the end of life, the value of the dissipation function explodes, thereby leading to material instability or failure. This is not to say that this theory is undesirable, for it is precisely this instability that continuum damage mechanics attempts to characterize.

Many researchers have used inelastic work as a parameter to characterize fatigue damage (e.g. refs. 28 to 31). The equation of damage evolution given in equation (36) differs from these earlier, largely empirical, energy criteria by including the influence of internal work. Albeit this is a lesser effect than that of inelastic work, nevertheless, it is believed not to be a negligible one, especially when time-dependent effects are present. Additional insight is gained from an equivalent expression for the dissipated work rate (eq. (34)), that is

---

[5] In accordance with equations (14) and (21), the quantities $-\dot\beta_{ij}/2h_b$ denote the rates of change in the thermodynamic displacements (or internal variables) conjugate to the thermodynamic forces β_{ij}. Therefore, the quantity $-\beta_{ij}\dot\beta_{ji}/2h_b$ can be interpreted as the rate of change in the internal work.

$$\dot{W} = \Sigma_{ij}\dot{\varepsilon}^{p}_{ji} + r_b(G)\,\frac{I_2}{h_b}\,(G) \tag{37}$$

which is obtained from equations (29) and (34). The first term in this relationship evolves with inelastic deformation and is a measure of fatigue damage. (See fig. 2.) The second term evolves with time at internal stress (I_2 is the second invariant of internal stress) and is a measure of the interactive creep damage. Thus, the interaction between fatigue and creep damage is specified. The temperature dependence for this measure of creep damage is accounted for, to a large extent, in the thermal recovery function r_b.

CONCLUDING REMARKS

A theory of viscoplasticity has been derived from conditions of stability and physical arguments, for an initially isotropic continua that exhibits internal damage. This material degradation was incorporated through the Kachanov-Rabotnov concept of a net stress. Damage was assumed to be an internal variable that evolves isotropically according to a Ponter-Leckie type constitutive assumption. A potential function was considered that extends the Robinson viscoplastic model by including the effects of isotropic hardening and material degradation. The yield strength was not considered to be an independent variable; rather, it was assumed to evolve with changes in threshold strength and temperature.

We determined that inelastic strain evolves according to a Prager type flow equation, and that Bailey-Orowan type kinetic equations govern the evolution of both internal stress and threshold strength. The internal stress hardens like a Prager hardening rule, whereas the threshold strength hardens with dissipated work - not inelastic path length - at a rate that depends on thermal history. Internal damage was shown to evolve with dissipated work leading to a loss of material stability. Dissipated work is the sum of inelastic work and internal work. Internal work is a continuum measure of the free energy stored in a material due to inelastic deformation.

APPENDIX

This appendix provides the derivations for the flow and evolutionary equations given in equations, (28), (29), (33), and (36).

By using equations, (15), (17), (19), (24), and (25), the flow law (eq. (20)) can be written as

$$\dot{\epsilon}^{p}_{ij} = \frac{\partial \Omega}{\partial F} \frac{\partial F}{\partial J_2} \frac{\partial J_2}{\partial \Sigma_{uv}} \frac{\partial \Sigma_{vu}}{\partial S_{mn}} \frac{\partial S_{nm}}{\partial \sigma_{ij}} \qquad \text{(A1)}$$

by the chain rule, where

$$\frac{\partial \Omega}{\partial F} = \frac{K^2 f(F)}{2\mu} \qquad \text{(A2)}$$

$$\frac{\partial F}{\partial J_2} = \frac{1}{K^2} \qquad \text{(A3)}$$

$$\frac{\partial J_2}{\partial \Sigma_{uv}} = \Sigma_{uv} \qquad \text{(A4)}$$

$$\frac{\partial \Sigma_{vu}}{\partial S_{mn}} = \delta_{vm}\delta_{un} \qquad \text{(A5)}$$

and

$$\frac{\partial S_{nm}}{\partial \sigma_{ij}} = \delta_{ni}\delta_{mj} - \frac{1}{3}\delta_{nm}\delta_{ij} \qquad \text{(A6)}$$

Combining these equations results in

$$2\mu\, \dot{\epsilon}^{p}_{ij} = f(F)\, \Sigma_{ij} \qquad \text{(A7)}$$

which is the flow equation (28).

By utilizing equations (16) to (19) and (24) to (26), the evolutionary law for internal stress (eq. (21)) can be written as

$$\dot{B}_{ij} = -2h_b(G) \left(\frac{\partial \Omega}{\partial F} \frac{\partial F}{\partial J_2} \frac{\partial J_2}{\partial \Sigma_{uv}} \frac{\partial \Sigma_{vu}}{\partial B_{mn}} + \frac{\partial \Omega}{\partial G} \frac{\partial G}{\partial I_2} \frac{\partial I_2}{\partial B_{mn}} \right) \frac{\partial B_{nm}}{\partial \beta_{ij}} \qquad \text{(A8)}$$

by the chain rule, where

$$\frac{\partial \Sigma_{vu}}{\partial B_{mn}} = -\delta_{vm}\delta_{un} \qquad \text{(A9)}$$

$$\frac{\partial \Omega}{\partial G} = K^2 g(G) \qquad \text{(A10)}$$

$$\frac{\partial G}{\partial I_2} = \frac{1}{K^2} \qquad \text{(A11)}$$

$$\frac{\partial I_2}{\partial B_{mn}} = B_{mn} \qquad \text{(A12)}$$

and

$$\frac{\partial B_{nm}}{\partial B_{ij}} = \delta_{ni}\delta_{mj} - \frac{1}{3}\delta_{nm}\delta_{ij} \qquad \text{(A13)}$$

Combining equations (A2) to (A4) with equations (A8) to (A13), we obtain

$$\dot{B}_{ij} = h_b(G)f(F)\,\frac{\Sigma_{ij}}{\mu} - 2h_b(G)g(G)B_{ij} \qquad \text{(A14)}$$

which when joined with the flow equation (eq. (A7)) results in

$$\dot{B}_{ij} = 2h_b(G)\dot{\varepsilon}^{p}_{ij} - r_b(G)B_{ij} \qquad \text{(A15)}$$

where $r_b(G)$ is defined to be $2h_b(G)g(G)$. This is the evolutionary equation for internal stress given in equation (29).

We define the following expression:

$$\dot{W} = -K\left(\frac{\partial\Omega}{\partial F}\frac{\partial F}{\partial K} + \frac{\partial\Omega}{\partial G}\frac{\partial G}{\partial K}\right) \qquad \text{(A16)}$$

From equations (18), (19), (25), and (26), we obtain

$$\frac{\partial F}{\partial K} = -\frac{\Sigma_{ij}\Sigma_{ji}}{K^3} \qquad \text{(A17)}$$

$$\frac{\partial G}{\partial K} = -\frac{B_{ij}B_{ji}}{K^3} \qquad \text{(A18)}$$

which when substituted into equation (A16), along with equations (A2) and (A10), gives

$$\dot{W} = \frac{f(F)\Sigma_{ij}\Sigma_{ji}}{2\mu} + g(G)B_{ij}B_{ji} \qquad \text{(A19)}$$

By substituting equations (A7) and (A15) into this relationship, it becomes

$$\dot{W} = S_{ij}\dot{\varepsilon}^{p}_{ji} - \frac{B_{ij}\dot{B}_{ji}}{2h_b}(G) \qquad \text{(A20)}$$

which can be expressed as

$$\dot{W} = \sigma_{ij}\dot{\epsilon}^{p}_{ji} - \frac{\beta_{ij}\dot{B}_{ji}}{2h_{b}}\,(G) \tag{A21}$$

because of equations (15) and (16), and the fact that $\dot{\epsilon}^{p}_{ij}$ and $\dot{B}_{ij}$ are deviatoric. This is the rate of dissipated work given in equation (34).

From equations (24) to (27), the evolutionary law for threshold strength (eq. (22)) can be written as

$$\dot{Z} = -h_{z}(Z)\left[\left(\frac{\partial\Omega}{\partial F}\frac{\partial F}{\partial K} + \frac{\partial\Omega}{\partial G}\frac{\partial G}{\partial K}\right)\frac{\partial K}{\partial Z} + z(Z)\right] \tag{A22}$$

by the chain rule, where

$$\frac{\partial K}{\partial Z} = \frac{K}{\kappa}\frac{\partial\kappa}{\partial Z} \tag{A23}$$

and where (from eq. (30)),

$$\frac{\partial\kappa}{\partial Z} = \Gamma - \int_{0}^{t}\frac{\partial\theta}{\partial Z}\dot{T}\,dt \tag{A24}$$

Joining equations (A16) and (A22) to (A24) results in

$$\dot{Z} = h_{z}(Z)\left(\Gamma - \int_{0}^{t}\frac{\partial\theta}{\partial Z}\dot{T}\,dt\right)\frac{\dot{W}}{\kappa} - r_{z}(Z) \tag{A25}$$

where $r_{z}(Z)$ is defined to be $h_{z}(Z)z(Z)$. This is the evolutionary equation for threshold strength given in equation (33).

By using equations (24) to (27), the evolutionary law for damage (eq. (23)) can be written as

$$\dot{\omega} = D(\omega)\left(\frac{\partial\Omega}{\partial F}\frac{\partial F}{\partial K} + \frac{\partial\Omega}{\partial G}\frac{\partial G}{\partial K}\right)\frac{\partial K}{\partial\omega} \tag{A26}$$

by the chain rule, where

$$\frac{\partial K}{\partial\omega} = -\frac{K}{1-\omega} \tag{A27}$$

Combining equations (A16), (A26), and (A27) results in

$$\dot{\omega} = D(\omega)\frac{\dot{W}}{1-\omega} \tag{A28}$$

which is the evolutionary equation for damage given in equation (36).

REFERENCES

1. Kachanov, L.M., "On the Time to Failure Under Creep Conditions," Izvestiya Akademii Nauk SSSR, Otdelenie Tekhnicheskikh Nauk, No. 8 (1958), pp. 26-31.

2. Rabotnov, Y.N., "On the Equation of State of Creep," Joint International Conference on Creep, Proceedings, Institution of Mechanical Engineers, Vol. 178, Pt. 3A (1963-4) pp. 2-117 to 2-122.

3. Chaboche, J.L., "Description Thermodynamique et Phenomenologique de la Viscoplasticite Cyclique avec Endommagement," Ph.D. thesis, University of Paris (1978).

4. Bodner, S.R., "A Procedure for Including Damage in Constitutive Equations for Elastic-Viscoplastic Work-Hardening Materials," IUTAM, Physical Nonlinearities in Structural Analysis, (eds. J. Hult and J. Lemaitre), Springer-Verlag (1982), pp. 21-28.

5. Walker, K.P. and Wilson, D.A., "Constitutive Modeling of Engine Materials," AFWAL/TR-84-4073 (1984).

6. Perzyna, P., "Stability of Flow Processes for Dissipative Solids with Internal Imperfections," Journal of Applied Mathematics and Physics, Vol. 35 (1984), pp. 848-867.

7. Leckie, F.A. and Onat, E.T., "Tensorial Nature of Damage Measuring Internal Variables," IUTAM, Physical Nonlinearities in Structural Analysis, (eds., J. Hult and J. Lemaitre), Springer-Verlag (1981), pp. 140-144.

8. Murakami, S. and Ohno, N., "A Continuum Theory of Creep and Creep Damage," Creep in Structures, 3rd Symposium, (ed., A. Ponter), Springer-Verlag (1982), pp. 422-444.

9. Betten, J., "Damage Tensors in Continuum Mechanics," Journal de Mecanique, Theorique et Appliquee, Vol. 2 (1983), pp. 13-32.

10. Lemaitre, J., "A Continuous Damage Mechanics Model for Ductile Fracture" Journal of Engineering Materials and Technology, Vol. 107 (1985), pp. 83-89.

11. Drucker, D.C., "Some Implications of Work Hardening and Ideal Plasticity," Quarterly of Applied Mathematics, Vol. 7 (1950), pp. 411-418.

12. Ponter, A.R.S., "Convexity and Associated Continuum Properties of a Class of Constitutive Relationships," Journal de Mecanique, Vol. 15 (1976), pp. 527-542.

13. Rice, J.R., "On the Structure of Stress-Strain Relations for Time-Dependent Plastic Deformation in Metals," Journal of Applied Mechanics, Vol. 37 (1970), pp. 728-737.

14. Martin, J.B., Plasticity: Fundamentals and General Results, MIT press (1975), pp. 886-890.

15. Ponter, A.R.S. and Leckie, F.A., "Constitutive Relationships for the Time-Dependent Deformation of Metals," Journal of Engineering Materials and Technology, Vol. 98 (1976), pp. 47-51.

16. Robinson, D.N., "Constitutive Relationships for Anisotropic High-Temperature Alloys," Nuclear Engineering and Design, Vol. 83 (1984), pp. 389-396.

17 Mises, R.V., "Mechanik der festen Korper im plastisch - deformablen Zustand," Nachrichten von der Koniglichen Gesellschaft der Wissenschaften, Mathematisch - Physikalische Klasse (1913), pp. 582-592. English translation: NASA TM-88448, (1986).

18. Bingham, E.C., Fluidity and Plasticity, McGraw-Hill (1922), pp. 215-218.

19. Prager, W., Introduction to Mechanics of Continua, Ginn and Co., Boston (1961), pp. 136-138.

20. Prager, W., "Recent Developments in the Mathematical Theory of Plasticity," Journal of Applied Physics, vol. 20 (1949), pp. 235-241.

21. Bailey, R.W., "Note on the Softening of Strain-Hardening Metals and its Relations to Creep," Journal of the Institute of Metals, London, Vol. 35 (1926), pp. 27-40.

22. Orowan, E., "The Creep of Metals," Journal of the West of Scotland Iron and Steel Institute, Vol. 54 (1946), pp. 45-96.

23. Robinson, D.N., "A Unified Creep-Plasticity Model for Structural Metals at High Temperature," ORNL/Tm-5969 (1978).

24. Robinson, D.N. and Swindeman, R.W., "Unified Creep-Plasticity Constitutive Equations for 2¼ Cr - 1 Mo Steel at Elevated Temperature," ORNL/TM-8444 (1982).

25. Mitra, S.K. and McLean, D., "Work Hardening and Recovery in Creep," Proceedings of the Royal Society of London, Ser. A, Vol. 295 (1966), pp. 288-299.

26. Robinson, D.N. and Bartolotta, P.A., "Viscoplastic Constitutive Relationships with Dependence on Thermomechanical History," NASA CR-174836 (1985).

27. Bodner, S.R. and Partom, Y., "Constitutive Equations for Elastic-Viscoplastic Strain-Hardening Materials," Journal of Applied Mechanics, Vol. 42 (1975), pp. 385-389.

28. Halford, G.R., "The Energy Required for Fatigue," Journal of Metals, Vol. 1 (1966), pp. 3-18.

29. Stowell, E.Z., "A Study of the Energy Criterion for Fatigue," Nuclear Engineering and Design, Vol. 3 (1966), pp. 32-40.

30. Ostergren, W.J., "A Damage Function and Associated Failure Equations for Predicting Hold Time and Frequency Effects in Elevated Temperature Low Cycle Fatigue," Journal of Testing and Evaluation, Vol. 4 (1976). pp. 327-339.

31. Garud, Y.S., "A New Approach to the Evaluation of Fatigue Under Multi-Axial Loadings," Methods for Predicting Material Life in Fatigue, (eds. W. Ostergren and J. Whitehead), American Society of Mechanical Engineers (1980), pp. 247-263.

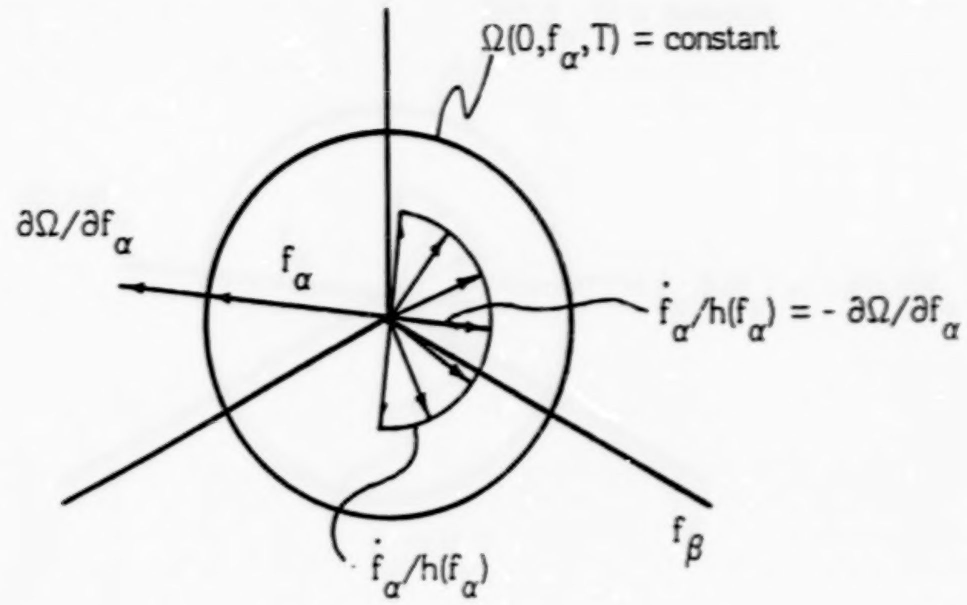
$\Omega(0,f_\alpha,T)$ = constant
$\partial\Omega/\partial f_\alpha$
f_α
$\dot{f}_\alpha/h(f_\alpha) = -\,\partial\Omega/\partial f_\alpha$
f_β
$\dot{f}_\alpha/h(f_\alpha)$

Figure 1. - In the stress free state $f_\alpha/h(f_\alpha)$ provides maximum internal dissipation during state recovery.

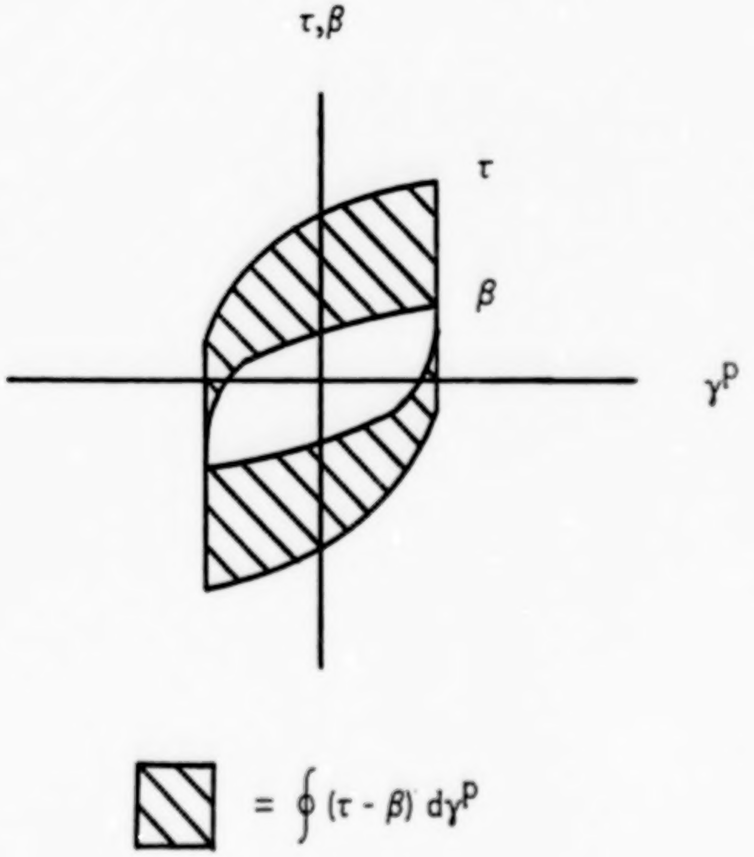
τ,β
τ
β
γ^P
$= \oint (\tau - \beta)\, d\gamma^P$

Figure 2. - Dissipated work in cyclic shear in the absence of thermal recovery.

N88
21509
UNCLAS

N88-21509

CREEP RUPTURE ANALYSIS OF A BEAM RESTING ON HIGH TEMPERATURE FOUNDATION

Randy J. Gu*
Oakland University
Rochester, Michigan 48063

Francis A. Cozzarelli
State University of New York at Buffalo
Buffalo, New York 14260

In this research, a simplified uniaxial strain-controlled creep damage law is deduced with the use of experimental observation from a more complex strain-dependent law. This creep damage law correlates the creep damage, which is interpreted as the density variation in the material, directly with the accumulated creep strain. Based on the deduced uniaxial strain-controlled creep damage law, a continuum mechanical creep rupture analysis is carried out for a beam resting on a high temperature elastic (Winkler) foundation. The analysis includes the determination of the nondimensional time for initial rupture, the propagation of the rupture front with the associated thinning of the beam, and the influence of creep damage on the deflection of the beam. Creep damage starts accumulating in the beam as soon as the load is applied, and a creep rupture front develops at and propagates from the point at which the creep damage first reaches its critical value. By introducing a series of fundamental assumptions within the framework of technical Euler-Bernoulli type beam theory, a governing set of integro-differential equations is derived in terms of the nondimensional bending moment and the deflection. These governing equations are subjected to a set of interface conditions at the propagating rupture front. A numerical technique is developed to solve the governing equations together with the interface equations, and the computed results are presented and discussed in detail.

1. INTRODUCTION

Tertiary creep involves the process of fracture leading ultimately to complete failure, and is associated with local reduction in cross-sectional area and more importantly with the nucleation and growth of voids and microracks along grain boundaries. This failure mode leads to eventual collapse of a structural component and is known in the literature as creep rupture or stress rupture. In order to meet the demands of designers and engineers concerned with the safety of equipment operating at elevated temperatures, researchers in recent decades have conducted extensive creep rupture experiments from which they hope to extract some useful "extrapolation" parameters. Such parameters are inevitably limited by the laboratory-allowed time scale and by the usual scatter of the empirical data, but they are employed to estimate the appropriate stress and temperature requirements for the practical service lives of equipment in operation. Amongst such extrapolation parameters methods are the ones of Larson-Miller (1952) [1], Manson-Haferd (1953) [2], Orr-Sherby-Dorn (1954) [3], and many others. Manson and Ensign [4] have presented an interesting review on the progress in extrapolation procedures for creep rupture; an excellent discussion of these is also given in the text by Conway [5].

In parallel with the development cited above, other researchers including some metallurgists have attempted to define and quantify a suitable variable which describes the damage state and measures the extent of damage in materials undergoing creep. The major hurdle in this line of research is the manner by which ones bridges the gap between the scalar damage variable obtained by macroscopic creep testing and the microscopic processes involved in the nucleation and growth of voids and microcracks at grain boundaries. Such variables are expected to be able to characterize the damage state from the physical and quantitative points of view, and furthermore to provide a useful tool for analytical modelling via continuum mechanics. Amongst such approaches are Robinson's linear cumulative creep damage law (1952) [6], Hoff's ductile creep rupture theory (1953) [7], Kachanov's brittle rupture theory (1961) [8], Robotnov's coupled damage creep theory (1969) [9], and many other modified theories such as the one due to Leckie and Hayhurst (1974) [10]. Comparative studies of the various theories may be found in [11-13]. Recently, scientists have observed a close relation between density change and the nucleation and growth of voids and microcracks associated with creep damage in polycrystalline materials. Extensive efforts have thus been made to identify and quantify creep damage in terms of the density variation which is attributed to cavitation in a creeping material. Following this concept, Piatti et al [14] developed a refined experimental technique to measure the density variation for use as a definition of creep damage. Using data obtained in this manner for steel, Belloni et al [15,16] proposed a statistically-based damage law in a complicated power law form similar to the one presented in Woodford's parametric study of creep damage [17].

Because of its inherent mathematical complexity, the creep damage law proposed in [15,16] is somewhat inconvenient for analytical treatment within the framework of continum creep damage mechanics. In addition, some arbitrariness remains in the determination of the material constants appearing in this damage law (see [18]). Accordingly, the first task in this work is to obtain a simplified yet still useful damage law. This task is addressed in Section 2 where we argue first from the microscopic point of view that density variation certainly is a proper index of damage in a material undergoing creep deformation. We then propose a simplified uniaxial strain-controlled damage law by introducing some assumptions based on experimental observation associated with the original damage law, and this strain-controlled damagelaw is demonstrated to be closely related not only to the original damage law but also to Kachanov's damage law (see [8]). We conclude Section 2 with the observation that, whereas a typical boundary value problem suffices to represent the problem in "the first stage of creep damage", we encounter in "the second stage of propagation of the rupture front" a moving boundary problem similar to the Stefan problem in heat conduction [19].

Utilizing the above strain-controlled creep damage theory, we present in Section 3 a continuum mechanics model for the creep rupture analysis of a beam resting on a high temperature elastic Winkler foundation which generates a prescribed thermal gradient in the thickness direction. Based on technical Euler-Bernoulli-type beam theory, we derive in Section 3 a set of governing differential equations for a region with a moving boundary (rupture front) which is prescribed by a set of interface equations. Owing to the inherent nonlinearity of the problem, closed form solutions generally do not exist. Accordingly, a successful treatment of the problem requires the application of a suitable numerical technique which is then presented in Section 4. In the latter part of Section 4, we consider a simple case for which a closed form solution does exist. We then present detailed numerical results for the problems in which temperature gradient is taken into account and the foundation is either present or absent. The results consist of the nondimensional forms for bending moment, deflection, and the geometric shapes of the rupture front.

2. STRAIN-CONTROLLED CREEP DAMAGE

2.1 Creep Damage Law Under Uniaxial Stress

Virtually all load-bearing structural components operating at elevated temperatures undergo the typical 3-stage creep phenomenon. Various phenomenological interpretations of the creep process have been devised, usually employing the concept that creep is essentially a competition between strain-hardening and recovery [20]. It is well understood that at elevated temperatures a crystalline solid may deform in accordance with several mechanisms such as dislocation creep and diffusion creep. Each such mechanism is most active is some range of stress and temperature [21], such that within certain regions of the stress-temperature space one mechanism is said to dominate the others. The pictorial maps constructed by this concept are known as Ashby's deformation-mechanism maps [21,22]. Raj and Ashby [23] have pointed out that the creep mechanisms mentioned above are in fact an "accommodation process" for grain boundary sliding. When a shear stress causes sliding to occur at a generally nonplanar grain boundary, some accommodation process (such as diffusional flow or plastic flow) is necessary to heal the crystalline structure at the deviation of the boundary from a perfect plane. In the event that this accommodation process does not develop fully at a boundary deviation during sliding, an "incompatibility" results in the form of voids and wedge cracks along the grain boundaries which are oriented roughly perpendicular to the tensile axis. As the material is strained further the coalescence of voids and cracks eventually leads to intergranular creep fracture. Clearly, as the cavity volume increases during the process of tertiary creep and eventual fracture, the material dilates. In this section, we shall focus on a strain-controlled constitutive continum damage law based on this close relation between creep damage and cavitation induced dilation in materials.

The type of damage described above is associated with power-law or dislocation creep [23,24]. Steady dislocation creep under constant uniaxial tensile stress σ_e is found experimentally to obey the constitutive relation[25]

$$\dot{\varepsilon}_s = A(T)\,\sigma_\circ^n \qquad (1)$$

in which n is the constant stress power. The reciprocal viscosity coefficient A(T) is expressed as the Arrhenius equation

$$A(T) = A^* \exp(-\Delta H/RT) \qquad (2)$$

where A^* is the relatively temperature insensitive pre-exponential cofficient, ΔH the activation energy for creep, R the gas constant and T the absolute temperature. Equation (1), which is also known as Norton's steady creep law, will be employed to describe the creep deformation process in the problem considered later in this work.

From the phenomenological point of view, creep rupture can be separated into two categories. Failure at high stress and low temperature is characterized by pronounced lateral contractions and the first continuum model for this process is known as Hoff's ductile creep rupture theory [7]. On the other hand, low stress levels together with high temperatures result in brittle type of rupture with little lateral contraction, and the first phenomenological theory for this process was formulated by Kachanov [8]. We shall not consider Hoff's theory further here (ample discussion is given in [13,26]), but we shall now review Kachanov's theory briefly. Kachanov defined the damage variable ω for a one-dimensional test specimen in accordance with

$$\omega = \frac{A_\circ - A_e}{A_\circ} = 1 - \frac{A_e}{A_\circ}$$

where A_o and A_e are, respectively, the original and the effective cross sectional areas carrying the load. Clearly, cavitation creates new internal surface area which in turn reduces the effective cross-sectional area carrying the load. Thus, the material in its virgin state has the damage ω equal to zero, while the damage in a completely deteriorated material approaches unity. A power law for the damage-rate was postulated by Kachanov for variable one-dimensional stress as

$$\dot{\omega} = C\left[\frac{\sigma}{1-\omega}\right]^{\nu} \tag{3}$$

where C,ν are material constants, and where C may be temperature dependent. Assuming that the material is initially undamaged, integration of the above equation gives

$$1 - (1-\omega)^{\nu+1} = C(1+\nu)\int_0^t \sigma^{\nu}(t')dt' \tag{4}$$

As pointed out earlier in this section, a close connection exists between creep damage and the cavitation induced dilation of a material. Belloni et al [15,16] have employed material density variation as the measure of damage in a creep material using refined techniques. They proposed a damage law at constant stress σ_o in the power form for the uniaxial tension test

$$D = c\,\epsilon_C^{\alpha}\,\sigma_o^{\gamma}\,t^{\delta} \tag{5}$$

where $D = -\Delta\rho/\rho_o$, ρ_o is the density of the material in the virgin state, and $\Delta\rho$ is the change in density due to the volume dilation of the material. In eqn.(5) ϵ_C denotes the creep strain, and C, α, γ, δ appear to be relatively insensitive to temperature, but c is highly temperature sensitive. In analogy with Kachanov's damage variable ω , the damage D has value equal to zero in the virgin state and is equal to a critical value at rupture D_r, which is a material constant. Employing statistical regression techniques, Belloni et al were able to correlate their experimental data with damage law (5). A close inspection in eqn.(5), however, reveals that some arbitrariness exists in the determination of the material constants (for details see [18]). This arbitrariness is a consequence of treating ϵ_C and σ_o as independent state variables in eqn.(5), without considering the constitutive creep law. One possible way of eliminating this arbitrariness is outlined by the sequence of simplifications given below.

First, based on the findings in [16] and related work [26,27] we shall make the simplifyig assumption

$$\gamma = \delta n \tag{6}$$

It will be shown later that eqn.(6) together with $\nu = n$ in eqn.(4) establishes an equivalence between Kachanov's formulation and the current one. We further assume that steady creep as described by eqn.(1) completely dominates the deformation behavior, i.e., the material is non-Newtonean viscous. A combination of eqns.(1) and (5), together with assumption (6), then gives

$$D = \frac{c}{A(T)^{\delta}} (\dot{\epsilon}_s t)^{\alpha+\delta} \tag{7}$$

or

$$D = \frac{c}{A(T)^{\delta}} \epsilon_s^{\alpha+\delta} \qquad (8)$$

in which ϵ_S is the creep strain under the steady creep condition. It has been found [28] that, for the rupture mechanism considered here, the product of steady-creep-rate, $\dot{\epsilon}_S$, and the time-to-rupture, t_R, is a constant, i.e.

$$\dot{\epsilon}_S t_R = C_{MG}$$

where C_{MG} is known as Monkman-Grant constant which has the dimension of strain. This relationship holds true for a wide range of temperature and stress. Therefore, at rupture eqn. (7) gives

$$D_r = \frac{c}{A(T)^{\delta}} (C_{MG})^{\alpha+\delta} \qquad (9)$$

where D_r is the critical value of damage at rupture. Belloni et al's data [15] showed that the critical value of damage in the high temperature range is relatively insensitive to temperature. The temperature independent character of both C_{MG} and D_r immplies that the $B/A(T)^{\delta}$ in eqn. (9) must also be temperature independent. Thus

$$\frac{c}{A(T)^{\delta}} = c_o$$

where c_o is a temperature independent material constant. Substituting this back into damage law (8) we then get the simplified form

$$D = c_o \epsilon_s^{\alpha+\delta} \qquad (10)$$

Although a significant simplification has been obtained, damage law (10) is still physically plausible. Note that, although damage is an explicit function of strain along, it is an implicit function of temperature and stress via creep constitutive law (1). In accordance with eqn.(10), a material exposed to stress experiences damage directly related to the creep strain, and rupture occurs as the available creep ductility is exhausted. Hanna and Greenwood [29] showed, for copper with pre-nucleated cavities subjected to low stress and with the creep rate linearly related to the stress, that

$$-\frac{\Delta\rho}{\rho_o} \propto \epsilon_C \tag{11}$$

Although a surprising analogy appears to exist between eqns. (10) and (11), conclusions may not be easily drawn on the material constants in eqn.(10). However, it does appear very reasonable to postulate that creep damage, as measured by density variation, be expressed explicity as a function of creep strain.

In many engineering practices, however, the stress may be varying with time due to effect such as load variation and stress relaxation. The extension of the original creep damage law, eqn.(5) , to the case of time dependent uniaxial stress has been presented in [30]. In the case of simplified eqn.(10) it suffices to employ the integral form of creep strain for variable stress, and thus integrating $\dot{\epsilon}_S = A(T)\sigma(t)^n$ we obtain

$$D(t) = C_* \left\{ \int_0^t A(T)\ \sigma^n(t')dt' \right\}^{\alpha+\delta} \tag{12}$$

Here, the reciprocal viscosity function, A(T), is retained inside the integral sign, in order to allow for the situation in which the temperature varies with time. If $\nu=n$ in Kachanov's theory [see eqn.(4)], eqns. (4) and (12) assume a very similar form; a more detailed comparison of strain-dependent theory with Kachanov's approach is given in [31].

2.2 Propagation of a Creep Rupture Front -- The Moving Boundary Problem

A nonuniform state of stress may be introduced by the irregular geometry of a structure, nonhomogeneous material properties, and nonuniform external loads. Under such circumstances the creep damage within the structure would be a function of the space coordinates in addition to time. Creep damage starts accumulating in the structure as soon as the loads are applied. As time elapses, the creep damage at some point within or on the surface of the structure would first reach the critical value, D_r, at which rupture takes place. This initial rupture time, t_I, is determined in accordance with eqn.(12) as

$$D_r = C_o \left\{ \int_o^{t_I} A(T)\, \sigma^n(t')dt' \right\}^{m+\beta} \tag{13}$$

A rupture front then develops generally as a smooth surface, and starts propagating through the structure until the entire structure collapses at some time t_{II}. It is readily seen that the lifetime of a structure may be divided into two time intervals or stages, i.e., $0 \leq t < t_I$ and $t_I \leq t < t_{II}$. In the first stage $0 \leq t < t_I$, which has been termed the stage of latent failure by Kachanov [8] or the incubation period by Johnson [32], the creep damage is assumed to be less than the critical value (D_r) everywhere in the structure. In the second stage $t_I \leq t < t_{II}$, which has been termed the stage of propagation of rupture, a rupture front Σ along which

$$D = D_r, \tag{14}$$

travels through the structure and complete collapse occurs at t_{II}.

A condition on the direction of travel for the rupture front Σ may be obtained by taking the total time derivative of eqn.(14). Accordingly, we obtain

$$\frac{\partial D}{\partial t} + \frac{\partial D}{\partial N}\frac{dN}{dt} = 0$$

in which N designates the coordinate normal to the rupture front. Similarly, the geometry of the rupture front Σ is constrained by

$$\frac{\partial D}{\partial t} + \frac{\partial D}{\partial x_j}\frac{dx_j}{dt} = 0 \qquad (15)$$

in which the x_j are the space coordinates.

This type of problem, more generally called moving (free) boundary problem, is well-known in heat conduction [19] with phase change and is known as the Stefan problem. Although the Stefan problem and the creep rupture problem share analogous mathematical characteristics, there are some significant physical differences. Instead of the temperature profile of the Stefan problem, we are now more concerned about the mechanical behavior of the structure, such as the coupling between the stress redistribution and the speed of the moving boundary (rupture front). Owing to the inherent nonlinearity of the problem, closed form solutions generally do not exist for moving boundary problems with a finite damain. Accordingly, a successful treatment of such problems will require the application of a suitable numerical technique. A thorough discussion and comparison of numerical methods currently used for moving boundary problems is given in [33]. Details of the numerical technique which we shall choose will be disclosed in subsequent sections as the need arises.

3. CREEP RUPTURE IN A BEAM ON A WINKLER FOUNDATION

3.1 Statement of the Problem

The beam problem to be studied is depicted in Fig. 1a. We consider a beam continuously supported by an elastic Winkler foundation, which exerts a restoring force as the beam deflects under the action of a distributed lateral load. Since the foundation is at an elevated temperature, a prescribed thermal gradient is assumed to exist in the z-direction (thickness) of the beam. It is assumed that this prescribed temperature distribution through the thickness of the beam is independent of time during the deformation and rupture processes. The physical model used to analyze the problem is shown in Fig. 1b. Here, the elastic foundation is modelled as an infinite series of infinitesimal springs with an elastic constant K [34], i.e. as an elastic Winkler foundation. Creep deformation starts to accumulate in the beam as soon as the lateral load is applied. In geophysical research this type of flexure model has recently yielded some interesting results on lithospheric flexures (eg. see McMullen et al [35]), where the temperature variation with z is due to the geothermal gradient and the Winkler foundation is due to the underlying mantle. In addition to the creep deformation, we shall also consider the effects of creep damage using the concepts previously developed. In brief, it is our major goal here to explore the propagation of a creep rupture front in a non-isothermal beam under distributed lateral load. During the second stage of damage the beam is thinning in a non-uniform manner, and accordingly the cross-section of the beam is not constant (see Fig. 1c). It will be seen later that a moving boundary problem is encountered as a consequence of this thinning behavior.

The problem presented here is extremely complex in nature. In order to reduce the mathematical difficulties somewhat, we present below a series of simplifying assumptions. Firstly, we assume that the material in the beam obeys the Norton law of steady creep, with viscosity dependent on the prescribed temperature gradient. Although the beam is of non-uniform cross-section during the second stage of damage, we assume that technical Euler-Bernoulli-type beam theory is valid throughout the entire process of creep damage. We also restrict our consideration to the case of small deformations and small rotations. Furthermore, we assume that no major cracks form in the unruptured segment of the beam during the process of rupture, and thus the effects of stress concentration at crack tips are excluded from the current study. Finally, we assume that the shear stresses are negligibly small when compared with the axial stresses due to flexure.

3.2 Mathematical Formulation of the Problem

The constitutive law governing the creep deformation in the beam is assumed to be of the Norton type [eqn. (1)]:

$$\dot{\epsilon}_c = A(z)\sigma^n \tag{16}$$

Here the stress state σ may vary with time as well as with the x- and z-coordinates. Note also that the reciprocal viscosity coefficient function A(z) is an implicit function of z via the temperature distribution (see Fig. 1c).

The geometry of the beam is shown is Fig. 1c; it has a rectangular cross-section of width b and thickness h and the length of the beam is 2L. For simplicity we will consider symmetric loading and thus only symmetric deformation in this work, and therefore only half of the span of the beam need be considered. Employing Euler-Bernoulli-type beam theory with h constant, we may derive the expression for stress in terms of the bending moment M as

$$\sigma = \frac{M}{\mathcal{J}_0}\left(\frac{z-e_0}{A(z)}\right)^{\frac{1}{n}} \qquad (17)$$

where e_o is the distance to the neutral axis (marked as N.A. in Fig.1c). Also, the governing equation in the bending moment M is obtained as

$$\frac{\partial^2 M}{\partial x^2 \partial t} + K\left(\frac{M}{\mathcal{J}_0}\right)^n = \frac{\partial^3 P}{\partial x^2 \partial t} \qquad (18)$$

where P is the applied lateral load, and we have introduced the notation for flexural rigidity

$$\mathcal{J}_0 = b\int_0^{h_0}\left[\frac{z'-e_0}{A(z')}\right]^{\frac{1}{n}} z'dz' \qquad (19)$$

The R.H.S. of eqn.(18) vanishes if we assume that the applied lateral load P(x,t) is expressed mathematically in the form

$$P(x,t) = P_* \, f(x) \, H(t) \qquad (20)$$

where P_* is the maximum load at x=0, f(x) is the symmetric shape function and H(t) represents the Heaviside unit step function. For a viscous material governed by eqn. (16) we have the initial condition in M as

$$\frac{d^2M(x,0^+)}{dx^2} = -f(x) \qquad (21)$$

For further simplicity, we also assume that the beam is simply supported at both ends and that the lateral load vanishes at both ends. Due to the symmetric nature of the problem as previously mentioned, the boundary conditions follow as

$$\frac{\partial M}{\partial x} = \frac{\partial^3 M}{\partial x^3} = 0 \qquad \text{at} \quad x=0 \tag{22a}$$

$$\frac{\partial^2 M}{\partial x^2} = M = 0 \qquad \text{at} \quad x=L \tag{22b}$$

It is important to point out that the neutral axis does not coincide with the centroidal axis in this beam problem since the viscosity is inhomogeneous due to its dependence on a non-uniform temperature distribution [36]. Since the axial force is zero in this problem, the distance to the neutral axis e_o may be determined in the first stage of damage from

$$\int_0^{h_o} \left[\frac{z'-e_o}{A(z')}\right]^{\frac{1}{n}} dz' = 0 \tag{23}$$

It is our task now to extend the above mathematical formulation, which is valid only for the first stage of creep damage, into the second stage of creep damage. The shear stresses in technical beam theory are usually negligibly small when compared with the axial stress. It is thus reasonable to utilize the uniaxial strain-controlled damage law. The creep damage then follows from eqn. (12), which with the use of eqn. (17) yields

$$D(x,z,t) = c_o \left\{ \int_0^t \left[\frac{M}{\mathcal{J}_o}\right]^n (z-e_o)dt' \right\}^{\omega+\beta} \tag{24}$$

Experimental evidence [37] has shown that there is virtually no creep damage in a crystalline material under compression. Therefore, the above equation is valid only in the region $e_0 < z \leq h_0$ (see Fig. 1c), while the creep damage is assumed to be identically zero in the remainder of the region. The initial rupture time t_I may now be obtained from the implicit relation

$$D_{cr} = c_0 \left\{ \int_0^{t_I} \left[\frac{M}{\mathcal{D}_0}\right]^n (z-e_0)\,dt' \right\}^{\alpha+\delta} \tag{25}$$

where the initial rupture clearly occurs at the midpoint of the bottom fiber (i.e. $x=0$ and $z=h_0$), since it is there that the tensile strain is maximum in magnitude.

Rupture thus starts at the point $x,z=0,h_0$, and then develops into a moving front which in turn causes the beam to thin (see Fig 1c). We shall call the region $0 \leq x < \delta(t)$ the thinning zone, and the remaining interval $\delta(t) \leq x \leq L$ the uniform zone since this interval is of uniform thickness. The quantities h and e, which designate the thickness and the distance to the neutral axis within the thinning zone of the beam, are clearly function of x and t. Furthermore, the flexural rigidity $\mathcal{D}$ in the thinning zone is also a function of x and t since it involves h and e. Governing equation (18) with P given by eqn. (20) may now be restated in the thinning zone as

$$\frac{\partial^5 M}{\partial x^4 \partial t} + K\left(\frac{M}{\mathcal{D}}\right)^n = 0 \qquad 0 \leq x < \delta(t), \quad t_I \leq t \tag{26a}$$

and in the uniform zone as

$$\frac{\partial^5 M}{\partial x^4 \partial t} + K\left(\frac{M}{\mathcal{D}_0}\right)^n = 0 \qquad \delta(t) < x \leq L, \quad t_I \leq t \tag{26b}$$

where

$$\mathcal{J} = \mathcal{J}(x,t) = b\int_0^{h(x,t)} \left[\frac{z'-e(x,t)}{A(z')}\right]^{\frac{1}{n}} z'dz', \quad 0\leq x<\delta(t), \quad t_I\leq t \qquad (27)$$

It is readily seen that governing equations (26) are subjected to a moving junction, which separates the thinning zone from the uniform zone. Note that the upper limit h(x,t) and the quantity e(x,t) in integral (27) are changing and unknown functions, and thus we must obtain conditions which govern the variables h, δ, and e. It may be shown that if the rupture front Σ is prescribed as

$$\Sigma : \quad z = h(x,t) \qquad t_I\leq t$$

eqn. (15) can be rewritten as

$$\frac{\partial D}{\partial t} + \frac{\partial h}{\partial t}\frac{\partial D}{\partial z} = 0 \qquad t_I\leq t \qquad (28)$$

Substitution of the expression for damage [eqn. (24)] into the above equation yields after some manipulation

$$\frac{\partial h}{\partial t} = -\left(\frac{M}{\mathcal{J}}\right)^n(h-e) \Big/ \left\{ \int_0^t \left(\frac{M}{\mathcal{J}}\right)^n dt' \right\}, \quad 0\leq x<\delta(t), \quad t_I\leq t \qquad (29)$$

The creep damage at the junction point Q in Fig. 1c with coordinates $x=\delta(t)$ and $z=h_0$ should be equal to the critical value, i.e.

$$D(x,z,t) = D_{cr}, \qquad x=\delta(t), \qquad z=h_0, \quad t_I\leq t$$

Following the same procedure employed for eqn. (29), the total time derivative of this equation now gives

$$\frac{d\delta(t)}{dt} = -M^n \Big/ \left\{ n \int_0^t M^{n-1} \frac{\partial M}{\partial x} \, dt' \right\}, \quad x=\delta(t), \quad t_I \leq t \qquad (30)$$

Note that the quantity $\mathcal{B}(x,t)$ does not appear in the above equation as it is a constant at the junction point Q (see Fig. 1c).

Finally, eqn. (23) for the distance to the neutral axis of the beam now becomes for the second stage of creep damage

$$\int_0^{h(x,t)} \left[\frac{z'-e(x,t)}{A(z')}\right]^{\frac{1}{n}} dz' = 0 \ , \quad 0 \leq x \leq \delta(t), \quad t_I \leq t$$

Differentiating the above equation with respect to time we obtain the equation

$$\frac{\partial e}{\partial t} = n\left[\frac{h-e}{A(h)}\right]^{\frac{1}{n}} \left(\frac{\partial h}{\partial t}\right) \Big/ \left\{ \int_0^h \frac{(z'-e)^{\frac{1}{n}-1}}{[A(z')]^{\frac{1}{n}}} \, dz' \right\}, \quad 0 \leq x < \delta(t), \quad t_I \leq t \qquad (31)$$

where A(h) is the reciprocal viscosity function A(z) evaluated at z=h.

We have thus obtained governing equations (26) subjected to interface equations (29), (30) and (31), and we must solve these equations for the unknowns M,h,δ, and e with boundary conditions (22). Although boundary conditions (22) are not applied at a moving boundary, we do have the interface equations which are applied at the moving junction. We shall thus use familiar terminology and call this problem a Stefan-like problem. It is readily seen that the present nonlinear problem is very complicated and numerically challenging; we shall present its numerical solution in the next section.

4. NUMERICAL TECHNIQUE AND RESULTS

4.1 Solution Technique

For convenience we introduce the following nondimensional variables:

$$\begin{array}{lll}
\bar{t} = \dfrac{t}{t_I}\ ,\ (\bar{t}_I=1) & \bar{e} = \dfrac{e}{h_o} & \bar{\delta} = \dfrac{\delta}{L} \\[2ex]
\bar{x} = \dfrac{x}{L}\ ,\ (0 \leq \bar{x} \leq 1) & \bar{D} = \dfrac{D}{D_{cr}}\ ,\ (0 \leq \bar{D} \leq 1) & \\[2ex]
\bar{z} = \dfrac{z}{h_o}\ ,\ (0 \leq \bar{z} \leq 1) & \bar{A} = \dfrac{A(z)}{A(z=0)} & \\[2ex]
\bar{h} = \dfrac{h}{h_o}\ ,\ (\bar{h}_o=1) & \bar{\mathscr{D}} = \dfrac{\mathscr{D}}{\mathscr{D}^*} & \\[2ex]
\bar{w} = \dfrac{wK}{P_o} & \bar{M} = \dfrac{M}{P_o L^2} &
\end{array} \tag{32}$$

In the above, $\mathscr{D}^*$ represents the flexural rigidity of a beam at a uniform temperature T_u, where T_u is the temperature at the upper surface of the present non-uniform beam. Thus

$$\mathscr{D}^* = \frac{nbh^{\frac{1}{n}+2}}{2(2n+1)[2A(z=0)]^{\frac{1}{n}}} \tag{33a}$$

and

$$\bar{\mathscr{D}} = \frac{(1+2n)2^{\frac{1}{n}+1}}{n} \int_o^h \left[\frac{\bar{z}'-\bar{e}}{\bar{A}(\bar{z}')}\right]^{\frac{1}{n}} \bar{z}'d\bar{z}' \tag{33b}$$

We now follow the practice that unless otherwise noted all variables without bars appearing in this section from this point on will be dimensionless variables. In accordance with the above definitions, governing equation (18) may be reformulated in terms of dimensionless variables as

$$\frac{\partial^5 M}{\partial x^4 \partial t} + B\left(\frac{M}{\mathcal{J}_o}\right)^n = 0 \tag{34}$$

in which we have introduced the dimensionless quantity

$$B = \frac{K t_I P_o^{n-1} L^{2n+2}}{\mathcal{J}_o^{*n}} \tag{35}$$

The variables appearing on the R.H.S. of eqn. (35) are all in dimensional form, and $\mathcal{J}_0^*$ is evaluated by setting $h=h_0$ in eqn. (33a). Note that the quantity B will be the key parameter in the present nondimensional study.

Employing the same techniques presented in [35], we may eliminate the spatial partial derivative appearing in eqn. (34) for the first stage. We thus obtain the integro-differential equations

$$\frac{\partial M}{\partial t} = \frac{B}{6}\left\{\int_o^x F(x,x')\left(\frac{M}{\mathcal{J}_o}\right)^n dx' + \int_o^1 G(x,x')\left(\frac{M}{\mathcal{J}_o}\right)^n dx'\right\} \tag{36a}$$

where

$$F(x,x') = -(x-x')^3 \tag{36b}$$

$$G(x,x') = 3x^2 - 3x^2x' - x'^3 + 3x'^2 - 2 \tag{36c}$$

The numerical solution to the above equation with geophysical data for a beam of constant thickness was presented in [35]. Here, we will employ a numerical technique other than the one presented in [35]. A discretization scheme using the method of lines in space is obtained from the above eqn. (36a). It follows that

$$\frac{\partial M_i}{\partial t} = \frac{B}{\delta}\left\{\int_0^{x_i} F(x_i,x')\left(\frac{M}{\mathcal{J}_o}\right)^n dx' + \int_0^1 G(x_i,x')\left(\frac{M}{\mathcal{J}_o}\right)^n dx'\right\}, \qquad i=1,2,\ldots,N_2 \tag{37a}$$

$$\frac{\partial M_i}{\partial t} = 0 \qquad i=N_2+1 \tag{37b}$$

where

$$x_i = (i-1)\Delta x = \frac{1}{N_2}(i-1)$$

Note that the first integral in eqn. (37a) vanishes at i=1, eqn. (37b) corresponds to boundary condition (22b), and N_2 designates the number of spatial increments. Evaluating the integrals by the Newton-Cotes formulas, we thus obtain a system of ODE's which may be solved by Gear's stiff ODE algorithm [38]. The result obtained above furnishes the solution in the first stage of damage, and provides the initial data for the second stage of damage.

Returning now to eqns. (26), we may again integrate out the spatial derivatives to obtain for the thinning zone in the second stage

$$\frac{\partial M}{\partial t} = \frac{B}{\delta}\left\{\int_0^{x} F(x,x')\left(\frac{M}{\mathcal{J}}\right)^n dx' + \int_0^{\delta(t)} G(x,x')\left(\frac{M}{\mathcal{J}}\right)^n dx' + \int_{\delta(t)}^{1} G(x,x')\left(\frac{M}{\mathcal{J}_o}\right)^n dx'\right\}, \qquad 0\leq x<\delta(t), \quad 1\leq t \tag{38a}$$

and for the uniform zone

$$\frac{\partial M}{\partial t} = \frac{B}{\delta}\left\{\int_{0}^{\delta(t)} F(x,x')\left(\frac{M}{\mathscr{I}}\right)^{n}dx' + \int_{\delta(t)}^{x} F(x,x')\left(\frac{M}{\mathscr{I}_0}\right)^{n}dx'\right.$$

$$\left. + \int_{0}^{\delta(t)} G(x,x')\left(\frac{M}{\mathscr{I}}\right)^{n}dx' + \int_{\delta(t)}^{1} G(x,x')\left(\frac{M}{\mathscr{I}_0}\right)^{n}dx'\right\}, \quad 0\leq x<\delta(t),\ 1\leq t \qquad (38b)$$

where $\mathscr{I}$ was defined in (33b), and F(x,x'), G(x,x') were defined in eqns. (36 b,c). Note that we have used continuity of M and its derivatives at the junction point, e.g. $M(x=\delta(t)^{+},t) = M(x=\delta(t)^{-},t)$. In other words, the bending moment, shear force, deflection, and slope of the beam are all continuous at the junction point.

In order to mathematically fix the moving junction and the limits of integration appearing in eqns. (38), we employ the concept of Landau's transformation [39] and introduce the variable changes

$$\zeta = \frac{x}{\delta(t)}, \quad \text{for thinning zone} \qquad 0\leq x<\delta(t) \qquad (39a)$$

$$\eta = \frac{x-\delta(t)}{1-\delta(t)}, \quad \text{for uniform zone} \qquad \delta(t)\leq x\leq 1 \qquad (39b)$$

Under such a transformation the partial time derivative ∂( )/∂t is replaced by the substantial time derivative D( )/Dt in accordance with

$$\frac{\partial(\ )}{\partial t} = \frac{D(\ )}{Dt} - \frac{dx}{dt}\frac{\partial(\ )}{\partial x}$$

With the use of the chain rule, the transformed governing equations are obtained for the thinning zone as

$$\frac{DM}{Dt} = \frac{\zeta}{\delta(t)} \frac{d\delta(t)}{dt} \frac{\partial M}{\partial \zeta} + \frac{B}{\delta} \left\{ \delta(t) \int_0^{\zeta} F(\zeta,\zeta') \left(\frac{M}{\mathcal{J}}\right)^n d\zeta' + \delta(t) \int_0^1 G(\zeta,\zeta') \left(\frac{M}{\mathcal{J}}\right)^n d\zeta' \right.$$

$$\left. + [1-\delta(t)] \int_0^1 G(\zeta,\eta') \left(\frac{M}{\mathcal{J}_o}\right)^n d\eta' \right\}, \quad 0 \le \zeta < 1, \quad 1 \le t \tag{40a}$$

and for the uniform zone as

$$\frac{DM}{Dt} = \frac{1-\eta}{1-\delta(t)} \frac{d\delta(t)}{dt} \frac{\partial M}{\partial \eta} + \frac{B}{\delta} \left\{ \delta(t) \int_0^1 F(\eta,\zeta') \left(\frac{M}{\mathcal{J}}\right)^n d\zeta' + [1-\delta(t)] \int_0^{\eta} F(\eta,\eta') \left(\frac{M}{\mathcal{J}_o}\right)^n d\eta' \right.$$

$$\left. + \delta(t) \int_0^1 G(\eta,\zeta') \left(\frac{M}{\mathcal{J}}\right)^n d\zeta' + [1-\delta(t)] \int_0^1 G(\eta,\eta') \left(\frac{M}{\mathcal{J}_o}\right)^n d\eta' \right\}, \quad \begin{matrix} 0 \le \eta \le 1, \\ 1 \le t \end{matrix} \tag{40b}$$

Similarly, an application of Landau's transformation to interface equations (29),(31) yields

$$\frac{Dh}{Dt} = \frac{\zeta}{\delta(t)} \frac{d\delta(t)}{dt} \frac{\partial h}{\partial \zeta} - \left(\frac{M}{\mathcal{J}}\right)^n (h-e) \Big/ \left\{ \int_0^t \left[\frac{M}{\mathcal{J}}\right]^n dt' \right\}, \quad 0 \le \zeta < 1, \quad 1 \le t \tag{41}$$

and

$$\frac{De}{Dt} = \frac{\zeta}{\delta(t)} \frac{d\delta(t)}{dt} \frac{\partial e}{\partial \zeta} + n\left[\frac{Dh}{Dt} - \frac{\zeta}{\delta(t)} \frac{d\delta(t)}{dt} \frac{\partial h}{\partial \zeta}\right]\left[\frac{h-e}{A(h)}\right]^{\frac{1}{n}} \Big/$$

$$\left\{ \int_0^h \frac{(z'-e)^{\frac{1}{n}-1}}{[A(z')]^{\frac{1}{n}}} dz' \right\}, \quad 0 \le \zeta < 1, \quad 1 \le t \tag{42}$$

The transformed interface equation (30) has the slightly different form

$$\frac{d\delta(t)}{dt} = -\delta(t)M^n \Big/ \left\{ n \int_0^t M^{n-1} \frac{\partial M}{\partial \zeta}\, dt' \right\}, \quad \zeta=1 \,, \quad 1\leq t \tag{43}$$

since $\delta(t)$ involves only the single variable t. By virtue of variable changes (39), the substantial (material) time derivative D( )/Dt appearing in the above transformed equations possesses a numerical value identical with $[\partial(\ )/\partial t]_\zeta$ or $[\partial(\ )/\partial t]_\eta$. It should be noted that fixing the moving junction unfortunately leads to governing equations of even more complicated form, and the above set of equations surely will not have a closed form solution. A numerical scheme will now be presented.

First, the method of lines in space [40] is utilized to eliminate the spatial derivatives from the above integro-differential equations in accordance with the discretization scheme shown in Fig. 2. Accordingly, we employ the central finite difference approximations for the interior points and one-sided three point formulas for the end points A,B and the junction point Q (see Fig. 2). Accordingly, eqns. (40-43) yield the following:

$$\frac{d\delta(t)}{dt} = -2\Delta\zeta\, \delta(t)\, M_i^n \Big/ \left\{ n \int_0^t M_i^{n-1}[M_{i-2}-4M_{i-1}+M_i]dt' \right\}, \qquad i=N_1+1 \tag{44}$$

$$\frac{DM_i}{Dt} = \frac{B}{\delta} \left\{ \delta(t) \int_0^1 G(\zeta_i,\zeta')\left(\frac{M}{\mathscr{S}}\right)^n d\zeta' + [1-\delta(t)] \int_0^1 G(\zeta_i,\eta')\left(\frac{M}{\mathscr{S}_o}\right)^n d\eta' \right\}, \quad i=1 \tag{45a}$$

$$\begin{aligned}\frac{DM_i}{Dt} = {} & \frac{\zeta_i}{2\Delta\zeta\, \delta(t)} \frac{d\delta(t)}{dt} [M_{i+1}+M_{i-1}] + \frac{B}{\delta} \left\{ \delta(t) \int_0^{\zeta_i} F(\zeta_i,\zeta')\left(\frac{M}{\mathscr{S}}\right)^n d\zeta' \right. \\ & \left. + \delta(t) \int_0^1 G(\zeta_i,\zeta')\left(\frac{M}{\mathscr{S}}\right)^n d\zeta' + [1-\delta(t)] \int_0^1 G(\zeta_i,\eta')\left(\frac{M}{\mathscr{S}_o}\right)^n d\eta' \right\}, \quad i=2,3,\ldots,N_1\end{aligned} \tag{45b}$$

$$\frac{DM_i}{Dt} = \frac{\zeta_i}{2\Delta\zeta\ \delta(t)} \frac{d\delta(t)}{dt} [M_{i-2}-4M_{i-1}+3M_i] + \frac{B}{\delta} \Big\{ \delta(t) \int_0^{\zeta_i} F(\zeta_i, \zeta') (\frac{M}{\mathcal{S}})^n d\zeta' + \delta(t) \int_0^1 G(\zeta_i, \zeta') (\frac{M}{\mathcal{S}})^n d\zeta' + [1-\delta(t)] \int_0^1 G(\zeta_i, \eta') (\frac{M}{\mathcal{S}_o})^n d\eta' \Big\} , \quad i=N_1+1 \tag{45c}$$

$$\frac{DM_i}{Dt} = \frac{1-\eta_i}{2\Delta\eta[1-\delta(t)]} \frac{d\delta(t)}{dt} [M_{i+1}-M_{i-1}] + \frac{B}{\delta} \Big\{ \delta(t) \int_0^1 F(\eta_i, \zeta') (\frac{M}{\mathcal{S}})^n d\zeta' + [1-\delta(t)] \int_0^{\eta_i} F(\eta_i, \eta') (\frac{M}{\mathcal{S}_o})^n d\eta' + \delta(t) \int_0^1 G(\eta_i, \zeta') (\frac{M}{\mathcal{S}})^n d\zeta' + [1-\delta(t)] \int_0^1 G(\eta_i, \eta') (\frac{M}{\mathcal{S}_o})^n d\eta' \Big\} , \quad i=N_1+2, N_1+3, \ldots, N_1+N_2 \tag{45d}$$

$$\frac{DM_i}{Dt} = 0 , \quad i=N_1+N_2+1 \tag{45e}$$

$$\frac{Dh_i}{Dt} = -(\frac{M_i}{\mathcal{S}_i})^n (h_i-e_i) \Big/ \Big\{ \int_0^t (\frac{M_i}{\mathcal{S}_i})^n dt' \Big\} , \quad i=1 \tag{46a}$$

$$\frac{Dh_i}{Dt} = \frac{\zeta_i}{2\Delta\zeta\ \delta(t)} \frac{d\delta(t)}{dt} [h_{i+1}-h_{i-1}] - (\frac{M_i}{\mathcal{S}_i})^n (h_i-e_i) \Big/ \Big\{ \int_0^t (\frac{M_i}{\mathcal{S}_i})^n dt' \Big\} , \quad i=2, 3, \ldots, N_1 \tag{46b}$$

$$\frac{Dh_i}{Dt} = 0 , \quad i=N_1+1 \tag{46c}$$

$$\frac{De_i}{Dt} = n \frac{Dh_i}{Dt} \left[\frac{h_i-e_i}{A(h_i)}\right]^{\frac{1}{n}} / \left\{ \int_0^{h_i} \frac{(z'-e_i)^{\frac{1}{n}-1}}{[A(z')]^{\frac{1}{n}}} dz' \right\} , \qquad i=1 \tag{47a}$$

$$\frac{De_i}{Dt} = \frac{\zeta_i}{2\Delta\zeta\ \delta(t)} \frac{d\delta(t)}{dt} [e_{i+1}-e_{i-1}] + n\left[\frac{Dh_i}{Dt} - \frac{\zeta_i}{2\Delta\zeta\ \delta(t)} \frac{d\delta(t)}{dt} (h_{i+1}-h_{i-1})\right] \cdot$$

$$\left[\frac{h_i-e_i}{A(h_i)}\right]^{\frac{1}{n}} / \left\{ \int_0^{h_i} \frac{(z'-e_i)^{\frac{1}{n}-1}}{[A(z')]^{\frac{1}{n}}} dz' \right\} , \qquad i=2,3,\dots,N_1 \tag{47b}$$

$$\frac{De_i}{Dt} = 0 , \qquad i=N_1+1 \tag{47c}$$

In the above

$$\zeta_i = (i-1)\Delta\zeta = \frac{1}{N_1}(i-1) , \qquad i=1,2,\dots,N_1$$

$$\eta_i = (i-N_1-1)\Delta\eta = \frac{1}{N_2}(i-N_1-1) , \qquad i=N_1+1, N_1+2, \dots, N_1+N_2+1$$

$$\Delta\zeta = \frac{1}{N_1} , \qquad \Delta\eta = \frac{1}{N_2}$$

and N_1, N_2 designates, respectively, the number of spatial increment in thinning zone and uniform zone, and $\mathcal{J}_i$ is obtained by setting $h=h_i$ is eqn. (33b).

Note that eqn. (45e) corresponds to boundary condition (22b). Moreover, Dh/Dt and De/Dt as given by eqns. (46c) and (47c) vanish at the junction point, since at any instant we always have h=1 and $e=e_o$ at this point. The

4.2 Solutions and Discussion

Our attention is first directed to a special case in which closed form solutions exist. Thus, let us delete the elastic Winkler foundation and also consider a beam with a uniform temperature distribution equal to T_u (a dimensional quantity). Under such circumstances, the bending moment M remains constant in time, and the neutral axis coincides with the centroidal axis owing to the homogeneous nature of the material properties. Moreover, we have the following values for the dimensionless quantities [see eqns. (32) and (33)]

$$e = \frac{1}{2} h$$

$$A(x) = 1$$

$$\mathcal{J} = h^{\frac{1}{n}+2}$$

The dimensionless governing equations for h,e [see eqns. (29) and (31)] in the thinning zone ($0 \leq x < \delta(t)$) follow for this special case as

$$\frac{\partial h}{\partial t} = - \frac{h^{-2n}}{2 \int_0^t h^{-1-2n} dt'} \ , \qquad 1 \leq t \tag{48a}$$

$$\frac{\partial e}{\partial t} = 2 \frac{\partial h}{\partial t} \ , \qquad 1 \leq t \tag{48b}$$

and that for $\delta(t)$ becomes

$$\frac{d\delta(t)}{dt} = - \frac{M}{nt \frac{\partial M}{\partial x}} \qquad x = \delta(t) \ , \quad 1 \leq t \tag{48c}$$

Note that these equations may be solved consecutively and that eqns. (48 a,b) include neither the x variable nor the input load function P(x,t) explicitly. Physically, eqn. (48b) indicates that although $2e_0=h_0=1$ initially, both quantities will be equal to zero at the instant the beam collapses. After eliminating the integral via differentiation, eqn. (48a) may be rewritten as

$$\frac{\partial}{\partial t}\left[\frac{\partial h}{\partial t}\cdot h^{2n-2}\right]=0 \qquad (49)$$

This differential equation may be solved analytically with the initial conditions

$$h=1 \quad \text{at} \quad t=t_I$$

and

$$\frac{\partial h}{\partial t}=-\frac{1}{2t_I} \quad \text{at} \quad t=t_I$$

where $t_I=t_I(x)$ designates the time required for a material point with coordinates (x,1) to reach the critical state. The second initial condition in the above was obtained by setting $t=t_I$ and $h=1$ in eqn. (48a). The solution to eqn. (49) is then obtained as

$$\frac{t}{t_I(x)}=\frac{2}{1-2n}h^{2n-1}-\frac{1+2n}{1-2n}\,, \quad 0\leq x<\delta(t)\,, \quad 1\leq t \qquad (50)$$

which is identical to the result derived in [8].

The solution to eqn. (48b) for e then follows directly from the solution of eqn. (50) for h. Here $t_I(x)$ may be expressed in terms of the bending moment $M(x)$. Since the point (0,1) reaches the critical state at time t=1 while the point (x,1) ruptures at time $t=t_I(x)$, it follows from eqn. (25) that

$$t_I(x) = (\frac{M_o}{M})^n \tag{51}$$

Here, M_o and M represent the bending moments at points with x-coordinates equal to 0 and x, respectively. Equation (50) thus becomes

$$(\frac{M}{M_o})^n t = \frac{2}{1-2n} h^{2n-1} - \frac{1+2n}{1-2n} , \quad 0 \leq x < \delta(t) , \qquad 1 \leq t \tag{52}$$

Although differential equation (48a) in h does not explicitly involve the variable x and the bending moment M, its solution (52) is seen to be directly related to M.

The function $t_I(x)$ in eqn. (51) may be inverted in the simple case that the bending moment $M(x)$ is monotonic in nature. In fact, for such a simple case the constraint on the moving juntion

$$x = \delta(t)$$

is invertible and is physically equivalent after inverstion to

$$t = t_I(x)$$

Consequently, witht he use of eqn. (51), eqn. (48c) attains the alternate form

$$\frac{d\delta(t)}{dt} = - \frac{M^{n+1}}{nM_o^n \frac{\partial M}{\partial x}} , \qquad x=\delta(t) , \quad 1 \leq t \tag{53}$$

Consider for the moment a very simple case in which a point-load is applied on the beam at x=0. The bending moment for this load is simply given as

$$M = M_0(1-x) \qquad (54)$$

and differential equation (53) becomes

$$\frac{d\delta(t)}{dt} = \frac{1}{n}\,[1-\delta(t)]^{n+1}\ , \qquad 1\leq t$$

With the initial condition δ at t=1 equal to 0, the above equation yields the solution

$$\delta(t) = 1 - t^{-\frac{1}{n}}\ , \qquad 1\leq t \qquad (55)$$

Note that solution (55) is also obtainable from the solution (52) by setting h=1 and using expression (54). The solutions of this special closed-form case are now complete.

We thus turn our attention to the original problem, containing in general both the Winkler term and a temperature gradient. A singularity appears in eqn. (39a) at time t=1 when δ=0, and this leads to numerical difficulties. This obstacle may be circumvented by introducing an "imperfection" [33] in eqn. (39a). Here, we follow the latter approach and introduce an imperfection in δ as

$$\delta(t) = 1.0\mathrm{x}10^{-4} \qquad \text{at} \quad t=1$$

Moreover, the temperature in the beam is assumed to be linearly distributed in the z-direction in accordance with (see Fig. 1c)

$$T = T_u + (T_b - T_u)z\ , \qquad 0\leq z\leq 1$$

where the dimensional surface and bottom temperatures are chosen respectively as

$$T_s = 300^\circ k \ , \quad T_b = 360^\circ k$$

Also, we use for the creep activation energy the dimensional value

$$\Delta H = 0.112x10^6 \ J\cdot mole^{-1}$$

Note that because of the nondimensional form of our governing equations it was not necessary to stipulate a specific material. Finally the number of increments chosen in the present beam problem were

$N_1 = 5$ for the thinning zone
$N_2 = 10$ for the uniform zone

which yield a total of 29 ODE's, or 45 if the equations for deflection are also included. In order to limit the complexity of this nonlinear problem, only the uniformly applied load is considered here. In this case, the shape function [see eqn. (20)] of the applied load is simply

$$f(x) = 1 \ , \qquad 0 \leq x \leq 1$$

The initial bending moment function $M(x,0^+)$ is obtainable from eqns. (21) and (22), and is given as

$$M(x,0^+) = (x^2-1)/2 \tag{56}$$

which will be used as the initial condition for eqns. (37).

The results we shall present may be separated into two groups, i.e. those with the foundation present and those with the foundation absent. In the latter case of the foundation absent, we have from eqn. (35) $B=0$ since in this case the spring constant for the foundation is identically zero. We consider the $B=0$ case first, and note that here the bending moment is independent of time, and is thus given simply by eqn. (56) after the lateral load is applied. (For the $B=0$ case, we did not calculate the deflection of the beam.) Figures 3 and 4 display the propagating rupture front for $B=0$ in the second stage of damage for $n=3$ and 5, respectively. In these figures the depth and axial coordinates z,x of the beam are given in nondimensional form. The sequence of curves inside the beam trace the propagation of the rupture front as time ellapses. The $\delta(t)$ function at time t is given by the distance along the bottom surface ($z=1$) from the point $x=0$ to the intersection of the curve for time t with the bottom surface. Note that the beam of $n=3$ material exhibits a wider thinning zone than does the beam of $n=5$ material. It would appear that the rupture front of the $n=5$ beam propagates faster than that of the $n=3$ beam. But you are reminded that this observation is made for a nondimensional time scale and will not necessarily follow for dimensional time. Each set of these curves for a parameter n required about 1 minute of computer time (CPU).

We now turn to the general case with the Winkler foundation present. The dimensionless parameter B [see eqn. (35)] contains a group of constants including the spring constant of the foundation, applied load, geometry and material properties of the beam, and is considered arbitrary in the present nondimensional study. Here we chose for illustration the value $B=1$ which requires that the numerator and denominator in eqn. (35) be of the same order. In addition to the bending moment M, we also computer the deflection w for this case. Due to the complicated nature of the governing large system of ODE's, a considerable amount of computer time was required to complete one run for a specific value of n. Thus we limited the computer time to 1000 seconds (about 16.7 minutes) per run, and accordingly obtained a reasonable number of solution curves for time steps in the early part of the second stage of damage. The computations could have easily been extended up to the point of final collapse of the beam, but for reasons of economy this was not done.

Figures 5a,b give respectively the nondimensional deflection of the beam for values 3 and 5 for the stress power n. Since the chosen load is uniformly distributed, these curves do not exhibit the characteristic "uplift" which often occurs under centrally concentrated loads or point loads on a beam with a Winkler foundation [34, 35]. According to the flexural model presented in [35], the deflections of a beam which experiences no damage approaches an asymptotic limit as the time tends to infinity. However, no asymptotic deflection solution exists in the present problem, since damage causes the beam to thin and accordingly the deflection is unbounded. This may readily be seen in Fig. 5b, in which the increment of beam deflection is clearly increasing in the final few time steps shown. Although we have used Norton's steady creep law, eqn. (16), to describe the creep behavior of the material, the nature of the deflection shown in Fig. 5b is similar in form to the typical creep curve with its three stages of creep. Such behavior coincides with the recent experimental investigations [41, 42] in which a beam with a deep notch was subjected to a uniform temperature and point load. This can be explained by the fact that as the beam starts thinning the remaining material carries the same load but with greater stress.

In [35] where no damage was included, McMullen et al noted that the bending moment relaxes after the load is applied and approaches zero as time tends to infinity. Figures 6a,b exhibit this same relaxation of the bending moment in the more general case where damage causes the beam to thin. Furthermore, Fig. 6b shows that the relaxation of the bending moment accelerates in the final few time steps shown; it is believed that Fig. 6a would also do the same if the computer time had been extended. Since the lifetime of the beam is finite, the beam should collapse before the bending moment vanishes. Figures 7a,b display the propagating rupture front for B=1 with n=3 and 5, respectively. As in the B=0 case, the rupture fronts in the present case have sharper profiles in the n=5 beam than in the n=3 beam. And the rupture front for the n=5 beam propagates faster than that for the n=3 beam relative to the nondimensional time scale. We also point out that the numerical scheme for the system of ODE's presented in the previous section is stiffer for n=5 than that for n=3, since within the chosen limit of compute time (100 seconds) the final time step reached was t=1.90 for the case of n=3 and only t=1.60 for the case of n=5.

It should be noted that the results displayed may contain some numerical error in the later time intervals, since we are restricted by the limitations of infinitesimal strain and small rotations. Although we have formulated the problem in an idealized manner, a significant amount of mathematical difficulty was still encountered. If one attemps to relax some of the assumptions imposed, the complexity of the problem could increase greatly and possibly preclude a successful numerical analysis.

REFERENCES

1. F.R. Larson and J. Miller, A Time-Temperature Relation for Rupture and Creep Stresses, Trans. A.S.M.E., Vol. 174, pp. 765-775, 1952.
2. S.S. Manson and A.M. Haferd, A Linear Time-Temperature Relation for Extrapolation for Creep and Stress Rupture Data, N.A.C.A. TN 2890, 1953.
3. R.L. Orr, O.D. Sherby and J.E. Dorn, Correlations of Rupture Data for Metals at Elevated Temperatures, Trans. ASM, Vol. 46, pp. 113-128, 1954.
4. S.S. Manson and C.R. Ensign, A Quarter-Century of Progress in the Development of Correlation and Extrapolation Methods for Creep Rupture Data, J. Eng. Mat. Tech., Vol. 101, pp. 317-325, 1979.
5. J.B. Conway, Stress-Rupture Parameters: Origin, Calculations and Use, Gordon and Breach, New York, 1969.
6. E.L. Robinson, Effect of Temperature Variation on the Long-Time Rupture Strength of Steels, Trans. A.S.M.E., Vol. 74, pp. 777-781, 1952.
7. N.J. Hoff, The Necking and Rupture of Rods Subjected to Constant Tensile Loads, J. of Applied Mechanics, Vol. 20, pp. 105-108, 1953.
8. L.M. Kachanov, Rupture Time Under Creep Conditions, Problems of Continuum Mechanics, contributions in honor of seventieth birthday of N.I. Muskhelishville, (ed. J.R.M. Radok), SIAM, Philadelphia, p. 202-218, 1961.
9. Y.N. Robotnov, Creep Rupture, Proc. 12th Int. Congr. Appl. Mech., Springer-Verlag, Berlin, 1969.
10. F.A. Leckie and D.R. Hayhurst, Creep Rupture of Structures, Proc. Roy. Soc. Londen, A340, pp. 323-347, 1974.
11. F.A. Leckie and D.R. Hayhurst, Constitutive Equations for Creep Rupture, Acta Metall, Vol. 25, pp. 1059-1071, 1977.
12. F.K.G. Odqvist, Mathematical Theory of Creep and Creep Rupture, 2nd edn., Oxford Clarendon Press, Oxford, 1974.

13. R. Penny and D. Marriot, Design for Creep, McGraw-Hill, New York, 1971.

14. G. Piatti, R. Lubek and R. Matera, The Measurement of Small Density Variations in Solids, JRC Techn. Note N.I.77.6 173/2. 10.1/3, Mar 1977.

15. G. Belloni, G. Bernasconi and G. Piatti, Damage and Rupture in AISI 310 Austenitic Steel, Meccanica, Vol. 12, pp. 84-96, 1977.

16. G. Belloni, G. Bernasconi and G. Piatti, Creep Damage Models, In Creep in Engineering Materials and Structures (eds. G. Bernasconi and G. Piatti), Ch.8, pp. 195-229, Applied Science Publ., London, 1980.

17. D.A. Woodford, A Parametric Approach to Creep Damage, Met. Sci, J., Vol. 3, pp. 50-53, 1969.

18. R.J. Gu, Strain-Controlled Creep Rupture in Non-Isothermal Materials, Ph.D. Dissertation, State University of New York at Buffalo, Sept 1984.

19. M.N. Ozisik, Heat Conduction, Wiley, New York, 1980.

20. G. Schoeck, Theories of Creep, in Mechanical Behavior of Materials at Elevated Temperatures (ed. J.E. Dorn), McGraw-Hill, 1961.

21. M. Ashby, A First Report on Deformation-Mechanism Maps, Acta Metall., Vol. 20, pp. 887-897, 1972.

22. M. Ashby, Strengthening Methods in Metals and Alloys, in The Microstructure and Design of Alloys, Proc. 3rd Int. Conf. on Strength of Metals and Alloys, Cambridge, England, Vol. 2, pp. 8-42, 1973.

23. R. Raj and M.F. Ashby, On Grain Boundary Sliding and Diffusion Creep, Metall. Trans., Vol. 2, pp. 1113-1127, 1971.

24. G.H. Edward and M.F. Ashby, Intergranular Fracture During Power-Law Creep, Acta Metall., Vol. 27, pp. 1505-1518, 1979.

25. A.K. Mukherjee, J.E. Bird and J.E. Dorn, Experimental Correlations for High-Temperature Creep, Trans. ASM, Vol. 62, pp. 155-179, 1969.

26. C.S. Lee, F.A. Cozzarelli and K. Burke, One-Dimensional Strain-Dependent Creep Damage in Inhomogeneous Materials, to appear in Int. J. Nonlinear Mechanics.

27. G. Piatti, G. Bernasconi, and F.A. Cozzarelli, Damage Equations for Creep Rupture in Steels, Proc. 5th Int. Conf. in Reactor Technology, paper L11/4, Berlin, August, 1979.

28. F.C. Monkman and N.J. Grant, An Impirical Relationship Between Rupture Life and Minimum Creep Rate in Creep Rate in Creep-Rupture Tests, Proc. ASTM, 56, 593, 1956.

29. H.D. Hanna and G.W. Greenwood, Cavity Growth and Creep in Copper at Low Stresses, Acta Metall., Vol. 30, pp. 719-724, 1982.

30. F.A. Cozzarelli and G. Bernasconi, Nonlinear Creep Damage Under One-Dimensional Variable Tensile Stress, Int. J. Non-Linear Mechanics, Vol. 16, No. 1, pp. 27-38, 1981.

31. K. Burke and F.A. Cozzarelli, On The Thermodynamic Foundations of Strain-Dependent Creep Damage and Rupture in Three Dimensions, Int. J. Solids Structures, Vol. 20, No. 5, pp. 487-497, 1984.

32. A.E. Johnson, J. Henderson and B. Khan, Complex-Stress Creep, Relaxation and Fracture of Metallic Alloys, H.M.S.O., Edinburg, 1962.

33. R.M. Furzeland, A Comparative Study of Numerical Methods for Moving Boundary Problems, J. Inst. Math. Applics., Vol. 26, pp. 411-429, 1980.

34. W. Flugge, Viscoelasticity, 2nd revised edn., Springer-Verlag, New York, 1975.

35. R.J. McMullen, D.S. Hodge and F.A. Cozzarelli, A Technique for Incorporating Geothermal Gradients and Nonlinear Creep into Lithospheric Flexure Models, J. of Geoph. Research, Vol. 86, pp. 1745-1753, 1981.

36. I.Finnie and W.R. Heller, Creep of Engineering Materials, McGraw-Hill, 1959.

37. P. Schiller, D. Boerman, P. Fenici, R. Matera, G. Pellegrini, G. Piatti and E. Ruedl, Testing and Modeling of Mechanical Properties of Metals, Highlights of Materials Science, EUR-5508, pp. 53-67, 1973-76.

38. C.W. Gear, Numerical Integration of Stiff Ordinary Differential Equations, Report No. 221, Dept. of Computer Science, University of Illinois, 1967.

39. H.G. Landau, Heat Conductions in a Melting Solid, Quart. of Appl. Math., Vol. 8, pp. 81-94, 1950.

40. R.M. Furzeland, Analysis and Computer Packages for Stefan Problems, Internal Report, Oxford University Computing Laboratory, 1979.

41. V.M. Radhakrishnan and A.J. McEvily, A Critical Analysis of Crack Growth in Creep, Trans, ASME, J. of Engg. Mat. and Tech., Vol. 102, pp. 200-206, 1980.

42. V.M. Radhakrishnan and A.J. McEvily, Effect of Temperature on Creep Crack Growth, Trans. ASME, J. of Engg. Mat. and Tech., Vol. 102, pp. 350-355, 1980.

1288G

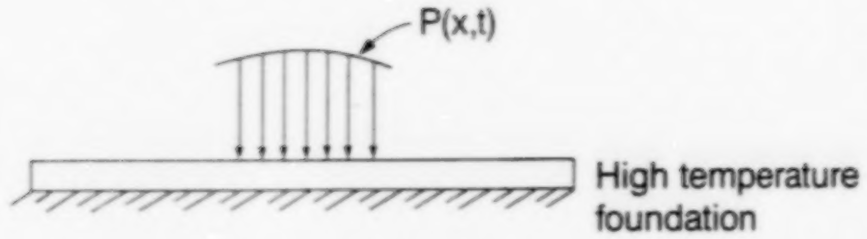
P(x,t)
High temperature foundation

Fig. 1a Beam on high temperature foundation, subjected to lateral load P(x,t).

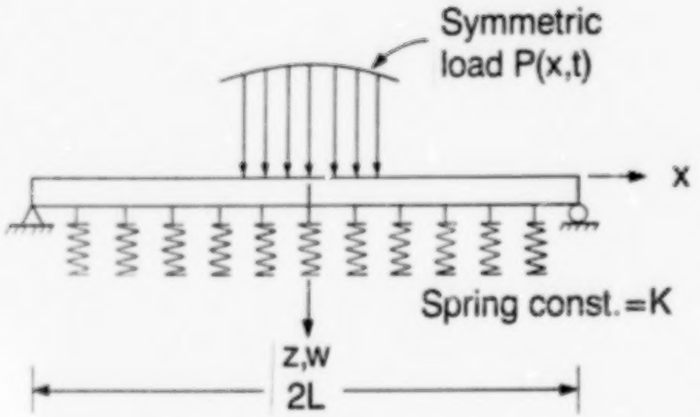
Symmetric load P(x,t)
x
Spring const.=K
z,w
2L

Fig. 1b Beam with simple end supports, elastic Winkler foundation, and symmetric load.

(4)

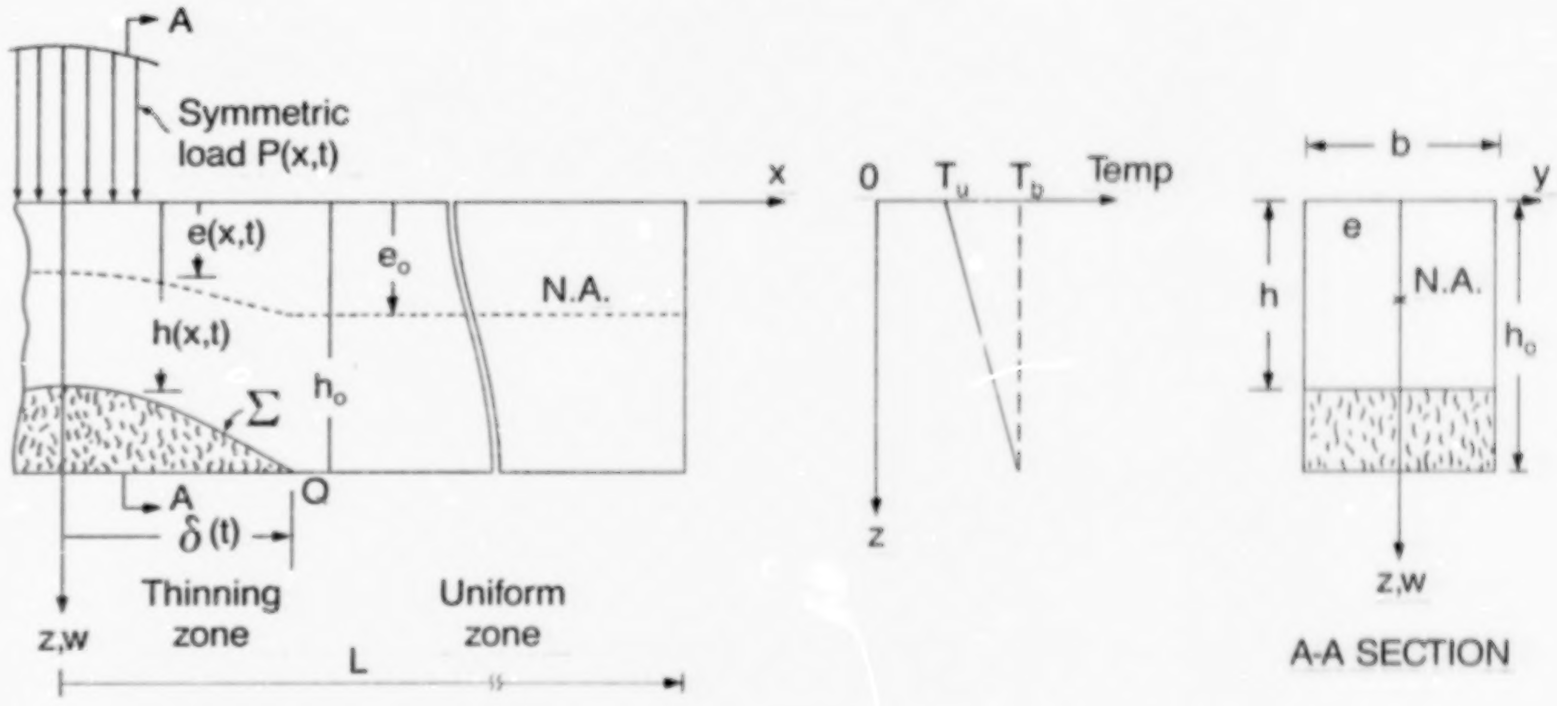
A
Symmetric
load P(x,t)
x
e(x,t)
e_o
N.A.
h(x,t)
h_o
Σ
A
O
δ (t)
z,w
Thinning
zone
Uniform
zone
L
0
T_u
T_b
Temp
z
b
y
e
h
N.A.
h_o
z,w
A-A SECTION

Fig. 1c Propagation of the rupture front and the linear temperature profile.

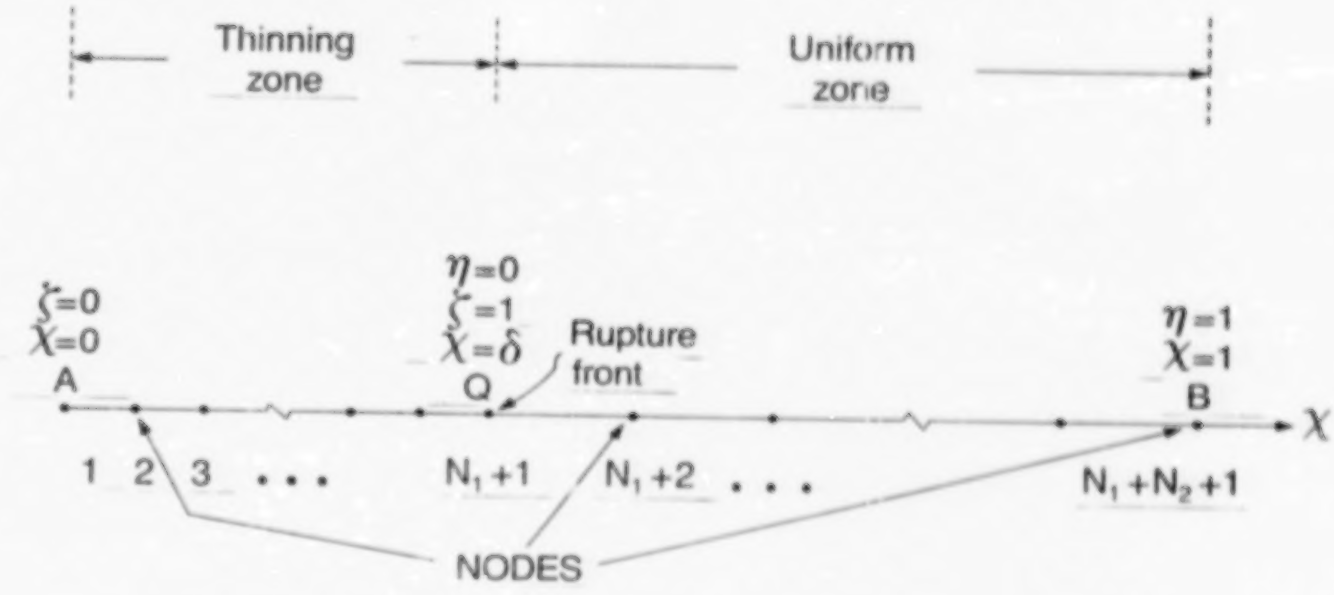
Thinning zone
Uniform zone
$\zeta=0$
$\chi=0$
A
$\eta=0$
$\zeta=1$
$\chi=\delta$
Q
Rupture front
$\eta=1$
$\chi=1$
B
χ
1
2
3
N_1+1
N_1+2
N_1+N_2+1
NODES

Fig. 2 Variable network in the second stage of creep damage.

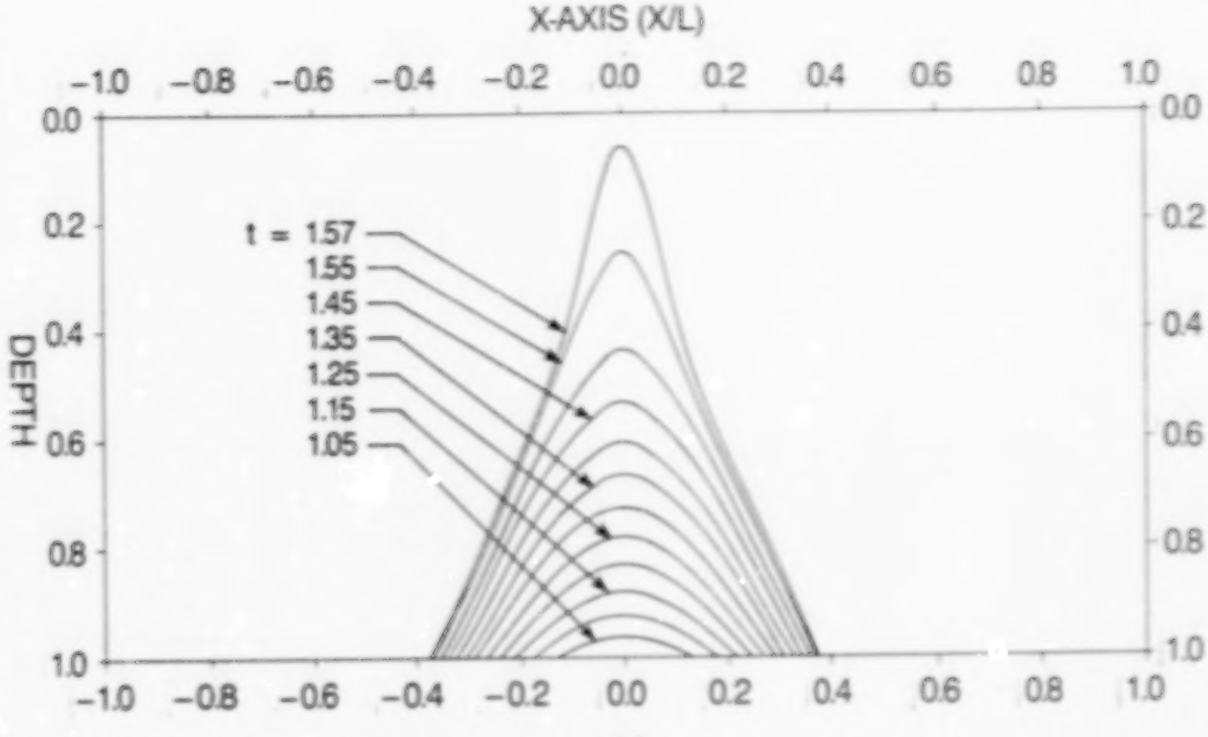

(a)

Fig. 3 Propagation of rupture front in a beam with no Winkler foundation — (a) B=0 and n=3, (b) B=0 and n=5.

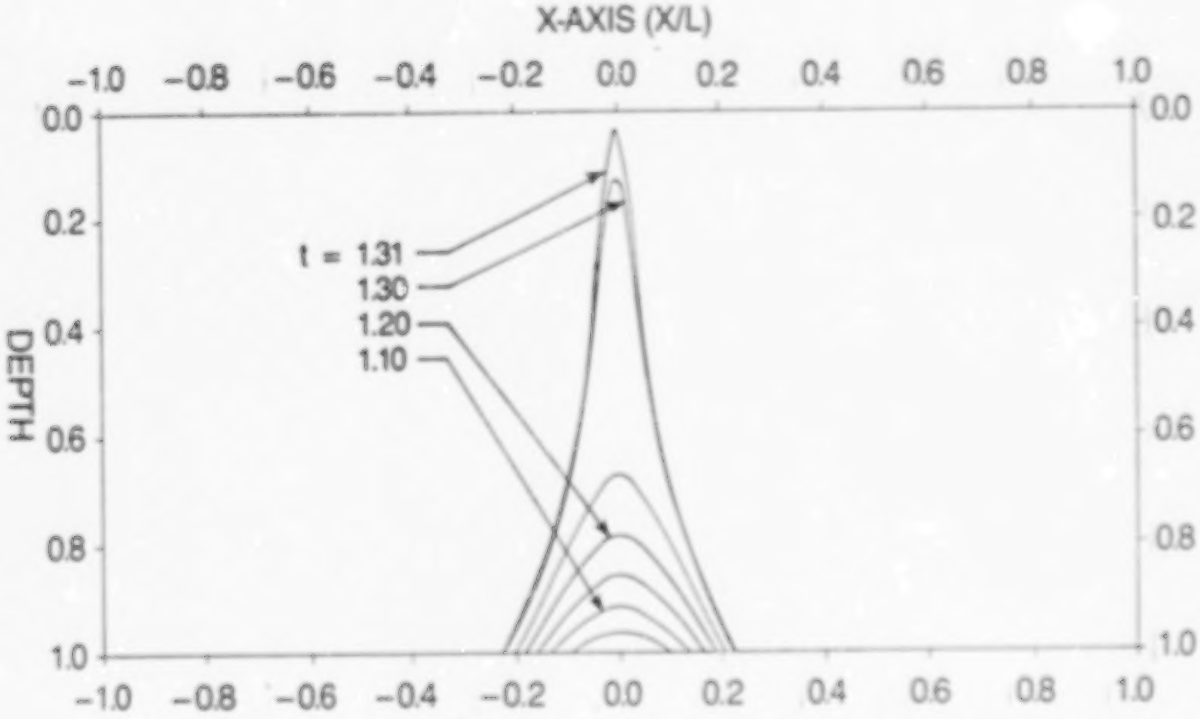

(b)

Fig 3. (continued

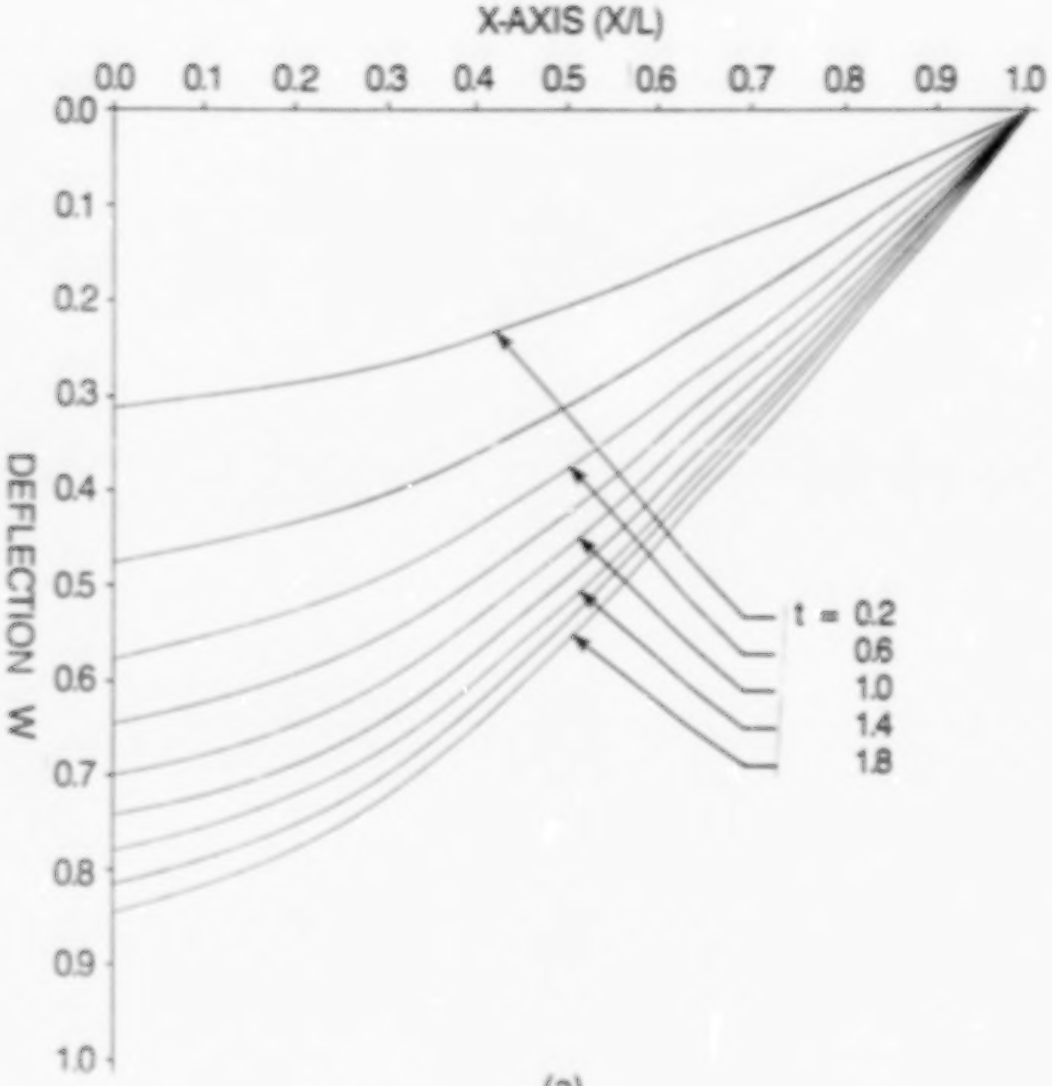

(a)

Fig. 4 Nondimensional deflection of a beam resting on Winkler foundation — (a) B=1, n=3, T_b=360°k and T_u=300°k, (b) B=1, n=5, T_b=360°k and T_u=300°k.

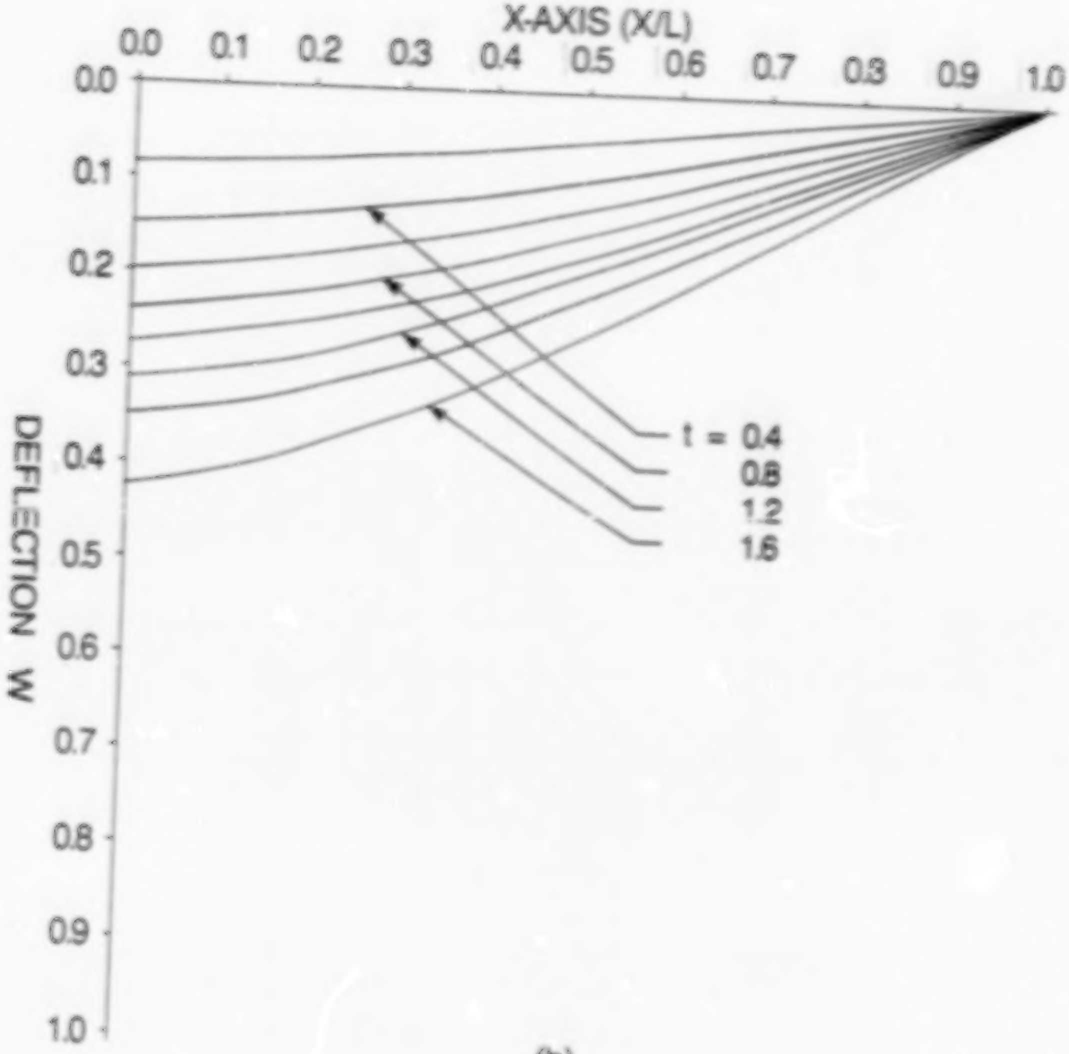

(b)

Fig 4. (continued)

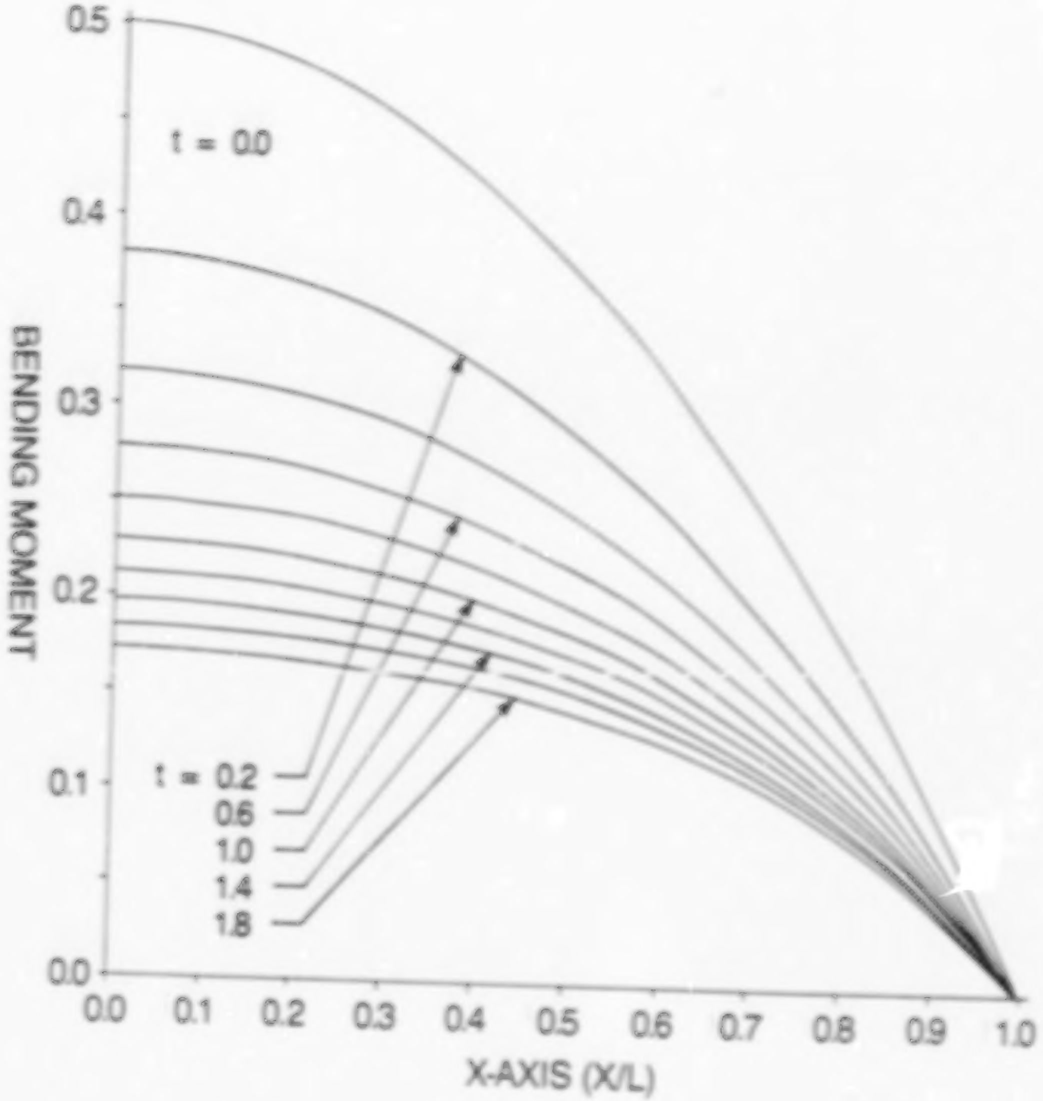

(a)

Fig. 5 Nondimensional bending moment along a beam on Winkler foundation — (a) B=1.0, n=3, T_b=360°k and T_u=300°k, (b) B=1.0, n=5, T_b=360°k and T_u=300°k.

Fig. 5 (continued)

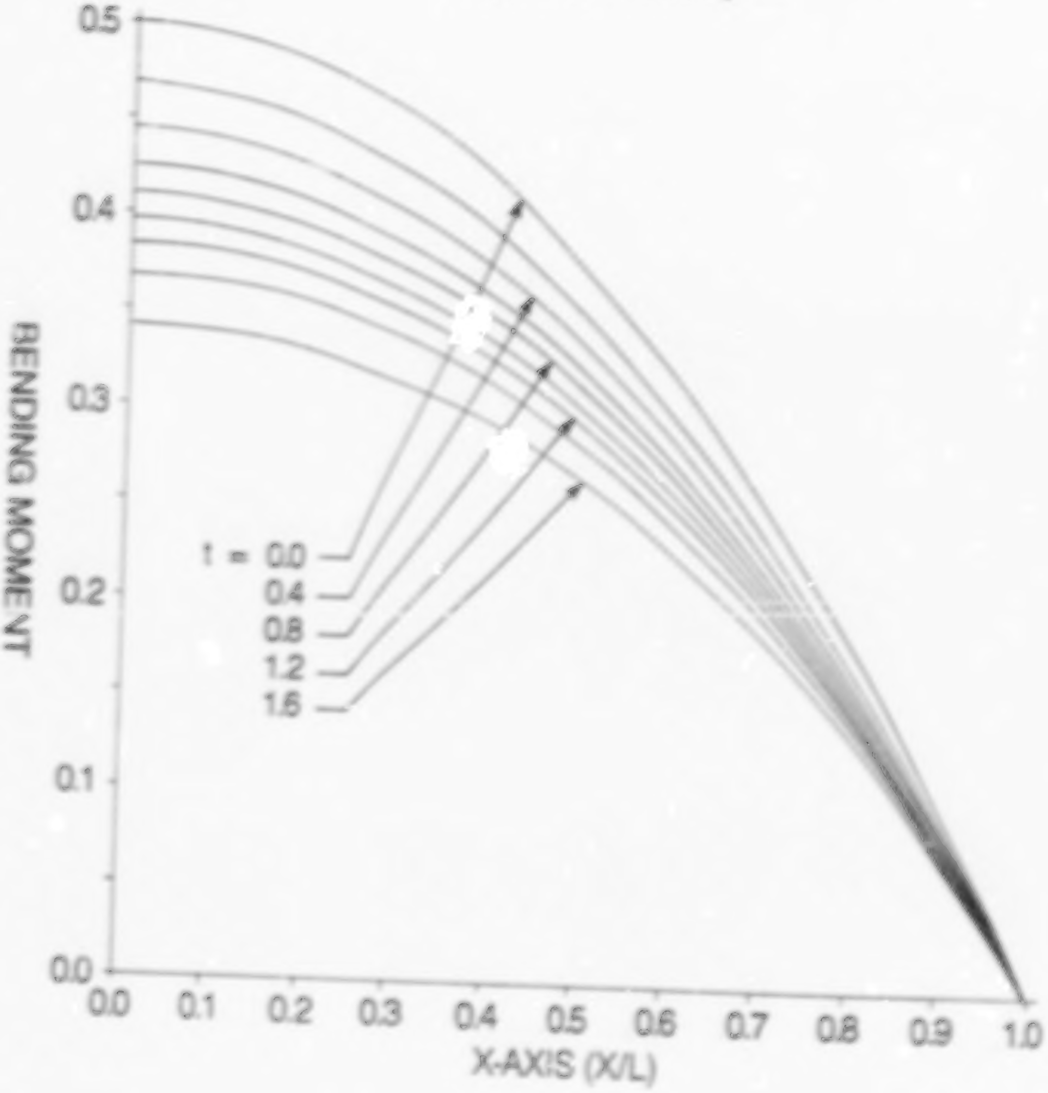

(b)

Fig. 5 (continued)

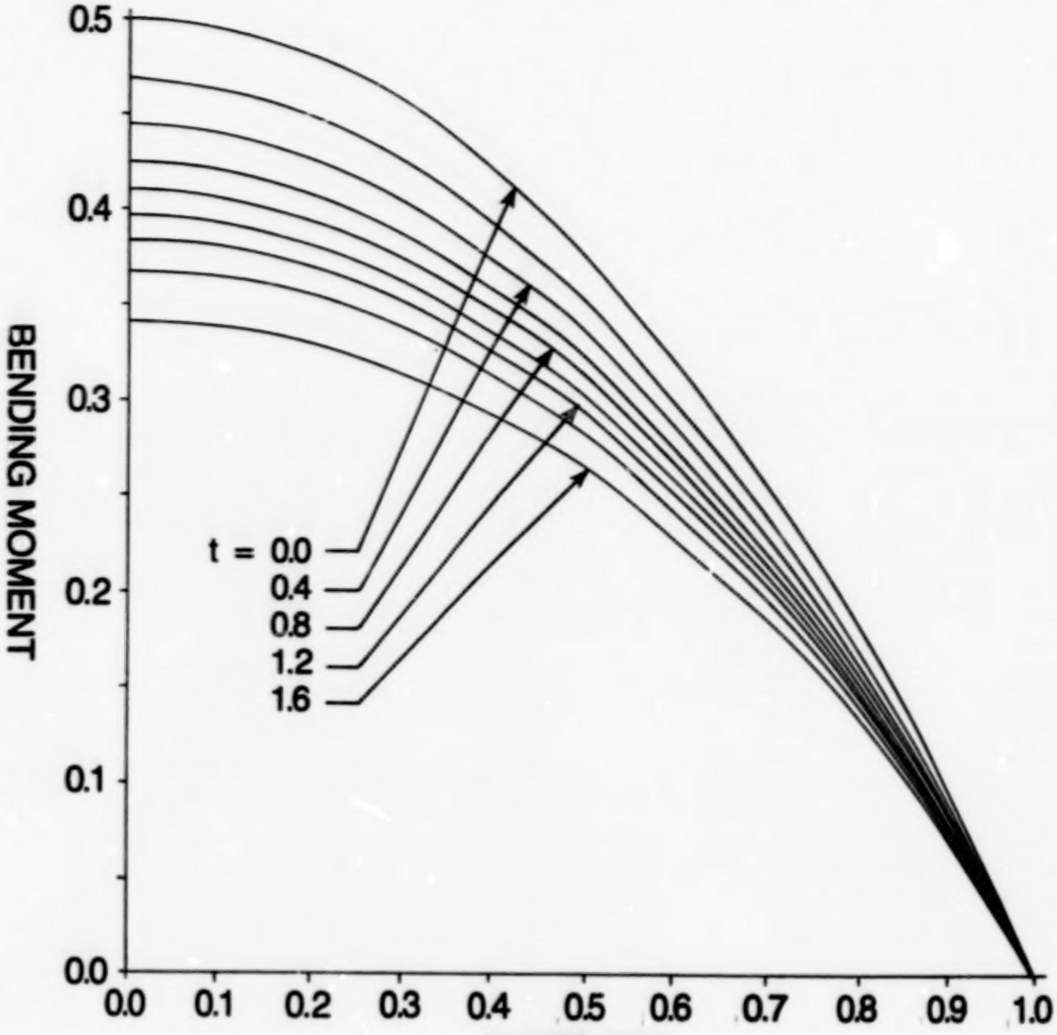

(b)

c-3

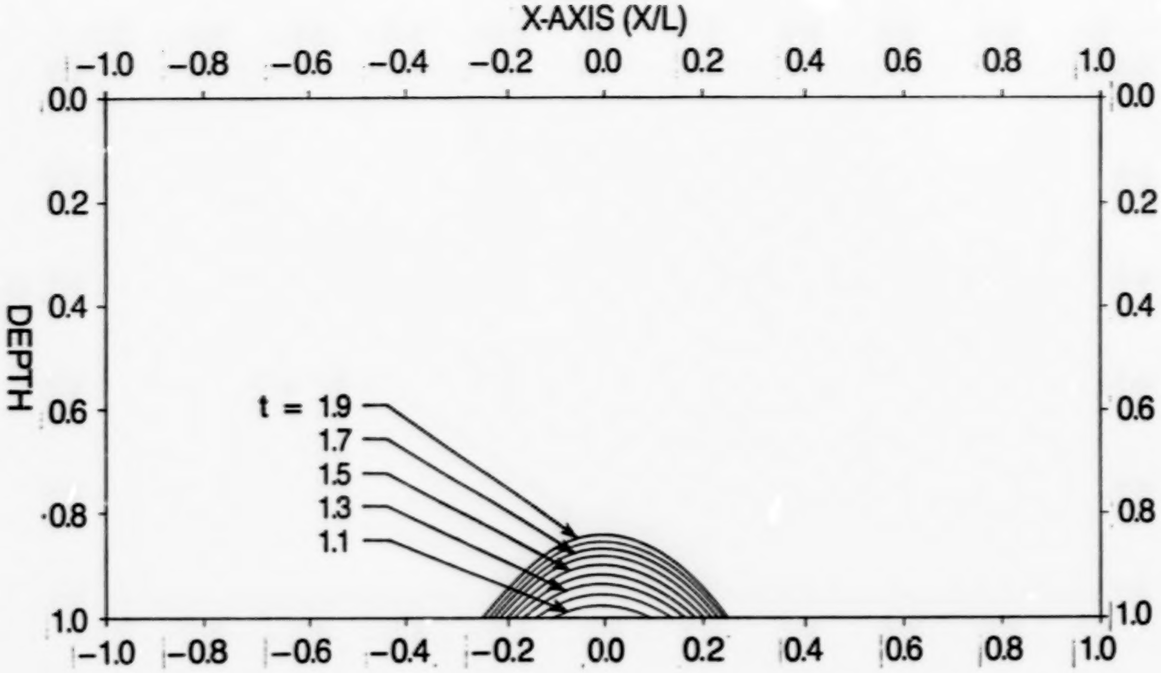

(a)

Fig. 6 Propagation of rupture front in a beam on Winkler foundation — (a) B=1, n=3, T_b=360°k and T_u=300°k, (b) B=1, n=5, T_b=360°k and T_u=300°k.

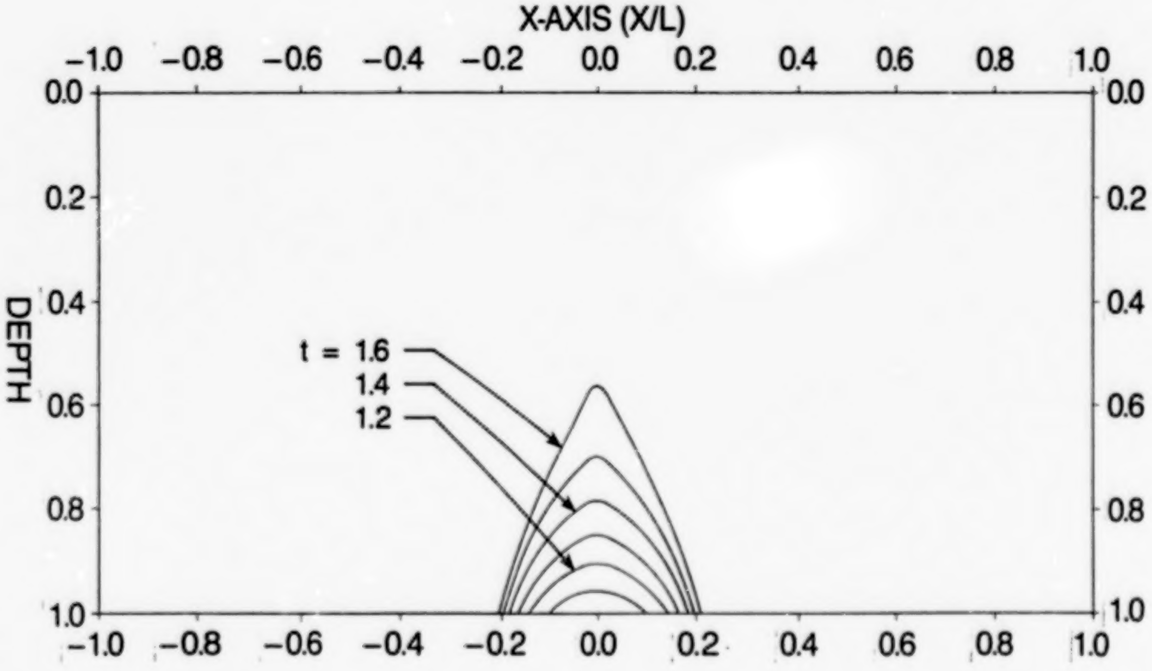

(b)

Fig. 6 (continued)

N88
21510
UNCLAS

N88-21510

A Constitutive Model With Damage for High Temperature Superalloys*

J.A. Sherwood and D.C. Stouffer
Department of Aerospace Engineering
and Engineering Mechanics
University of Cincinnati
Cincinnati, Ohio 45221

I. Introduction

The goal of the research is to develop a unified constitutive model that is applicable for high temperature superalloys used in modern gas turbines. The formulation will be considered successful if: (1) the resulting formulation is efficient for numerically intensive computation such as found in nonlinear finite element models, (2) there is a direct correspondence between the material parameters and experimental data, and (3) the resulting formulations are reasonably accurate for a variety of loading conditions.

Two unified inelastic state variable constitutive models have been evaluated for use with the damage parameter proposed by Kachanov [1]. The first is the model of Bodner and Partom [2,3] in which hardening is modeled through the use of a single state variable that is similar to drag stress. The other constitutive model is an extension of the Bodner-Partom flow proposed by Ramaswamy [4] that employs both a drag stress and back stress. This extension has been successful for predicting the tensile, creep, fatigue, torsional and nonproportional response of Rene' 80 at several

---

* This research was supported, in part, by the National Aeronautics and Space Administration Lewis Research Center and the Air Force Wright Aeronautical Laboratory at Wright Patterson Air Force Base by grant NAG-3-511 to the University of Cincinnati.

PRECEDING PAGE BLANK NOT FILMED

temperatures. In both formulations a cumulative damage parameter is introduced to model the changes in material properties due to the formation of microcracks and microvoids that ultimately produce a macroscopic crack. Calculations have shown that the drag stress/damage model is reasonable for predicting the tensile and creep responses of IN100 at 1350°F and Rene' 95 at 1200°F, but the model is not entirely satisfactory for predicting the cyclic response of these materials. In this study a back stress/drag stress/damage model has been evaluated for Rene' 95 at 1200°F and is shown to predict the tensile, creep, and cyclic loading responses reasonably well.

II. Drag Stress/Damage Model

The initial phase of this research is based on a constitutive model using only one hardening variable, Z, to simulate the drag stress of the material and a damage variable, ω, to model the changes in the material properties due the formation of microcracks and microvoids. The inelastic flow equation of Bodner was used in the following form

$$\dot{\varepsilon}^{I}_{ij} = D_0 \exp\left(-\frac{n+1}{2n}\left(\frac{Z^2(1-\omega)^2}{J_2}\right)^n\right) \frac{S_{ij}}{\sqrt{J_2}} , \qquad (1)$$

where S_{ij} is the deviatoric stress tensor and $J_2 = S_{ij} S_{ij}$. The value of n controls strain rate sensitivity and D_0 is the limiting strain rate. The evolution equations for the state variables Z and ω were developed using the Hemholtz free energy as potential function similar to the work in [7]. The results show that the flow law and evolution equations are thermodynamically associated and are not free to be derived independently.

The damage parameter, as proposed by Kachanov, was defined to exist on the interval [0,1]. A value of zero represents no damage and a value of one for ω denotes complete failure. Calculations for Rene' 95 and IN100 indicated that a value for the damage state variable of much less than one corresponds to failure.

The values of the material constants and initial value of the state variables were determined from experimental data that was obtained in a previous study. The experimental work was conducted by the Air Force Wright Aeronautical Laboratory, WPAFB, Ohio and Mars-Test Inc., Cincinnati, Ohio [5,6]. The correlation of the constitutive model to experimental observations of monotonic tensile and creep tests on IN100 at 1350°F and Rene' 95 at 1200°F was very good. The calculated response for IN100 is shown in Figures 1 and 2.

Extending the drag stress/damage model to predict fatigue loop responses was not completely successful. The model appeared to have trouble capturing the shape of the fatigue loop. This shortcoming is possibly due to how the state variable Z quantifies dislocation movements for a particular type of loading. Drag stress is metallurgically associated with the retardation of dislocation movement due to the interaction with precipitates which results in dislocation jogs or looping for example. Back stress is associated with the pile-up of dislocations at a barrier, such as a grain boundary, which cannot be overcome. During cyclic loading the back stress oscillates with the applied load while the drag stress either increases monotonically or remains essentially constant. Since the dislocation movement was only in one direction for the tensile and creep tests, the contributions of the drag stress and back stress to the total resistance of dislocation motion could be simulated by one state variable monotonically increasing to a steady state value. Although this lumping of resistances to dislocation motion worked well for monotonic loadings, it appears inadequate for cyclic loadings.

III. Drag Stress/Back Stress/Damage Model

Based on the metallurgical considerations given above and the success of the drag stress/back stress model proposed by Ramaswamy for predicting the fatigue response of Rene' 80, a drag stress/back stress/damage model is proposed. The drag stress scalar Z simulates long term cyclic hardening while the back stress tensor Ω_{ij} models the short term strain or work hardening. The governing equations are:

Inelastic Flow Equation,

$$\dot{\varepsilon}^{I}_{ij} = D_0 \exp - \left[\left(\frac{Z^2(1-\omega)^2}{3K_2}\right)^n\right] \frac{(S_{ij}-\Omega_{ij})}{\sqrt{K_2}} \tag{2}$$

Back Stress Evolution Equation,

$$\dot{\Omega}_{ij} = f_1\dot{\varepsilon}^{I}_{ij} + f_1|\dot{\varepsilon}^{I}_{ij}|\Omega_{ij}/\Omega_s + f_3\dot{\sigma}_{ij} \tag{3}$$

Drag Stress Evolution Equation,

$$\dot{Z} = m(Z_1-Z)\dot{W}^{I} \tag{4}$$

Damage Evolution Equation,

$$\dot{\omega} = g_2\dot{\varepsilon}^{IT}_{max} \tag{5}$$

and

Back Stress Relaxation Equation

$$\dot{\Omega}_s = -B\left(\frac{\sqrt{J_2}}{\sigma_0}\right)^r (\Omega_s-\Omega_{sat}) \tag{6}$$

where $K_2 = (S_{ij}-\Omega_{ij})(S_{ij}-\Omega_{ij})$. In the back stress evolution equation f_1 and f_3 are material constants. In the drag stress evolution equation the value of m controls the hardening rate, Z_1 is the saturated value of Z, and $\dot{W}^{I}$ is the inelastic work rate. The parameter g_2 in the damage evolution equation is a material function and damage growth is assumed to be proportional to the maximum principal tensile inelastic strain rate $\dot{\varepsilon}^{IT}_{max}$. Initially damage is assumed to be absent in the material before loading. In the back stress relaxation equation Ω_s is the steady state value of the back stress, Ω_{sat} is the maximum saturated value of the back stress observed in uniaxial tensile tests, the constant σ_0 is introduced to nondimensionalize stress, and B and r are material constants to control the time dependence. The proposed model reduces to that of Ramaswamy for $\dot{\omega} = \omega = 0$.

In uniaxial loading Rene' 95 response displays tension-compression asymmetry as shown in Figure 5. At constant strain rate the compressive tests saturate at a higher magnitude of stress than do the tensile tests. The experimental fatigue response as given in Figure 9 for example shows that for the same level of stress the tensile strain is less than the compressive strain. It is also shown in [5] that the minimum creep rates observed in compression are much less than those in tension at corresponding values of stress. These pieces of information are used to substantiate that a higher initial value of hardness for the material in compression than in tension. For the uniaxial exercise this asymmetry was included in the model by having two drag stress state variables, Z^+ and Z^-similar to kinematic hardening components. The corresponding evolution equations are:

Tensile Drag Stress Evolution Equation,

$$\dot{Z}^+ = m^+(Z_1^+ - Z^+)\dot{W}^I \qquad (7)$$

and

Compressive Drag Stress Evolution Equation,

$$\dot{Z}^- = m^-(Z_1^- - Z^-)\dot{W}^I. \qquad (8)$$

When the stress is greater than zero $Z=Z^+$ and when the stress is less than zero $Z=Z^-$. The $\dot{Z}^+$ evolution equation was only active for stresses greater than zero and the $\dot{Z}^-$ equation was only active for stresses less than zero.

IV. Evaluation of Material Parameters

The values of D_0, n, Ω_{max}, Z_1^+ and Z_1^- were found using a nonlinear regression analysis of the inelastic strain rates corresponding to saturated stress levels observed in the tensile tests. The values of the material constants f_1, f_2, m^+ and m^- were determined using an iterative computer program with the tensile, creep, and cyclic test data as inputs. The program iterated until it converged on stable values for these material constants. For Rene'95 at 1200°F the values of Z_1^+ and Z_1^- are equal.

The damage function, g_2, was determined as the final step after all other constants had been found. The damage growth was evaluated from the tertiary creep response for small values of accumulated inelastic strain and the long term fatigue response corresponding to large values of accumulated inelastic strain. Using both the creep and cyclic tests the values of g_2, relating damage to the accumulated inelastic strain, were found as shown in Figure 3. This damage curve demonstrates that the greatest damage growth occurs early in the loading of the specimen and the rate of damage accumulation approaches a steady-state value rather rapidly.

The maximum value of the back stress is observed in the short time tensile tests when the stress saturates. During long time loading such as creep, the maximum value of the back stress has a lower value than that in the short time tests. This lower value was seen by Ramaswamy [4] for Rene' 80 at 1400°F and 1600°F. This reduced back stress value is also present in

Rene' 95 at 1200°F. Figure 4 shows how the maximum back stress Ω_s decreases from the maximum value Ω_{sat} as a function of the applied stress. Without test data to for substantiation a lower bound has been artificially imposed. The value of σ_o was arbitrarily chosen as 200 Ksi to nondimensionalize stress. Since the time required for a given creep test to reach a stable back stress can be observed, the values of B and r were determined by a linear regression of the back stress relaxation equation and the test data.

V. Comparisons of Experimental and Calculated Results

The strain rate control test data for Specimens 1-1 and 6-1 in Figure 6 show that the saturation stress for Rene' 95 is essentially strain rate independent. The model predictions show a small amount of strain rate dependence; however the predictions are reasonable for both the stress rate controlled and strain rate controlled tests.

The comparison of the observed and predicted creep response is shown in Figure 7. The creep stresses range from 146 Ksi to 175 Ksi. The experimental data is ordered except for the 146 Ksi test. The model predicts reasonably well the primary, secondary, and tertiary creep responses for all of the tests except the 146 Ksi test. The slight dip in the predicted creep response connecting the secondary and tertiary creep regions is a consequence of matching the constants in the back stress relaxation equation with the damage growth equation. However, once the back stress is stabilized the model predictions are parallel to the experimental creep responses.

A typical stress control cyclic test is shown in Figures 8 and 9. The predicted and experimental peak strains as a function of time are shown in Figure 9. The experimental tensile peak strain is observed to remain relatively constant while the compressive peak strain decreases with each additional loop until a steady state response is reached. The observed error in the model prediction is due to a combination of factors. However since test 5-3, Ref. [5], is for a stress range of ± 168 Ksi the deformation is well into the plastic range. It can be seen from the tensile tests in Figure 6 that a small deviation in the peak stress produces a large variation in the predicted tensile peak strain. Since the trends are clearly correct the predicted tensile strain is considered acceptable. Figure 8 shows how the shape of the fatigue loop changes with increasing cycles. A displacement limit of 0.02 in/in was defined as failure since the model does not include a criteria for the transition from damage accumulation to crack growth. The model has been used to predict the fatigue life up to cracking for two stress control tests 5-3 and 3-6 of Ref. [5] at ±168 Ksi and ±158 Ksi, respectively. In these calculations the damage growth appears to be reasonably accurate. Additional fatigue calculations will be made in the future to further evaluate the model. Finally, future work to use the model to predict the material deformation to combined creep and cyclic loadings is planned.

VI. References

1. Kachanov, L.M., "Time to Fracture Under Conditions of Creep," Meknanika i Mashinostr. No. 8, [in Russian], pp. 26-31, 1958.
2. Bodner, S.R. and Partom, Y., "Constitutive Equations for Elastic-Viscoplastic Strain-Hardening Materials," ASME Journal of Applied Mechanics, Vol. 42, pp 385-389, 1975.
3. Bodner, S.R., Partom, I., and Partom, Y., "Uniaxial Cyclic Loading of Elastic-Viscoplastic Materials," ASME Journal of Applied Mechanics, Vol. 46, pp 805-810, 1979.

4. Ramaswamy, V.G., "A Constitutive Model for the Inelastic Multiaxial Response of Nickel Base Superalloy Rene' 80," Ph.D. Dissertation, University of Cincinnati, 1985.

5. Stouffer, D.C., Papernik, L. and Bernstein, H., "On the High Temperature Response of a Super Alloy; Part 1: The Mechanical Properties of Rene' 95," AFWAL-TR-80-4163, 1980.

6. Stouffer, D.C., "A Representation for the Mechanical Response of IN100 at Elevated Temperature," AFWAL-TR-81-4083, 1981.

7. Abuelfoutouh, N.M., "A Thermodynamically Consistent Constitutive Model for Inelastic Flow of Materials," Ph.D Dissertation, University of Cincinnati, 1983.

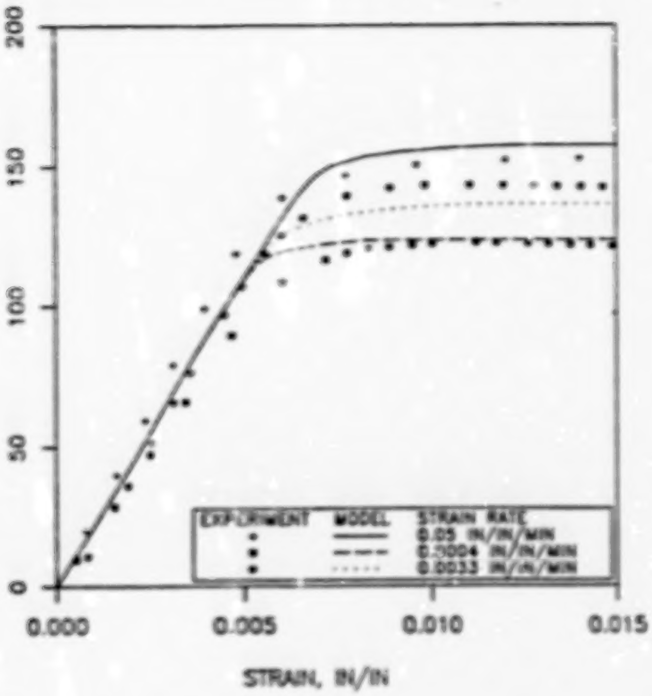

Figure 1. Predicted and Experimental Tensile Response of IN100 at 1350°F

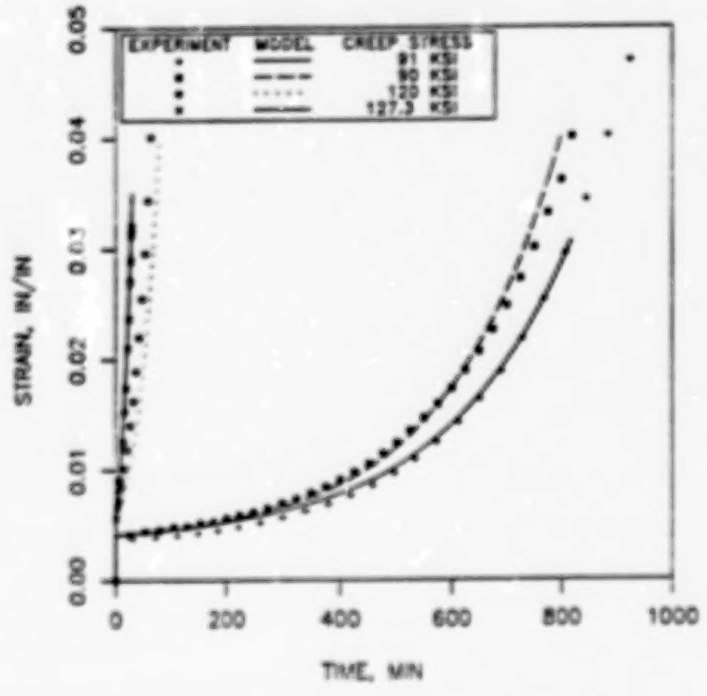

Figure 2. Predicted and Experimental Creep Response of IN100 at 1350°F

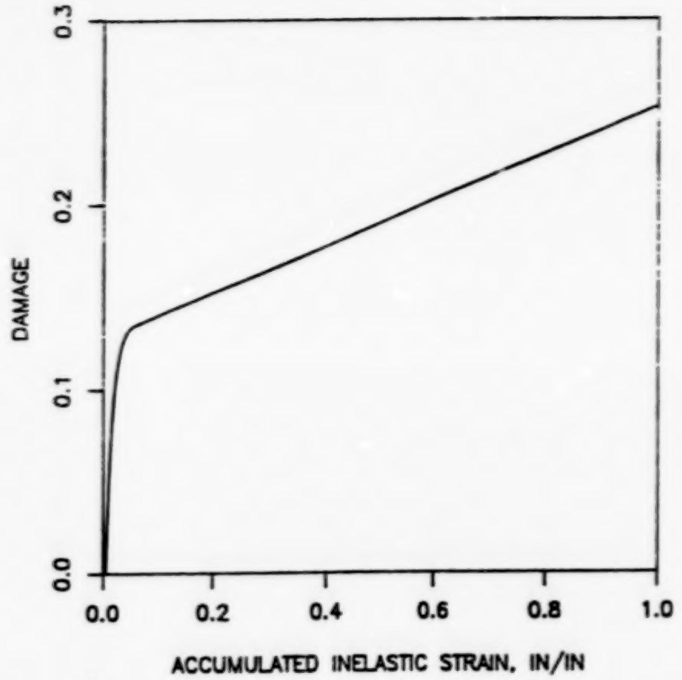

Figure 3. Damage as a Function of Accumulated Inelastic Tensile Strain for Rene' 95 at 1200°F

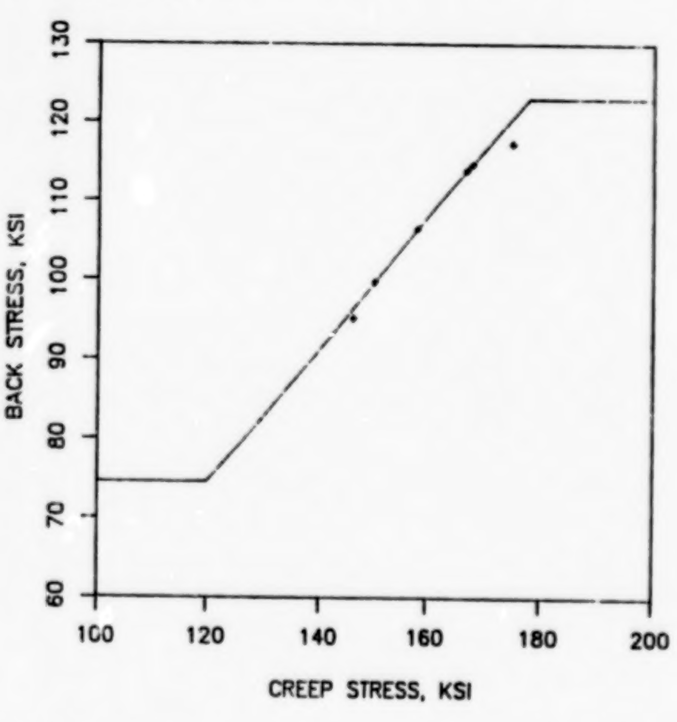

Figure 4. Variation of Saturated Back Stress with Applied Stress for Rene' 95 at 1200°F

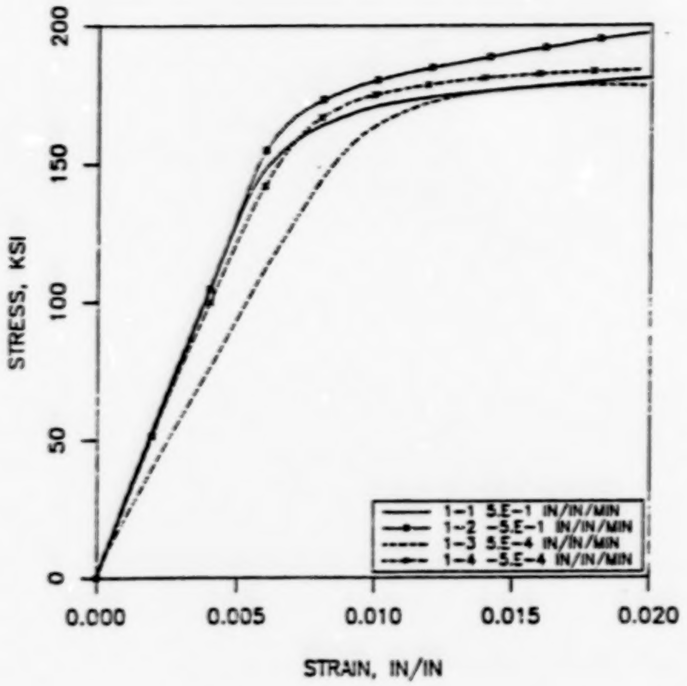

Figure 5. Comparison of Experimental Tensile and Compressive Responses of Rene' 95 at 1200°F

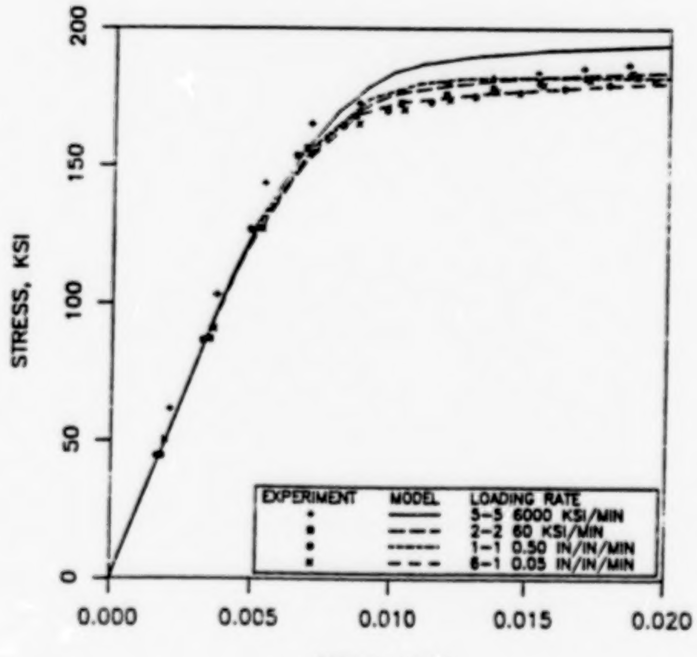

Figure 6. Predicted and Experimental Tensile Response of Rene' 95 at 1200°F

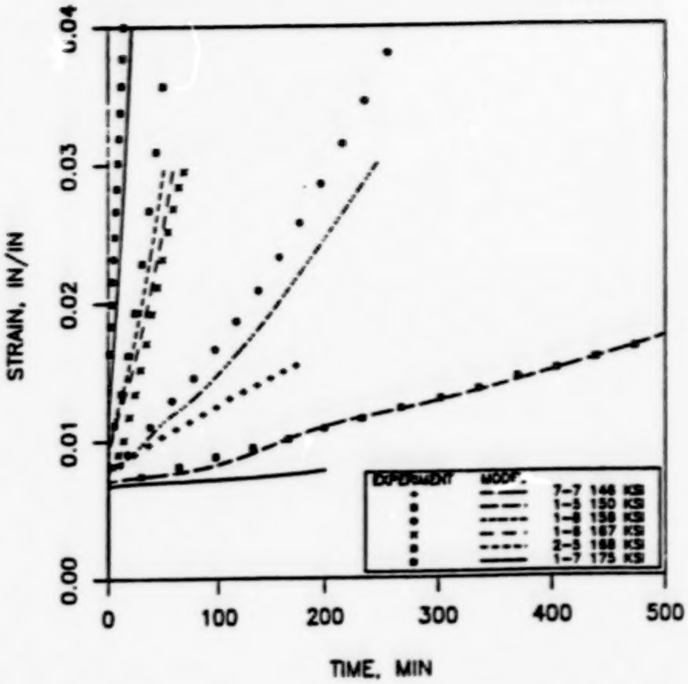

Figure 7. Predicted and Experimental Creep Response of Rene' 95 at 1200°F

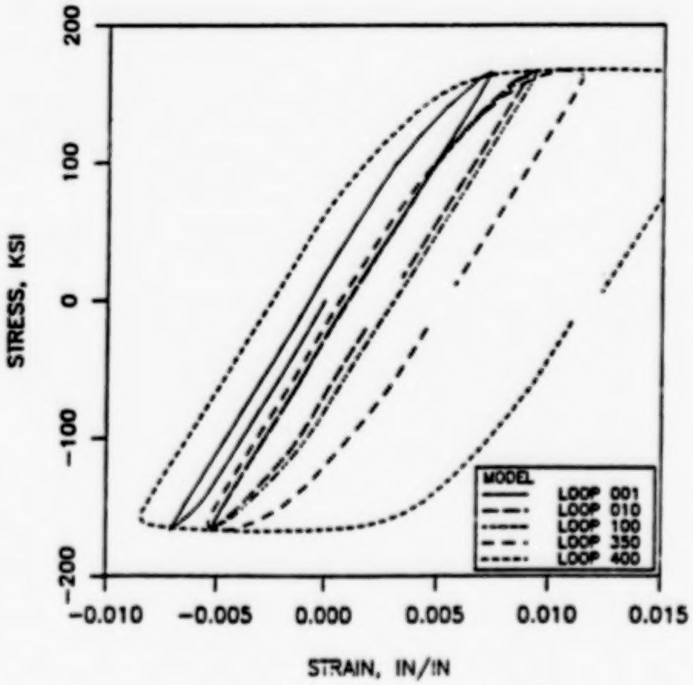

Figure 8. Variation of Fatigue Loop for Specimen No. 5-3 Loaded at ±168 Ksi at 10 Cycles per Second for Rene' 95 at 1200°F

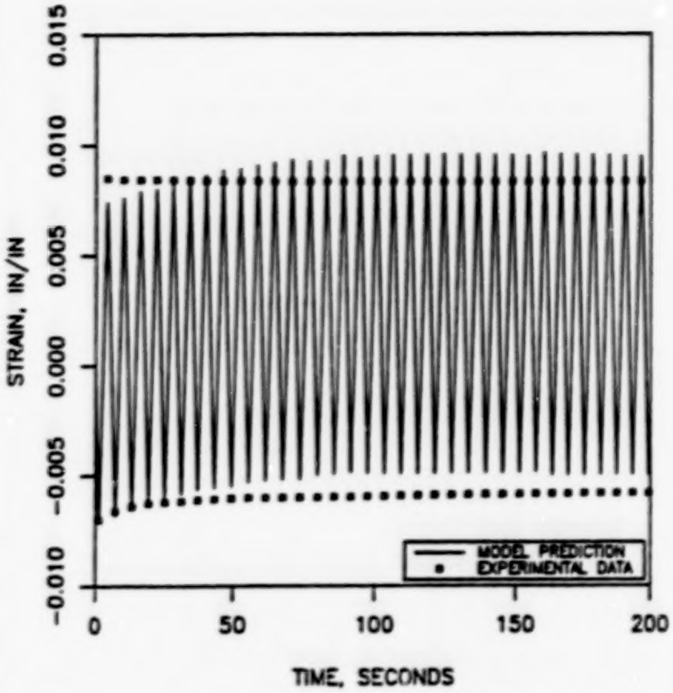

Figure 9. Predicted and Experimental Strains for Specimen No. 5-3 Loaded at ±168 Ksi at 10 Cycles per Second for Rene' 95 at 1200°F

N88
21511
UNCLAS

N88-21511

EVALUATION OF STRUCTURAL ANALYSIS METHODS FOR LIFE PREDICTION

A. Kaufman,* J.F. Saltsman, G.R. Halford, and M. Tong*
National Aeronautics and Space Administration
Lewis Research Center
Cleveland, Ohio 44135

INTRODUCTION

Hot section components of gas turbine engines are subject to severe thermomechanical loads during each mission cycle. Inelastic deformation can be induced in localized regions leading to eventual fatigue cracking. Assessment of durability requires reasonably accurate calculation of the structural response at the critical location for crack initiation.

Nonlinear finite-element computer codes, such as MARC (ref. 1), have become available for calculating inelastic structural response under cyclic loading. The plasticity computations in these codes have been based on classical incremental theory using a hardening model to define the cyclic yield surface, a yield criterion, and a flow rule. Generally the von Mises yield criterion and the normality flow rule are used. Creep analyses are based on a separate creep constitutive model that is not directly coupled to the plasticity model. However, analytical studies of hot section components such as turbine blades (ref. 2) and combustor liners (ref. 3) have demonstrated that existing nonlinear finite-element computer codes based on classical methods do not always predict the cyclic response of the structure accurately because of the lack of interaction between the plasticity and creep deformation response.

Under the HOST Program, the NASA Lewis Research Center has been sponsoring the development of unified constitutive material models and their implementation in nonlinear finite-element computer codes for the structural analysis of hot section components (refs. 4 to 7). The unified constitutive theories are designed to encompass all time-dependent and time-independent aspects of inelasticity including plasticity, creep, stress relaxation, and creep recovery. These theories avoid the noninteractive summation of inelastic strain into plastic and creep components and most of them avoid specifying yield surfaces to partition stress space into elastic and elastic-plastic regions. In discarding these overly simplified assumptions of classical theory, unified models can more realistically represent the behavior of materials under cyclic loading conditions and high temperature environments.

A major problem with nonlinear, finite-element computer codes is that they are generally too costly to use in the early design stages for hot section components of aircraft gas turbine engines. A program has been underway at NASA Lewis to develop a simplified and more economical procedure for performing nonlinear structural analysis using only an elastic finite-element solution or local strain measurements as input (refs. 8 and 9). Development of the simplified method was based on the assumption that the inelastic regions in the structure are local and that the total strain history can be defined by elastic analyses. Corrections have been incorporated in the method to account for strain redistribution under applied mechanical loading. This procedure was implemented in a computer program and has been exercised on a wide variety of problems including multiaxial loading, nonisothermal conditions, various materials and constitutive models, and dwell times at various points in the cycles. Comparisons of the results of the simplified analyses with nonlinear finite-element solutions for these problems have shown reasonably good agreement.

---

*Sverdrup Technology, Inc., Lewis Research Center Group.

More than 30 methods for predicting low-cycle fatigue life have been identified in a recent review article by Halford (ref. 10). These methods differ somewhat in the structural analysis parameters used for life prediction. Basic structural response information required by various life prediction methods includes the total and inelastic strain ranges, inelastic strain rate, proportion of time-dependent and time-independent inelastic deformation, peak tensile and mean stresses, stress range, and cycle frequency.

The purpose of this study was to evaluate several nonlinear structural analysis methods (of different levels of sophistication) with regard to their effect on the life prediction of a hot section component. The methods selected for evaluation were nonlinear finite-element analyses based on both classical and unified theories, as well as the simplified nonlinear procedure.

The component under consideration was the airfoil of an air-cooled turbine blade being studied for use in the first-stage, high pressure turbine of a commercial aircraft engine. A mission cycle typical of a transatlantic flight was assumed for the analyses. Initially, this airfoil and mission were used for a demonstration problem involving a Walker unified model by Pratt & Whitney (P&W) (ref. 7) under contract to NASA as part of the HOST Program.

MARC nonlinear finite-element analyses were conducted for this airfoil problem at NASA Lewis to calculate the stress-strain hysteresis loop at the critical location for life prediction purposes. The classical type of analysis used conventional creep-plasticity models, whereas the unified analyses were based on two quite different constitutive theories, those of Bodner and Walker (ref. 6). The simplified procedure was also applied to this problem using elastic finite-element solutions for three peak temperature points of the cycle. Comparisons were made of calculated fatigue lives based on these structural analysis results by using the total strain version of the strain range partitioning (TS-SRP) life prediction method (ref. 11).

PROBLEM DESCRIPTION

The turbine blade under study is a Pratt & Whitney (P&W) generic design for use in the high-pressure-stage turbine of a commercial aircraft engine. The airfoil span measures about 6 cm; the chord width, 2.5 cm; and the tip-to-hub radius ratio is 1:15. Material properties and model constants for a cast nickel-base superalloy, B1900+Hf (ref. 6), were used for the analyses.

The three-dimensional finite-element model created by P&W for the MARC analyses of the turbine blade airfoil is shown in figure 1. A total of 173 solid elements with 418 nodes and 1086 unsuppressed degrees of freedom was used to model the airfoil shell. This model included twenty-four 20-node elements around the expected high strain region of the leading edge and 149 8-node elements for the remainder of the airfoil. Displacements were tied at the interfaces of the two types of elements to prevent separation around midside nodes. Boundary conditions were applied to constrain all nodes at the base of the model to lie on the base plane of the airfoil. Additional boundary conditions were applied to prevent rigid body motion.

Figure 2 illustrates the flight mission originally selected by P&W and subsequently used for these analyses. This type of cycle is representative of a transatlantic flight for an advanced commercial aircraft engine. High, transient, thermal stresses and inelastic strains are induced during the engine takeoff, climb, and descent parts of the cycle. Creep occurs during the maximum takeoff, climb, and cruise steady-state hold times. On shutdown at the end of each cycle, a uniform airfoil temperature of 429 °C and a rotational speed of 200 rpm were assumed.

ANALYTICAL PROCEDURE

Finite-Element Analyses

Metal temperatures were calculated from MARC transient and steady-state three-dimensional heat transfer analyses. The input for these heat transfer analyses are proprietary P&W information. The calculated metal-temperature, cycle-time profiles for the midspan leading edge, trailing edge, and cold spot locations are shown in figure 3. Figure 4 shows the temperature distribution at the maximum takeoff condition when the highest temperatures occurred.

The MARC code was also used to perform elastic and nonlinear structural analyses for the airfoil. The mission cycle was subdivided into 81 load-time increments. Structural analyses were carried out for two complete flight cycles. Plasticity calculations were performed for the transient parts of the cycle and creep calculations during the steady-state maximum takeoff, maximum climb, and cruise hold times. The classical creep-plasticity analyses used temperature-dependent cyclic stress-strain and creep properties for B1900+Hf alloy. Plasticity calculations were based on a kinematic hardening rule and the von Mises yield criterion; creep was determined from a power law model in conjunction with a time hardening rule.

MARC finite-element analyses were also performed with the unified models of Bodner and Walker. The Walker model is of the common back-stress, drag-stress form; where the back stress is a tensor internal variable defining the directional hardening (Bauschinger effect), and the drag stress is a scalar internal variable defining the isotropic hardening. Of the many unified models which have been proposed in the literature, the Walker model has undergone the most development for finite-element analysis. All 14 material constants of this model are temperature-dependent.

The major exception to the back-stress, drag-stress form is the Bodner model. This model has one internal variable which is partitioned into directional and isotropic hardening components. Since it lacks a back stress, it assumes that the inelastic strain rate vector is coincident with the direction of the deviatoric stress. Another difference between the Bodner model and the more common back-stress, drag-stress model is that the former uses the plastic work rate as the measure of hardening whereas the latter uses the magnitude of the inelastic strain rate. There are essentially nine material constants to be determined for this model, only three of which have been found to be temperature-dependent for most materials studied.

Under a NASA sponsored effort with Southwest Research Institute and Pratt & Whitney Aircraft, the unified constitutive theories of Bodner and Walker were evaluated and further developed to model the high-temperature cyclic behavior of B1900+Hf alloy. A detailed discussion of these unified constitutive models, as well as the material constants for both models, are presented in the contractor annual status reports (refs. 6 and 7). The models were implemented into the MARC code through a user subroutine, HYPELA. The model constitutive equations were integrated using an explicit Euler technique and a self-adaptive solution scheme.

Simplified Analysis

The basic assumption of the simplified procedure is that the inelastic region is localized and, therefore, the material cyclic response can be approximated using as input the total strain history obtained from elastic analyses. One version of the procedure uses Neuber corrections to account for strain redistribution due to mechanical loading; however, this version was not utilized for this study because of the dominance of the thermal loading during the peak strain parts of the cycle. Classical incremental plasticity methods are used; the material is characterized by a von Mises yield criterion, to describe yielding under multiaxial stress states, and a bilinear kinematic hardening model, to describe the motion of the yield surface under cycling.

Only elastic solutions for peak strain points in the cycle are normally required to create the strain history input; these are linearly subdivided into a sufficient number of increments to define the stress-strain cycle. The strain states calculated from the elastic finite-element analyses are correlated in the form of von Mises effective strains. To compute cyclic hysteresis loops for life prediction purposes, the input effective strains must be given signs, usually on the basis of the signs of the dominant principal stresses and strains. In this case, elastic finite-element analyses were performed for the startup, maximum takeoff, and shutdown conditions in order to create the input strain history at the critical location.

The increments are analyzed sequentially to obtain the cumulative plastic strains and to track the yield surface. Creep computations are performed for increments involving dwell times by using the creep characteristics incorporated in the code. Depending on the nature of the problem, the creep effects are determined on the basis of one of three options: (1) stress relaxation at constant strain, (2) cumulative creep at constant stress, or (3) a combination of stress relaxation and creep.

A FORTRAN IV computer program (ANSYMP) was created to automatically implement the simplified analytical procedure. Previous papers (refs. 8 and 9) on the development of this procedure present a detailed description of the calculational scheme.

DISCUSSION OF RESULTS

The entire discussion of the structural and life analyses results for the airfoil presented herein are based on the critical location at the leading edge at midspan, which was the hot spot as indicated in figure 4. This location contained the element and Gaussian integration point which exhibited the largest total strain change during a mission cycle.

The calculated stress-strain hysteresis loops at the critical location for the first two mission cycles are shown in figures 5 to 7 for MARC finite-element analyses (using the classical creep-plasticity, Bodner, and Walker models, respectively), and in figure 8 for the simplified analysis. Figures 5 to 7 are plotted in terms of von Misses effective stress and strain with a sign criterion based on the sign of the dominant normal stress. Comparison of figures 5 to 7 shows that the maximum compressive strain, which occurs at the hot end of the cycle, was about the same for the classical and unified model finite-element analyses on the first cycle. This result is to be expected since the problem was largely thermally driven, and it indicates that the thermal strain calculations were consistent among these three analyses from startup at room temperature to maximum takeoff. However, the stress-strain loops on subsequent cycling were substantially different among the models, especially in regard to the peak strains during the cold part of the cycle in descending to shutdown. These differences result in a smaller cyclic strain range for the unified analyses than for the classical creep-plasticity analysis. The calculated stress-strain loops shown in figure 6 for the Bodner model are questionable because of computational instabilities that were encountered in the analysis on the cooldown part of the cycle. These instabilities are apparently due to a discontinuity in the isotropic hardening term of the model's internal variable when the stress sign changes during a steady-state hold time; it is believed that this problem can be circumvented by refinements to the numerical procedure for integrating the constitutive equations. The maximum compressive strain for the simplified analysis (shown in fig. 8) was somewhat smaller than for the finite-element analyses because the maximum compressive strain did not quite occur at maximum takeoff. Therefore, the selection of the maximum takeoff condition as one of the mission points for a finite-element analysis resulted in a slight truncation in the calculated peak strain and strain range. In all the analytical cases, except with the Bodner model, the stress-strain response had essentially stabilized by the end of the second cycle.

The results from these structural analyses (elastic-plastic-creep, Bodner unified, Walker unified, and simplified) are summarized in table I in terms of the total strain range and mean stress for the second cycle. CPU (central processor unit) times for two complete analytical cycles are indicated in the first column. The CPU time for the simplified analysis, including 81 sec to perform the elastic finite-element analyses for the startup, maximum takeoff, and shutdown conditions, and 1 sec for the actual simplified procedure, was 50 times faster than for the MARC classical finite-element analysis. The MARC analysis using the Walker model was somewhat more economical in CPU time than with the creep-plasticity models. Because of the computational problems that were encountered with the Bodner model, it used somewhat more CPU time than the classical models.

Also presented in table I are predicted cyclic lives to crack initiation using the TS-SRP method. These predictions were based on unpublished NASA data for out-of-phase bithermal behavior of B1900+Hf alloy at maximum and minimum temperatures of 871 and 483 °C, respectively. Comparisons of the calculated strain ranges and lives (shown in table I) for the different structural analysis methods demonstrate the sensitivity of life prediction to the constitutive models and analytical methodologies employed. In the present case, the lowest cyclic life prediction was obtained using the classical nonlinear finite-element analysis, and the largest using the Walker unified model. The simplified procedure probably would have given the most conservative life prediction if the maximum compressive strain used for the input total strain history had been more accurately defined.

SUMMARY OF RESULTS

This paper evaluates the utility of advanced constitutive models and structural analysis methods in predicting the cyclic life of an air-cooled turbine blade for a gas turbine aircraft engine. Structural analysis methods of various levels of sophistication were exercised to obtain the cyclic stress-strain response at the critical airfoil location. Calculated strain ranges and mean stresses from the stress-strain cycles were used to predict crack initiation lives by using the TS-SRP life prediction method. The major results of this study were as follows:

1. The predicted strain range and life varied with the constitutive model used. Differences in the calculated strain ranges between the unified and classical models were mainly due to differences in the peak strains computed at the cold end of the cycle. However, the maximum compressive strain on the first cycle was not significantly affected by the constitutive model, thereby indicating that the thermal expansion calculations were consistent.

2. The stress-strain responses calculated by using the Bodner and Walker unified models were very similar. Computational instabilities encountered with the Bodner model during the steady-state hold times probably can be circumvented by refinements in the numerical integration procedure.

3. Because of the differences in the calculated strain ranges, the lowest predicted cyclic life resulted from using the classical nonlinear finite-element analysis and the highest one from using the Walker unified model. The simplified procedure probably would have given the most conservative life prediction if the input total strain peak at the hot end of the cycle had been more accurately defined.

4. The simplified procedure, including the computing times for the initial elastic finite-element analyses, was about 50 times faster than the cyclic finite-element analyses, and about 4000 times faster for just the cyclic inelastic computations. The CPU time for the MARC finite-element analyses was somewhat less for the Walker unified model than the classical creep-plasticity models. Because of its computational problems, the Bodner model analysis used the most CPU time.

N88
21512
UNCLAS

N88-21512

REFERENCES

1. MARC General Purpose Finite Element Program. Vol. A: User Information Manual; Vol. B: MARC Element Library; Vol. C: Program Input; Vol. D: User Subroutines and Special Routines. MARC Analysis Research Corporation, 1986.

2. McKnight, R.L.; Laflen, J.H.; and Spamer, G.T.: Turbine Blade Tip Durability Analysis. (R81AEG372, General Electric; NASA Contract NAS3-22020) NASA CR-165268, 1981.

3. Moreno, V.: Combustor Liner Durability Analysis. (PWA-5684-19, Pratt and Whitney Aircraft; NASA Contract NAS3-21836) NASA CR-165250, 1981.

4. Ramaswamy, V.G., et al.: Constitutive Modeling for Isotropic Materials. NASA CR-174805, 1984.

5. Ramaswamy, V.G., et al.: Constitutive Modeling for Isotropic Materials. NASA CR-175004, 1985.

6. Lindholm, U.S., et al.: Constitutive Modeling for Isotropic Materials. NASA CR-174718, 1984.

7. Lindholm, U.S., et al.: Constitutive Modeling for Isotropic Materials. (SWRI-7576/30, Southwest Research Institute; NASA Contract NAS3-23925) NASA CR-174980, 1985.

8. Kaufman, A.: Development of a Simplified Procedure for Cyclic Structural Analysis. NASA TP-2243, 1984.

9. Kaufman, A.; and Hwang, S.Y.: Local Strain Redistribution Corrections for a Simplified Inelastic Analysis Procedure Based on an Elastic Finite-Element Analysis. NASA TP-2421, 1985.

10. Halford, G.R.: Low-Cycle Thermal Fatigue. NASA TM-87225, 1986.

11. Saltsman, J.F.; and Halford, G.R.: An Update of the Total-Strain Version of SRP. NASA TP-2499, 1985.

TABLE I. TURBINE BLADE STRUCTURAL ANALYSIS RESULTS

Analytical Method (CPU time, sec)	Strain Range, Microstrain	Mean Stress MPa	Predicted Cyclic Life
Elastic-Plastic Creep (4038)	2886	2	42,400
Unified (Bodner) (4938)	2440	50	89,500
Unified (Walker) (3660)	2360	90	103,800
Simplified (81+1)	2771	-5	50,700

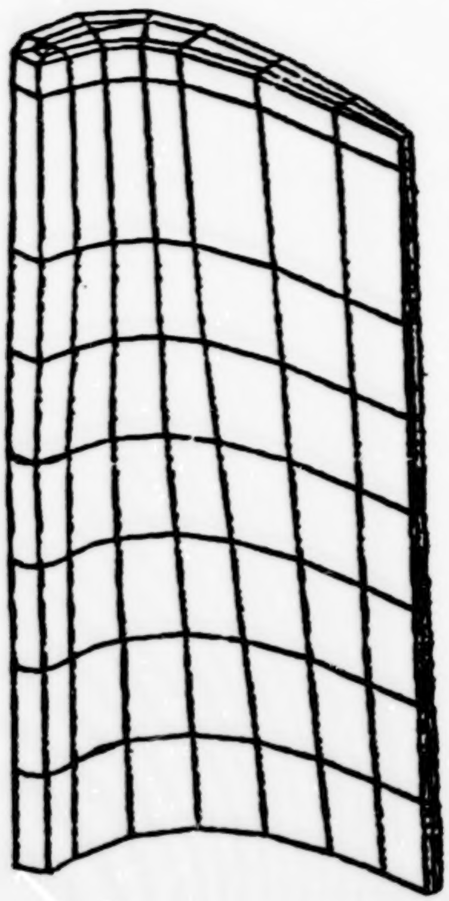

FIGURE 1. - AIRFOIL FINITE-ELEMENT MODEL

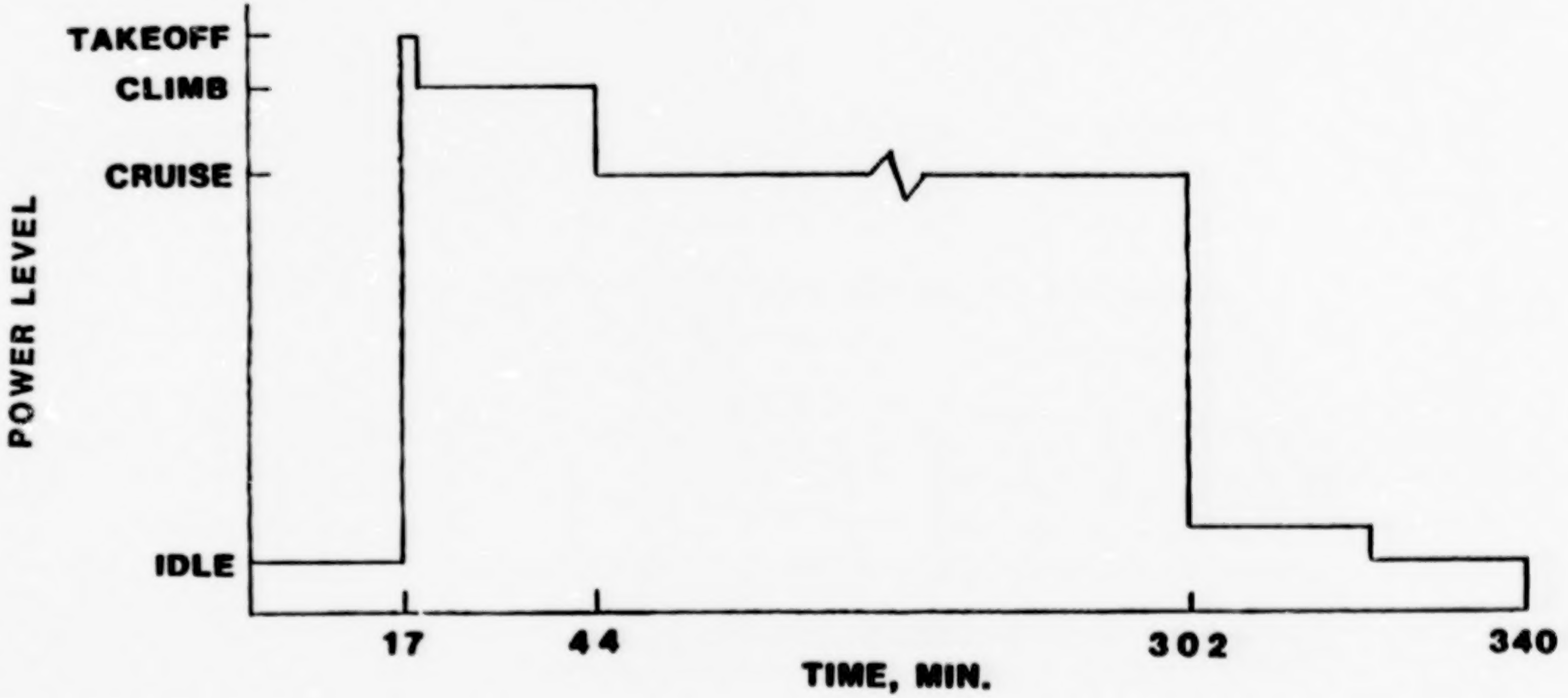

FIGURE 2. - MISSION CYCLE USED FOR ANALYSIS

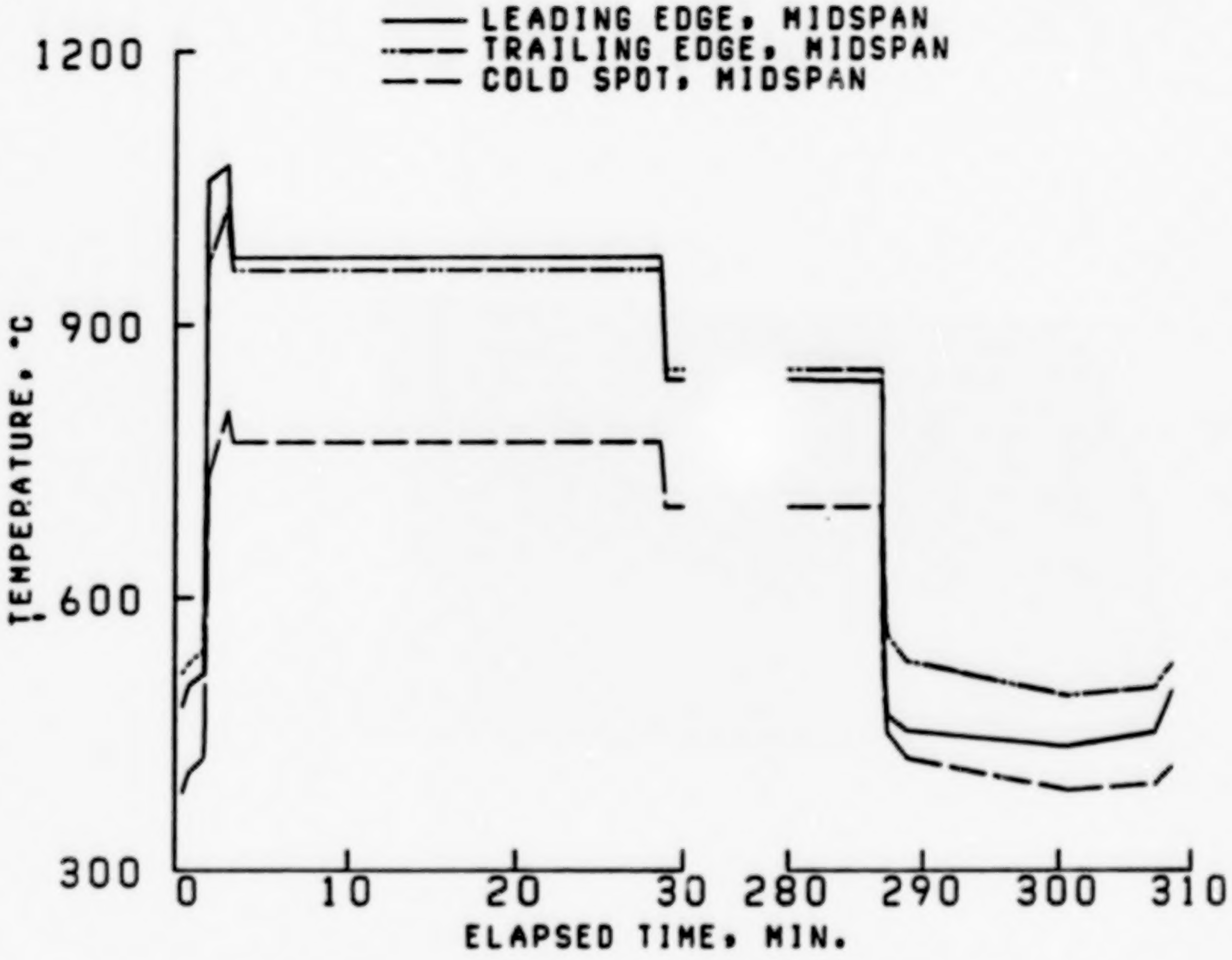

FIGURE 3. AIRFOIL TEMPERATURE CYCLE

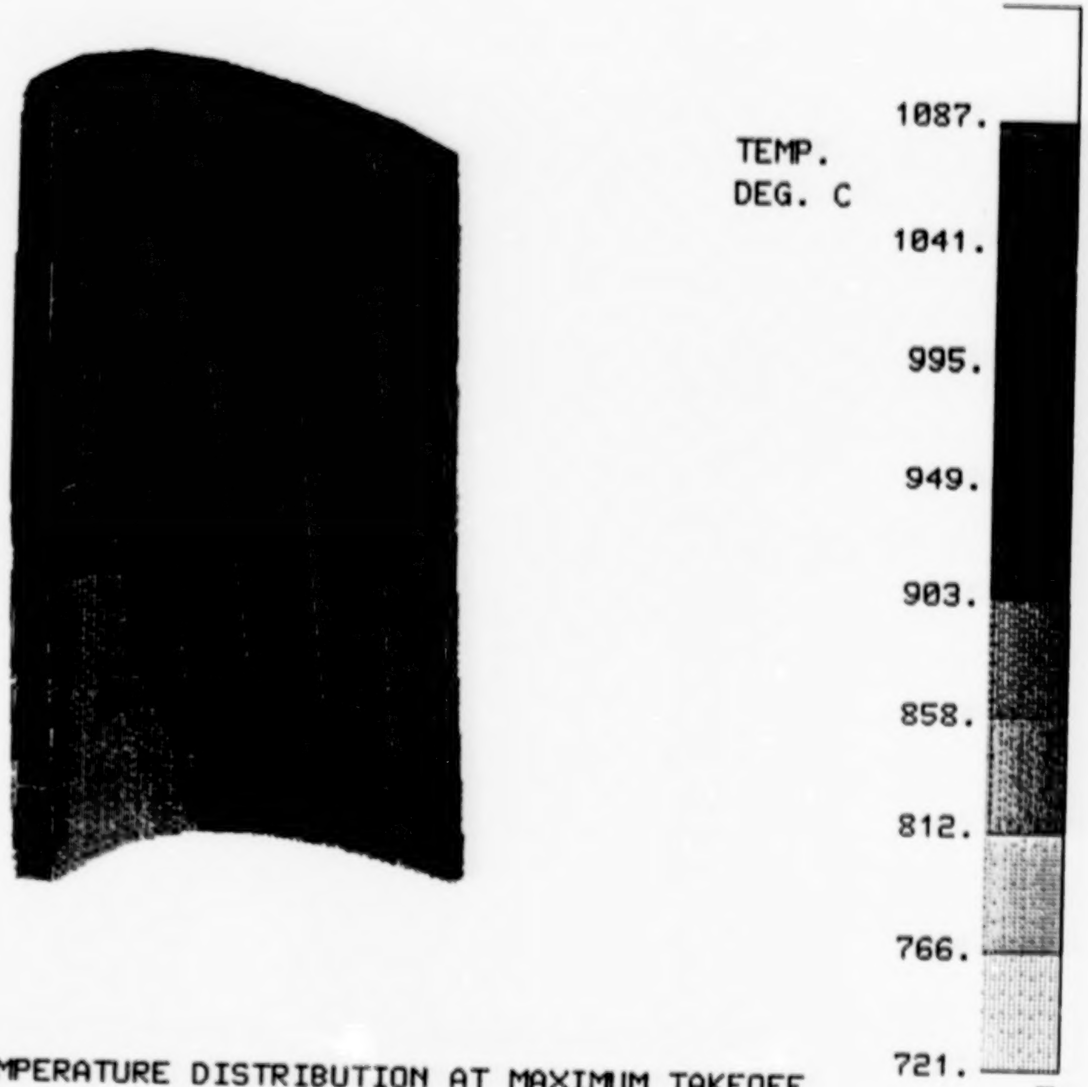

FIGURE 4. - AIRFOIL TEMPERATURE DISTRIBUTION AT MAXIMUM TAKEOFF

ORIGINAL PAGE IS
OF POOR QUALITY

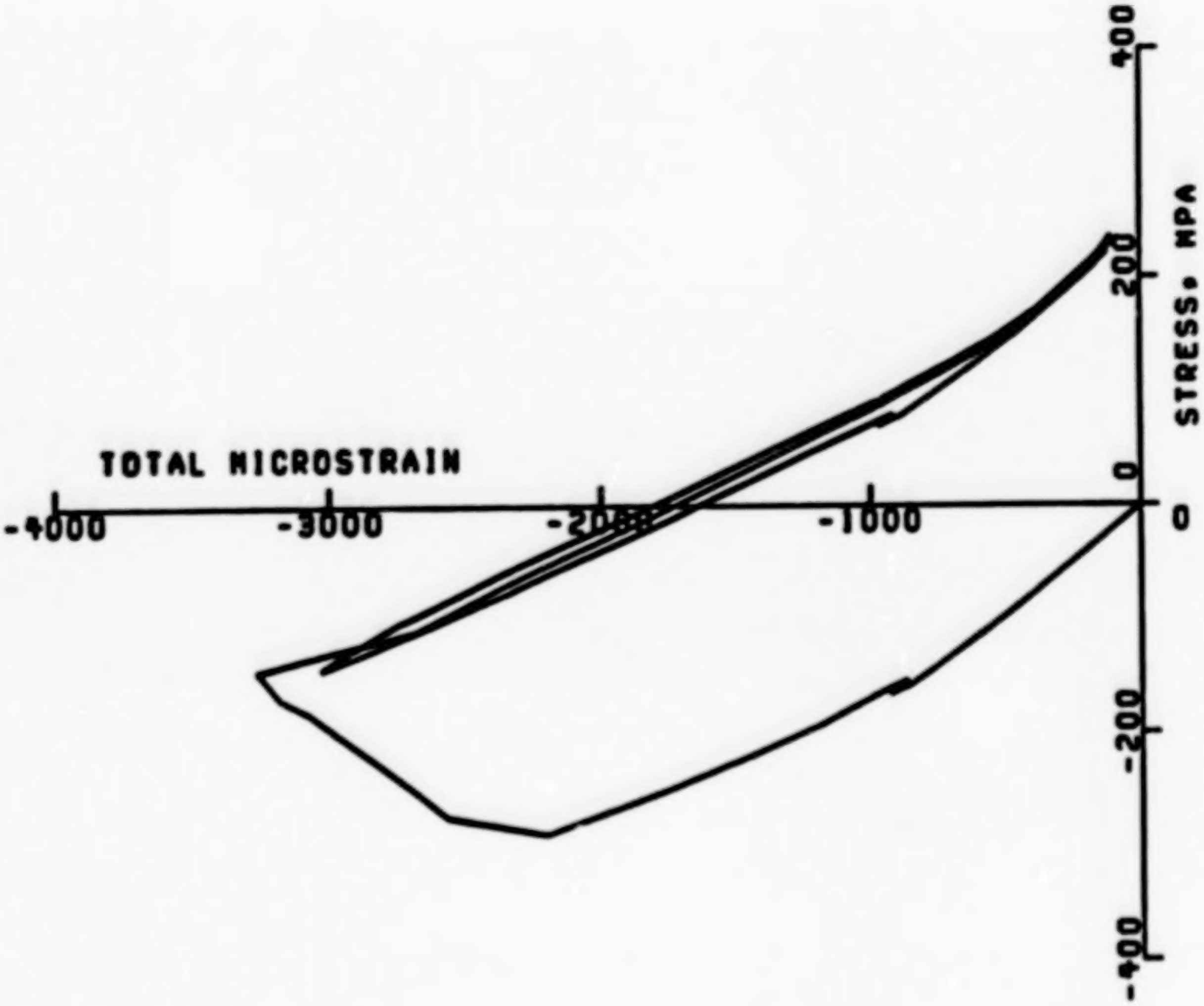

FIGURE 5. - MARC FINITE-ELEMENT ANALYSIS STRESS-STRAIN CYCLE USING CLASSICAL CREEP-PLASTICITY MODELS

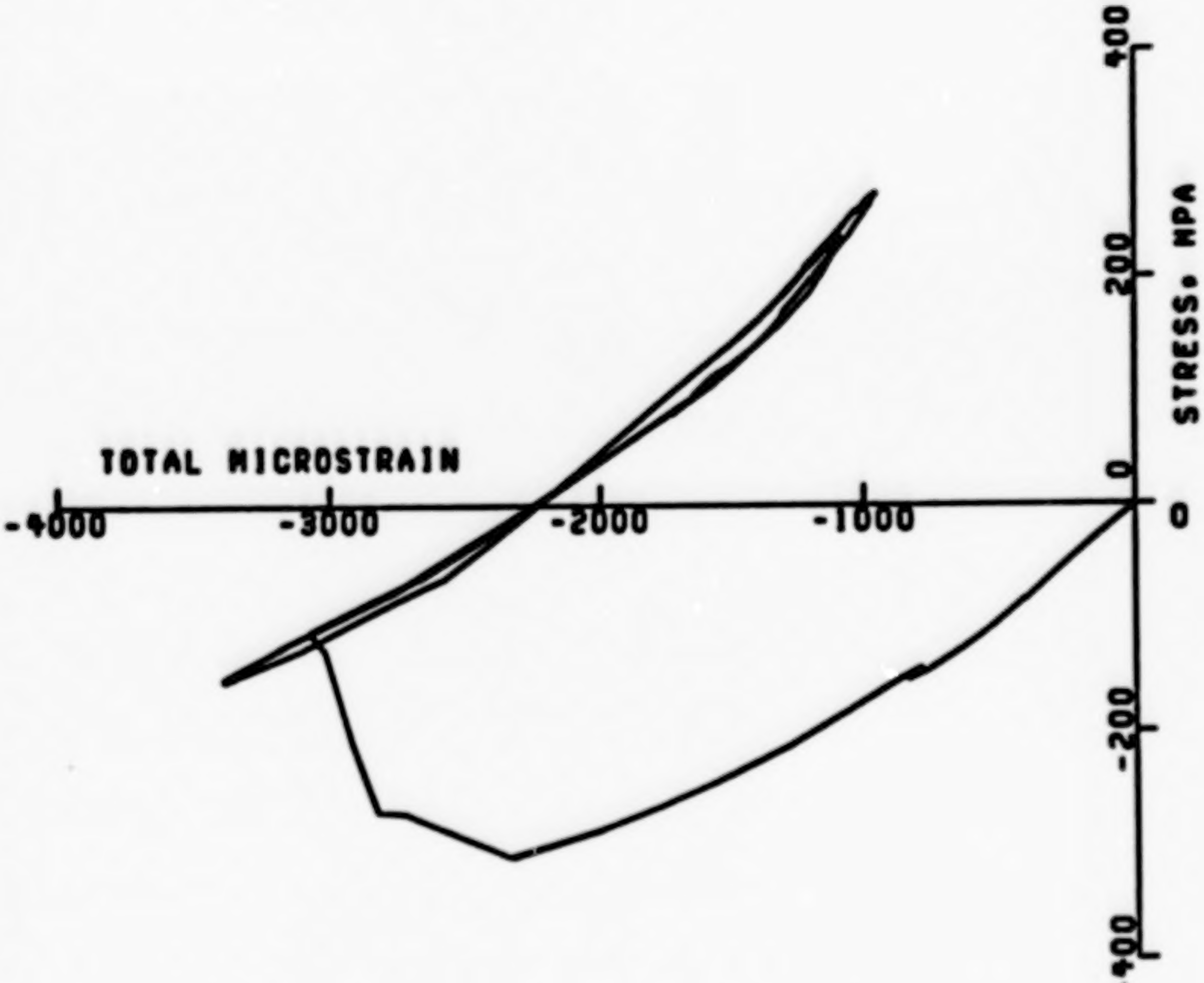

FIGURE 6. - MARC FINITE-ELEMENT ANALYSIS STRESS-STRAIN CYCLE USING BODNER UNIFIED MODEL

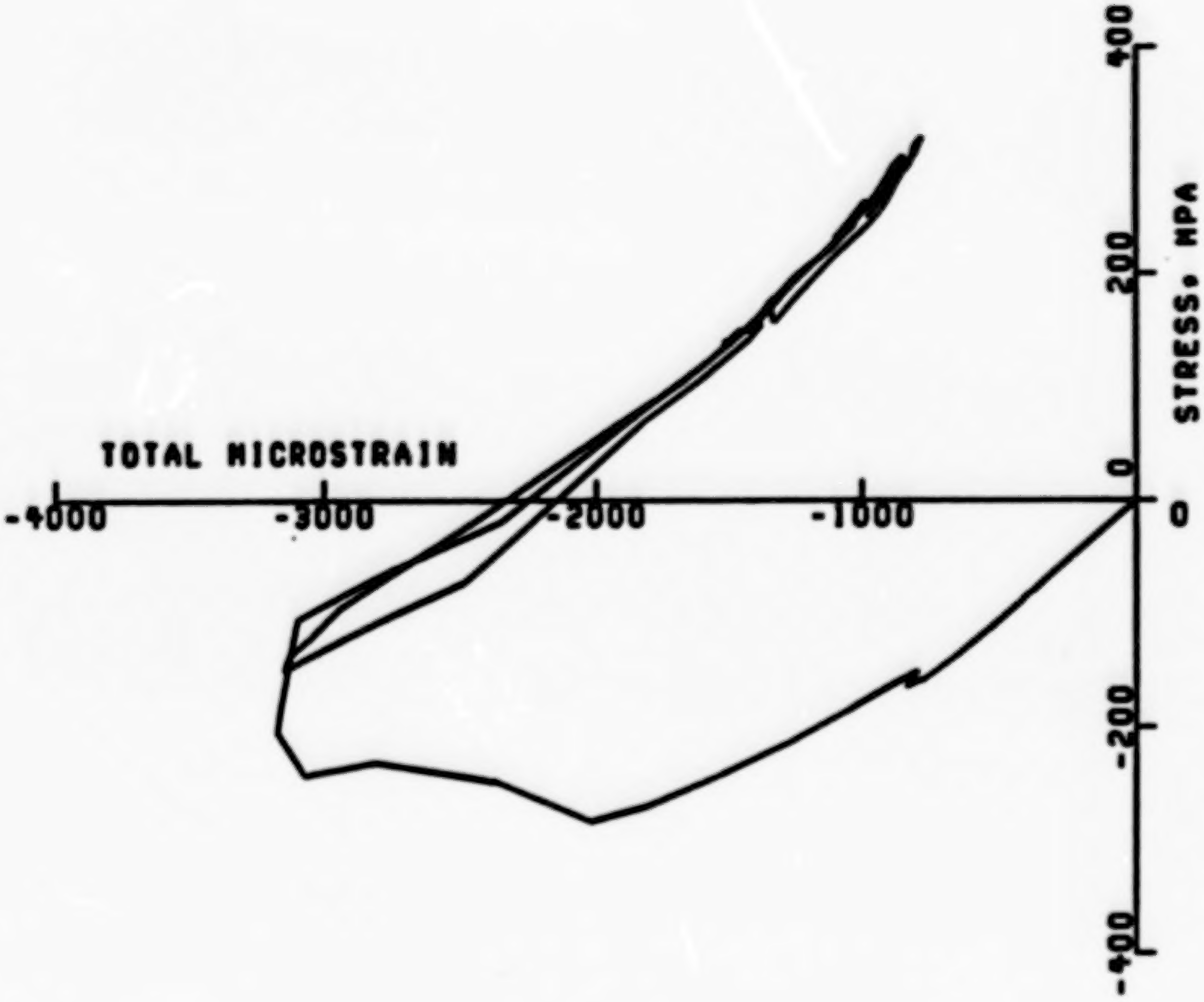

FIGURE 7. - MARC FINITE-ELEMENT ANALYSIS STRESS-STRAIN CYCLE USING WALKER UNIFIED MODEL

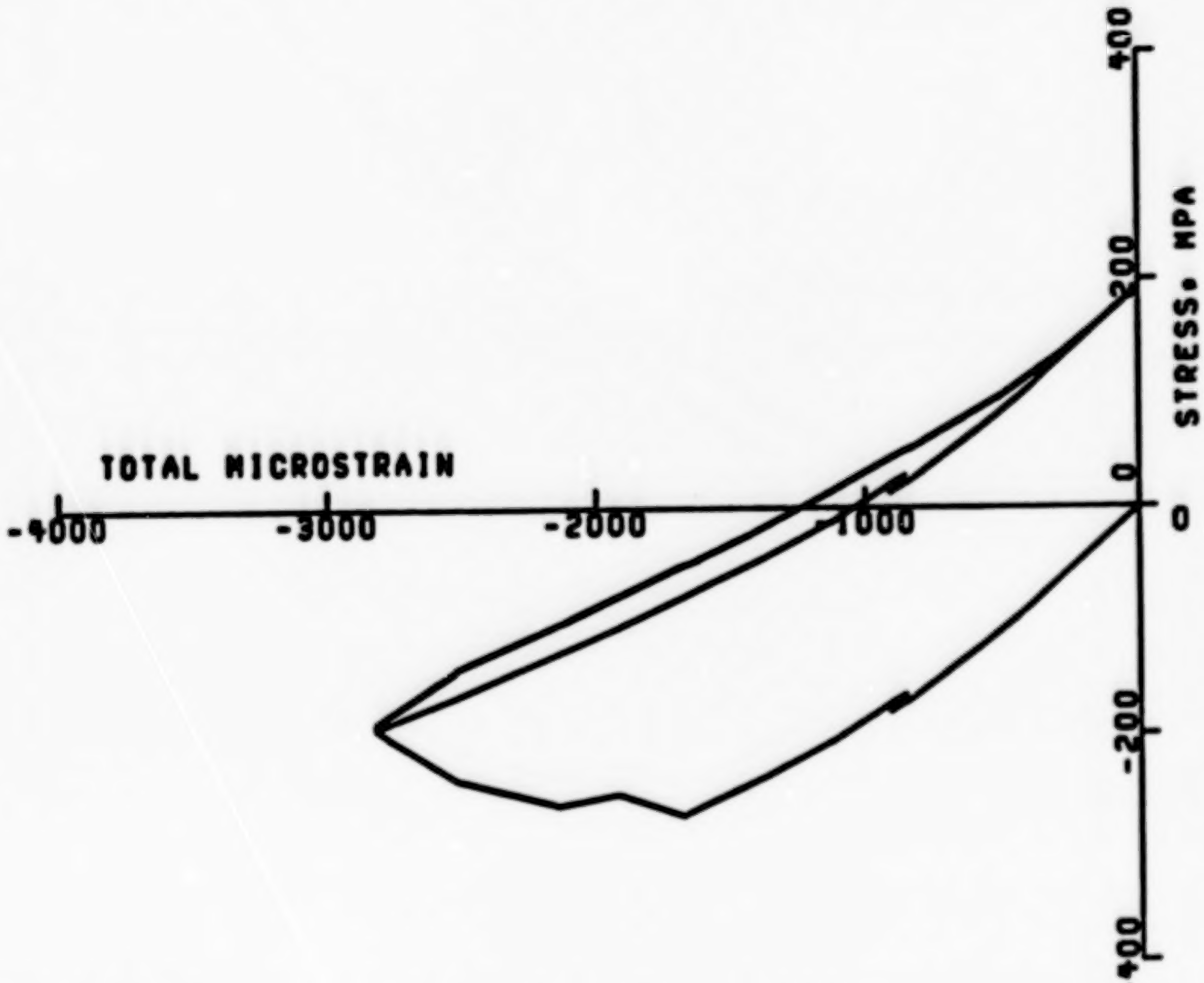

FIGURE 8. - SIMPLIFIED ANALYSIS STRESS-STRAIN CYCLE

DATA REQUIREMENTS TO MODEL CREEP IN 9CR-1MO-V STEEL *

R. W. Swindeman
Metals and Ceramics Division
Oak Ridge National Laboratory
Oak Ridge, Tennessee 37831

Models for creep behavior are helpful in predicting response of components experiencing stress redistributions due to cyclic loads, and often the analyst would like information that correlates strain rate with history assuming simple hardening rules such as those based on time or strain. On the other hand, much progress has been made in the development of unified constitutive equations that include both hardening and softening through the introduction of state variables whose evolutions are history dependent. Although it is difficult to estimate specific data requirements for general application, there are several simple measurements that can be made in the course of creep testing and results reported in data bases. The issue is whether or not such data could be helpful in developing unified equations, and, if so, how should such data be reported. Data produced on a martensitic 9Cr-1Mo-V-Nb steel were examined with these issues in mind.

---

*Research sponsored by the U. S. Department of Energy, AR&TD Fossil Energy Materials Program under contract no. DE-AC05-84OR21400 with Martin Marietta Energy Systems, Inc.

Approximately 40 creep tests were performed on the steel in the temperature range 475 to 650 C and for times to beyond 10,000 h. The initial creep rate, time to 0.2% creep strain, and minimum creep rate data were taken and used to examine two types of creep models. In the first model, strain hardening was assumed and the 0.2% creep data used to estimate the parameters for a simple Norton-Bailey power law creep equation. In the second model, the initial and minimum creep rate data were used to estimate the evolution of a kinematic state variable that reduces the effective stress included in a simple power law creep equation. In addition to the above data, more than 100 creep rate data from stress and temperature change tests were obtained and examined in connection with the expectations of the two deformation models.

An example of the creep response to changing stresses in a test lasting 13,000 h is shown in Fig. 1. Here the stresses ranged from 0 to 241 MPa at 500 C, and creep response included both softening and hardening features. Analysis of these and other data are shown in Fig. 2 which compares the creep rates from constant and variable stress-temperature conditions with the rates calculated from a simple strain hardening rule and creep law. Data and calculations agree within reasonable bounds, although there is some tendency for the rates to be greater than expected. These comparisons do not include results from short-time transients. In such situations the strain hardening model was found to underestimate creep rates for stress increases and overestimate creep rates for stress decreases.

In the unified equation, the creep rate was assumed to be proportional to the function $(S-\alpha)^n$, where α may be a kinematic state variable (called the "back stress"), as many other investigators have postulated. The choice of 4 for the stress exponent is quite common in the literature, and the proportionality factor may be written as A(T)/D, where A(T) is some function of temperature and D is either constant or slowly changing as a result of the metallurgical aging produced by time-temperature-strain exposure. Assuming that α is initially 0 and that D does not change permits the use of the initial creep rate data to calculate α for any condition where the instantaneous creep rate is known. Fig. 3 shows a comparison of the calculated α against the applied stress for the minimum creep rate condition. The calculated values are proportional to stress at low stresses but approach a maximum that depends on the testing temperature. Calculations of the hardening and recovery parameters in the Orowan-Bailey growth law for α requires more data, however. Here the rate of change in α is given by the difference $H\dot{e}-\mathrm{R}\alpha$, where H is a hardening term, $\dot{e}$ is creep rate, and R is the recovery term. Examples of H and R obtained from the creep tests are shown in Figs. 4 and 5.

Stress change data at various stages of creep are needed to determine whether or not it is necessary to evaluate changes in D. If the α calculated from the initial creep rate and the minimum creep rate does not agree with the α determined from a recovery creep experiment, then either the model is totally wrong or D is changing. The latter situation seems to be the case for the 9Cr-1Mo-V-Nb steel. Either way, the data base needed to fully develop unified equations from creep tests is fairly substantial. It may be easier to least squares fit entire data sets together rather than to correlate parameters from individual tests and restructure a model from the these elements.

ORIGINAL PAGE IS
OF POOR QUALITY

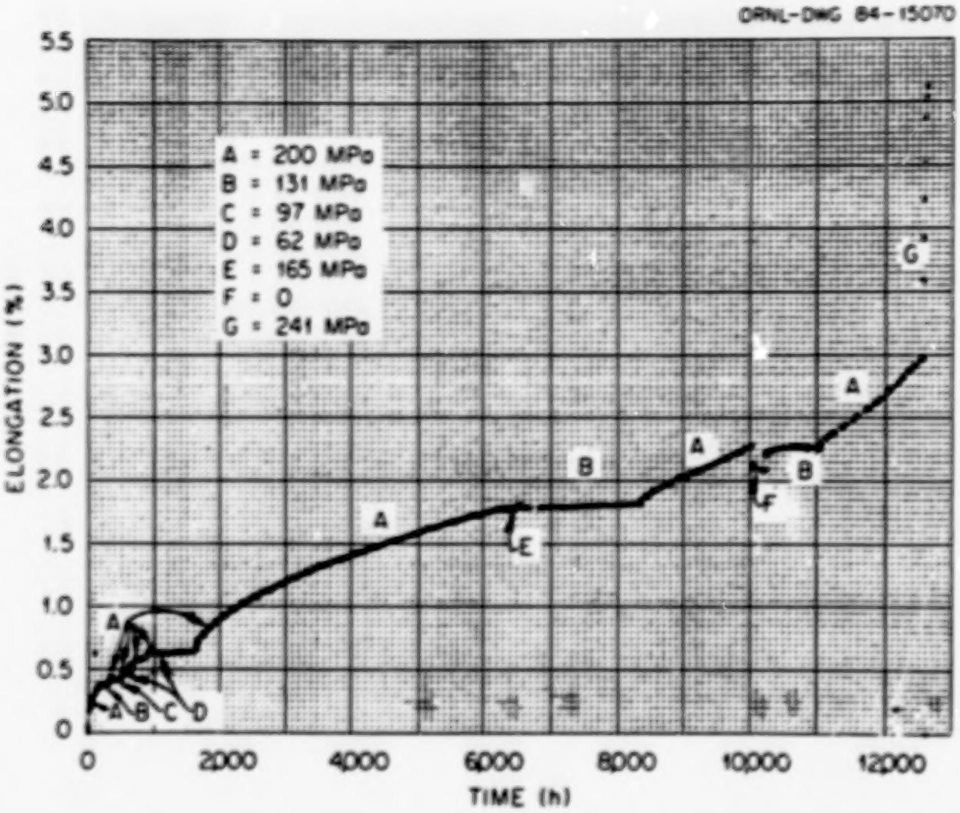

Fig. 1. Creep response of 9Cr-1Mo-V-Nb steel during stress changes at 550 C.

ORIGINAL PAGE IS
OF POOR QUALITY

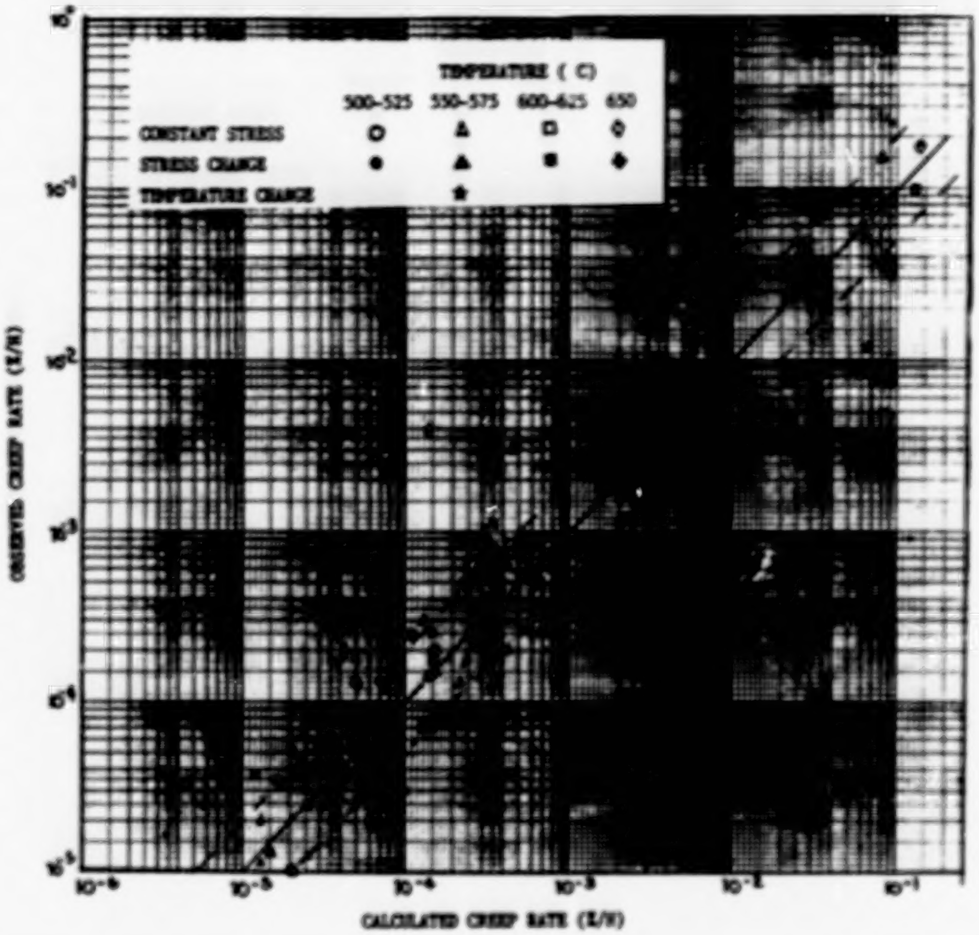

Fig. 2. Comparison of calculated and observed creep rate data produced from constant, variable stress, and variable temperature testing.

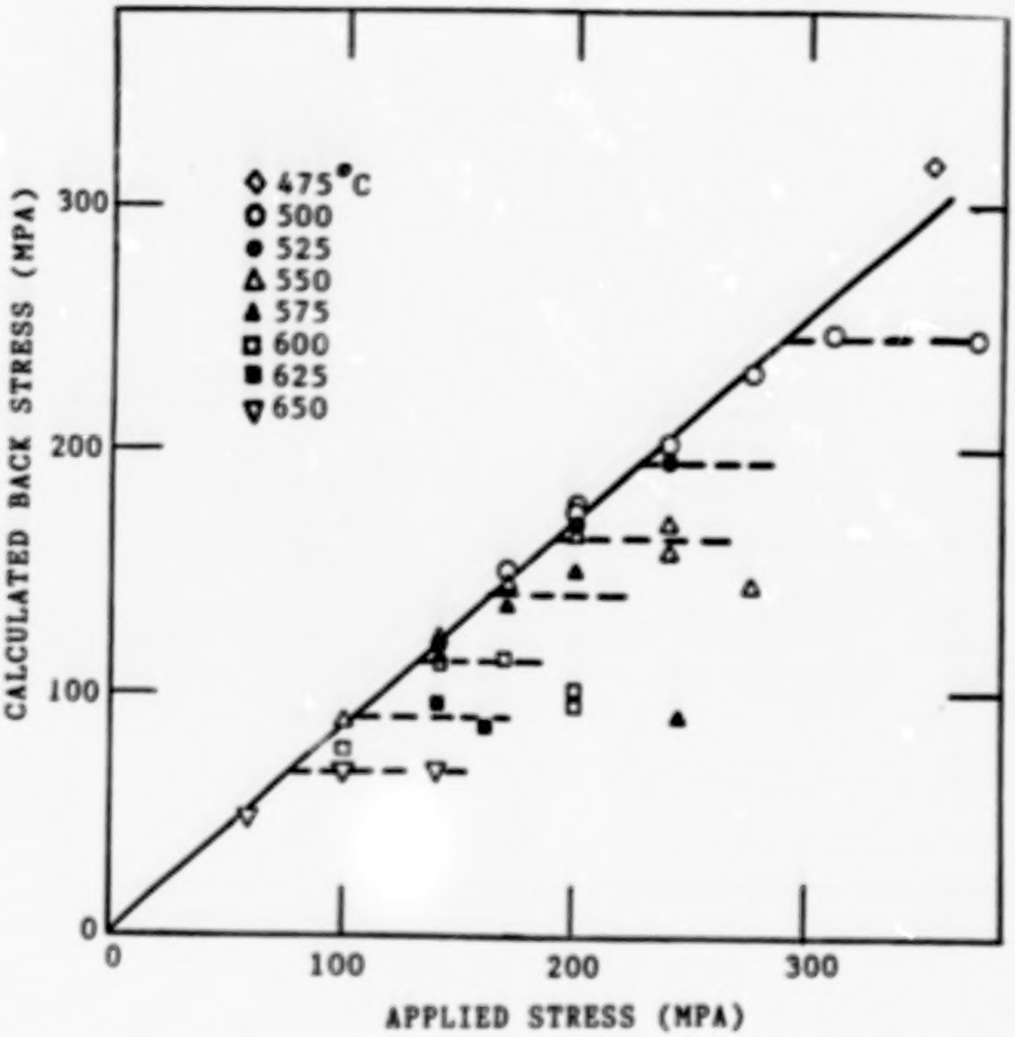

Fig. 3. Calculated back stress versus applied stress.

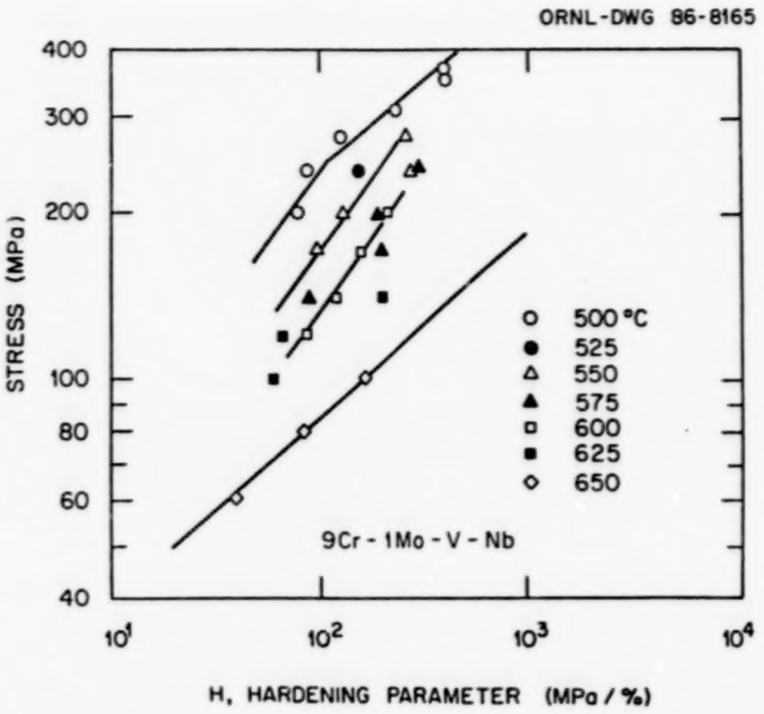

Fig. 4. Log stress versus log of the calculated hardening parameter of the Orowan-Bailey equation.

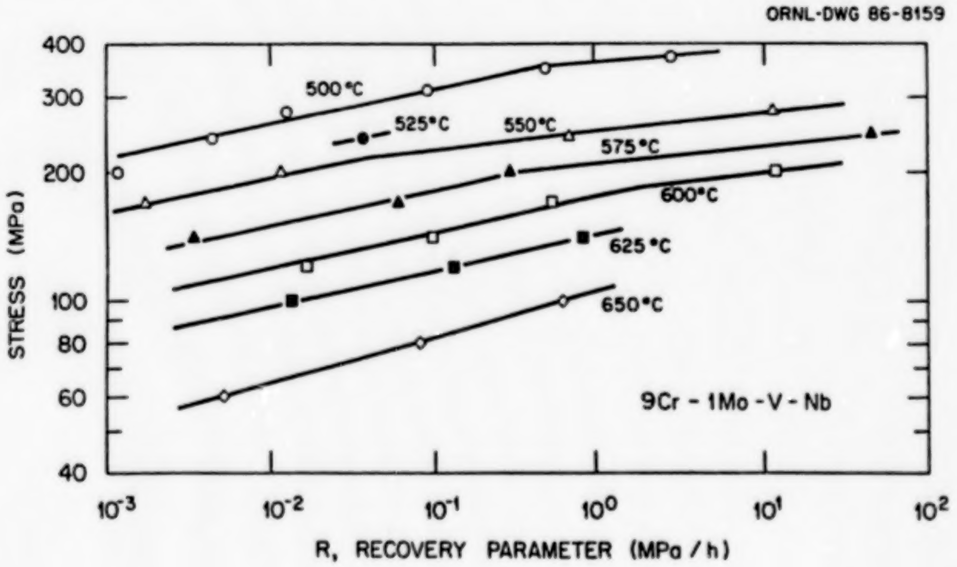

Fig. 5. Log stress versus the log of the calculated recovery parameter of the Orowan-Bailey equation.

N88
21513
UNCLAS

N88-21513

CONTROLLED-STRAIN RATE TESTS AT VERY LOW STRAIN RATES OF 2618 ALUMINUM AT 200°C

J.L. Ding, S.R. Lee
Department of Mechanical Engineering
Washington State University
Pullman, Washington 99164-2920

Constant strain rate tests and constant load creep tests were performed on 2618 aluminum at 200°C. The strain rates used in the constant strain rate tests were 10^{-6}, 10^{-7}, 10^{-8}, and 10^{-9}/sec. Due to the fact that the strain rates in both tests were comparable to each other, the similarities between them can therefore be studied.

It was concluded that metals are essentially rate sensitive at elevated temperatures. The traditional definition of creep and plasticity used in the classical creep analysis is actually a reflection of the material behavior under different loading conditions. A constitutive equation based on the test data under one loading condition should work well for other loading conditions as long as the strain rates are in the same range as those under which the material constants are determined.

PRECEDING PAGE BLANK NOT FILMED

Introduction

Classically the constitutive equations used in the design of components of fast breeder reactor (FBR) or pressure vessels are mostly based on the idea that the total strain can be decomposed into elastic strain, plastic strain, creep strain, and thermal strain (1). The elastic strain and the plastic strain are defined as the instantaneous response to stress change which is time-independent, while the creep strain is defined as the time-dependent strain under constant load. The constitutive equations for the plastic strain component are based on the classical rate-independent plasticity theory in which the concept of yield surface plays a very important role; and those for the creep strain component are generally based on strain-hardening viscous flow rule which, in most of the cases, needs to be modified in order to incorporate the anisotropy induced by deformation (2). Since the inelastic strain is decomposed into plastic strain and creep strain, there have also been some followup studies on the interaction between creep and plasticity (3).

The new trend in modelling the inelastic material behavior, however, is toward a unified approach in which the traditional creep and plasticity are treated by a unified equation. This approach is reasonable based on the fact that both creep strain and plastic strain are contributed mainly by the same deformation mechanism, i.e., dislocation motion. On the other hand, the way to distinguish creep strain from plastic strain in the traditional approach is also somewhat too arbitrary. It is actually based on the way the material is tested. For example, in the study of creep-plasticity interaction, the material testing usually started with a constant strain rate loading followed by a period of constant-load loading, or vice versa. The inelatic strain accumulated during constant strain rate loading is considered as plastic strain, while the strain accumulated during the constant load period is treated as creep strain. This definition probably follows the tradition that plasticity is usually studied with constant strain rate tests, while creep is studied with the constant load test.

In the current study, both constant strain-rate tests and creep tests were performed on 2618 aluminum alloy. The strain rates adopted were in the range from 10^{-9}/sec to 10^{-6}/sec. The similarities between these two tests were investigated. The purposes of this study are:

1) To justify the unified theory for creep and plasticity.
2) To study the concept of creep-plasticity interaction.
3) To compare the steady state response of engineering materials under constant-strain rate loadings with that under constant-load loadings.

In addition, one test under combined tension and torsion loadings was also performed to study the effects of shear stress on the axial stress-strain relation at constant strain rate.

Material and Specimen

The material employed in the present work was aluminum forging alloy 2618-T61 which was the same kind of material as that used in previous work (4-7), but obtained three years later from the same source, probably from a different batch. The heat treatment was carried out at different place too. Some variations in the mechanical properties were found between these two batches. However, since previous work were not referred in the current study, these variations may be disregarded.

Specimens were thin-walled tubes of circular cross section. The nominal outside diameter, wall thickness, and gage length were 25.4, 1.5, and 101.6 mm respectively.

Experimental Apparatus

All the tests were performed with a combined tension and torsion creep machine whose details can be found in the paper by Findley and Gjelsvik (8). The relative axial displacement between the gage points was measured by a matched pair of linear variable differential transformers (LVDT) using an AC-null balance system. One LVDT was attached to the gage points through four invar rods and the other (reference LVDT) was connected to a micrometer. Before the test, the outputs of these two LVDT's cancelled each other, i.e., balanced. During the test some imbalance was induced, due to the relative displacement between the gage points, which would be balanced out again with the reference LVDT by turning the micrometer. The relative displacement could then be read from the micrometer.

In order to use the current machine to perform controlled strain-rate tests, some modificiations were necessary. The desired strain rates were obtained by use of several AC reversible synchronous motors to drive the reference LVDT at specified speeds and an servohydraulic system to apply the load in such a way that the output from the LVDT attached to the specimen always matches with that of the reference LVDT, i.e., the specimen is stretched at a speed determined by the motor. Unlike the tests done in a conventional tensile testing machine with constant "crosshead" speed, the current tests are truly strain rate controlled tests because the servo-hydraulic system is driven directly by the output from the extensometer.

The specimen was heated internally by a quartz-tube, radiant heating lamp and externally by two resistance heaters at the ends just outside the gage length. The lamp and the end heaters were controlled separately by two sets of Research Incorporated temperature controller and power controller. The test temperature was 200°C. Prior to testing, the specimen was soaked at the testing temperature for approximately 18 hours. The details of the choice of 18 hours as the soaking time can be found in the paper by Ding and Findley (7).

Experimental Results

The experimental results are shown in the attached figures. In figure 1(b) the solid line is the test data on the stress-strain relation for a controlled-strain-rate test under stepwise increased strain rates, namely 1.04×10^{-8}/sec, 1.0×10^{-7}/sec, and 1.0×10^{-6}/sec followed by unloading at a strain rate of 1.04×10^{-8}/sec as shown in figure 1(a). Figure 2 is another controlled strain rate test under stepwise decreased strain rates. For both tests, a steady state can be found for each particular strain rate in which the stress remains constant. The steady state stress at each step in figure 1(b) is lower than that in the corresponding step with the same strain rate in figure 2(b), respectively. This may be due to the different strain histories and strain rate histories involved in these two tests. In figure 1(b), it can also be seen that the slope during unloading is higher than that during loading. This may be explained as follows: during loading, the time-dependent strain is developed in the same direction as the imposed strain rate direction, while during unloading, they are opposite to each other. Therefore, for the same imposed strain rate, less stress may be required during loading than during unloading. Similar observations can also be found in figure 7(b). However, loading and unloading were carried out at different strain rates in this test.

The creep test data under step loadings are shown in figure 3. The stress at each step was chosen the same as the steady state stress at the corresponding step in figure 1, namely, 172.5 MPa, 195 MPa, and 216 MPa, respectively. Similar to figure 1, a steady state was also found in each loading step. A comparison of the material responses between these two tests is shown in figure 4. The steady state responses at each step are quite close to each other. The deviation is within 10%. The major differences between these two tests seem mainly on the transient responses.

Shown in figure 5 are the test results of axial loading at constant strain rate combined with stepwise varied torsional loadings. The effect of shear stress on the ongoing axial material response to a constant-strain-rate loading can be clearly seen. It is quite interesting to notice that the combination of axial stress and shear stress at new steady state for steps 2, 3, and 4 satisfy the Tresca relation, i.e, $\sigma^2 + 4\tau^2 = \text{constant}$, as shown in figure 5(c). However, the implication of this relation is not quite clear in this case. From figure 5(b), it can also be seen that the steady state axial stress in the later stage, i.e., when the shear stress is completely released, is lower than the initial steady state stress before the shear stress was applied. Similar observations can also be found for the two steps with the same shear stress, namely 55.6 MPa. This may indicate that some kind of softening may have occurred.

Discussion of the Experimental Results

In figure 6, the stress-strain curves at different strain rates discussed earlier were put together. As shown in this figure, a distinguishable elastic region can be found for each curve. The point at which the curve starts to deviate from the straight line may be defined as the so-called yield stress and the dependence of the yield stress on strain rate may be interpreted as the rate-sensitive yielding in the theory of viscoplasticity. From these results, the first conclusion we may draw is that the yield stress is not a well-defined term at high temperature due to its dependence on the loading condition. In other words, yield stress is not a material property. The applicability of classicial rate-independent plasticity theory, in which the concept of yield stress is essential, to describe the deformation at high temperature is therefore questionable.

Secondly, following the proposal by Rice (9), the above rate-sensitive yielding can actually be interpreted as a reflection of the role of the time-dependent strain (or creep strain). If the loading rate is high, the time-dependent strain does not have enough time to develop during loading, a well-defined elastic region may be found. When the loading rate gets lower, this elastic region should gradually diminish due to the involvement of the time-dependent strain. When the materials reach the steady state, the time-dependent strain rate at a particular stress level is fixed. In a constant strain rate test, when the stress is increased to a level in which the time-dependent strain rate is equal to the imposed strain rate, the stress will stay constant. At room temperature, the creep rate of most structural materials is so low that the stress-strain curve based on loading times of order of minutes does not differ significantly from those based on seconds, hours, or days. This may be considered as a limiting case for which the rate-independent plasticity theory could be applied.

Based on the above discussion, we may conclude that at high temperature, all the materials are essentially rate-sensitive, i.e., time-dependent. The traditional definition of plastic strain and creep strain at high temperature based on material testing only refers to different macroscopic material behavior under different loading conditions, i.e., constant strain rate loading versus constant load loading. The "instantaneous" response has no meaning unless the loading rate (or strain rate) is specified. Consequently, there seems no physical background to study the so-called creep-plasticity interaction. In fact, when the steady state is reached, both load and strain rate are constant. There is even no distinction between creep test and constant strain rate test any more.

Modeling of the Experimental Results

In the previous work (4-7), a viscous-viscoelastic model was developed to model the experimental results of creep under variable biaxial loadings. The material constants were determined by quite a few creep and creep recovery tests. As mentioned earlier, since there exist some variations in the mechanical properties between the specimens in the current study and those in previous work no attempts was made to use previous theoretical model to predict the current experimental results or to redetermine the material constants due to the limited amount of specimen. Instead, some other constitutive equations were considered.

Due to its simplicity, the constitutive equation proposed by Bodner (10) and Mertzer (11,12) were tried to model the current experimental results.

For uniaxial stress state, the constitutive equation can be stated as follows:

$$\dot{\epsilon}^P = \frac{2D_o}{\sqrt{3}} \left(\frac{\sigma}{|\sigma|}\right) \exp\left[-(1/2)(z^2/\sigma^2)^n\right] \qquad (1)$$

and

$$\dot{z} = m(z_1 - z)\sigma\dot{\epsilon}^P - A(z - z_o)^q \qquad (2)$$

where $\dot{\epsilon}^P$ is the inelastic strain rate, σ is the applied stress, z is a scalar state variable whose initial value and the saturation value are z_o and z_1 respectively, and is assumed to be a function of plastic work. D_o, n, m, A, q are the material constants. As shown in eqn. (2), the rate of change of $z(\dot{z})$ is governed by work-hardening, $m(z_1 - z)\ \sigma\dot{\epsilon}^P$, and softening due to thermal recovery, $A(z - z_o)^q$.

As shown in the paper by Merzer and Bodner (11), if neglecting the recovery term, the above constitutive equation can be integrated to get an explicit stress-plastic strain relation for the case when the plastic strain rate is constant. The assumption of constant plastic strain rate can actually be applied to the later stages of the three curves shown in figure 6 because the stress increment and thus the elastic strain increment, is almost zero.

By fitting the integrated equation to these three curves, the material parameters used in equations (1) and (2) can be determined for the current material. The values of these constants are: D_o: 10^{-4} $\sec^{-1}$; n: 0.79; m: 19.0 MPa^{-1}; z_o: 525 MPa; z_1: 1092 MPa. The theoretical results are shown in figures 1(b), 2(b), and 3(b) as dotted lines. Because equations (1) and (2) was for uniaxial stress state, no theoretical predictions was made for the data shown in figure 5.

Discussion of The Theoretical Model

The theoretical results shown in figures 1(b) and 2(b) showed some discrepancies with the experimental data. Furthermore, the predicted steady state stress at each step in figure 1(b) is almost the same as that at the corresponding step in figure 2(b) with the same imposed strain rate, respectively. This was found to be due to the fact that in both cases the scalar state variable z almost reached its saturation value z_1 at the end of the first step and stayed there for the whole test. With a constant value of z, a unique stress should of course be expected for a specified strain rate.

When equations (1) and (2) are applied to the creep test, figure 3, it can be seen that the general trend of the material behavior seems satisfactorily described especially for the transient response at the first loading step. The results could be improved by including the thermal recovery term which seems quite important in the low strain rate tests. However, the current experimental information is not enough for identifying this term.

Based on the above results, it seems reasonable to conclude that constitutive equations based on the data from constant strain rate material testing should be able to predict the material behavior in a constant load creep test or vice versa, i.e., a unified equation should work well for various kinds of loadings. However, there is one very important point which needs to be clarified here. In the current tests, all the constant strain rate tests were performed at the strain rates which are comparable to those during a constant load creep test, namely 10^{-9}/sec to 10^{-6}/sec. However, the strain rates usually used in the study of plasticity, e.g., creep-plasticity interaction, are in the range from 10^{-5}/sec to 10^{-2}/sec which are generally available in a commercial testing machine. In this case, the constitutive equation derived from the data from creep tests may not be able to predict the material behavior during a constant strain rate tests because of different ranges of strain rates involved. Therefore, it seems important to keep in mind that in order to develop a unified constitutive equation which can interpret the traditional creep-plasticity interaction, test data covering a wide range of strain rates seems necessary.

Conclusions

Metals are essentially rate sensitive at elevated temperatures. The traditional definition of creep and plasticity used in the classical creep analysis is actually a reflection of the material behavior under different loading conditions. A unified constitutive equation should work well for various kinds of loading conditions as long as the strain rates are comparable to each other.

Acknowledgement

This study was supported in part by funds provided by Washington State University and the National Science Foundation under Grant No. MEA-84029. The authors are grateful to Prof. W.N. Findley (Division of Engineering, Brown University) for helpful discussions. Thanks are also due to Ms. Jo Ann Rattey for typing the manuscript.

References

1. Pugh, C.E., "Progress in developing constitutive equations for inelastic analysis," J. of Pressure Vessel Tech., 105, 273-276, 1983.

2. Kraus, H., Creep Analysis, Wiley, New York, 1980.

3. Ohashi, Y., Kawai, M., and Shimizu, H., "Effects of prior creep on subsequent plasticity of Type 316 stainless steel at elevated temperature," ASME J. Eng. Mat'ls and Tech., 105, 257-273, 1983.

4. Ding, J.L. and Findley, W.N., 1984a, "48 Hour multiaxial creep and creep recovery of 2618 aluminum alloy at 200°C," ASME J. of Appl. Mech., 51, 125-132.

5. Ding, J.L. and Findley, W.N., 1984b, "Multiaxial creep of 2618 aluminum under proportional loading steps," ASME J. Appl. Mech., 51, 133-140.

6. Ding, J.L. and Findley, W.N., 1985, "Nonproportional loading steps in multiaxial creep of 2618 aluminum," ASME J. of Appl. Mech., 52, 621-628.

7. Ding, J.L. and Findley, W.N., 1986, "Simultaneous and mixed stress relaxation in tension and creep in torsion of 2618 aluminum," ASME J. Appl. Mech. (to appear).

8. Findley, W.N. and Gjelsvik, A., "A biaxial testing machine for plasticity, creep or relaxation under variable principal stress ratios," Proceedings, ASTM, 62, 1103-1118, 1962.

9. Rice, J.R., "on the structure of stress-strain relations for time-dependent plastic deformation in metals," ASME J. Appl. Mech., 728-737, 1970.

10. Bodner, S.R. and Partom, Y., "Constitutive equations for elastic-viscoplastic strain hardening materials," ASME J. Appl. Mech., 42, 385-389.

11. Merzer, A.M. and Bodner, S.R., "Analytical formulation of a rate and temperature dependent stress-strain relation," ASME J. of Eng. Mat'l Tech., 101, 254-257.

12. Merzer, A.M., "Steady and transient creep behavior based on unified constitutive equations," ASME J. of Eng. Mat'l Tech., 104, 18-25.

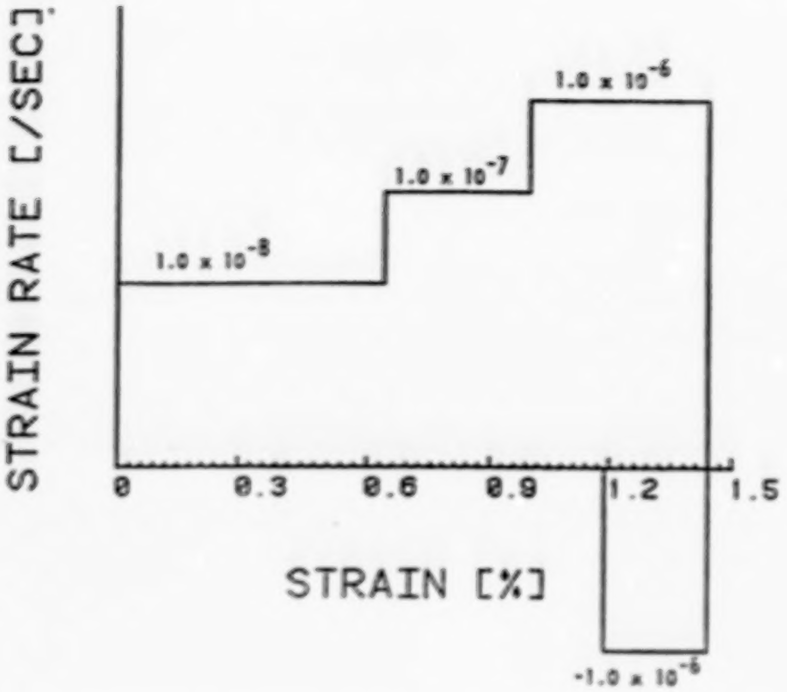

Figure 1(a): Loading program for a controlled strain rate test under stepwise increased strain rates.

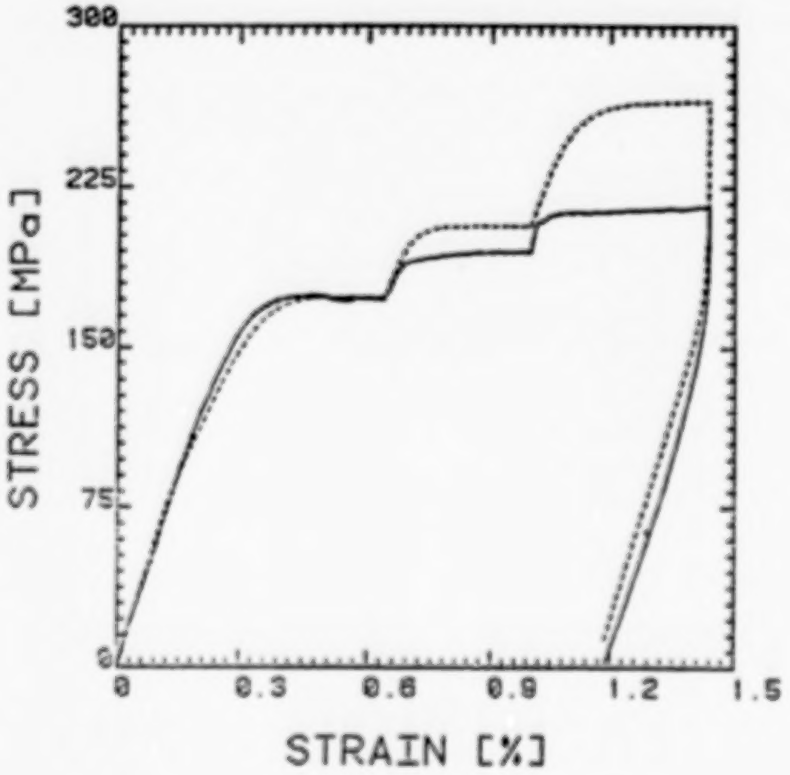

Figure 1(b): Experimental (solid lines) and theoretical (dotted lines) results for the loading program shown in figure 1(a).

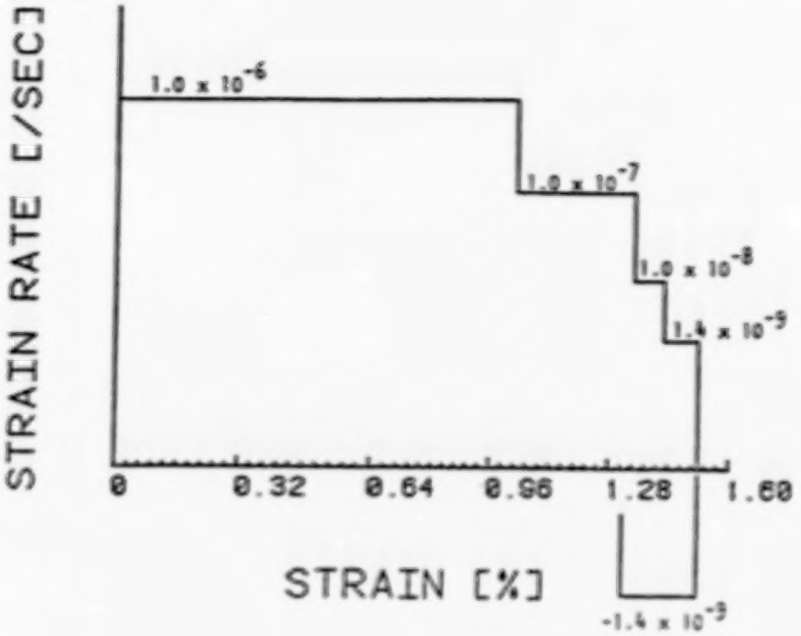

Figure 2(a): Loading program for a controlled strain rate test under stepwise decreased strain rates.

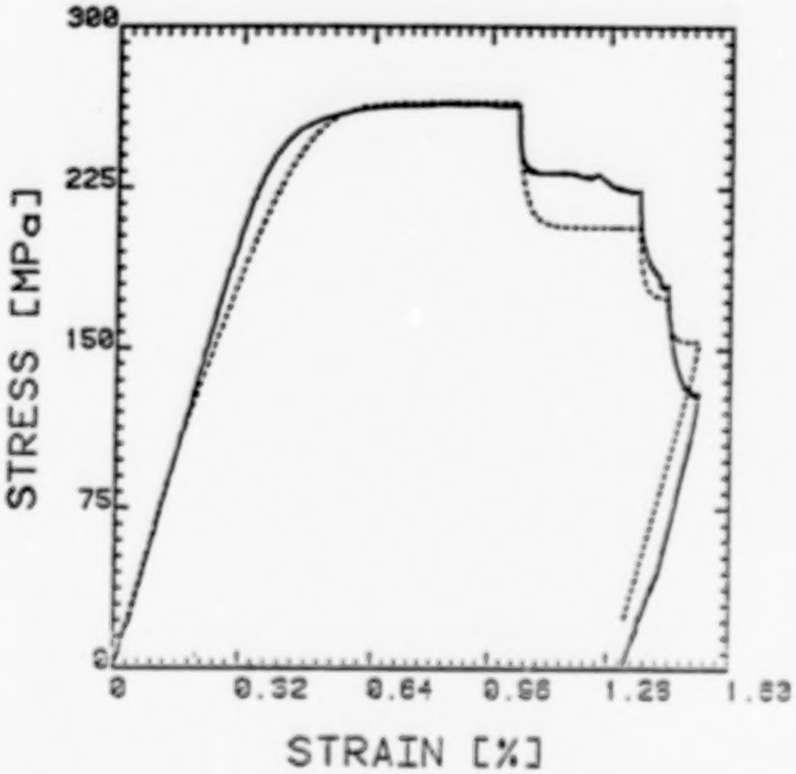

Figure 2(b): Experimental (solid lines) and theoretical (dotted lines) results for the loading program shown in figure 2(a).

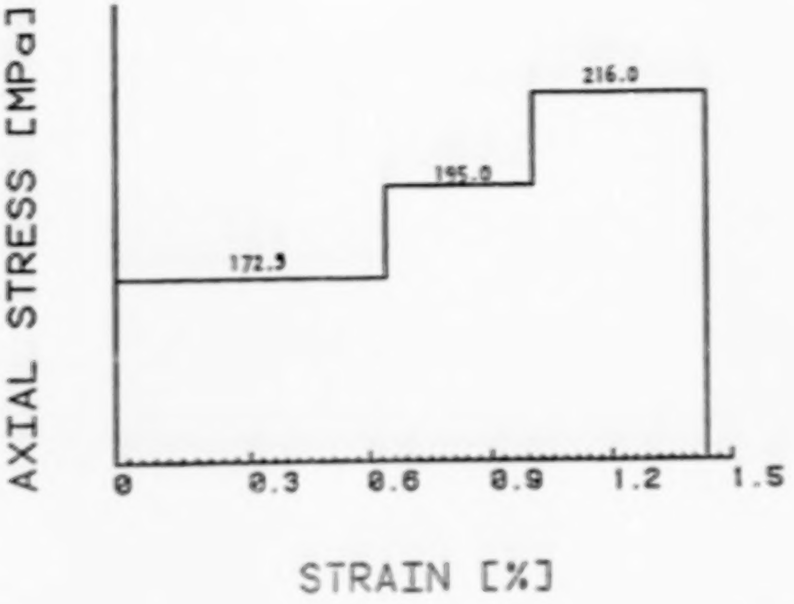

Figure 3(a): Loading program for a creep test under stepwise increased stresses. The stress at each step is equal to the steady state stress at the corresponding step in figure 1(b), respectively.

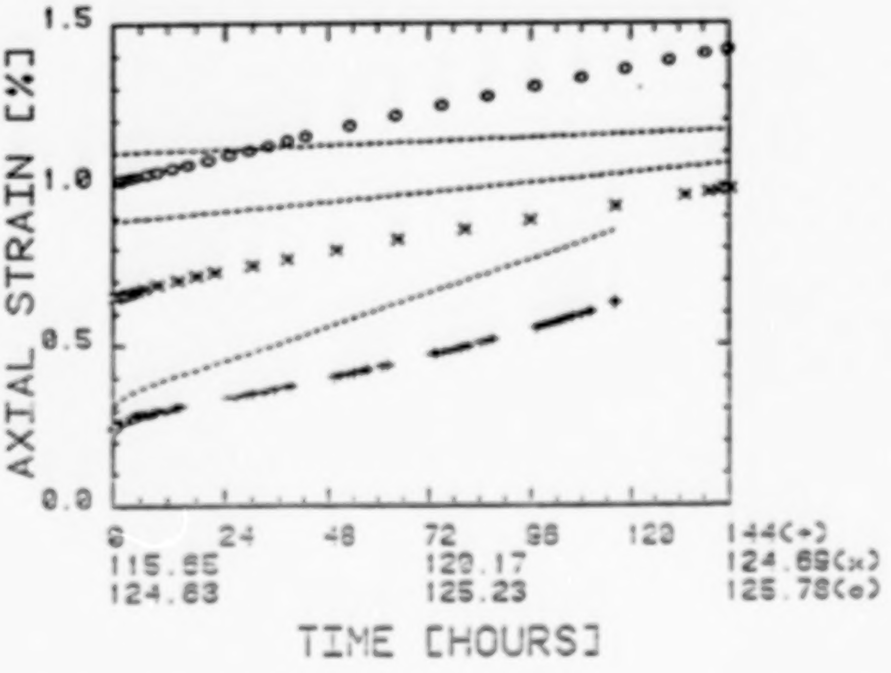

Figure 3(b): Experimental (solid lines) and theoretical (dotted lines) results for the loading program shown in figure 3(a). Notice that different time scales were used for each step.

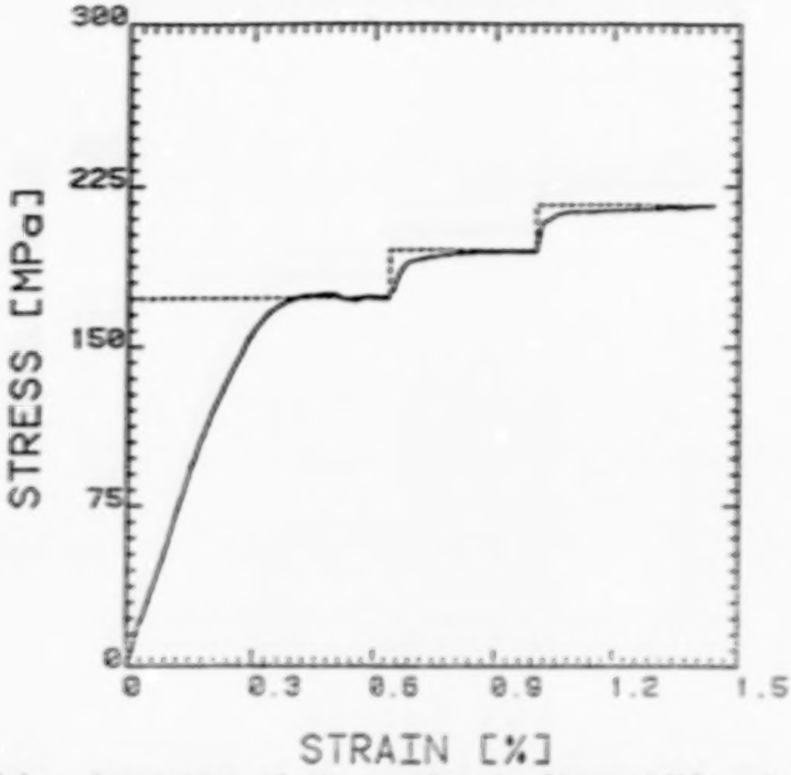

Figure 4(a): Comparison of the results in figure 1(b) and figure 3(a) in terms of stress and strain. Solid lines are the results of constant strain rate test, while dotted lines are the loading program for creep test.

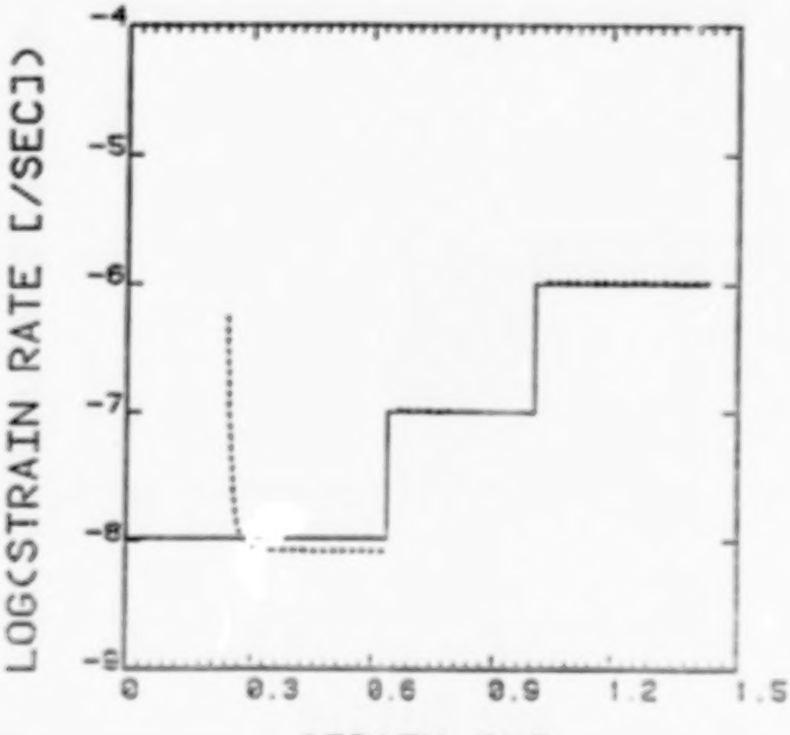

Figure 4(b): Comparison of the results in figure 1(a) and figure 3(b) in terms of strain rate and strain. Solid lines are the loading program for constant strain rate tests, while dashed lines are the results of creep tests.

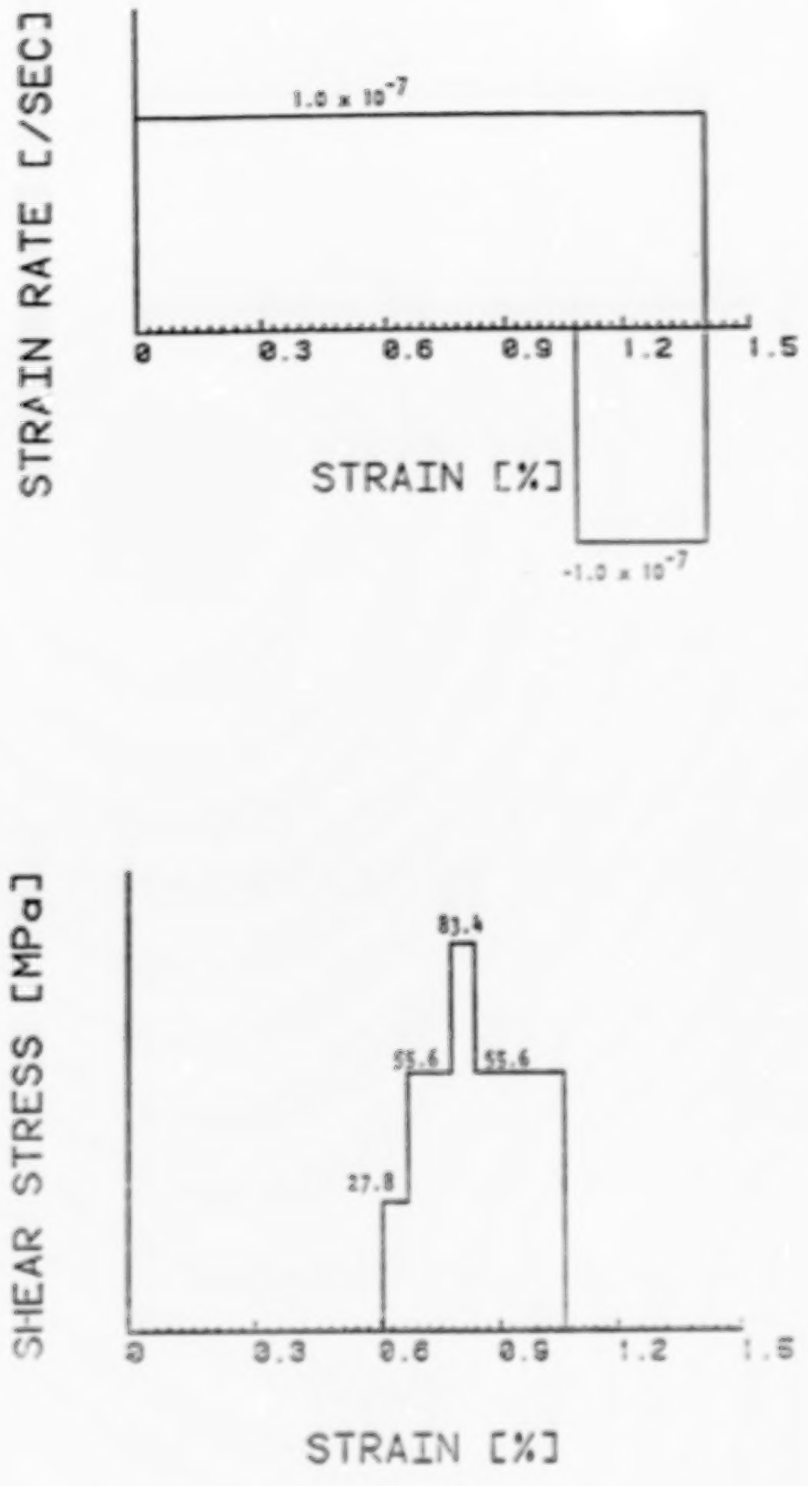

Figure 5(a): Loading program for a test under constant-strain-rate axial loading combined with stepwise varied torsional loadings.

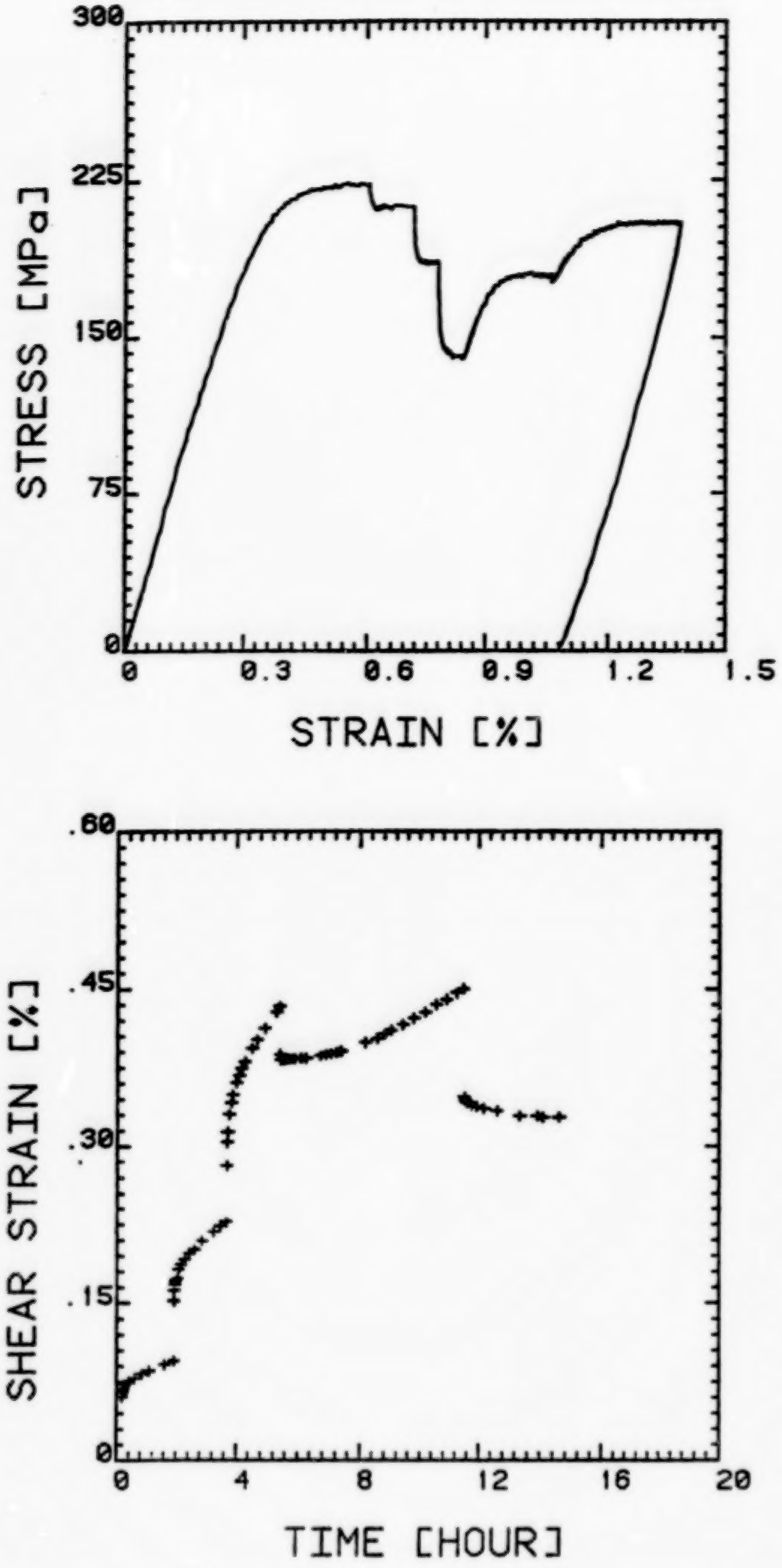

Figure 5(b): Experimental results for the loading programs shown in figure 5(a).

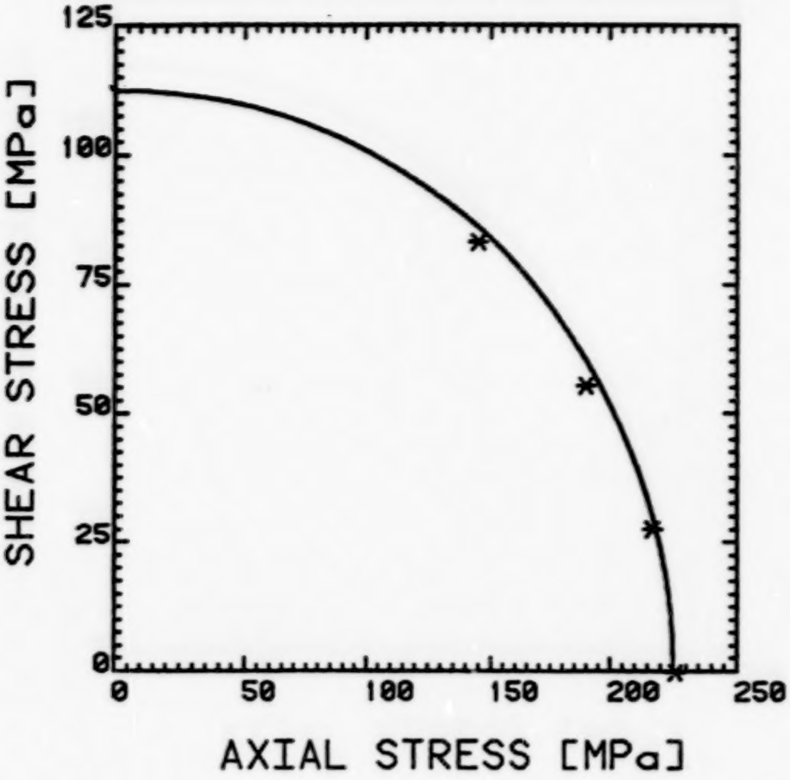

Figure 5(c): Stresses at steady states for steps 2, 3, and 4 shown in a two-dimensional stress space. The solid line is the Tresca curve.

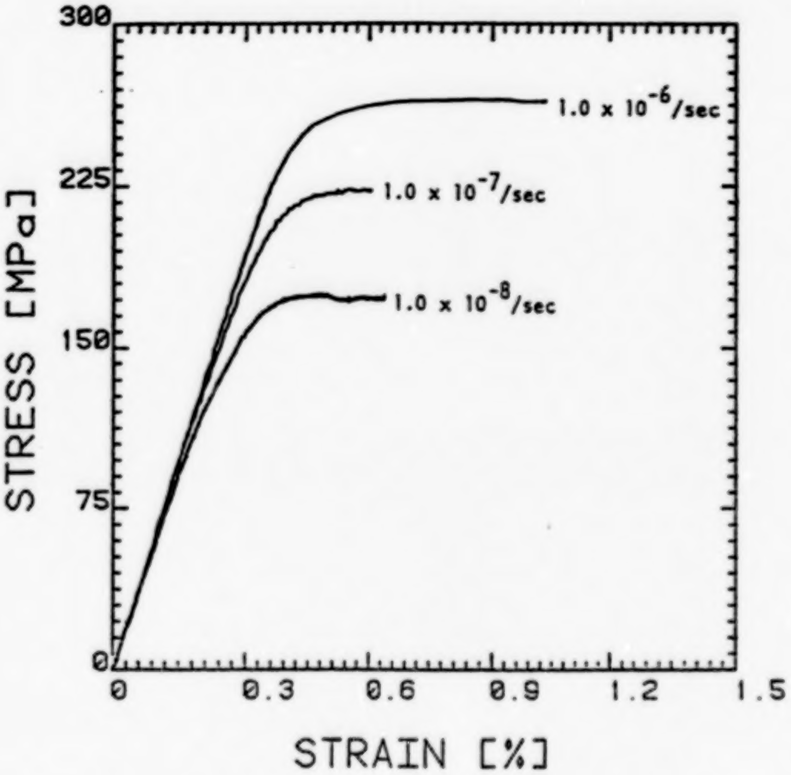

Figure 6: Stress-strain relations at different strain rates.

N88
21514
UNCLAS

N88-21514

CYCLIC UNIAXIAL AND BIAXIAL HARDENING OF TYPE 304 STAINLESS STEEL MODELED BY THE VISCOPLASTICITY THEORY BASED ON OVERSTRESS

David Yao and Erhard Krempl
Department of Mechanical Engineering,
Aeronautical Engineering & Mechanics
Rensselaer Polytechnic Institute
Troy, NY 12180-3590

The isotropic theory of viscoplasticity based on overstress does not use a yield surface or a loading and unloading criterion. The inelastic strain rate depends on overstress, the difference between the stress and the equilibrium stress, and is assumed to be rate-dependent. Special attention is paid to the modeling of elastic regions.

For the modeling of cyclic hardening, such as observed in annealed Type 304 Stainless Steel, an additional growth law for a scalar quantity which represents the rate-independent asymptotic value of the equilibrium stress is added. It is made to increase with inelastic deformation using a new scalar measure which differentiates between nonproportional and proportional loading.

The theory is applied to correlate uniaxial data under two-step amplitude loading including the effect of further hardening at the high amplitude and proportional and nonproportional cyclic loadings. Results are compared with corresponding experiments.

INTRODUCTION

For the modeling of the rate(time)-dependent, cyclic neutral, inelastic deformation behavior of metals, the theory of viscoplasticity based on overstress (VBO) with a differential growth law for the equilibrium stress was proposed [1]. When compared with biaxial experiments it was shown to predict the room temperature deformation behavior of an Aluminum alloy under both monotonic and cyclic proportional and nonproportional loadings [2].

Some alloys such as annealed copper [3], Type 304 Stainless Steel [4,5] and 316L Stainless Steel [6,7] exhibit complicated cyclic hardening phenomena. For their modeling an additional growth law for a scalar quantity is introduced in VBO. Its growth with inelastic deformation is governed by a new scalar measure which differentiates between proportional and nonproportional loadings. The effect is similar to isotropic hardening in classical plasticity. Unlike other approaches, e.g. [6], neither an updating rule (or help function) nor a loading-unloading criterion is needed in this formulation.

The purposes of the present paper are to give an isotropic formulation of VBO applicable for cyclic hardening and to demonstrate its predictive capability in proportional and nonproportional strain-controlled cyclic loadings. Some results of numerical experiments are compared with corresponding room temperature results on Type 304 Stainless Steel.

The isotropic formulation consists of the following differential equations and functions:

$$\dot{\underset{\sim}{e}} = \frac{1+\nu}{E}\,\dot{\underset{\sim}{s}} + \frac{1+\nu}{Ek[\Gamma_o]}\,(\underset{\sim}{s} - \underset{\sim}{g}^d) \quad , \qquad (1)$$

$$\dot{\underset{\sim}{g}} = \psi[\Gamma_o, A]\,\underset{\sim\sim}{T}\dot{\underset{\sim}{\varepsilon}} - (\underset{\sim}{g} - E_t \underset{\sim\sim}{T}\underset{\sim}{\varepsilon})\,\frac{\dot{\phi}}{b[\Gamma_o, A]} \quad . \qquad (2)$$

$$\mathrm{tr}(\dot{\underset{\sim}{\varepsilon}}) = \frac{1-2\nu}{E}\,\mathrm{tr}(\dot{\underset{\sim}{\sigma}}) \quad , \qquad (3)$$

$$b[\Gamma_o, A] = \frac{A}{\psi[\Gamma_o, A] - E_t} \quad , \qquad (4)$$

$$\Gamma_o = \left(\frac{3}{2}\,\mathrm{tr}(\underset{\sim}{s} - \underset{\sim}{g}^d)^2\right)^{1/2} \quad , \qquad (5)$$

$$\dot{\phi} = \left(\frac{2}{3}\,\mathrm{tr}(\dot{\underset{\sim}{\varepsilon}}^{in})^2\right)^{1/2} \quad , \qquad (6)$$

$$\dot{P}_1 = \left(\mathrm{tr}\left(\dot{\underset{\sim}{\varepsilon}}^{in}(\underset{\sim}{\varepsilon}^{in})^2\,\dot{\underset{\sim}{\varepsilon}}^{in}\right)\right)^{1/2} \quad , \qquad (7)$$

$$\dot{P}_o = \left(\mathrm{tr}(\underset{\sim}{\Omega}\underset{\sim}{\Omega}^T)\right)^{1/2} \quad , \qquad (8)$$

$$\underset{\sim}{\Omega} = \underset{\sim}{\varepsilon}^{in}\dot{\underset{\sim}{\varepsilon}}^{in} - \dot{\underset{\sim}{\varepsilon}}^{in}\underset{\sim}{\varepsilon}^{in} \quad , \qquad (9)$$

$$\dot{A}^* = a_1\dot{P}_1^{\,a_2} + a_5\dot{P}_o^{\,a_6} - a_3(A - A_o)^{a_4} \quad , \qquad (10)$$

$$\dot{A} = a_7|\dot{A}^*| + a_8\dot{A}^* \quad . \qquad (11)$$

where $T_{ijk\ell} = \frac{1}{1+\nu}\left(\frac{1}{2}(\delta_{ik}\delta_{j\ell} + \delta_{i\ell}\delta_{jk}) + \frac{\nu}{1-2\nu}\,\delta_{ij}\delta_{k\ell}\right)$, $a_7 + a_8 = 1$ and $a_8 - a_7 = u$ $(0 \le u \le 1)$. For cyclic neutral behavior the constants a_1, a_3, a_5 are zero; a_7, a_8, and Eqs.(7)-(11) are not necessary.

The system of differential equations introduced in the above is similar to that obtained in [2] with the exception that a dependence of ψ on A and a growth law for A are added. The former ensures that the linear elastic regions expand when A increases. In addition to the inelastic strain path length defined in (6), two additional scalar measures are introduced in (7) and (8). The last measure is nonzero when the inelastic strain and the inelastic strain rate are not collinear. This occurs in nonproportional loading. The quantity defined in (7) is of the same order as the one defined in (8) and accumulates in every inelastic loading. These quantities have been used to correlate experimental data [8].

To illustrate the capability of the newly proposed growth law for A consider two axial-torsion tests; one with proportional straining and the other with 90° out-of-phase straining. It is clear that, though $\dot{P}_i$ are not zero, $\dot{P}_o = 0$ in the former case and $P_o \neq 0$ in the latter case. Therefore Eq.(10) gives a different growth in the two cases which is reflected in the magnitude of $\dot{P}_o$. If we consider two cyclic tests with different strain ranges, again Eq.(10) gives a different growth depending on the inelastic strain because ε^{in} is included in P_o and $\dot{P}_i$. The model can predict a further hardening at the high amplitude under two-step amplitude loading even if saturation was reached at the first amplitude. If a small strain range is performed following a large strain range in the two-step amplitude loading, the model predicts a stabilized stress corresponding to the most recent level irrespective of the prior history. Equation (11) is introduced to delay the process of reaching the stabilized value.

Aside from these qualitative predictions, the details of deformation behavior must be evaluated through numerical experiments. The constants and functions of the theory were selected to represent the Type 304 Stainless Steel. All numerical integrations were performed using IMSL routine DGEAR on an IBM AT personal computer.

NUMERICAL EXPERIMENTS AND DISCUSSIONS

The procedure introduced in [1,2] for determining the constants and functions is still useful. Stabilized stresses for different strain ranges under both uniaxial and 90° out-of-phase loadings are necessary for the identifications of the constants associated with the growth law for A. The details can be found in [9]. The constants and functions for annealed Type 304 SS are listed in Table 1.

Simulations of the following four tests are reported, all conducted at the same equivalent strain rate of $\dot{\varepsilon}_e = 0.0003\ s^{-1}$. The first test is a two amplitude step-up uniaxial test with $\varepsilon_a = 0.0056$ for 15 cycles followed by 15 cycles with $\varepsilon_a = 0.008$. In the second test the sequence of the applied strain amplitudes is reversed. In the third test the second block consisted of a 90° out-of-phase loading for 5 cycles with the same equivalent strain amplitude as the previous uniaxial cycling to near saturation. Lastly a 90° out-of-phase cyclic test without any prior deformation was performed with $\varepsilon_e = 0.0056$ for 5 cycles.

The results for the first three tests are presented in Figure 1. The theory correlates the experimental result reasonably well in normal cyclic hardening tests and gives similar responses as reported in [6] in both further hardening and partial fading memory cases. It also demonstrates that an additional hardening is experienced in 90 degrees out-of-phase loading even when the material had almost saturated under proportional loading with the same strain range. This behavior is found in experiments [3,5]. It was shown [5] that the cyclic hardening behavior during in-phase loading (axial, torsional and proportional loading) can be correlated on the basis of the v. Mises equivalent stress and the accumulated strain path length, the integral of (6). The present theory uses these quantities, see (5) and (6). On the basis of the results in Fig. 1 it is reasonable to assume that the theory can correlate the hardening in in-phase loading.

The correlation for the 90° out-of-phase loading is shown in Figure 2 where the experimental result for the 5th cycle is also plotted. Comparison of the saturation levels for out-of-phase loading in Fig. 1 (path AB") and Fig. 2 (saturation is almost reached after 5 cycles) shows that they are almost equal. It was found in [3] that the saturated stress was not dependent on prior history. This fact is represented by the present theory. Even though the model gives a correct stabilized stress in 90° out-of-phase loading, the description of the transient behavior needs improvement.

ACKNOWLEDGMENT

This research was made possible by a grant from the National Science Foundation.

REFERENCES

[1] Krempl, E., J. McMahon and D. Yao, "Viscoplasticity Based on Overstress with a Differential Growth Law for the Equilibrium Stress," *Mechanics of Materials* (in press).

[2] Yao, D. and E. Krempl, "Viscoplasticity Theory Based on Overstress. The Prediction of Monotonic and Cyclic Proportional and Nonproportional Loading Paths of an Aluminum Alloy," *Int'l. J. Plasticity, 1*, pp.259-274, 1985.

[3] Lamba, H. S. and O. M. Sidebottom, "Cyclic Plasticity for Nonproportional Paths: Part I - Cyclic Hardening, Erasure of Memory, and Subsequent Strain Hardening Experiments," *Trans. ASME, J. Engineering Materials and Technology, 100*, pp.96-103, 1978.

[4] Lu, H., Ph.D. Dissertation, Rensselaer Polytechnic Institute, Troy, NY, May 1985.

[5] Krempl, E. and H. Lu, "The Hardening and Rate-Dependent Behavior of Fully Annealed Type 304 Stainless Steel under Biaxial In-phase and Out-of-Phase Strain Cycling at Room Temperature," *Trans. ASME, J. Engineering Materials and Technology, 106*, 376-382, 1984.

[6] Chaboche, J. L., K. Dang Van and G. Cordier, "Modelization of the Strain Memory Effect on the Cyclic Hardening of 316 Stainless Steel," SMIRT 5, Berlin, Germany, 1979, Paper L 11/3.

[7] Nouailhas, D., J. L. Chaboche, S. Savalle and G. Cailletaud, "On the Constitutive Equations for Cyclic Plasticity under Nonproportional Loading," *Int'l. J. Plasticity, 1*, pp.317-330, 1985.

[8] Krempl, E. and H. Lu, "Proportional and Nonproportional Cycling of Type 304 Stainless Steel at Room Temperature. The Path Dependence of Hardening and Two New Measures of Strain Path Length," Second Int. Conference on Biaxial/Multiaxial Fatigue, Sheffield, UK, Dec. 1985, submitted for publication in the Proceedings.

[9] Yao, D., Ph.D. Dissertation, Rensselaer Polytechnic Institute, Troy, NY (expected December 1986).

TABLE 1 MATERIAL CONSTANTS AND FUNCTIONS*

Material constants:

$E = 195000$ MPa

$E_t = 2000$ MPa

$A_o = 115$ MPa

$\nu = 0.5$

$a_1 = 380000$ MPa $s^{-(1-a_2)}$

$a_2 = 0.925$

$a_3 = 0.0653$ MPa$^{1-a_4}$ s^{-1}

$a_4 = 0.703$

$a_5 = 41.17$ MPa $s^{-(1-a_6)}$

$a_6 = 0.2062$

$a_7 = 0.495$

$a_8 = 0.505$

Viscosity function:

$$k[x] = k_1\left(1+\frac{|x|}{k_2}\right)^{-k_3} ,$$

$k_1 = 314200$ s, $k_2 = 60$ MPa, $k_3 = 21.98$.

Shape modulus function:

$$\psi[x,y] = c_1[y] + (c_2 - c_1[y])\exp(-c_3 x) ,$$

$$c_1[y] = H_1 + H_2 y ,$$

$c_2 = 182500$ MPa, $c_3 = 0.0783$ MPa^{-1}, $H_1 = 74740$ MPa, $H_2 = 37.04$

---

*All x and y are in units of MPa.

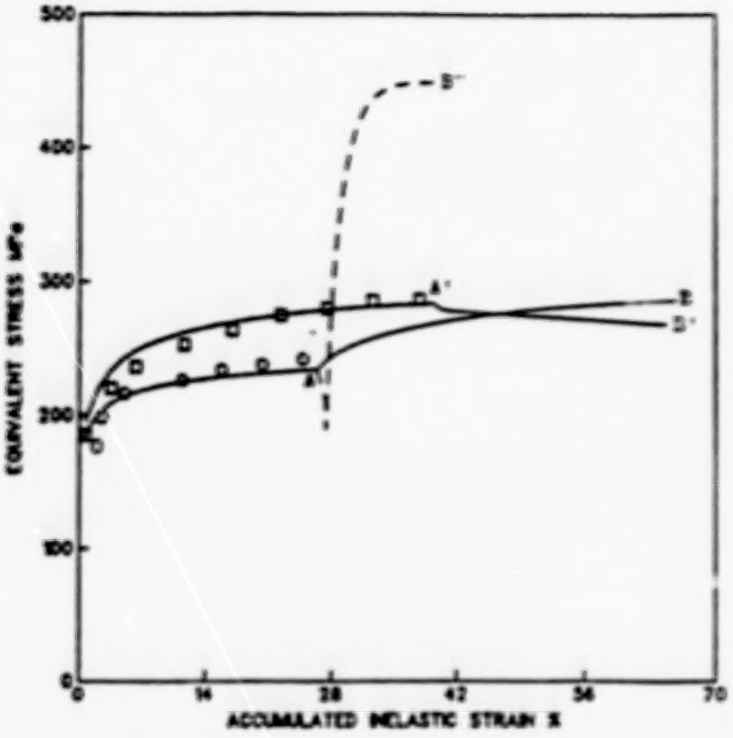

Figure 1. The equivalent stress vs accumulated inelastic strain.
Solid and dotted lines: theory.
Strain history:
OAB uniaxial cycling with amplitude increase
- 15 cycles with $\epsilon_a = 0.0056$ followed by
15 cycles with $\epsilon_a = 0.008$;
OA'B' uniaxial cycling with amplitude decrease
- 15 cycles with $\epsilon_a = 0.008$ followed by
15 cycles with $\epsilon_a = 0.0056$;
OAB" uniaxial cycling followed by 90° out-of-phase
cycling for 5 cycles at the same effective
strain amplitude.
All tests were performed with $\dot{\epsilon}_e = 0.0003\ s^{-1}$.

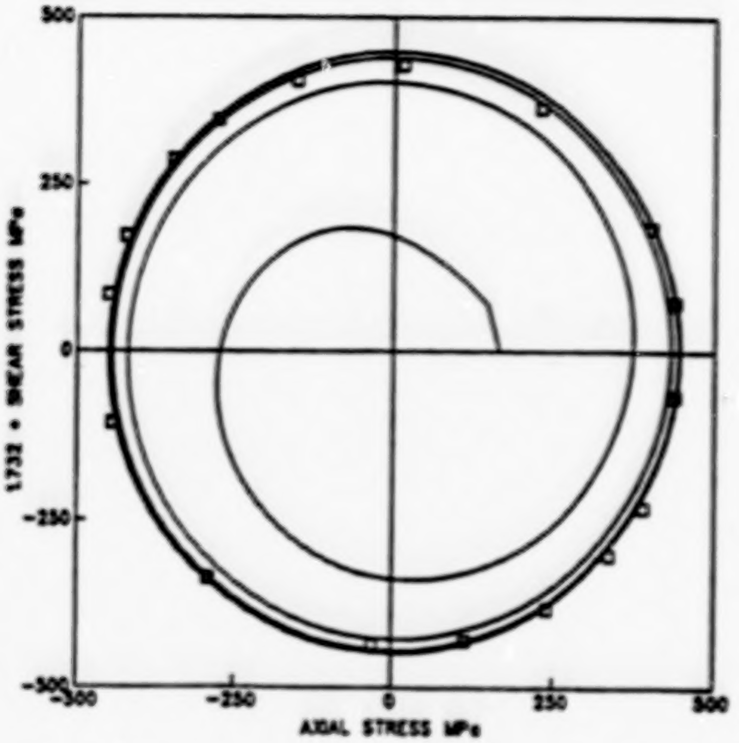

Figure 2. The $\sqrt{3}$ × shear stress vs axial stress under 90° out-of-phase loading with $\epsilon_e = 0.0036$ and $\dot{\epsilon}_e = 0.0003\ s^{-1}$. Solid lines: theory. Experimental data only show the 5th cycle.

N88
21515
UNCLAS

N88-21515

SOME IMPLICATIONS FOR CYCLIC PLASTIC AND VISCOPLASTIC EQUATIONS BASED ON NONPROPORTIONAL LOADING EXPERIMENTS

D.L. McDowell, J. Moosbrugger, M. Doumi
Georgia Institute of Technology
Atlanta, Georgia 30332

E.H. Jordan
University of Connecticut
Storrs, Connecticut 06268

A number of different formulations exist for state variable or "unified" creep-plasticity theory [1-10]. There is, however, a common isothermal framework for many of these models which include backstress, e.g.

$$\dot{\underset{\sim}{\varepsilon}}^{n} = f(||\underset{\sim}{s} - \underset{\sim}{\alpha}||,\kappa)\ (\underset{\sim}{s} - \underset{\sim}{\alpha}) \tag{1}$$

$$\dot{\underset{\sim}{\alpha}} = h_{\alpha}\ \dot{\underset{\sim}{\xi}} - r_{\alpha}\ \underset{\sim}{\Omega} \tag{2}$$

$$\dot{\kappa} = h_{\kappa}\left|\left|\dot{\underset{\sim}{\varepsilon}}^{n}\right|\right| - r_{\kappa} \tag{3}$$

where h_{α} and h_{κ} are scalar hardening functions, r_{α} and r_{κ} are scalar recovery functions, $\underset{\sim}{\alpha}$ is the backstress, κ is the drag stress, $\underset{\sim}{s}$ is deviatoric stress, $\dot{\underset{\sim}{\varepsilon}}^{n}$ is the inelastic strain rate, and $||\dot{\underset{\sim}{\varepsilon}}^{n}|| = [\dot{\underset{\sim}{\varepsilon}}^{n}:\dot{\underset{\sim}{\varepsilon}}^{n}]^{1/2}$.

---

[1] School of Mechanical Engineering, Georgia Institute of Technology, Atlanta, GA 30332.

[2] Mechanical Engineering, University of Connecticut, Storrs, CT 06268.

PRECEDING PAGE BLANK NOT FILMED

It is usual to first select hardening and recovery functions which encompass relevant uniaxial phenomenological behavior, and then to fit the associated material constants to this data using appropriate multivariate error minimization procedures. There is a somewhat prevalent assertion among existing theories that the directional index for the hardening term in equation (2) is the inelastic strain rate, i.e.

$$\dot{\underset{\sim}{\xi}} = \dot{\underset{\sim}{\varepsilon}}^{n} \tag{4}$$

Several theories [2-3, 11-12] include a dynamic recovery term with $\underset{\sim}{\alpha}$ as the directional index, i.e.

$$\dot{\underset{\sim}{\xi}} = \dot{\underset{\sim}{\varepsilon}}^{n} - h_{\alpha}{}^{-1} h_{D} \underset{\sim}{\alpha} \, || \dot{\underset{\sim}{\varepsilon}}^{n} || \tag{5}$$

where h_D is a scalar dynamic recovery function. Uniaxial testing alone is insufficient to validate the directional index of the dynamic recovery term since $\underset{\sim}{\alpha}$ is collinear with $\dot{\underset{\sim}{\varepsilon}}^{n}$. This collinearity is also likely responsible for the absence of the dynamic recovery term in many theories.

An important attribute of multiaxial nonproportional loading is the noncollinearity of $\dot{\underset{\sim}{\varepsilon}}^{n}$ and $\underset{\sim}{\alpha}$. As will be shown in this paper, the need for the dynamic recovery term can be established from cyclic nonproportional biaxial tests. Furthermore, it is possible to comment on the relative magnitude of the direct hardening and dynamic recovery coefficients and to assess the accuracy of the direct hardening and dynamic recovery directional indices based on selected tests. Axial-torsional experiments conducted with type 304 stainless steel at room temperature and Hastelloy-X at 649°C will be discussed.

Brief Discussion of Results

The need for the dynamic recovery term is evidenced in analysis of the type 304 stainless steel response. As shown in Figure 1, the backstress rate direction much more accurately approaches tangency to the backstress path (assuming constant, rate-independent Mises yield surface radius) with the addition of the dynamic recovery term.

Allowing for rate-dependent response, data from sinusoidal 90° out-of-phase tests on Hastelloy-X were analyzed. Two possibilities were considered. Firstly, the coefficients of the direct and dynamic recovery terms, h_a and h_D in equation (5), were considered scalars. Secondly, they were considered as tensor operators of diagonal form. Several admissible backstress paths were determined by fixed point iteration of an equation reflecting the constraint that backstress must lie along the backward projection of the inelastic strain rate direction from the current stress point. Each assumed initial value of backstress produced a unique, possible backstress path. For each path, the direct hardening and dynamic recovery coefficients were determined by least squares fit to the loading cycle. It was determined that the coefficient of direct hardening is accurately described as a scalar, inferring adequacy of the inelastic strain rate as the directional index. For the dynamic recovery term, however, the data suggest that a tensor-valued coefficient $\underset{\sim}{h}_D$ is appropriate, inferring the inadequacy of backstress $\underset{\sim}{a}$ as a directional index. Refer to Figure 2 for a comparison of the correlation achieved by using scalar and tensor-valued coefficients.

Though limited in number and scope, these results indicate the potential utility of nonproportional biaxial testing in generalization of state variable cyclic viscoplasticity theories.

Conclusions

From cyclic, strain-controlled, nonproportional tests on type 304 stainless steel and Hastelloy-X, the following statements may be made:

1. A dynamic recovery term is essential to properly model the backstress evolution.
2. From analysis of Hastelloy-X data obtained at 649°C, the inelastic strain rate appears to be a satisfactory directional index for direct hardening, but the backstress appears to be an inappropriate directional index of dynamic recovery.
3. Sinusoidal, 90° out-of-phase axial torsional tests can be very useful in aiding determination of backstress evolution functions, including both directional indices and scalar hardening functions, by virtue of the associated approximately constant magnitudes of overstress, inelastic strain rate, and effective stress. Such tests have previously been associated with the study of nonproportional hardening effects but have more far ranging applications.

Acknowledgments

Professor McDowell would like to acknowledge the support of the U.S. National Science Foundation (NSF MEA-840 4080). Professor Jordan conducted the experiments on Hastelloy-X with the support of a grant from NASA (NAG 3-160).

References

1. Perzyna, P., "The Constitutive Equations for Rate Sensitive Plastic Materials," Quarterly of Applied Mechanics, Volume 20, 1963.

2. Miller, A., "An Inelastic Constitutive Model for Monotonic, Cyclic and Creep Deformation, Part I: Equation Development and Analytical Procedure," J. Eng. Mat. and Technology, Trans. ASME, Volume 98, 1976.

3. Miller, A., "An Inelastic Constitutive Model for Monotonic Cyclic and Creep Deformation: Part II: Application to Type 304 Stainless Steel," J. of Eng. Mat. and Technology, Trans. ASME, Volume 98, 1976.

4. Robinson, D.N., "A Unified Creep-Plasticity Model for Structural Metals at High Temperature," ORNL/TM-5669, Oct. 1978.

5. Krieg, R.D., Swearengen, J.C. and Rohde, R.W., "A Physically-based Internal Variable Model for Rate-Dependent Plasticity," Inelastic Behavior of Pressure Vessels and Piping Components, Montreal, 25-29 June, 1978, edited by T.Y. Chang and E. Krempl.

6. Lagneborg, R., "A Modified Recovery-Creep Model and its Evaluation," Metal Science Journal, Volume 6, 1972.

7. Ponter, A.R.S., and Leckie, F.A., "Constitutive Relationships for the Time-Dependent Deformation of Metals," J. of Eng. Mat. and Technology, Trans. ASME, Volume 98, 1976.

8. Hart, E.W. "Constitutive Relations for Non-Elastic Deformations of Metals," J. of Eng. Mat. and Technology, Trans. ASME, Volume 98, 1976.

9. Chan, K.S., Bodner, S.R., Walker, K.P., and Lindholm, U.S., "A Survey of Unified Constitutive Theories," Proc. 2nd Symp. on Nonlinear Constitutive Relations for High Temperature Applications, NASA Lewis Research Center, June 13-15, 1984.

10. Allen, D.H. and Beek, J.M., "On the Use of Internal State Variables in Thermoviscoplastic Constitutive Equations," Proc. 2nd Symp. on Nonlinear Constitutive Relations for High Temperature Applications, NASA Lewis Research Center, June 13-15, 1984.

11. Chaboche, J.L., Bulletin de L'Academie des Sciences, serie des Science Techniques, Vol. XXV, No. 1, 1977, p.33.

12. Lee, D., and Zaverl, F., Jr., Acta Met., Vol. 26, No. 11, 1975, p. 385.

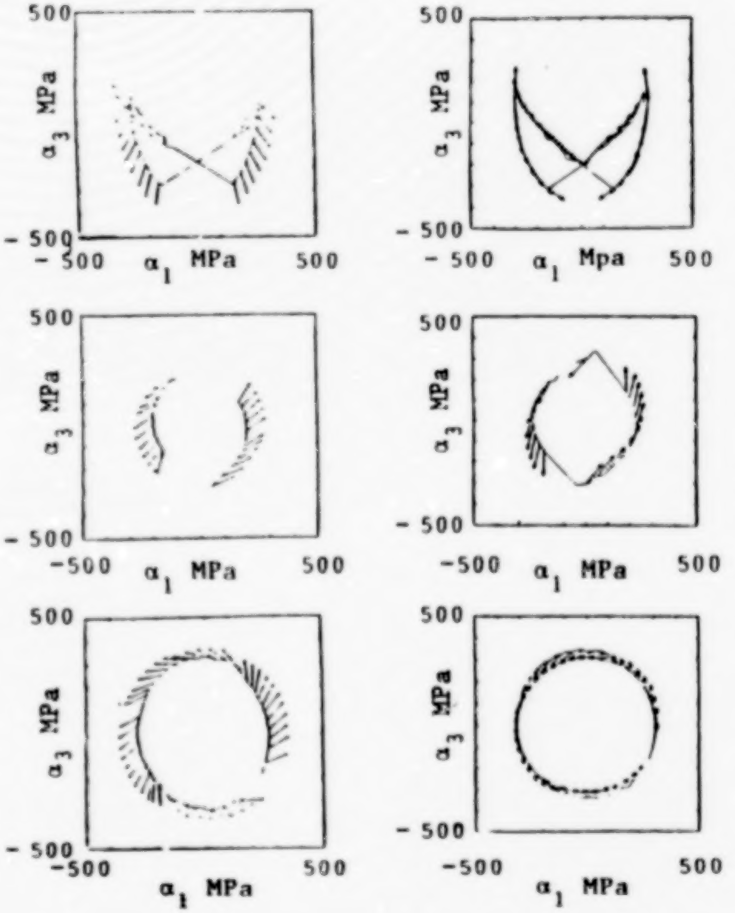

Fig. 1 Backstress rate directions predicted using (left column) direct hardening only, and (right column) with inclusion of dynamic recovery term for AISI Type 304 Stainless Steel at room temperature. Included are stable cycles from three nonproportional histories. Assumed Mises yield surface radii are (left column) 200 MPa and (right column) 160 MPa.

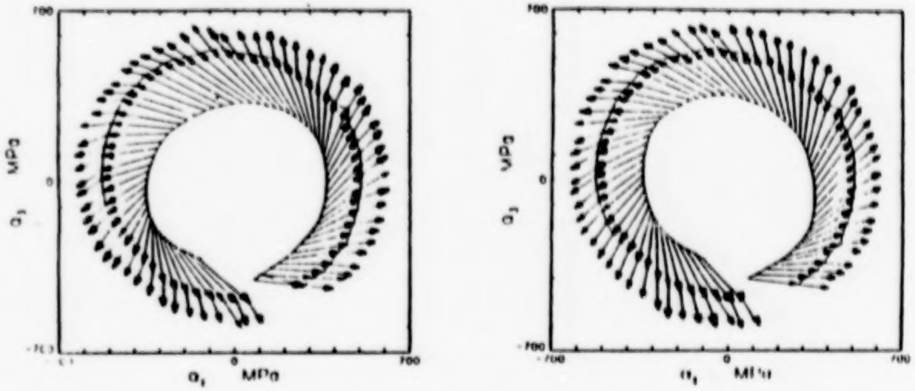

Fig. 2 Direction of inelastic strain rate (short vectors) and associated overstress vectors $\underline{\sigma}-\underline{\alpha}$ for a 90 deg. out-of-phase history on Hastelloy-X at 593°C. Backstress $\underline{\underline{\alpha}}$ is obtained by Euler integration of (left) scalar direct hardening and dynamic recovery coefficients and (right) tensor-valued coefficients. In each case, the assumed initial value of backstress was 60% of the initial stress. Note the improved collinearity and backstress path shape for the case of tensorial coefficients.

ORIGINAL PAGE IS
OF POOR QUALITY

N88
21516
UNCLAS

N88-21516

AN EXPERIMENTAL COMPARISON OF SEVERAL CURRENT VISCOPLASTIC CONSTITUTIVE MODELS AT ELEVATED TEMPERATURE

G.H. James, P.K. Imbrie, P.S. Hill, D.H. Allen, W.E. Haisler
Texas A&M University
College Station, Texas 77843

Four current viscoplastic models are compared experimentally for Inconel 718 at 593° C. This material system responds with apparent negative strain rate sensitivity, undergoes cyclic work softening, and is susceptible to low cycle fatigue. The models used include Bodner's anisotropic model, Krieg, Swearengen, and Rhode's model, Schmidt and Miller's model, and Walker's exponential model. Schmidt and Miller's model and Walker's model correct for negative strain rate sensitivity response. A correction similar to Schmidt's is applied to the models of Bodner and Krieg, et al.

A series of tests has been performed to create a sufficient data base from which to evaluate material constants. A method to evaluate the constants is developed which draws on common assumptions for this type of material, recent advances by other researchers, and iterative techniques. A complex history test, not used in calculating the constants, is then used to compare the predictive capabilities of the models.

The combination of exponentially based inelastic strain rate equations and dynamic recovery is shown to model this material system with the greatest success. The method of constant calculation developed in this work was successfully applied to the complex material response encountered. Backstress measuring tests were found to be invaluable and warrant further development.

INTRODUCTION

This paper experimentally compares four current viscoplastic models for metals at elevated temperature. The primary objective of this work is to uncover the mathematical forms which model reality most successfully and to develop basic understanding of the models. A secondary objective is to develop methods of constant calculation which are systematic and repeatable. A final objective is to develop experimental tests and test software to support viscoplastic modeling.

This research produces many positive results. First, the aspects of each model which need further development are uncovered. Also, the most accurate mathematical forms of the models are determined. Third, basic understanding of the models is generated. Such understanding is necessary for actual engineering application of the models and for expanding the capabilities of the models. Fourth, systematic methods of material parameter evaluation are developed which draw on advances by all the modelers. Systematic constant calculation methods make the models much easier to use by researchers and engineers in the field and advance the technology toward automation and standardization. Finally, experimental techniques and needs are developed or reported which can either lead or support theoretical advances.

MATERIAL CONSIDERATIONS

The material used in this work was Inconel 718 and was provided by NASA Lewis Research Center in Cleveland, Ohio. The temperature used was 593° C. (1100° F.). The average value of Young's modulus was 169.9 GPa. The material used in this work had .2% yield stress values between 792 and 903 MPa. The material cyclically work softened. Strain ageing and negative strain rate sensitivity effects were observed between the strain rates of $1X10^{-5}$ sec^{-1} and $1X10^{-3}$ sec^{-1}. A fatigue life of 5 to 30 cycles resulted when specimens were cycled at strain amplitudes over $\pm 1\%$ strain. Lower strain rates and the inclusion of creep hold times also adversely affected the fatigue life.

All samples were subjected to the same heat treatment prior to testing. The heat treatment used was given by the Metals Handbook [1]. The material was annealed at 954° C for one hour and then oil quenched. The next step was ageing at 718° C. for eight hours with a furnace cool. The furnace used was a Hevi Duty Electric Co. type 66-P. Temperature was monitored with a Keithly 871 Digital Thermometer. The resulting material state was found to be the easiest to machine. Therefore, the heat treatment was carried out before machining and again before testing.

OVERVIEW OF MODELS

The models chosen for this work include Bodner's anisotropic model [2], Krieg, Swearengen, and Rhode's model [3], Schmidt and Miller's model [4], and Walker's exponential model [2]. These models were chosen because they are under active development, methods of determination of the constants have been reported, and some attempt has been made or is being made to expand them to transient temperature modeling. The material utilized in this work responded with negative strain rate sensitivity due to strain ageing. The models of Schmidt and Miller and Walker were able to handle this phenomenon. The models of Bodner and Krieg, et al. needed corrections to handle this effect. The models are reviewed below.

Bodner's Anisotropic Model

The growth laws for Bodner's anisotropic model have the following form:

$$\dot{\epsilon}^I = \frac{2}{\sqrt{3}} D_0 \exp\left[- \frac{1}{2} \left[\frac{Z}{\sigma}\right]^{2n}\right] \operatorname{sgn} \sigma \tag{1}$$

$$Z = Z^I + Z^A = Z^I + B \operatorname{sgn} \sigma \tag{2}$$

$$\dot{Z}^I = m_1 [Z_1 - Z^I] \dot{W}_p - A_1 Z_1 \left[\frac{Z^I - Z_2}{Z^1}\right]^{r_1} \tag{3}$$

$$\dot{B} = m_2 [Z_3 \operatorname{sgn} \sigma - Z^A] \dot{W}_p - A_2 Z_1 \left[\frac{|B|}{Z_1}\right]^{r_2} \operatorname{sgn} Z^A \tag{4}$$

where D_0, n, m_1, Z_1, Z_2, A_1, r_1, m_2, Z_3, A_2, and r_2 are material constants.

The flow law is exponentially based as seen in equation (1). The model gives a limiting strain rate in shear of D_0 [5]. The term $-m_1 Z^I \hat{W}_p$ is a dynamic recovery term for Z^A in the isotropic growth law (3) and $- A_1 Z_1 [(Z - Z_2) Z_1^{-1}]^{r_1}$ is a static thermal recovery term. B is a uniaxial representation of a second order tensor in the multiaxial state which handles directional or anisotropic hardening. B is assumed to act as an isotropic variable on an incremental basis [6]. The growth law for B (4) has the same components as the growth law for D (3).

Bodner's model is seen to use the rate of plastic work instead of inelastic strain rate as the measure of work hardening (3,4). This is designed to allow for better modelling of strain rate jump tests [7]. The correction used to account for the strain ageing effects was Schmidt and Miller's non-interactive solute strengthening correction [4]. The inelastic strain rate equation was then written in the following form:

$$\dot{\varepsilon}^I = \frac{2}{\sqrt{3}} D_0 \exp\left[-\frac{1}{2}\left(\frac{Z + F_{sol}}{\sigma}\right)^{2n}\right] \operatorname{sgn} \sigma \tag{5}$$

$$F_{sol} = F \exp\left\{-\left[\frac{\log(|\dot{\varepsilon}^I|) - \log(J)}{\beta}\right]^2\right\} \tag{6}$$

where F is the maximum correction, J is the strain rate of maximum correction, and β is the width of correction.

Krieg, Swearengen, and Rhode's Model

Krieg, et al.'s growth laws have the following form:

$$\dot{\varepsilon}^I = C\left(\frac{\sigma - B}{D}\right)^n \operatorname{sgn} \sigma \tag{7}$$

$$\dot{B} = A_1\dot{\varepsilon}^I - A_2 B^2\left[e^{(A_3 B^2)} - 1\right] \operatorname{sgn} B \tag{8}$$

$$\dot{D} = A_4\dot{\varepsilon}^I - A_5(D - D_0)^n \tag{9}$$

where C, n, A_1, A_2, A_3, A_4, and A_5 are material constants.

The flow law is seen to be a power law based equation. The back stress and drag stress growth laws (8,9) contain static thermal recovery terms but no dynamic recovery terms. The recovery term in (8) is based on a dislocation climb model by Friedel. The recovery term in (9) is based on a special case of the same climb recovery model used in (8) [3,8].

Schmidt and Miller's non-interactive solute strengthening correction was again used with this model to produce the following inelastic strain rate equation:

$$\dot{\varepsilon}^I = C\left(\frac{\sigma - B}{D + F_{sol}}\right) \operatorname{sgn}(\sigma - B) \tag{10}$$

$$F_{sol} = F \exp\{ - [\frac{\log(|\dot{\varepsilon}^I|) - \log(J)}{\beta}]^2\} \quad (11)$$

Schmidt and Miller's Model

Schmidt and Miller's growth laws have the following form:

$$\dot{\varepsilon}^I = B'\{ \sinh(\frac{\sigma - B}{D + F_{sol}})^{1.5}\}^n \operatorname{sgn}(\sigma - B) \quad (12)$$

$$\dot{B} = H_1\dot{\varepsilon}^I - H_1B'\{ \sinh(A_1|B|) \}^n \operatorname{sgn}(B) \quad (13)$$

$$\dot{D} = H_2|\dot{\varepsilon}^I|(C_2 + |B| - \frac{A_2}{A_1} D^3) - H_2C_2B'\{ \sinh(A_2D^3) \}^n \quad (14)$$

$$F_{sol} = F \exp\{ - (\frac{\log(|\dot{\varepsilon}^I|) - \log(J)}{\beta})^2\} \quad (15)$$

where B', n, H_1, A_1, H_2, C_2, A_2, F, J, and β are material constants.

The flow law has the form of a hyperbolic sine. This form was chosen to model creep response better [9]. This same form is found in the static thermal recovery terms of the back stress and drag stress growth laws (13,14). The drag stress hardening term contains a hardening term, a dynamic recovery term, and a term which couples drag stress hardening to back stress magnitude. These three terms provide the proper cyclic, hardening, softening and saturation behavior [9]. The same non-interactive solute strengthening correction (F_{sol}) as mentioned earlier is seen in this model.

Walker's Exponential Model

The growth laws for Walker's exponential model have the following form [2,10]:

$$\dot{\varepsilon}^I = \frac{\exp(\frac{\sigma - B}{D}) - 1}{\beta} \operatorname{sgn}(\sigma - B) \quad (16)$$

$$\dot{B} = n_2 - B \{ [n_3 + n_4\exp(-n_5| \log(\frac{|\dot{R}|}{\dot{R}_0}) |)] \dot{R} + n_6\} \quad (17)$$

$$D = D_1 + D_2\exp(-n_7R) \quad (18)$$

$$\dot{R} = |\dot{\varepsilon}^I| \quad (19)$$

where β, n_2, n_3, n_4, n_5, $\dot{R}_0$, n_6, D_1, D_2, and n_7 are material constants.

This version of Walker's flow law (16) is based on an exponential function. The term $n_2\dot{\epsilon}^I$ is seen to be a work hardening term in the back stress growth law. The term $B\ [\ n_3 + n_4 \exp(-n_5|\log(|\dot{R}|/\dot{R}_0|)|]\ \dot{R}$ is a dynamic recovery term. Negative strain rate sensitivity effects can be modelled with the term $n_4 \exp(-n_5|\log(|\dot{R}|/\dot{R}_0)|)$. Back stress thermal recovery is handled by the $B\ n_6$ term. Drag stress hardening is modelled through the $D_2 \exp(-n_7 R)$ term. No provision is made for drag stress recovery in this model.

EXPERIMENTAL PROGRAM

The basic experimental program consisted of the following tests:

(1) 2 monotonic tension tests to 1.5% strain (strain rates of $3.15\text{X}10^{-3}$ $\sec^{-1}$ and $7.25\text{X}10^{-6}$ $\sec^{-1}$);

(2) 5 fully reversed cyclic tests to ± .8% strain (strain rates between $1.00\text{X}10^{-3}$ $\sec^{-1}$ and $7.63\text{X}10^{-6}$ $\sec^{-1}$);

(3) 5 constant load creep tests (applied stresses between 820 MPa and 958 MPa);

(4) 4 back stress measuring tests during cyclic loading and 4 during secondary creep; and

(5) 1 complex history test.

Table 1 provides more specific information on the test program. Column 1 provides the test number. The type of test is given in column 2. The strain rate and strain limits are given in columns 3 and 4. The applied stresses for the creep tests are given in column 5. A complete data set in tabular form is provided in reference [11].

Back Stress Measuring Tests

Back stress measuring tests during secondary creep as described by Krieg, et al. [3] and during saturated cyclic loading as used by Walker [12] were performed in this work. The cyclic back stress numbers were obtained by holding a saturated cyclic test at various points on the unloading curve, switching to load control and monitoring the strain rate following the hold. The material was recycled and a hold time at another stress value was carried out. Fatigue lifetime problems for the material used in this work did not permit complete saturation of the microstructure for fear of sample fracture. The criterion used to define saturation in this work was a cycle to cycle variation of the maximum stress of less than 6.89 mpa. These conditions

Table 1 - Test Program

Test	Type	$\dot{\epsilon}_{app}$ sec^{-1}	ϵ_{lim}	σ_{app} MPa
70	tension	3.151E-3	1.5%	
71	tension	7.253E-6	1.5%	
86	cyclic	1.002E-3	+/-.8%	
56	cyclic	9.966E-4	+/-.8%	
65	cyclic	3.127E-4	+/-.8%	
83	cyclic	9.926E-5	+/-.8%	
80	cyclic	3.054E-5	+/-.8%	
72	cyclic	7.626E-6	+/-.8%	
64	creep			956.3
63	creep			922.6
62	creep			875.0
61	creep			854.4
60	creep			819.9
84	back	2.812E-3	+/-.8%	
88	back	9.272E-4	+/-.8%	
81	back	8.635E-4	+/-.8%	
65	back	3.127E-4	+/-.8%	
63	back			922.6
62	back			875.0
61	back			854.4
60	back			819.9
89	complex			

were met after 10 to 15 cycles for this material.

A linear least squares regression to the strain rate data provided a strain rate at each hold time. Each transient test had to be individually scrutinized to decide how many points to consider in the regression analysis as the onset of thermal recovery following a hold time was a very subjective decision. The back stress was assumed to be equal to the hold stress at which a zero strain rate was produced. This hold stress was determined by the use of a linear least squares curve fit to the strain rate versus hold stress data.

The creep back stress numbers were obtained in a similar fashion. The stress on a sample in secondary creep was dropped to various lower levels. The inelastic strain rate immediately following each drop was analyzed in the same manner as with the cyclic tests.

The back stress numbers were invaluable in estimating some material constants. The results were also promising enough to warrant further study. The procedures used here could be greatly enhanced by equipment with greater resolution such as used by Jones, et al. [13] and less subjective methods of data reduction such as the method of Blum and Finkel [14]. Other techniques such as torsional cycling used by Ellis and Robinson could also be considered [15]. The stress transient test [16] might also provide information for a material such a Inconel 718 which suffers from a short fatigue life when cycled. Reference [11] contains more information on the results observed and software developed for these tests.

EXPERIMENTAL APPARATUS

The load frame utilized in these tests was an MTS (Materials Test System) model 880 electrohydraulic testing machine shown in Fig. 1. MTS 652.01 Water-cooled hydraulic grips allowed fully reversed cyclic tests to be carried out at high temperature. The frame was controlled by a Digital Micro PDP-11 computer. Computer programs were written to run monotonic tension tests, cyclic tests, cyclic tests with hold times, creep tests, and creep stress drop tests. The Micro PDP-11 also handled data acquisition functions. An MTS 661.21A-02 50 KN load cell was the load transducer. An MTS 632.41B-02 axial extensometer was the strain transducer. This device had quartz extension rods which contacted the sample at two 120° punch holes. The material samples designed to ASTM E606-77T specifications for low cycle fatigue specimens.

An MTS 652 three-zone clamshell furnace and three Research Incorporated 63911 Process Temperature and Power Controllers were used for temperature control. Temperature Measurement was handled by six 28 gauge K-type thermocouples. These were placed in contact with the sample. Three thermocouples were fed into a Fluke 2176A Digital Thermometer for readout. These were placed with one each at the top, middle, and bottom of the gauge section. The other three thermocouples were fed into the temperature controllers. These were placed in the center of the furnace zone each was to sense with one thermocouple placed in the center of the gauge section and one on each grip.

The thermocouples were fastened to the grips by fiberglass thread attached to the sample by self-supporting means. The thermocouples at the top and bottom of the gauge section were wound around the sample. The thermocouples used in the center of the gauge section were brought into the oven from different directions and tied to each other. These thermocouples were then wound around the sample for contact. Welding the thermocouples to the sample would have produced harder contacts with more reliable temperature measurement. However premature failure occurred at the welds.

CALCULATION OF MATERIAL CONSTANTS

The complex response of Inconel 718 at 593° C prompted flexible methods of constant calculation to be developed. The method for calculating constants for the models began by making a series of judicious assumptions which allowed commonly used constant calculation schemes to produce initial estimates of the constants. Some nonlinearity was avoided in this step and was reintroduced by a series of repeatable iterations to the final constants. The iterative step numerically integrated the models to predict the stress-strain response at a certain point. One material constant was then changed to match the prediction to the experimental value at this point. Another material constant was then changed to match another material point.

Physical insight, familiarity with the uncertainty in the data set, and engineering intuition guided the organization of the calculation process. However, the actual process was carried out as systematically as possible. The eventual creation of systematic and automatable methods to calculate constants has been a major driver in this phase of the work. The method used to calculate the material constants will be summarized using a generic viscoplastic model in the first subsection of this section. The generic model used as an example will be presented first followed by a subsection outlining the general method of initial calculations and a subsection outlining the iterative step.

Generic Viscoplastic Model

The growth laws for the example model are presented below:

$$\dot{\varepsilon}^I = \left(\frac{\sigma - B}{D}\right)^n \tag{20}$$

$$\dot{B} = C_1\dot{\varepsilon}^I + C_2 B\,\dot{\varepsilon}^I + C_3 B \tag{21}$$

$$\dot{D} = C_4|\dot{\varepsilon}^I| + C_5 D \tag{22}$$

n is a constant measuring strain rate sensitivity. C_1 is a constant measuring back stress hardening. C_2 is handling back stress dynamic recovery and C_3

measures back stress thermal recovery. C_4 produces drag stress hardening and C_5 models drag stress recovery.

Initial Assumptions

The following initial assumptions were made in this work:

(1) back stress was assumed responsible for hardening in monotonic tension;

(2) drag stress was assumed responsible for cyclic softening;

(3) thermal recovery was assumed negligible for rapid tests $(\dot{\varepsilon}^I \geq 1.0\text{X}10^{-4}\,\text{sec}^{-1})$;

(4) drag stress thermal recovery was present in low strain rate saturated cyclic tests; and

(5) back stress thermal recovery was present in creep tests.

These assumptions allowed the constants for the inelastic strain rate equations, back stress hardening, drag stress hardening, drag stress recovery, and back stress recovery to be calculated in that general order. These assumptions also allowed much of the constant calculation schemes reported in the literature to be utilized with this material [2,3,4,5,9,12,17,18].

The first step was to estimate the constants in the back stress growth law assuming thermal recovery was negligible. The back stress growth law took on the following form:

$$\dot{B} = [C_1 + B\,C_2]\,\dot{\varepsilon}^I \qquad (23)$$

Differential techniques for calculating work hardening such as seen in Chan's gamma and theta plot concepts [2] were useful. Experimental estimations of back stress values such as used by Krieg, et al. [3] and Walker [12] were usually necessary. Relationships between saturated stresses and saturated back stresses as used by Miller [9] have also been used.

The next step was to calculate the strain rate sensitivity constant n and the initial value of drag stress denoted by D_0. Rewriting the inelastic strain rate equation in the following form was useful:

$$\ln(\ \sigma - B\ ) = \frac{1}{n}\ln(\ \dot{\varepsilon}^I) + \ln(\ D_0) \qquad (24)$$

A linear fit to several data points typically provided 1/n as the slope and $\ln(\ D_0\ )$ as the intercept. This is a technique commonly used with Bodner's model [19]. The ability to estimate saturated stresses and back stresses using techniques such as the gamma or theta plot [2] and relations between saturated stress and back stress are useful [9,2].

Initial determination of the drag stress parameter C_4 was carried out by assuming that thermal recovery could be neglected for rapid tests. The cumulative inelastic strain was calculated at a point on the cyclic curve where B and D could be estimated. The drag stress recovery parameter C_5 was then calculated by assuming the drag stress growth law was equal to zero for the saturated cycle of a low strain rate test. The back stress recovery parameter C_3 was calculated by assuming the growth law for back stess was zero for creep tests.

Computer Iterations

The computer iterations began by pairing each material constant with an experimental stress-strain point which the constant should intuitively have the greatest effect in predicting in a sequential fashion. The constants in the generic model were paired in the following fashion for this work:

(1) D_0 was paired with a stress-strain point at .8% strain on test 70 ($\dot{\epsilon} = 3.151X10^{-3}$ sec^{-1});
(2) C_2 was paired with a stress-strain point at 1.3% strain on test 70;
(3) C_1 was used to assure that the theoretical back stress values were in the same range expected from experimental values;
(4) n was paired with a stress-strain point at .8% strain on test 71 ($\dot{\epsilon} = 7.253X10^{-6}$ sec^{-1});
(5) C_3 was paired with a point at 1.3% strain on test 71;
(6) C_4 was paired with a point at .8% on the 10th cycle of test 86 ($\dot{\epsilon} = 1.002X10^{-3}$ sec^{-1});
(7) C_5 was paired with a point at .8% ot the 4th cycle of test 72 ($\dot{\epsilon} = 7.626X10^{-6}$ sec^{-1});

The iterative procedure then progressed by numerically integrating the model to predict the experimental stress-strain value for a specific constant. The constant was altered to match this point while the others were held constant. Then another constant was altered to produce the proper prediction at its paired experimental point. The expected order with which these steps were to be carried out is shown in Table 2. The x marks indicate which constant is being altered during the step indicated in column 1. Steps 1 through 5 are setting the back stress hardening characteristics. Steps 6 through 9 are setting the strain rate sensitivity of the model. Steps 10 through 12 are setting the drag stress hardening constant. The back stress recovery constants are being set in steps 13 through 15. Drag stress recovery is set in steps 16 through 18.

Table 2 - An Example Set of Iterations

Step	D_0	C_2	C_1	n	C_4	C_3	C_5
1	x						
2		x					
3			x				
4	x						
5		x					
6				x			
7	x						
8		x					
9				x			
10					x		
11		x					
12					x		
13						x	
14		x					
15						x	
16							x
17						x	
18							x

This method allows the entire process to be recorded. Automation of such a method is also possible if the initial calculations produce values which are close to the final constants. A systematic set of iterations may also allow a standard method for calculating constants to be produced. The lack of correction for strain ageing effects in the initial calculations caused problems in implementing this iterative scheme. Reference [11] provides some suggestions to avoid this as well as the specific application of this method to the models used in this work. Table 3 gives the final values of the constants with stress units of MPa, strain units of cm/cm, and time units of sec.

MODEL RESULTS

The forms of the models to be covered in this section include Bodner's model without a correction for solute strengthening, Bodner's model with a

Table 3 - Final Constants for Models

Krieg, Swearengen and Rhode's Model	
Constant	Final Value
n	15.00
C (1/sec)	2.000E-4
A1 (MPa)	9,646
A2 (1/(MPa sec))	0.000
A3 (MPaE-2)	2.387E-5
A4 (MPa)	-3445
A5 (MPaE(1-n)/sec)	-1.137E-19
D0 (MPa)	689.0
F (MPa)	379.0
β	1,000
J	7.000E-6

Schmidt and Miller's Model	
Constant	Final Value
n	7.0
A1 (1/MPa)	1.451E-4
A2 (MPaE-3)	.030572
B' (1/sec)	1.5E6
C2 (MPa)	-2.067E5
D0 (MPa)	.006890
H1 (MPa)	.4823
H2 (secE(1/n))	1E-7
F (MPa)	.04823
β	3.5
J	1E-9

Bodner's Anisotropic Model	
Constant	Final Value
n	.8132
A1 (1/sec)	-.0010
A2 (1/sec)	0.000
M1 (1/MPa)	.007257
M2 (1/MPa)	.05805
r1	.4926
r2	.4926
Z0 (MPa)	6201
Z1 (MPa)	4823
Z2 (MPa)	6201
Z3 (MPa)	2184
F (MPa)	-2412
β	3.0
J	1.0E-6

Walker's Exponential Model	
Constant	New Value
C	1.000E40
D1 (MPa)	4.823
D2 (MPa)	2.067
n2 (MPa)	2.274E5
n3	750.0
n4	-250.0
n5	.6600
n6	2.5E-4
n7	18.00
R0	3.050E-5

solute strengthening correction, the model of Krieg, et al. with and without a correction for solute strengthening, Schmidt and Miller's model, and Walker's exponential model. The models were numerically integrated with an Euler forward integration scheme on a Perkin-Elmer 32-10 computer. The time steps used ranged from $5.0\text{X}10^{-4}$ sec for test 70 to $5.0\text{X}10^{-2}$ sec for test 71.

Reproduction of Test Data

Fig. 2 shows the response of the models as compared to test 70 ($\dot{\varepsilon} = 3.151\text{X}10^{-3}$ sec^{-1}). The models are all oversquare except for Walker's. Walker's model is showing adverse effects from its dynamic recovery term as the stress is decreasing at higher strain levels. This is more of a problem with the method of constant calculation than the model itself. The iterative portion of the constant calculation process was performed with access to only two points on this curve. Using three points or interactive graphics would have solved this problem.

Fig. 3 compares the model outputs to test 71 ($\dot{\varepsilon} = 7.253\text{X}10^{-6}$ sec^{-1}). Walker's model is still following the shape of the curve best. The dynamic recovery problem still exists with the Walker model. The Krieg, et al. model is showing some numerical instability due to the presence of the solute strengthening parameters. The uncorrected versions of Bodner and Krieg, et al. are much lower than the other models. The F_{sol} parameter was simply set to zero in these versions. The other constants remained the same as in the corrected versions. Therefore, the reponse of the uncorrected versions could have been averaged over the strain range better. However, the basic strain rate sensitivity would have remained the same.

Fig. 4 interpolates the model response and experimental response between these two strain rates presented above by picking off stress values at .8% total strain for tests of intermediate strain rates and plotting these values versus the log of the applied strain rate. The tests used in Fig. 2 and Fig. 3 are shown on this figure also. Walker's model is exhibiting negative strain rate sensitivity and the corrected Bodner model is showing no strain rate sensitivity. The other models clearly produce positive strain rate sensitivity.

Fig. 5 shows the stress values at +.8% strain for the saturated cycle response. The slowest strain rate provides data from the fourth cycle and the other points are from the 10th cycle. The trend has changed and all the models with correction for solute strengthening are exhibiting negative strain rate sensitivity. This is probably an effect of the drag stress thermal recovery parameters and the cyclic work softening response.

Fig. 6 allows interpolation between the first cycle and the 10th cycle of test 86 ($\dot{\varepsilon} = 1.002X10^{-3}$ sec^{-1}) by presenting the values at +.8% strain for each cycle. The corrected Krieg, et al. model and the uncorrected Bodner model reproduce this data closest. Fig. 7 provides the same data for test 80 ($\dot{\varepsilon} = 9.926X10^{-5}$ sec^{-1}). This strain rate shows Walker's model following the experiment the closest. The peak value at the second cycle is reproduced with this model only. Fig. 8 presents the cyclic data for test 72 ($\dot{\varepsilon} = 7.626X10^{-6}$ sec^{-1}). The corrected Bodner model is following the data closest. The Walker model is clearly suffering from the lack of a drag stress thermal recovery term.

Predictive Capabilities

The predictive capabilities of the models were explored by the use a complex history test. This experimental test was not used in the calculation of the material constants. Table 4 gives the input history of this test. Fig. 9 through Fig. 14 show the comparison of the models to this complex history test. The corrected Bodner model in Fig. 10 is the least affected by strain rate jumps. Bodner attributes this to the use of plastic work as the measure of work hardening [7]. The interaction of the solute strengthening corrections of all the models may be having an effect on this aspect of all the models. The uncorrected versions in Fig. 9 and Fig. 11 are very suseptible to these jumps. Yao and Krempl report that the overshoots and undershoots observed during the strain rate jumps are a transient effect of the behavior of a system of coupled nonlinear differential equations [20].

A comparison of the response of the corrected and uncorrected versions of the Bodner and Krieg, et al. models at the zero strain hold time shows that the F_{sol} correction negates the effects of thermal recovery in such instances. This could be a result of the low value of J or the inelastic strain rate of maximum correction used in these models. The corrected Bodner model had $J = 1.0X10^{-6}$ sec^{-1}, the model of Krieg, et al had $J = 7.0X10^{-6}$ sec^{-1}, and Schmidt and Miller had $J = 1.0X10^{-9}$sec^{-1}. Schmidt and Miller's model showed no thermal recovery at this hold either. The small inelastic strain rates produced by thermal recovery terms would meet increasing hardness if their magnitude was below J. Increasing hardness would tend to drive the stresses up and oppose the action of the thermal recovery terms.

Table 4 - Complex History Test Input

Interval	Beginning Strain	Ending Strain	Strain Rate	Time(sec)
1	0.0	.004	9.991E-5	40
2	.004	.006	4.784E-4	4
3	.006	.008	9.762E-4	2
4	.008	0	-5.0E-3	1.6
5	0	0	0.0	60
6	0	-.004	-9.878E-4	4
7	-.004	-.009	-9.795E-5	50
8	-.009	.006	9.933E-4	15
9	.006	008	9.532E-6	200
10	.008	.01	5.0E-3	.4
11	.01	.01	0	60
12	.01	.015	4.95E-4	10
13	.015	0	-1.4925E-3	15

The Walker model follows the shape of the stress strain curve better than the other models. This could be a result of the better modelling of the back stress growth and the lack of an inelastic strain rate exponent. The model of Krieg, et al. had n = 15.0 and Schmidt and Miller had n = 7.0. The constant values of work hardening have also been reported as reasons for this [3,21]. Bodner's model may be suffering from the lack of a back stress or the effects of the plastic work measure of strain hardening. However, further study would be required to show this. The corrected model of Krieg, et al. reproduces the actual stress levels best after initial yield. No explanation can be given for this at this time.

CONCLUSIONS AND RECOMMENDATIONS

Conclusions and Recommendations based on the Models

The theories of Walker and Bodner with exponentially based inelastic strain rate equations and dynamic recovery terms handle the strain rate sensitivity the best. Bodner's model shows less sensitivity to strain rate jumps possibly due to the plastic work rate measure of strain hardening. The reproduction of the general shape using Walker's model may be aided by better modelling of the back stress term and by the exponentially based inelastic strain rate equation. The drag stress growth law of the Walker model provided the closest fit to data over several cycles at higher strain rates. The second cycle peak seen at the lower strain rates was modelled only by Walker. Bodner's model handled cyclic response best over several cycles at the lower strain rates due to the thermal recovery term. The solute strengthening correction caused numerical instability, negating the effect of thermal recovery during hold times and may have lessened the sensitivity to strain rate jumps.

Future study of these models could take two directions. First, a comparison to a material which does not exhibit strain ageing effects would be beneficial. The corrections necessary to account for this phenomenon masked some of the information which could have been obtained in this work. An example of this is information about the effect of strain jumps on the predictive capabilities of the models. The thermal recovery capabilities of the models were also adversely affected by the strain ageing corrections. The methods for calculating constants should be checked with a positive strain rate sensitive material.

Second, further study which concentrates on the specific model form should be carried out by the use of extended models. These would be models extended from the existing ones. An example of this would be to replace the inelastic strain measure of work hardening in the model of Krieg, et al. with a measure based on plastic work. The inelastic work measure in Bodner's model could be replaced with an inelastic strain measure. The extended models could then provide true insight into the ramifications of using a measure of plastic work. The effect of using an inelastic strain rate equation based on exponential, power law, and hyperbolic sine functions could be studied. The advantages and disadvantages of providing a model with a back stress term could be studied by providing the Bodner model with one as Moreno and Jordan have done [22].

Conclusions and Recommendations based on the Calculation of Constants

The initial assumptions that back stress is responsible for hardening in monotonic tension and drag stress is responsible for cyclic hardening/softening appear to be good assumptions for this material system. These assumptions were used for every model in the hand calculations and the computer iterations with success. Krempl, McMahon, and Yao report that a changing drag stress parameter alters the strain rate sensitivity of the model [23]. This effect was not considered in this work and might warrant further study. The initial assumptions that thermal recovery is negligible for rapid tests ($\dot{\varepsilon} > 1.0\text{X}10^{-14}\ \text{sec}^{-1}$), drag stress recovery dominates in low strain rate cyclic tests, and back stress recovery dominates in creep tests appear difficult to apply in the presence of solute strengthening effects. This material system requires that a correction for solute strengthening be employed before recovery effects can be calculated. The recovery effects were much smaller than the original hand calculations for the models of Krieg, et al., Bodner, and Walker produced. This observation leads to the conclusion that the recovery effects are largely insignificant for $\dot{\varepsilon} > 1.0\text{X}10^{-5}\ \text{sec}^{-1}$. Miller's model requires the recovery terms to be much more active than the other models. This inflexibility gave some problems in the calculation of Miller's constants.

The solute strengthening effects also masked the true strain rate sensitivity of the material. Information on the strain rate sensitivity needs to be obtained outside the region of solute strengthening effects. The following initial assumptions would have been more appropriate based on these observations:

(1) back stress was assumed responsible for hardening in monotonic tension;

(2) drag stress was assumed responsible for cyclic softening;

(3) thermal recovery effects were small and masked by solute strengthening effects;

(4) solute strengthening or strain aging effects masked the basic positive strain rate sensitivity of the material.

The model of Krieg et, al. was an easy model to work with since each term in the growth laws could be scaled somewhat separately of the others. An interesting observation of this model was that the constants of the inelastic strain rate equation could be swept over a broad range but the monotonic hardening remained relatively constant. There was also a mathematical ambiguity between the constant C and the scaling of the drag stress. The scaling could be transferred from one parameter to the other without any visible change in model response.

Bodner's model "converged" to the final constants with fewer iterations than the other models using the iterative scheme developed in this work. This was probably due to the lack of a back stress parameter. A mathematical ambiguity existed between n and the scaling of the internal state variables when information was not available to calculate n. This is why a value for n can often be picked and still produce a workable model.

Miller's model was highly coupled in that the recovery terms were not separated from the hardening terms. The recovery terms can therefore change the same order of magnitude as the hardening terms. Miller readily admits that this model is designed for materials which have a very active drag stress parameter [9]. He states that this model may not be applicable for this type of material system. However, a reevaluation of the constants for Miller's model might prove fruitful. A majority of the constants should be calculated outside the region of solute strengthening effects and without artificially separating the hardening and recovery terms. A solute strengthening parameter would then be added to fit the response to the negative strain rate sensitive region.

Miller's model also maintains control over the saturated states of the internal state variables B and D with the A_1 and A_2 constants. A correction for strain ageing as well as cyclic work softening might be possible by controlling these saturated states. A recommendation for further study based on this model would contain an expanded study of back stress magnitudes over the entire strain rate region considered. A possible method for this is disscussed in reference 11. The latest form of Miller's model [24] should also be studied, as it may be used with material systems similar to this.

Walker's model holds promise for automating the calculation procedure for this type of material. Walker's model has fewer constants, appears to be tailored for this type of material, and can utilize the theta plot concept [2]. The drag stress scaling performs the same strain rate sensitivity functions as the n in the power law related models. Expanding knowledge of the back stress values would also be useful for this model.

Conclusions and Recommendations Based on the Experimental Work

The back stress measuring tests both in creep and in cyclic loading were very subjective and uncertain. However, their extreme usefulness and relative success in application with an automated test set-up warrant further study. It appears possible that these tests can be developed into useful inputs to the constant calculation process. More sensitive data acquisition devises with greater resolution and a smaller and less massive load frame for more precise control would greatly enhance the usefulness of these tests. The subjectivity could be lessened by using a method such as proposed by Blum and

Finkel [14] to analyze the data.

The back stress measuring tests during creep were useful for strain rates less than 1.0X10^{-7} sec^{-1}. The cyclic back stress measuring tests were useful for strain rates greater than 1.0X10^{-4} sec^{-1}. The region between these two tests could be filled by performing tests during monotonic tension such as the stress transient test mentioned by Soloman, Alhquist and Nix [16]. This type of test takes on greater usefulness for a material such as Inconel 718 which exhibits good ductility in tension and high susceptibility to low cycle fatigue.

An automated load frame was invaluable in this work for the complex tests. A smaller load frame might provide more stability during highly sensitive and mode-switching tests. A dead weight load frame would also be useful for the creep and creep-stress drop tests. A more advanced and controllable method of load-up would be a necessity. It would also be useful to utilize the same grips, furnace, extensometer, and data aquisition equipment as with the automated load frame. This would remove some relative errors between the two systems.

REFERENCES

1. *Metals Handbook*, 9th edition, Volume 4 *Heat Treating*, American Society for Metals, Metals Park, Ohio.

2. U. S. Lindholm, K. S. Chan, S. R. Bodner, R. M. Weber, K. P. Walker, and B. N. Cassenti, Constitutive modelling for isotropic materials (HOST), Second annual contract report, NASA CR-174980 (1985).

3. R. D. Krieg, J. C. Swearengen, and R. W. Rhode, A physically-based internal variable model for rate-dependent plasticity. *Proc. ASME/CSME PVP Conference*, 15-27 (1978).

4. C. G. Schmidt, *A Unified Phenomenological Model for Solute Hardening, Strain Hardening, and Their Interations in Type 316 Stainless Steel*, Ph. D. Dissertation, Stanford University, Department of Materials Science and Engineering, (1979).

[illegible]. P. K. Imbrie, W. E. Haisler, and D. H. Allen, Evaluation of the numerical stability and sensitivity to material parameter variations for several unified constitutive models. MM 4998-85-61, Texas A&M University, (1985).

6. S. R. Bodner, Evolution equations for anisotropic hardening and damage of elastic-viscoplastic materials. *Plasticity Today: Modelling, Methods, and Applications*, Elsevier Applied Science Pub., Barking, England, (1984).

7. S. R. Bodner, Review of a unified elastic-viscoplastic theory. AFOSR-84-0042, (1984).

8. J. Friedel, *Dislocations*, Addison Wesley, 277-279, (1967).

9. A. K. Miller, An inelastic constitutive model for monotonic, cyclic, and creep deformation. part I-equations development and analytical procedures, part II-application to type 304 stainless steel. *J. Eng. Mat. Tech.* 98H, 97-113 (1976).

10. K. P. Walker and D. A. Wilson, Creep crack growth predictions in INCO 718 using a continuum damage model. *Pro-ceedings of the 2nd Symposium on Nonlinear Constitutive Relations for High Temperature Applications*, Cleveland, Ohio, (1984).

11. G. H. James, *An experimental comparison of several viscoplastic models at elevated temperature*, M.S. thesis, Texas A&M University, (1986).

12. K. P. Walker, Representation of Hastelloy-X behavior at elevated temperature with a functional theory of viscoplasticity. ASME Pressure Vessels Conference, San Francisco, California, (1980).

13. W. B. Jones, R. W. Rhode, and J. C. Swearengen, Deformation modelling and the strain transient dip test. *Mechanical Testing for Deformation Model Development*, STP 765, ASTM, 102-118 (1982).

14. W. Blum and A. Finkel, *Acta Met.* 30, 1705 (1982).

15. J. R. Ellis and D. N. Robinson, Some advances in experimentation supporting development of viscoplastic constitutive models. *Pro-ceedings of the 2nd Symposium on Nonlinear Constitutive Relations for High Temperature Applications*, Cleveland, Ohio, (1984).

16 A. A. Soloman, C. N. Ahlquist, and W. D. Nix, The effect

of recovery on the measurement of mean internal stresses. *Scripta Met.*, 4, 231, (1970).

17. K. P. Walker, Research and development program for nonlinear structural modelling with advanced time-temperature dependent constitutive relationships. CR-165533, NASA, (1981).
18. J. M. Beek, *A comparison of current models for nonlinear rate-dependent material behavior of crystalline solids*, M. S. Thesis, Texas A&M University, (1986).
19. D. C. Stouffer, A constitutive representation for In-100. AFWAL-TR-81-4039, Wright-Patterson AFB, (1981).
20. D. Yao and E. Krempl, Viscoplasticity theory based on overstress. The prediction of monotonic and cyclic proportional and nonproportional loading paths of an aluminum alloy, *Int. J. of Plasticity*, 1/3, (1985), pp. 259-274.
21. A. K. Miller, Modelling of cyclic plasticity: improvements in simulating normal and anomalous Bauschinger effects. *J. Eng. Mat. Tech.* 102, 215-220 (1980).
22. V. Moreno, and E. H. Jordan, Prediction of material thermomechanical response with a unified viscoplastic constitutive model. *Pro. of the 26th Structures, Structural Dynamics, and Materials Conference*, Orlando, Florida, (1985).
23. E. Krempl, J. J. McMahon, and D. Yao, Viscoplasticity based on overstress with a differential growth law for the equilibrium stress. *Proc. of the 2nd Symposium on Nonlinear Constitutive Relations for High Temperature Applications*, Cleveland, Ohio, (1984).
24. T. C. Lowe and A. K. Miller, Improved constitutive equations for modelling strain softening - part 1: conceptual development and part 2: predictions for aluminum, *J. Eng. Mat. Tech.*, 106, 337-348 (1984).

ORIGINAL PAGE IS
OF POOR QUALITY

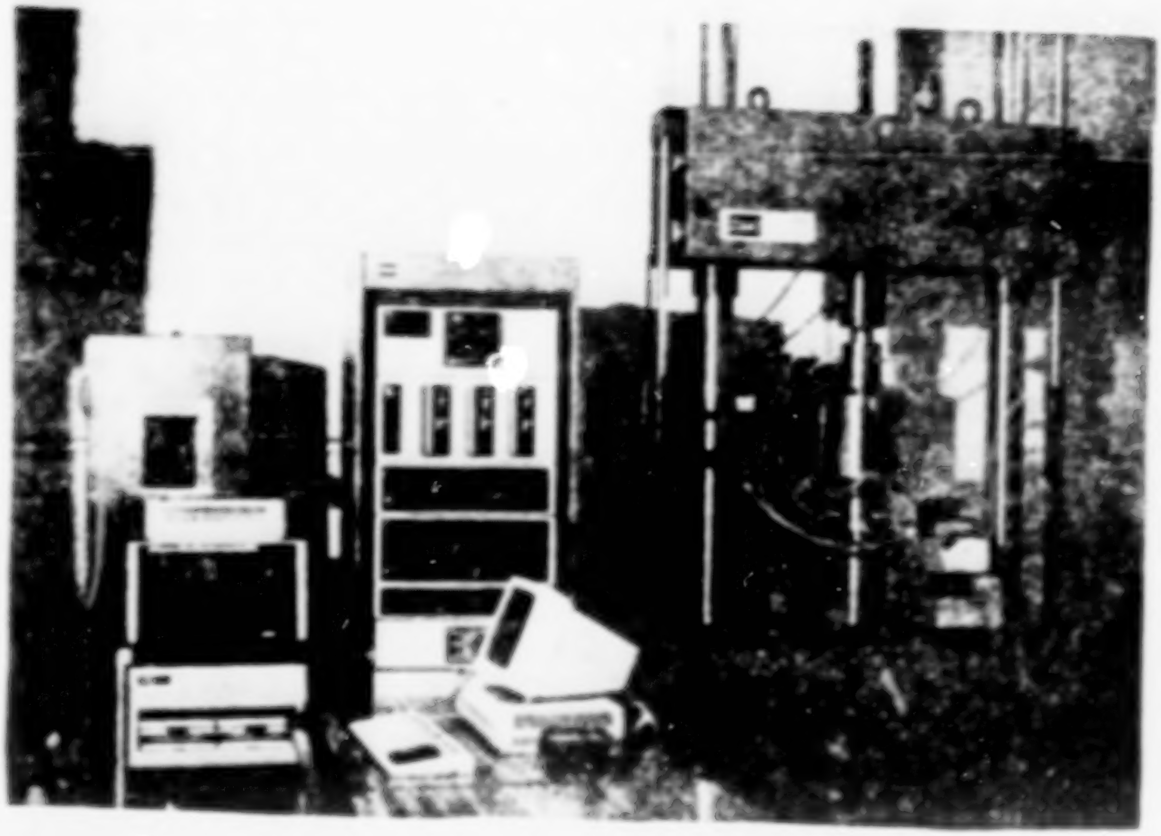

Fig. 1. MTS Configuration

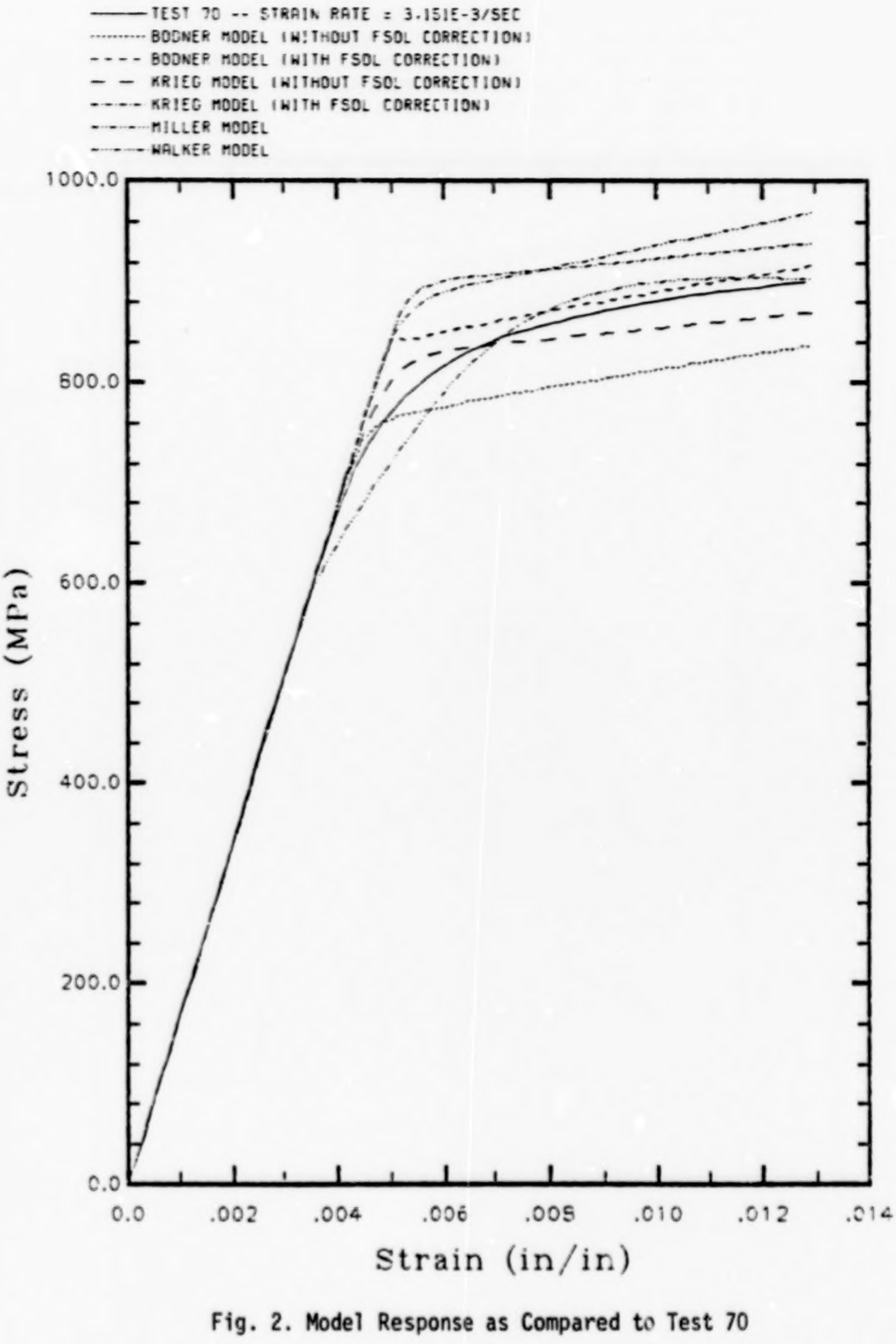

Fig. 2. Model Response as Compared to Test 70

C-4

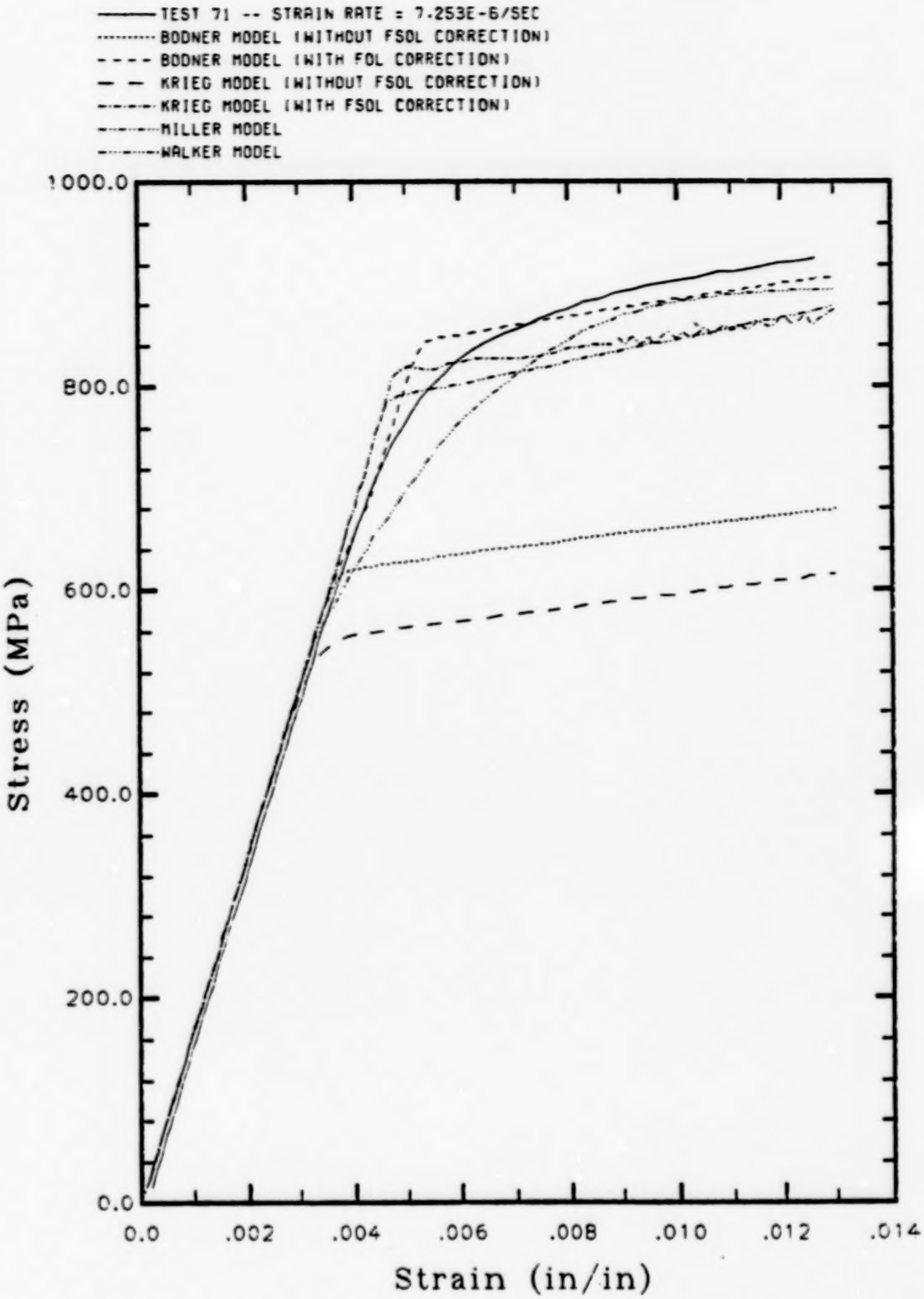

Fig. 3. Model Response as Compared to Test 71

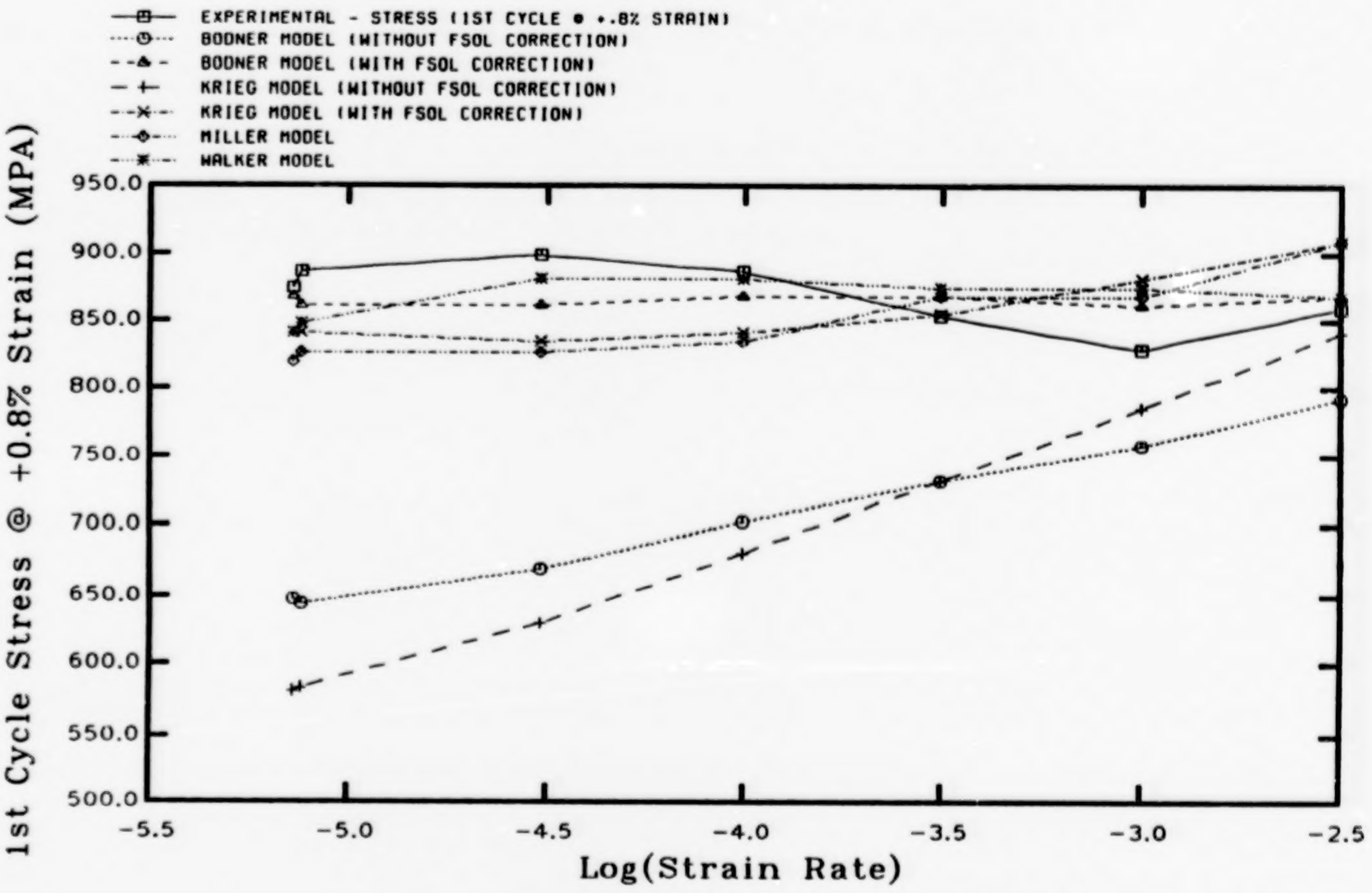

Fig. 4. Stress-Strain Response at +.8% for Cycle 1

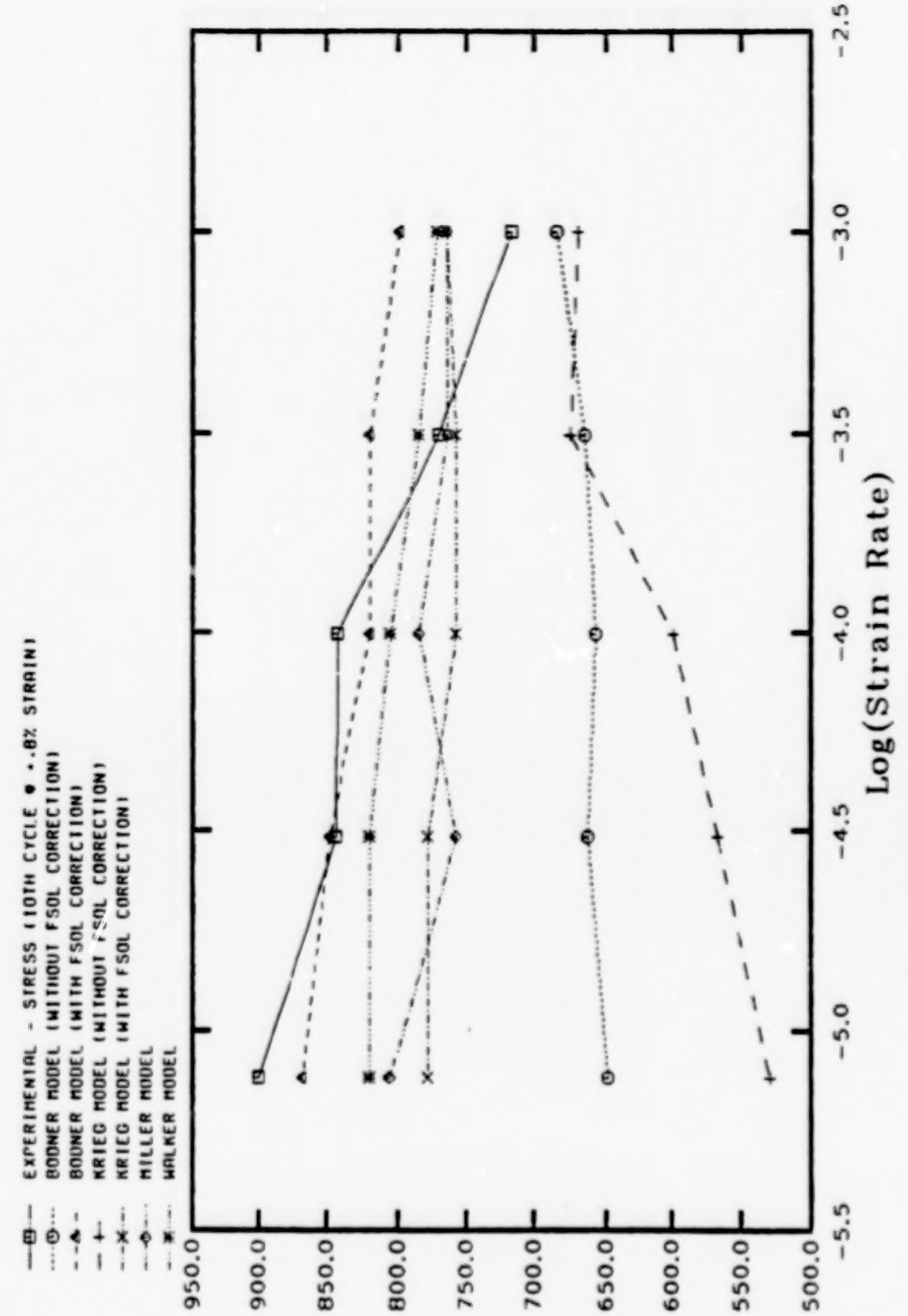

Fig. 5. Stress-Strain Response at +.8% Saturated Cycle

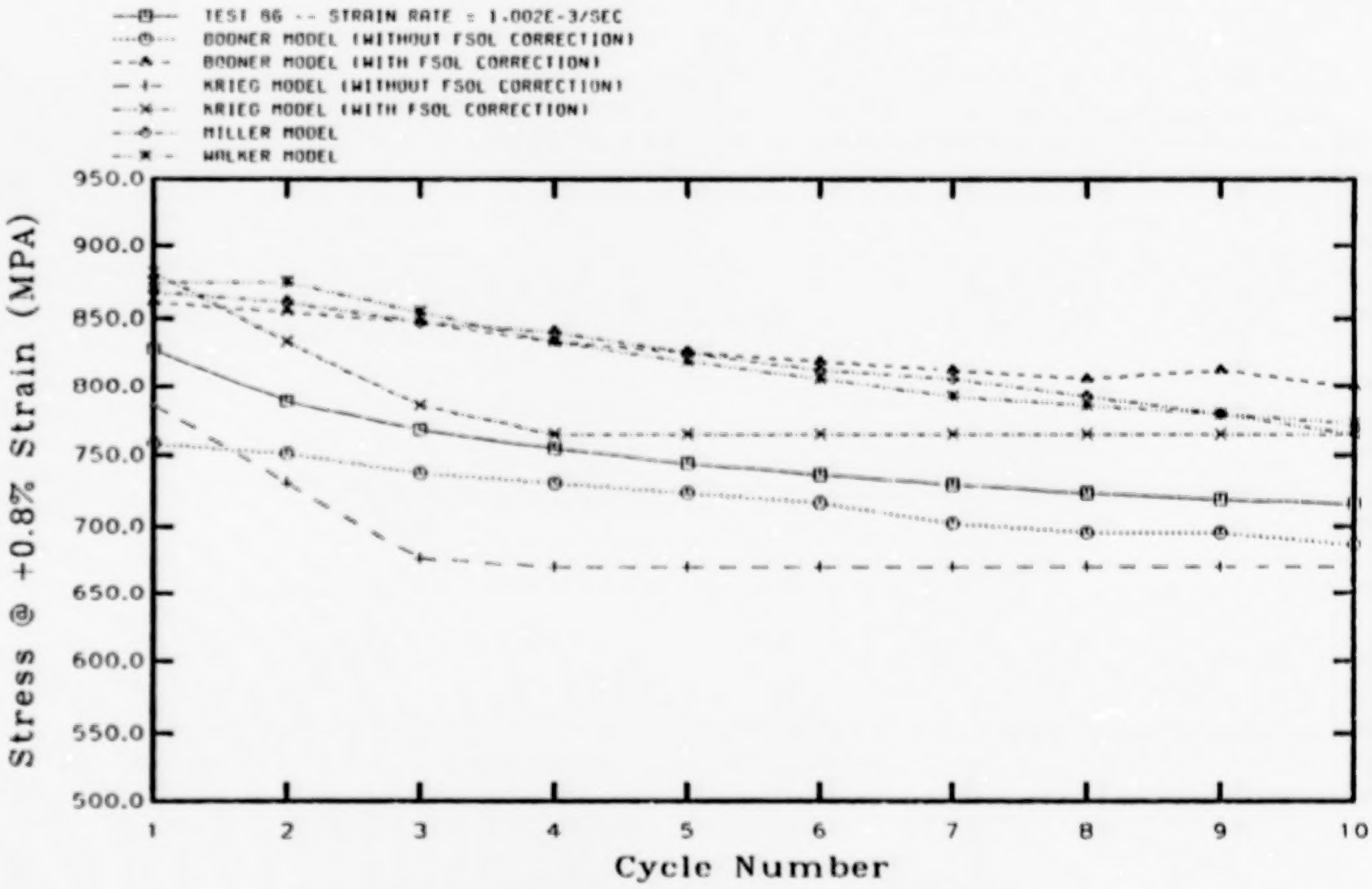

Fig. 6. Test 86 +.8% Response at Each Cycle

ORIGINAL PAGE IS
OF POOR QUALITY

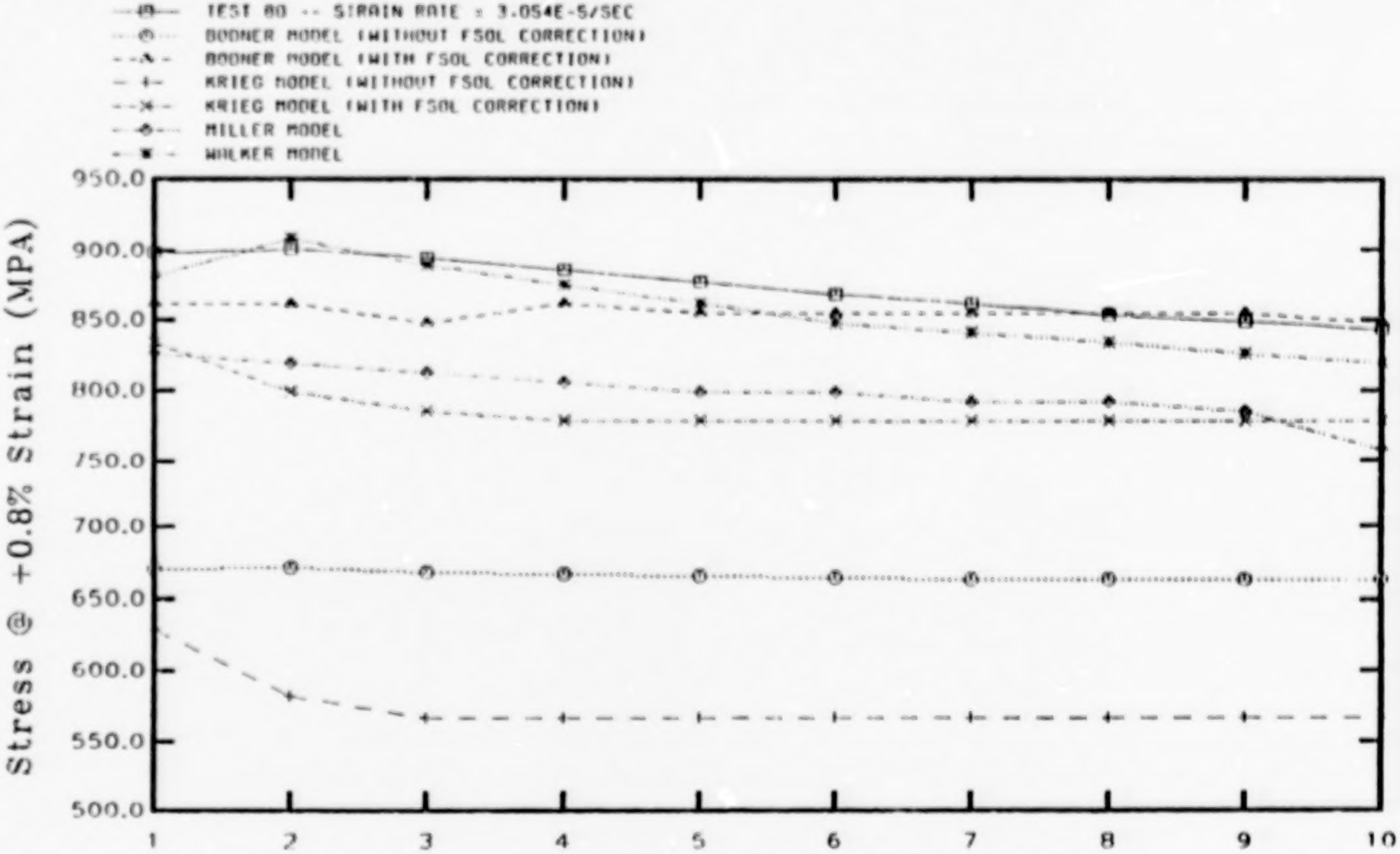

Fig. 7. Test 80   +.8% Response at Each Cycle

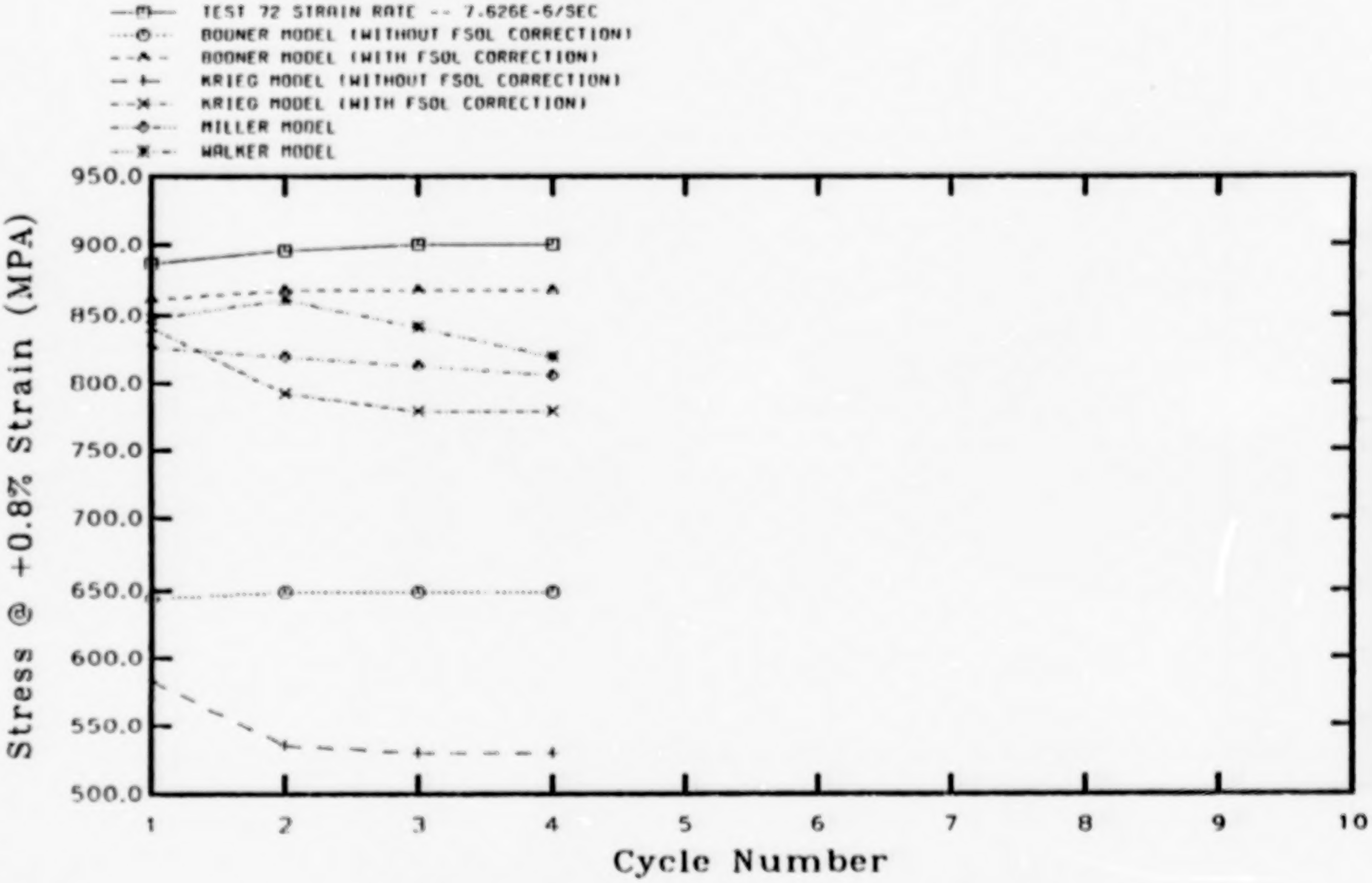

Fig. 8. Test 72 +.8% Response at Each Cycle

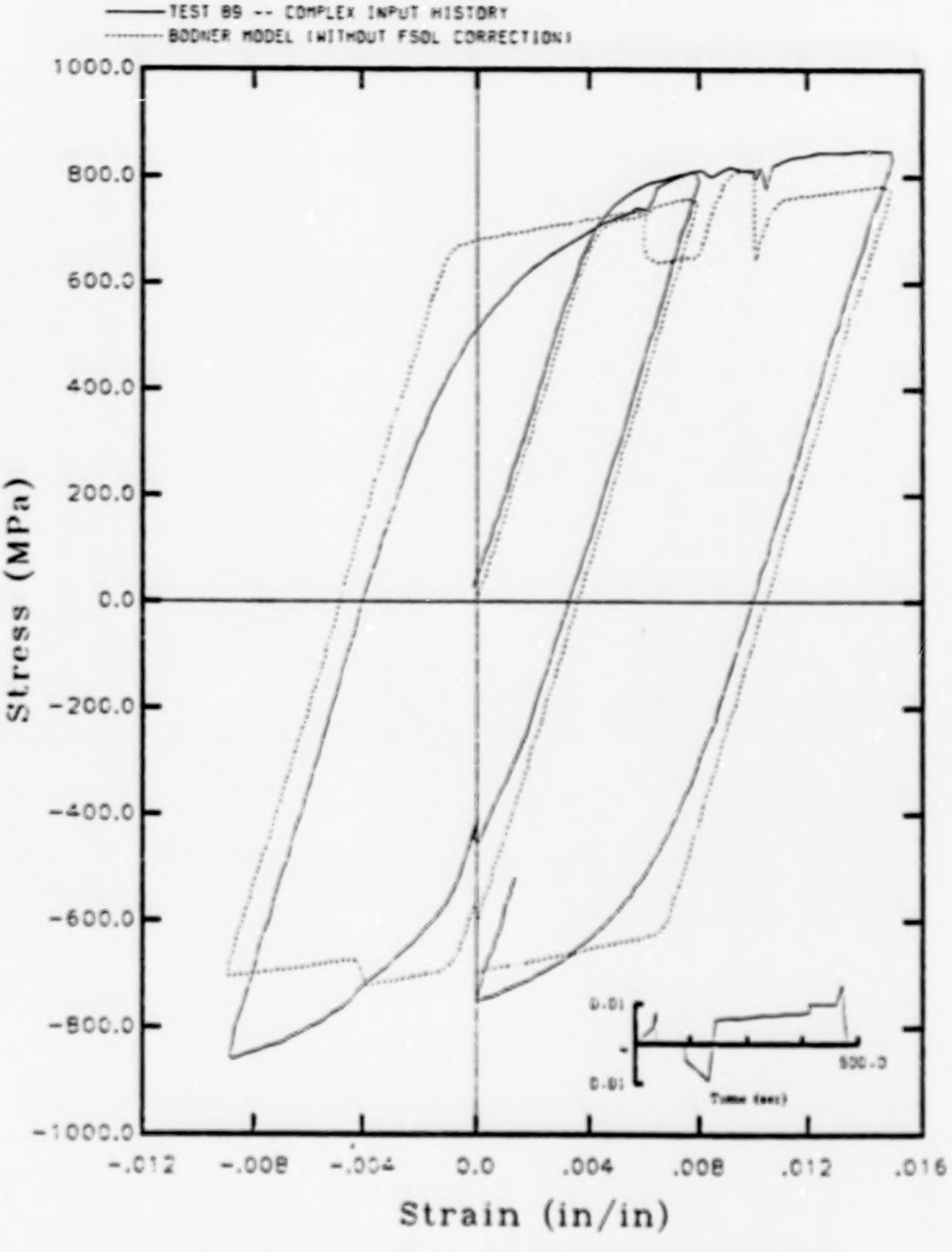

Fig. 9. Complex History - Bodner's Uncorrected Model

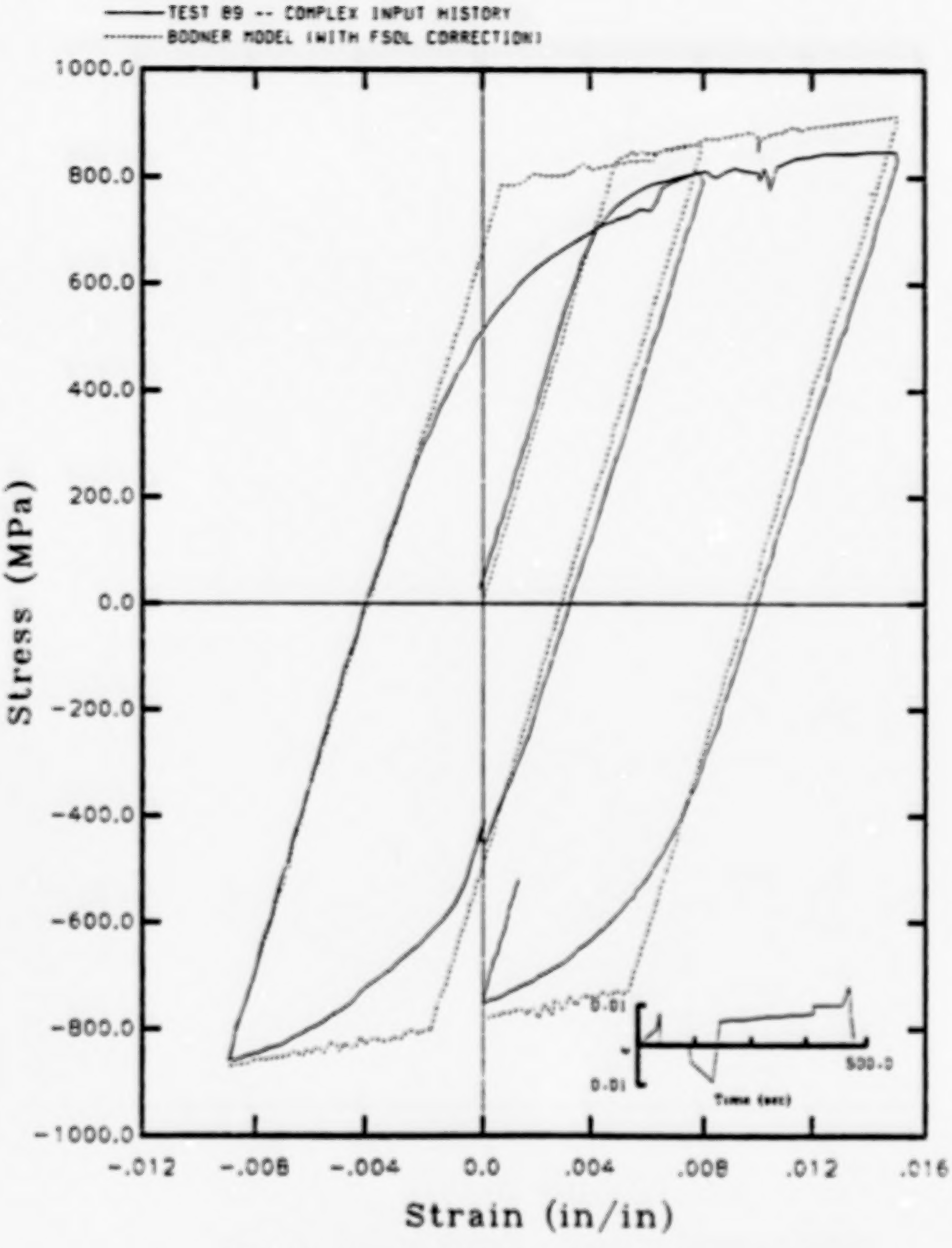

Fig. 10. Complex History - Bodner's Corrected Model

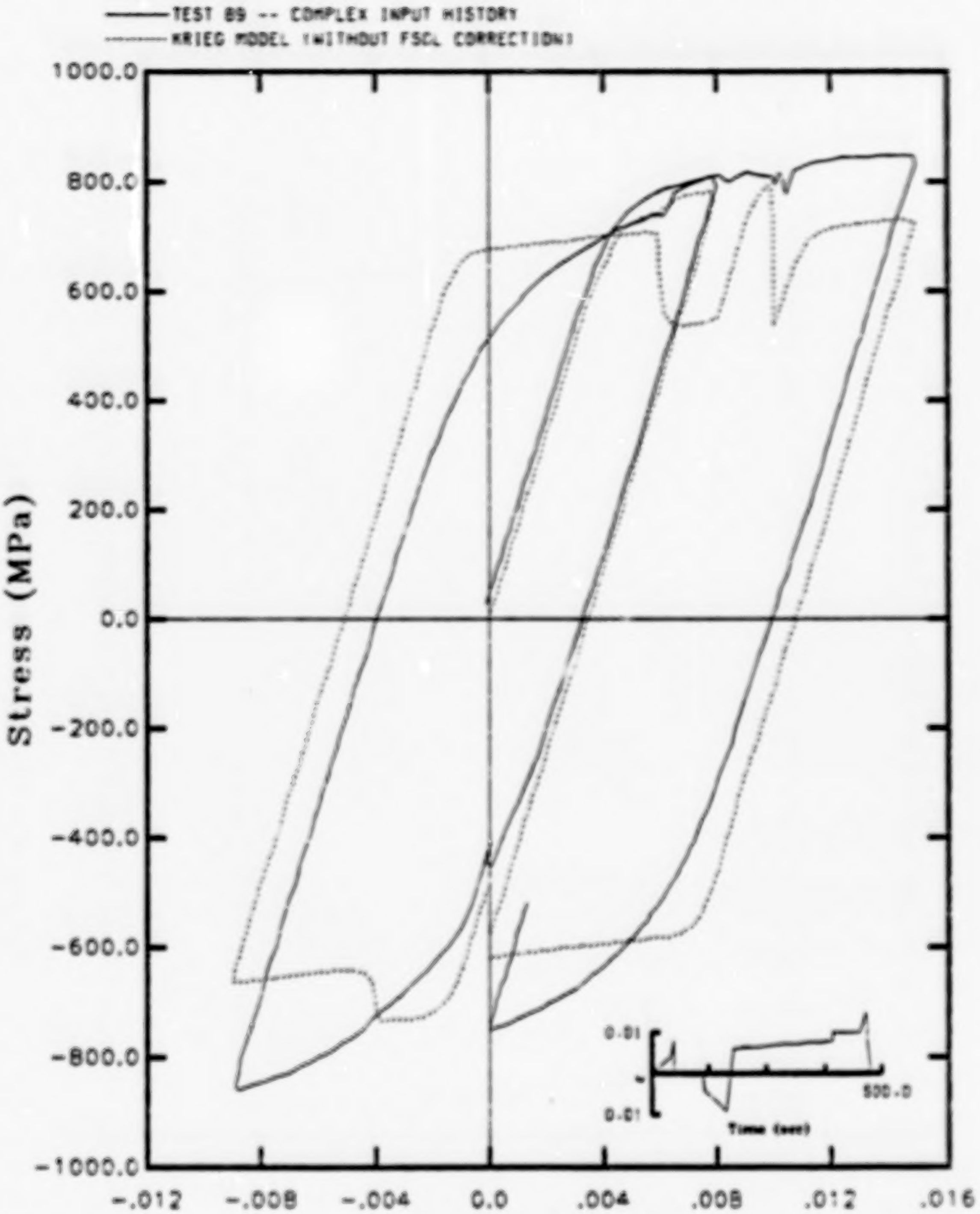

Fig. 11 Complex History - Uncorrected Model of Krieg, et al.

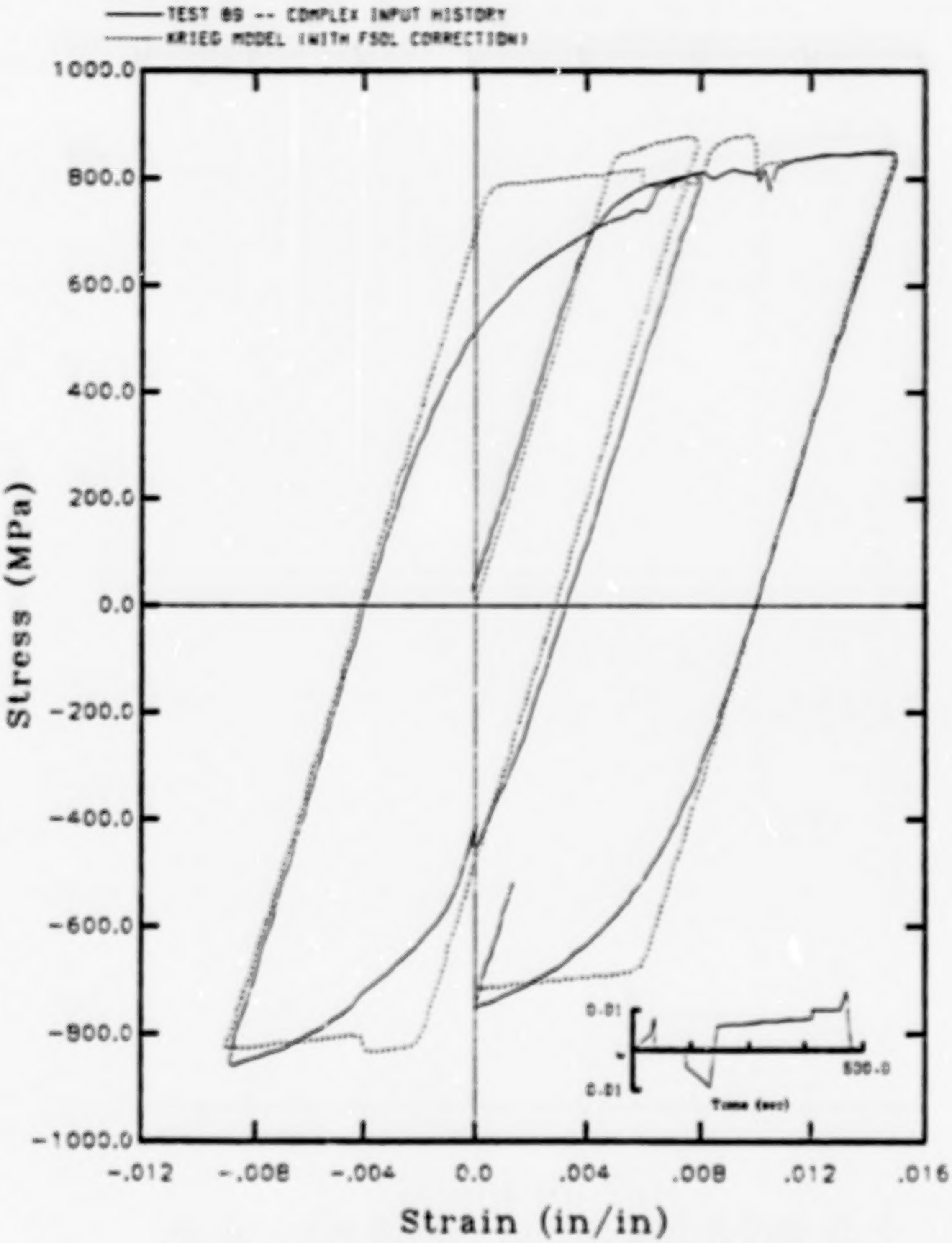

Fig. 12. Complex History - Corrected Model of Krieg, et al.

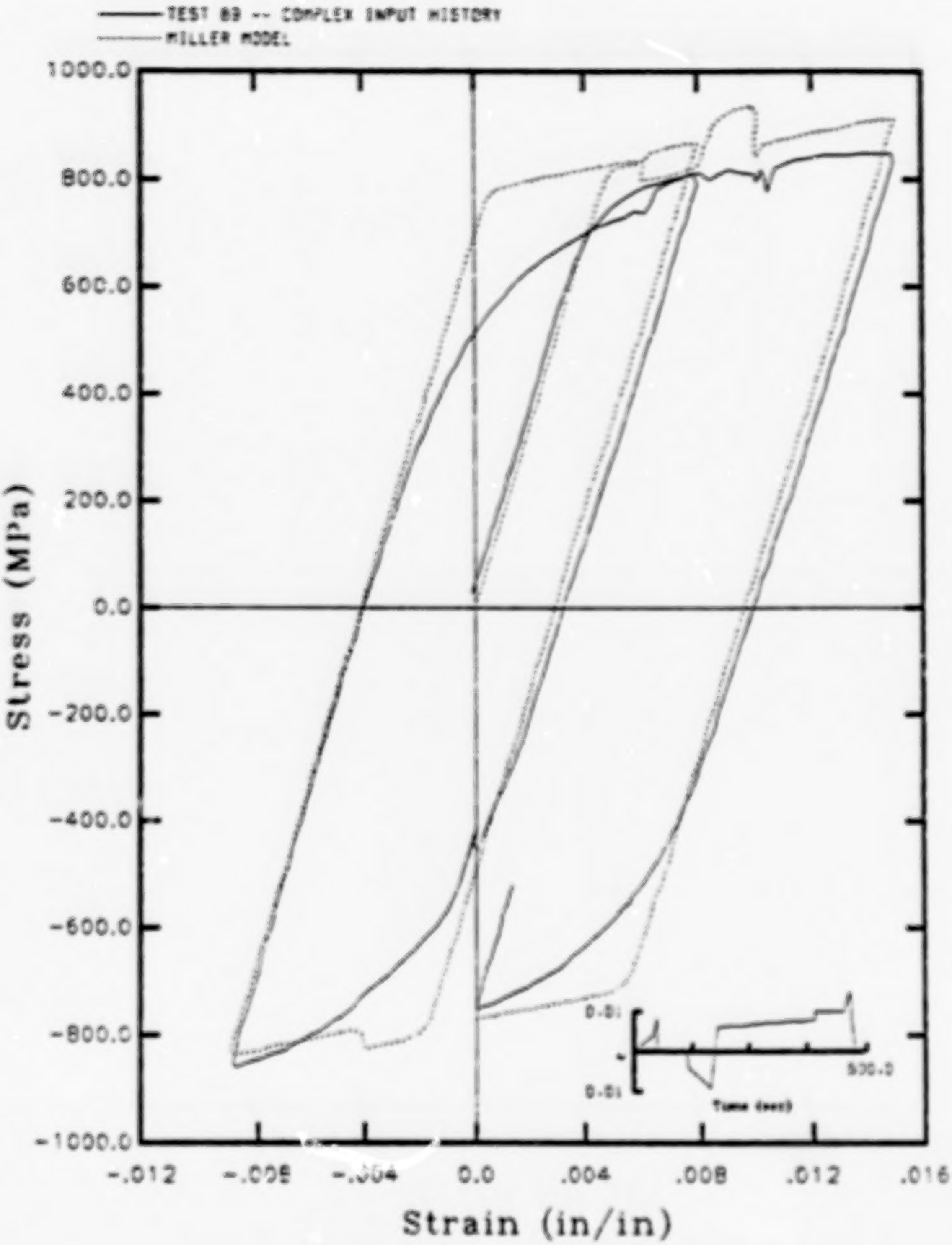

Fig. 13. Complex History - Schmidt and Miller's Model

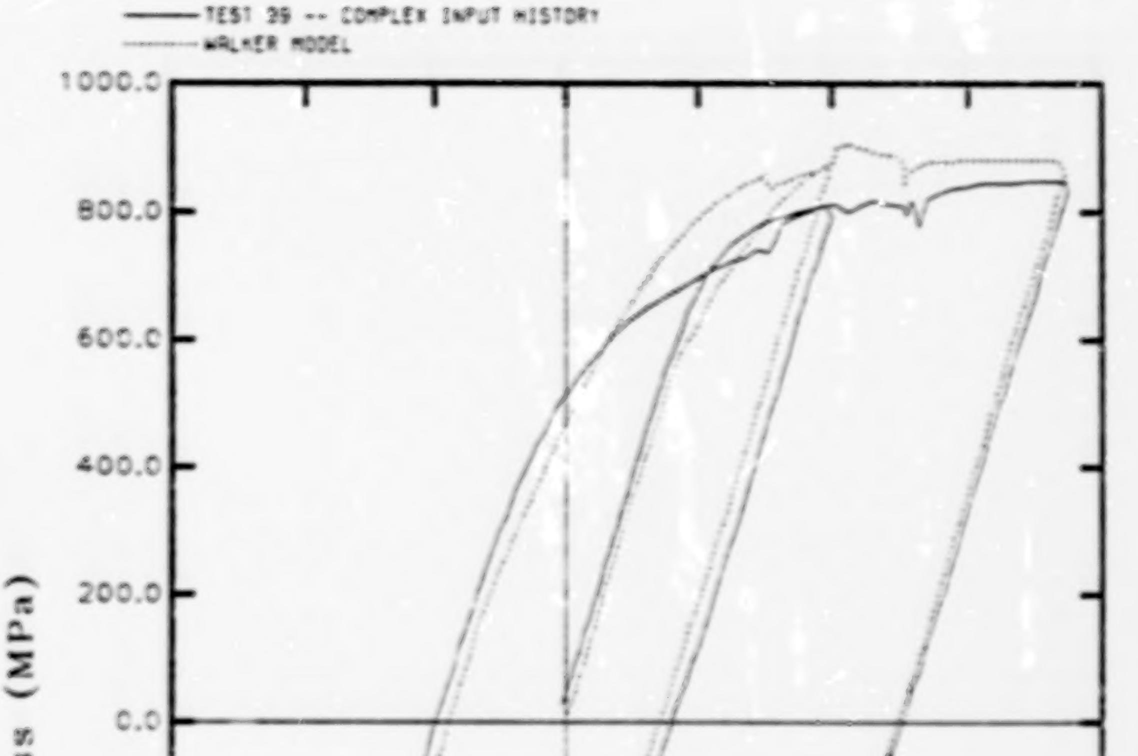

Fig. 14. Complex History - Walker's Model

N88
21517
UNCLAS

N88-21517

THE EFFECTS OF TEMPERATURE AND STRAIN RATE ON THE YIELDING BEHAVIOR OF THE SINGLE CRYSTAL SUPERALLOY PWA 1480

Walter W. Milligan and Stephen D. Antolovich
Fracture and Fatigue Research Laboratory
School of Materials Engineering
Georgia Institute of Technology
Atlanta, Georgia 30332-0245

Recent advances in precision casting techniques and alloy development have allowed the introduction of directionally solidified and single crystalline turbine blades in aircraft gas turbine engines and advanced rocket engines. Because these alloys exhibit complex anisotropic elastic and plastic properties, the conventional continuum-mechanical approach to constitutive modelling is frequently inadequate. This has led designers and analysts to try to understand fundamental metallurgical deformation and damage mechanisms in these alloys, and to incorporate some of these mechanisms in their models. The goal of this project is to characterize these fundamental mechanisms in the nickel-base superalloy PWA 1480, and to interact with the mechanics-oriented analysts in an attempt to develop physically-based constitutive models for this alloy.

In addition to the anisotropic elastic and plastic properties which are inherent to a single crystal, nickel-base superalloy single cyrstals also exhibit complex behavior due to their miocrostructures. The alloys are strengthened by the precipitation of the γ' phase, and this phase is the dominant microstructural feature (about 60 volume % of the alloy). Because γ' is an ordered phase, it shows an anomolous increase in strength with temperature, and also exhibits very complicated orientation-dependent behavior.(1) Because the superalloy is composed of 60% γ', some of this behavior is also evident in the superalloy. However, it must be stressed that the superalloy is a composite structure, consisting of two phases. It is of the highest importance to determine how dislocations interact with the precipitates and with the matrix/precipitate interfaces during deformation. These interactions are very dependent on temperature, strain rate, and stress state.

The first phase of the poject has been completed.(2) Interrupted tensile tests were conducted on <001> oriented single crystals at temperatures from 20-1093°C. Two strain rates were used, 0.5 and 50%/min. After the tests were conducted, the deformation substructures were characterized by transmission electron microscopy (TEM). Although the cyclic work has just recently begun, the results to-date include some unexpected deformation behavior. If these trends are also evident in the cyclic testing, they will have strong implications for the applicability of current constitutive models.

PRECEDING PAGE BLANK NOT FILMED

Figure 1 is a summary of the yield strength data. It can be seen that below 760°C, the strength is independent of temperature and strain rate. Above 760°C, the strength becomes of function of temperature and strain rate, due to the fact that the plastic deformation in this regime is thermally activated. Frequently, thermally activated processes can be characterized very well by an Arrhenius-type relationship of the form:

$$\sigma = A(\exp[Q/RT])$$

where
Q = Activation energy
T = Temperature
R = Gas constant
A = Constant

Figure 2 is a plot of the data in this form. It is seen that the data falls naturally into three temperature regimes. Analysis of the deformation substructures resulted in the same three regimes, and the boundaries of the regimes were the same. Reference (2) should be consulted for details, but a short summary is presented below.

At low temperatures, when the strength was independent of temperature, slip was very crystallographic. Deformation occurred by shearing of the γ' on $\{111\}$ planes. In this regime, the crystallographic models which add plastic shear strains on different systems (both inside and outside the γ') would appear to be generally applicable.

At high temperatures, where the activation energy for yielding was independent of strain rate, slip was extremely homogeneous. Additionally, the γ' was not sheared during deformation. The particles were by-passed by diffusion-controlled climb. In this regime, the γ' was not sheared, so the crystallographic models which consider cube slip within the precipitates would not be applicable.

Intermediate temperatures resulted in transitional behavior.

It must be stressed that the above discussion is limited to deformation during the initial stages of a tensile test, and only the $\{001\}$ orientation was tested. Later in the program, cyclic and off-axis studies will be conducted to see if the conclusions are more general.

References

1. D. P. Pope and S. S. Ezz: Int'l. Metals Review, 1984, vol. 29, p. 136.

2. W. W. Milligan: NASA CR-175100, 1986.

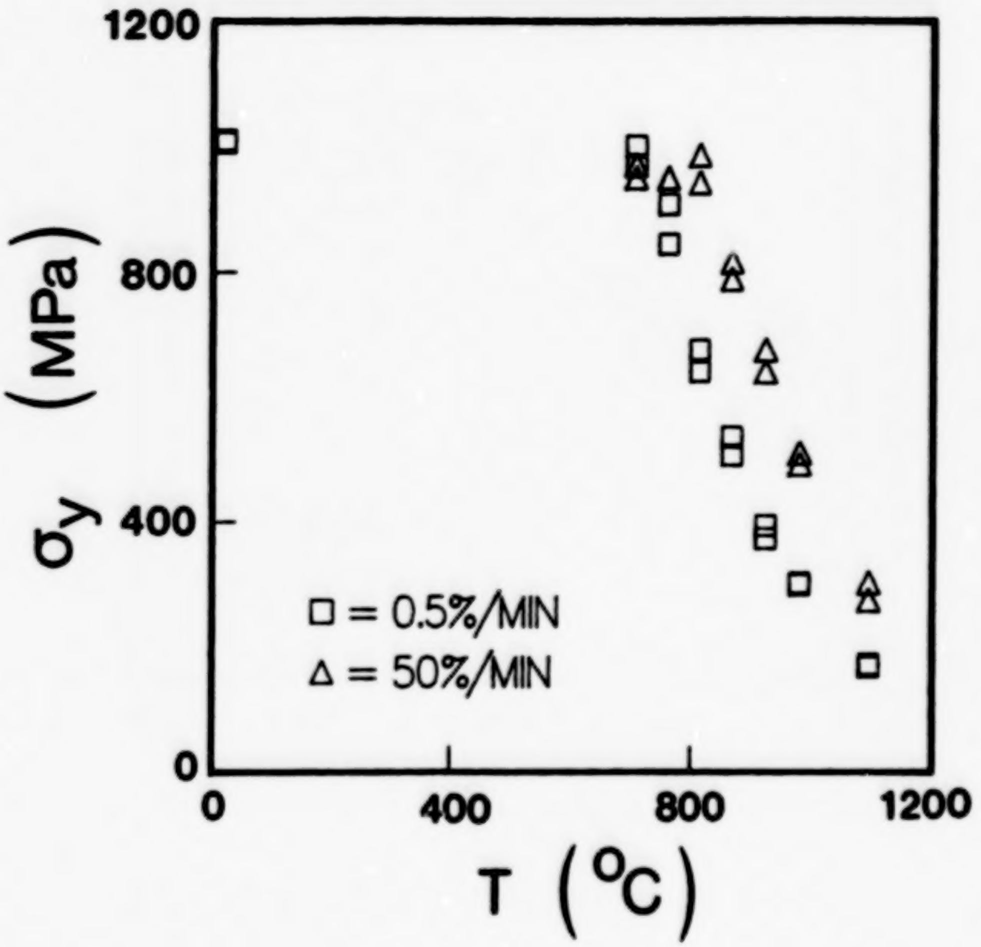

Figure 1. Yield strength at 0.05% offset vs. temperature.

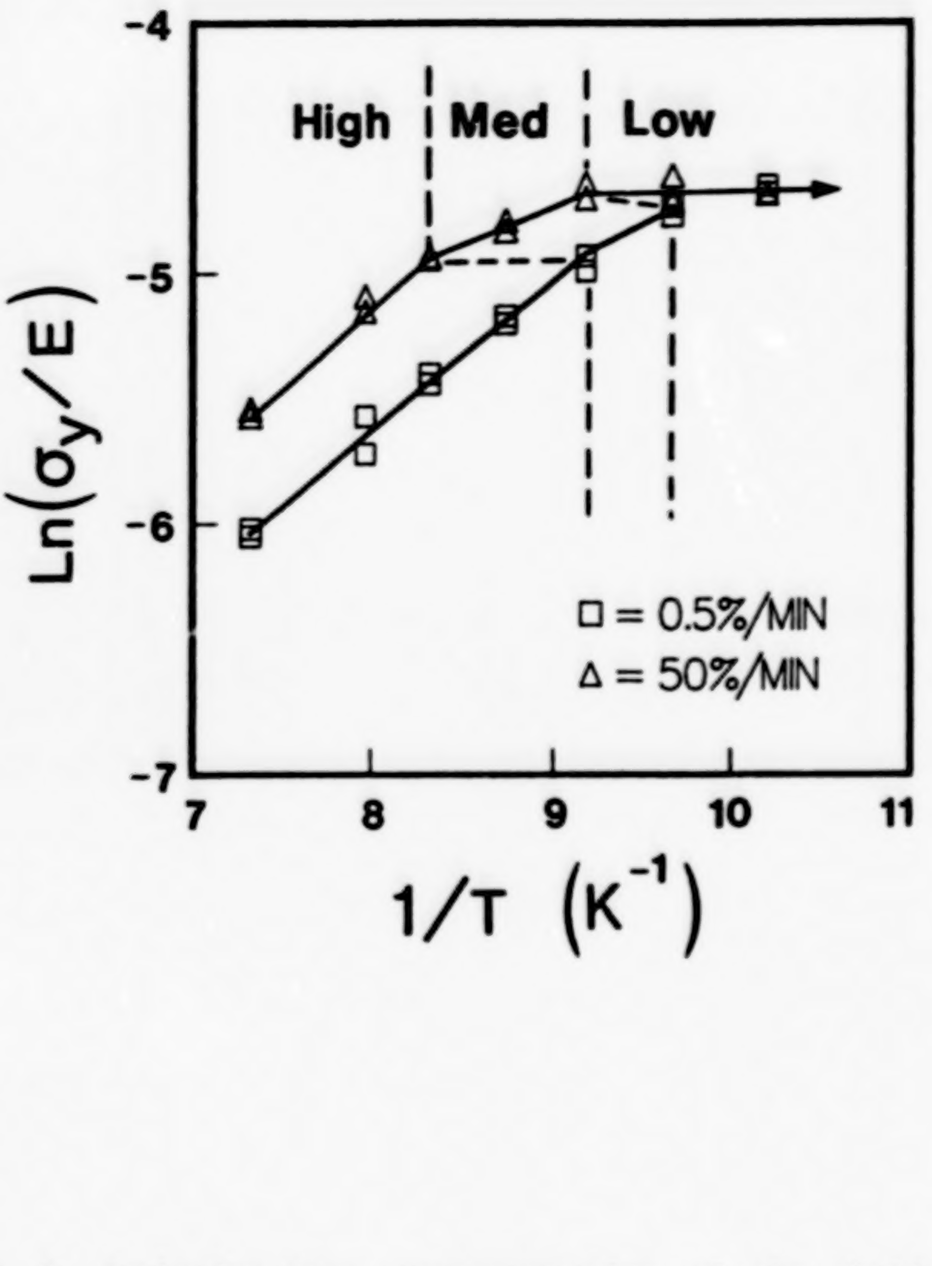

Figure 2. Arrhenius-type respresentation of the yield strength data.

N88
21518
UNCLAS

N88-21518

A Unified Creep-Plasticity Model Suitable for Thermo-Mechanical Loading

D. Slavik, Research Assistant
H. Sehitoglu, Assistant Professor
Department of Mechanical and Industrial Engineering
University of Illinois at Urbana-Champaign
1206 West Green Street
Urbana, IL 61801

1.1 INTRODUCTION

Various unified creep-plasticity constitutive models have been proposed to account for time-dependent material behavior and temperature affects [1-6]. Material constants for the flow rule and the evolution equations are generally determined from a number of material behavior experiments. Model limitations may exist if material behavior predictions are considered outside the temperature or strain rate regime where the material constants have been established. New deformation mechanisms identified in deformation mechanism maps [7] could dramatically affect material behavior, but they may not be represented in the unified equations.

A constitutive model is needed that can account for relative rate insensitive material behavior obtained at low temperatures (plasticity deformation mechanism) as well as highly rate sensitive material behavior observed at high temperatures (power law creep and diffusional flow deformation mechanisms). This is necessary to provide an accurate time-dependent material model for a wide range of temperatures and strain rates.

A constitutive model with accurate rate and temperature predictive capabilities could then be checked with critical thermo-mechanical loading experiments. This is necessary to identify model capabilities and explore model limitations.

1.2 PURPOSE AND SCOPE

In this study:

(1) a unified model is presented for isothermal and thermo-mechanical loading. Predictions are compared to experiments for a wide range of temperatures and strain rates.

(2) deformation mechanisms operative for the alloys considered are incorporated into the constitutive equations.

2. THE CONSTITUTIVE EQUATIONS

The proposed unified creep-plasticity model contains two state variables. The state variable S^c_{ij} is the deviatoric back stress. It is a tensor that defines the center of the stress surface in deviatoric stress space. The second state variable K is the drag stress. It is a scalar that defines the radius of the stress surface in deviatoric stress space. In general, the state variables will evolve throughout the deformation history consistent with the Bailey-Orowan theory [8,9]. The coupled differential equations are

$$\dot{\epsilon}_{ij} = \dot{\epsilon}^{e}_{ij} + \dot{\epsilon}^{in}_{ij} + \delta_{ij}\,\dot{\epsilon}^{th} \tag{1}$$

$$\dot{\epsilon}^{in}_{ij} = f\left[\frac{(S_{ij} - S^{c}_{ij})}{K}\right] \frac{(S_{ij} - S^{c}_{ij})}{\sqrt{\frac{2}{3}(S_{ij} - S^{c}_{ij})(S_{ij} - S^{c}_{ij})}} \tag{2}$$

$$\dot{S}^{c}_{ij} = \frac{2}{3}\, h_{\alpha}\, \dot{\epsilon}^{in}_{ij} - r_{\alpha}\, S^{c}_{ij} \tag{3}$$

$$\dot{K} = h_K - r_K + \theta \dot{T} \tag{4}$$

where $\dot{\epsilon}_{ij}$ is the total strain rate, $\dot{\epsilon}^{e}_{ij}$ is the elastic strain rate (determined with Hook's law), $\dot{\epsilon}^{in}_{ij}$ is the inelastic strain rate, $\dot{\epsilon}^{th}$ is the thermal strain rate, δ_{ij} is the Kronecker delta, $S_{ij} = \sigma_{ij} - \sigma_{kk}\,\delta_{ij}/3$ is the deviatoric stress, $S^{c}_{ij} = \alpha_{ij} - \alpha_{kk}\,\delta_{ij}/3$ is the deviatoric back stress, σ_{ij} is the stress, α_{ij} is the back stress, $\dot{S}^{c}_{ij}$ is the deviatoric back stress rate, $\dot{K}$ is the drag stress rate, $\dot{T}$ is the temperature rate, h_{α} and h_{K} are the hardening functions, r_{α} and r_{K} are the recovery functions, f is the flow rule function, and Θ is a temperature dependence term.

3. 1070 STEEL

A detailed systematic method has been established for determining the material constants from experimental data [10]. Two different flow rules shown in Fig. 1 are considered. Flow rule 1 is determined with plasticity deformation mechanism material behavior only. Flow rule 2 is determined from material behavior operating in the plasticity and power law creep deformation mechanism regimes. The flow rules and evolution equation constants for 1070 steel are shown in Table 1.

Flow rule 1 provides accurate material response simulations when the plasticity deformation mechanism is operative, but it is inaccurate for slow strain rate high temperature simulations when the power law creep deformation mechanism is operative. In Fig. 2, 600°C material response experiments and predictions with flow rule 1 are shown. For $\dot{\epsilon}$ = 2.0e-3 sec^{-1} (plasticity), the predicted response is accurate. For $\dot{\epsilon}$ = 2.0e-6^{-1} sec^{-1}, a different mechanism is operative (power law creep), and the predicted stresses are significantly higher than the experimental values. Deformation mechanisms need to be incorporated into the flow rule and evolution equations to provide accurate strain rate effects.

Flow rule 2 accounts for the high strain rate sensitivity at higher temperatures. In Fig. 3, stable 600°C experimental and predicted response is shown. Accurate rate affects have been achieved. Through the flow rule and evolution equations the model can account for these two deformation mechanisms for a wide range of temperature and strain rates.

Thermo-mechanical total constraint material response is shown in Figs. 4 and 5. The mechanical strain is the sum of the elastic and inelastic strain components. Cycle numbers are shown on the figures at the maximum stress levels. These predictions are independent of the thermal experimental response and provide a good check for the constitutive model. For the thermo-mechanical response, plasticity (low temperature end) and power law creep (high temperature end) are both activated during a cycle. Predictions compare favorably with experiments.

4. CONCLUSIONS AND FUTURE WORK

An experimentally based unified creep-plasticity constitutive model has been implemented for 1070 steel. Accurate rate and temperature affects have been obtained for isothermal and thermo-mechanical loading by incorporating deformation mechanisms into the constitutive equations in a simple way.

Further work on low temperature material behavior for 1070 steel ($T < 400°C$) and on different materials is presently being considered. Preliminary work on 304 stainless steel and nickel alloys show the model applicability to a variety of engineering materials.

REFERENCES

1. Miller, A., "An Inelastic Constitutive Model for Monotonic, Cyclic, and Creep Deformation: Part I and Part II," J. of Engineering Materials and Technology, Vol. 98, pp. 97-113, April 1976.

2. Bodner, S. R., and Merzer, A., "Viscoplastic Constitutive Equations for Copper with Strain Rate History and Temperature Effects," J. of Engineering Materials and Technology, Vol. 100, pp. 388-394, 1978.

3. Walker, K. P., "Research and Development Program for Non-Linear Structural Modelling with Advanced Time-Temperature Dependent Constitutive Relationships," PWA-5700-50, United Technologies Research Center, (also NASA CR-165533), 1981.

4. Robinson, D. N., and Swindeman, R. W., "Unified Creep-Plasticity Constitutive Equations for 2-1/4 Cr-1 Mo Steel at Elevated Temperature," ORNL/TM-8444, October 1982.

5. Abrahamson, T. E., "Modeling the Behavior of Type 304 Stainless Steel with a Unified Creep-Plasticity Theory," Ph.D. Thesis, University of Illinois at Urbana-Champaign, 1983.

6. Slavik, D. C., and Sehitoglu, H., "Constitutive Models Suitable for Thermal Loading," to appear in J. of Engineering Materials and Technology, 1986.

7. Frost, H. J., and Ashby, M. F., Deformation-Mechanism Maps, The Plasticity and Creep of Metals and Ceramics, Pergamon Press, 1982.

8. Bailey, R. W., "Note on the Softening of Strain Hardening Metals and It's Relation to Creep," J. of Institute of Metals, Vol. 35, pp. 27-40, 1926.

9. Orowan, E. J., "The Creep of Metals," West Scotland Iron and Steel Institute, Vol. 54, pp. 45-53, 1946.

10. Slavik, D. C., "A Unified Creep-Plasticity Model for Thermal Loading," Master of Science Thesis, University of Illinois at Urbana-Champaign, 1986.

Table 1 1070 Steel Material

Constitutive Functions

$$\dot{\epsilon}^{th} = \beta \dot{T}$$

$$f\left[\frac{(S_{ij} - S^c_{ij})}{K}\right] = A\ (\bar{\sigma}/K)^n$$

where $A = A' \exp\ [-\Delta H/RT]$

$$\bar{\sigma} = \sqrt{\frac{3}{2}\ (S_{ij} - S^c_{ij})\ (S_{ij} - S^c_{ij})}$$

$$h_\alpha = \begin{cases} a - b\,\bar{\alpha} & \text{for } S^c_{ij}\ \dot{\epsilon}^{in}_{ij} \geq 0 \\ a & \text{for } S^c_{ij}\ \dot{\epsilon}^{in}_{ij} < 0 \end{cases}$$

$$\bar{\alpha} = (\tfrac{3}{2}\ S^c_{ij}\ S^c_{ij})^{\ 1/2}$$

$$r_\alpha = c(\bar{\alpha}/\alpha^*)^d$$

where $c = c' \exp\ [-G/RT]$

$$h_K = 0,\ r_K = 0$$

$$E = e_1 - e_2\ T$$

$$K_0 = h_1 - h_2\ T$$

$$\theta = -h_2$$

Constitutive Constants

Flow Rule #1

$n = 27.9$

Flow Rule #2

for $\bar{\sigma}/K \leq 1$, $n = 5.4$
for $\bar{\sigma}/K > 1$, $n = 27.9$

$\beta = 1.7 \times 10^{-5}/K$
$A' = 4.0 \times 10^{9}\ \text{sec}^{-1}$
$\Delta H = 210.6$ KJ/mole
$a = 40000$ MPa
$b = 100$
$\sigma^* = 100$ MPa
$d = 3.2$
$c' = 5.0 \times 10^{14}\ \text{sec}^{-1}$
$G = 248.4$ KJ/mole

For $T \leq 713$ K (440°C)

$e_1 = 210710$ MPa, $e_2 = 31.0$ MPa/K
$h_1 = 273.6$ MPa, $h_2 = 0.04$ MPa/K

For $T > 713$ K (440°C)

$e_1 = 385260$ MPa, $e_2 = 275.7$ MPa/K
$h_1 = 501.3$ MPa, $h_2 = 0.32$ MPa/K

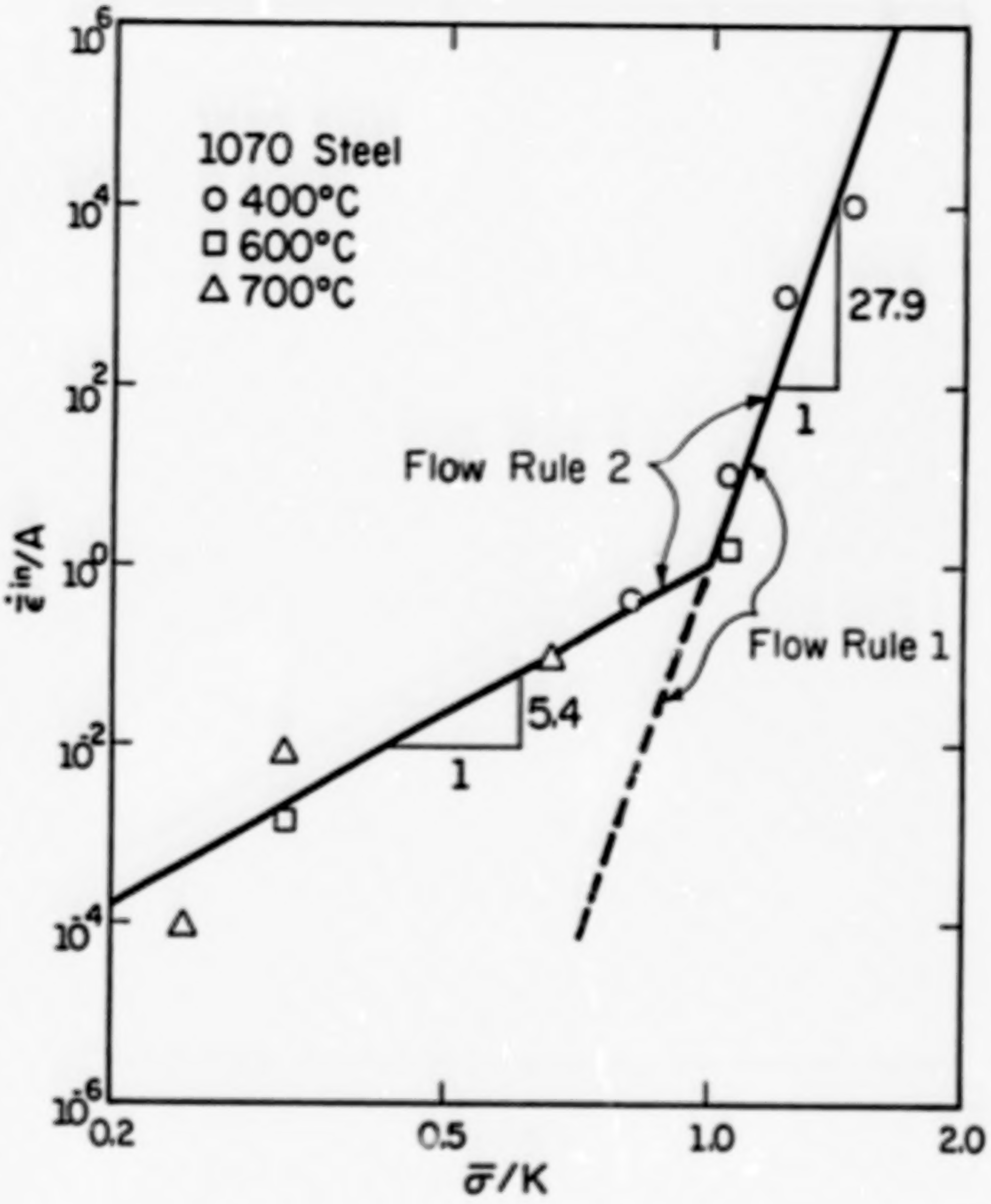

Figure 1 1070 Steel Flow Rule (400°C - 700°C)

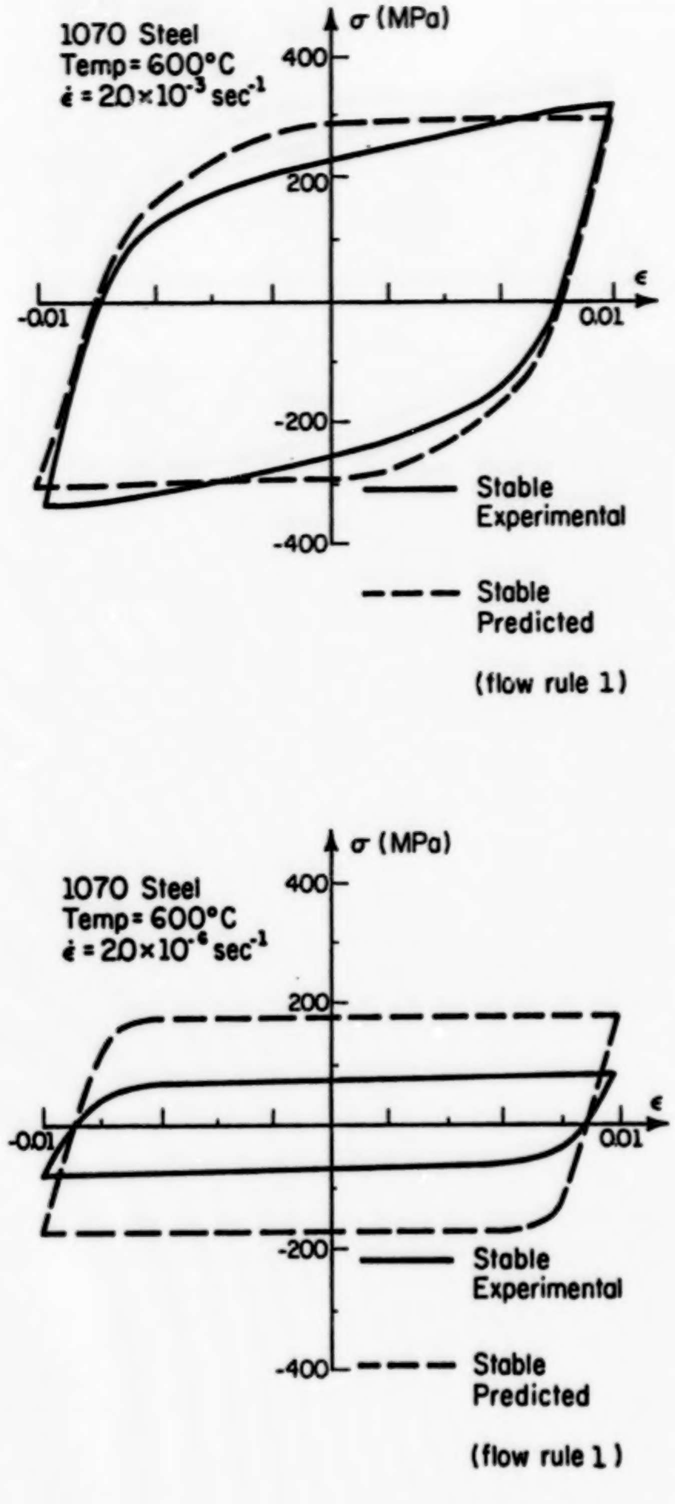

Figure 2 1070 Steel Experimental and Predicted Material Response, 600°C (flow rule 1)

(a) $\dot{\epsilon} = 2.0 \times 10^{-3}\mathrm{sec}^{-1}$ (b) $\dot{\epsilon} = 2.0 \times 10^{-6}\mathrm{sec}^{-1}$

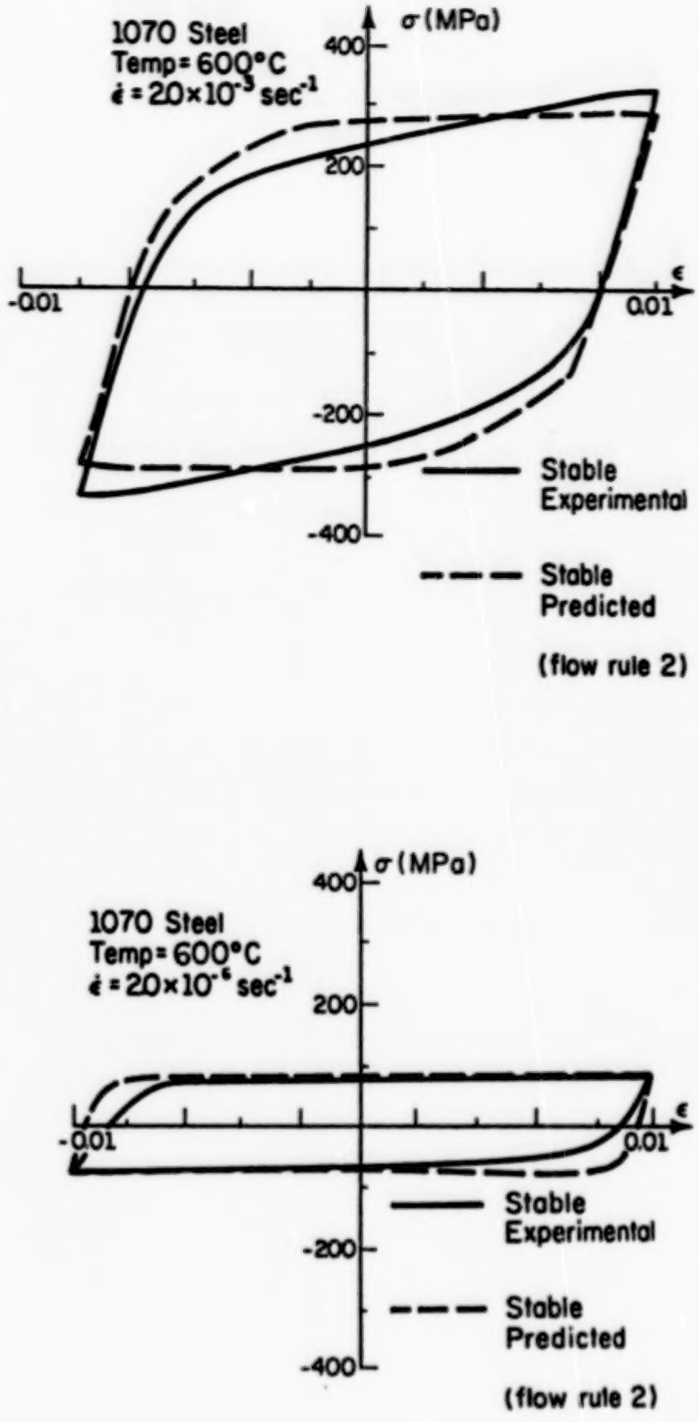

Figure 3 1070 Steel Experimental and Predicted Material Response, 600°C (flow rule 2)

(a) $\dot{\varepsilon} = 2.0 \times 10^{-3} \text{sec}^{-1}$ (b) $\dot{\varepsilon} = 2.0 \times 10^{-6} \text{sec}^{-1}$

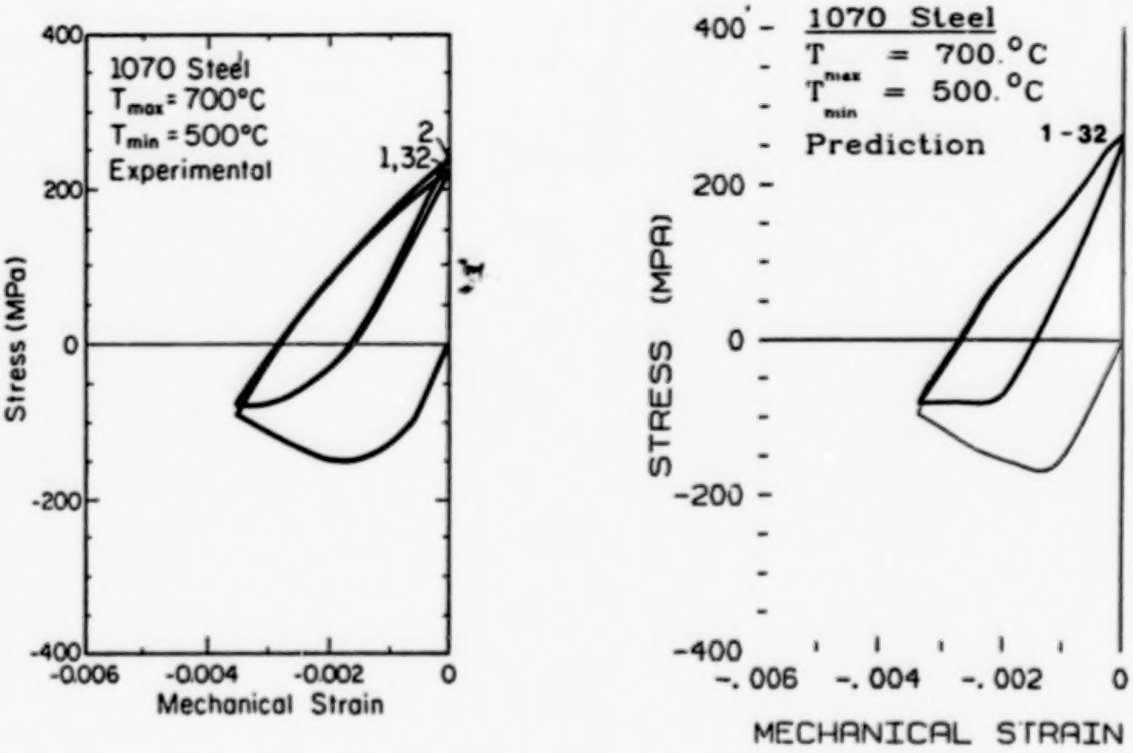

Figure 4 1070 Steel Thermo-Mechanical Material Response, 500°C - 700°C

(a) Experiment (b) Prediction

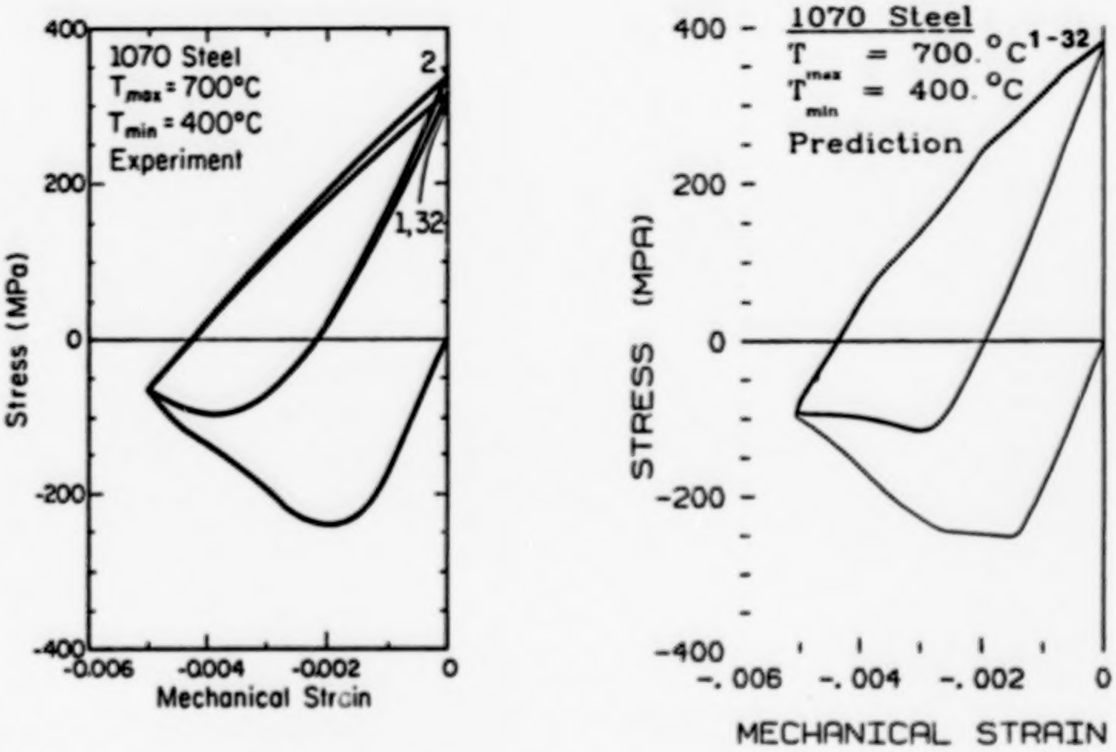

Figure 5 1070 Steel Thermo-Mechanical Material Response, 400°C - 700°C

(a) Experiment (b) Prediction

N88
21519
UNCLAS

N88-21519

On the Global/Local Time Incrementing for Viscoplastic Analysis

A. F. Saleeb, T. Y. Chang, J. Y. Chen
Department of Civil Engineering
The University of Akron
Akron, Ohio 44325

1. INTRODUCTION

There has been a great deal of research work in modeling the inelastic deformation behavior of materials at the elevated temperature environment. It appears that a unified approach in the form of viscoplastic relations has been most popular for prediction of material responses. In this context, a number of viscoplastic material models have been published in the literature [e.g. 1-6]. The unified approach differs from the conventional creep and plasticity theory in that both the creep and plastic deformations, or alternately termed inelastic deformations, are treated as time-dependent quantities. Based on the experimental and theoretical studies performed by various investigators [3,4,7-9], it is known that viscoplastic constitutive relations, in principle, are capable of predicting material responses at high temperatures such as cyclic plasticity, rate sensitivity, long-term creep deformations, strain-hardening or softening, etc. The degree of success of a constitutive relationship varies depending on the extent of parameters considered in or mathematical sophistication of a specific model.

Although most of viscoplastic models give improved material response predictions over the classical approach, the associated constitutive differential equations have stiff regimes which present numerical difficulties in time-dependent structural analysis. The numerical difficulty is indeed an important concern when the viscoplastic relations are applied to large scale finite element structural analysis.

In finite element analysis for viscoplastic materials, two issues of primary concern in connection with the associated material nonlinearity: 1) solution convergence in solving the global (incremental) equilibrium equations, 2) integration of the constitutive rate equations at the local material points (or element integration points). Numerically, these two issues are inter-related. On the one hand, global equilibrium can not be achieved if the stresses calculated at local material points are grossly inaccurate. On the other hand, the constitutive relations and stresses are not representative to the material if the strains computed from the nodal displacements are in error.

In view of the above discussion, we have therefore investigated a combined global/local incrementing scheme for the finite element analysis of viscoplastic materials.

2. GLOBAL INCREMENTING

Due to the material nonlinearity, a viscoplastic problem is effectively formulated by an incremental approach, in which the finite element equilibrium equations can be linearized. In order to solve these equations successfully, the analyst must be able to specify "appropriate" load steps. If the loading increments are too large, the solution may not converge, or it is far from being accurate. Alternatively, if the loading increments are very small, the computation cost will become prohibitively high. Therefore, it is desirable to implement an automatic incrementing procedure in which the selection of (global) load steps can be made by the program, rather than the analyst.

Use of automatic load stepping for solving nonlinear problems is not new and most of the applications were concentrated at time independent problems [10-11]. Herein, we adopted similar concepts for the solution of time dependent viscoplastic problems. The procedure involves two major steps: 1) initiation of incremental solution, and 2) selection of subsequent load increments. Each of the two steps is briefly outlined below.

(1) Initiation of incremental solution - the solution begins with a specified load vector, i.e.

$$\underset{\sim}{R}_1 = \alpha \cdot \underset{\sim}{R} \qquad (1)$$

where α = a load factor, < 1.

$\underset{\sim}{R}$ = a reference load vector.

With the above load vector, solution will proceed with equilibrium iterations. When the number of iterations reaches four and the solution has not yet converged, an estimate is made to project the number of iterations required according to

$$n = i + \ln(DTOL/d_i)/(\ln d_i - \ln d_{i-1}) \qquad (2)$$

where i = number of iterations already performed.

DTOL = iteration tolerance for displacements.

d_i = ratio between the incremental displacement norm of the i-th iteration and total displacement norm.

$= | \Delta \underset{\sim}{U}_i | \, / \, | \underset{\sim}{U}_i |$

If n is greater than a maximum number of iteration cycles allowed, then a new load vector is set to be $\underset{\sim}{R}_1^{NEW} = \tau \underset{\sim}{R}_1$, $\tau<1$.

(2) Subsequent load increments - The load increments, subsequent to the first step, are determined on the basis of a constant arc length method [12-14]. In this method, let the current load vector be

$$\underset{\sim}{R}_{i+1} = \lambda_{i+1} \underset{\sim}{R} \tag{3}$$

where λ_{i+1} = a load parameter corresponding to the (i+1)-th iteration

$$= \lambda_i + d\,\lambda_{i+1} \tag{4}$$

and d λ_{i+1} is calculated from a quadratic algebraic equations [13].

3. LOCAL INCREMENTING

Once the global load increment is determined from the method outlined in the above, a sub-incrementing method is incorporated at the material point level to integrate the rate constitutive equation. For the purpose of discussion, the viscoplastic constitutive equations are written in the form

$$\dot{\underset{\sim}{y}} = \underset{\sim}{f}\,(\underset{\sim}{y}, t) \tag{5}$$

where $\underset{\sim}{y}$ represents the vector of stress, inelastic strain and state variables, and $\underset{\sim}{f}$ is a vector of nonlinear functions. To integrate the preceding equations, we have developed an automatic procedure based on the variable-step Runge-Kutta (R-K) method. In this method, the global time increment Δt is divided into a number of sub-increments, i.e. $h = \Delta t/n$. Corresponding to h, the vector $\underset{\sim}{y}$ for iteration (i+1) is evaluated by the 4th order and 5th order R-K formulas, respectively, i.e. $\underset{\sim}{y}_{i+1}^{(4)}$ and $\underset{\sim}{y}_{i+1}^{(5)}$. Then an error can be estimated from

$$E_{st} = \| \underset{\sim}{y}_{i+1}^{(5)} - \underset{\sim}{y}_{i+1}^{(4)} \| / h \tag{6}$$

The calculated error must be within the following tolerance

$$E_{st} < \epsilon \; || \underset{\sim}{y_i} || / \Delta t \tag{7}$$

If the above condition is violated, a revised sub-increment h' is then obtained from

$$h' = \tau h$$

$$\tau = \left\{ \frac{\epsilon \; || \underset{\sim}{y_i} ||}{E_{st} \cdot \Delta t} \right\}^{\frac{1}{4}} \tag{8}$$

The foregoing procedure is repeated until the criterion in Eq. (7) is satisfied.

4. NUMERICAL EXAMPLE

Several problems have been analyzed using the procedure outlined in the preceding sections. Presented herein is a thick walled cylinder subjected to an internal pressure, varying linearly from 0 to 14.6 psi for $t \in [0, 40\text{sec.}]$ The cylinder material is assumed to be 2-1/4 Cr-Mo common steel at 811° k and Robinson's viscoplastic model is adopted. For finite element analysis, five 4-noded axisymmetric elements are used.

The analysis was performed by using four different combinations of numerical algorithms:

1) Automatic global and local incrementing (G + L)
2) Automatic global incrementing (G) with constant local steps $h = \Delta t/n_s$, $n_s = 2, 4,$ and 8
3) Automatic local sub-incrementing (L) with constant global steps, N = 5, 10, 16, and 20.
4) Constant global and local steps.

Summarized in Table 1 are the algorithm details, CPU time on IBM-3033 computer, and radial displacement at the outer surface of the cylinder. It is seen that with the automatic global/local incrementing algorithm, the lowest CPU time was consumed. Convergence difficulty was experienced if only the automatic global or local incrementing scheme was optioned unless the number of solution steps or the number of sub-increments is significantly increased. Shown in Figure 1 is the load vs. radial displacement at the outer surface of the cylinder calculated from two different algorithms, i.e. automatic global/local incrementing and constant global stepping with automatic local incrementing. Both algorithms gave almost identical results.

5. CONCLUSION

Presented in this paper is a global/local time incrementing scheme for viscoplastic analysis of structures. The scheme is very efficient and useful for conducting large scale nonlinear finite element analysis involving viscoplastic materials.

REFERENCES

1. Miller, A.K., "An Inelastic Constitutive Model for Monotonic Cyclic, and Creep Deformation", ASME Journal of Engineering Materials and Technology, Vol. 98, 1976, pp. 97-113.

2. Kreig, R.D., Swearingen, J.C., and Rohde, R.W., "A Physically-based Internal Variable Model for Rate-Dependent Plasticity", Inelastic Behavior of Pressure Vessel and Piping Components, T.Y. Chang and E. Krempl Eds., ASME PVP-PB-028, 1978, pp. 15-28.

3. Walker, K.P., "Representation of Hastelloy-X Behavior at Elevated Temperature with a Functional Theory of Viscoplasticity", Paper presented at ASME/PVP Century 2 Energy Technology Conference, San Francisco, CA, Aug. 1980.

4. Hart, E.W., "Constitutive Relations for the Nonelastic Deformation of Metals", ASME Journal of Engineering Material and Technology, Vol. 98, 1976, pp. 193-202.

5. Robinson, D.N., "A Unified Creep-Plasticity Model for Structural Metals at High Temperature", ORNL/TM-5969, Oak Ridge National Laboratory, Oct. 1978.

6. Bodner, S.R., and Patrom, Y., "Constitutive Equations for Elastic-Viscoplastic Strain-Hardening Materials", ASME Journal of Applied Mechanics, Vol. 42, 1975, pp. 385-389.

7. Chaboche, J.L., and Rousselier, G., "On the Plastic and Viscoplastic Constitutive Equations", Inelastic Analysis and Life Prediction in Elevated Temperature Design, Edited by G. Baylac, ASME PVP-Vol. 59, 1982, pp. 33-35.

8. Larsson, B., and Storakers, B., "A State Variable Interpretation of Some Rate-Dependent Inelastic Properties of Steel", ASME Journal of Engineering Materials and Technology, Vol. 100, 1978, pp. 395-401.

9. Snyder, M.D., and Bathe, K.J., "A Solution Procedure for Thermo-Elastic-Plastic and Creep Problems", Journal of Nuclear Engineering and Design, Vol. 64, 1981, pp. 49-80.

10. Bathe, K.J., and Dvorkin, E.N., "On the Automatic Solution of Nonlinear Finite Element Equations", Computers & Structures, Vol. 17, No. 5-6, 1983, pp. 871-879.

11. Crisfield, M.A., "A Fast Incremental/Iterative Solution Procedure that Handles Snap-Through", Computers & Structures, Vol. 13, 1981, pp. 55-62.

12. Riks, E., "An Incremental Approach to the Solution of Snapping and Buckling Problems", Int. J. Solids Structures, 15, 1979, pp. 529-551.

13. Ramm, E. "Strategies for Tracing Nonlinear Responses Near Limit Points", In Nonlinear Finite Element Analysis in Structural Mechanics, Edited by Wunderlich et al., Springer-Verlag, New York, 1981, pp. 63-89.

14. Crisfield, M.A., "Variable Step-Lengths for Nonlinear Structural Analysis", TRR Lab., Rep. 1049, 1982.

Table 1 A COMPARISON OF DIFFERENT SOLUTION ALGORITHMS FOR A THICK-WALLED CYLINDER

Case No.	Option	Global Steps	Local Substeps	CPU Unit	$U_0 10^{-2}$ Inch
1	G + L	16	--	11	0.1851
2A	G	16	8	100	0.1851
2B	G	16	4	57	0.1851
2C	G	--	2	solution diverged,	(note 5)
3A	L	20	--	35	0.1851
3B	L	16	--	36	0.1856
3C	L	10	--	45	0.1879
3D	L	5	--	solution diverged,	(note 6)
4A	N	20	4	37	0.1851
4B	N	20	2	solution diverged,	(note 5)

Note:

1. G+L - both global and local automatic incrementing.
2. L - local automatic incrementing only.
3. G - global automatic incrementing only.
4. N - manual incrementing
5. In cases 2C and 4B, solution diverged at steps 6 and 3, respectively, because the values of material state variables are out of bound.
6. In case 3D, solution diverged at step 5 because out-of-balance load was greater than incremental load.
7. U_0 is the radial displacement at outer surface of the cylinder.

ORIGINAL PAGE IS
OF POOR QUALITY

Geometry and Idealization:

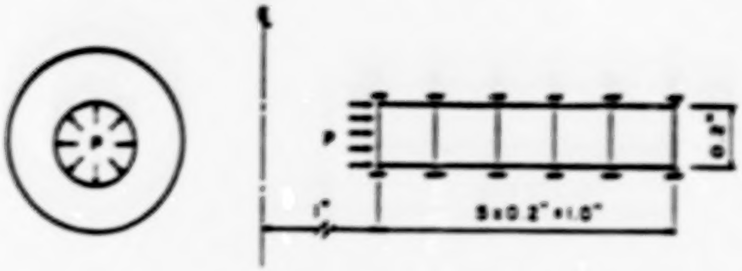

Loading History

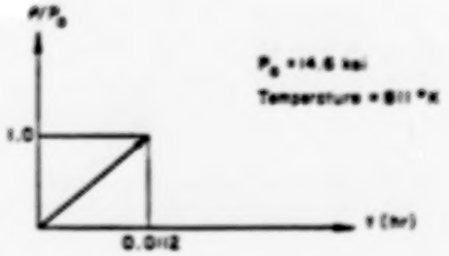

P/P$_0$
P_0 = 14.5 ksi
Temperature = 811 °K
1.0
0.0112
t (hr)

Material Model:

Robinson Viscoplastic Model

CR-MO $2\frac{1}{4}$ common steel

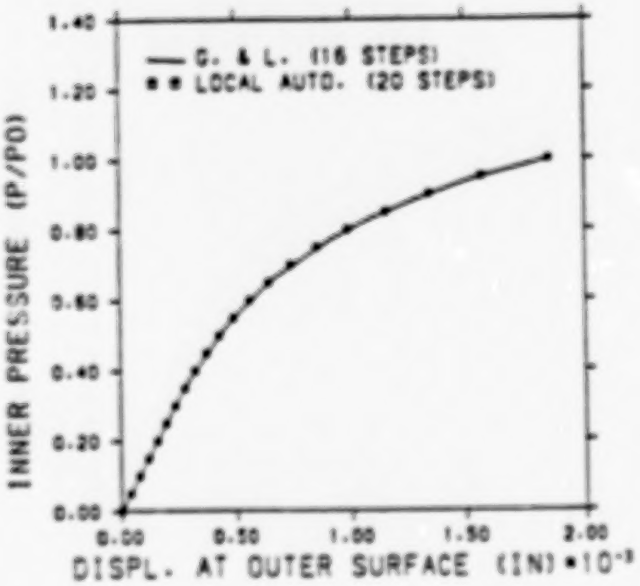

Figure 1. A Thick-Walled Cylinder
Under Internal Pressure

N88
21520
UNCLAS

N88-21520

AN AUTOMATED PROCEDURE FOR MATERIAL PARAMETER EVALUATION FOR VISCOPLASTIC CONSTITUTIVE MODELS

P.K. Imbrie, G.H. James, P.S. Hill,
D.H. Allen, and W.E. Haisler
Texas A&M University
College Station, Texas 77843

An automated procedure is presented for evaluating the material parameters in Walker's exponential viscoplastic constitutive model for metals at elevated temperature. Both physical and numerical approximations are utilized to compute the constants for Inconel 718 at 1100°F. When intermediate results are carefully scrutinized and engineering judgement applied, parameters may be computed which yield stress output histories that are in agreement with experimental results. A qualitative assessment of the θ-plot method for predicting the limiting value of stress is also presented. The procedure may also be used as a basis to develop evaluation schemes for other viscoplastic constitutive theories of this type.

PRECEDING PAGE BLANK NOT FILMED

INTRODUCTION

A large number of unified viscoplastic theories are currently being developed for metals[1]. These models generally require the evaluation of numerous material parameters before they can be utilized. These constants are highly coupled to one another, and, due to the nonlinearity and stiffness of the governing equations, they are difficult to evaluate. The evaluation of these parameters is normally accomplished in a heuristic way due to the complexity of the models, so that the values of the constants are dependent on the person evaluating them. The purpose of this research was to develop an automated procedure for the evaluation of material parameters utilized in Walker's exponential viscoplastic constitutive model for metals at elevated temperature[2,3]. The procedure developed herein entails a synthesis of physical and numerical approximations which use various combinations of experimental data, as well as engineering intuition to determine the constants. The impetus for this work was two-fold. First, automated procedures for determining the material parameters are needed if standardized material parameters are ever to be realized. Second, in order to improve the present theories, a thorough understanding of the approximations and/or assumptions made during their development and subsequent usage is required.

While the model developed by Walker is only one of many currently being used, similarities are notable in a number of other theories such as those proposed by Krieg, Swearengen, and Rhode[4], Bodner[3], and Schmidt and Miller[5]. Therefore, it is believed by these authors that the general procedure presented herein may be applied to other models such as those mentioned above.

THE MODEL

The model proposed by Walker is a viscoplastic theory which uses a flow law for the inelastic strain rate, which is an exponential in stress. The growth law modeling back stress is of the hardening/recovery form and accounts for both dynamic and static thermal recovery. The drag stress term models isotropic hardening, thus accounting for the cyclic hardening or softening characteristics of metals. The uniaxial differential form of Walker's exponential model may be written as:

$$\dot{\epsilon}^I = \frac{\exp(\frac{\sigma - B}{D}) - 1}{\beta} \operatorname{sgn}(\sigma - B) \quad , \tag{1}$$

$$\dot{B} = n_2\dot{\epsilon}^I - B(|n_3 + n_4 \exp(-n_5|\log(\frac{\dot{R}}{\dot{R}_0})|)|\ \dot{R} + n_6) , \tag{2}$$

$$D = D_1 - D_2 \exp(-n_7 R) \ , \tag{3}$$

$$\dot{R} = |\dot{\epsilon}^I| \ , \tag{4}$$

where σ is the applied stress, ϵ^I is the inelastic strain, B is the back stress, and D is the drag stress. A superposed dot above the variables denotes differentiation with respect to time. The material parameters for this model are β, n_2, n_3, n_4, n_5, n_6, n_7, D_1, and D_2 . Therefore, nine constants need to be evaluated, in addition to Young's Modulus E and the strain aging parameter $\dot{R}_0$. These same constants are required for the multiaxial formulation, in addition to Poisson's ratio.

The experiments required to determine the constants for Walker's model using the procedure developed herein include: 1) A series of constant strain rate steady state hysteresis loops under fully reversed strain controlled conditions (Fig. 1); 2) cyclic hold tests performed on the unloading branch of the cyclic tests (Fig.2); and 3) long term monotonic tension tests (Fig. 3).

The cyclic hold tests are used to measure the back stress and are performed by cycling a material until saturated conditions are reached. Hold times are then inserted at various points in the unloading region as shown in Fig. 2. If the test frame is in load control, then the back stress is equal to the applied stress when no creep is observed for a given hold time.

The monotonic tension and cyclic hold tests are used to evaluate the material parameters found in the inelastic strain rate equation and the back stress growth law, whereas the cyclic hysteresis tests are used primarily to obtain constants for the isotropic hardening variable. The monotonic tests may not be necessary if acceptable values of the limiting stress (σ_{1im}) can be obtained from the first half cycle of the cyclic tests. The aforementioned experiments were performed on Inconel 718 at 1100° F. A complete description of the test procedures and results may be found in reference [6].

DETERMINATION OF THE CONSTANTS

The procedure for determining the material parameters in Walker's theory is described in the ensuing paragraphs. The equations, which are a result of both physical and numerical approximations, can be coalesced into a single interactive computer code. Since approximations are made, from time to time the user may have to judiciously select some constants in order to complete the constant calculation process. The reason for this can be an insufficient data base, poor experimental results, or a material response that the model cannot handle.

Evaluation of the material parameters begins by plotting σ_{1im} versus ln $(\dot{\varepsilon}^I)$. A nonlinear representation signifies that strain aging and/or thermal recovery effects are present and thus need to be modeled. If σ_{1im} is not obtained experimentally, it can be estimated in a manner similar to that proposed by Lindholm, et al.[2].

If σ_{1im} is to be estimated, then under conditions of uniaxial tension loading, when $\dot{\varepsilon}^I$ is assumed to be a constant and equal to the applied strain rate and $\exp(\frac{\sigma-B}{D}) >> 1$,eq. (1) may be written as:

$$\sigma = D \ln (\beta\dot{\varepsilon}^I) + B \quad . \tag{5}$$

Using the evolution equation defining the back stress (eq. (2)) and the assumption that D remains constant during monotonic loading, then $d\sigma/d\varepsilon^I$ (or Θ) may be written as:

$$\Theta = n_2 - B[n_3 + n_4 \exp(-n_5 |\log (\frac{\dot{R}}{\dot{R}_0})|) + n_6/\dot{\varepsilon}^I] \quad . \tag{6}$$

Thus, equations (5) and (6) can be combined, yielding

$$\Theta = -N\sigma + [n_2 + ND\ln(\beta\dot{\varepsilon}^I)] \quad , \tag{7}$$

where

$$N = n_3 + n_4 \exp(-n_5|\log(\frac{\dot{R}}{\dot{R}_0})|) + n_6/\dot{\varepsilon}^I \quad . \tag{8}$$

Therefore, equation (7) indicates that a plot of Θ versus σ should be linear at low inelastic strains, having a slope of N and an x-intercept of σ_{1im} . The θ- plot is obtained by plotting stress versus inelastic strain (as shown in Fig. 4(a)) to find $\sigma(\varepsilon^I)$, which in general is a n^th order polynomial. This function is then numerically differentiated and plotted versus stress to produce the θ- plot (see Fig. 4(b)). Hence, values of N and σ_{1im} can be obtained for each monotonic tension test using a linear regression scheme. If acceptable values of σ_{lim} are obtained experimentally, the θ- plot may still be used to determine N. In this situation, the linear fit results in a slope which is forced to pass through σ_{lim} .

The constant n_5 is computed by determining where the effect of strain aging is considered negligible and may be written as:

$$n_5 = -[\ln(\tau)/|\log(\frac{\dot{R}_1}{\dot{R}_0})|] . \qquad (9)$$

The constants $\dot{R}_0$ and $\dot{R}_1$ represent the strain rate at which the strain aging correction is a maximum and minimum, respectively, and τ denotes the residual correction at rate $\dot{R}_1$. It should be noted that τ also affects the rate of decay of the strain aging correction and selection of too small a value will result in a very localized correction.

The next step in this procedure is to compute the dynamic and static thermal recovery constants n_3, n_4, and n_6 using equation (8). Assuming that a limiting value of stress has been obtained, then $\dot{\varepsilon}=\dot{\varepsilon}^I$ and eq. (8) can be written a number of times, corresponding to the different monotonic tests (denoted by the subscript i) as:

$$N_i = n_3 + n_4 f_i + n_6/\dot{\varepsilon}_i^I , \qquad (10)$$

where

$$f_i = \exp(-n_5|\log(\frac{\dot{R}_i}{\dot{R}_0})|) . \qquad (11)$$

Thus, the three parameters n_3, n_4, and n_6 may be obtained simultaneously using a multiple linear regression scheme. A plot of this curve fit will indicate if acceptable values of the dynamic and thermal recovery parameters have been found. In the event that poor results are obtained (as shown in Fig.5) , one of the following actions can be taken: 1) The data base can be scrutinized more carefully, using additional tests to capture the desired effect or deleting tests that do not appear consistent; 2) values of n_3, n_4, and n_6 can be assigned using engineering intuition; or 3) an uncoupled method (to be discussed below) for evaluating the constants can be used.

The uncoupled formulation assumes that thermal recovery effects can be neglected for high strain rate tests. Thus, eq. (10) may be written as:

$$N_i = n_3 + n_4 f_i \quad . \tag{12}$$

Therefore, n_3 and n_4 can be computed by a linear least squares algorithm where n_3 is the intercept and n_4 is the slope (see Fig. 5). If this method is used, the constant n_6 should be initially set to zero and determined later in the procedure.

The hardening coefficient n_2 is computed on the basis that B saturates to B_{lim} at large inelastic strains. Hence, $\dot{B}=0$ and equation (2) reduces to

$$B_{lim} = \frac{n_2}{n_3 + n_4 f + n_6/\dot{\varepsilon}^I} \quad . \tag{13}$$

If it is assumed that the ratio σ_{exp}/B_{exp} will remain constant for the limiting condition at sufficiently large inelastic strains, then

$$\frac{\sigma_{exp}}{B_{exp}} = \frac{\sigma_{lim}}{B_{lim}} \quad . \tag{14}$$

Substituting eq. (13) into (14) and solving for n_2 results in

$$n_2 = \frac{[n_3 + n_4 f + n_6/\dot{\varepsilon}^I]\sigma_{lim}}{\sigma_{exp}} \cdot \frac{B_{exp}}{\sigma_{exp}} \qquad . \tag{15}$$

where σ_{lim} values are obtained from long term monotonic tension tests or σ-plots and B_{exp}/σ_{exp} values come from cyclic hold tests. The final value of the hardening coefficient is then computed as the arithmetic mean of the number of experiments. If an acceptable value of n_2 is not obtained, it can be specified, noting that this parameter effects the rate of hardening.

The initial value of drag stress D_0 and the inelastic strain rate scalar β are determined by rewriting equation (15) using the limiting values of σ and B as:

$$\sigma_{lim} - B_{lim} = D_0 \ln(\dot{\varepsilon}^I) + D_0 \ln(\beta) \ . \tag{16}$$

Since B_{lim} is given by equation (13), it can be substituted into equation (16), resulting in

$$\delta_{\sigma B} \equiv \sigma_{lim} - \frac{n_2}{n_3 + n_4 f + n_6/\dot{\varepsilon}^I} = D_0 \ln(\dot{\varepsilon}^I) + D_0 \ln(\beta) \quad . \tag{17}$$

Equation (17) indicates that a plot of $\delta_{\sigma B}$ versus $\ln(\dot{\varepsilon}^I)$ should be linear (the piecewise curve shown in Fig. 6 is an artifact of the strain aging correction in the dynamic recovery term of the back stress evolution equation), having a slope of D_0 and an intercept of $D \ln(\beta)$ which are obtained from a linear regression analysis. Hence, β can be computed directly once the value of the intercept is known.

If thermal recovery effects were previously neglected, the constant n_6 can now be evaluated. Since β and D_0, n_2, n_3, and n_4 are known, eq. (13) can be substituted into eq. (16) yielding an expression for n_6 :

$$n_6 = \dot{\varepsilon}^I \, (n_2 \, [\sigma_{lim} - D_0 \, \ln(\beta\dot{\varepsilon}^I)]^{-1} - n_3 - n_4 f) \quad . \tag{18}$$

The thermal recovery parameter is then computed for a number of low strain rate monotonic tension tests and averaged.

Up to this point, the only tests that are needed in order to compute the material parameters are monotonic tension and cyclic hold tests. To obtain the isotropic hardening and recovery constants D_1, D_2, and n_7, saturated cyclic hysteresis data are required. By estimating the cumulative inelastic strain from applied stress, strain amplitude, and E, in addition to assuming that D saturates to D_1 , then n_7 can be approximated by:

$$n_7 = -\ln(\tau)/R_{avg} \quad , \tag{19}$$

where R_{avg} is the average of R for a number of tests and τ is a number approaching zero.

On the physical basis that B saturates much more rapidly than D, equation (5) can be written as:

$$D_{lim} = D_1 = \frac{\sigma_{lim} - B_{lim}}{\ln(\beta\dot{\varepsilon}^I)} \quad , \tag{20}$$

where

$$B_{lim} = n_2/N \quad . \tag{21}$$

The values of σ_{lim} and N in equations (20) and (21) are estimated from the θ-plot using data from the tension half-cycle after cyclic saturation has occurred. If several tests are used, D_1 is computed as the arithmetic mean.

The final parameter to be determined is D_2 . When R=0 equation (3) reduces to

$$D_0 \overset{\bullet}{=} D_1 - D_2 \ . \tag{22}$$

from which D_2 may be computed directly, completing the constant calculation procedure.

The primary equations used in the procedure described above are summerized below and a flow chart of the associated computer code is shown in Fig. 7. The program is written to compute the constants in a totally automated fashion or, alternately, the parameters can be modified and/or recomputed through user intervention. While the flow chart depicts the procedure as a sequential series of evaluations, the user may alter the program flow to iterate on a specific constant or series of constants.

1) Values of σ_{lim} and N from monotonic tension tests are computed using equation (7) and a least squares procedure.
2) After selecting $\dot{R}_0$, $\dot{R}_1$, and τ, n_5 is evaluated using equation (9).
3) The parameters n_3, n_4, and n_6 are determined, in a coupled formulation, by equations (10) and (11) using a multiple linear regression scheme, or

alternately, using an uncoupled formulation by equations (12) and (18).

4) The back stress hardening coefficient n_2 is computed directly from equation (15).

5) The constants D_3 and β are evaluated using equation (17) via a least squares procedure.

6) After computing the cumulative inelastic strain from the experimental data, n_7 is evaluated directly from equation (19).

7) D_1 and D_2 are computed using equation (20) and (22).

DISCUSSION OF THE PROCEDURE AND RESULTS

The parameter evaluation program, described in the previous section, does not require an entire experimental data base. Instead, summary information which is composed of both measured quantities and pre-processed values is all that is necessary. Data tabulated from fully reversed cyclic tests, cyclic hold tests and long term monotonic tension tests on Inconel 718 at 1100° F may be found in Table 1. These data were used to compute an initial set of constants (see Table 2) in a totally automated fashion. Comparisons between Walker's exponential model and several tension experiments may be seen in Fig.'s 8-10. It is apparent that the initial set of parameters did not enable the model to capture the true response of the material. Therefore, a critical review of both the procedure and experimental data was necessary.

For the purpose of this discussion, it was assumed that the data base accurately represented the material behavior. Therefore, steps in the procedure which require user interpretation were examined first and the following observations were made.

When constructing the θ-plot, there are several points to consider. First, proper evaluation of σ_{lim} and N require that ε^I be computed after $\dot{\varepsilon}^I$ becomes constant. This is generally assumed to occur at the 0.2% offset yield stress. However, if this is not true, the computed value of N will be too large, which in turn will yield a value of σ_{lim} that is too low. A second area of interest is in the differentiation of the σ versus ε^I curve. Usually the stress is expressed as an nth order polynomial function of the inelastic strain. However, depending upon the viscoplastic model and material system, a logarithmic, power law or exponential curve fit may be more suitable. In addition, a finite difference approximation can be used, thus eliminating the curve fitting requirement altogether. Since a poor curve fit will yield a θ-plot that is difficult to interpret, care should be taken in selecting the proper form of the equation. Lastly, one needs to consider the strain amplitude necessary to obtain an accurate prediction of σ_{lim}.

The θ-plots for the material system considered herein were constructed using a combination of third and fourth order polynominal curve fits (see Fig. 4). Figure 11 shows that the values of N are scattered and have no specific trends when they are plotted against $\ln(\dot{\varepsilon})$. In a similar fashion, Fig. 12 shows anomalies in the prediction of σ_{lim}. While the sigmoidal shape of the curve was expected, the large discrepancies make interpretation difficult.

To illustrate how scatter such as that depicted in Fig.'s 11 and 12 can occur, consider the following points. First, Fig. 13 shows a θ-plot constructed using a fourth order polynomial curve fit, evaluating $\sigma(\varepsilon^I)$ over various strain amplitudes. While there is only a 6% change in predicted σ_{lim}, there is over a 50% change in N. Some of the discrepancy can be attributed to the fact that $\dot{\varepsilon}^I$ was not constant. In addition, the order of the curve fit drastically changed the shape of the θ-plot making interpretation difficult . Second, Fig. 14 shows a θ-plot generated from a logarithmic curve fit. While not shown, evaluation of σ_{lim} and N over different strain amplitudes did not adversely affect their values. Finally, Fig. 15 depicts a θ-plot constructed using finite differences. It is apparent that numerical differentiation by this method yields unacceptable results. In summary, one must carefully consider both the constitutive model and material system before selecting the type of curve fit that will be used in the construction of the θ-plot.

It was also determined that the multiple linear regression scheme used to compute dynamic and static thermal recovery constants in a coupled fashion did not work well when the material exhibited substantial strain aging. Therefore, by neglecting thermal recovery, n_3 and n_4 were computed using an uncoupled procedure. Figures 8 through 10 show that Walker's model, using the final parameters (see Table 2), was able to reproduce the input data fairly well except in the initial yield region. Test 80 showed the largest deviation between actual and predicted stress, underestimating it by 6% at a strain amplitude of 0.8%.

Figures 16 through 18 show the model behavior for the last cycle of several cyclic hysteresis tests. Figures 17 and 18 indicate that the computed value of D_1 was too large, which resulted in an excess of material softening under cyclic loading. However, the opposite trend can be seen in Fig. 16 (test 86 was the fastest cyclic test run), wherein the peak stress amplitude was overpredicted. A review of the monotonic tension data reveals the same tendency. This would lead to the conclusion that the full effect of the strain aging correction was not captured.

A complex history test (one which was not used to evaluate the constants) was used to show the predictive capabilities of Walker's model using the final set of parameters. In general, Fig. 19 indicates the numerical simulation matches the test fairly well. The only major problem encountered was a 7.5% overprediction in stress at large strain amplitudes.

CONCLUSIONS

A method for obtaining the material parameters for Walker's model has been developed which is a synthesis of both physical and numerical approximations. The associated computer algorithm allows the user to specify either a totally automated procedure or engineering intuition at selected points when computing constants. In addition, qualitative assessments were made regarding the use of the θ-plot in determining σ_{lim} and N. It was noted that the method of differentiating the σ versus ϵ^I curve depends on both the constitutive model being used and the material system.

Walker's viscoplastic constitutive model for metals at elevated temperature was compared to experiment results for Inconel 718 at 1100°F. This material system responds with apparent strain aging, undergoes cyclic work softening, and is susceptible to low cycle fatigue. It was shown that Walker's model was able to capture the response of the material. It has also been shown that the use of the linearized equations can lead to unacceptable simulations if care is not used to interpret the results. The procedure yields initial values for the constants which may then be used in an iterative scheme to arrive at the final parameters.

REFERENCES

1. D.H. Allen, and J.M. Beek, "On the Use of Internal State Variables in Thermoviscoplastic Constitutive Equations," Nonlinear Constitutive Relations for High Temperature Application - 1984, NASA CP 2369, pp. 83-102, 1984.

2. K.P. Walker and D.A. Wilson, "Creep Crack Growth Predictions in INCO 718 Using a Continuum Damage Model," 2nd Symposium on Nonlinear Constitutive Relations for High-Temperature Applications, Cleveland, OH, 1984.

3. U.S. Lindholm, K.S. Chan, S.R. Bodner, R.M., Weber, K.P. Walker, and B.N. Cassenti, "Constitutive Modeling for Isotropic Materials," CR-174980, NASA (Host), 1985.

4. R.D. Krieg, J.C. Swearengen, and R.W. Rhode, "A Physically-based Internal Variable Model for Rate Dependent Plasticity," Proc. ASME/CSSME PVP Conference, 1978.

5. C.G. Schmidt, A Unified Phenomenological Model for Solute Hardening, Strain Hardening, and Their Interactions in Type 316 Stainless Steel, Ph.D. Dissertation, Stanford University, Dept. of Materials Science and Engineering, 1979.

6. G.H. James III, "An Experimental Comparison of Current Viscoplastic Constitutive Models at Elevated Temperature, M.S. Thesis, Texas A&M University, 1986.

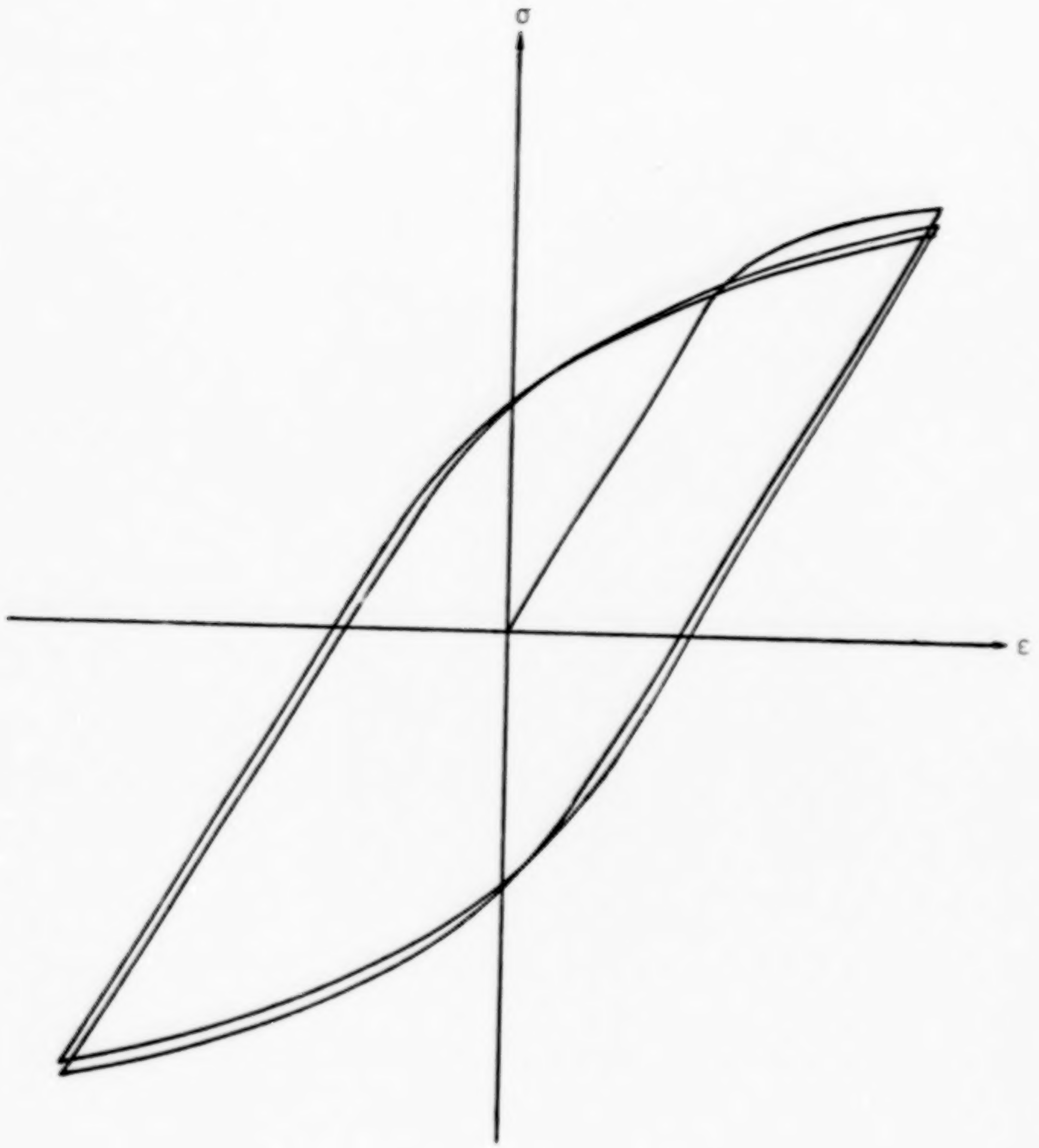

Figure 1. Cyclic Hysteresis Test

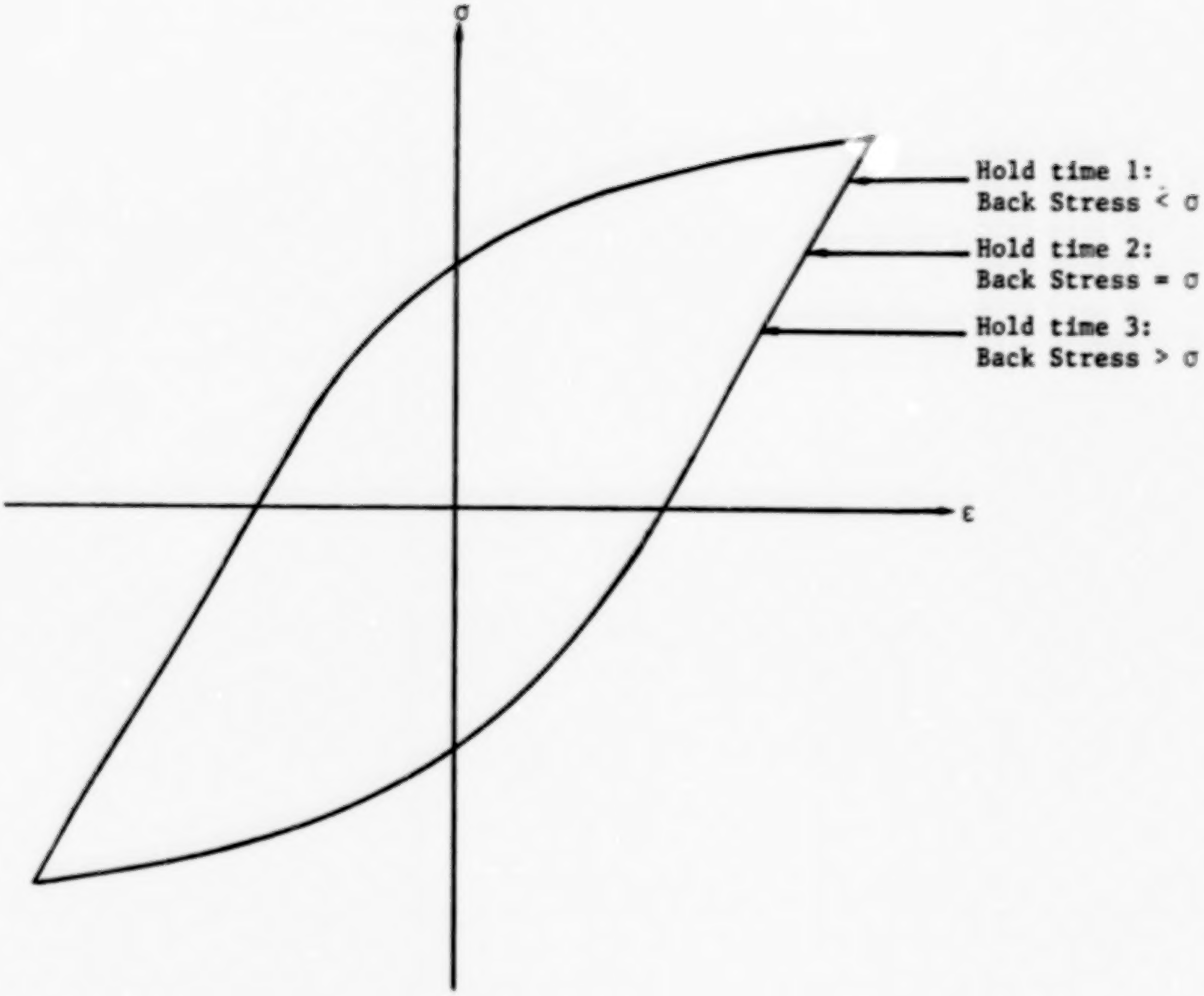
σ
ε
Hold time 1:
Back Stress < σ
Hold time 2:
Back Stress = σ
Hold time 3:
Back Stress > σ

Figure 2. Cyclic Hysteresis Test with Hold Times

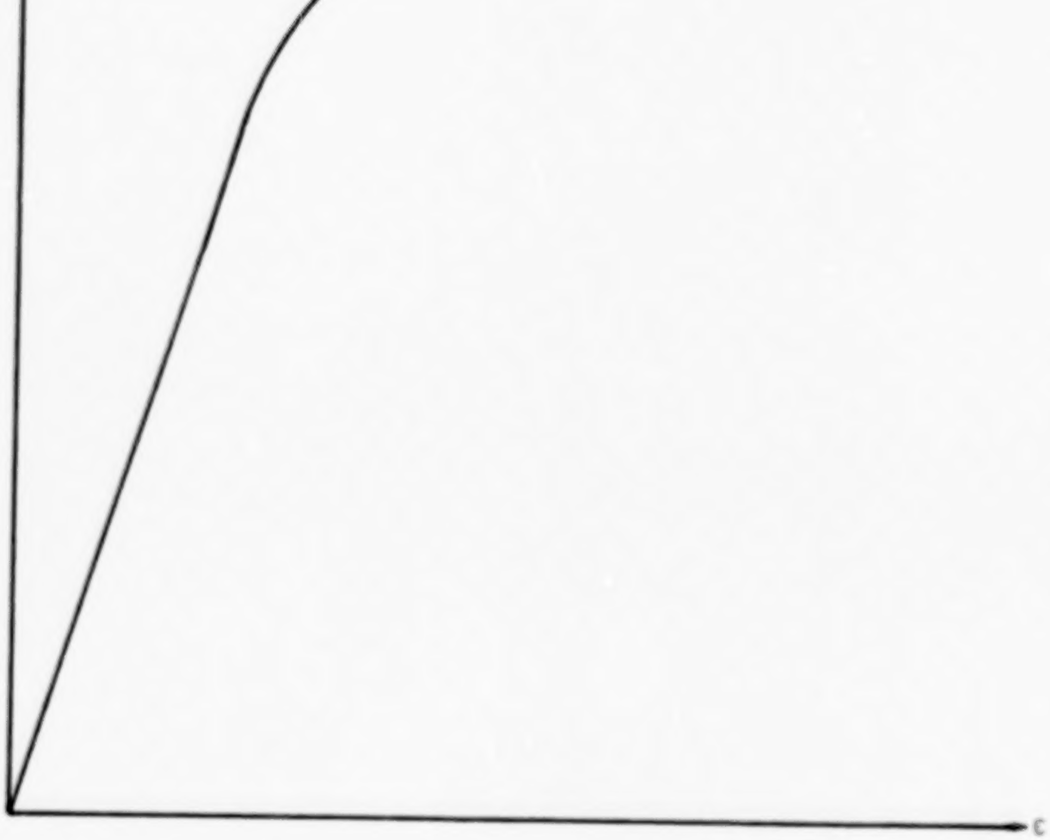

Figure 3. Long Term Monotonic Tension Test

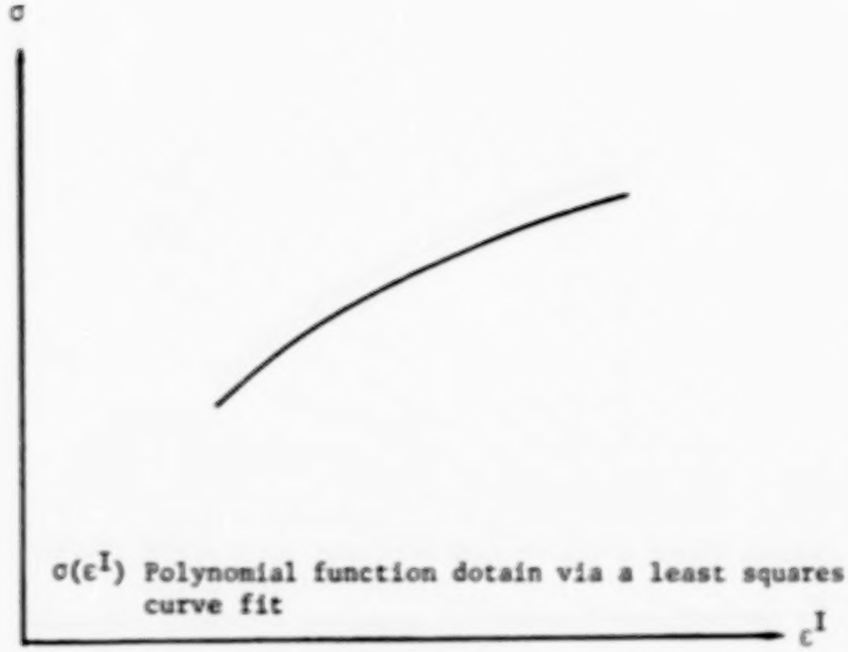

Figure 4(a). Stress versus inelastic strain

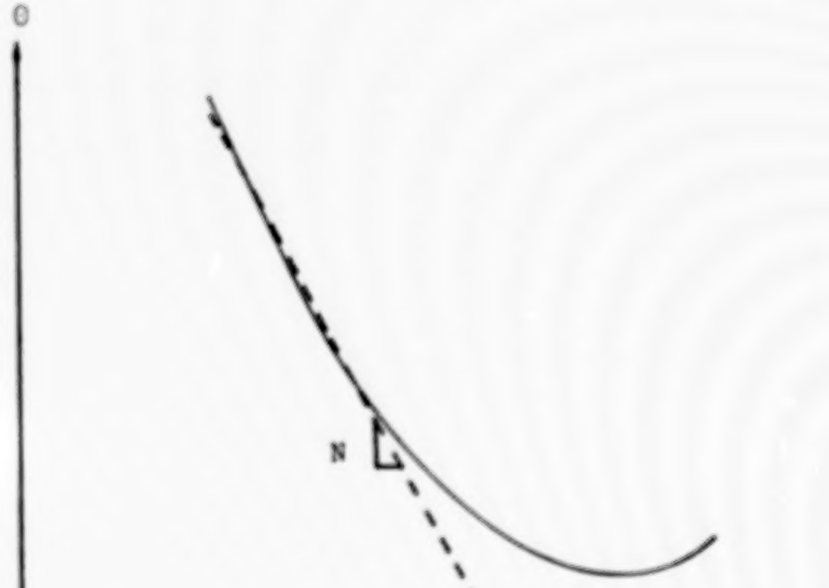

Figure 4(b). Typical Θ-plot

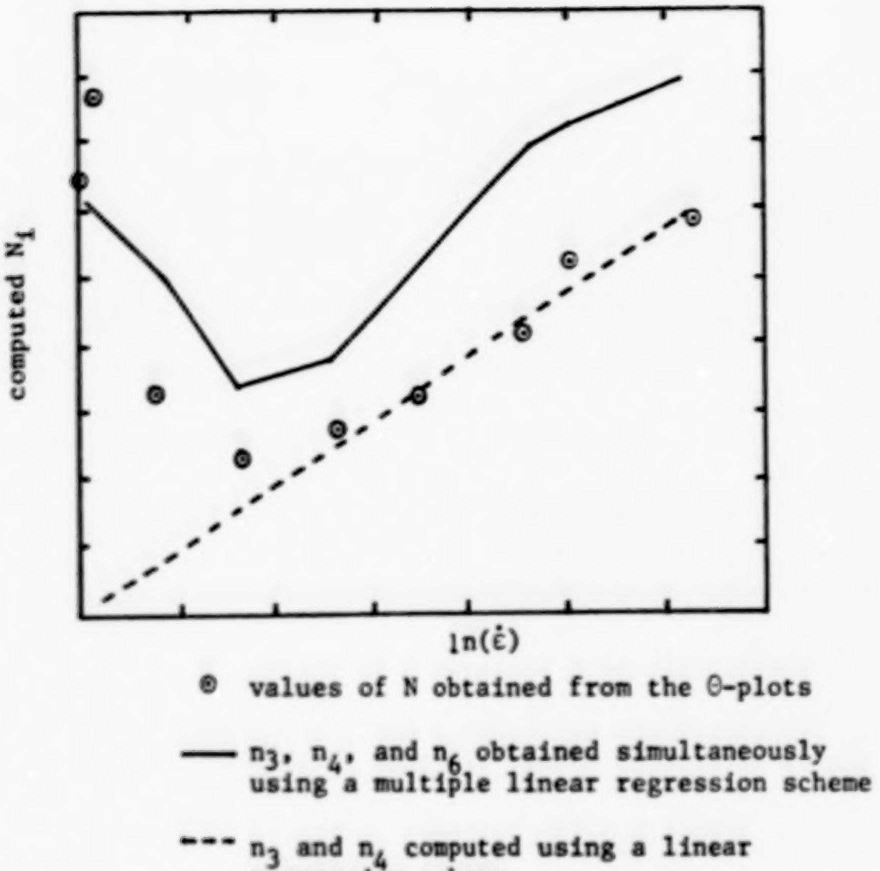

Figure 5. Least squares fit of N as a function $\dot{\varepsilon}^I$ (note: the abscissa is shown as ln($\dot{\varepsilon}$) instead of $\dot{\varepsilon}$ for pictorial purposes only)

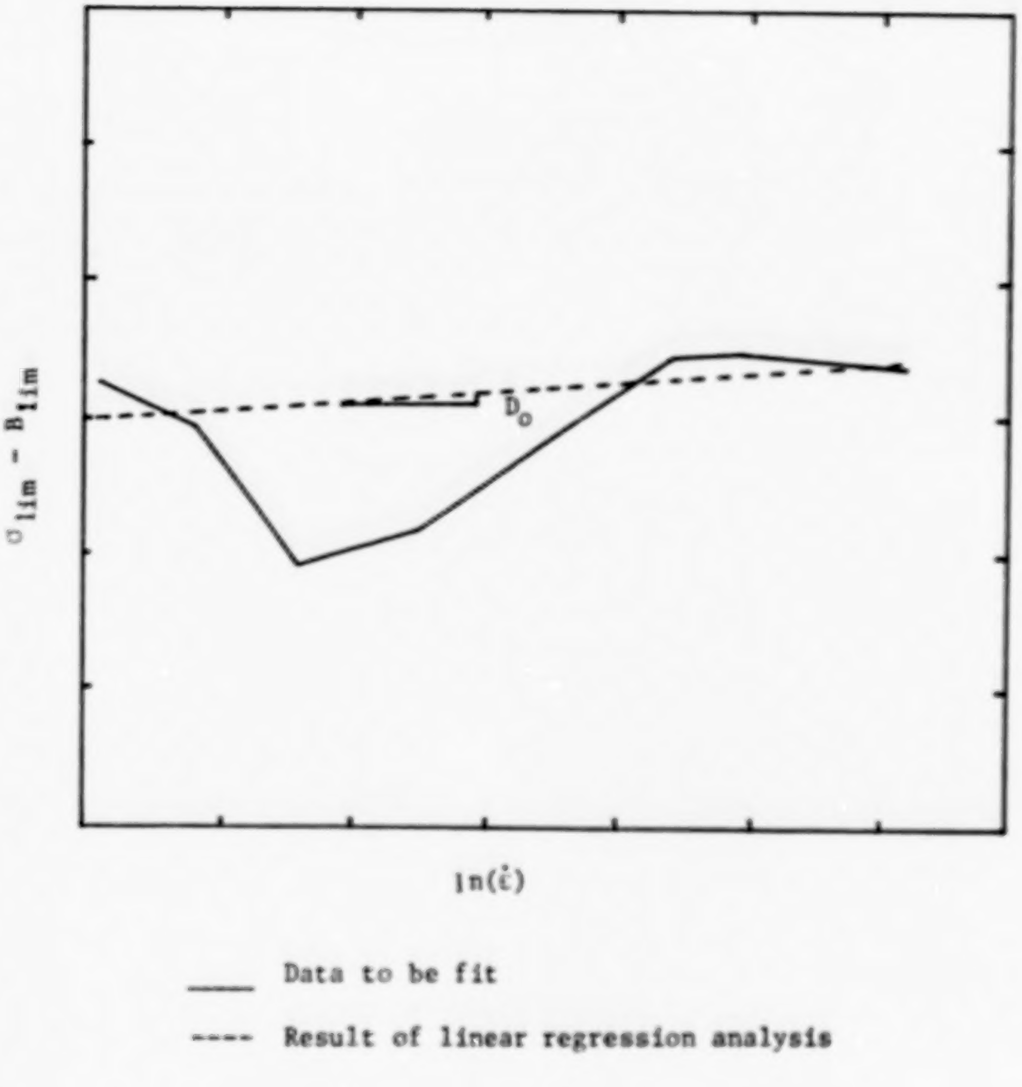

Figure 6. Least squares fit of $\delta_{\sigma B}$ as a function $\ln(\dot{\varepsilon}^I)$

ORIGINAL PAGE IS
OF POOR QUALITY

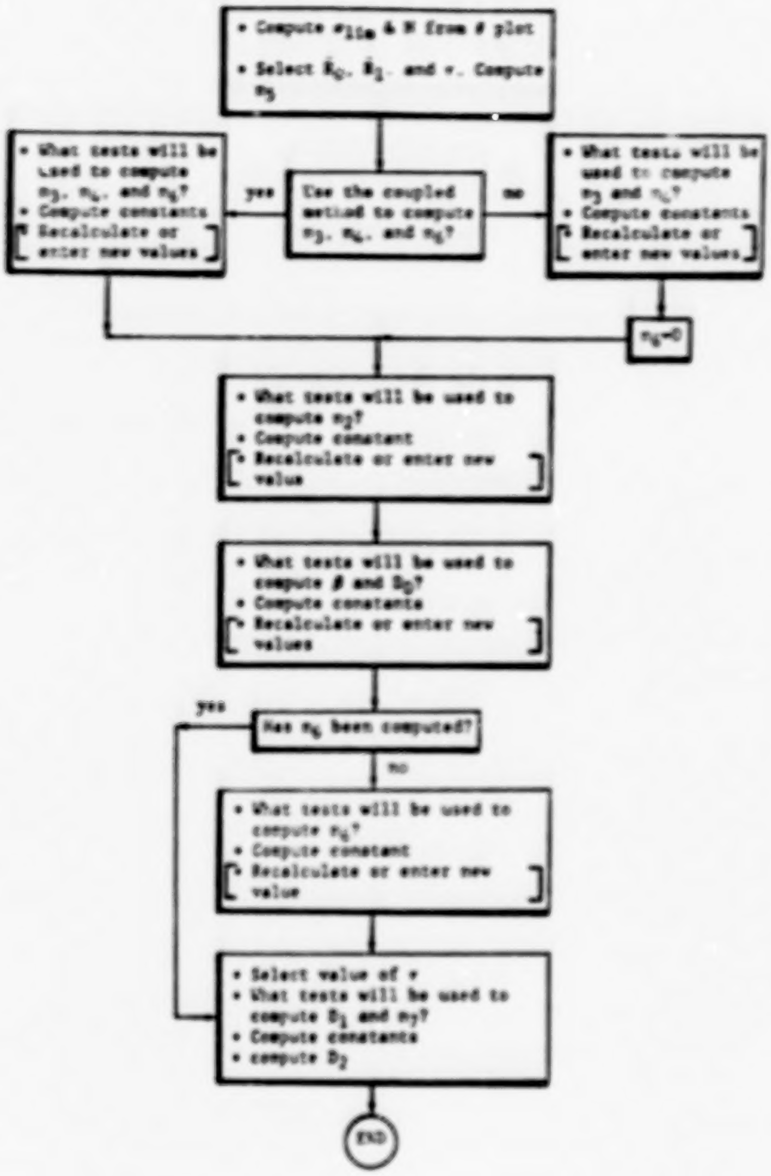
• Compute σ_{11a} & N from ϕ plot
• Select $\dot{\varepsilon}_0$, $\dot{\varepsilon}_1$, and ν. Compute n_5
• What tests will be used to compute n_3, n_4, and n_6?
• Compute constants
• Recalculate or enter new values
yes
Use the coupled method to compute n_3, n_4, and n_6?
no
• What tests will be used to compute n_3 and n_4?
• Compute constants
• Recalculate or enter new values
$n_6=0$
• What tests will be used to compute n_2?
• Compute constant
• Recalculate or enter new value
• What tests will be used to compute β and D_0?
• Compute constants
• Recalculate or enter new values
yes
Has n_6 been computed?
no
• What tests will be used to compute n_6?
• Compute constant
• Recalculate or enter new value
• Select value of ν
• What tests will be used to compute D_1 and n_7?
• Compute constants
• compute D_2
END

[ ] Modifications requiring user intervention

Figure 7. Flowchart of Walker's Procedure

ORIGINAL PAGE IS
OF POOR QUALITY

Test No. P	E	ℓ	σ_{exp}	σ_{lim}	σ_y	δ_{exp}	N	R
1	70	3.151×10^{-3}		132.527	97.83		287.293	
2	88	1.002×10^{-4}		120.938	91.677		307.181	
3	56	9.966×10^{-4}		118.217	95.575		305.438	
* 4	35	9.235×10^{-4}		136.3			277.2	
* 5	37	6.941×10^{-4}		137.5			246.9	
6	65	3.127×10^{-4}		134.143	97.84		268.17	
* 7	39	1.793×10^{-4}		133.6			206.61	
8	83	9.926×10^{-5}		134.536	94.56		337.399	
* 9	34	7.637×10^{-5}		142.1			319.8	
* 10	36	5.703×10^{-5}		138.5			241.6	
11	60	3.054×10^{-5}		141.821	100.941		310.777	
* 12	42	1.914×10^{-5}		137.6			291.8	
* 13	38	1.410×10^{-5}		140.7			212.4	
14	72	7.626×10^{-6}		138.155	101.71		358.549	
15	71	7.253×10^{-6}		135.584	97.67		342.254	
* 16	40	7.026×10^{-6}		138.3			328.5	
17	84	2.812×10^{-5}	116.49	132.527		68.3		
18	88	9.272×10^{-4}	100.98	120.938		62.47		
19	88	9.272×10^{-4}	100.98	118.217		62.47		
20	81	8.635×10^{-4}	116.45	120.938		64.65		
21	81	8.635×10^{-4}	116.45	118.217		64.65		
22	65	2.751×10^{-4}	107.64	134.143		80.00		
23	88	1.002×10^{-3}		108.326			288.42	0.0773
24	56	9.966×10^{-4}		105.867			294.58	0.0799
25	65	3.127×10^{-4}		121.427			246.02	0.0707
26	83	9.926×10^{-5}		138.699			267.179	0.0293
27	80	3.054×10^{-5}		135.899			255.534	0.0579
28	72	7.262×10^{-6}		139.38			375.035	0.0205

* Different Material System

Table 1. Input Data for Parameter Evaluation

Parameters	Initial Values	Final Values
β (sec)	0.288E34	0.280E70
D_1 (ksi)	0.580E00	0.520E00
D_2 (ksi)	-0.000E00	-0.120E00
$\dot{\epsilon}_o^I$ in/in/sec	0.454E-4	0.454E-4
E (ksi)	0.247E05	0.247E05
n_2 (ksi)	0.264E05	0.140E05
n_3	0.370E03	0.390E03
n_4	-0.200E03	-0.200E03
n_5	0.530E00	0.103E01
n_6 (/sec)	0.400E-4	0.4000-4
n_7 (/sec)	0.179E02	0.179E02

Table 2. Parameters for Walker's model

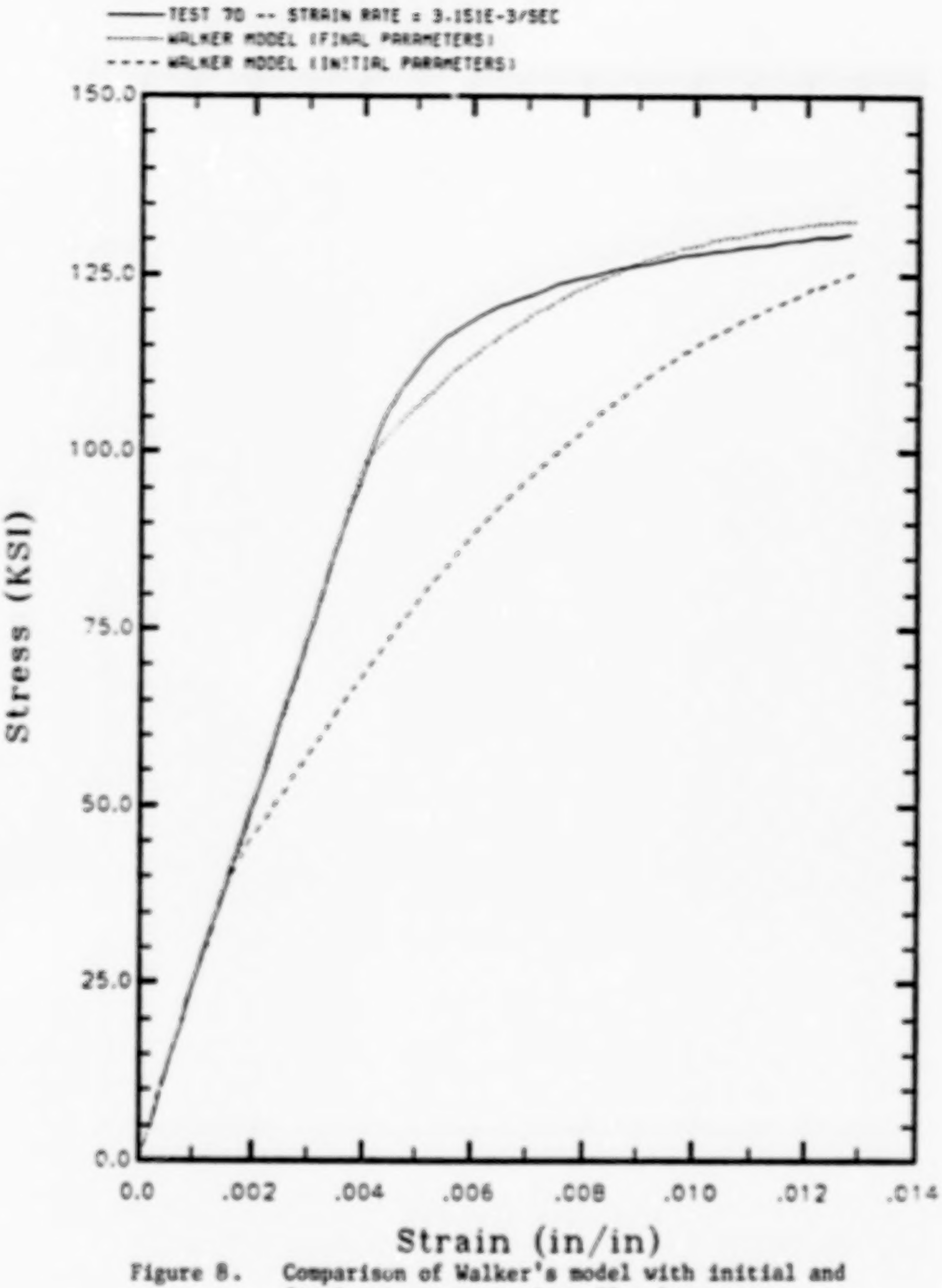

Figure 8. Comparison of Walker's model with initial and final parameters to Test 70-a long term monotonic tension test.

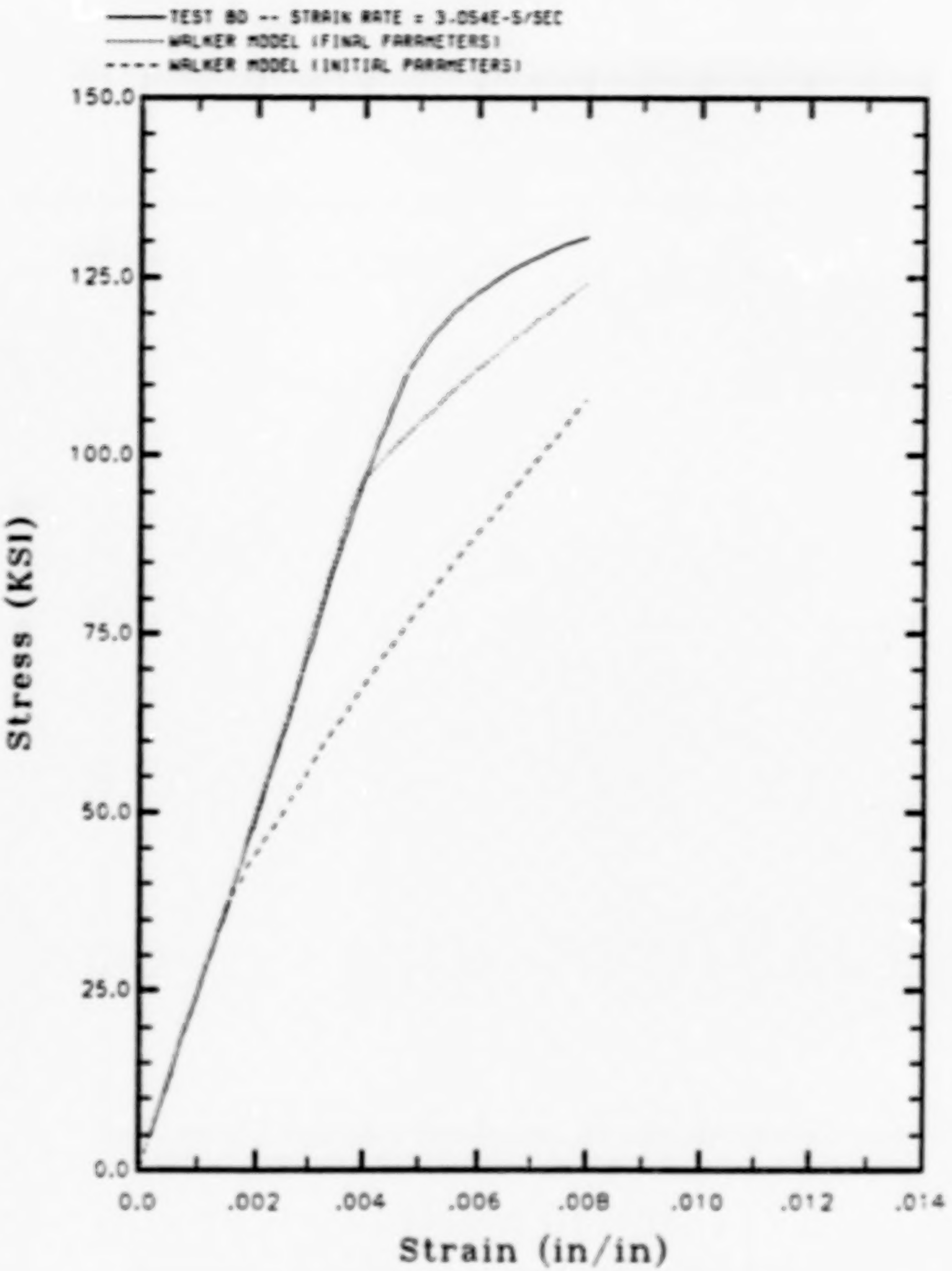

Figure 9. Comparison of Walker's model with initial and final parameters to Test 80-a short term monotonic tension test.

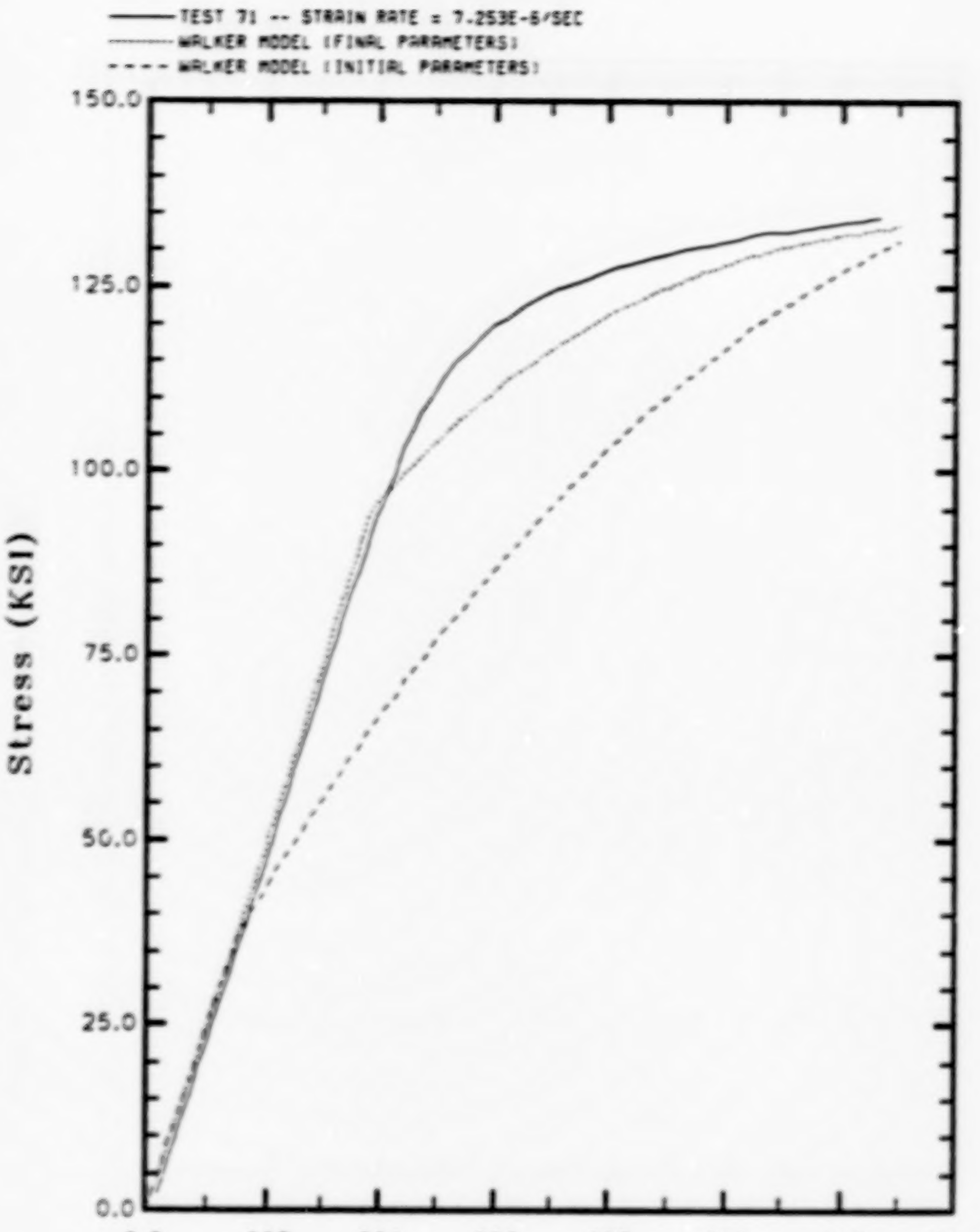

Figure 10. Comparison of Walker's model with initial and final parameters to Test 71-a long term monotonic tension test.

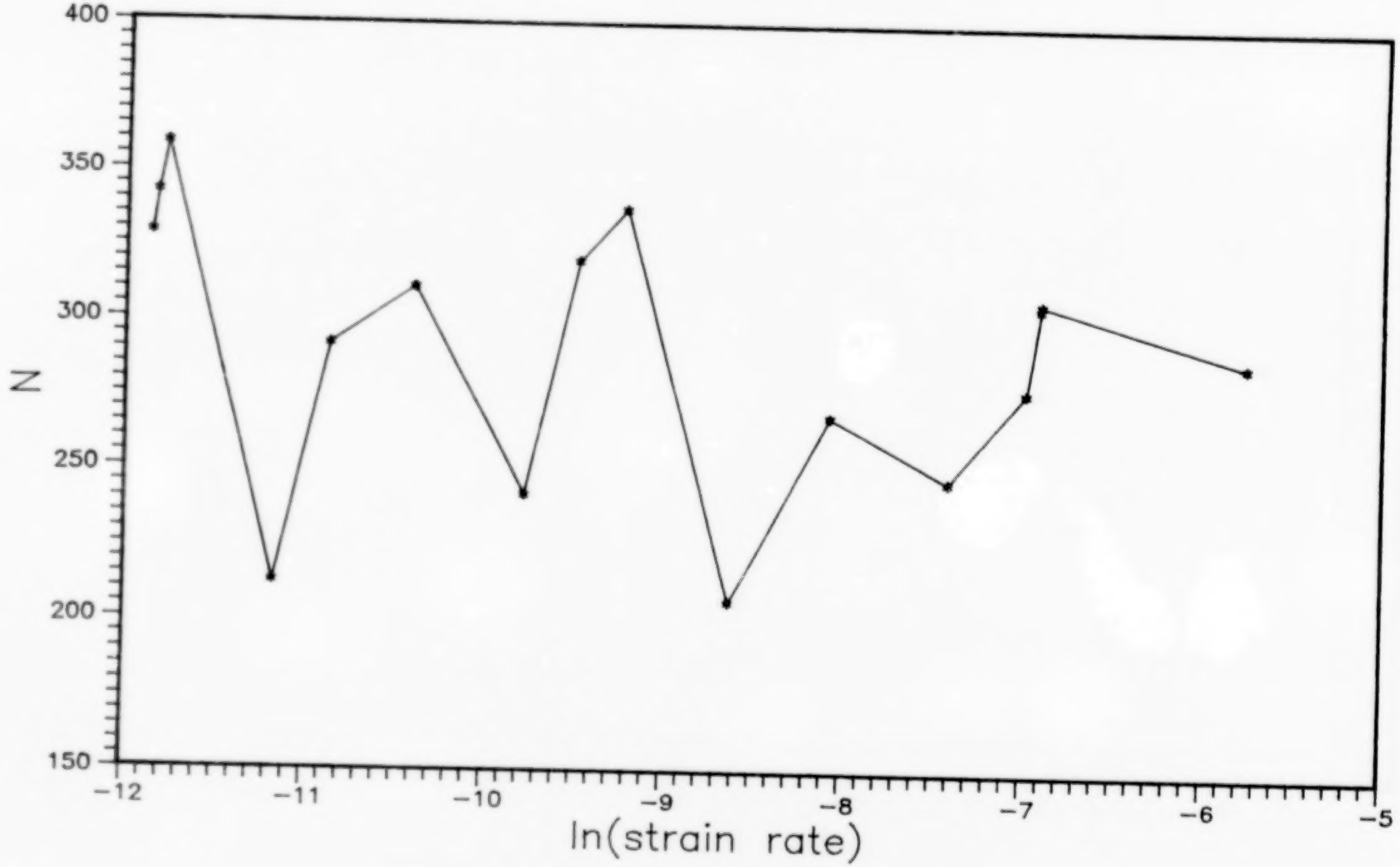

Figure 11. Computed values of N from the Θ-plot

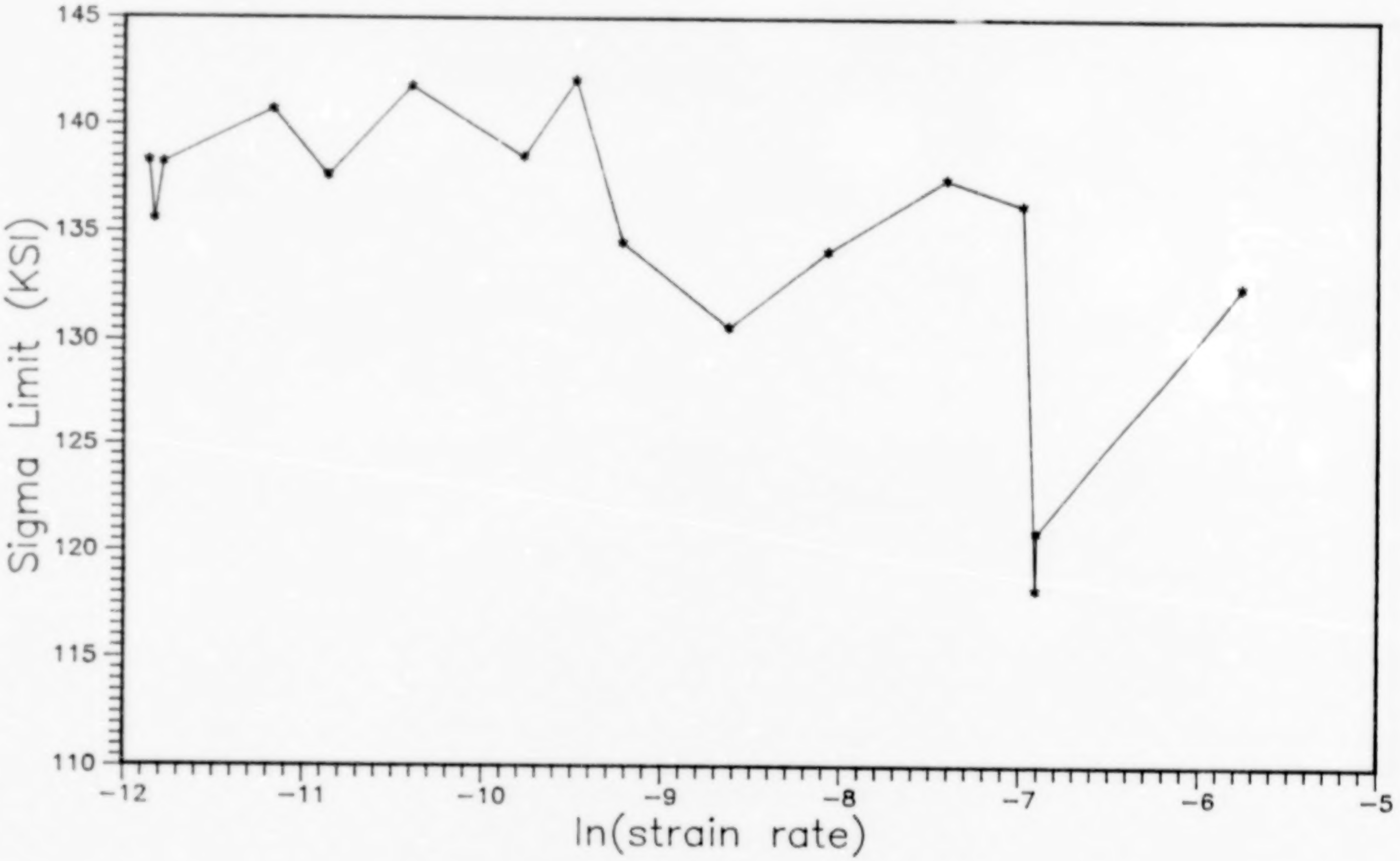

Figure 12. Predicted σ_{lim} from the Θ-plot

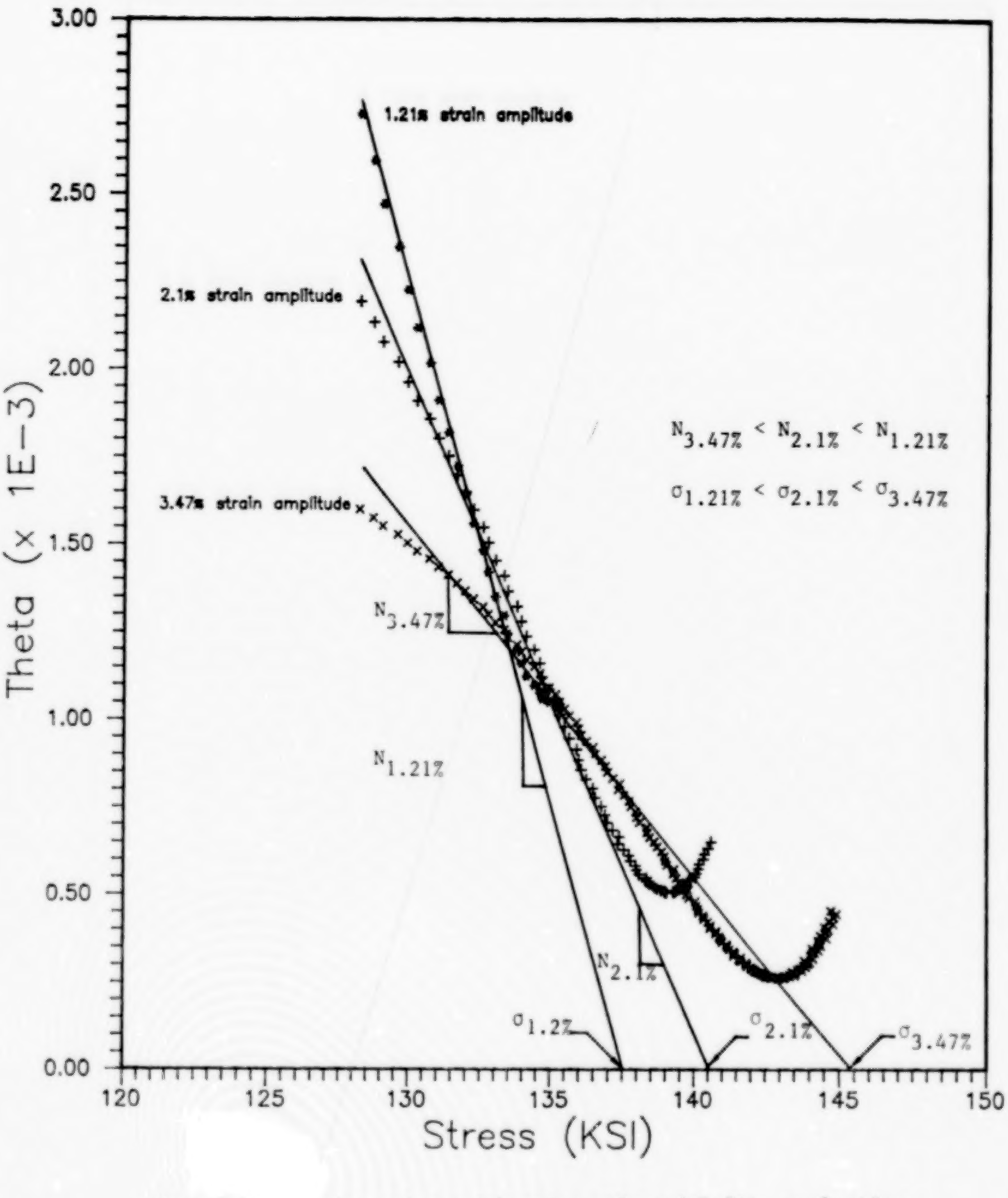

Figure 13. -plot using a 4th order polynomial fit, evaluating $\sigma(\varepsilon^I)$ over different strain amplitudes

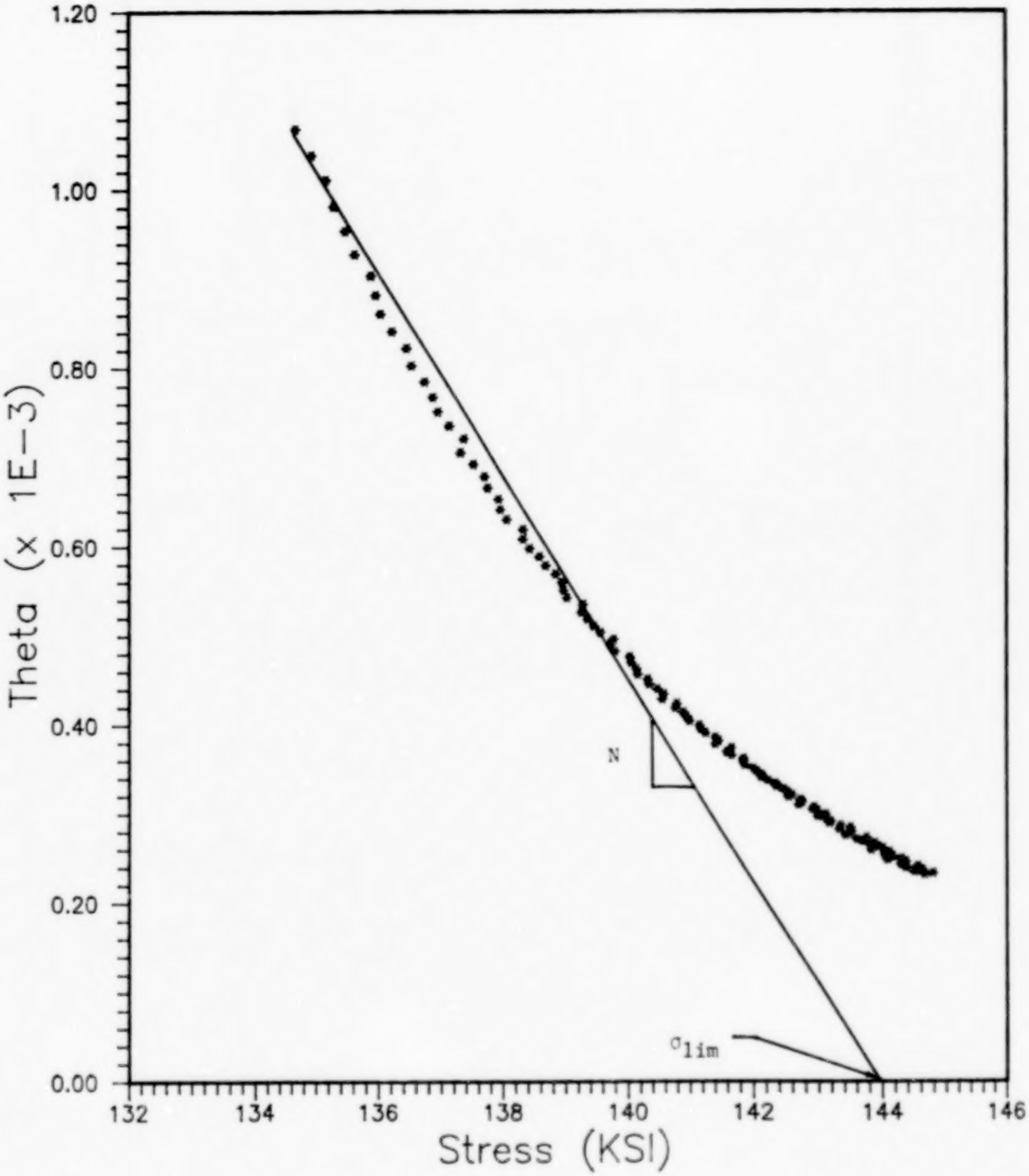

Figure 14. Θ-plot using a logarithmic curve fit of σ vs ε^I

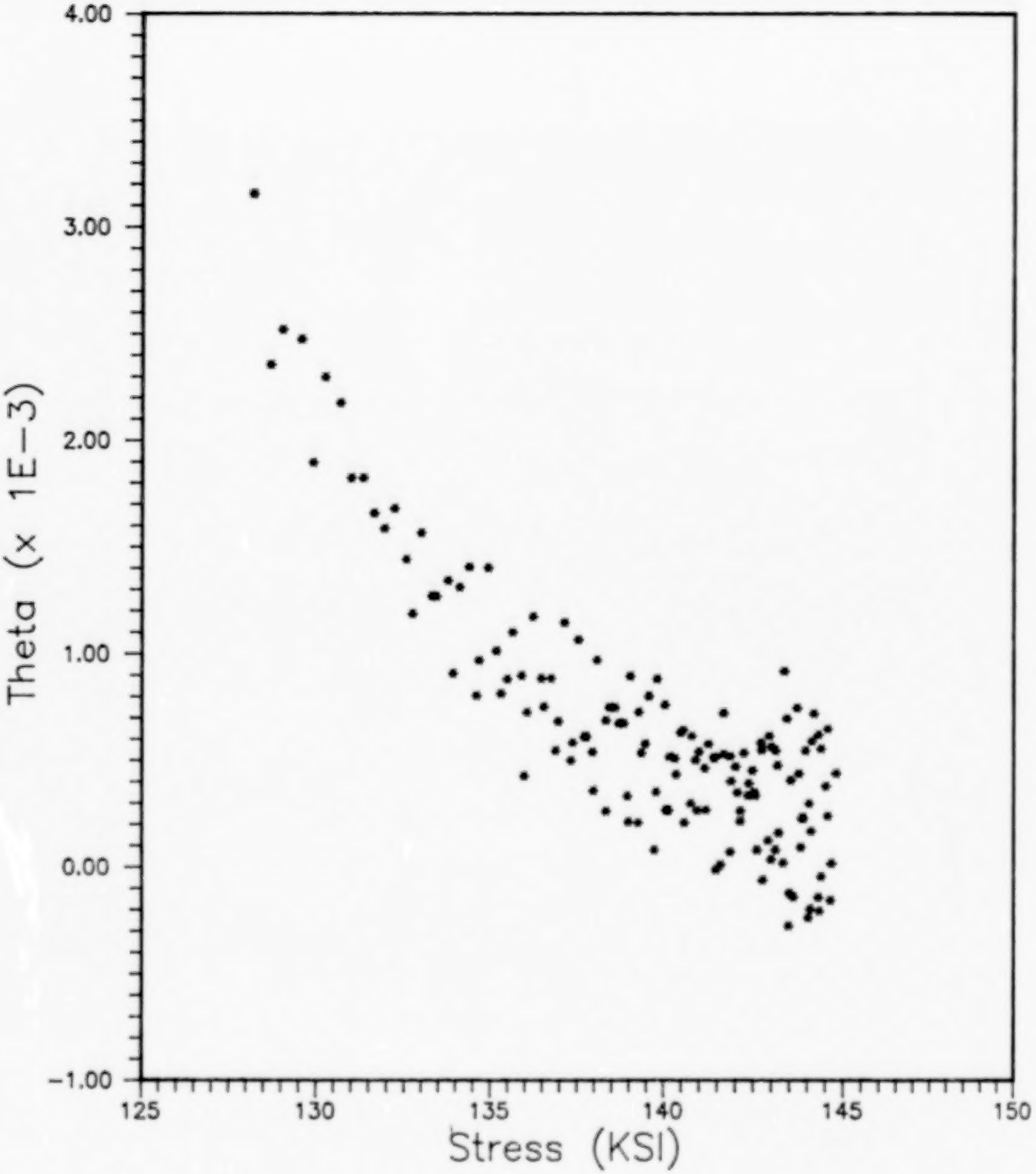

Figure 15. Θ-plot constructed by finite difference

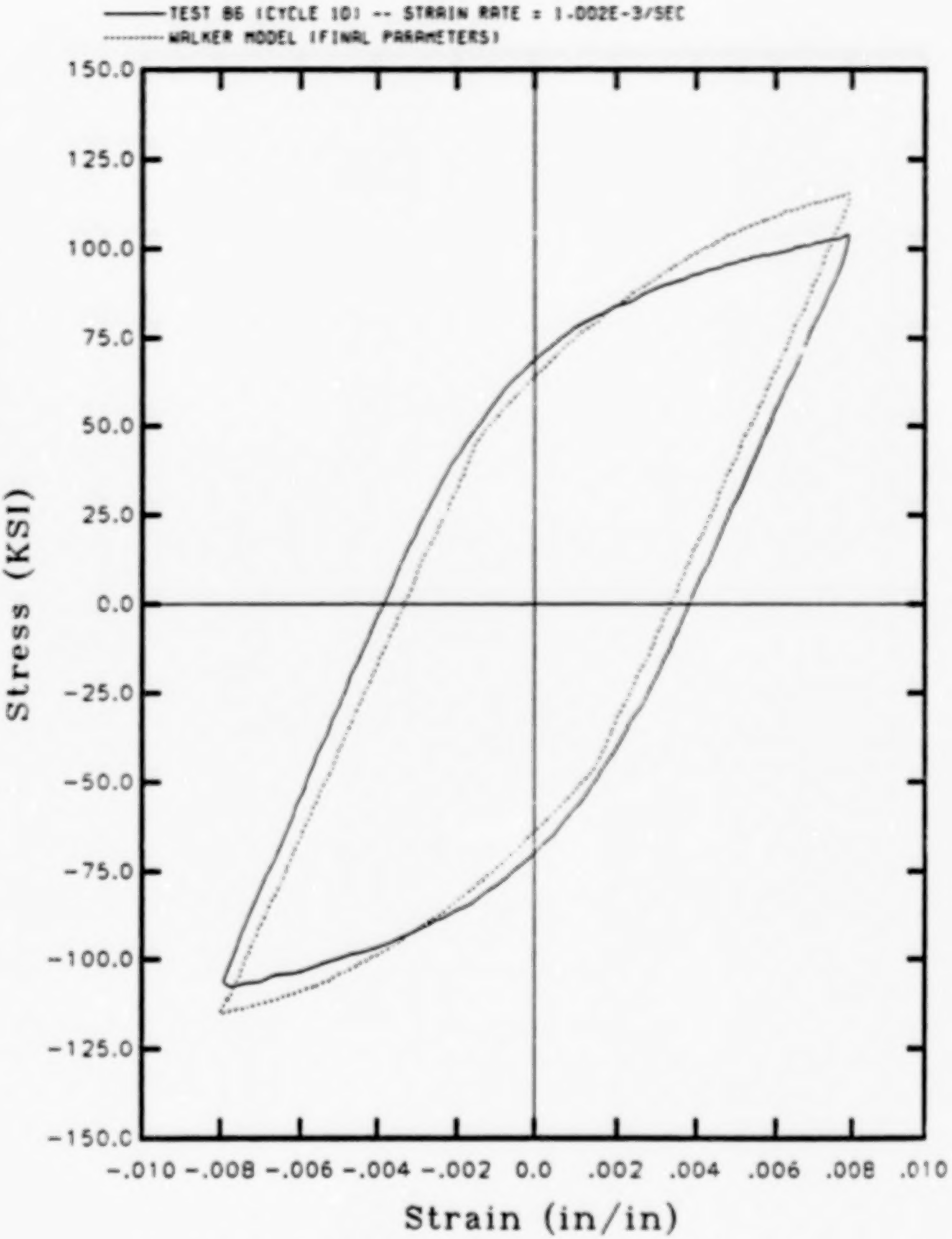

Figure 16. Comparison of Walker's model to the last cycle of Test 86.

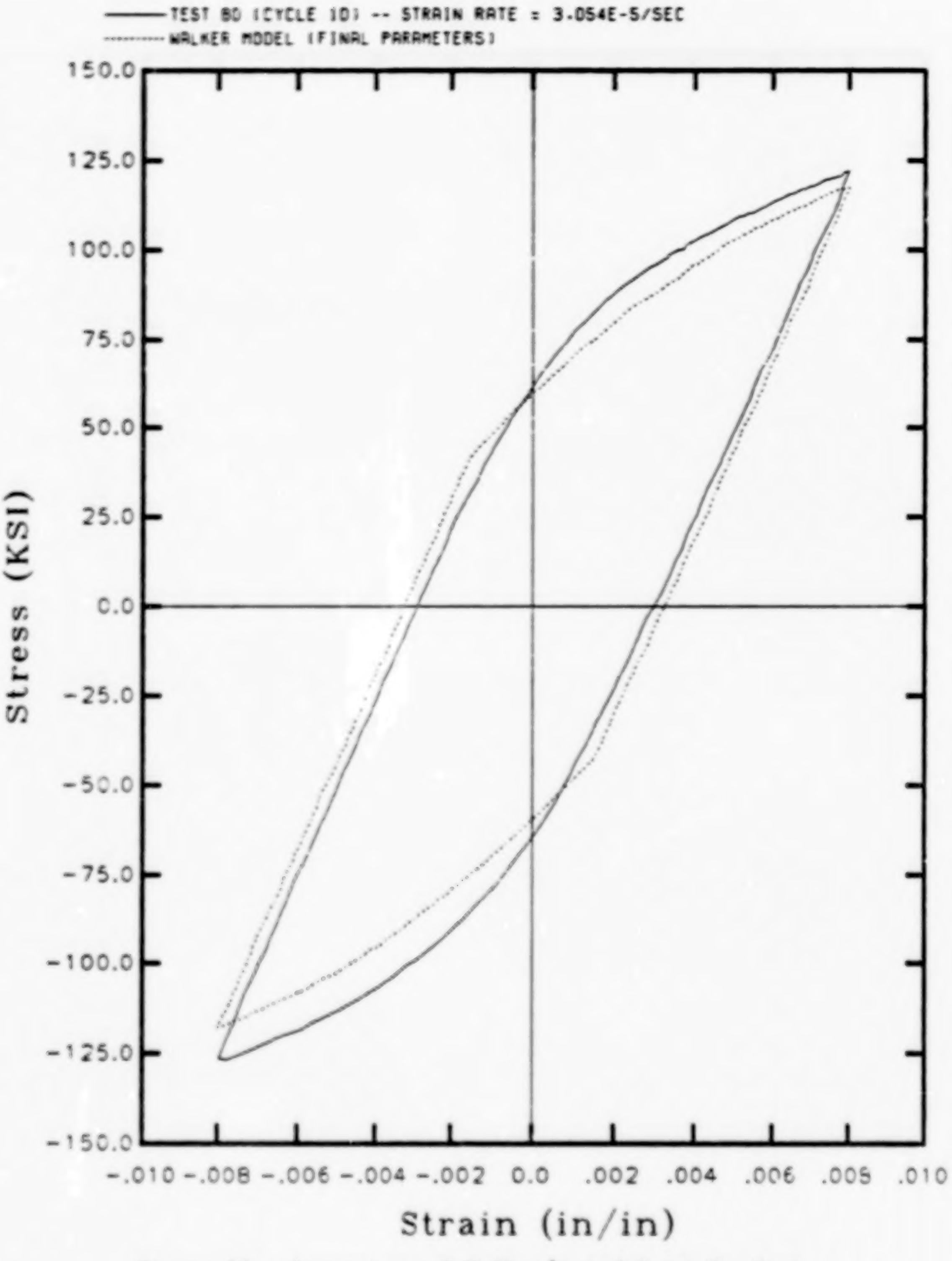

Figure 17. Comparison of Walker's model to the last cycle of Test 80.

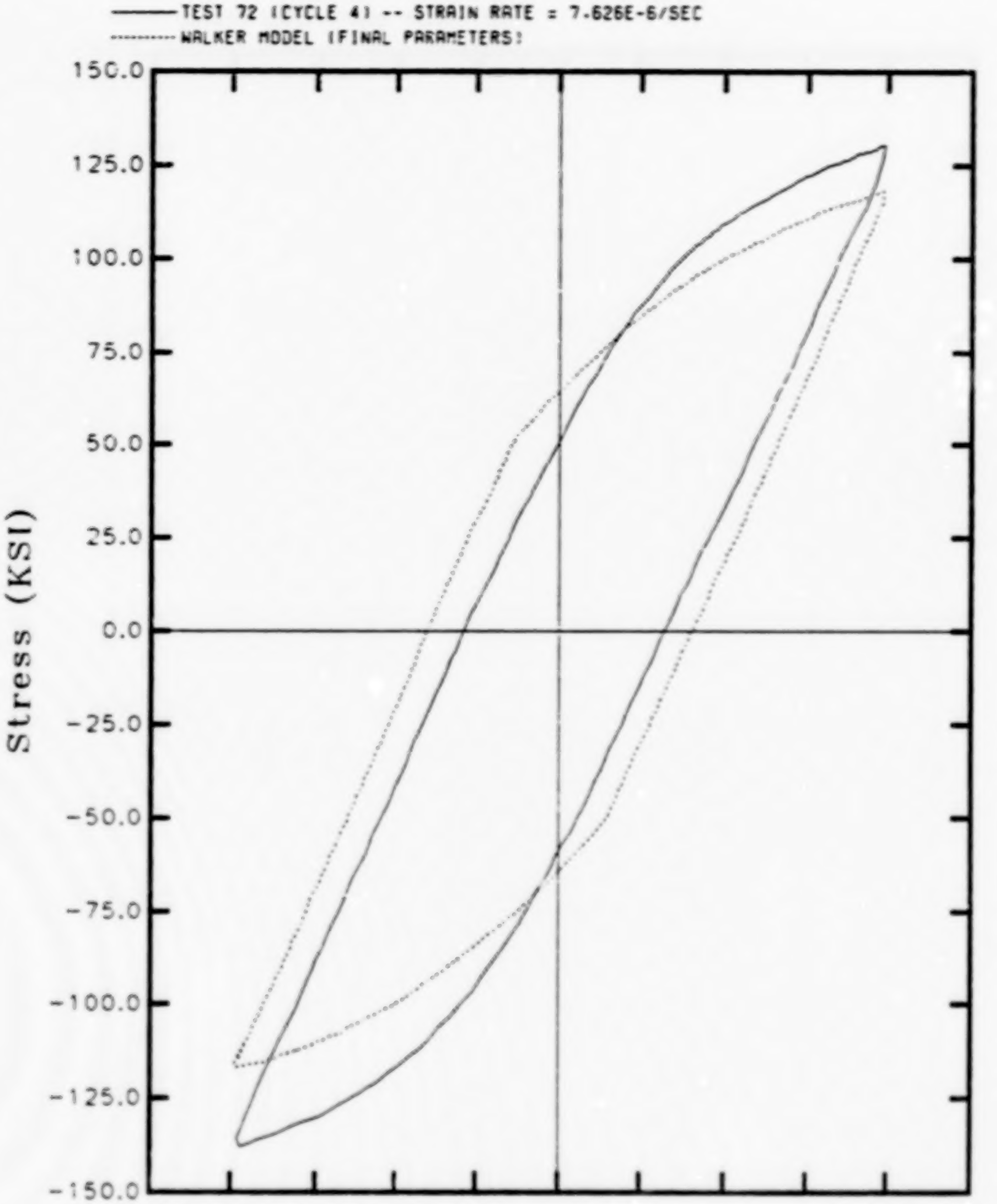

Figure 18. Comparison of Walker's model to the last cycle of Test 72.

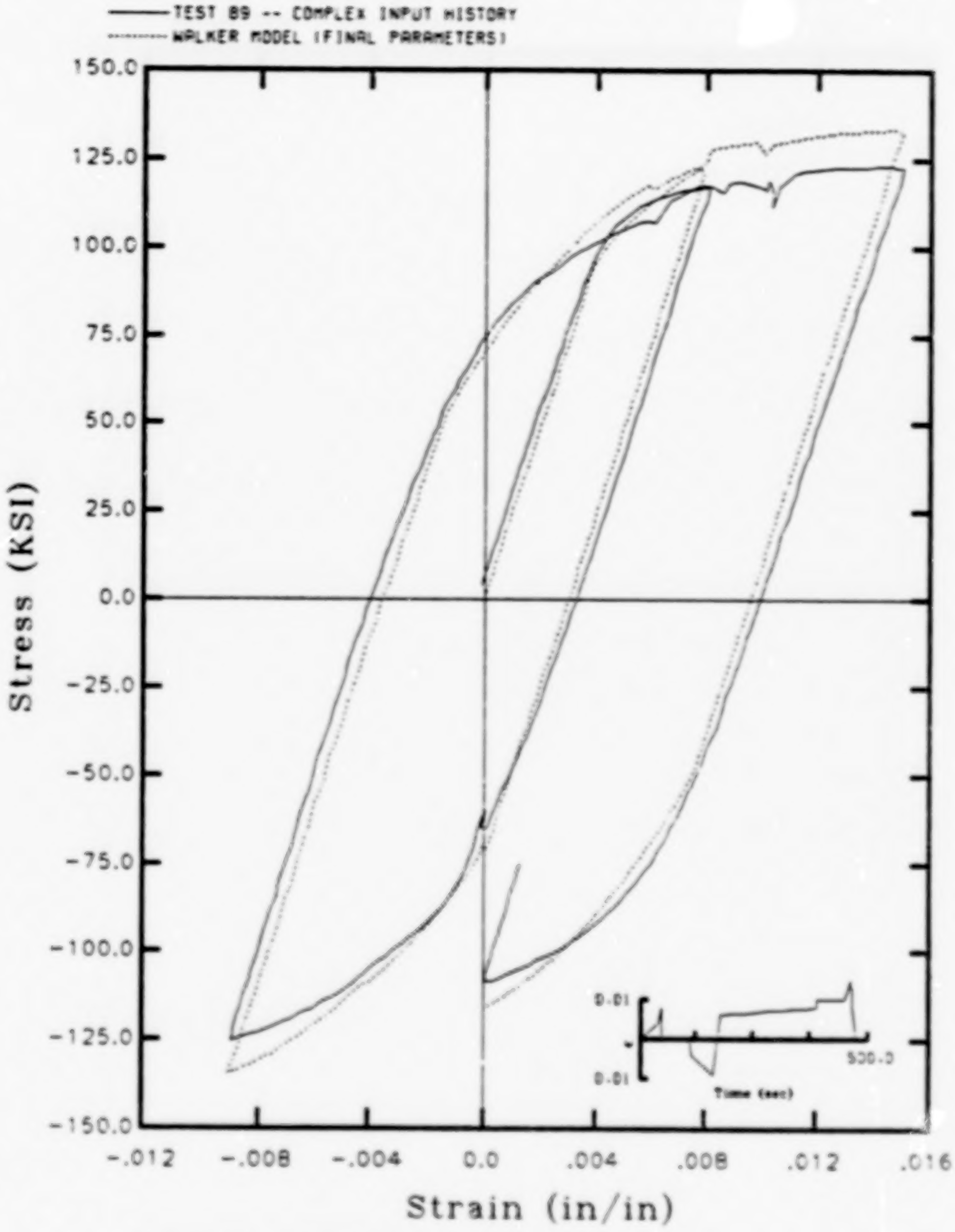

Strain (in/in)

Figure 19. Comparison of Walker's model to a complex history test.

N88
21521
UNCLAS

N88-21521

A CONSTITUTIVE MATERIAL MODEL FOR NONLINEAR FINITE ELEMENT STRUCTURAL ANALYSIS USING AN ITERATIVE MATRIX APPROACH

Herbert A. Koenig
University of Connecticut
Storrs, Connecticut 06268

Kwai S. Chan
Southwest Research Institute
San Antonio, Texas

Brice N. Cassenti
United Technologies Research Center
East Hartford, Connecticut 06108

Richard Weber
Pratt & Whitney
East Hartford, Connecticut 06108

A unified numerical method for the integration of stiff time-dependent constitutive equations is presented. The solution process is directly applied to a constitutive model proposed by Bodner. The theory confronts time-dependent anelastic behavior coupled with both isotropic hardening and directional hardening behaviors. Predicted stress-strain responses from this model are compared to experimental data from cyclic tests on uniaxial specimens. An algorithm is developed for the efficient integration of the Bodner flow equation. A comparison is made with the Euler method for integrating these relations. Additional comparisons are made with the model developed by Walker using the Euler integration method. An analysis of computational time is presented for the three algorithms.

I. Introduction

The development of constitutive models for the use in the structural analysis of aircraft gas turbine engine components has been an on-going process for many years.

Recent investigators have chosen to combine the physical aspects of the various non-linear effects into a unified theory in which all phenomena are coupled. One such theory was proposed by Bodner and Partom (1). This theory forms the basis for the investigations in this paper.

The usual approach for the integration of this type of model is either an Euler integration technique of direct "marching" or the second-order Adams-Moulton predictor-corrector technique (2).

II. Method

A new approach which uses a matrix integration technique has been presented by Tanaka (3). This approach solves for all the variables at the same time, thereby proposing to shorten the computational process and result in a stable integration scheme. The process should allow for larger time steps to be chosen than the Euler technique to achieve the same accuracy. The process is also stable. Therefore short computational times are the goal to be achieved for a given problem. Unified computative models such as

$$\underline{\dot{\sigma}} = \underline{D} \{ \underline{\dot{\epsilon}} - \underline{\dot{\epsilon}}^{N} \} \tag{1}$$

$$\underline{\dot{\epsilon}}^{N} = \underline{f} \{ \sigma, \underline{x}, T \} \tag{2}$$

$$\underline{\dot{x}} = \underline{g} \{ \underline{\dot{\epsilon}}^{N}, \underline{x}, T \} \tag{3}$$

may be treated by this technique.

Equation (3) may be enhanced by including work hardening and recovery formats, i.e.,

$$\underline{\dot{x}} = \underline{h} \{ \underline{\sigma}, \underline{x}, T \} \underline{\dot{\epsilon}}^{N} - \underline{r} \{ \underline{\sigma}, \underline{x}, T \} \tag{4}$$

Algorithm:

A numerical algorithm has been developed to numerically solve for the state variables represented in equations (2) - (4) subjected to a time - varying total strain function.

Equations (2) - (4) are formed into a matrix of the form

$$M x = b$$

Where M is the system Jacobian matrix, x is the vector of unknown variables, and b is the solution and error correction matrix.

This matrix is successively reformed and inverted to affect the solution of the state variables. No attempt is made to iterate on the matrix construction during a particular strain incremental step. Thus, the process constructed herein is a matrix extension of an Euler method in which all variables are calculated simultaneously based upon a driver of the state variables from the previous strain state.

Results:

The basic disadvantage in using Tanaka's NONSS (Noniterative Self-Correcting Solution) technique is the solution time which is excessive. The execution times for the load cases studied are summarized in Table I. The times shown are for a single load history at 2000 F, a strain rate of 4 x 10 -5 per second, a strain range of .6%, and a R-ratio of minus infinity. All computation times shown in Table I represent actual numerical computation time, the computer time spent for I/O and for accessing the clock were subtracted since the three routines differed in their respective I/O burdens. The convergence criterion used in each of the three routines was identical, namely the calculated out-of-plane stress for the uniaxial specimen was forced to be within a small tolerance of zero.

The first 5 cases shown in Table I summarize the experience with the NONSS integration method. It can be seen that the method is in general slower than the other two routines studied (Bodner's model using Euler integration shown as cases 6 through 10 and Walker's model using Euler integration shown as cases 11 through 15). In addition it can be seen that there is a tendency to fail to converge for coarser time steps. One difference between the NONSS routine and the other two studied is the lack of a self adaptive time step. This is evident in the comparison of the computing times in cases 3 and 4 where the number of integration time subincrements was doubled resulting in an approximately doubled computing gime. For the other two routines the number of subincrements was set initially for each increment, but underwent an automatic readjustment internally (self-adaptive time steps). This self adaptive feature often results in the same overall computation time even though the initial subincrement value was high. Inclusion of a self adaptive time step with the NONSS method would likely have prevented the convergence failures which occurred in cases 1 and 2 without significant loss of efficiency.

The present study supports the conclusion reached by Kumar et. al. (7) and by Imbrie, Haisler, and Allen (6); namely that the Euler forward difference or a minor modification of it is the most efficent method. Evidence of this for the NONSS and Euler methods is seen by comparing cases 5 and 9 in Table II. For case number 10, the self adaptive time stepping was suppressed in order to get a direct comparison of the two methods.

The cases 6 through 9 and 12 through 14 compare the response of Bodner's and Walker's models to various initializations of the subincrement parameter. For Walker's model the self adaptive time step quickly finds the lowest level and consequently completes the integration in the same amount of computing time regardless of the initial value of the subincrement. For Bodner's model this is also true to some extent. However an examination of case number 7 shows that initializing the subincrement parameter at too small a value can actually increase the total integration time. Thus there appears to be an inherent instability for Bodner's model which detracts from the overall efficiency. Additional study is required to identify the source of this instability and to determine if strategies exist which might prevent it.

A detailed analysis of the portions of each code where the computing time was actually spent showed that nearly 33% of computing time consumed by the NONSS method was spent in matrix inversion. This result suggests that considerable efficiency for the NONSS method could be gained if the inverted matrix were assembled directly. It was also noted that the algorithm used for Walker's model contained some redundant calculations which, if removed, would save approximately 20% of computing time.

References

1. Bodner, S.R. and Partom, Y., "Constitutive Equations for Elastic-Visco plastic Strain-Hardening Materials," Journal of Applied Mechanics, Vol.42, June 1975, pp 385-389.

2. Kaufman A., and Laflen, J.H. and Lindholm, U.S., "Unified Constitutive Material Models for Nonlinear Finite Element Structural Analysis", AIAA/SAE/ASME/ASEE 21st Joint Propulsion Conference, July 8-10, 1985, paper AIAA-85-1418.

3. Tanaka, T.G., "A Unified Numerical Method for Integrating Stiff Time-Dependent Constitutive Equations for Elastic/ Visco-Plastic Deformation of Metals and Alloys", A Ph.D thesis in Material Science and Engineering, Stanford University, May 1983.

4. "Constitutive Modeling For Isotropic Materials (HOST) (Second Annual Status Report), NASA CR 174980, July, 1985.

5. P. K. Imbrie, Private Correspondence, Texas A&M University, September 19, 1985.

6. P. K. Imbrie, W. E. Haisler, D. H. Allen, "Evaluation of the Numerical Stability and Sensitivity to Material Parameter Variations for Several Unified Constitutive Models", Texas A&M University, May, 1985.

7. V. Kumar, M. Morjaria and S. Mukherjee, "Numerical Integration of Some Stiff Constitutive Models of Inelastic Deformation," Transaction of the ASME, Journal of Engineering Materials and Technology, Vol. 102, pp 92-96, January, 1980.

Table I

A Comparison of Computing Times For 3 Constitutive Model Routines

CASE #	THEORY	METHOD	CYCLES	INCREMENTS	SUB-INCREMENTS	TIME
1.	Bodner-Partom	NONSS	2	80	2	failed
2.			2	80	3	failed
3.			2	80	4	3.50
4.			2	80	8	6.34
5.			2	320	1	3.53*
6.	Bodner-Partom	Euler (self-adaptive)	2	80	1	1.28
7.			2	80	3	1.62
8.			2	80	4	1.26
9.			2	80	8	1.26
10.			2	320	1	1.76
11.	Bodner-Partom	Euler self-adaptive, without directional hardening terms	2	320	1	1.43
12.	Walker	Euler (self-adaptive)	2	80	1	0.45
13.			2	80	2	0.45
14.			2	80	8	0.45
15.			2	320	1	1.03**

* 0.78 to assemble matrix, 1.15 to invert matrix

** 0.81 when adjusted for excess material properties calculations

N88
21522
UNCLAS

N88-21522

NONLINEAR STRUCTURAL ANALYSIS OF A TURBINE AIRFOIL USING THE WALKER VISCOPLASTIC MATERIAL MODEL FOR B1900 + Hf

T.G. Meyer, J.T. Hill, R.M. Weber
Pratt & Whitney
East Hartford, Connecticut 06108

A viscoplastic material model for the high temperature turbine airfoil material B1900 + Hf has been developed under NASA contract NAS3-23925, "Constitutive Modeling for Isotropic Materials (HOST)"[1], and has been demontrated in a three dimensional finite element analysis of a typical turbine airfoil. The demonstration problem is a simulated flight cycle and includes the appropriate transient thermal and mechanical loads typically experienced by these components. The Walker viscoplastic material model was shown to be efficient, stable and easily used. The following report summarizes the demonstration analysis and evaluates the performance of the material model.

Background

In recent years unified constitutive models have been developed as alternatives to the classical elastic-plastic-creep models for modeling nonlinear material behavior. These unified models are mathematically and functionally elegant and are capable of representing material nonlinear behavior over a wide range of temperatures and loading conditions while avoiding the simplifying assumptions of classical theory. The unified models are characterized by the use of a kinetic equation to relate inelastic strain rate to the applied stress and one or more internal state variables. Evolutionary equations are used to describe the variation of the internal state variables with loading history. Models of this kind have been shown to be capable of treating all aspects of inelastic deformation including plasticity, creep and stress relaxation.

PRECEDING PAGE BLANK NOT FILMED

ORIGINAL PAGE IS OF POOR QUALITY

Several unified models are being evaluated in a current NASA sponsored technical program, "Constitutive Modeling for Isotropic Materials (HOST)"[1]. Part of the evaluation includes a demonstration in an analysis of gas turbine component under simulated flight conditions. This paper presents the results of the demonstration of one of the unified models; the two state variable model patterned after Walker[2,3]. In this model, the general form of the inelastic flow law realtes the plastic strain rate tensor, $\dot{C}ij$, to the applied deviatoric stress, Sij, by the simple realtionship:

$$\dot{C}ij = f\left(\frac{Sij - \Omega ij}{K}\right)$$

where Ωij represents the "equilibrium" or "back" stress; and K, a scalar quantity, represents the degree of isotropic hardening. This two state variable unified model was developed by Walker[2,3] and modified during the present NASA program[1], and includes the increased computational efficiency features developed by Cassenti[4].

Component Finite Element Model Descrition

The component chosen for the demonstration of the B1900 + Hf viscoplastic material model is the airfoil portion of a typical cooled turbine blade. The foil was analyzed using the MARC[5] finite element program. Figure 1 shows the finite element mesh used in the analysis. A total of 173 elements and 418 nodes were used to describe the geometry, resulting in 1086 degrees of freedom. Two element types were used in the mesh. The bulk of the airfoil was modeled using 8 noded solid elements (MARC element type 7), but a portion of the leading edge was modeled with higher order 20 noded solid elements (MARC element type 21). A total of twenty four higher order elements were used in this region.

Boundary Conditions and Loading

The loading and boundary conditions were chosen to simulate a typical commercial engine flight. The flight simulation is shown schematically in Figure 2 and includes periods of Taxi, Take-Off, Climb, Cruise, Descent , Taxi and finally Shutdown. The Take-Off potion includes a momentary pause in engine acceleration to more faithfully simulate actual "rolling take-off" conditions. The range of foil temperatures and the centrifugal load spectrum encompassed in the simulated flight excercises the material model over most of its range of applicability.

Radial deflections were specified to be zero at the radially innermost section of the foil. Additional nodal boundary conditions were imposed in this plane to fully suppress rigid body motion.

The flight cycle was described in the stress analysis as a series of load increments which accounted for time steps and corresponding centrifugal loads and temperature profiles which were accessed from a previously generated thermal tape. The analysis proceeded until the cyclic response of the foil was noted to be stable from one flight to the next.

To allow the possibility of a very small load increments in the stress analysis, temperature profiles were defined frequently on the thermal tape. The maximum nodal temperature change from one profile to the next was 50C. In the Take-Off portion of the flight, where foil temperatures change rapidly, 25 time points were used. During the Cruise portion of the flight, the temperature profile is essentially constant. However, the material model state variables continue to evolve (e.g. creep deformation), so that step size is still important. Consequently, a large number of increments, (twenty-eight), were used in this portion of the flight. In total, 83 loading increments were used for each flight.

Stress Analysis Results; Accuracy and Stability

Two locations on the airfoil have been selected to illustrate the the results of the analysis. The behavior at these locations was expected to be very different and to provide an evaluation of the model over the widest possible range of conditions on the airfoil. Figure 3 shows the location of these points superimposed on the temperature profile during Cruise. Point A corresponds to the integration point nearest the external wall at the leading edge "hot spot", and was expected to have the largest amount of inelasticity in the foil. Point B corresponds to the integration point nearest the internal wall at an adjacent "cool spot". Both points are in the region of the model having higher order solid elements.

Figure 4 shows the strain - temperature history at the locations of interest during the first flight. The Take-Off portion is shown in more detail than the remainder of the flight. The various parts of the flight are labeled consistently with the flight definition shown in Figure 2. Figures 5 and 6 show the stress - strain response during all three flights at locations A and B respectively. The two locations present somewhat different pictures of the cyclic response: At location A, it is appears that a stabiblized hysteresis loop is achieved after just three flights. At the end of Take-Off, the largest variation in stress or strain between the second and third flights is less than 2% (see Table 1) and this is much less than the change between the first and second flight. However at location B the change between successive flights is decreasing less rapidly (5% and 4%). Thus the analysis predicts that different parts of the foil stabilize at different rates, which is reasonable since the loading and temeratures vary significantly from one location to another. In an actual airfoil it could be expected that the cyclic response from one flight to the next may be very similar even though it may never completely "stabilize" due to load redistribution from adjacent sections. As a result the hysteresis loop at any location may ratchet throughout the service life. Consequently, it is not appropriate to judge the material model stability based on the stress - strain response alone. More useful criteria are those of smoothness and sensitivity to step size. The stress - strain response in Figures 5 and 6 shows no tendancy to severe oscillation. The "looping" observed during initial loading at location A is a result of the complex thermal and mechanical loading on the foil during the "rolling take-off" portion of the flight and should not be interpreted as of a material model deficiency.

Table 1

Change in stress and strain from one flight to the next

Values at the end of Take-Off

	Flight	Stress (MPa)	Strain (%)	Inelastic Strain (%)
At Location A				
	1st	-235.9	-0.339	-0.239
	2nd	-213.1	-0.344	-0.267
	3rd	-209.7	-0.343	-0.276
At Location B	1st	629.7	0.365	0.068
	2nd	594.5	0.371	0.096
	3rd	569.0	0.376	0.119

Additional insight regarding the behavior of the material model and the adequacy of the solution can be gained by examining the evolution of key state variables and the inelastic strains. Figure 7 shows the evolution of the back stress in the radial direction at locations A and B during the first flight. Once again, the Take-Off pause is easily identified. The evolution of the inelastic strain in the radial direction during the first flight is shown in Figure 8 for location A. It is clear that these variables evolve smoothly, adding confidence in the behavior of the model and the fidelity of the analysis.

Figure 8 shows the accumulation of inelastic strain at location A during all three flights. Several observations can be made. First, the bulk of the inelastic strain is accumulated during Take-Off on the first flight. Secondly, the element exhibits some degree of reversed inelasticity as evidenced by the decrease in the inelastic strain during Cruise and Descent. The Take -Off portions of the second and third flights have nearly the same amounts of inelastic strain accumulation, indicating that the overall hysteresis loop shape is essentially unchanged.

A further check on the model can be made by checking that the effective stress and effective strains during initial stages of loading coincide with the normal monotonic tensile behavior. This check is valid only during early stages of loading before significant inelastic history has been accumulated. This check was made for location A at increment 19 which shows the first significant amount of inelastic strain. At increment 19, the inelastic strain is approximately 10% of the total mechanical strain. On the previous increment the inelastic strain was only 4% of the total strain. Figure 9 shows the monotonic stress - strain curve predicted by the material model (at a temperature and strain rate consistent with increment 19) along with the effective stress/ effective strain calculated for that increment.

Sensitivity to Step Size and Efficiency

A study was conducted to determine the sensitivity of the solution and material model behavior to step size. The reults reported above, (Base Case), were obtained using 23 increments to describe the Take-Off portion between ground Idle and the end of Take-Off. In this study, this same period was described in 10 increments, (Case 2), and in 6 increments, (Case 3). Only the first flight was studied. Figure 10 shows the resulting stress - strain response at location A . Case 3 failed to converge to a solution on increment 8. The convergence failure occurred at an element other than location A. Case 2 converged for all increments and produced results at the end of Take-Off which are in very good agreement with the Base Case.

It should also be noted that the improved efficiency integration techniques introduced by Cassenti[4] resulted in very fast solution times for the nonlinear analysis. Computing times for the nonlinear analysis were compared to computing times for a conventional elastic analysis at various times in the flight cycle. It was found that the matrix solution times were the same, indicating that the material model routines are very efficient. The efficiency measures developed by Cassenti avoid matrix inversion on each increment. Instead, the stiffness matrix is assemble at a reference temperature only, and any change in the stiffness due to temperature dependent elastic properties is passed to the main MARC program as an incremental inelastic stress vector. The reference temperature stiffness matrix is assembled only at the start of the inelastic analysis and each time the inelastic analysis is restarted. The net effect is that an inelastic analysis involving several increments actually uses less computing time than an equal number of separate elastic analyses, because each separate elastic analysis requires the stiffness matrix to be assembled anew.

Conclusions

The two state variable (Walker) viscoplastic model for B1900 has been successfully demonstrated in an analysis of a turbine airfoil under complex and realistic flight cycle loading. The model behaved very stably thoughout the flight cycle, was easily used and is very efficient. Each inelastic solution is no more expensive that an ealstic solution. The model was demonstrated using both linear strain and higher order three dimensional elements. A sensitivity study indicates that surprisingly large time/temperature/load steps could be used.

References

1. Constitutive Modeling for Isotropic Materials (HOST), NASA3-23925.
2. Walker, K.P., "Research and Development Program for Nonlinear Modeling with Advanced Time-Temperature Dependent Constitutive Relationships", Final Report, NASA CR-165533.
3. Walker, K.P., "Constitutive Modeling of Engine Materials", Final Report FR-17911, AFML Contract F33615-81-C-5040, November 1983.
4. Cassenti, B.N., " Research and Development Program for Nonlinear Structural Modeling with Advanced Time-Temperature Dependent Constitutive Relationships, Vol. I - Theoretical Discussion." Final Report NASA CR168191, July, 1983.
5. MARC General Purpose Finite Element Program, MARC Corporation, Palo Alto, Ca.

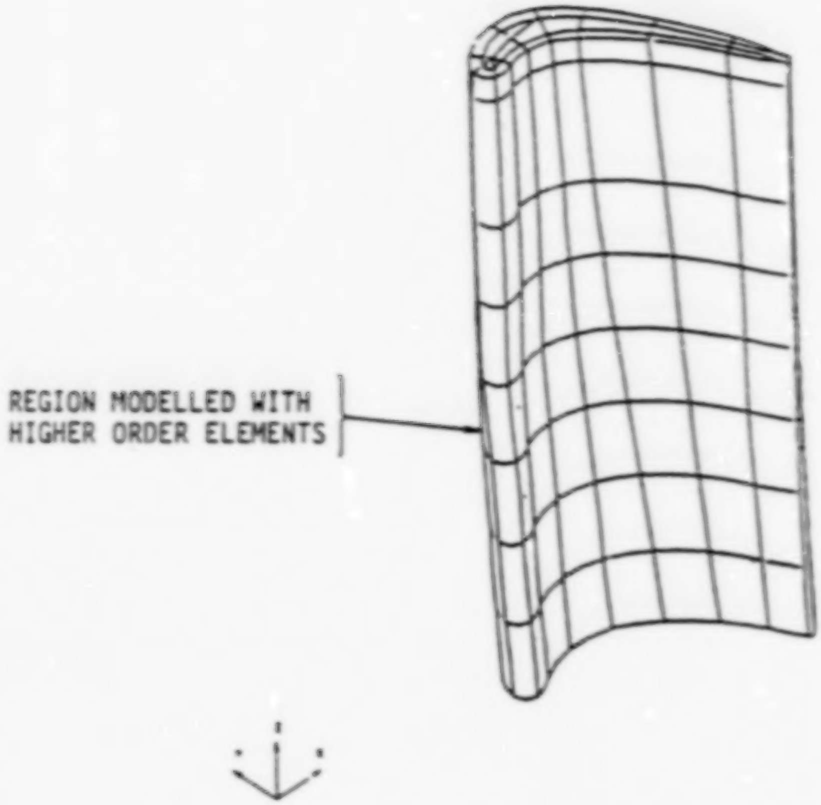
REGION MODELLED WITH
HIGHER ORDER ELEMENTS

Figure 1. Finite Element Mesh Used for Constitutive Model Demonstration

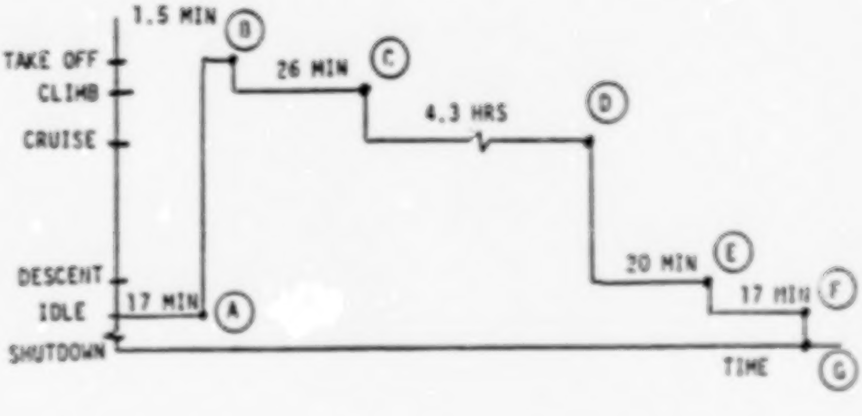

Figure 2. Simulated Flight Used in The Demonstration Analysis

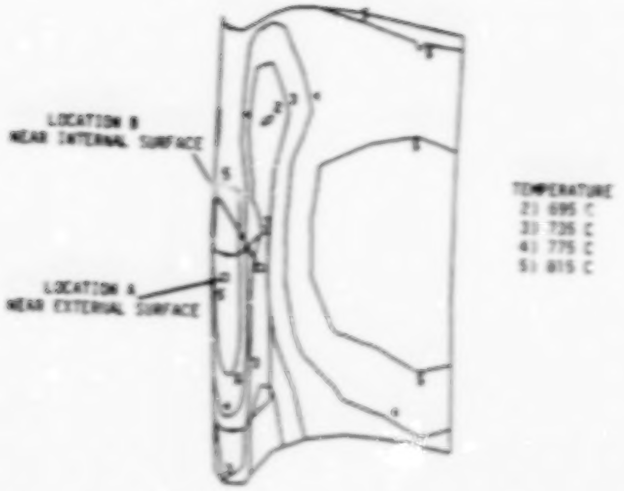
LOCATION B
NEAR INTERNAL SURFACE
LOCATION A
NEAR EXTERNAL SURFACE
TEMPERATURE
2) 695 C
3) 735 C
4) 775 C
5) 815 C

Figure 3. Steady State Temperature Profile During Cruise and Locations A and B Examined in Detail

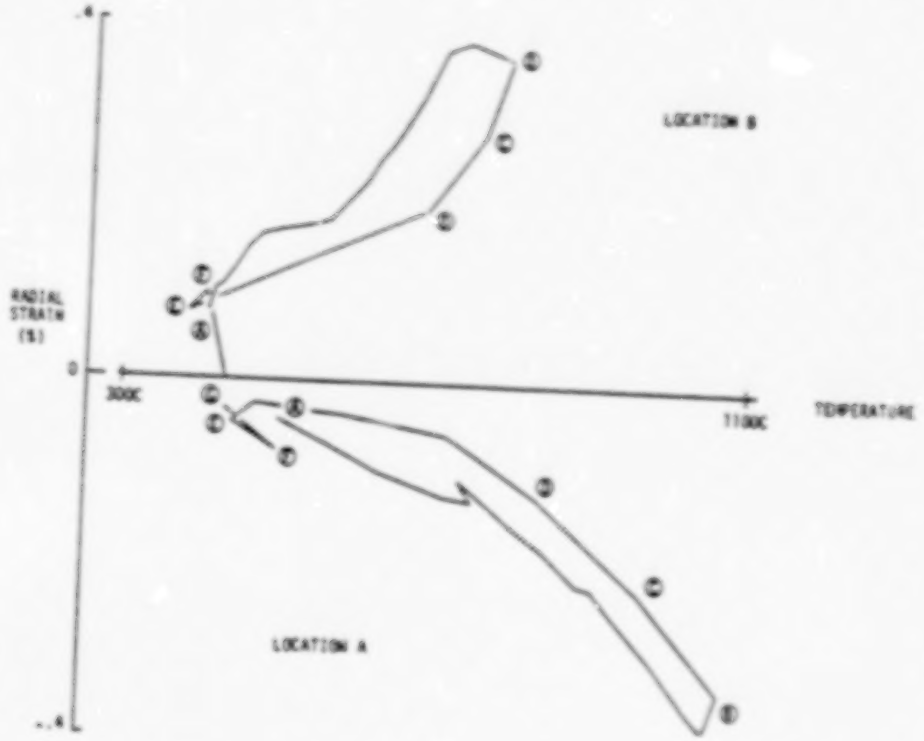

Figure 4. Strain-Temperature History at Locations A and B During First Flight

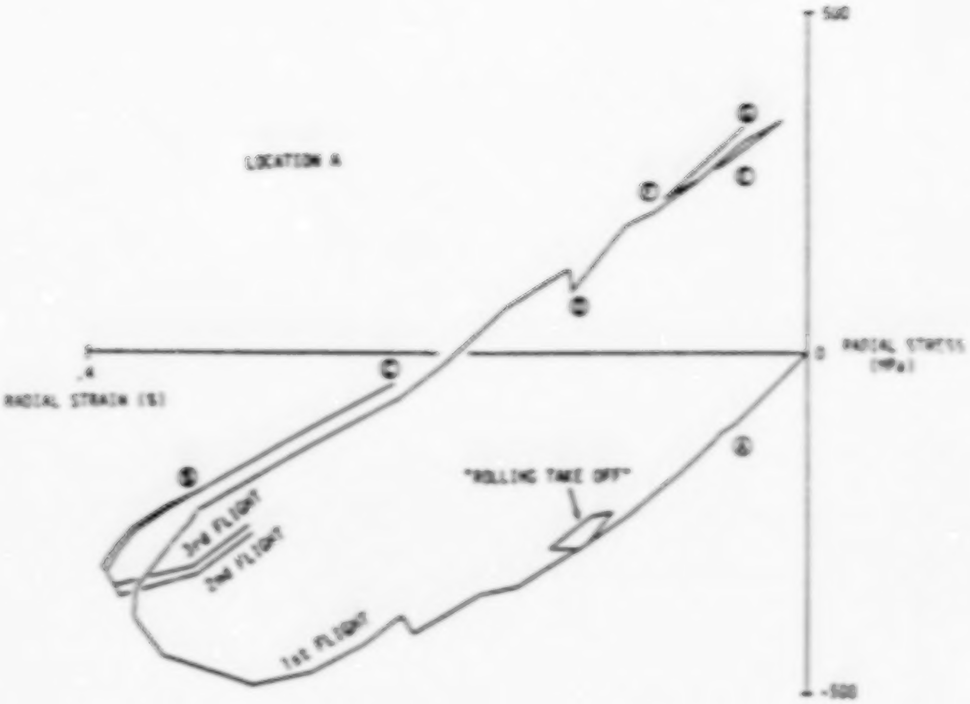

Figure 5. Stress-Strain Response at Location A

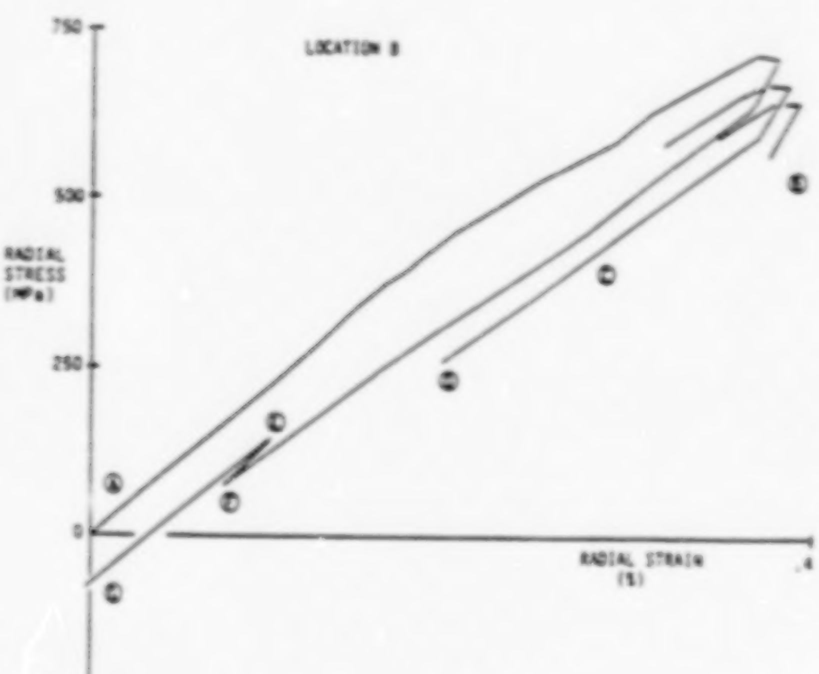

Figure 6. Stress-Strain Response at Location B

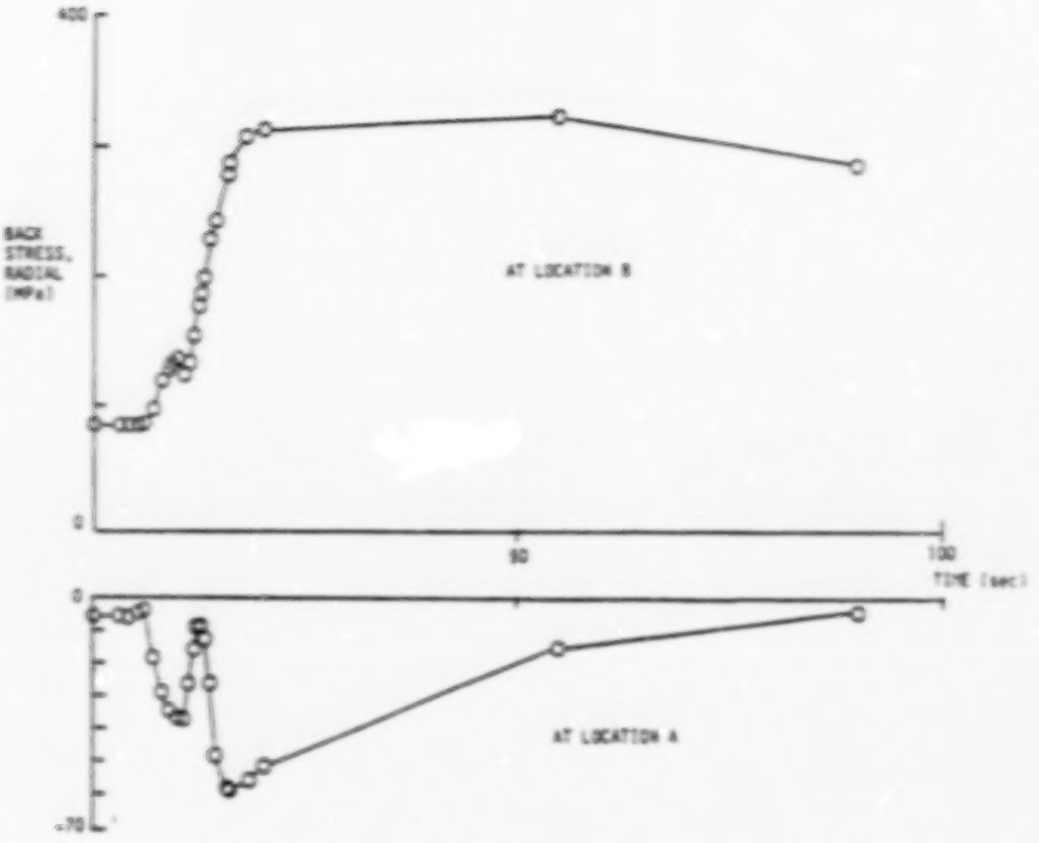

Figure 7. Evolution of Back Stress During Take-Off in the First Flight

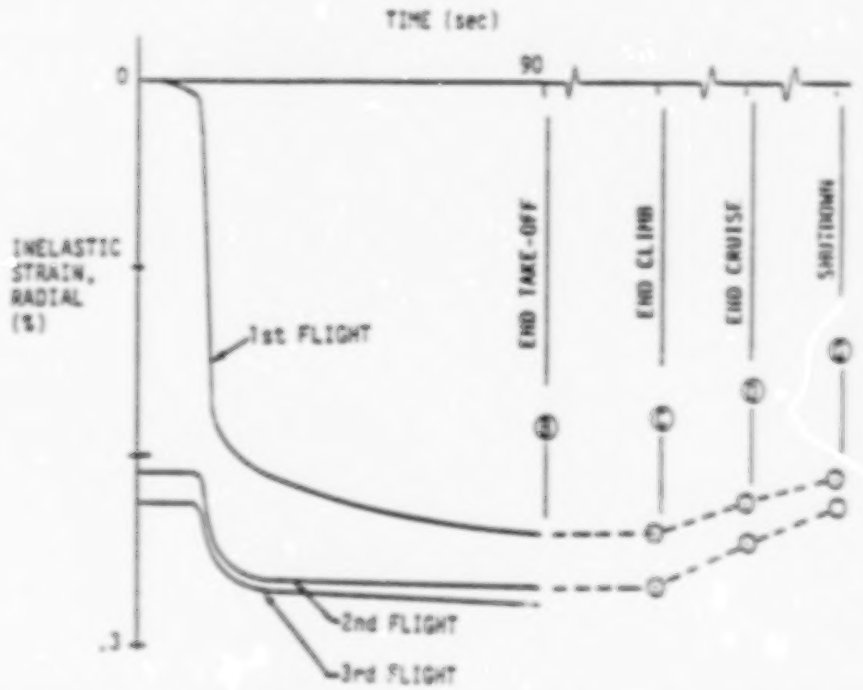

Figure 8. Accumulation of Inelastic Strain at Location A During Three Flights.

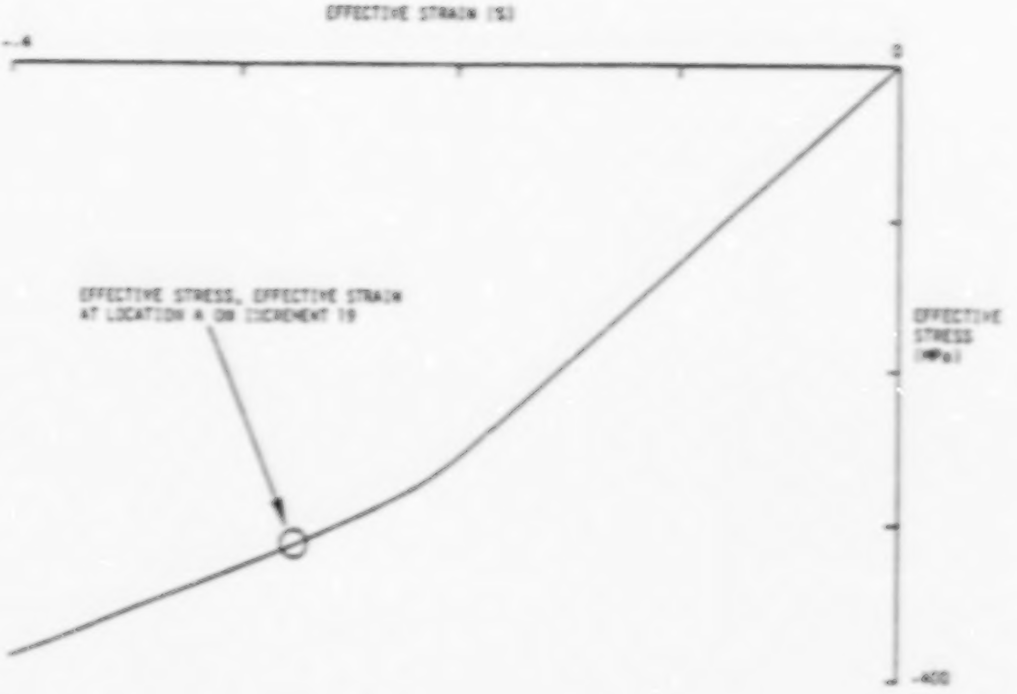

Figure 9. The Effective Stress/Effective Strain at Location A Follows the Expected Monotonic Curve.

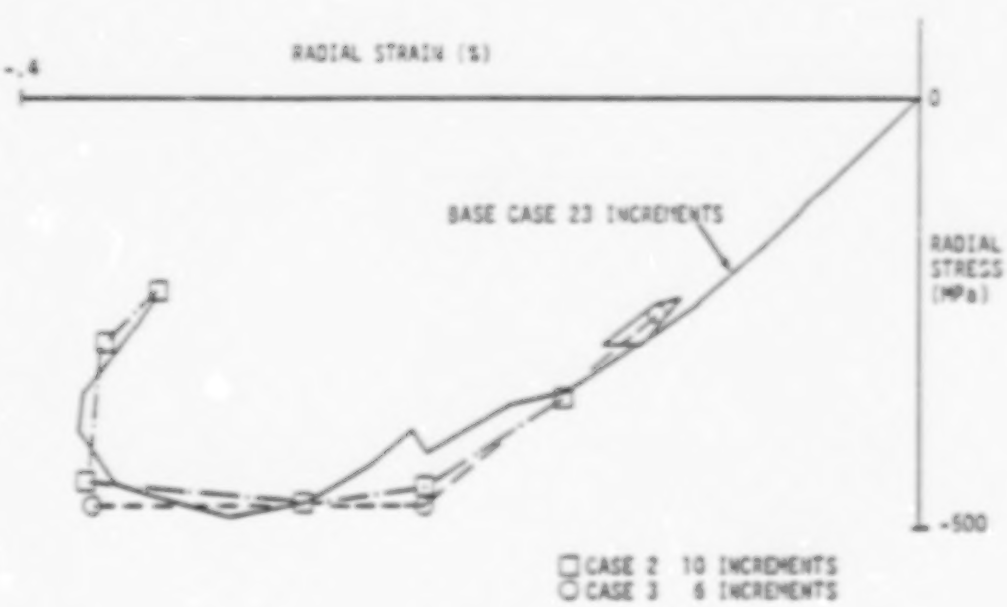

Figure 10. Effect of Step Size During Take-Off of the First Flight

N88
21523
UNCLAS

N88-21523

UNIFIED CONSTITUTIVE MODELS FOR HIGH-TEMPERATURE STRUCTURAL APPLICATIONS[*]

U.S. Lindholm, K.S. Chan
Southwest Research Institute
San Antonio, Texas

S.R. Bodner
Technion-Israel Institute of Technology
Haifa 32000, Israel

R.M. Weber
Pratt & Whitney
East Hartford, Connecticut 06108

K.P. Walker
Engineering Scientific Software, Inc.
Smithfield, Rhode Island 02917

Unified constitutive models are characterized by the use a single inelastic strain rate term for treating all aspects of inelastic deformation, including plasticity, creep, and stress relaxation under monotonic or cyclic loading. The structure of this class of constitutive theory pertinent for high temperature structural applications is first outlined and discussed. The effectiveness of the unified approach for representing high temperature deformation of Ni-base alloys is then evaluated by extensive comparison of experimental data and predictions of the Bodner-Partom and the Walker models. The use of the unified approach for hot section structural component analyses is demonstrated by applying the Walker model in finite element analyses of a benchmark notch problem and a turbine blade problem.

INTRODUCTION

It is well-known that accurate prediction of component fatigue lives is critically dependent on the success with which local inelastic stress/strain states in the vicinity of holes, fillets, and other strain concentration sites can be calculated. Stress/strain computations for hot section components are complicated by two factors: (1) complex component geometries, and (2) nonlinear material behavior associated with high temperature creep-plasticity effects. The latter factor is particularly significant for turbine engine components in view of the fact that the combinations of centrifugal, aerodynamic, thermal and other mechanical loads that typically occur in a flight operation are so severe that they tend to drive the underlying material response beyond accepted limits for linear elastic behavior and into the regime characterized by inelastic, time- and temperature-dependent deformation, thereby rendering elastic analysis methodologies inapplicable. Thus, an accurate account of geometrical complexities, three-dimensional and inelastic effects of hot section components requires a nonlinear finite-element methodology with an advanced material constitutive model appropriate for high temperature applications.

---

[*] Work supported by NASA Lewis Research Center through Contract No. NAS3-23925.

C-5

Advanced constitutive models which have been developed for high temperature applications are generally based on the unified approach, utilizing a single inelastic term to encompass all aspect of inelasticity, including plasticity, creep, and stress relaxation. Unified constitutive models which have been proposed in the literature include those of Walker [1], Bodner-Partom [2,3], Miller [4], Krieg, Swearengen and Rhode [5], Chaboche [6], Robinson [7], Hart [8], and Lee and Zaverl [9]. Of these newly proposed constitutive models, only a small number of them have been used in conjunction with finite-element methods for structural analysis applications. Despite the limited experience, the earlier works [1] clearly demonstrated that the unified approach is entirely compatible with three-dimensional inelastic finite-element formulations, and constitutes a new approach for structural analysis which has heretofore been based on classical concepts with uncoupled creep-plasticity models. In avoiding the simplified assumptions of classical theory, the unified theory can more realistically represent the behavior of materials under cyclic loading conditions and high temperature environments.

A joint effort by Southwest Research Institute and Pratt & Whitney Aircraft has been underway for the past two years [10,11] to: (1) develop unified constitutive models for representing high-temperature, time-dependent inelastic deformation of initially isotropic cast nickel-base alloys, and (2) apply a unified constitutive model for hot section component analysis. This effort is funded under the HOST (Hot Section Technology) Program managed by NASA Lewis Research Center. The objective of this paper is to summarize the results to date concerning the use of the unified approach for modeling high temperature deformation of nickel-base alloys and for structural analysis. In this paper, the structure of unified constitutive theories pertinent for high-temperature structural applications is first outlined and discussed. The use of the unified approach for representing high temperature deformation is then evaluated by extensive comparison of experimental data of a nickel-base alloy and predictions of two unified models: the Bodner-Partom and the Walker models. Finally, the use of the unified approach for hot section structural component analyses is demonstrated by applying the Walker model to finite element analyses of a benchmark notch problem and a turbine blade problem.

OVERVIEW OF UNIFIED CONSTITUTIVE MODELS

The "unified" models are inherently incremental (rate formulation), retaining the separation of elastic and inelastic behavior and the assumption of plastic incompressibility. Thus,

$$\dot{\varepsilon}_{ij} = \dot{\varepsilon}^{e}_{ij} + \dot{\varepsilon}^{p}_{ij} \tag{1a}$$

and

$$\dot{\varepsilon}^{p}_{kk} = 0. \tag{1b}$$

All inelastic behavior is represented in the single term $\dot{\varepsilon}^{p}_{ij}$. For small deformation, the elastic term, $\dot{\varepsilon}^{e}_{ij}$, follows Hooke's law. Development of the inelastic strain rate term generally includes three components: a flow law, a kinetic relation, and a set of evolutionary equations for the internal variables describing the development of hardening and recovery processes due to deformation and thermal histories. An extensive review of the general forms for these components is given in [10,12].

Most models use the generalized form of the Prandtl-Reuss flow law, i.e.

$$\dot{\varepsilon}^p_{ij} = \lambda(S_{ij} - \Omega_{ij}) \tag{2}$$

where S_{ij} is the deviatoric stress, Ω_{ij} is also a deviatoric tensor often referred to as the equilibrium stress, back stress, or kinematic hardening variable, and λ is a scalar coefficient incorporating isotropic hardening. In one model examined (Bodner-Partom), the Ω_{ij} is dropped and directional hardening is included in an incremental scalar fashion in the coefficient λ. Eq. 2 defines the direction of inelastic flow with respect to the applied deviatoric stress S_{ij} or the effective stress $S_{ij} - \Omega_{ij}$.

The functional relationship between the scalar increments of strain rate and stress and the temperature, T, and internal variables, X_i, is called the kinetic relation, e.g.:

$$D^p_2 = F(J_2, T, X_i) \ , \tag{3}$$

where

$$D^p_2 = \frac{1}{2} \dot{\varepsilon}^p_{ij} \dot{\varepsilon}^p_{ij}$$

and

$$J_2 = \frac{1}{2}(S_{ij} - \Omega_{ij})(S_{ij} - \Omega_{ij}) \ .$$

The number of internal variables, X_i, used is arbitrary but usually is restricted to two; one representing isotropic hardening and the other directional (kinematic) hardening. At high temperatures, the evolutionary equations for the internal variables are based on the well-accepted Bailey-Orowan theory for a hardening process proceeding with accumulating deformation and a recovery or softening process proceeding with time. The evolution rate of an internal variable is then the difference between the hardening rate and the recovery rate.

Thermal history effects are generally modeled by including thermal terms in the evolution equations for the isotropic and directional hardening variables [12,13]. The general forms of the evolution equations for the isotropic hardening variable, K, and the directional hardening variable, Ω_{ij}, are [12]:

$$\dot{K} = h_1(K)\dot{M}_1 - r_1(T,K) + \theta_1(K,T)\dot{T} \tag{1}$$

$$\dot{\Omega}_{ij} = h_2(\Omega_{ij})\dot{M}_{ij} - d(\Omega_{ij},T)\dot{N}_{ij} - r_2(\Omega_{ij},T)V_{ij} + \theta_2(\Omega_{ij},T)\dot{T}\, W_{ij} \qquad (2)$$

where h_1, r_1, and θ_1 represent, respectively, the hardening, static thermal recovery, and thermal history functions for K; h_2, d, r_2, and θ_2 represent the hardening, dynamic recovery, static thermal recovery, and thermal history functions for Ω_{ij}, respectively; $\dot{N}_{ij}$, V_{ij} and W_{ij} are directional indices related to unit vectors representing plastic strain rate, stress, or the directional hardening variable [12]. The measure of the hardening rate, $\dot{M}$, is taken as either the inelastic strain rate $\dot{\epsilon}^p_{ij}$ or the inelastic work rate, $\dot{W}_p = \sigma_{ij}\dot{\epsilon}^p_{ij}$.

The appropriate forms of θ_1 and θ_2 are not very well established at this time. A general approach for modeling thermal history effects is to express θ_1 and θ_2 as functions of the internal variable and temperature [12,13]. New internal variables may also be introduced [14]. In a particular approach [1,11], θ_1 and θ_2 are assumed to depend on temperature only and are taken as functions represented by variations of material constants with respect to temperature [1,11].

In the following sections, extensive experimental correlations with two specific models, Bodner-Partom [2,3] and Walker [1], will be presented. While following the general form outlined above, these two models differ considerably in detail but both have found considerable use in high-temperature problems. Details of both sets of equations are given in Tables 1 and 2.

EVALUATION OF THE BODNER-PARTOM AND THE WALKER MODELS

Extensive experiments were conducted on a cast turbine blade or vane alloy (PWA B1900+Hf) over the entire range of conditions experienced by hot section components, which include temperature ranging from room temperature to 1093C, strain rates from 10^{-7} to 10^{-2} $\sec^{-1}$ and strain of ± 1 percent. The B1900+Hf alloy has a grain size of .8 mm (ASTM No. -2 to -3), a γ' size of 0.9 μm in the fully heat-treated condition, and low porosity. All specimens were obtained from a single heat.

Testing included isothermal tension, creep, stress relaxation, cyclic loading (with and without mean stress or hold time), thermomechanical fatigue (TMF) cycles, and proportional and nonproportional biaxial strain cycles. Details of the experimental procedures are described elsewhere [11]. As described in [11], the material constants for the Bodner-Partom model were derived from uniaxial tension data only, while the Walker model required, in addition, a small amount of cyclic data. Tables 3 and 4 summarize the Bodner-Partom and the Walker model constants for B1900+Hf, respectively. Formalized procedures for developing model constants are being developed [11]. In the past, this function has been a major detraction from use of these models. The remaining cyclic, creep, relaxation, and biaxial data are predictions from each model.

A. Deformation Under Uniaxial Tension, Creep, and Cyclic Loading

Figure 1 shows monotonic tensile results and corresponding model calculations at three temperatures and a constant strain rate of 8.3×10^{-5} sec^{-1}. These monotonic stress vs strain data are used to establish the constants for the evolutionary equations of the internal variables describing hardening and recovery behavior. In the case of the Walker model, the cyclic stress-strain curves are needed, in addition, in order to differentiate between the isotropic and directional components. Similar tensile data over a wide range in temperature and strain rate are given in Figure 2. Temperature and rate variations are needed to fix the constants related to the kinetic equations. At 760 C (1400 F), hardening mechanisms are dominant, while at 1093 C (2000 F), the recovery terms in the evolutionary equations become dominant. The transition between hardening and recovery is dependent on both temperature and strain rate. At 760 C, the Walker model includes a strain-aging term which accounts for the region of negative strain-rate sensitivity.

Figure 3 shows the correlation for steady-state creep rate as a function of the applied stress at four temperatures. The hardening-recovery transition is evident in these data also. These results are predictions obtained from the monotonic tensile data.

A sample cyclic stress-strain curve at 1093 C is given in Figure 4. These are saturated (stable) loops after a small amount of cyclic hardening. Cyclic hardening or softening is included in the models. Cyclic stress-strain data obtained by incrementally increasing the strain range for completely reversed cycling (R = -1) is summarized in Figure 5 for four different temperatures. Here again, it should be emphasized that the Bodner-Partom model predictions are based on monotonic input data only.

The effects of imposed compressive and tensile mean strains on the cyclic constitutive behavior of B1900+Hf have also been investigated. The results for 760 C are summarized in Figure 6, with corresponding model predictions using both the Bodner-Partom and the Walker theories. For purposes of comparison the half stress range ($\Delta\sigma/2$), half cyclic plastic strain range ($\Delta\epsilon_p/2$) and mean cyclic stress at both the first and sixth cycle are plotted versus the half strain range ($\Delta\epsilon/2$) for R ratios (minimum strain/-maximum strain) of 0, -1, and $-\infty$. Two important observations in Figure 6 are: (1) the experimental and theoretical saturated cyclic stress-strain curves ($\Delta\sigma/2$ - $\Delta\epsilon/2$ curves) appear to be unique at a particular strain rate and temperature and are independent of the R ratio, and (2) both unified models predict a drift in the mean cyclic stress which is not always observed in the experimental data.

Stress relaxation tests were performed by holding strain at various locations of the hysteresis loops for a two minute period. Figure 7 compares model predictions and experimental results of stress relaxation during strain hold on the unloading portion of the saturated hysteresis loop of B1900+Hf at 1093 C. The Bodner-Partom calculations agree well with the experimental data for strain holds at .6% and .55%. At .5%, the experimental result indicates reverse stress relaxation as the stress is slightly increased from compression to tension during the hold period while the Bodner-Partom model predicts a constant stress with essentially no stress relaxation. In principle, the reverse stress relaxation process is capable of prediction by the equilibrium stress approach. However, no stress relaxation calculations are currently available for the Walker model.

B. Deformation Under Thermomechanical Cycling

In practice, component parts are subject to simultaneous load and thermal cycling and a dominant failure mode is thermomechanical fatigue (TMF). The ability of a unified constitutive model to predict response to TMF cycling is of prime interest and constitutes a rigorous test of the model. It is of further interest to determine whether a model based on equilibrium isothermal data can handle the nonisothermal response problem. Numerous experimental TMF cycles have been run with both in-phase and out-of-phase temperature-strain cycles and with and without hold time. Figure 8 presents a typical data vs model correlation for a simple in-phase cycle. Similar results are obtained for an out-of-phase cycle with a 60 second strain hold at maximum compressive strain, Figure 9. The cycle time for both the in-phase and out-of-phase cycles was 60 seconds. The correlation with both isothermally-based models is reasonably good, indicating that no obvious correction is needed to account for the rate of change in temperature. For materials exhibiting strong dynamic strain aging effect or microstructural changes during thermomechanical cycling, this may no longer be the case and extra terms in the constitutive model may be required.

C. Deformation Under Biaxial Loading

Another critical test for the unified models is their ability to handle complex multiaxial stress or strain histories. Hardening laws under nonproportional loading still pose a problem in classical rate-independent plasticity. Most of these theories are based on initial yield and subsequent multiple loading surfaces with a normality rule. While unified theories can be developed based upon yield surface or plastic potential concepts [6-9], the models studied here assume viscoplastic flow occurs at all finite stress states other than $S_{ij} = \Omega_{ij}$ (Bodner-Partom assumes $\Omega_{ij} = 0$). The evolutionary equations in combination with the flow law define the incrementally-developed hardened state for each material direction.

Figure 10 shows experiment-model correlations for a strongly nonproportional strain cycle in which the axial and torsional strain are controlled to have the same effective cyclic strain amplitude with a 90° phase difference between the two inputs. This results in the nearly circular stress trajectories shown in Figure 10 along with the individual stress-strain hysteresis loops. The models, based on uniaxial data, show good qualitative agreement with some overestimate of the stress amplitudes.

Previous results with Hastelloy X [10] had shown that cyclic strain hardening under similar out-of-phase, nonproportional loading was significantly greater than that obtained under uniaxial or other proportional loading paths. For B1900+Hf, sequential proportional and nonproportional straining histories produced no differences in hardening behavior at all temperatures from 20 C to 980 C. There seems to be a difference in this aspect of hardening between the precipitation-hardened alloys and dominantly solid solution alloys. The nonproportional strain paths also provide useful information on the correct form of the flow law. In the strain trajectories of Figure 10, there is observed a phase lag of approximately 20° between the inelastic strain rate $\dot{\epsilon}^p_{ij}$ and the deviatoric stress S_{ij}. This phase lag is reasonably predicted by the Walker model through the use of the equilibrium or back stress term, Ω_{ij}. In the Bodner-Partom approach, $\dot{\epsilon}^p_{ij}$ and S_{ij} are assumed coincident.

Figure 11 shows another more complex nonproportional path where the frequency of the shear strain is twice that of the axial strain. Again, qualitative agreement with the models is good; however, the hysteretic energy loss seems to be greater in the models than in the experiment.

HIGH TEMPERATURE STRUCTURAL ANALYSES

Preliminary effort to demonstrate the utility of the unified models for component analysis has been accomplished at Pratt & Whitney Aircraft. For this purpose, the MARC nonlinear finite element computer program was the vehicle for incorporating the viscoplastic models. The incorporation in the MARC program was achieved by means of an initial stress technique. All of the material nonlinearity in the constitutive equations is put into an initial load vector and treated as a pseudo body force in the finite element equilibrium equations. Because the models form a "stiff" system of differential equations, it is necessary to form the incremental constitutive equation appropriate to the finite element load increment by means of a subincrement technique. Then the constitutive equations are integrated over the small subincrements to form an accurate representation over the finite element load increment. The integration of the constitutive equations is currently performed by using explicit Euler forward differences with subincrement time step sizes determined by convergence and stability criteria. Other integration schemes are under investigation in the attempt to improve computational efficiency.

A. Benchmark Notch Analyses

The MARC finite-element code and the Walker model were used to analyze a number of benchmark notch problems. Elevated temperature testing of instrumented notch round specimen was also conducted to generate notch displacement data for verification of the analytical methodologies. The benchmark notch testing was conducted on specimens of design shown in Figure 12a for six load patterns at 871°C over load ranges sufficient to result in short time inelastic behavior and over load time sufficient to induce significant time-dependent inelastic notch strain. The loading conditions and the experiment procedures for the benchmark notch experiments are described in [11]. In these experiments, the radial and the diametrial displacements at the notch throat were measured.

The finite-element mech for the benchmark notch specimen is shown in Figure 12b. In one of the benchmark experiment, the notch specimen was loaded under monotonic tension at a nominal strain rate of 2×10^{-5} $\sec^{-1}$. The variation in the diametrial displacement at the notch throat with the applied load is presented with model prediction in Figure 13. At the imposed nominal strain rate of 2×10^{-5} sec^{-1}, the limit load was 35,800N (8050 lb). Finite element load versus displacement predictions agree well with the test data at low values of diametrial displacement, but diverge at strain conditions indicative of bulk yielding in the notch. The limit load is overestimated by 18%.

In another benchmark experiment involving dwell, the notched specimen was cycled at ± 331, ±352, ±365, ±386, and ± 414 MPa for 10 cycles at each stress level. Additionally, a minute hold was applied at both maximum tension and compression. The variation of the peak-to-peak notch displacement and the cyclic inelastic notch displacement with the cycle number is shown in Figures 14a and b, respectively. As noted in Figures 14a and b, the finite element analysis predicts the peak-to-peak variation in the throat diametrial displacement to within 14%, but underestimates the cyclic inelastic notch displacement by nearly 60% at the highest test loads. However, it should be noted that the inelastic notch displacements are quite small.

B. Inelastic Turbine Blade Analysis

The MARC code along with the Walker constitutive model were used to analyze a turbine blade under a simulated flight loading spectrum. The FEM blade model with the temperature and engine RPM flight history are given in Figure 15. The flight history, representative of a commercial airline, has some high transient response early followed by steady cruise conditions. While thermal and mechanical response is computed continuously for the complete blade, we will present here a comparison only for a selected element between a totally elastic analysis and the viscoplastic analysis. This comparison is given in Figure 16. Besides showing the difference in response for a given problem by including viscoplastic behavior, this exercise provides some comparison of the relative computational times for the two problems. In this case, the viscoplastic computation time was about seven times as great as for the elastic case. More recent work has reduced this ratio to less than two [15].

CONCLUSIONS

Rapid advances are being made in the development of strongly nonlinear, time- and temperature-dependent constitutive models for metals used in gas turbine hot section components. These models, in conjunction with finite element structural analysis codes, will allow accurate prediction of stress histories and strain accumulation of components in service. This capability, particularly for regions of local stress concentration, is essential for reliable input into cumulative damage or crack initiation algorithms used for component life prediction. An increased coupling between constitutive models describing stable deformation states and limit conditions describing the initiation of local material instability or failure is needed.

ACKNOWLEDGEMENTS

The authors are grateful for the financial support provided by NASA Lewis Research Center through Contract No. NAS3-23925.

REFERENCES

1. K. P. Walker, NASA Contract Report NASA CR 165533, 1981.

2. S. R. Bodner and Y. Partom, ASME J. of Applied Mechanics, Vol. 42, 1975, p. 385.

3. S. R. Bodner, "Evolution Equations for Anisotropic Hardening and Damage of Elastic-Viscoplastic Materials," Pro. Conference on Plasticity Today, Udine, Italy, 1983.

4. A. K. Miller, ASME J. of Eng. Mat. & Tech., Vol. 96, 1976, p. 97.

5. R. D. Krieg, J. C. Swearengen, and R. W. Rohde, in "Elastic Behavior of Pressure Vessel and Piping Components," PVP-PB-028, p. 15.

6. J. L. Chaboche, Bulletin de L'Academie des Sciences, Serie des Science Techniques, Vol. XXV, No. 1, 1977, p. 33.

7. D. N. Robinson, ORNL Report/TM-5969, 1978.

8. E. W. Hart, ASME J. of Eng. Mat. and Tech., Vol. 98, 1976, p. 193.

9. D. Lee and F. Zaverl, Jr., Acta Met., Vol. 26, No. 11, 1975, p. 385.

10. U. S. Lindholm, K. S. Chan, S. R. Bodner, R. M. Weber, K. P. Walker, and B. N. Cassenti, NASA CR-174718, May 1984.

11. U. S. Lindholm, K.S. Chan, S. R. Bodner, R. M. Weber, K. P. Walker, and B. N. Cassenti, NASA CR-174980, July 1985.

12. K. S. Chan, U. S. Lindholm, S. R. Bodner, and K. P. Walker, "A Survey of Unified Constitutive Theories," Prof. Second Symposium on Nonlinear Constitutive Relations for High Temperature Applications, NASA Lewis Research Center, Cleveland, Ohio, NASA Conf. Pub. 2369, Oct. 1984.

13. D. N. Robinson and P. A. Bartolotta, "Viscoplastic Constitutive Relationships with Dependence on Thermomechanical History," NASA Contractor Report 174836, 1985.

14. G. Cailletaud and J. L. Chaboche, "Macroscopic Description of the Microstructural Changes Induced by Varying Temperature," ICM3, Vol. 2, 1979.

15. K.S. Chan, U.S. Lindholm, S.R. Bodner, J.T. Hill, R.M. Weber, and T.G. Meyer, Third Annual Status Report, NASA Contract No. NAS 3-23925, Southwest Research Institute, 1986.

TABLE 1. SUMMARY OF BODNER-PARTOM MODEL

1. Flow Law:

$$\dot{\varepsilon}_{ij} = \dot{\varepsilon}_{ij}^{e} + \dot{\varepsilon}_{ij}^{p}$$

$$\dot{\varepsilon}_{ij}^{p} = \lambda S_{ij} \; ; \; \dot{\varepsilon}_{kk}^{p} = 0$$

with $S_{ij} = \sigma_{ij} - \frac{1}{3}\delta_{ij}\sigma_{kk}$

2. Kinetic Equation:

$$D_2^p = D_0^2 \exp\left\{-\left[\frac{Z^2}{3J_2}\right]^n\right\}$$

with $Z = Z^I + Z^D$

$$D_2^p = \frac{1}{2}\dot{\varepsilon}_{ij}^{p}\dot{\varepsilon}_{ij}^{p}$$

$$J_2 = \frac{1}{2}S_{ij}S_{ij}$$

$$\lambda^2 = D_2^p / J_2$$

3. Evolution Equations of Internal Variables:

a. Isotropic Hardening

$$\dot{Z}^I = m_1\left[Z_1 + \alpha Z_3 - Z^I\right]\dot{W}_p - A_1 Z_1\left[\frac{Z^I - Z_2}{Z_1}\right]^{r_1}$$

where $\dot{\alpha} = m_2(\alpha_1 - \alpha)\dot{W}_p \sin\theta$

$$\theta = \cos^{-1}(v_{ij}\bar{v}_{ij}) \quad \text{or} \quad \theta = \cos^{-1}(u_{ij}\bar{u}_{ij})$$

$$v_{ij} = \beta_{ij}/(\beta_{kl}\beta_{kl})^{1/2}, \; \bar{v}_{ij} = \dot{\beta}_{ij}/(\dot{\beta}_{kl}\dot{\beta}_{kl})^{1/2}$$

$$u_{ij} = \sigma_{ij}/(\sigma_{kl}\sigma_{kl})^{1/2}, \; \bar{u}_{ij} = \dot{\sigma}_{ij}/(\dot{\sigma}_{kl}\dot{\sigma}_{kl})^{1/2}$$

with $Z^I(0) = Z_0 \; ; \; \dot{W}_p = \sigma_{ij}\dot{\varepsilon}_{ij}^{p} \; ; \; W_p(0) = 0; \; \alpha(0) = 0$

b. Directional Hardening

$$\dot{\beta}_{ij} = m_2(Z_3 u_{ij} - \beta_{ij})\dot{W}_p - A_2 Z_1\left[\frac{(\beta_{kl}\beta_{kl})^{1/2}}{Z_1}\right]^{r_2} v_{ij}$$

with $Z^D = \beta_{ij}u_{ij} \; ; \; Z^D(0) = 0 , \; \beta_{ij}(0) = 0$

Material Constants: D_0, Z_0, Z_1, Z_2, Z_3, m_1, m_2, α_1
A_1, A_2, r_1, r_2, n, and elastic constants

In most cases can set: $r_1 = r_2$, $A_1 = A_2$, $Z_0 = Z_2$

TABLE 2. SUMMARY OF THE MODIFIED WALKER THEORY (DIFFERENTIAL FORM)

$$\dot{\varepsilon}^{p}_{ij} = \frac{\left(\frac{3}{2}S_{ij} - \Omega_{ij}\right)}{\sqrt{\frac{2}{3}\left(\frac{3}{2}S_{ij} - \Omega_{ij}\right)\left(\frac{3}{2}S_{ij} - \Omega_{ij}\right)}} \left\{\exp\left(\frac{\sqrt{\frac{2}{3}\left(\frac{3}{2}S_{ij} - \Omega_{ij}\right)\left(\frac{3}{2}S_{ij} - \Omega_{ij}\right)}}{K}\right) - 1\right\} / \beta \qquad (1)$$

$$K = K_1 - K_2 e^{-n_7 R} - K_3 e^{-n_8 I} \qquad (2)$$

$$\dot{I} = \left|\sqrt{\frac{2}{3}\dot{\varepsilon}^{p}_{ij}\dot{\varepsilon}^{p}_{ij}} - \left|\dot{\overline{\sqrt{\frac{2}{3}\varepsilon^{p}_{ij}\varepsilon^{p}_{ij}}}}\right|\right| \qquad (3)$$

$$\dot{R} = \sqrt{\frac{2}{3}\dot{\varepsilon}^{p}_{ij}\dot{\varepsilon}^{p}_{ij}} \qquad (4)$$

$$\Omega_{ij} = \Omega_{ijo} + \Omega_{ij1} + \Omega_{ij2} \qquad (5)$$

$$\dot{\Omega}_{ij1} = n_2\dot{\varepsilon}^{p}_{ij} - \Omega_{ij1}\left([n_3 + n_4 e^{-n_5|\log \frac{\dot{R}}{\dot{R}_o}|}]\dot{R} + n_6 + \frac{1}{n_2}\frac{\partial n_2}{\partial\theta}\dot{\theta} - \frac{1}{n_3}\frac{\partial n_3}{\partial\theta}\dot{\theta}\right) + \left(\frac{n_2}{n_3} - \Omega_{ij1}\right)\frac{\partial n_3}{\partial\theta}\varepsilon^{p}_{ij}\dot{\theta} \qquad (6)$$

$$\Omega_{ij2} = n_{11}\dot{\varepsilon}^{p}_{ij} - \Omega_{ij2}\left(n_9\dot{R} + n_{10} + \frac{1}{n_{11}}\frac{\partial n_{11}}{\partial\theta}\dot{\theta} - \frac{1}{n_9}\frac{\partial n_9}{\partial\theta}\dot{\theta}\right) + \left(\frac{n_{11}}{n_9} - \Omega_{ij2}\right)\frac{\partial n_9}{\partial\theta}\varepsilon^{p}_{ij}\dot{\theta} \qquad (7)$$

$$\dot{\overset{\circ}{\Omega}}_{ij} = 3\overset{\circ}{\Omega}\left[\frac{\dot{C}_{ik}C_{kj}}{C_{pq}C_{pq}} + \frac{C_{ik}\dot{C}_{kj}}{C_{pq}C_{pq}} - \left(\frac{2C_{ik}C_{kj}}{C_{pq}C_{pq}}\right)\left(\frac{C_{rs}\dot{C}_{rs}}{C_{uv}C_{uv}}\right)\right] + \left[3\frac{C_{ik}C_{kj}}{C_{pq}C_{pq}} - \delta_{ij}\right]\frac{\partial\dot{\overset{\circ}{\Omega}}}{\partial\theta} \qquad (8)$$

$$S_{ij} = \sigma_{ij} - \frac{1}{3}\delta_{ij}\sigma_{kk} \qquad (9)$$

Material Constants: λ, μ, $\overset{\circ}{\Omega}$, β, n_2, n_3, n_4, n_5, n_6, n_7, n_8, n_9, n_{10}, n_{11}, K_1, K_2, K_3, dependent on temperature, θ

TABLE 3. BODNER-PARTOM MODEL CONSTANTS FOR B1900+Hf

- **Temperature-Independent Constants**

$m_1 = .270\ \text{MPa}^{-1}$

$m_2 = 1.52\ \text{MPa}^{-1}$

$\alpha_1 = 0.0$

$Z_1 = 3000\ \text{MPa}$

$Z_3 = 1150\ \text{MPa}$

$r_1 = r_2 = 2$

$D_0 = 1 \times 10^4\ \text{sec}^{-1}$

- **Temperature-Dependent Constants**

Constants	Temperature, °C			
	$T \leq 760$°C	871°C	982°C	1093°C
n	1.055	1.03	.850	.70
Z_0 (MPa)	2700	2400	1900	1200
$A_1 = A_2$ (sec^{-1})	0	.0055	.02	.25
$Z_2(=Z_0)$ (MPa)	2700	2400	1900	1200

- **Elastic Moduli for B1900+Hf**

$E = 1.987 \times 10^5 + 16.78\ T - .1034\ T^2 + 1.143 \times 10^{-5}\ T^3$ MPa with T in °C.

$G = 8.650 \times 10^4 - 17.58\ T + 2.321 \times 10^{-2}\ T^2 - 3.464 \times 10^{-5}\ T^3$ MPa with T in °C

TABLE 4. CONSTANTS FOR THE EXPONENTIAL FORM OF WALKER'S MODEL FOR B1900+HF

Temp, °C	21	427	538	649	760	871	982	1093
E (Modulus), MPa	1.900 E+5	1.900 E+5	1.900 E+5	1.800 E+5	1.655 E+5	1.438 E+5	1.249 E+5	1.161 E+5
ν (Poisson's Ratio)	.322	.328	.331	.334	.339	.374	.351	.351
K_1, MPa	12.4	12.4	12.4	12.4	13.8	16.6	13.8	9.0
K_2, MPa	0	0	0	0	0	0	0	0
K_3, MPa	0	0	0	0	0	0	0	0
n, MPa	1.73 E11	1.73 E11	1.73 E11	3.062 E10	2.55 E10	5.50 E12	4.20 E10	5.57 E19
n_2, MPa	2.41 E6	2.41 E6	2.41 E6	8.27 E5	8.27 E5	2.36 E6	9.65 E4	2.36 E4
n_3	4794.	4794.	4794.	1714.	1080.	621.2	400.6	270.7
n_4	0	0	0	0	-505	0	0	0
n_5	.3117	.3117	.3117	.3117	.3117	.3117	.3117	.3117
n_6	0	0	0	0	0	8.71 E-4	4.29 E-4	4.83 E-2
n_7	0	0	0	0	0	0	0	0
n_8	0	0	0	0	0	0	0	0
n_9	11.87	11.87	11.87	16.64	19.83	59.31	136.0	136.0
n_{10}	0	0	0	0	2.44 E-3	2.44 E-3	2.44 E-3	2.44 E-3
n_{11}, MPa	4.70 E3	4.70 E3	4.70 E3	4.70 E3	4.70 E3	9.65 E2	0	0
$\dot{\omega}$, MPa	0	0	0	0	0	0	0	0

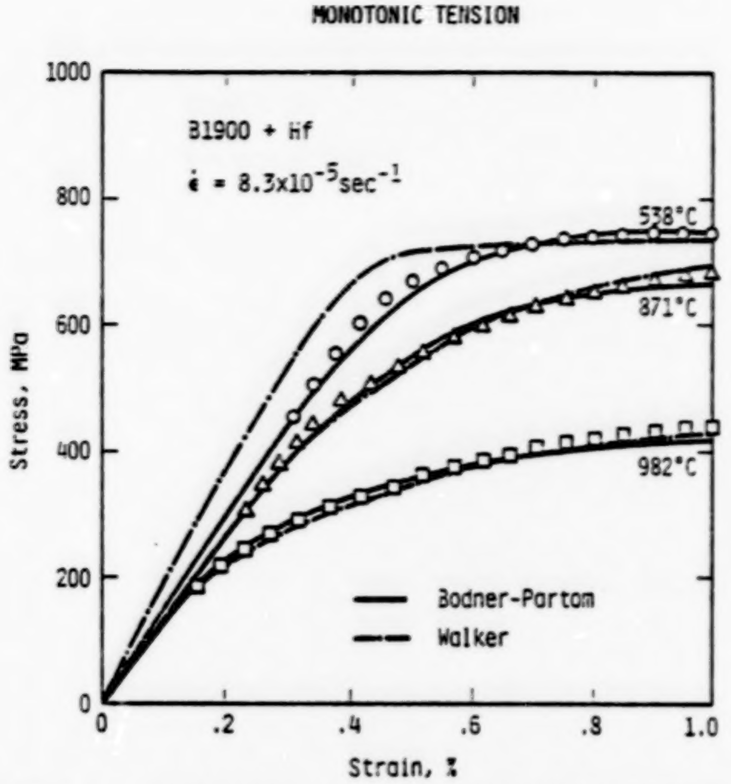

FIGURE 1. COMPARISON OF CALCULATED AND EXPERIMENTAL STRESS-STRAIN CURVES AT THREE TEMPERATURES

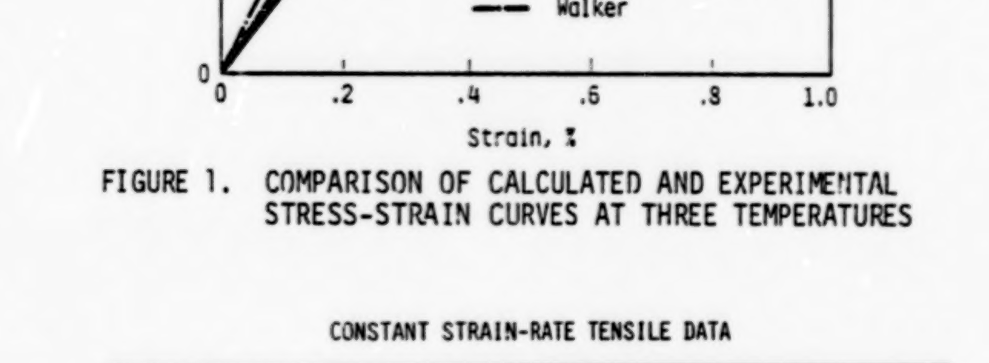

FIGURE 2. CALCULATED AND EXPERIMENTAL RESULTS FROM CONSTANT STRAIN-RATE TENSILE TESTS

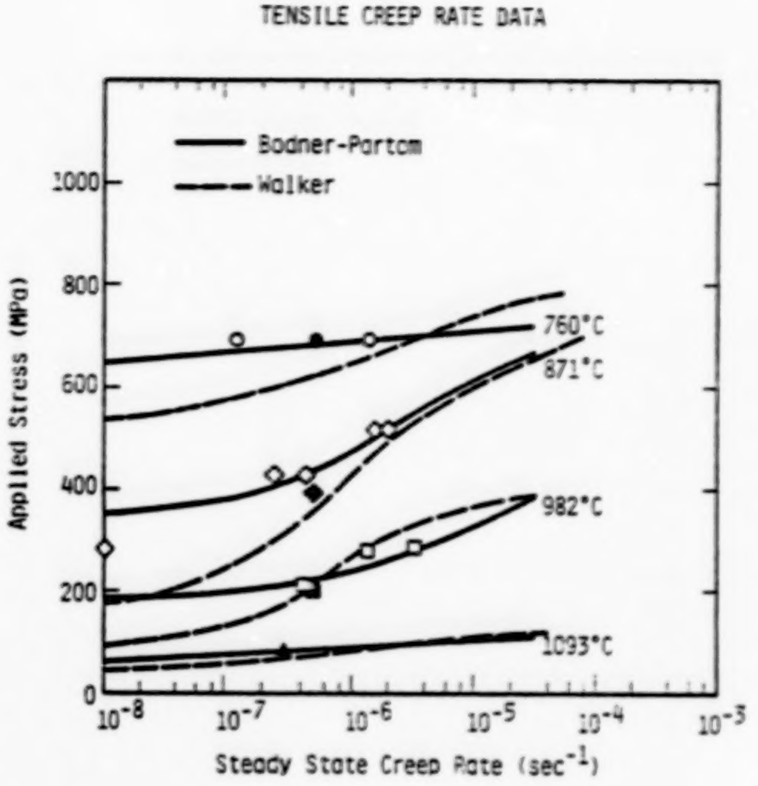

FIGURE 3. CALCULATED AND EXPERIMENTAL RESULTS OF CONSTANT LOAD CREEP TESTS

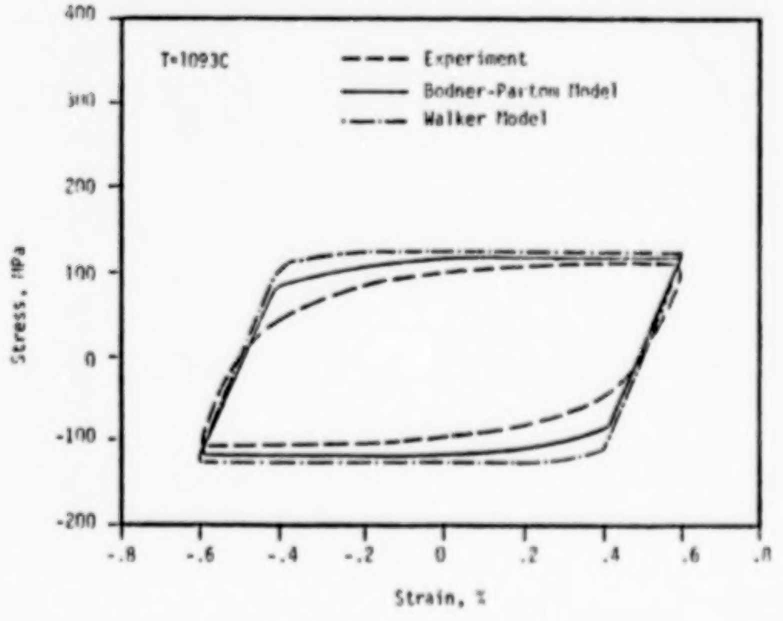

FIGURE 4. COMPARISON OF THE EXPERIMENTAL AND CALCULATED STABLE HYSTERESIS LOOPS AT 1903 C

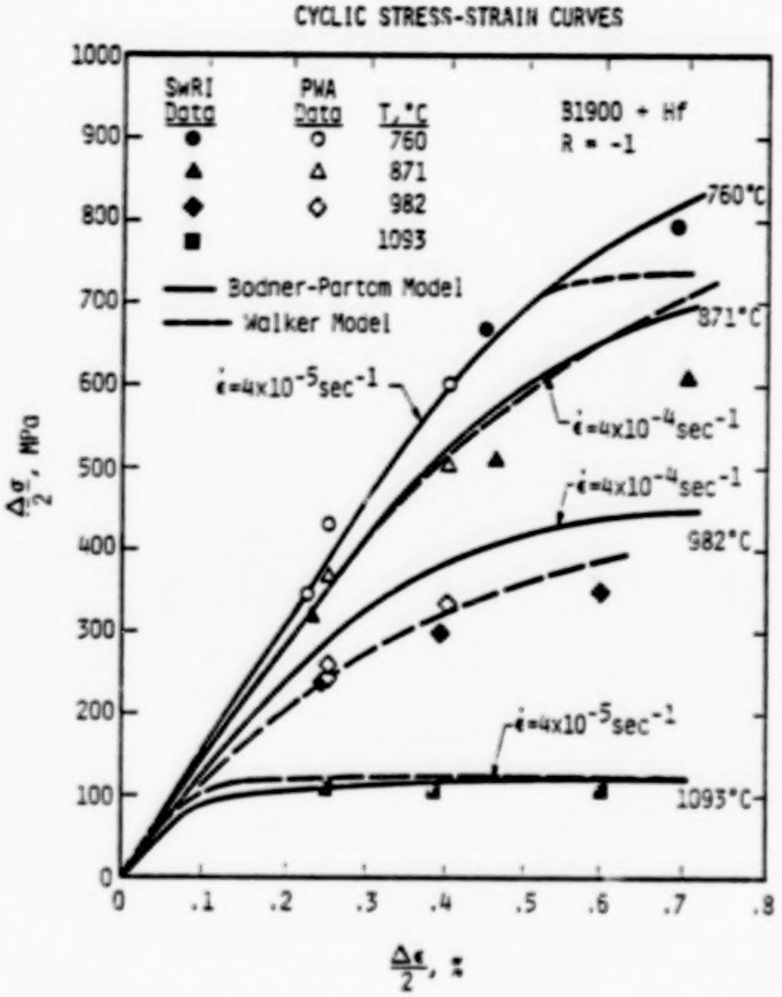
CYCLIC STRESS-STRAIN CURVES

FIGURE 5. CYCLIC STRESS-STRAIN CURVE AT VARIOUS TEMPERATURES

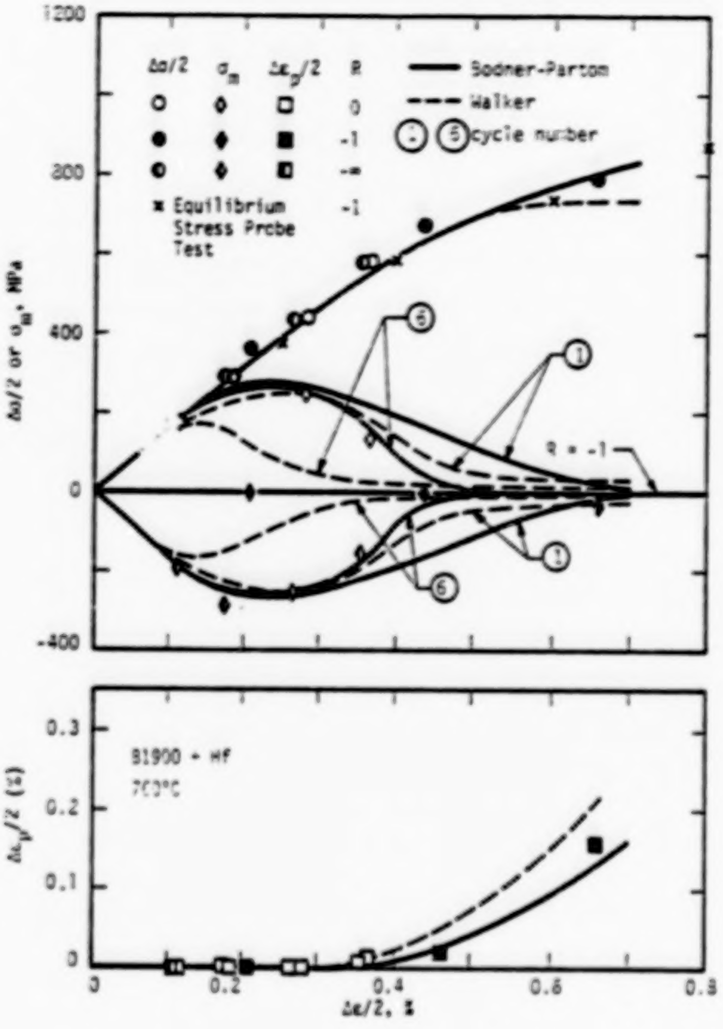

FIGURE 6. CORRELATION OF CYCLIC STRESS-STRAIN DATA WITH MODEL PREDICTIONS AT 760°C

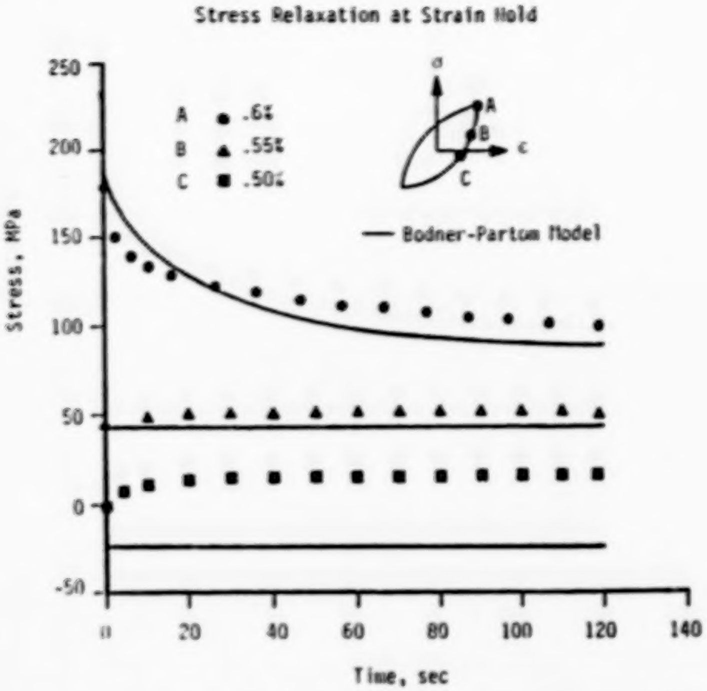

FIGURE 7. STRESS RELAXATION DATA AT THE UNLOADING BRANCH OF A HYSTERESIS LOOP COMPARED WITH BODNER-PARTOM MODEL PREDICTION AT 1093°C

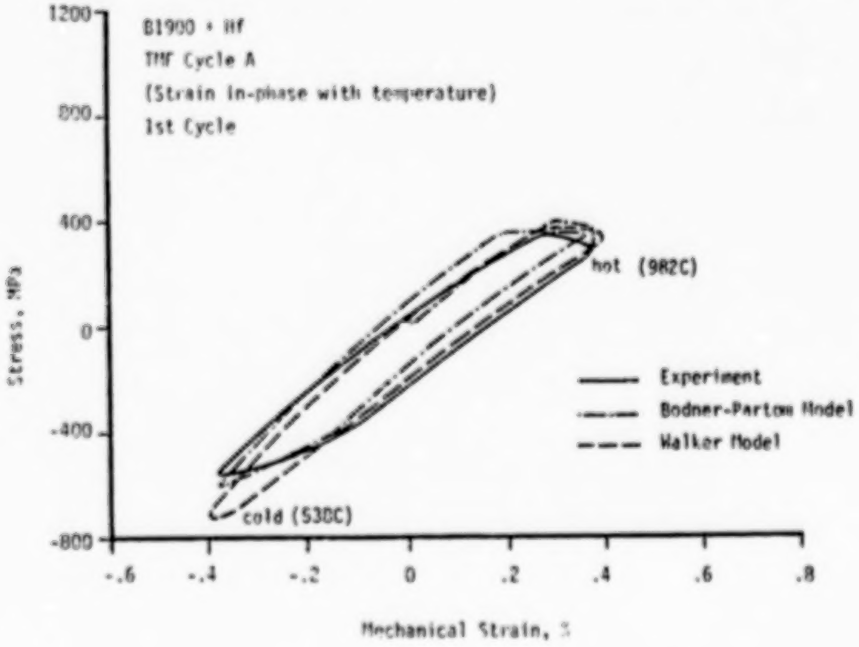

FIGURE 8. THERMOMECHANICAL CYCLIC DATA COMPARED WITH THE WALKER AND THE BODNER-PARTOM MODEL PREDICTIONS FOR THE IN-PHASE TMF CYCLE

ORIGINAL PAGE IS
OF POOR QUALITY

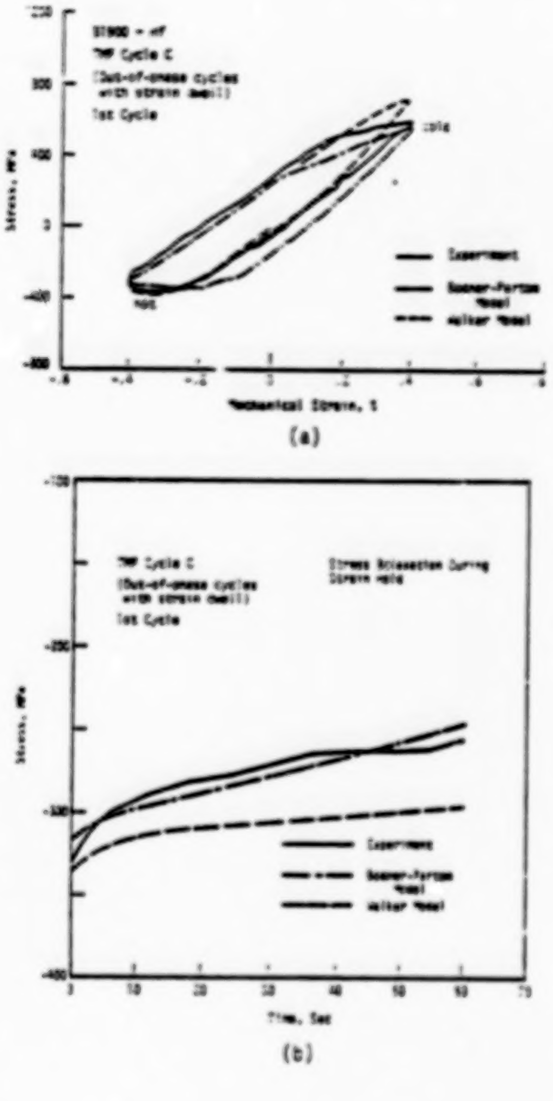

(a)

(b)

FIGURE 9. THERMOMECHANICAL DATA COMPARED WITH THE WALKER AND THE BODNER-PARTOM MODEL PREDICTIONS FOR THE OUT-OF-PHASE TMF CYCLE WITH STRAIN HOLD: (A) STRESS-STRAIN RESPONSE DURING OUT-OF-PHASE CYCLE, (B) STRESS RELAXATION RESPONSE DURING STRAIN HOLD

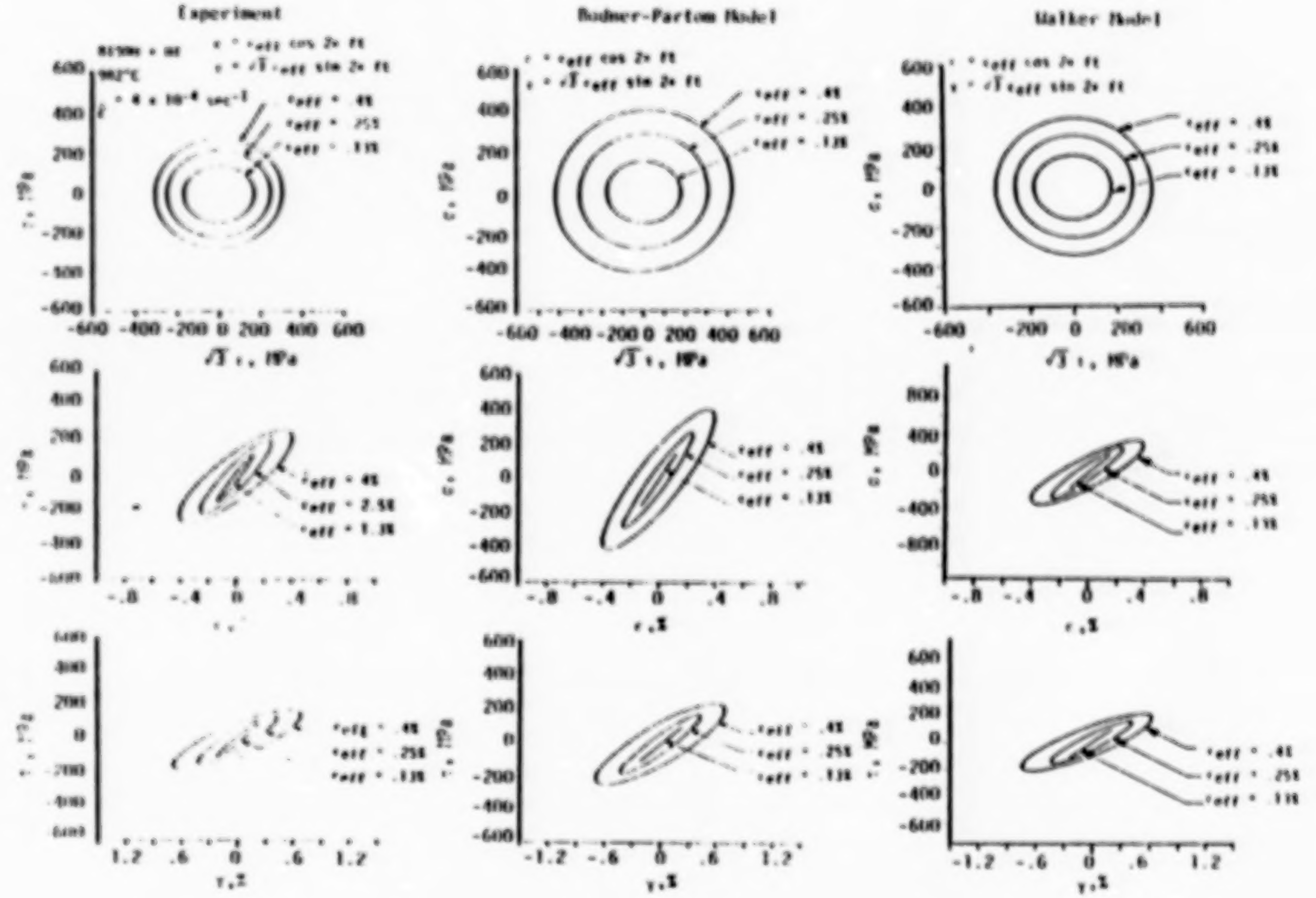

FIGURE 10. COMPARISON OF EXPERIMENTAL DATA AND MODEL CALCULATIONS SUBJECTED TO 90° OUT-OF-PHASE LOADING AT THREE EFFECTIVE STRAIN LEVELS (T = 982 C)

ORIGINAL PAGE IS
OF POOR QUALITY

ORIGINAL PAGE IS
OF POOR QUALITY

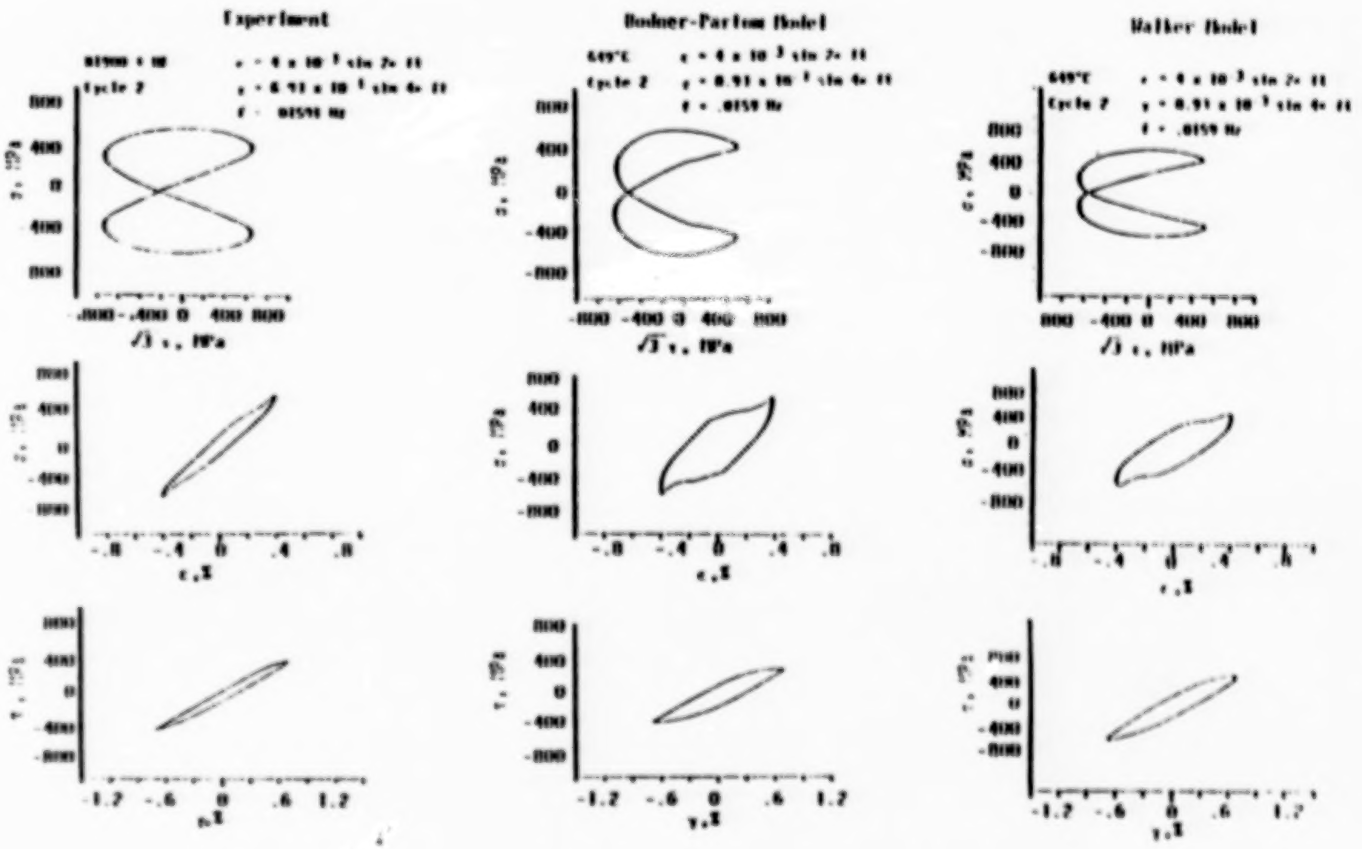

FIGURE 11. MODEL CALCULATIONS AND NONPROPORTIONAL MULTIAXIAL DATA WITH DOUBLE FREQUENCIES (T = 649 C)

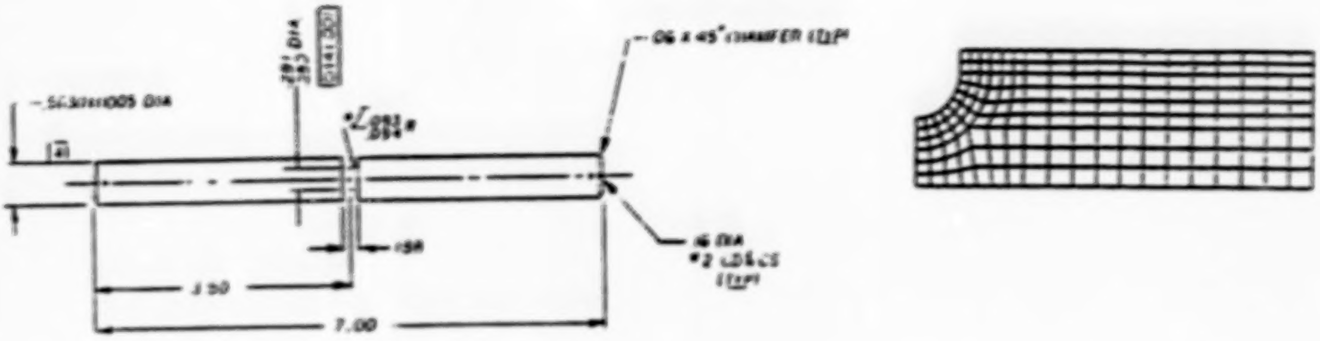
.563±.005 DIA
.281 DIA
.283
.06 X 45° CHAMFER (TYP)
.092
.094 R
.150
3.50
7.00
.16 DIA
2 LOCS
(TYP)

(a)

(b)

FIGURE 12. BENCHMARK NOTCH SPECIMEN: (a) SPECIMEN DESIGN WITH DIMENSIONS IN INCHES, AND (b) FINITE-ELEMENT MECH

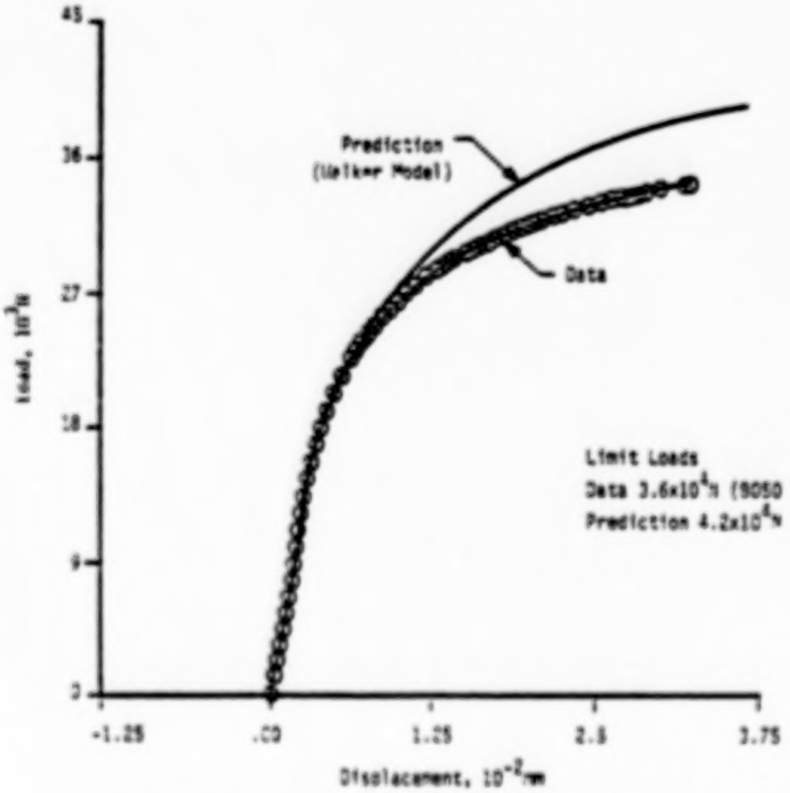

FIGURE 13. COMPARISON OF EXPERIMENT AND FINITE-ELEMENT RESULT OF SPECIMEN UNDER MONOTOMIC TENSILE LOADING

ORIGINAL PAGE IS
OF POOR QUALITY

ORIGINAL PAGE IS
OF POOR QUALITY

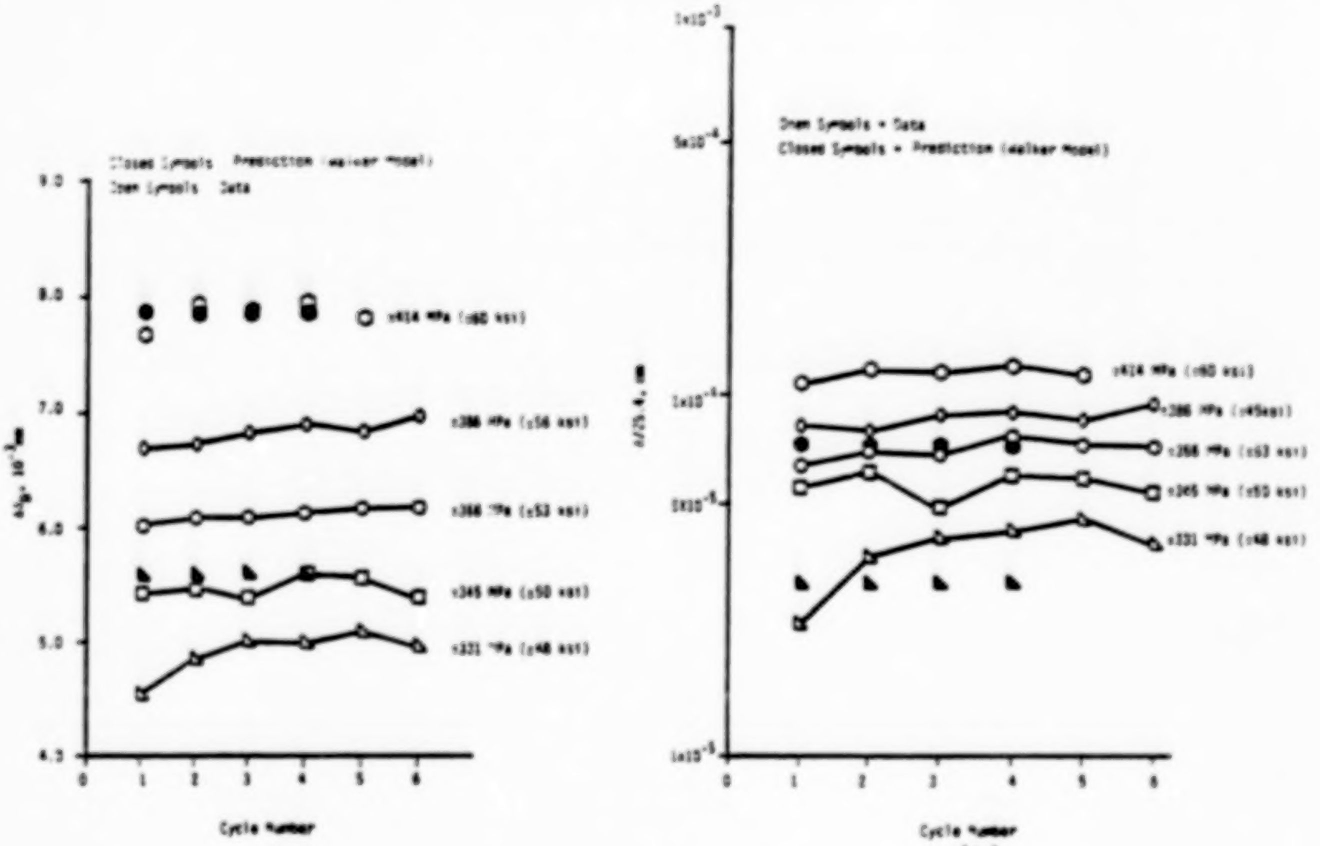

(a) (b)

FIGURE 14. BENCHMARK NOTCH SPECIMEN UNDER FULLY REVERSED LOADING AT 871 C WITH ONE MINUTE HOLD AT TENSION AND COMPRESSION: (a) PEAK-TO-PEAK NOTCH DISPLACEMENT, AND (b) CYCLIC NOTCH INELASTIC DISPLACEMENT.

CONSTITUTIVE MODEL DEMONSTRATED IN A THERMAL-MECHANICAL FLIGHT SIMULATION OF A TURBINE BLADE

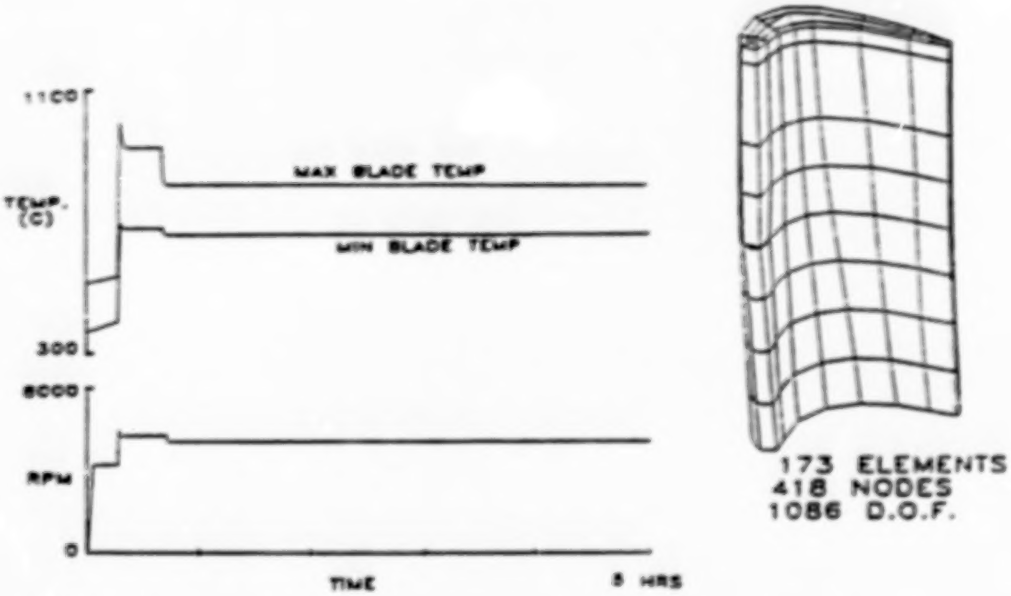

FIGURE 15. FLIGHT SPECTRUM AND FEM BLADE MODEL USED IN A THERMAL-MECHANICAL FLIGHT SIMULATION

ELASTIC VS INELASTIC ANALYSES FOR A SELCTED ELEMENT

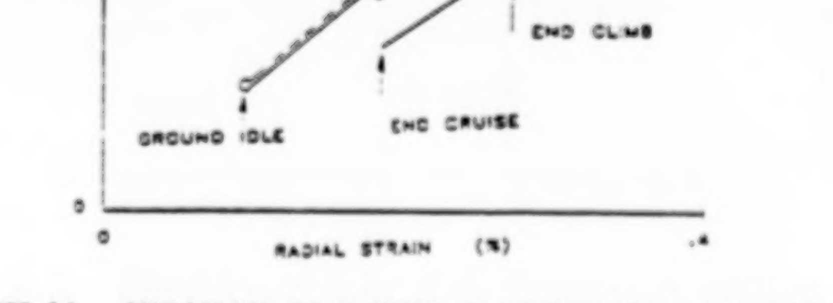

FIGURE 16. COMPARISON OF ELASTIC VS VISCOPLASTIC ANALYSIS FOR A SELECTED BLADE ELEMENT

N88
21524
UNCLAS

N88-21524

CONSTITUTIVE RESPONSE OF RENÉ 80 UNDER THERMAL MECHANICAL LOADS

K.S. Kim, T.S. Cook, R.L. McKnight
General Electric Company
Cincinnati, Ohio 45215

Accurate prediction of structural response in the high temperature environment is a prerequisite for reliable life prediction of hot section components of gas turbine engines. In many situations, this involves the use of general purpose finite element code capable of modeling nonlinear material behavior. The constitutive models of material behavior may be either classical, i.e. separation of creep and plastic deformation, or unified, wherein inelastic deformation as a whole is considered. While there is considerable interest in the unified theories, these models require further development of capabilities and experimental verification under realistic loading conditions. At present, the implementation of unified theories in numerical analysis is not widespread. The classical theories, on the other hand, are relatively well established and available in many finite element codes. Therefore, the prediction of cyclic deformation in this study was made using a classical model rather than a unified theory. The objective of the study was to examine the accuracy of a classical constitutive model when applied to thermomechanical fatigue (TMF) of Rene' 80. Using isothermal creep and cyclic stress-strain data, two approaches were used to predict the half life thermal mechanical hysteresis loops. An elastic-plastic analysis using appropriate stress-strain-rate data was followed by an elastic-plastic-creep analysis. This latter approach used high strain rate data for the elastic-plastic analysis and relied on the explicit inclusion of creep to develop the appropriate time dependent behavior. Comparison of the two approaches provides an indication of the importance of explicitly modeling the rate effects in the thermal mechanical cycles of Rene' 80.

MATERIAL

The material selected for this study is the conventionally cast superalloy Rene' 80. The composition (wt. pct.) is: 3.0 pct. Al, 5.0 pct. Ti, 14.0 pct. Cr, 3.9 pct. W, 4.0 pct. Mo, 9.8 pct. Co, 0.17 pct. C, and the balance Ni. This nickel-base material is a typical high temperature alloy and is quite widely used for turbine blades and nozzle vanes. The microstructure of this alloy has been described by Antolovich and Domas [1,2], but it consists of large (ASTM 2 to 3), irregular grains with a distribution of grain boundary carbides and borides. There are several strengthening mechanisms but the major one is uniformly distributed cuboidal gamma prime precipitates. These precipitates tend to coarsen with increasing temperature and strain rate and are at least partially responsible for the temperature dependence of cyclic deformation. At the lowest test temperature, the deformation is largely within the matrix leading to matrix failure when a critical dislocation density is achieved. At the higher temperatures, the large precipitates tend to disperse the slip, yielding more homogeneous deformation. The damage accumulates at grain boundaries, leading to the formation of oxide spikes [1]; hence, not only the deformation but also the failure mechanisms are temperature dependent.

MECHANICAL TESTING

Solid cylindrical specimens were cast to size and final machined using low stress procedures. The specimens had a diameter of 6.35mm and were 92.1mm in length. The specimen ends were threaded for attachment purposes.

A broad sequence of thermomechanical and isothermal tests were carried out to develop and evaluate a TMF model. Isothermal cyclic stress-strain (CSS), low cycle fatigue (LCF), creep, and relaxation tests were conducted at three temperatures under a variety of test conditions. The CSS behavior was examined as a function of strain rate, as was the LCF life. Creep and relaxation were examined in tension and compression; mean stress effects and creep-plasticity interactions were investigated. All these results will not be reported here; this paper will concentrate on the time dependent behavior of Rene' 80.

All testing was carried out in conventional servohydraulic fatigue machines with extensometry. For the displacement controlled tests, total longitudinal strain was controlled. The same test setup was used for the creep tests so that the creep curve was obtained. Data were obtained at three temperatures, 760, 871, and 982^{o}C; the majority of the testing was done at the highest temperature. Cyclic testing was done at strain rates of 10, 2, and 1 percent/minute, with a few tests at 0.2 percent/minute. Previous testing had established stress-strain behavior at high strain rates, 40-50%/min. [2,3]. Triangular waveforms were used in these tests with several strain ratios ($R_{\varepsilon} = \varepsilon_{min}/\varepsilon_{max}$) employed.

The cyclic stress-strain data was obtained in two ways. At a strain rate of one percent/minute, fully reversed cyclic tests with open hysteresis loops were conducted. By recording the loops, the material's approach to stable behavior was observed. A loop at the estimated half life was selected as representative of the cyclic amplitude curve. Other strain rate data was obtained from the LCF tests; the stress-strain values at 0.5 N_f were taken as points on the cyclic curve. A summary of the cyclic behavior at the three temperatures and four strain rates is shown in Figure 1. The data shows a complex pattern of temperature dependent behavior. At 760C, there is very little effect of strain rate. At 871C, the strength shows a significant increase with rate, while the 982C stress-strain curve increases only at the very high rate. This behavior reflects the temperature dependent deformation mechanism of Rene' 80.

Since the TMF cycles had a period of less than three minutes, the creep tests concentrated on the early part of the creep curve. The stress levels employed were typical of the TMF loads and the initial load was applied at approximately the rate of the TMF tests. There was slight plasticity in a few cases but most of the initial loading was elastic. The majority of the creep tests lasted two to three hours, although a few were taken to failure.

The creep data was analyzed using a nonlinear regression routine and fitted with the creep curve

$$\varepsilon^{c} = K\,\sigma^{m}t^{n} + Q\,\sigma^{r}t \quad , \tag{1}$$

where K, m, n, Q, and r are constants determined by the regression.

Both the tensile and compressive creep data were analyzed using this expression. It was found that the compression curves could be reasonably predicted by the tensile data and vice versa. In addition, when the creep rates were examined, at 982C (the only temperature examined at present), the same creep rates were occurring at the same creep strain regardless of the sign of the load. Figure 2 shows the tensile creep data and the resulting curve fits at 982 and 871C. Since there does not appear to be any variation in creep associated with the sign of the load, this same fit was used to describe both the tensile and compressive creep in the modeling.

The Rene' 80 TMF specimens were subjected to the three temperature and strain waveforms shown in Figure 3. The general testing procedure has been described by Embley and Russell [4] and consists of two control loops, one for strain and one for temperature. Induction heating was employed and controlled by calibrated thermocouples mounted on the specimen shoulders. The TMF cycle was limited by the solid specimens; forced air cooling would induce undesirable temperature gradients and was not employed. A strain rate of one percent per minute was used in the TMF experiments; this resulted in a period of 1.6 to 2.6 minutes. This consideration restricted the temperature cycle to 100-150^{0}C. This cycle is, of course, not representative of an entire flight cycle, but it does simulate parts of the cycle, for example, a thrust reversal [5].

Load-displacement hysteresis loops were recorded periodically throughout the TMF and LCF tests. Load and strain data were recorded on calibrated strip charts and used to determine cycles to crack initiation, N_i, and failure, N_f. The Rene' 80 softened at a constant rate for much of the fatigue test; an acceleration in the softening rate was used to define crack initiation. Cycles to failure was defined as 50 percent load drop. The hysteresis loop nearest $N_f/2$ was used as the definition of cyclic values. Stress values and strain ranges were obtained from this loop. The measured plastic strain range was defined as the maximum width of the stress-strain hysteresis loop.

THERMAL MECHANICAL ANALYSIS

Analyses of the thermal mechanical hysteresis loops were made using the four constant strain triangle model shown in Figure 4. The finite element program developed by McKnight [6] was used throughout the study. Two approaches were taken to account for the inelastic deformation at high temperatures. In the first approach, only the elastic and plastic deformation was considered. The creep was not explicitly included in the analysis. Instead, the stress-strain curves at the strain rate used in the TMF tests were input to the analysis. It may be assumed that the creep was implicitly included in this case since the creep effects are reflected in the rate-dependent stress-strain curves.

In the second approach, the creep deformation was explicitly included. The stress-strain curves at high strain rates, 50%/min, along with creep constants, were input to the analysis. It was assumed that the creep deformation is negligible at the high strain rate. All the stress-strain curves used as input in the analysis are half-life curves, as are the hysteresis loops being calculated in this paper. From the standpoint of life prediction, using half life data is more practical than relying on the data based on continuous changes of cyclic response, which is difficult to predict for the classical constitutive models.

The thermal mechanical cycles analyzed in this study are (Figure 3):

(i) 760 - 871°C, $R_\varepsilon = -1$, $\Delta\varepsilon = 1\%$, $\dot{\varepsilon} = 1\%/\text{min}$; LIP, CWD, LOP
(ii) 871 - 982°C, $R_\varepsilon = -1$, $\Delta\varepsilon = 1\%$, $\dot{\varepsilon} = 1\%/\text{min}$; LIP, CWD, LOP

For comparison purposes, isothermal cycles are also presented:

(iii) 871°C, $R_\varepsilon = -1$, $\Delta\varepsilon = 1.0\%$, $\dot{\varepsilon} = 2\%/\text{min}$
(iv) 982°C, $R_\varepsilon = -1$, $\Delta\varepsilon = 1.3\%$, $\dot{\varepsilon} = 2\%/\text{min}$ and $10\%/\text{min}$

For the elastic-plastic analysis, the six cycles in (i) and (ii) were analyzed. For elastic-plastic-creep analysis, conditions (ii), (iii) and (iv) were considered. The 760-871°C cycles were not considered in the latter approach because the creep tests were completed only for 871°F and 982°C at this time.

For completeness of presentation, the constitutive model used herein is outlined in the following:

(I) Time-Independent Deformation

The strain component can be written as the sum of the elastic, plastic and thermal parts:

$$\varepsilon_{ij} = \varepsilon_{ij}^{e} + \varepsilon_{ij}^{p} + \varepsilon_{ij}^{\theta} \quad . \tag{2}$$

The elastic and thermal strains are given by:

$$\varepsilon_{ij}^{e} = \frac{1+\nu}{E}\sigma_{ij} - \frac{\nu}{E}\delta_{ij}\sigma_{kk} \quad , \tag{3}$$

$$\varepsilon_{ij}^{\theta} = \alpha\delta_{ij}\Delta T \quad , \tag{4}$$

where E is the Young's modulus, ν is the Poisson ratio, α is the thermal expansion coefficient, δ_{ij} is the Kronecker delta and ΔT is the relative temperature. For the plastic deformation, the classical incremental plasticity theory which utilizes the Prandtl-Reuss flow rule, Von Mises yield criteria and the kinematic hardening rule in the strain space, has been used in this study. The Besseling's subvolume method [7] is used within this constitutive framework. In the subvolume method a strain-hardening material is considered as a composition of several subvolumes, each of which is an elastic-ideally plastic material. The subvolumes have identical elastic constants but different yield stresses. The yield function for the k-th subvolume is given by

$$f_k = (e_{ij} - e_{ijk}^{p})\;(e_{ij} - e_{ijk}^{p}) - P_k^{\,2} \quad , \tag{5}$$

where e_{ij} is the strain deviator, e^p_{ijk} is the plastic component of e_{ij} for the k-th subvolume and P_k is the radius of the k-th subvolume yield surface ($P_1 < P_2 < \ldots$). Notice that the kinematic hardening rule in the strain space is used in Eq. (5). The plastic deformation for each subvolume is assumed to be isochoric, i.e., $\dot{\varepsilon}_{iik}=0$, which implies $\dot{\varepsilon}^p_{ijk}=\dot{e}^p_{ijk}$. The plastic strain rate of the k-th subvolume is given by

$$\dot{e}^p_{ijk} = \frac{(e_{ijk} - e^p_{ijk})\,(e_{mn} - e^p_{mnk})\,\dot{e}_{mn}}{P_k^{\,2}} \quad , \tag{6a}$$

if

$$f_k = 0 \text{ and } (e_{ij} - e^p_{ijk})\,\dot{e}_{ij} > 0$$

and

$$\dot{e}^p_{ijk} = 0 \text{ , otherwise.} \tag{6b}$$

The total plastic strain can be written as the weighted sum of the plastic strains of the subvolumes satisfying Eq. (6a):

$$\dot{e}^p_{ij} = \sum_k \Psi_k \, e^p_{ijk} \tag{7}$$

The determination of Ψ_k, and also P_k in Eq. (5), can be done by considering the uniaxial stress-strain curves. For details, the reader is referred to Besseling [7].

The elastic properties and the stress-strain curves are input at several temperatures. In a time-varying temperature field, for example, the thermomechanical process under consideration, the material data, E, ν, α, P_k and Ψ_k, are linearly interpolated using the input data at nearest temperatures.

(II) Time-Dependent Deformation

The total strain in the presence of creep is given by

$$\epsilon_{ij} = \epsilon^{e}_{ij} + \epsilon^{p}_{ij} + \epsilon^{c}_{ij} + \epsilon^{\theta}_{ij} \quad , \tag{8}$$

where ϵ^{c}_{ij} is the creep strain and others are as given in equation (2). The creep strain components are given by

$$\dot{\epsilon}^{c}_{ij} = \lambda\, S_{ij} \tag{9}$$

where S_{ij} is the stress deviator, λ is a function of the history of creep deformation. Defining $\dot{\bar{\epsilon}}^{c}$ such that

$$\dot{\bar{\epsilon}}^{c} = \sqrt{\frac{2}{3}\,\dot{\epsilon}^{c}_{ij}\,\dot{\epsilon}^{c}_{ij}} \tag{10}$$

it can be shown that

$$\lambda = \frac{3}{2}\,\frac{\dot{\bar{\epsilon}}^{c}}{\bar{\sigma}} \tag{11}$$

where

$$\bar{\sigma} = \sqrt{\frac{3}{2}\,S_{ij}\,S_{ij}} \tag{12}$$

The constancy of the volume in creep deformation $\dot{\epsilon}^c_{kk} = 0$, is again assumed here. The effective creep strain, $\bar{\epsilon}^c$, is determined by the primary creep term of the Bailey-Norton type and a steady state creep term;

$$\bar{\epsilon}^c = K\bar{\sigma}^m t^n + Q\bar{\sigma}^r t \quad , \tag{13}$$

where the constants are those from (1) and

$$\bar{\epsilon}^c = \int_0^t \dot{\bar{\epsilon}}^c \, dt \quad . \tag{14}$$

Differentiating (13) with respect to time and using equations (9), (11) and (12), one can show that

$$\dot{\epsilon}^c_{ij} = \frac{3}{2} \, S_{ij} K n \bar{\sigma}^{m-1} t^{n-1} \tag{15}$$

for small times where the primary creep dominates. In terms of accumulated creep strain, equation (15) can be written as

$$\dot{\epsilon}^c_{ij} = \frac{3}{2} \, S_{ij} K^{\frac{1}{n}} n \bar{\sigma}^{\frac{m}{n}-1} (\bar{\epsilon}^c)^{1-\frac{1}{n}} \tag{16}$$

Equation (15) is called "the time-hardening formulation" and equation (16) is called the "strain-hardening formulation" in the context of the creep analysis under time-varying stress field. In this study, the strain-hardening formulation was used simply because it is somewhat favored over the time-hardening relation from the standpoint of correlating test data. In the case where the steady state creep is not negligible, the creep time for a given creep strain must be determined numerically. Then, the creep strain rate is determined from Eq. (15) with an additional term for the steady state creep. In this study, the secondary creep was included even though the primary creep was dominant.

The stress reversal was assumed to occur if

$$(\varepsilon_{ij}^{c} - \varepsilon_{ij}^{*})\,\sigma_{ij} < 0 \tag{17}$$

where ε_{ij}^{*} is the strain origin which is updated, if necessary, after each stress reversal. Further explanation of the stress reversal and also the algorithm of application of the strain-hardening rule can be found in Kraus [8].

In the finite element analysis, the creep constants K, m, n, Q, and r are input at a number of temperatures. The creep constants at an intermediate temperature are linearly interpolated using the data at nearest temperatures.

DISCUSSION OF RESULTS

(I) Elastic-Plastic Analysis

The stress-strain curves at the 1%/min strain rate which were input to the analysis are shown in Figure 1. Note in the figure that the strain rate effects below the rate of 10%/min are rather small at 982°C, but they were considerably larger at 871°C. The analysis results obtained are shown in Figures 5 and 6 for 760-871°C in-phase and 871-982°C 90° out-of-phase cycles, respectively. The point "P" on the curves designates the point where plasticity develops. For further details of the results, the reader is referred to Cook, et al. [9]. In general, the agreement between the computed and the experimental hysteresis loops was very good. In particular, excellent correlation between analysis and test results was found for 871-982°C cycles for all three phases. The 760-871°C results were satisfactory but not as good as the 871-982°C results. This could reflect the changing inelastic deformation mechanisms over the 760-871°C temperature range as discussed by Antolovich, et al. [1,10]. It should be possible to improve the correlation by incorporating more stress-strain curves between the two temperatures. Unfortunately, such data are unavailable at this time.

(II) Elastic-Plastic-Creep Analysis

The material data base for this model, the high strain rate CSS curves and the creep curves, are those in Figures 1 and 2. Using these data, the elastic-plastic-creep analysis modeled the cycle using linear strain ramps; the cycle was divided into 38 identical time steps. For each step, the elastic-plastic stress analysis was done for the strain increment; then the stress was relaxed in the strain hold over the time increment. The average values of the stress in the strain hold were used in the hysteresis loop plots. The maximum stress relaxation in a step was approximately 70 MPa. The temperature in the strain hold was set equal to the temperature at the midpoint of the time step.

First, the isothermal temperature hysteresis loops were obtained at 2%/min and 10%/min strain rates. The 2%/min hysteresis loops at 871°C and 982°C are shown in Figures 7 and 8. The correlation between prediction and observation is excellent for both temperatures.

The 871-982°C thermal mechanical cycles were reanalyzed for the three phases. The hysteresis loops are presented in Figures 9, 10 and 11 and are compared to the experimental curves and the elastic-plastic results. The shapes of the hysteresis loops agree very well; in particular note the flattening of the loops in the region of the maximum temperature. The general features of the CWD loop are accurately reproduced but note that the loop bears more resemblance to the in-phase than the out-of-phase cycle. This qualitative observation is supported by the TMF life prediction model work of Reference 9. That investigation showed that, in terms of life modeling, the CWD cycle was similar to the LIP cycle and the same stress/temperature parameters could be used in both.

A comparison of the three 871-982C cycles predicted by the elastic-plastic and elastic-plastic-creep models shows that there is not much difference in the results of the two models. The elastic-plastic model is marginally better at predicting the hysteresis loop of the CWD cycle but the results are quite similar for the other two cycles. The plastic strain range agreement is excellent; the time dependence of the load shows some variation among the two models and the experimental results. The discrepancies in hysteresis loop prediction seem to be associated with temperature increasing from 871 to 982C and indicate too high a strength level in this regime. It has not been determined whether this is due to the material data or the constitutive model itself. It must be pointed out that the predicted versus observed loops were not as good for the lower temperature cycle, 760-871°C, in Reference 9. The generation of creep data at 760C is presently underway and it will be very interesting to see whether the inclusion of explicit time dependence improves the prediction. The results for this one temperature cycle suggest that the use of high strain rate and creep data can produce hysteretic behavior that is nearly as good as an analysis based on the correct strain rate.

CONCLUSIONS

This paper examines the applicability of a classical constitutive model for stress-strain analysis of a nickel-base superalloy, Rene' 80, in the gas turbine TMF environment. A variety of tests were conducted to generate basic material data and to investigate the material response under cyclic thermomechanical loading. Isothermal stress-strain data were acquired at a variety of strain rates over the TMF temperature range. Creep curves were also generated over the same temperature regime. Three TMF cycles were examined at two temperature ranges, 871-982C and 760-871C. Only the former temperature cycle was modeled in this paper as some of the 760C creep data had to be regenerated.

Two approaches were taken to analytically predict the hysteresis loops. In the first approach, the elastic-plastic deformation was considered with rate-dependent stress-strain curves. In the second approach, the creep deformation was explicitly included and the stress-strain curves at high strain rates were input to the analysis. The results indicate that both approaches provide accurate hysteretic behavior of Rene' 80 under the TMF loading. The correlation of the predicted and observed hysteresis loops was excellent over 871-982°C for all three cycles using both approaches. The elastic-plastic model predictions did not compare with experiment as well for the temperature range 760-871°C [9]. As soon as the appropriate data is available, this cycle will be examined with the elastic-plastic creep model. For the cycles examined, either model approach can be employed depending on the material data available.

The results of this paper provide optimism on the ability of the classical constitutive model for high temperature applications, at least for the material under consideration. Further efforts with wider range of temperature cycles and more general loading, including the effects of hold time, mean stress and strain, would be worthwhile.

REFERENCES

1. Antolovich, S. D., Domas, P. A., and Strudel, J. L., Met. Trans. A, 10A, December 1979, pp. 1859-1868.

2. Domas, P. A., "An Investigation of Notch Low Cycle Fatigue Life Behavior of Rene' 80 at High Temperature," Ph.D. Dissertation, University of Cincinnati, 1981.

3. Miller, M. A., Unpublished Research, General Electric Aircraft Engine Group, Cincinnati, Onio.

4. Embley, G. T. and Russell, E. S., Proceedings of the First Parsons International Turbine Conference, Institute of Mechanical Engineers, 1984, p. 157.

5. McKnight, R. L., Laflen, J. H., and Spamer, G. T., "Turbine Blade Tip Durability Analysis," NASA Report 165268, National Aeronautics and Space Administration, February 1982.

6. McKnight, R. L., "Finite Element Cyclic Thermoplasticity Analysis by the Method of Subvolumes," Ph.D. Dissertation, Department of Aerospace Engineering, University of Cincinnati, 1975.

7. Besseling, J. F., "A Theory of Plastic Flow for Anisotropic Hardening in Plastic Deformation of an Initially Isotropic Material," Report S. 410, National Aeronautical Research Institute, Amsterdam, 1953.

8. Kraus, H., Creep Analysis, Wiley-Interscience, 1980, Chapter 2.

9. Cook, T. S., Kim, K. S., McKnight, R. L., "Thermal Mechanical Fatigue of Cast Rene' 80," presented at the ASTM Symposium on Low Cycle Fatigue - Directions for the Future, 30 Sept.-4 Oct., 1985, Lake George, N.Y., In Press.

10. Antolovich, S. D., Baur, R., and Liu, S., in Superalloys 1980, J. K. Tien, et al. eds, ASM, 1980, pp. 605-613.

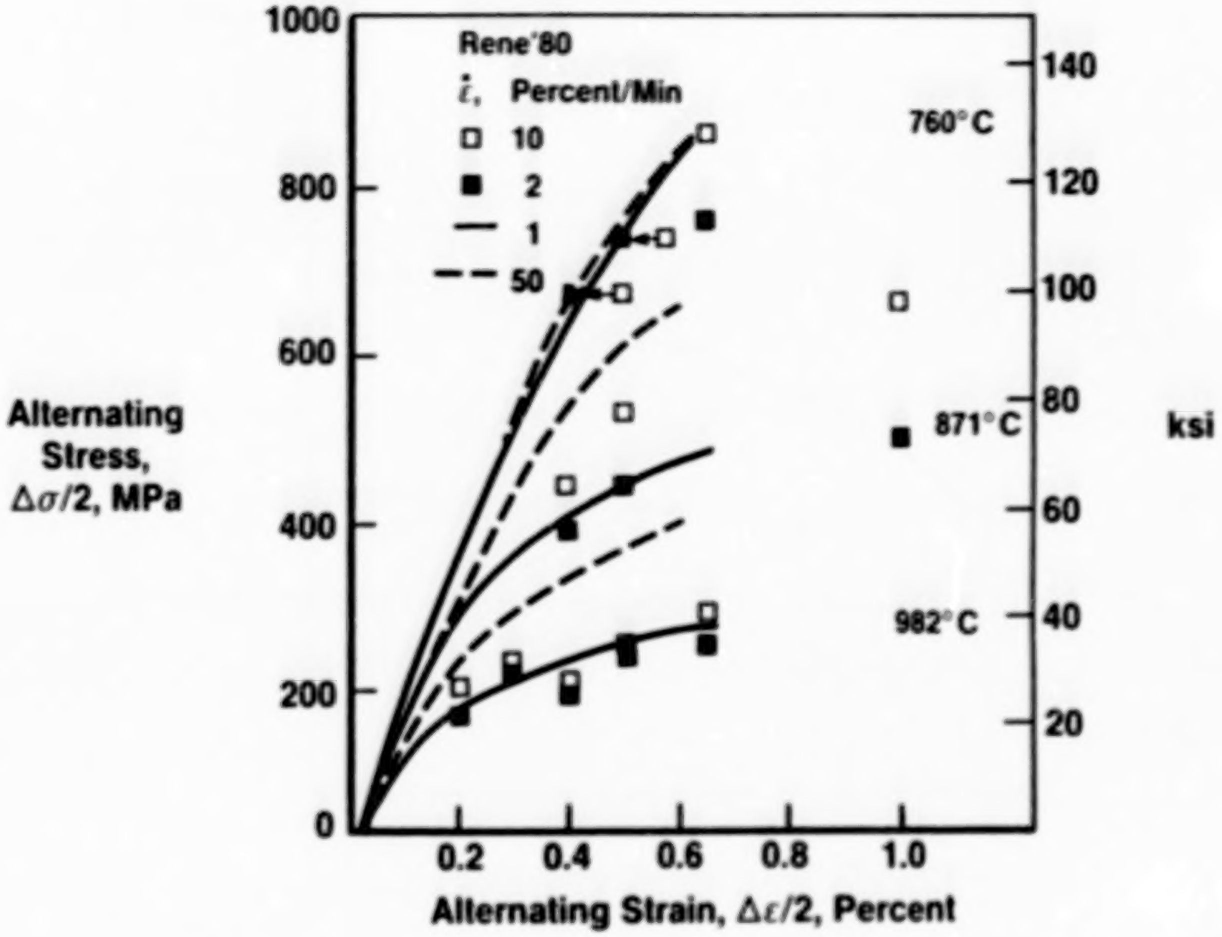

Figure 1. - Cyclic Stress-Strain Behavior for Rene' 80

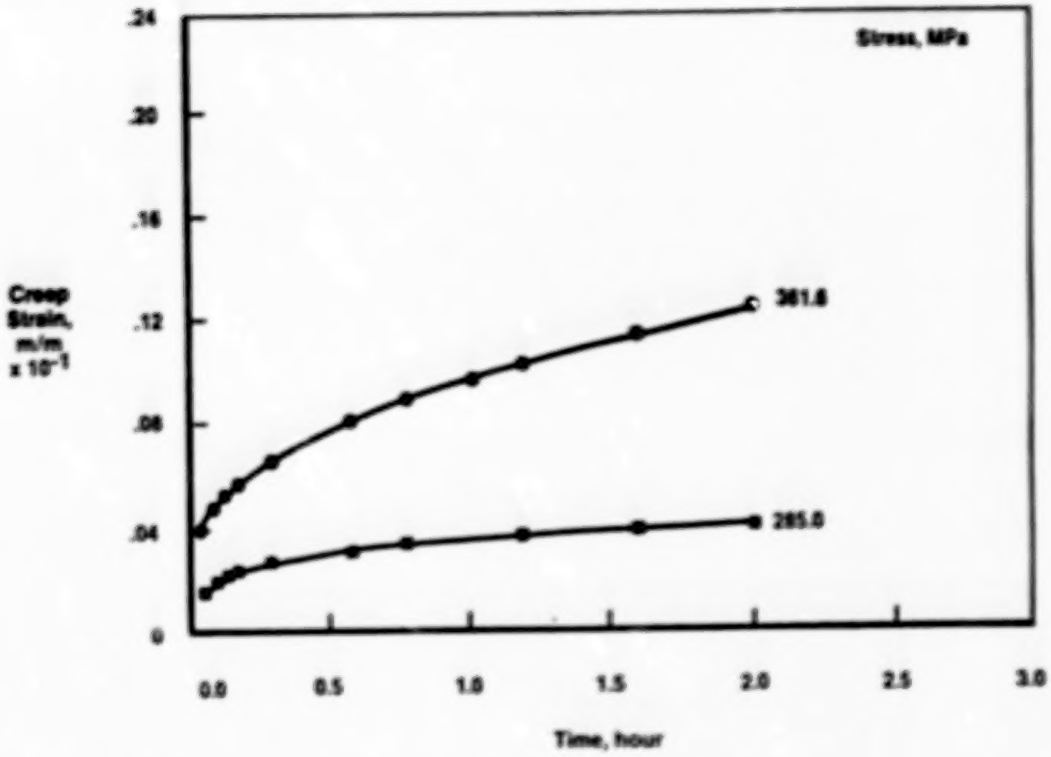

Figure 2a. - Creep Data and Curve Fits at 871°C

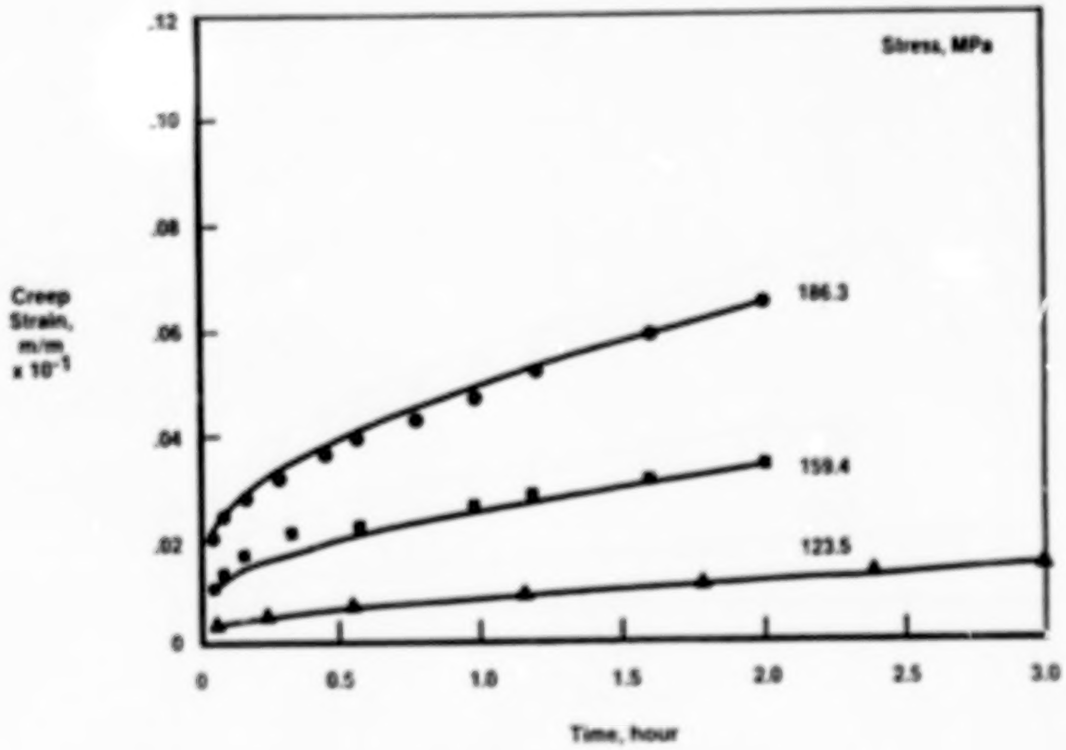

Figure 2b. - Creep Data and Curve Fits at 982°C

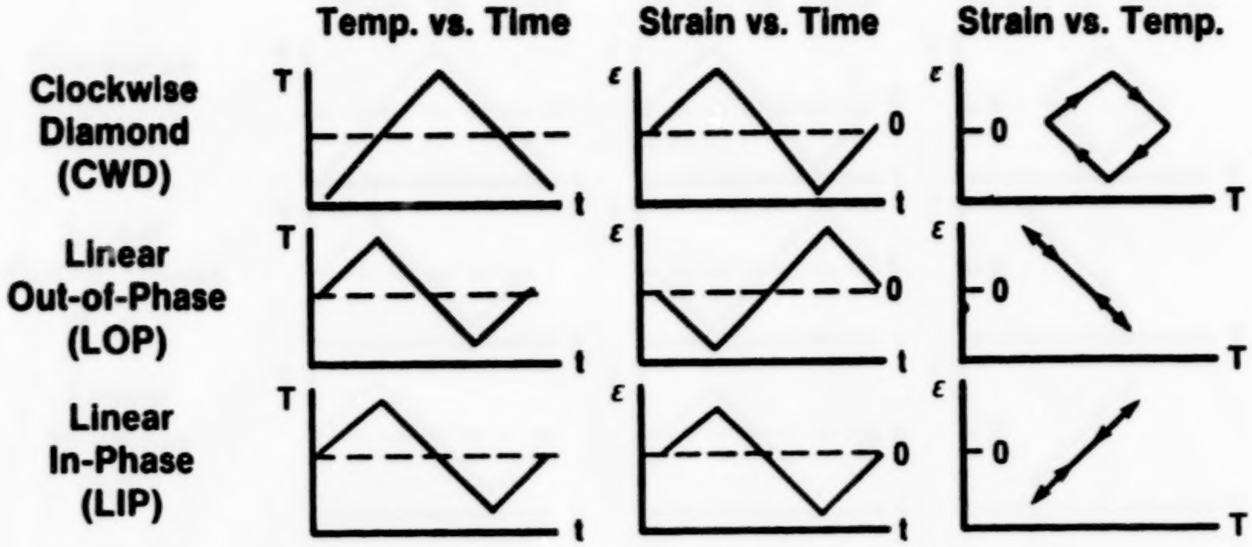
Temp. vs. Time
Strain vs. Time
Strain vs. Temp.
Clockwise Diamond (CWD)
Linear Out-of-Phase (LOP)
Linear In-Phase (LIP)
T
t
ε
0
T

Figure 3. - Thermal Mechanical Cycles Examined in the Investigation

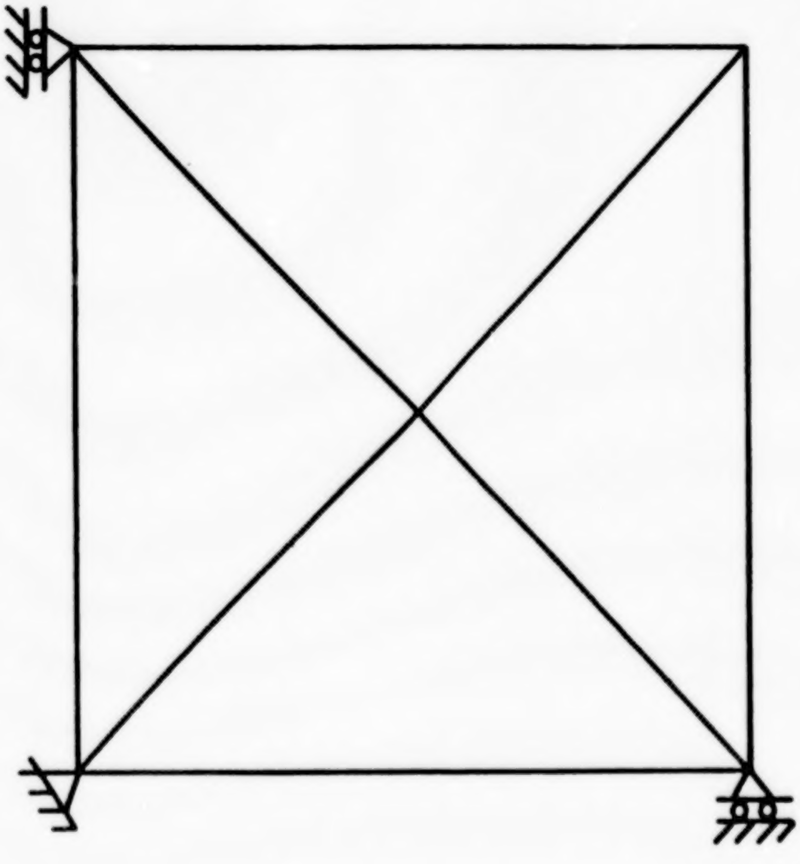

Figure 4. - Finite Element Model Used in TMF Modeling

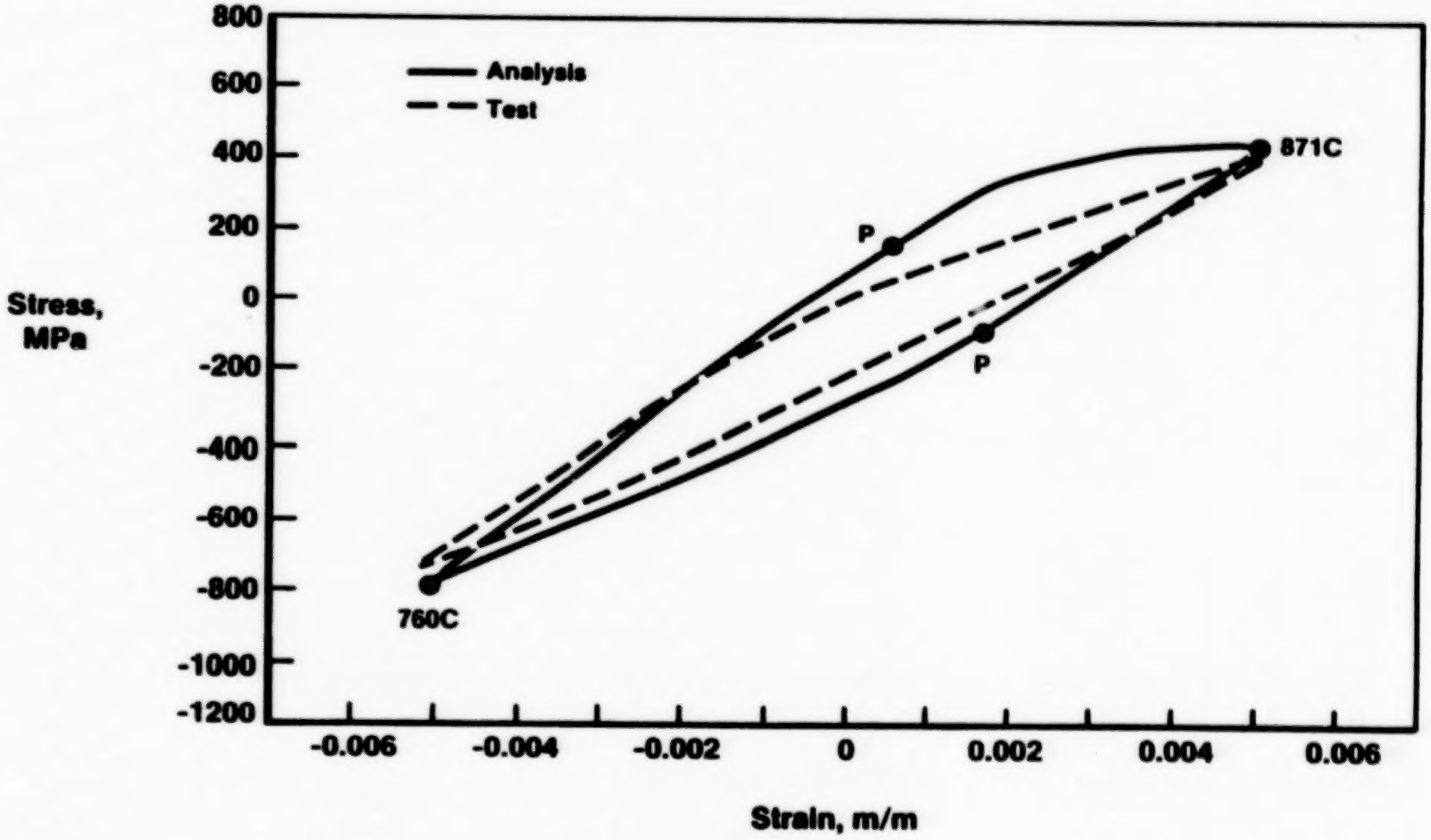

Figure 5. - Predicted Vs. Observed Constitutive Behavior, 760-871°C LIP TMF Cycle, Elastic-Plastic Analysis

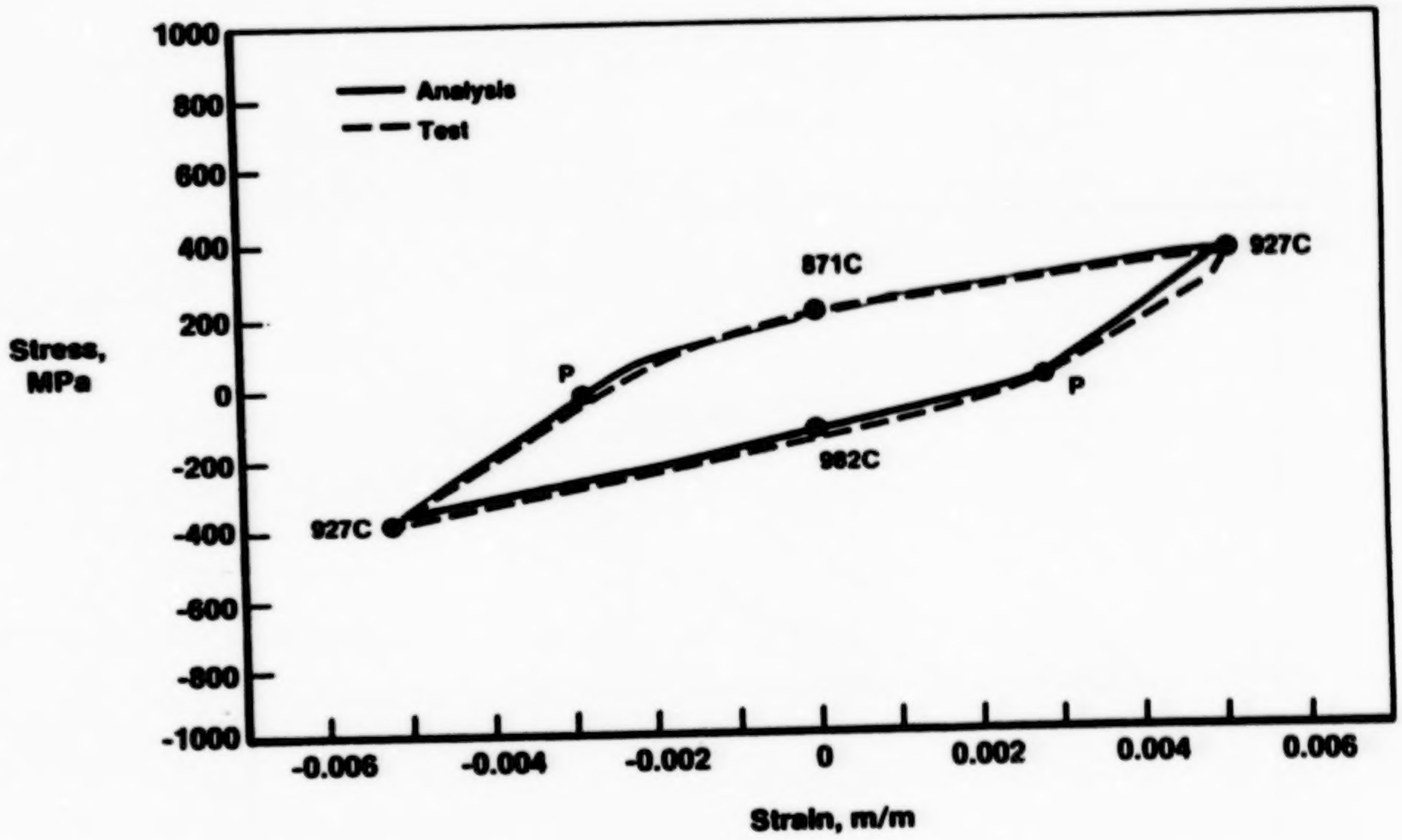

Figure 6. - Predicted Vs. Observed Constitutive Behavior 871-982°C CWD TMF Cycle, Elastic-Plastic Analysis

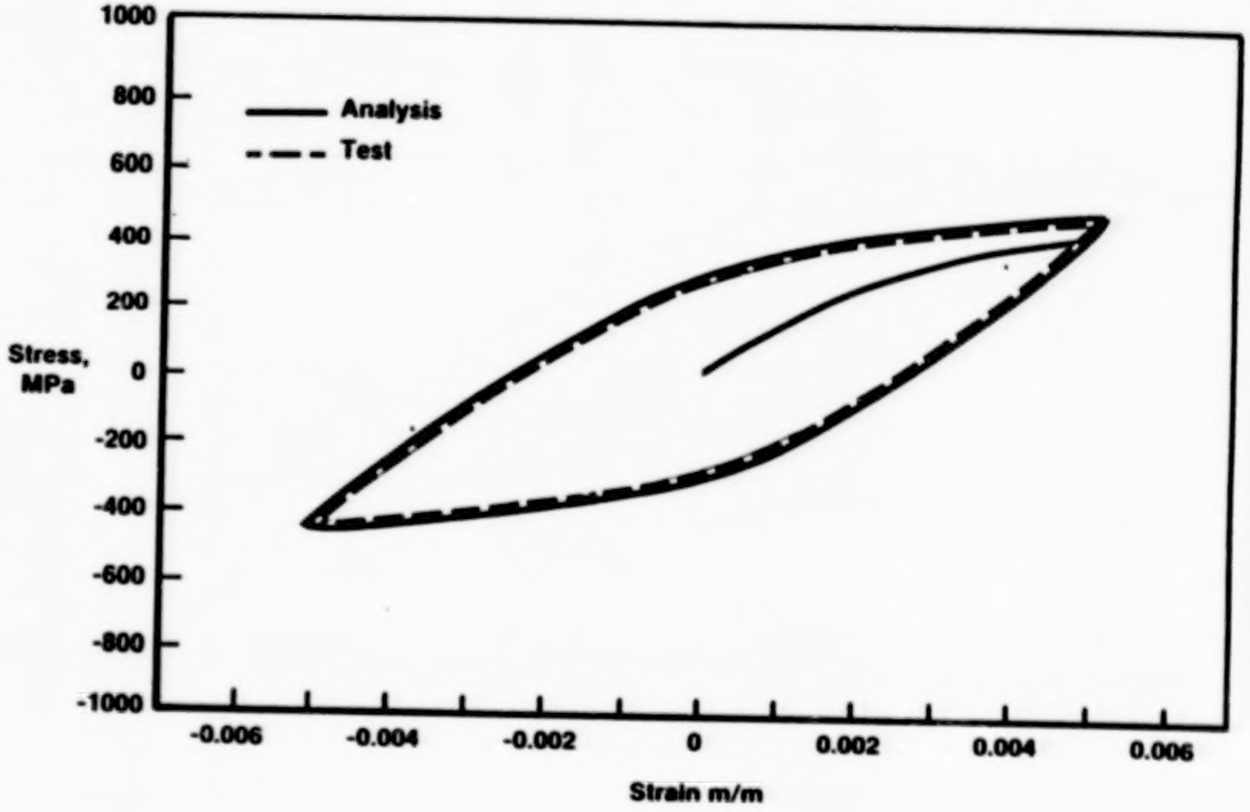

Figure 7. - Predicted Vs. Observed Constitutive Behavior, 871°C, 2%/min, Elastic-Plastic-Creep-Analysis

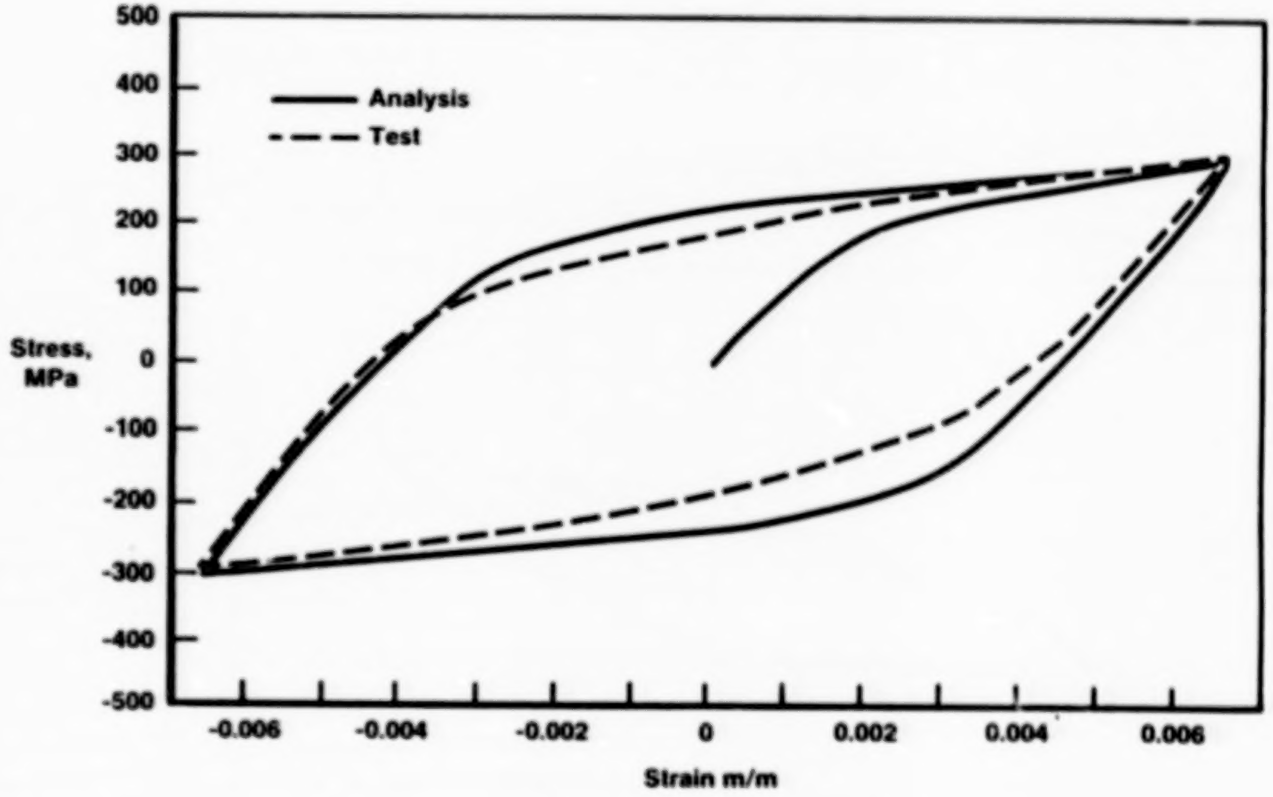

Figure 8. - Predicted Vs. Observed Constitutive Behavior, 982°F, 2%/min, Elastic-Plastic-Creep-Analysis

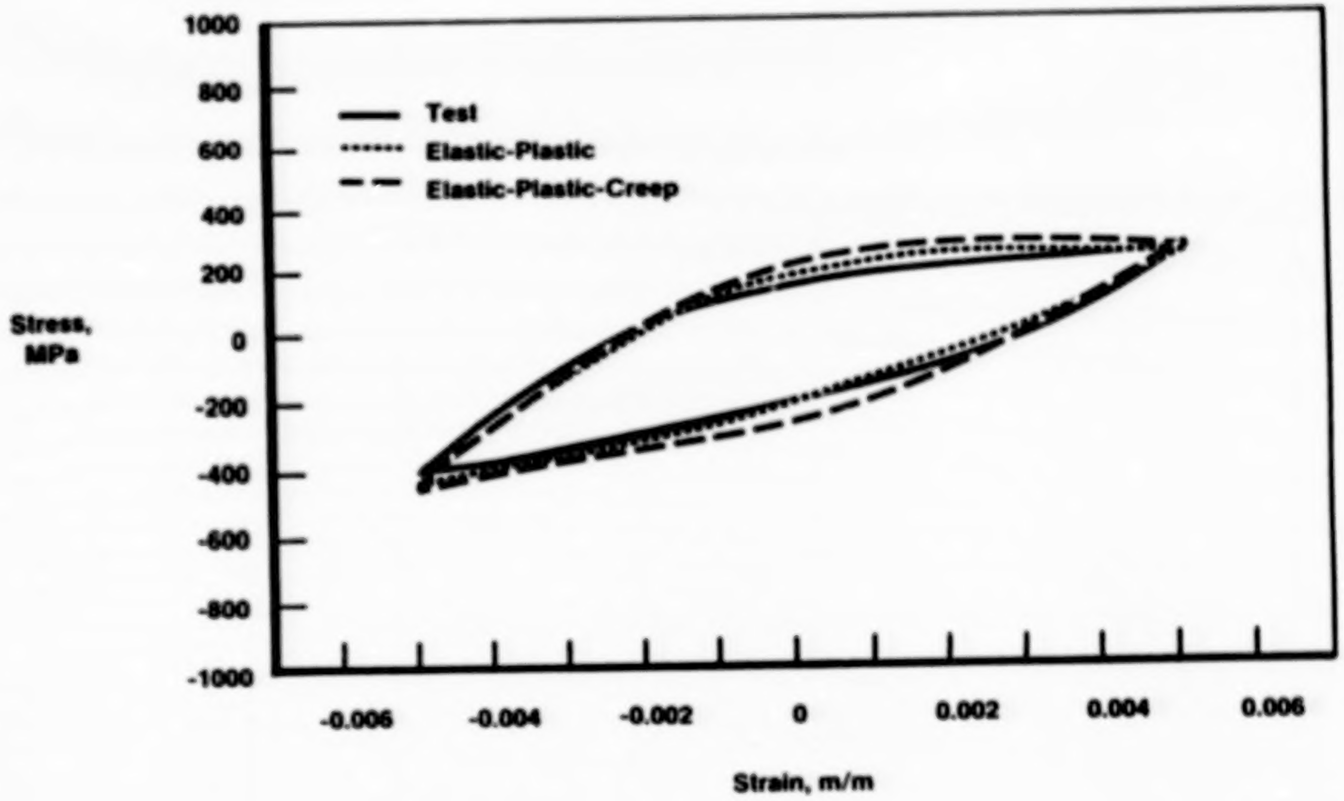

Figure 9. -Predicted Vs. Observed Constitutive Behavior, 871-982°C, LIP TMF Cycle, Elastic-Plastic-Creep and Elastic-Plastic Analysis

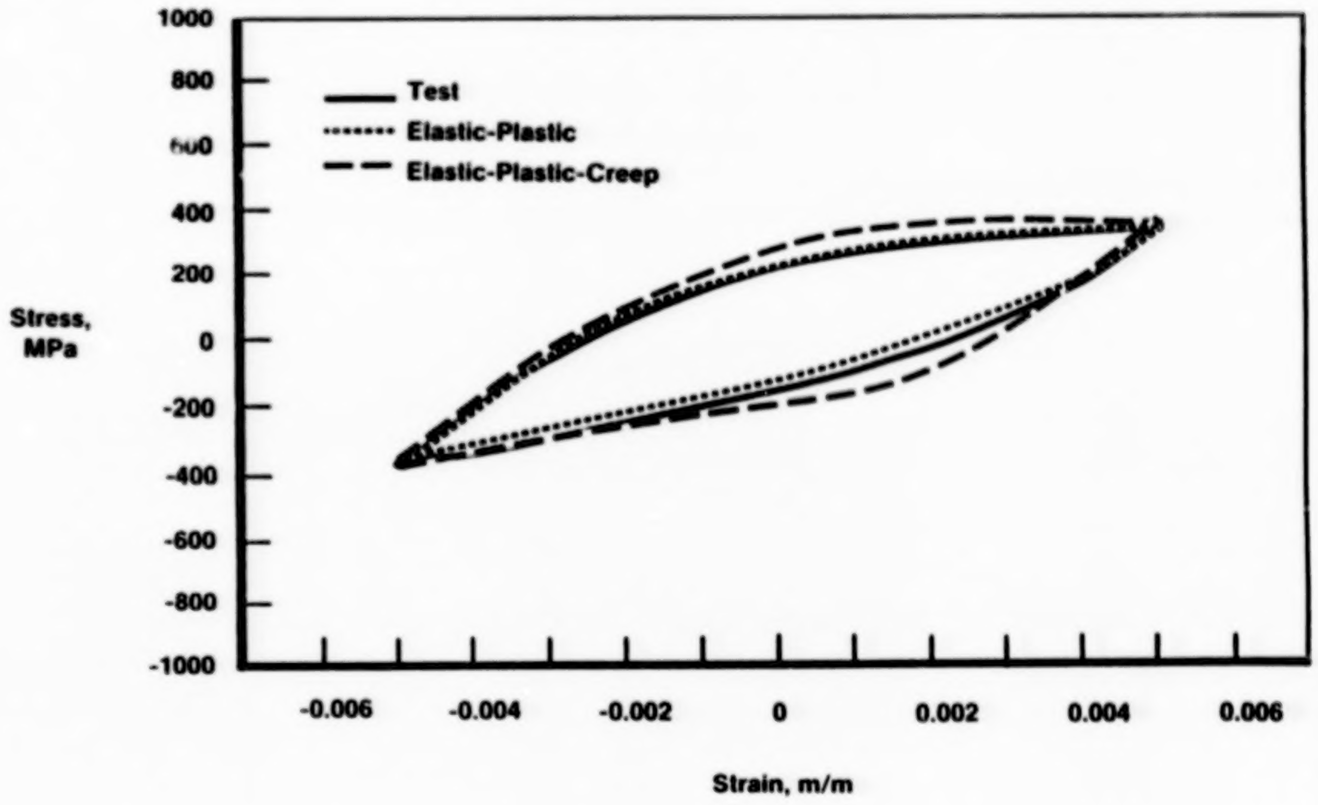

Figure 10. - Predicted Vs. Observed Constitutive Behavior, 871-982°C, CWD TMF Cycle, Elastic-Plastic-Creep and Elastic-Plastic Analysis

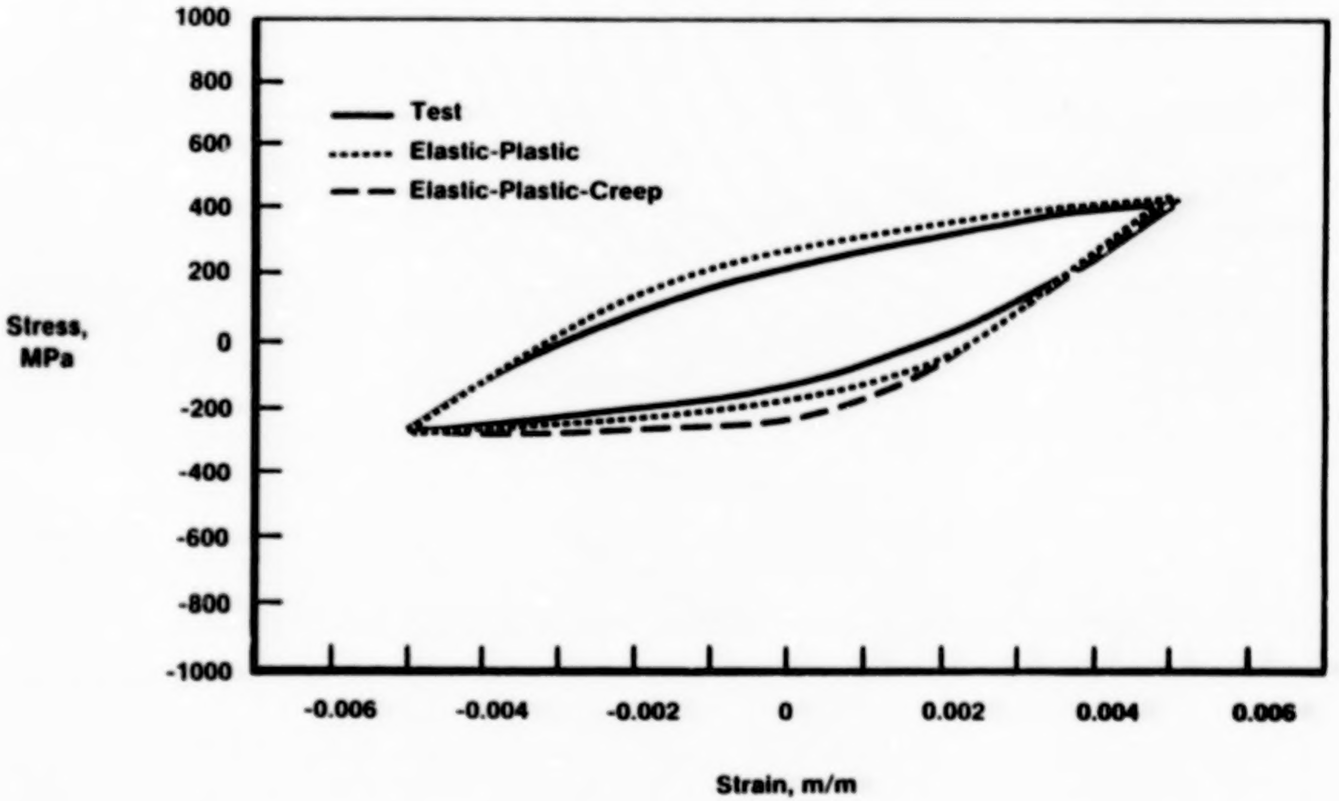

igure 11. -Predicted Vs. Observed Constitutive Behavior, 871-982°C, LOP TMF Cycle, Elastic-Plastic-Creep and Elastic-Plastic Analysis

N88
21525
UNCLAS

N88-21525

A CONSTITUTIVE MODEL FOR AN OVERLAY COATING

D.M. Nissley, G.A. Swanson
Pratt & Whitney
East Hartford, Connecticut 06108

Coatings are frequently applied to gas turbine blades and vanes to provide protection against oxidation and corrosion. One class of coatings, known as overlay, usually has a nickel base with various protective elements added. Since no strengthening elements are included, it has a very low strength and becomes highly inelastic in real turbine airfoil applications. By contrast, turbine blades and vanes are cast from highly strengthened superalloys, which experience very little plasticity even though the thermomechanical loadings are severe. Strains generated in the superalloy airfoils during engine operation are imposed on the much thinner and weaker coating, subjecting it to severe cyclic damage, which leads to cracking of the coating. These cracks, in turn, are fatigue initiation sights for the airfoil. Hence, the inelastic behavior of the overlay coating plays an integral role in controlling the thermomechanical fatigue life of an advanced turbine blade or vane. This paper reports the results of an experimental and analytical study to develop a constitutive model for an overlay coating. Specimens were machined from a hot isostatically pressed (HIP) billet of PWA 286 (NiCoCrAlY + Hf + Si). The tests consisted of isothermal stress relaxation cycles with monotonically increasing maximum strain and were conducted at various temperatures. The results were used to calculate the constants for various constitutive models, including the classical, the Walker isotropic, a simplified Walker, and the Stowell models. A computerized regression analysis was used to calculate model constants from the data. The best fit (lowest standard deviation) was obtained for the Walker model, with the simplified Walker and classical models close behind. The Stowell model gave the poorest correlation.

Nomenclature

σ = stress (psi)

ε_t = total strain (in/in)

ε_e = elastic strain (in/in)

ε_{in} = $\varepsilon_p + \varepsilon_c$ = inelastic strain (in/in)

$\dot{\varepsilon}_{in}$ = inelastic strain rate (sec^{-1})

ε_p = plastic strain (in/in)

ε_c = creep strain (in/in)

$\varepsilon_{in\ eff}$ = effective inelastic strain (in/in)

$\dot{\varepsilon}_{in\ eff}$ = effective inelastic strain rate (sec^{-1})

E = elastic modulus (psi)

t = time (sec)

T = absolute temperature (°R)

R = universal gas constant (1545 $\frac{\text{ft-lbf}}{\text{lb}_m\text{-mole-°R}}$)

ΔH = apparent activation energy ($\frac{\text{ft-lbf}}{\text{lb}_m\text{-mole}}$)

Ω = instantaneous back stress (kinematic hardening parameter) (psi)

Ω_2 = component of instantaneous back stress (psi)

K = instantaneous drag stress (isotropic hardening parameter) (psi)

Temperature dependent material constants (in consistent units):

$A_1, A_2, A_3, A_4, n, n_1, n_7, n_9, n_{10}, n_{11}, m_0, K_1, K_2, s, \sigma_0$

Introduction

One of the major goals of the NASA Hot Section Technology (HOST) program, which has sponsored this work, is the investigation and development of improved durability models for gas turbine hot section alloys. This broad activity addresses the durability issue considering both crack initiation and crack propagation of traditional isotropic (polycrystalline) and anisotropic (single crystal and directionally solidified) materials.

In application, many hot section components are coated to prevent oxidation and corrosion damage (e.g., combustors and turbine vanes and blades). Traditionally, coated thermomechanical fatigue life prediction methods applied to those components simply correlated coated specimen lives without regard to coating/substrate interactions. Although the significant effect of coatings on component thermomechanical fatigue life has been established (References 1-9), little experimental or analytical work has been conducted to evaluate the coating constitutive behavior necessary to provide input to a coating cracking life prediction model.

In this paper, the application of four constitutive models: (1) Classical, (2) Walker isotropic, (3) simplified form of Walker isotropic, and (4) the Stowell equation to NiCoCrAlY overlay coating behavior is presented. Initially, the models are applied to a baseline data set which represents typical low and high temperature tests conducted to obtain model constants. Next, each model is used to predict a thermomechanical cycle verification data set. To facilitate model-to-model comparisons, an identical baseline data set and automated material constant regression technique was used for each model. Standard deviation between the observed and calculated coating stress was used as the quantitative comparison criteria for the baseline data. Finally, a simple two-bar mechanism analysis of a coating/substrate composite structure, exposed to an out-of-phase thermomechanical cycle, is presented to demonstrate the vast dissimilarity between coating and substrate behavior.

Material and Test Specimen Descriptions

NiCoCrAlY + Si + Hf (PWA 286) is a typical vacuum plasma sprayed overlay type coating used to provide oxidation protection of gas turbine airfoil superalloys. Overlay coatings are easily distinguishable from diffusion type coatings in that virtually no interfacial diffusion zone occurs as a result of the application process. Due to that fact and also the small grained structure of overlay coatings in general, PWA 286 is considered isotropic in the plane of the airfoil surface. As such, bulk specimens were considered useful in determining overlay coating constitutive behavior.

The PWA 286 tested in this research effort was obtained in powder form, hot isostatically pressed (HIP) into an ingot, and then heat treated per normal engine hardware specifications. Constitutive specimens for both isothermal and thermomechanical experiments were then machined from the ingot into the geometry presented in Figure 1. In general, the airfoil applied coating contains some porosity near the coating/substrate interface region which was not observed in the specimen due to the HIP fabrication process.

Test Facility

The test facility used for the isothermal baseline tests included a servo-controlled, closed loop screw driven testing machine with set point controllers, an electrical resistance clamshell furnace, and a thermocouple for temperature monitoring. Axial deflection measurement was accomplished with a capacitance type extensometer. The extensometer specimen contact arms were placed into small dimples located at the gage section extremities.

The test facility used for the thermomechanical verification test included a servo-controlled, closed loop hydraulic testing machine with MTS controllers, a 7.5 kW - 10 kHz TOCCO induction heater, and an Ircon infrared radiation pyrometer for temperature measurement. Axial deflection measurement was accomplished with an MTS extensometer. The extensometer quartz rods, which define a one-inch gage section, are spring loaded against the specimen and did not show any signs of slippage during testing.

Baseline Data

The baseline data consists of isothermal stress relaxation experiments of the sort shown schematically in Figure 2. Although the baseline tests were conducted at several elevated temperatures spanning the operating range of 1000-2000°F, the present discussion is limited to the 1000°F and 1800°F data which is representative of low and high temperature behavior. The data from these two experiments are presented in Figure 3. Similar information at other temperatures is available in Reference 1.

Candidate Constitutive Models

For the sake of simplicity, only the one-dimensional forms of the models that were used to correlate the uniaxial data are discussed. Expanding the models into three-dimensional forms required by nonlinear finite element computer codes was considered unnecessary until such time that the most promising candidate model is chosen for continued development.

o Classical

The classical approach (e.g., Reference 10) was one of the first attempts at developing a nonlinear model which recognized the observed dissimilarity between monotonic tensile and creep inelastic material response. Time independent inelasticity (plasticity) and time dependent inelasticity (creep) are considered as uncoupled components of the total inelastic strain.

$$\varepsilon_{in} = \varepsilon_p + \varepsilon_c \tag{1}$$

Thus, the total strain function, neglecting thermal strain, is written:

$$\varepsilon_t = \varepsilon_e + \varepsilon_p + \varepsilon_c \tag{2}$$

or

$$\varepsilon_t = \sigma/E + f(\sigma) + g(\sigma,t) \tag{3}$$

Both plastic and creep strain functions $f(\sigma)$, $g(\sigma,t)$ are chosen to provide adequate duplication of the material behavior. From tests of PWA 286, it was determined that both functions could be described by simple power law relationships:

$$df = \frac{A_2}{K_1}\left(\frac{\sigma}{K_1}\right)^{A_2-1} d\sigma \tag{4}$$

$$dg = \left(\frac{\sigma}{K_3}\right)^{A_4} dt \tag{5}$$

o Walker

The Walker model (Reference 11) is among a new generation of constitutive models based on a unified viscoplastic approach which considers all nonlinear behavior as time dependent inelasticity. No distinction is made between plastic and creep inelastic action as in the Classical model. Walker, from his earlier work on Hastelloy X, chose to express inelastic behavior by a power law relationship which can be written as:

$$\dot{\varepsilon}_{in} = \left(\frac{\sigma-\Omega}{K}\right)^n \tag{6}$$

where n is a constant and Ω, back stress, and K, drag stress, are strain history dependent internal state variables which describe kinematic and isotropic cyclic hardening, respectively.

The back stress term is a quantity which physically corresponds to the asymptotic stress state under relaxation conditions. Qualitatively, the evolutionary expression for back stress is a sum of opposing hardening and thermal and dynamic recovery components which can be characterized as:

$$\dot{\Omega} = f\,(\dot{\varepsilon}_{in}, \varepsilon_{in}, T, t) - g\,(\dot{\varepsilon}_{in}, \Omega, T, t) \tag{7}$$

Drag stress is a quantity which represents a resistance to inelastic flow, and is considered a function of the effective strain, $\varepsilon_{in\ eff}$.

$$K = K_1 - K_2 \exp\,(-n_7\, \varepsilon_{in\ eff}) \tag{8}$$

where: K_1 = fully hardened/softened drag stress

$K_1 - K_2$ = initial drag stress.

Thus, the drag stress function is a monotonically increasing relationship describing isotropic hardening ($K_2>0$) or softening ($K_2<0$). The Walker model form used for this investigation is given below:

$$\dot{\varepsilon}_t = \dot{\varepsilon}_e + \dot{\varepsilon}_{in} \tag{9a}$$

$$\dot{\varepsilon}_{in} = \left(\frac{\sigma-\Omega}{K}\right)^n \tag{9b}$$

$$K = K_1 - K_2 \exp\,(-n_7\, \varepsilon_{in\ eff}) \tag{9c}$$

$$\Omega = n_1\, \varepsilon_{in} + \Omega_2 \tag{9d}$$

$$\dot{\Omega}_2 = n_{11}\, \dot{\varepsilon}_{in} - \Omega_2\,\left(\dot{G}_2 - \frac{1}{n_{11}} \frac{\partial n_{11}}{\partial T}\, \frac{dT}{dt}\right) \tag{9e}$$

$$\dot{G}_2 = n_9\, \dot{\varepsilon}_{in\ eff} + n_{10}\, \Omega_2^{(m_0-1)} \tag{9f}$$

$$\dot{\varepsilon}_{in\ eff} = |\dot{\varepsilon}_{in}| \tag{9g}$$

References 11 and 12 provide a detailed discussion of Walker's and other unified approaches.

o Simplified Walker

This model is identical to the Walker model except that all back stress terms were eliminated.

$$\dot{\varepsilon}_{in} = (\sigma/K)^n \tag{10}$$

the expression for $\dot{\varepsilon}_{in}$ is equivalent to the Classical model power law creep equation; however, in this case, the drag stress term, K, is not a constant, but an evolutionary variable. From a simplicity standpoint, this model is very attractive.

o Stowell

The Stowell model (References 13 through 15) is another form of a unified viscoplastic approach initially developed to simulate heating rate effects on yielding of metals. It considers inelastic action based on an apparent activation energy level and uses a hyperbolic sine stress function.

$$\dot{\varepsilon}_{in} = 2s\ T\ \exp\left(\frac{-\Delta H}{RT}\right) \sinh\left(\frac{\sigma}{\sigma_0}\right) \tag{11}$$

Verification Data

Qualitative evaluation of the predictive capabilities of the candidate constitutive models was accomplished by application to verification data consisting of an out-of-phase thermomechanical waveform. Thermomechanical cycles include complex material behavior such as stress relaxation and plasticity which is useful for exercising the models. The out-of-phase cyclic condition is of particular interest in that such conditions are typical of gas turbine airfoil external surfaces where many thermomechanical fatigue cracks originate in the coating.

Correlation of Baseline Data

Baseline data correlation by each candidate constitutive model is presented in Figures 4 and 5, and a summary of the corresponding standard deviations is given in Table I. The material constants for each model obtained from the baseline tests are presented in Table II.

As expected, the Classical model regression indicated that plasticity dominates the inelastic response at low temperature while creep dominates at high temperature. The Walker and Simplified Walker models correlate the data similarly. It seems that the added complexity of incorporating back stress is unnecessary for modeling this isothermal data set. The Stowell model correlated the baseline information the poorest.

Based on standard deviation and the given baseline data set, the candidate constitutive models can be listed in order of correlation capability as follows: (1) Walker, (2) Simplified Walker, (3) Classical, and (4) Stowell.

Prediction of Thermomechanical Verification Data

Experimental and predicted thermomechanical fatigue (TMF) waveforms are presented in Figure 6.

The high temperature response of the TMF cycle was fairly well predicted by all the models, but none were able to predict the extent of the low temperature tensile inelasticity. In fact, only the Walker and Classical models managed to predict any low temperature yielding. The Simplified Walker and Stowell models predicted thermoelastic tensile responses.

The ability of the Walker model to predict the observed tensile yielding trend can be explained as follows: during the compression/heating portion of the cycle (points A to B), the material relaxes, creating a compressive back stress. Then, during the tensile/cooling portion of the cycle (points B to C), the back stress moves deeper into compression due to temperature rate effects. Thus, the "effective" stress ($\sigma - \Omega$), at which yielding initiates, occurs at a lower applied tensile stress.

The ability of the Classical model to predict some low temperature yielding reflects the fact that this model did not reproduce the observed low temperature yielding trend. Had the Classical model correlated the 1000°F behavior better, it is felt that the low temperature tensile portion of the TMF prediction would have been more like the Simplified Walker and Stowell models...thermoelastic.

Simulation of Coated Superalloy Constitutive Behavior

A simple one dimensional two-bar mechanism simulation of coating and substrate constitutive behavior was performed to help visualize the coating response to TMF cycling as would occur on an airfoil. A schematic of the two-bar mechanism and the predicted results are presented in Figure 7.

A thermo-elastic creep model was used for the PWA 1480 <001> and the Walker model was used for the PWA 286. Note that the mechanical strain range of the PWA 286 is 0.25 percent higher than the PWA 1480 substrate. This is due to the thermal growth and strength characteristics of both materials. Upon load reversal, high stress and plasticity are generated in the coating as the structure is cooled.

Summary and Conclusions

1. Four candidate coating constitutive models were evaluated based on the ability to correlate a baseline data set consisting of isothermal stress relaxation experiments. The four models presented can be ranked as follows: (1) Walker, (2) Simplified Walker, (3) Classical, and (4) Stowell based on the standard deviation of the correlation.

2. An out-of-phase thermomechanical cycle was used to evaluate the four candidate models. Although none of the models accurately predicted the TMF cycle, a back stress formulation such as is incorporated in the Walker model is considered necessary to duplicate the observed material behavior.

3. A one-dimensional two bar mechanism was utilized to calculate PWA 286 coating behavior on a PWA 1480 <001> substrate during out-of-phase thermomechanical cycling. The coating was predicted to have significantly larger mechanical strain range and reverse inelasticity than the PWA 1480 substrate.

Acknowledgements

The experimental testing and analytical work were conducted by Pratt & Whitney, United Technologies Corporation, East Hartford, Connecticut under sponsership of the NASA Lewis Research Center, Contract NAS3-23939.

References

1. G. A. Swanson, I. Linask, D. M. Nissley, P. P. Norris, T. G. Meyer, K. P. Walker, "Life Prediction and Constitutive Models for Engine Hot Section Anisotropic Materials Program; First Annual Report," NASA CR-174952, February, 1986.

2. K. R. Bain, "The Effect of Coatings on the Thermomechanical Fatigue Life of a Single Crystal Turbine Blade Material," 21st Joint Propulsion Conference, AIAA-85-1366, July, 1985.

3. D. P. DeLuca and B. A. Cowles, "Fatigue and Fracture of Advanced Blade Materials," Final Report to AFWAL, FR-18518, Pratt & Whitney, 1984.

4. R. H. Barkalow, "Effect of Cyclic Strain/Temperature Exposure on Fatigue Life of Coated Turbine Alloys," Interim Report to AFWAL/ML, FR-18605, Pratt & Whitney, September, 1984.

5. P. K. Wright, "TMF Failure Models in Single Crystal Rene' N4," NASA TMF Workshop, November 15-16, 1984.

6. T. E. Strangman, "Thermal Fatigue of Oxidation Resistant Overlay Coatings," Ph.D. Thesis, University of Connecticut, 1978.

7. I. Linask and J. Dierberger, "A Fracture Mechanics Approach to Turbine Airfoil Design," ASME Gas Turbine Conference and Products Show, March 2-6, 1975.

8. M. Gell, G. R. Leverant and C. H. Wells, "The Fatigue Strength of Nickel-Base Superalloys," Achievement of High Fatigue Resistance in Metals and Alloys, STP 467, ASTM, 1970, pp. 113-153.

9. G. R. Leverant and M. Gell, "The Elevated Temperature Fatigue of a Nickel-Base Superalloy, Mar-M200," Trans. Metallurgical Society of AIME, Vol. 246, 1969, pp. 1167-1173.

10. H. Kraus, Creep Analysis, John Wiley & Sons, Inc., New York, Chapter 2, 1980.

11. K. P. Walker, "Research and Development Program for Nonlinear Structural Modeling with Advanced Time-Temperature Dependent Constitutive Relationships," NASA CR-165533, November, 1981.

12. U. S. Lindholm, et al, "Constitutive Modeling for Isotropic Materials (HOST)," NASA CR-174718, May, 1984.

13. E. Z. Stowell, et al, "Predicted Behavior of Rapidly Heated Metal in Compression," NASA TR R-59, 1960.

14. E. Z. Stowell, "The Properties of Metals Under Rapid Heating Conditions," J. Aeron Sci., pp. 922-923, December, 1957.

15. E. Z. Stowell, "A Phenomenological Relation Between Stress Strain Rate, and Temperature for Metals at Elevated Temperature," NASA TR-R1343, February, 1957.

Table I

Summary of Constitutive Model Regression Fit Standard Deviation (1 std dev., in psi)

	1000°F	1400°F	1600°F	1800°F	2000°F
Walker	2000	1815	633	153	101
Simplified Walker	2041	1717	876	220	119
Classical	2255	1878	736	300	127
Stowell	6541	2091	1044	377	140

TABLE II

Summary of Constitutive Model Regressed Temperature Dependent Material Constants

	1000°F	1400°F	1600°F	1800°F	2000°F
E	.185E8	.1E8	.8E7	.3E7	.1E7
Walker					
n	26.85	3.318	2.240	2.036	1.649
n_1	1617.0	704.6	806.0	1316.0	1573.0
n_7	2369.0	1202.0	2653.0	1900.0	184.3
n_9	253.3	58.5	131.7	38.87	113.7
n_{10}	.2389E-4	.1469E-3	.5504E-3	.2184E-3	.1340E-3
n_{11}	.4955E7	.4006E6	.5625E6	.7500E5	.3312E5
m_0	1.2	1.2	1.2	1.2	1.2
K_1	.1736E6	.5845E6	.5410E6	.2053E6	.1435E6
K_2	.3315E5	.2048E6	.3624E6	-.1094E4	-.4711E5
Simplified Walker					
n	29.57	3.554	3.424	3.295	3.295
n_7	787.7	770.4	405.3	100.6	156.0
K_1	.1865E6	.5164E6	.1545E6	.5044E5	.1408E5
K_2	.4351E5	.2302E6	.4906E5	.2370E5	.5820E4
Classical					
A_1	.3054E6	.5153E6	.3325E6	.8385E5	.4753E5
A_2	7.579	2.711	2.026	2.261	2.183
A_3	.7778E6	.4885E6	.1928E6	.4861E5	.8368E4
A_4	7.325	3.627	3.207	3.214	3.909
Stowell					
s	.1156E-11	.7814E-10	.1529E-9	.1202E-8	.7478E-9
ΔH	.2198E7	.4471E6	.3640E6	.1668E7	.1121E7
σ_0	.1376E5	4971.	1682.	681.6	191.3

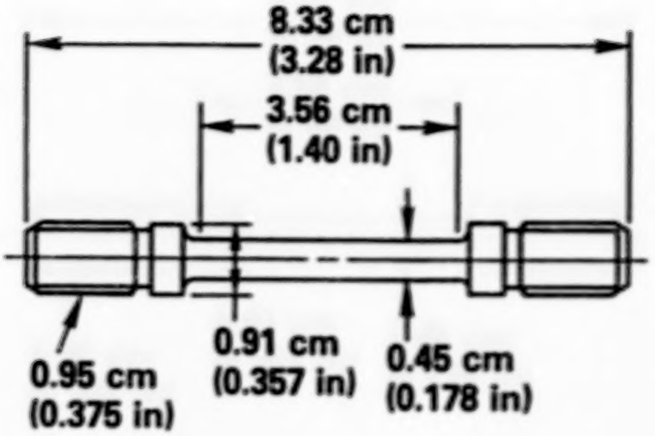
8.33 cm
(3.28 in)
3.56 cm
(1.40 in)
0.95 cm
(0.375 in)
0.91 cm
(0.357 in)
0.45 cm
(0.178 in)

Figure 1 PWA 286 Stress Relaxation Specimen Design

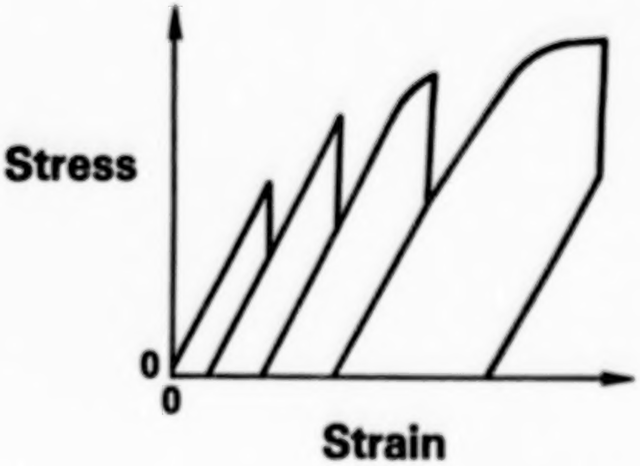

Figure 2 Typical Isothermal Stress Relaxation Experiment

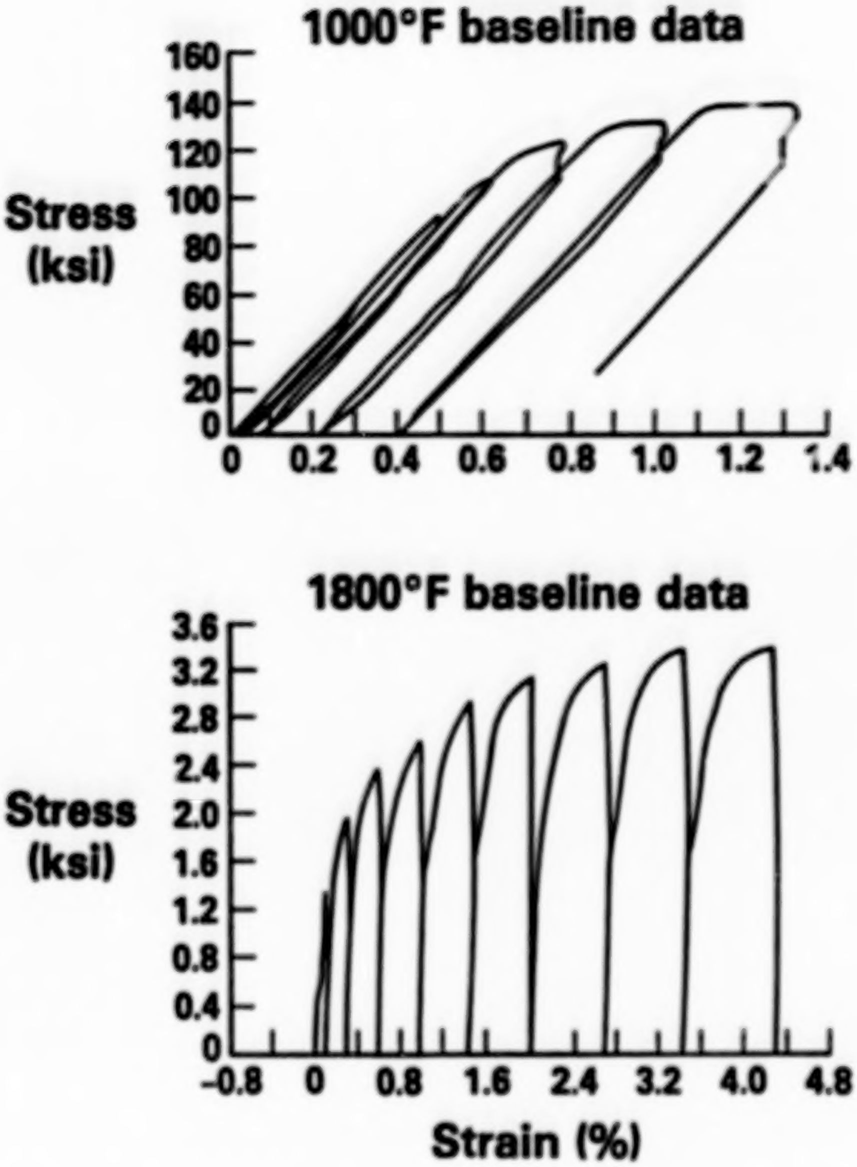

Figure 3 1000°F and 1800°F PWA 286 Baseline Stress Relaxation Data

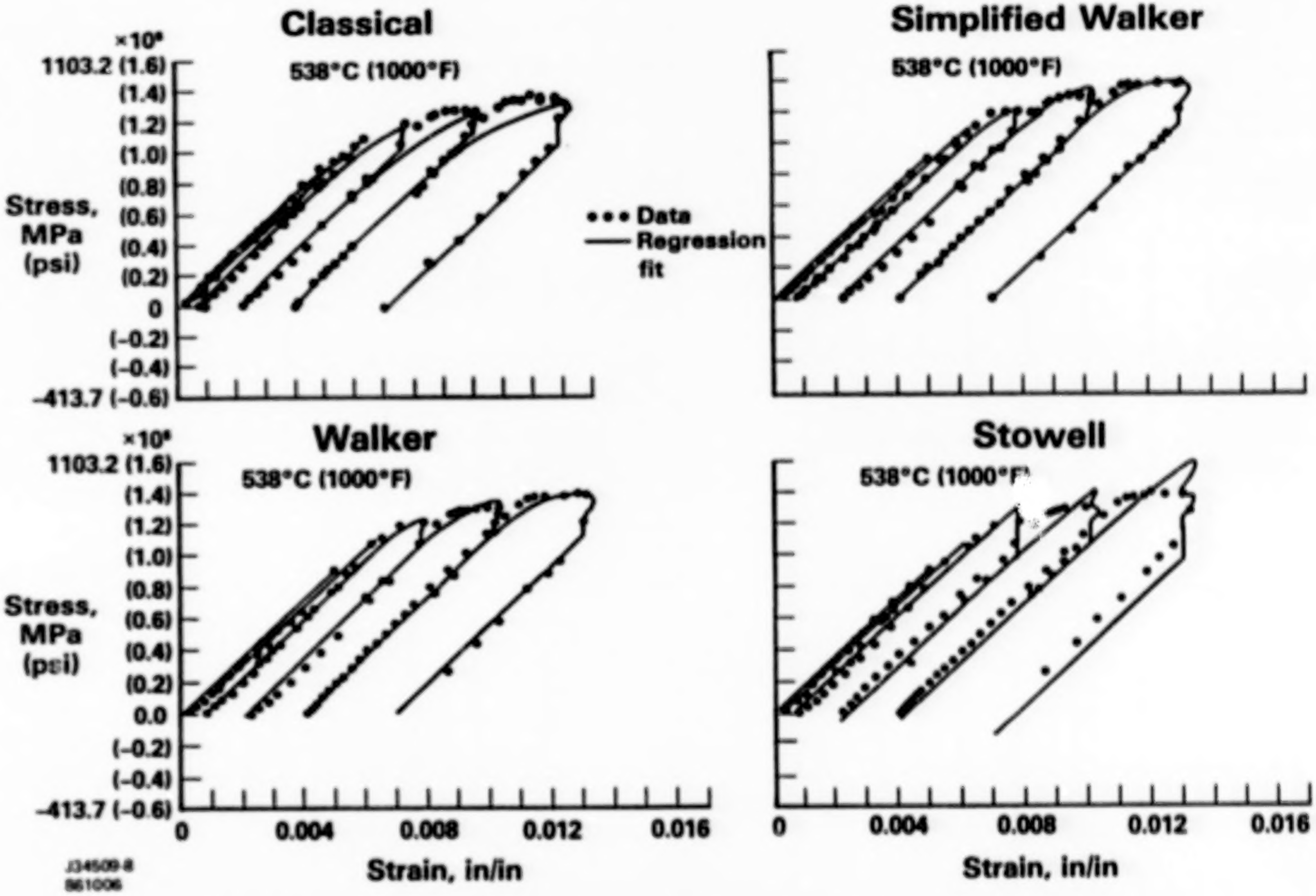

Figure 4 Low Temperature Regression Fit of PWA 286 Stress Relaxation Data

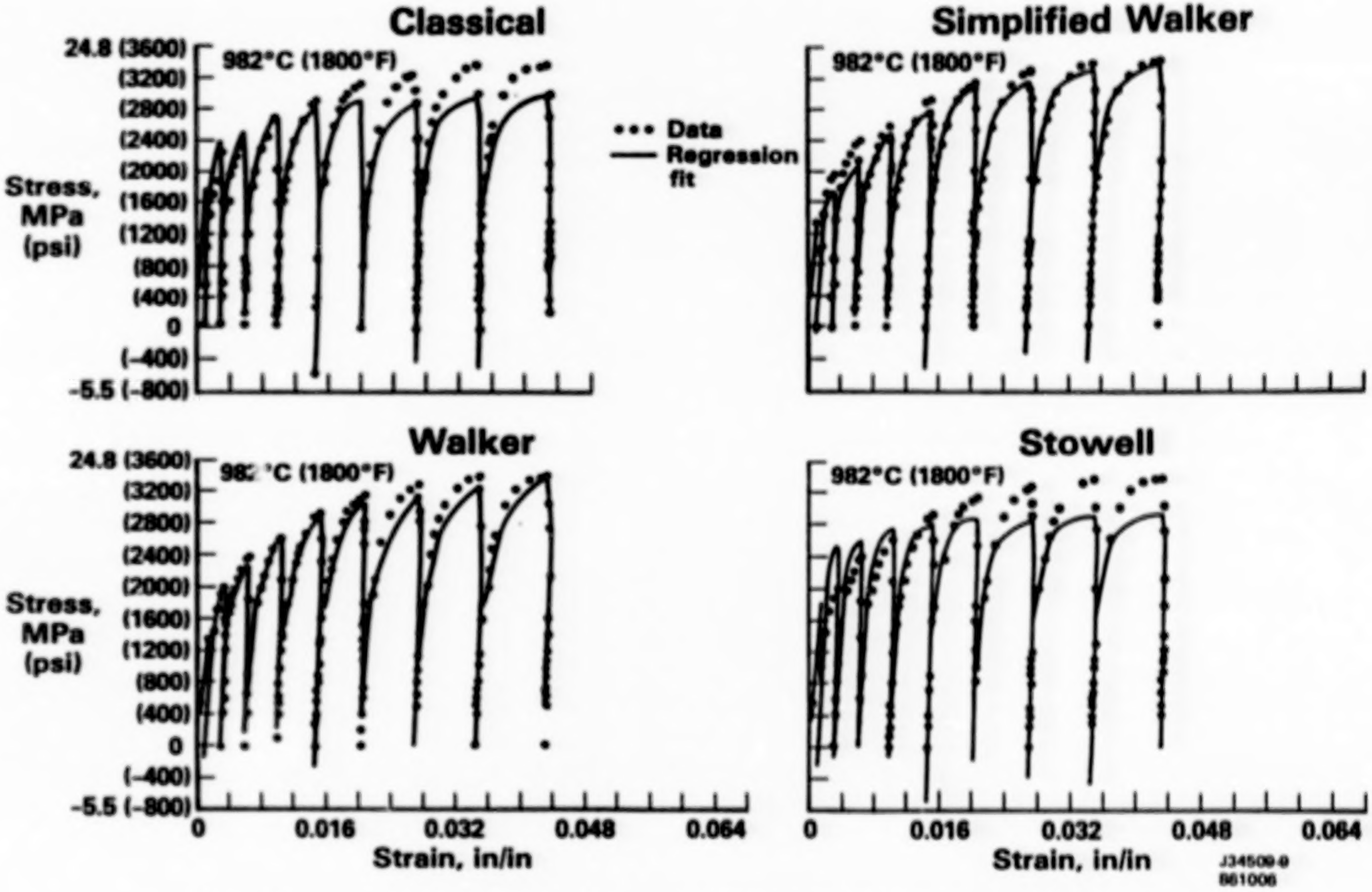

Figure 5 High Temperature Regression Fit of PWA 286 Stress Relaxation Data

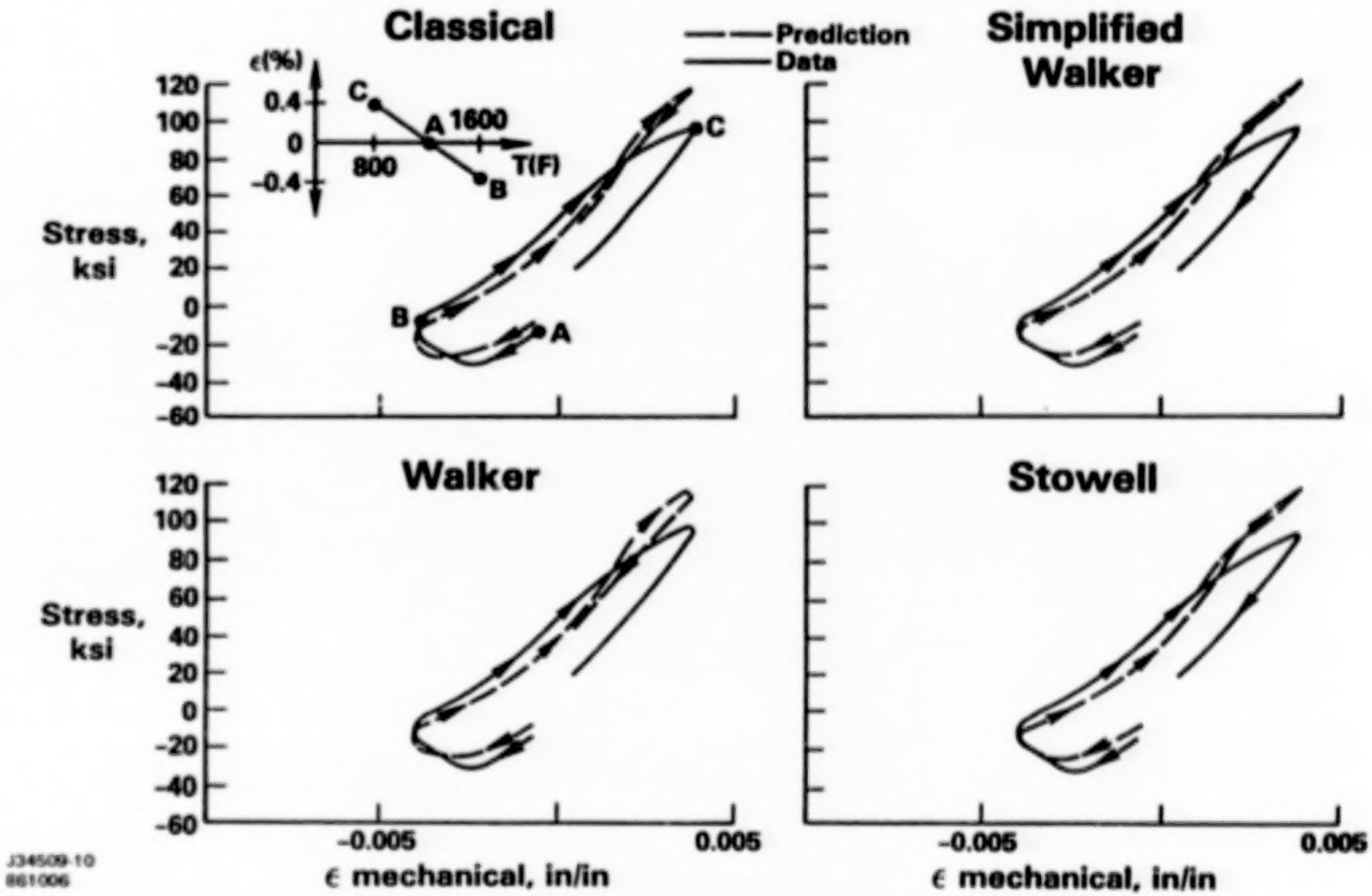

Figure 6 PWA 286 Thermo-Mechanical Test - 1st Cycle Prediction Vs. Test Data

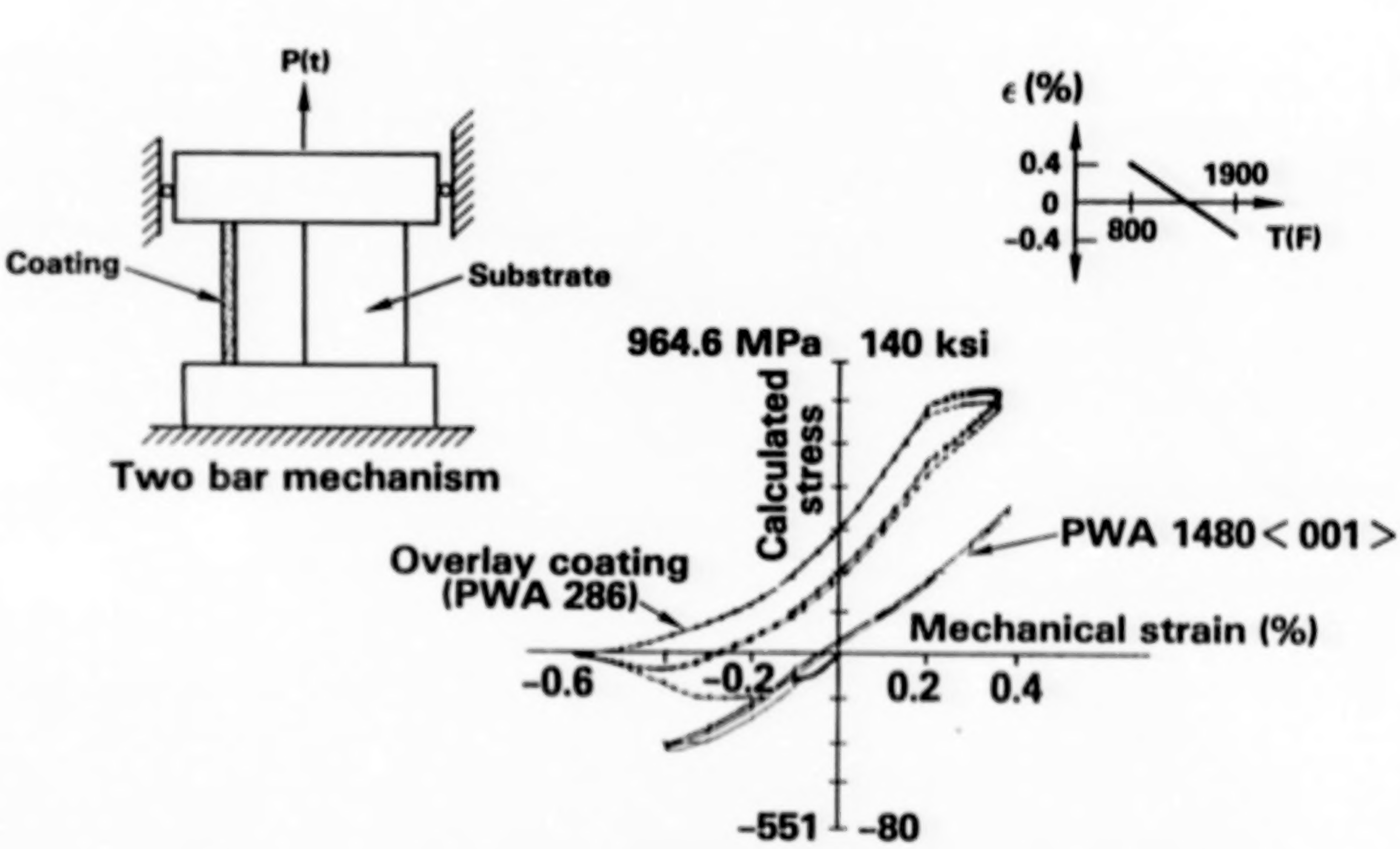

Figure 7 "Two-Bar" Mechanism and Predicted Coating/Substrate Hysteretic Response of a 427-1038°C (800-1900°F), ±0.4%, Out-of-Phase TMF Test

N88
21526
UNCLAS

N88-21526

NON-ISOTHERMAL ELASTOVISCOPLASTIC ANALYSIS OF PLANAR CURVED BEAMS[†]

G. J. Simitses[*] R. L. Carlson[**] and R. Riff[*]
Georgia Institute of Technology
Atlanta, Georgia 30332

The paper focuses on the development of a general mathematical model and solution methodologies, to examine the behavior of thin structural elements such as beams, rings, and arches, subjected to large non-isothermal elasto-viscoplastic deformations. Thus, geometric as well as material-type nonlinearities of higher order are present in the analysis.

For this purpose a complete true abinito rate theory of kinematics and kinetics for thin bodies, without any restriction on the magnitude of the transformation is presented. A previously formulated elasto-thermo-viscoplastic material constitutive law is employed in the analysis.

The methodology is demonstrated through three different straight and curved beams problems. Moreover importance of the inclusion of large strains is clearly demonstrated, through the chose applications.

[†] This work was performed under NASA Grant NAG 3-54.

[*] Professor and Assistant Professor, respectively; School of Engineering Science and Mechanics.

[**] Professor; School of Aerospace Engineering.

~~PRECEDING PAGE BLANK NOT FILMED~~

1. Introduction

The prediction of inelastic behavior of metallic materials at elevated temperatures has increased in importance in recent years. The operating conditions within the hot section of a rocket motor or a modern gas turbine engine present an extremely harsh thermo-mechanical environment. Large thermal transients are induced each time the engine is started or shut down. Additional thermal transients from an elevated ambient occur, whenever the engine power level is adjusted to meet flight requirements. The structural elements employed to construct such hot sections, as well as any engine components located therein, must be capable of withstanding such extreme conditions. Failure of a component would, due to the critical nature of the hot section, lead to an immediate and catastropic loss in power and thus cannot be tolerated. Consequently, assuring satisfactory long term performance for such components is a major concern for the designer.

Traditionally, this requirement for long term durability has been a more significant concern for gas turbine engines rather than rocket motors. However, with the advent of reusable space vehicles, such as the Space Shuttle, the requirement to accurately predict future performance following repeated elevated temperature operations must now be extended to include the more extreme rocket motor application.

Under this kind of severe loading conditions, the structural behavior is hightly nonlinear dut to the combined action of geometrical and physical nonlinearities. On one side, finite deformation in a stressed structure introduces nonlinear geometric effects. On the other side, physical nonlinearities arise even in small strain regimes, whereby inelastic phenomena play a particulary important role. From a theoretical standpoint, nonlinear constitutive equations should be applied only in connection with nonlinear transformation measures (implying both deformation and rotations). However, in almost all of the works in this area (See Ref. 1), the two identified sources of nonlinearities are always separated. This separation yields, at one end of the spectrum, problems of large response, while at the other end, problems of viscous and/or non-isothermal behavior in the presence of small strain.

The classical theories, in which the material response is characterized as a combination of distinct elastic, thermal, time independent inelastic (plastic) and time dependent inelastic (creep) deformation components cannot explain some phenomena, which can be observed in complex thermo-mechanical loading histories. This is particularly true when high-temperature non-isothermal processes should be taken into account. There is a sizeable body of literature[1,2] on phenomenological constitutive equations for the rate - and temperature - dependent plastic deformation behavior of metallic materials. However, almost all of these new "unified" theories are based on small strain theories and several suffer from some thermodynamic inconsistencies.

In a previous paper[3], the authors have presented an alternative constitutive law for elastic-thermo-viscoplastic behavior of metallic materials, in which the main features are: (a) unconstrained strain and deformation kinematics, (b) selection of reference space and configuration for the stress tensor, bearing in mind the rheologies of real materials, (c) an intrinsic relation which satisfies material objectivity, (d) thermodynamic consistency, and (e) proper choice of external and internal thermodynamic variables. Accuracy of the formulation was checked on a wide range of examples[4].

The formulation presented in this paper focuses on a mathematical model to examine the behavior of thin structural elements subjected to large non-isothermal elasto-viscoplastic deformations. Thus, geometric as well as material-type nonlinearities of higher order are present in the analyses. Such thin elements, including beams, rings and arches, are intended to present generic types of components, which might be located within or adjacent to the hot section of a rocket motor or gas turbine engine.

The rate form of the constitutive equations suggests that[5] a rate approach be taken toward the entire problem so that flow is viewed as history dependent process rather than an event. A direct consequence of the consistent adoption of the rate viewpoint in a spatial reference frame is that the problem is found to be governed by quasi-linear differential equations in time and in space. Hence, the analysis requires solution of an initial- and boundary- value problem involving instantaneously linear equations. The quasi-linear nature of the problem not only suggests an incremental approach to numerical solution, but also provides confidence in the completeness of the incremental equations. In this case, finite element solution capability is established; it should be noted, however, that the linearity of the instantaneous governing equations admits use of a wide variety of other established numerical procedures for spatial integration. A complete true ab initio rate theory of kinematics and kinetics for continuum and double curved thin structures, without any restriction on the magnitude of the strains or the deformation was formulated in Ref. 4 and will be rephrased here.

Formulation of problems concerned with finite deformation of beams has followed two different paths[6]. Prescribing the beam by its deformed or undeformed centroidal axis and cross section, one may introduce at the outset beam stress resultants and their conjugate kinematic variables characterizing displacement and rotation of the cross section. Together with appropriate beam constitutive equations and a global balance law a consistent theory is obtained. Alternatively, one may imbed beam theory in the setting of deformable solid continua, in which case one is concerned with local constitutive equations connecting the stress tensor with a strain tensor, which may in turn be expressed in terms of a combination of undetermined beam kinematic variables and functions of the beam coordinates. Momentum may then be balanced globally by integrating the local equations over the deformed beam configuration. Both paths will be considered in what follows.

2. Two-Dimensional Plane Beams (A Plane Stress Problem)

2.2 - Kinematics of the Continuum

Let a continuum in space be described by two systems of coordinates, the x^i-system, which stays at rest (the fixed system) and the u^α-system, which is associated with materials points (the convected material system). The transformation equations from one system to the other are:

$$dx^i = f^i_\alpha \, du^\alpha \tag{1}$$

$$du^\alpha = u^\alpha_i \, dx^i \tag{2}$$

where

$$f^i_\alpha \triangleq \frac{\partial x^i}{\partial u^\alpha} \tag{3}$$

$$f^\alpha_i \triangleq \frac{\partial u^\alpha}{\partial x^i} \tag{4}$$

The covariant components of the metric tensor in the material system u^α are:

$$g_{\alpha\beta} = r^i_\alpha \, r^j_\beta \, G_{ij} \tag{5}$$

where G_{ij} are the covariant components of the metric tensor in the fixed system x^i. For the fixed cartesian system (Euclidian space) we have,

$$G_{ij} = \delta_{ij} \tag{6}$$

where δ_{ij} are the components of the Kronecker delta. The coordinate lines of the x^i-system are assumed to "deform" with the continuum in order to enable the material points to keep their coordinates (in the u^α-system) unchanged.

The contravariant components of the velocity vector in the fixed system are defined by:

$$v^i = \frac{dx^i}{dt} \tag{7}$$

It is impossible to define velocity as a change in the coordinates in the material system, however, distances are obviously changing. The length of the elementary arc in the material coordinates is given by:

$$ds^2 = g_{\alpha\beta} \, du^\alpha \, du^\beta \tag{8}$$

Defining the rates of change in the material system by $\frac{\partial}{\partial t}$, the rate of change of the elementary arc is,

$$\frac{\partial}{\partial t}(ds^2) = \frac{\partial g_{\alpha\beta}}{\partial t} \, du^\alpha \, du^\beta \tag{9}$$

From Eq (9) one may conclude also that

$$\frac{1}{ds}\left(\frac{\partial(ds)}{dt}\right) = \frac{\partial}{\partial t}(\log ds) = \frac{1}{2}\,\frac{\partial g_{\alpha\beta}}{\partial t}\,\frac{du^\alpha}{ds}\,\frac{du^\beta}{ds} \tag{10}$$

The clue for the intrinsic rates of change may be unraveled, then, by the derivation of the rates of change of the metric tensor.

It can be shown[4] that the rate of change of the metric tensor in the material coordinates is given by

$$\frac{\partial g_{\alpha\beta}}{\partial t} = v_{\alpha,\beta} + v_{\beta,\alpha} \tag{11}$$

where

$$v_{\alpha,\beta} = g_{\gamma\alpha}\, v^{\gamma}{}_{,\beta} = g_{\gamma\alpha}\, f^{\gamma}_{i}\, v^{i}{}_{,\beta} = g_{\gamma\alpha}\, f^{\gamma}_{i}\, \frac{\partial}{\partial t}\left(f^{i}_{\beta}\right) \tag{12}$$

So $\frac{\partial}{\partial t}(f^{i}_{\beta})$ or $v^{i}{}_{,\beta}$ is the velocity in the fixed system as observed in the material system. The components of the deformation rate tensor defined as follows,

$$d_{\alpha\beta} \triangleq \frac{1}{2}\frac{\partial g_{\alpha\beta}}{\partial t} = \frac{1}{2}(v_{\alpha,\beta} + v_{\beta,\alpha}) = d_{\beta\alpha} \tag{13}$$

and the components of the spin tensor as,

$$\omega_{\alpha\beta} \triangleq \frac{1}{2}(v_{\alpha,\beta} - v_{\beta,\alpha}) = -\,\omega_{\beta\alpha} \tag{14}$$

Substitution of Eq. (13) into Eq. (10) yields,

$$\frac{\partial}{\partial t}\left(\log ds\right) = d_{\alpha\beta}\, \lambda^{\alpha}\, \lambda^{\beta} \qquad \left(\lambda^{\alpha} = \frac{du^{\alpha}}{ds}\right) \tag{15}$$

As soon as the deformation rate is established as the time derivative of the metric tensor, the intrinsic characteristics of the continuum, being metric properties of space, are readily differented (with respect to time). For more details see Ref. 4.

2.2 The Rate of Global Principles

The principle of virtual power (or of virtual velocities),

$$\int_V \sigma^{ij}\, \delta v_{j,i}\, dV - \int_V \rho\, f^{j}\, \delta v_{j}\, dV - \int_A \nu T^{j}\, \delta v_{j}\, dA = 0 \tag{16}$$

is equivalent to the equations of equilibrium along with the complete set of boundary conditions. In Eq. (16), σ^{ij} are the contravariant components of the Cauchy stress tensor, ρ the mass density, and f^j is a vector of specific body forces.

Total differentiation of Eq. (16) yields[4],

$$\int_V \left(\frac{d\sigma^{ij}}{dt} + \sigma^{ij} d^k_{\cdot k} = v^i{}_{,k}\, \sigma^{kj}\right) \delta v_{j,i}\, dV - \int_V \rho \frac{df^j}{dt}\, \delta v_j dV$$

$$- \int_A \gamma \frac{dT^j}{dt}\, \delta v_j dA + \int_V \sigma^{ij} \frac{d\delta v_j}{dt}{}_{,i}\, dV - \int_V \rho f^j \frac{d\delta v_j}{dt}\, dV$$

$$- \int_A \gamma T^j \frac{d\delta v_j}{dt}\, dA = 0 \tag{17}$$

At any instant Eq. (17) must be satisfied. The virtual velocity and its time derivative are, then, independent. Moreover, the last three terms of Eq. (17) are equivalent to Eq. (16). Hence, the principle of the rate of virtual power may be obtained in its concise form. For further classifications, the total derivative of the stress components will be represented by the Jauman derivative, namely

$$\frac{d\sigma^{ij}}{dt} = \overset{\nabla}{\sigma}{}^{ij} + \omega^i_{.k}\, \sigma^{kj} + \omega^j_{.k}\, \sigma^{ik} \tag{18}$$

and the following integrals are defined by

$$I_e = \int_V \overset{\nabla}{\sigma}{}^{ij}\, \delta v_{j,i} dV \tag{19}$$

$$I_d = \int_V \left(\sigma^{ij} d^k_{.k} - \sigma^{kj} d^i_{.k}\right) \delta v_{j,i} dV \tag{20}$$

$$I_r = \int_V \omega^j_{.k}\, \sigma^{ik}\, \delta v_{j,i}\, dV \tag{21}$$

Then, substitution in Eq. (17) yields the final form of the principle of the rate of virtual power,

$$I = I_e + I_d + I_r = \int_{r} \rho \frac{df^j}{dt} \delta v_j \, dV + \int_{A} \gamma \frac{dT^j}{dt} \delta v_j \, dA \qquad (22)$$

which is equivalent to

$$\frac{d\sigma^{ji}}{dt}_{,i} - v^k_{\ ,i} \, \sigma^{ij}_{\ \ ,k} + \rho \frac{df^j}{dt} - \rho d^k_{.k} f^j = 0 \qquad (23)$$

and

$$\frac{d(vT^j)}{dt} = \frac{d(\sigma^{ij} v_j)}{dt} \qquad (24)$$

A similar process can be applied[4] to obtain the principle of the rate of balance of energy from the first law of thermodynamics.

2.3 Constitutive Equations

In a previous paper[3], the authors have presented a complete set of constitutive relations for nonisothermal, large strain, elasto-viscoplastic behavior of metals. It was shown there[3] that the metric tensor in the convected (material) coordinate system can be linearly decomposed into elastic and (visco) plastic parts. So a yield function was assumed, which is dependent on the rate of change of stress on the metric, on the temperature and a set of internal variables. Moreover, a hypoelastic law was chosen to describe the thermo-elastic part of the deformation.

A time and temperature dependent "viscoplasticity" model was formulated in this convected material system to account for finite strains and rotations. The history and temperature dependence were incorporated through the introduction of internal variables. The choice of these variables, as well as their evolution, was motivated by thermodynamic considerations.

The nonisothermal elasto-viscoplastic deformation process was described completely by "thermodynamic state" equations. Most investigators[1,2] (in the area of viscoplasticity) employ plastic strains as state variables. This study[3] shows that, in general, use of plastic strains as state variables may lead to inconsistencies with regard to thermodynamic considerations. Furthermore, the approach and formulation employed in previous works leads to the condition that all the plastic work is completely dissipated. This, however, is in contradiction with experimental evidence, from which it emerges that part of the plastic work is used for producing residual stresses in the lattice, which, when phenomenologically considered, causes hardening. Both limitations were excluded from this formulation.

The constitutive relation will be rephrased here as follows

$$\text{a) if} \quad F = (t^i_k - C\,\rho_0\,g\,\beta^i_k)(t^k_i - C\,\rho_0\,g\,\beta^k_i) - \kappa^2(\overset{P}{W},T) = 0 \qquad (25)$$

where, s^i_k, the Kirchhoff stress tensor, $s^i_k = \frac{\rho_0}{\rho}\,\sigma^i_k$, and the temperature T are independent process variables, t^i_k being the deviator of the Kirchhoff stress s^i_k, and $\overset{P}{W}$ and β^i_k are internal parameters, then

$$d^i_k = \underbrace{\frac{1}{2G}\{\overset{\nabla}{s}{}^i_k - \frac{\nu}{1+\nu}\,\overset{\nabla}{s}{}^r_r\,\delta^i_k\} + \alpha\,\dot{T}\,\delta^i_k}_{\overset{E}{d}{}^i_k} + \underbrace{2\dot{\lambda}(\bar{t}^i_k - C\,\rho_0\,g\,\beta^i_k)}_{\overset{P}{d}{}^i_k} \qquad (26)$$

with

$$\dot{\lambda} = \frac{1}{4\eta}\{[\frac{(t^i_k - C\,\rho_0\,g\,\beta^i_k)(t^k_i - C\,\rho_0\,g\,\beta^k_i)}{\kappa^2}]^{1/2} - 1\} \qquad (27)$$

$$\bar{t}^i_k = \frac{1}{1 + 4\,n\dot{\lambda}}\,(t^i_k - C\,\rho_o\,\varepsilon\,s^i_k) + C\,\rho_o\,\varepsilon\,s^i_k \qquad (28)$$

$$\overset{P}{\dot{W}} = \frac{1}{\rho_o}\,\bar{t}^i_k\,\overset{P}{d}{}^k_i \qquad (29)$$

$$\overset{\nabla}{s}{}^i_k = \zeta\,\overset{P}{d}{}^i_k \qquad (30)$$

b) if $F = 0$ (31)

and $$\frac{\partial F}{\partial s^i_k}\,\overset{\nabla}{s}{}^i_k + \frac{\partial F}{\partial T}\,\dot{T} > 0 \qquad (32)$$

then $$d^i_k = \overset{E}{d}{}^i_k \qquad (33)$$

$$\overset{P}{d}{}^i_k = 0 \qquad \overset{\overset{P}{\nabla}}{d}{}^i_k = 2\dot{\lambda}(t^i_k - C\rho_o\,\varepsilon s^i_k) \qquad (34)$$

with $$\dot{\lambda} = \frac{1}{8nk^2}\,\{2(t^i_k - C\,\rho_o\,\varepsilon\,s^i_k)\,\overset{\nabla}{t}{}^k_i - \frac{\partial k^2}{\partial T}\,\dot{T}\} \qquad (35)$$

c) if $F = 0$ and $\frac{\partial F}{\partial s^i_k}\,\overset{\nabla}{s}{}^i_k + \frac{\partial F}{\partial T}\,\dot{T} \le 0$ (36)

or $F < 0$ (37)

then $$d^i_k = \overset{E}{d}{}^i_k \tag{38}$$

$$\overset{P}{\dot{W}} = 0 \tag{39}$$

$$\overset{\nabla}{\beta}{}^i_k = 0 \tag{40}$$

2.4 Plane Stress Approximation

By definition, a body is said to be in the state of plane stress parallel to the u^1, u^2 plane when the stress components σ^{13}, σ^{23}, σ^{33} vanish[7]. It is well known in literature that the case of plane stress is difficult to handle theoretically. Even linear elasticity has to treat this case in an approximate manner. To remove some of theoretical difficulties Durban and Baruch[5] introduced the notion of Generalized Plane Stress, where instead of dealing with the quantities themselves, one deals with their average values.

In our case the problem is even more difficult. The nonlinearities, which the general three-dimensional theory takes into account will also cause a large change of the geometrical quantities in the u^3 direction. Clearly, some assumptions are needed to treat the case of plane stress as a two-dimensional case.

The first basic assumption is that the thickness, h, of the plate defined by the coordinates u^1, u^2 located in its middle plane, is small as compared with the other two dimensions. A second assumption is that the external forces act in the u^1, u^2 directions and are symmetrically distributed with respect to the middle plane.

In a way similar to the procedure proposed by Durban and Baruch[5], all the kinematic expressions are obtained by averaging the three-dimensional expressions.

A basic assumption for the case of plane stress is that the components connected with the third direction are small and can be neglected. So, a new concept of generalized stress tensor is introduced

$$\tau_k^i = \frac{\sigma_k^i h}{h_0} \tag{41}$$

It must be noted that in the linear theory of elasticity, where the geometry does not change, the averaged and generalized stress tensors coincide.

So the three-dimensional incremental elasto-viscoplastic theory, developed previously, can be adopted for two-dimension plane stress problems.

3. A Thin Curved Beam

3.1 Doubly Curved Element

A complete rate theory of kinematics and kinetics for doubly and singly curved thin structures, without any restriction on the magnitude of the strain or the deformation, was presented in Ref. 4.

Five different shell theories (approximations), in rate form, starting with the simple Kirchhoff-Love theory and finishing with a completely unrestricted one, were considered there[4].

The kinematic and kinetic equations for intrinsic shell dynamics, introduced in Ref. 4 are presented here, in compact form, together with basic notations. For simplicity we consider here Kirchhoff motion only[8].

The components of the velocity vector $w = \dot{y}$ are

$$w_\alpha = \dot{y} \cdot y_\alpha \quad w^\alpha = \dot{y} \cdot y^\alpha, \quad w_n = \dot{y} \cdot \bar{n} \tag{42}$$

where $\bar{n}$ is the unit normal to y, and y is the weighted motion.

Expressions for the couponents of the velocity gradients, $\dot{y}$, follow from differentiation of Eq. (42)

$$d_{\alpha\beta} = y_\alpha \cdot \dot{y}_\beta = w_{\alpha;\beta} - \bar{b}_{\alpha\beta}\, w_n \tag{43}$$

$$\bar{w}_\alpha = \bar{n} \cdot \dot{y}_\beta = w_{n,\alpha} + \bar{b}_{\alpha\beta}\, w^\beta \tag{44}$$

The time rates of the components of the metric and curvature tensors follow immediately from the above as

$$\dot{\bar{a}} = d_{\alpha\beta} + d_{\beta\alpha} \quad , \quad \dot{\bar{b}}_{\alpha\beta} = \bar{\omega}_{\alpha;\beta} + d^\gamma_\alpha\, \bar{b}_{\beta\gamma} \tag{45}$$

To complete the kinematics, we get the components of the acceleration vector by time differentiation of Eq. (42) and through use of Eqs. (43) and (44),

$$\begin{aligned} \ddot{y} \cdot y^\alpha &= \dot{w}^\alpha + d^\alpha_\beta\, w^\beta - \bar{\omega}^\alpha\, w_n \\ \ddot{y} \cdot \bar{n} &= \dot{w}_n + \bar{\omega}\, w^\alpha \end{aligned} \tag{46}$$

The accelerations form the right sides of the equations of motion. The left sides are the static terms that can, for example, be expressed in terms of symmetrical stress resultants[8]. The result becomes

$$\dot{w}^\alpha = \bar{m}^{-1} [\bar{n}^{\beta\alpha}_{;\beta} + \bar{b}^\alpha_{\lambda;\beta} + \bar{m}^{\lambda\beta} + 2\bar{b}^\alpha_\lambda\, \bar{m}^{\beta\lambda}_{;\beta} + \bar{p}^\alpha] - d^\alpha_\beta\, w^\beta + \bar{\omega}^\alpha\, w_n \tag{47}$$

ORIGINAL PAGE IS
OF POOR QUALITY

$$\dot{w}_n = \bar{m}^{-1}[\bar{n}^{\alpha\beta}\,\bar{b}_{\alpha\beta} + \bar{b}^{\lambda}_{\beta}\,\bar{b}_{\alpha\lambda}\,\bar{m}^{\alpha\beta} - \bar{m}^{\alpha\beta}_{;\alpha\beta} + \bar{p}] - \bar{\omega}^{\alpha}\,w_{\alpha}. \tag{48}$$

where $\bar{p}^{\alpha}$, $\bar{p}$, m are loading components and mass, respectively, per unit area of γ.

3.2 A Simplified Version of Curved Beam Element

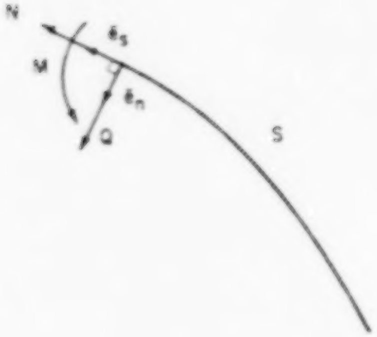

Fig. 1 - Reference Line of a Curved Beam

A portion of the reference line for a curved beam is shown on Fig. 1. The current arc length is denoted by s, while φ is the current angle of inclination of the normar to the reference line, and ρ is the radius of curvature.

The stress resultants acting on the beam cross section are the bending moment M, the axial force N, and the shear force Q. The external load, measured per unit of current length of the reference line, has the components p_s and p_n in the direction of the unit vectors $\bar{e}_s$ and $\bar{e}_n$ respectively.

If v_s and v_n denote the velocity components in the direction of the unit vectors $\bar{e}_s$ and $\bar{e}_n$ respectively, the rate of extension is

$$d = \frac{\partial v_s}{\partial s} - \frac{v_n}{\rho} \tag{49}$$

The rate of rotation, $\dot{\phi}$, of a given section is given by

$$\omega = \dot{\phi} = \frac{\partial v_n}{\partial s} + \frac{v_s}{\rho} \tag{50}$$

while the generalized rate of deformation associated with bending is

$$\dot{k} = \frac{\partial \dot{\phi}}{\partial s} = -\frac{\partial}{\partial s} \left(\frac{\partial v_n}{\partial s} + \frac{v_s}{\rho}\right) \tag{51}$$

The rate of equilibrium equations for this simplified version may be put in the following form:

$$\begin{gathered}
\frac{\partial \dot{N}}{\partial s} - Q \frac{\partial \phi}{\partial s} - \dot{Q} \frac{\partial \phi}{\partial S} + \dot{p}_s + d\, p_s = 0 \\
\frac{\partial \dot{Q}}{\partial s} + N \frac{\partial \dot{\phi}}{\partial s} + \dot{N} \frac{\partial \phi}{\partial s} + \dot{p}_n + d\, p_n = 0 \\
\frac{\partial \dot{M}}{\partial s} + \dot{Q} + dQ = 0
\end{gathered} \tag{52}$$

4. Numerical Solution

The quasi-linear nature of the velocity equilibrium equations suggests the adoption of an incremental approach to numerical integration with respect to time. The availability of the field formulation provides assurance of the completeness of the incremental equations and allows the use of any convenient procedure for spatial integration over the domain B. In the present instance the choice has been made in favor of a simple first order expansion in time for the construction of incremental solutions from the results of finite element spatial integration of the governing equations.

The procedure employed permits the rates of the field formulation to be interpreted as increments in the numerical solution. This is particularly convenient for the construction of incremental boundary condition histories.

The finite element method for spatial discretization has been well documented (see, e.g. Zienkiewicz[9] or Oden[10]) and will not be detailed here. It should be noted, however, that as a consequence of the present formulation, the velocity equilibrium equations are not symmetric. This feature precludes implementation of a Ritz procedure as commonly employed in finite element analysis of infinitesimal deformation. Linear algebraic equations governing the discrete model for the finite case are developed employing the method of Galerkin.

The spatial discretization results in:

$$[K]\,\{v\} = \{\dot{R}\} \tag{53}$$

where [K] is the nonsymmetric stiffness matrix, $\{v\}$ is the vector containing the generalized nodal velocities, and $\{\dot{R}\}$ is the rate of the load. The solution to Eq. (53) at time to provides a basis for evaluation of a deformation increment and associated changes in internal stresses and boundary loading. The incremental solution defines the deformed configuration and stress rate at $t = t_0 + \delta t$ thereby permitting definition of a new spatial problem at the later time.

5. Applications

The capabilities of the models presented here in have been evaluated through three simple numerical examples. The first example demonstrates the capability of the plane stress approximation to predict deflections and [illegible] in a beam loaded by a constant moment. Figure 2 illustrates the beam and the finite element model. A quarter of the beam was divided into six elements in the vertical direction and into five elements in the horizontal direction. The external moment was introduced by six parallel forces acting on the section BC (see Fig. 2).

The value of the external moment is 3500 kg/cm, and the material of the beam is CMR-17. The viscoplastic properties of the material were obtained experimentally from uniaxial tests in Ref. 1. This properties were collaborated into the present material model.

The variation of the deflection of point E as a function of time is given in Fig. 3. It is important to point out the value of the large deformation analysis. After ten minutes of the deformation is increased by [illegible] and at the same time there are important changes in the stress field (see Fig. 4).

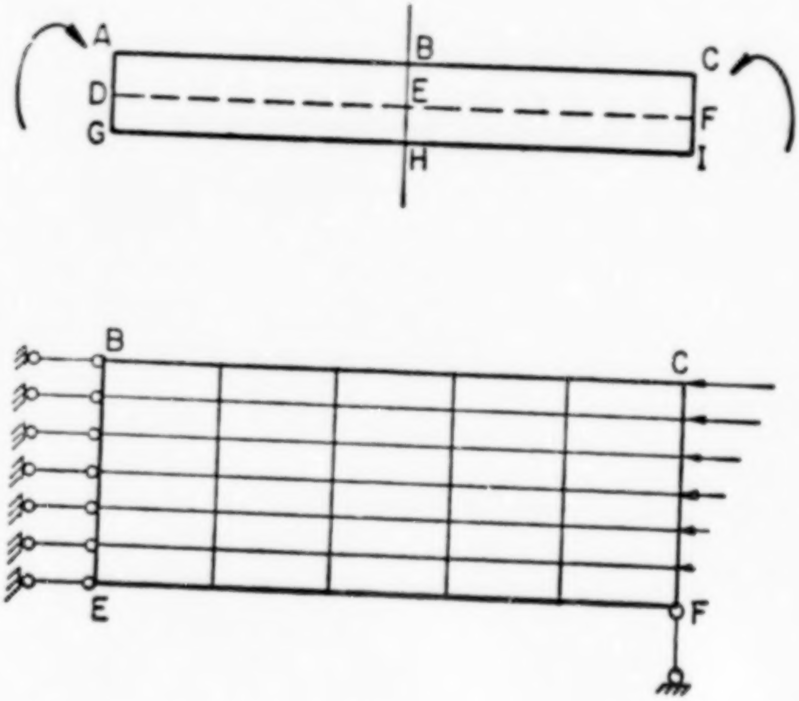

Fig. 2 - The Beam Model

ORIGINAL PAGE IS
OF POOR QUALITY

ORIGINAL PAGE IS
OF POOR QUALITY

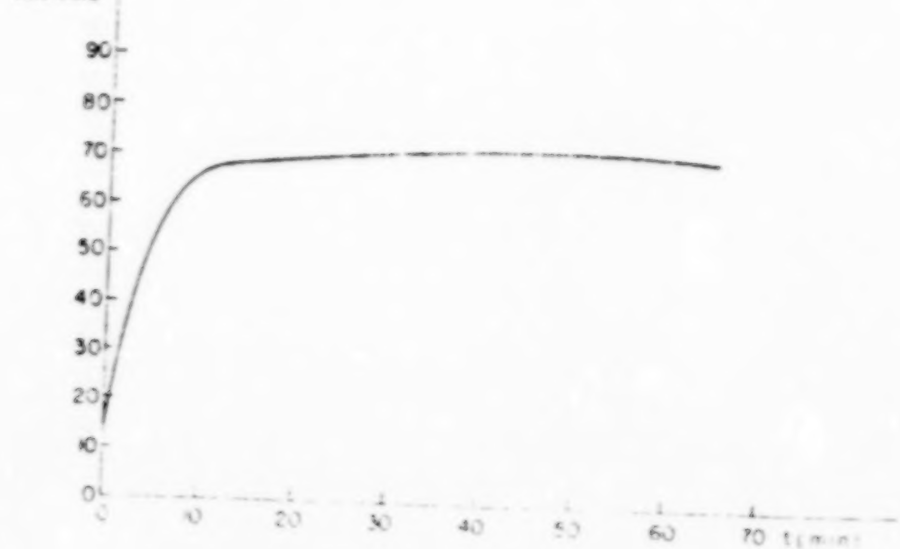

Fig. 3 - Point E Deflection

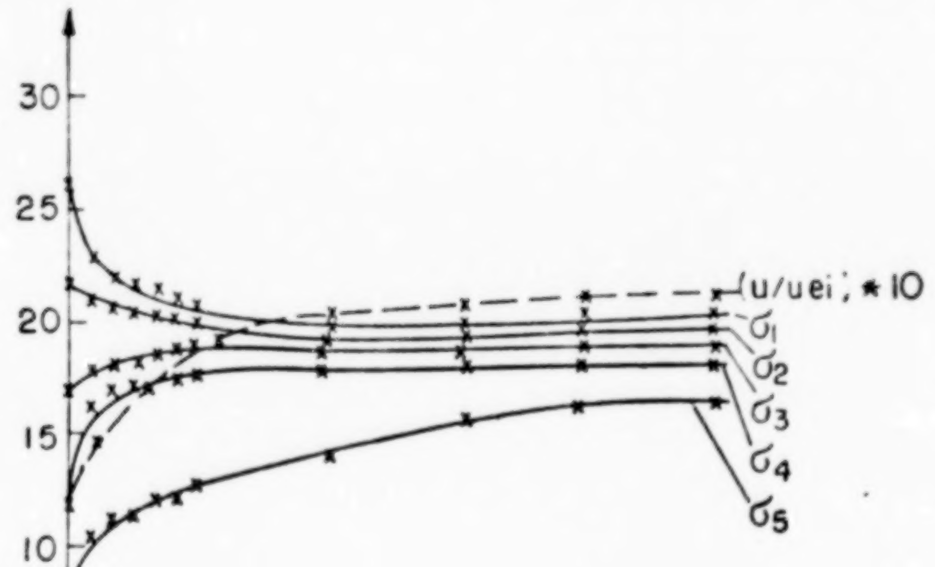

Fig. 4 - Stress Distribution

The next example consists of a straight simply supported beam, loaded by a transverse concentrate force at the midspan. The beam is 25 inches long, two inches high and one inch wide. The material is stainless steel 304 (Heat 9T2796). The material constants in sub section 2.3 were correlated with the uniaxial tension experimental results given in Ref. 12. The beam was subjected to a load of 2000 pounds at 1100°F, this load was then held constant for 312 hr., and then increased to 2250 pounds at 1400°F.

The primary purpose of this example is to compare the results, obtained by the two previously discussed models. The first one is the two-dimensional plane stress model, and the second one is the thin beam model as derived from thin shell theory. Figure 5 presents results in the form of load versus midspan deflection. The finite element model consists of five simple plane stress elements (dashed line in Fig. 5) or five sophisticated beam elements (full line in Fig. 5).

It can be seen (Fig. 5) that the results agree quite well up to the 312-hour hold period (points 3,4). During the hold period, the material hardens and only the beam model can represent this behavior after the load is further increased.

The last example presents an analysis of a circular arch. The geometry of the shallow circular arch is shown on Fig. 6. The material is once again the 304 stainless steel. The arch is fixed at both ends and carries a concentrated load at the center. The elasto-viscoplastic analysis of this arch is performed with the aid of a ten curved beam elment model and with the inertia terms taken into account. The load P is assumed to be applied in a quasi-static manner at t = 0. The results of this analysis are shown on Fig. 6, as the time-history of the midspan

ORIGINAL PAGE IS
OF POOR QUALITY

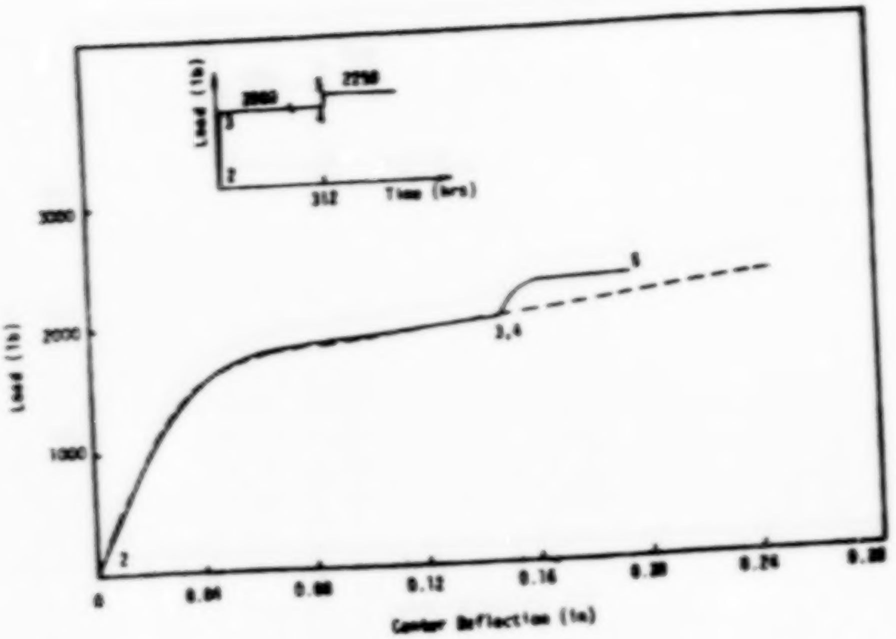

Fig 5 - Deflection vs Load

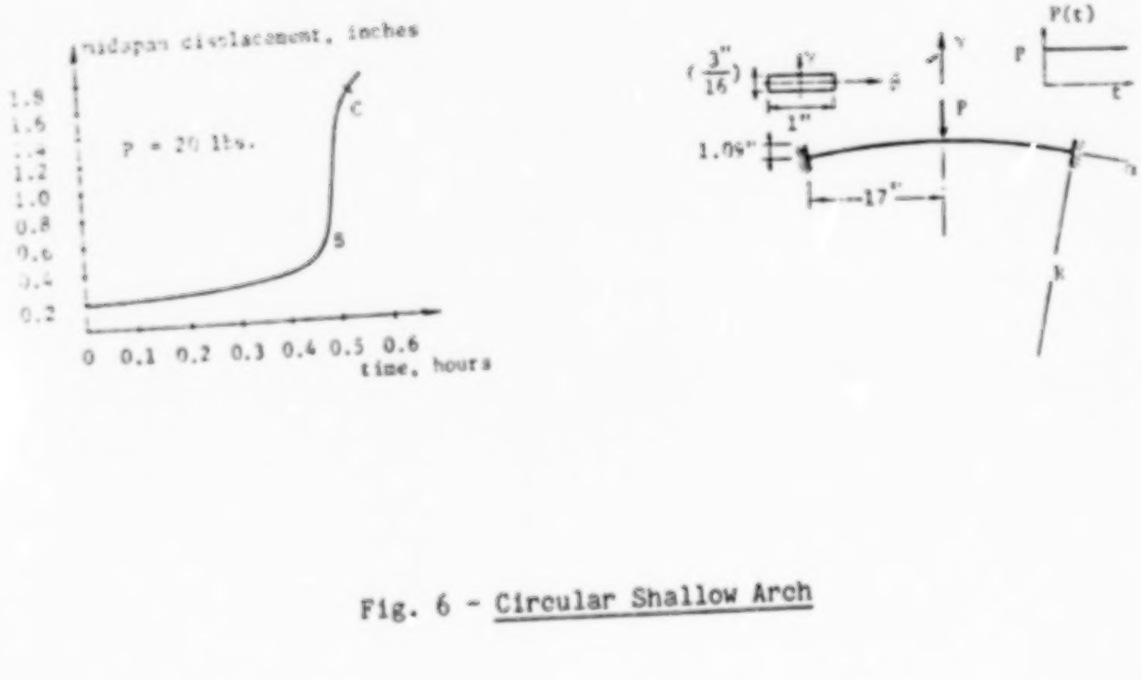

Fig. 6 - Circular Shallow Arch

displacement. The response of the arch starts with the instantaneous elastic deformation at t = 0, followed by slow deformation up to point B, which can be considered as a limit point for the given value of the load P. Beyond point B, the displacements increase rapidly towards point C. This may suggest the existence of critical time for the prescribed load.

REFERENCES

1. Walker, K. P., "Research and Development Programs for Nonlinear Structural Modeling with Advanced Time-Temperature Dependent Constitutive Relations", NASA Contract Report, NASA CR 165533; 1981.

2. Chan, K. S., Bodner, S. R., Walker, K. P., and Lindholm, U. S., "A Survey of Unified Constitutive Theories", NASA Contract Report, NASA-23925, 1984.

3. Riff, R. Carlson, R. L., and Simitses, G. J., "The Thermodynamically Consistent Constitutive Equations For Nonisothermal Large Strain, Elasto-Plastic, Creep Behavior", AIAA/ASME/ASCE/AHS 26th SDM Conference, Orlando, Florida, April 1985, paper No. 85-0621-CP, also to be published in AIAA J.

4. Simitses, G. J., Carlson, R. L., and Riff, R., "Formulation of the Nonlinear Analysis of Shell-Like Structures, Subjected to Time-Dependent Mechanical and Thermal Loading", NASA Report, 1986.

5. Durban, D., Baruch, M., "Incremental Behavior of an Elasto-Plastic Continuum", Technion - I.I.T., TAE Rep. No. 193, February 1975.

6. Pinskey, P. M., Taylor, R. L., and Pister K. S., "Finite deformation of elastic beams", in Variational Methods in The Mechanics of Solids (ed. S. Nemat-Nasser), Pergamon Press, 1980.

7. Mendelson, A., Plasticity: Theory and Application, The MacMillan Co., New York, 1968.

8. Libai, A., and Simmonds, J. G., "Nonlinear Elastic Shell Theory", in Advances in Applied Mechanics, (Ed. Htchinson, J. W. and Wu, T. Y.) Vol. 23, 1983.

9. Zienkiewicz, O.C., and Cheung, Y.K., The Finite Element Method in Structural and Continuum Mechanics, McGraw-Hill, 1967.

10. Oden, J. T., Finite Elements of Nonlinear Continua, McGraw-Hill, 1972.

11. Riff, R., and Baruch, M., "Development of Incremental Elasto-Plastic Finite Element in Space", Technion-I.I.T., TAE Rep. No. 348, 1981.

12. J. A. Clinard, J. M. Corum, and W. K. Sarotory, "Comparison of Typical Inelastic Analysis Predictions with Benchmark Problem Experimental Results. Pressure Vessels and Piping: Verification and Qualification of Inelastic Analysis Computer Programs", pp. 79-98 ASME Publication G00088 (1975).

N88
21527
UNCLAS

N88-21527

EFFECTS OF STATE RECOVERY ON CREEP BUCKLING UNDER VARIABLE LOADING

D.N. Robinson* and S.M. Arnold†
University of Akron
Akron, Ohio 44325

Structural alloys embody internal mechanisms that allow recovery of state with varying stress and elevated temperature; that is, they can return to a softer state following periods of hardening. Such material behavior is known to strongly influence structural response under some important thermomechanical loadings; for example, those involving thermal ratcheting. Here, we investigate the influence of dynamic and thermal recovery on the creep buckling of a column under variable loading. The column is taken as the idealized (Shanley) sandwich column. The constitutive model, unlike the commonly employed Norton creep model, incorporates a representation of both dynamic and thermal (state) recovery. The material parameters of the constitutive model are chosen to characterize Narloy-Z, a representative copper alloy used in thrust nozzle liners of reusable rocket engines. Variable loading histories include rapid cyclic unloading/reloading sequences and intermittent reductions of load for extended periods of time; these are superimposed on a constant load. The calculated results show that state recovery significantly affects creep buckling under variable loading. Failure to account for state recovery in the constitutive relations can lead to nonconservative predictions of the critical creep-buckling time.

INTRODUCTION

The influence of dynamic and thermal recovery on the high temperature behavior of structural alloys is well recognized (refs. 1 and 2). (See figs. 1 and 2.) For example, recovery is believed to play a major role in one of the central structural problems relating to liquid metal breeder reactor design, the problem of thermal ratcheting. Failure to account for recovery effects in structural analyses involving repeated thermal transients has been shown to give qualitatively incorrect and nonconservative predictions of ratcheting in some instances (ref. 3). Special provisions for taking recovery into account (e.g., the so called α-reset procedure (ref.4)) are now finding their way into documents guiding structural analysis in the U.S. nuclear industry. The effects of thermal ratcheting have also been observed in thrust nozzle liners of reusable rocket engines.

A second area in which recovery effects are thought to play a primary role, and one that impacts essentially all high temperature system design, is that of creep crack growth under creep-fatigue (variable stress) conditions.

---

*NASA Lewis Resident Research Associate.
†Now at NASA Lewis Research Center.

PRECEDING PAGE BLANK NOT FILMED

Creep (state) recovery is believed to be one of the main causes of acceleration of crack growth in the creep regime and under variable loads. A study by Kubo (ref. 5), using the same constitutive relations (refs. 2 and 6) employed in the present work, shows that the experimentally observed acceleration of creep cracks under variable stress can be predicted through the inclusion of appropriate mechanisms of recovery in the constitutive relations.

In this paper we discuss a third area of mechanics in which recovery is expected to have significant influence, that is the problem of creep buckling under variable loading. The presence of mechanisms of recovery can allow creep strain rates to increase following periods of hardening and thus cause acceleration of creep buckling. Load reversals may be accompanied by dynamic recovery as in figure 1, and load reductions by thermal recovery as in figure 2; in either case, creep rates are increased upon reloading, which tends to reduce the critical time to buckling.

In the vast majority of creep-buckling studies the constitutive model used has been of the Norton type (refs. 7 to 9) wherein the (steady state) creep rate is taken as a function of stress and temperature alone. Some investigations have made use of hardening theories (refs. 10 to 12) that include a primary creep phase. However, these theories do not generally allow for inelastic state recovery and, consequently, for rejuvenation of primary creep. These constitutive theories are adequate in the case of constant loading but may significantly over predict the time to buckling under certain types of variable loading.

Here, we examine the elevated temperature creep-buckling problem under variable loading using the simple Shanley model (ref. 13) of a column but with a constitutive model (refs. 2 and 6) that embodies a representation of both dynamic and thermal recovery. The constitutive model is that developed principally by Robinson at Oak Ridge National Laboratory and NASA Lewis Research Center; and that used by Kubo in studies concerning creep crack growth.

The present study was motivated partly by the occurence of what appears to be local ratcheting-buckling failures in the throat liner of the main thrust nozzles of reusable rocket engines, notably the NASA Space Shuttle main engine. For that reason the material parameters used in the constitutive equations are chosen to represent a copper alloy, Narloy-Z, which is typical of materials used in rocket engine thrust nozzle liners.

We shall first state the constitutive model and, secondly, specify the geometry of the Shanley column model. We then investigate creep-buckling behavior under constant loading; cyclic loading which includes relatively rapid load reductions and reversals (dynamic recovery); and cyclic loading which includes intermittent reductions of load for extended periods of time (thermal recovery). Some of the calculations, using a roughly equivalent Norton type creep model, are repeated for comparison. Some physical aspects associated with the constitutive model are discussed along with the results. Finally, we state the conclusions drawn from the study.

THE CONSTITUTIVE THEORY

We make use of the constitutive law reported in references 2 and 6, which gives the complete multiaxial statement of the model. Here, we state the model in uniaxial terms together with the corresponding parameter values appropriate for the copper alloy Narloy-Z.

Flow law:

$$\dot{\epsilon}^p = \begin{cases} AF^n \operatorname{sgn}(\sigma-\alpha); & F > 0 \text{ and } \sigma(\sigma-\alpha) > 0 \\ 0 & ; F \leq 0 \text{ or } F > 0 \text{ and } \sigma(\sigma-\alpha) \leq 0 \end{cases} \tag{1}$$

Evolutionary law:

$$\dot{\alpha} = \begin{cases} \dfrac{H}{|\alpha|^{\beta}}\, \dot{\epsilon}^p - R|\alpha|^{m-\beta} \operatorname{sgn} \alpha; & \alpha > \alpha_0 \text{ and } \sigma\alpha > 0 \\ \dfrac{H}{\alpha_0{}^{\beta}}\, \dot{\epsilon}^p - R\alpha_0^{m-\beta} \operatorname{sgn} \alpha; & \alpha \leq \alpha_0 \text{ or } \sigma\alpha \leq 0 \end{cases} \tag{2}$$

in which

$$F = \frac{(\sigma-\alpha)^2}{\kappa^2} - 1 \tag{3}$$

and

$$\begin{aligned} A &= 1.60\times10^{-8} \\ n &= 4 \\ m &= 8.73 \\ \beta &= 1.07\times10^{-6}\,(T^2) + 1.60 \\ \kappa^2 &= 209.6 - 0.20(T) \\ H &= 1.46\times10^{7} \\ R &= 1.06\times10^{-7} \\ \alpha_0 &= 0.2 \end{aligned} \tag{4}$$

Also, $\dot{\epsilon}^p$ indicates the inelastic strain rate in hr^{-1} and σ, the applied uniaxial stress in MPa. In the general form of the theory, κ (MPa) is a Bingham-Prager threshold stress playing the role of a scalar state variable; here it is taken to have the constant value given above. For present purposes, α (MPa) is the single inelastic state variable. It represents the uniaxial component of a tensorial state variable (internal stress) that appears in the multiaxial formulation of the theory. The minimum attainable value of $|\alpha|$ is α_0 which plays a primary role in the representation of dynamic recovery. (See Discussion.) The remaining parameters, in some cases functions of temperature (T), are consistent with the units MPa, hr, and degrees Kelvin. The elastic response is characterized by a linearly temperature dependent Young's modulus E (MPa) given by

$$E = 1.47\times10^{5} - 70.5(T) \tag{5}$$

Equations (1) to (4) incorporate both dynamic and thermal recovery and therefore are capable of predicting the type of behavior illustrated in figures 1 and 2.

The parameter values for Narloy-Z were determined from uniaxial tensile and stress relaxation test data. Because the complete data base normally required to characterize a particular alloy by using the present constitutive theory was not available, the tensile and relaxation data had to be considered sufficient.

Tensile data were found (ref. 14) over a wide temperature range (~30 to 811 K) but at only a single strain rate 0.002/sec. Limited stress relaxation data (ref. 15) were found at the temperature 811 K (1000 °F); these were used in the absence of creep data. The most serious data deficiency in the present context is the lack of tests giving a direct measurement of recovery effects; that is such tests as strain or stress transient dip tests or open loop cyclic tests involving partial stress reversals. Nevertheless, it is believed that the material characterization is adequate for a reasonably quantitative study of creep-buckling behavior under variable stress.

Figure 3 shows a comparison of the tensile data with predictions based on equations (1) to (4). Figure 4 similarly compares typical relaxation responses with a prediction. Neither figure is intended as a demonstration of the predictive capability of the constitutive model but simply as an assessment of correlation with existing data. The predictive capability of the constitutive theory has been adequately demonstrated relative to other alloys in earlier publications (refs. 2 and 6).

THE SHANLEY COLUMN

The column model adopted here is the sandwich idealization introduced by Shanley (ref. 13) and used by Kachanov (ref. 16) and others. The column geometry is indicated in figure 5. All of the deformation is presumed to occur in the slender bar elements 1 and 2 of length h and cross sectional area A/2. The remainder of the column of length L (L>>h) remains rigid. The width of the column, that is, the distance separating bars 1 and 2, is also taken as h.

The column is loaded by a time dependent load P(t) (shown positive); the lateral displacement of the load point at any time is denoted by u(t). The stress and total strain in bars 1 and 2 are denoted by σ_1, σ_2, and $e_1 = \delta_1/h$ and $e_2 = \delta_2/h$, respectively.

Equilibrium requires that

$$\sigma_2 + \sigma_1 = 2\sigma_0 \tag{6}$$

and

$$\sigma_2 - \sigma_1 = \frac{4\sigma_0 u}{h} \tag{7}$$

where $\sigma_0 = P/A$.

Differentiation with respect to time provides the rate form of the equilibrium equations,

$$\dot{\sigma}_2 + \dot{\sigma}_1 = 2\dot{\sigma}_0 \tag{8}$$

and

$$\dot{\sigma}_2 - \dot{\sigma}_1 = \frac{4u}{h}\dot{\sigma}_0 + 4\sigma_0\frac{\dot{u}}{h} \tag{9}$$

From geometric considerations (fig. 5) the compatibility condition is obtained as

$$\frac{\delta_1 - \delta_2}{h} = \frac{u - u_0}{L} \tag{10}$$

or

$$e_1 - e_2 = \frac{u - u_0}{L} \tag{11}$$

in which u_0 is the initial displacement (imperfection). The rate form of the compatibility relation is

$$\dot{e}_1 - \dot{e}_2 = \frac{\dot{u}}{L} \tag{12}$$

Decomposing the total strain rates in each bar into elastic and inelastic contributions gives

$$\dot{e}_1 = \frac{\dot{\sigma}_1}{E} + \dot{\varepsilon}_1^p \tag{13}$$

$$\dot{e}_2 = \frac{\dot{\sigma}_2}{E} + \dot{\varepsilon}_2^p \tag{14}$$

where E is the Young's modulus as specified in equation (5). The inelastic strain rates $\dot{\varepsilon}_1^p$ and $\dot{\varepsilon}_2^p$ are, of course, obtained by applying the inelastic constitutive equations (1) to (4) to each bar.

Combining the equilibrium equations (8) and (9), the compatibility equation (12), and the constitutive relationships (13) and (14) leads to

$$\dot{\sigma}_1\left(1 + \frac{4L}{Eh}\sigma_0\right) = \dot{\sigma}_0\left(1 + \frac{4L}{Eh}\sigma_0 - \frac{2u}{h}\right) - \frac{2L}{h}\sigma_0\left(\dot{\varepsilon}_1^p - \dot{\varepsilon}_2^p\right) \tag{15}$$

C-6

Under constant compressive stress (i.e., $\sigma_0 < 0$ and $\dot{\sigma}_0 = 0$), and in the absence of inelasticity ($\dot{\varepsilon}_1^p = \dot{\varepsilon}_2^p = 0$), equation (15) gives the Euler critical stress for the idealized column as

$$\sigma_c = \frac{Eh}{4L} \tag{16}$$

Further, calling

$$\rho = \frac{\sigma_0}{\sigma_c} \tag{17}$$

and

$$\eta = \frac{2u}{h} \tag{18}$$

where η is termed the nondimensional displacement, we have from equation (15)

$$\dot{\sigma}_1 = \frac{\dot{\sigma}_0}{1 + \rho} (1 + \rho - \eta) - \frac{\rho}{1 + \rho} \frac{E}{2} \left(\dot{\varepsilon}_1^p - \dot{\varepsilon}_2^p\right) \tag{19}$$

Now, from equation (6)

$$\dot{\sigma}_2 = 2\dot{\sigma}_0 - \dot{\sigma}_1 \tag{20}$$

and from equations (12), (13), (14), and (18)

$$\dot{\eta} = \frac{E}{2\sigma_c} \left(\frac{\dot{\sigma}_1}{E} + \dot{\varepsilon}_1^p - \frac{\dot{\sigma}_2}{E} - \dot{\varepsilon}_2^p\right) \tag{21}$$

The coupled system of equations (1), (2), (3), (19), (20), and (21) together with the appropriate initial conditions, including the initial imperfection $\eta_0 = \eta(0)$, allow the (nondimensional) displacement $\eta(t)$ to be calculated for a specified temperature T, Euler critical stress σ_c, and history of loading $\sigma_0(t)$. The results of several such calculations for various loading histories are presented in the following section.

RESULTS

All of the calculated results are isothermal with the temperature taken to be 811 K (1000 °F). The Euler critical stress σ_c is 200 MPa and the loading/unloading ramp rate $|\dot{\sigma}_0|$ is 96 MPa/sec. The governing system of equations was integrated using a self-adapting Adams-Bashforth predictor-corrector method with a fourth-order Runge-Kutta method as a starter. The calculations were performed in double precision on a Prime 850 computer with an upper error bound of 10^{-4}.

In all cases, the criterion defining the critical time to buckling t_c is taken as

$$\eta = \frac{2u}{h} = 1 \tag{22}$$

This is equivalent, under constant load, to the criterion

$$\sigma_1 = 0 \tag{23}$$

that is, the stress in bar element 1 becoming zero.

Behavior Under Constant Load

In all calculations the compressive load is first applied from zero, where the deforming elements are considered in a virgin state (i.e., $\alpha_1 = \alpha_2 \approx 0$), to a nominal value of the applied stress ($\sigma_0 = P/A$) of -35 MPa. Thus, with the Euler stress $\sigma_c = 200$ MPa the nominal value of the ratio ρ (eq. (17)) is

$$\rho = \frac{\sigma_0}{\sigma_c} = \frac{-35}{200} = -0.175 \tag{24}$$

In this section we present the calculated results for a constant load ρ held at the above value. Figure 6 shows a response $\eta(\tau)$ under these conditions for four different values of initial (nondimensional) displacement η_0 = 0.02, 0.05, 0.10, and 0.2. The time $\tau = t/t_0$ in figure 6 is nondimensional, being normalized with respect to the critical time corresponding to $\eta_0 = 0.02$; that is, $t_0 \approx 6$ hr.

Figure 6 shows that the critical time to buckling is reduced by a factor of almost 8 with an order of magnitude increase in the initial displacement.

For the sake of comparison, all subsequent calculations are taken to have the initial imperfection $\eta_0 = 0.02$ and are presented in terms of the nondimensional time $\tau = t/t_0$.

Behavior Under Variable Load

We first consider the effect of rapid load reductions and reversals superimposed on the constant load $\sigma_0 = -35$ MPa ($\rho = -0.175$). As shown in the inserts of figure 7, load interruptions occur at time intervals of $\tau_0 = 0.15$ with varying amplitude. These include reductions (in the tensile direction) of σ_0 to -20 MPa and to 0 MPa (insert (a)), to +20 MPa (insert (b)), and a complete reversal to +35 MPa (insert (c)). The calculated effects of these histories on the creep-buckling response $\eta(\tau)$ are shown in the respective curves (a), (b), and (c) of figure 7.

Curve (a) corresponds to the loading histories indicated in insert (a); reductions to -20 and 0 MPa. The response curve for each is identical to that of figure 6 for the same initial displacement 0.02, thereby indicating that no change in the buckling response has occurred. Response curve (b) corresponds to insert (b) in which there is a load reversal to $\sigma_0 = +20$ MPa. Here, we begin to see a measurable change in the calculated creep-buckling response, the critical time having diminished from the constant load case by about 10 percent. Finally, in curve (c) we observe a reduction of more than 30 percent in the time to buckling. This corresponds to the history of insert (c) where a complete load reversal from $\sigma_0 = -35$ MPa to $\sigma_0 = +35$ MPa occurs at each load interruption. Immediately following each reversal, we see evidence of the reappearance of primary creep. This is attributed to the presence of dynamic recovery (fig. 1) where creep (or relaxation) is observed to be accelerated with stress reversals — even in the absence of significant reversed inelastic strain. Although, to the knowledge of the authors, these effects have not been observed directly in creep-buckling phenomena, it is expected that such effects can occur, on the basis of the experimental observations illustrated schematically in figure 1.

The influence of dynamic recovery is best understood by considering the state space (σ,α) of figure 8. Note that in figure 8 and all subsequent representations of the state space, compressive σ and α are shown as positive and are plotted upward and to the right, respectively. Hereafter, the relevant quadrants of the state space will be referred to as the first $(\sigma\alpha > 0)$ and the fourth $(\sigma\alpha < 0)$. In figure 8 the trajectory of the state point (σ_2, α_2) for bar element 2 is shown corresponding to the constant load response curve (a) in figure 6. The segment OA traces the path of the state point during initial load-up to $\sigma_0 = -35$ MPa. Some inelasticity is indicated over path OA by the increase in the inelastic state variable α_2. As σ_0 is held constant, bar 2 creeps under nearly constant stress, and the state point moves toward B. As the geometric nonlinearity becomes prevalent, the stress in bar 2 increases (as that in bar 1 decreases), and the state point moves toward C. Point C corresponds to the buckled condition $\eta = 1$ in figure 6 (curve (a)).

Similarly, figure 9 shows the trajectory of the state point for the loading histories illustrated in insert (a) of figure 7; load reductions to $\sigma_0 = -20$ MPa and to $\sigma_0 = 0$. Here, we see the effect of the abrupt load changes as vertical (elastic) trajectories in the state space, resulting in no overall change in the state path OABC from that just considered for a constant load. This, of course, results in the same creep-buckling response observed earlier for the constant load.

The state path of figure 10 relates to the loading history of insert (b) in figure 7. Here, we begin to see evidence of state recovery. The load variations now produce stress reversals in bar 2 and the state point trajectories are not simply vertical (elastic) lines as before, but now follow curved paths as the state point penetrates into the fourth quadrant $(\sigma\alpha < 0)$ corresponding to a reversal of stress. The state recovers with the stress reversal, resulting in a relatively softer state (smaller α_2) upon reloading. Correspondingly, the creep rate is increased in response to each load cycle. Evidence of increased creep rate following reloading is apparent in curve (b) (fig. 7).

Load histories involving larger stress reversals produce increased state recovery. Figure 11 shows the state path in bar 2 for the fully reversed load depicted in insert (c) (fig. 7). In figure 11, the effect of dynamic recovery at each unloading/reloading cycle returns the state point well back into the primary creep regime. As observed earlier, clear evidence of the rejuvenation of primary creep after each loading cycle is seen in curve (c), with the total effect of diminishing the critical buckling time by about 30 percent.

Since the period of application of the rapid loading cycles ($\tau_0 = 0.15$) was chosen quite arbitrarily, we now investigate the effect of the frequency of load cycles. Figure 12 shows the buckling response curves $\eta(\tau)$ for load histories involving a full reversal; that is, $\sigma_0 = -35$ to +35 MPa (as in insert (c) fig. 7), with periods τ_0, $\tau_0/2$, $\tau_0/4$, and $\tau_0/8$. (The constant load response curve is also shown for reference.) We see the pronounced effect of more frequent (shorter period) stress reversals. Reversals with period $\tau_0/8$ reduce the time to buckling by more than a factor of 3.

Next, we examine the influence of load reductions of extended duration on the creep-buckling time. The loading histories considered are shown in the inserts of figure 13. Case a (i.e., insert (a) and response curve (a)) is equivalent to one of those considered previously (insert (a) of figure 7), where the time duration at the reduced load $\sigma_0 = 0$ is effectively zero. This history produces no change in the buckling response over the constant load case.

Insert (b) depicts the history where the load, having been applied for period τ_0, is abruptly removed (at a rate $|\dot{\sigma}_0| = 96$ MPa/sec) and held at zero for a period τ_1; a time comparable to the actual critical time ($\tau_0 = 6$ hr) of the column under constant load. The sequence is then repeated. This history reduces the critical time as shown in curve (b) by about 15 percent. Here, the time τ includes only that time in which the load $\sigma_0 = -35$ MPa is applied.

This behavior is best visualized in the state space (σ_2, α_2), figure 14. State recovery is observed as, in time, the state point moves at zero stress toward smaller α_2; for example, on the first load reduction from point D to E. Reloading returns the state point to a softer state than before the load reduction and, correspondingly, to a higher creep rate. Repetition of the sequence thus causes acceleration of the creep-buckling process.

Insert (c) of figure 13 shows a loading history in which the time at zero stress is now increased a hundredfold to $100\tau_1$. The corresponding response curve (c) shows a further decrease in the critical time, about 30 percent. The related state point trajectory shown in figure 15 is qualitatively similar to that of figure 14 but now shows significantly increased recovery with the hundredfold increase in hold time at the reduced stress.

Comparison With Predictions by Norton Law

In this section we compare the results presented with those for identical loading histories based on a classical creep law of the Norton-Bailey type; that is,

$$\dot{\epsilon}^p = B\sigma^N \mathrm{sgn}(\sigma) \tag{25}$$

A roughly equivalent representation was obtained by calculating the steady state creep rates for various stress levels using equations (1) to (4) and fitting equation (25) to these "data" by choosing optimal values of B and N in a least squares sense. This process yielded the following:

$$B = 2.03\mathrm{x}10^{-19}$$

$$N = 9.375$$

which are consistent with units of σ in MPa and $\dot{\epsilon}^p$ in hr^{-1}. By using equation (25), the critical time to buckling (corresponding to the constant load case of curve (a) figure 6) turned out to be $t_0' = 7.8$ hr; slightly greater than the earlier reference $t_0' = 6$ hr. Thus, in the calculated results presented here (fig. 16), the nondimensional time τ is obtained by normalization with respect to t_0'. The time plotted is that for which the load $\sigma_0 = -35$ MPa is applied. On this basis, calculations of creep-buckling response $\eta(\tau)$ for all of the loading histories presented earlier have been included in figure 16. As expected, the time to buckling is completely unaffected by any of the variable loading histories. This is because the classical Norton-Bailey representation (eq. (25)) fails to account for state recovery in any form.

DISCUSSION

Dynamic recovery, as illustrated in figure 1 and by the state point trajectories of figures 10 and 11, is characterized in the present constitutive model through the dual analytical forms of the evolutionary law (eqs. 2)). This description is consistent with the viewpoint of Onat (ref. 17) in representing inelastic behavior through the specification of analytically different mathematical forms corresponding to various regions of the state space. Here, different analytical forms are specified depending on whether the state point lies in the first (third) quadrant $\sigma\alpha > 0$ or the fourth (second) quadrant $\sigma\alpha < 0$ of the state space. In effect, this permits the state point to recover rapidly upon reversing the stress, even in the absence of significant reversed inelastic strain (fig. 1). This formulation is intended as an idealization of a physical process wherein the dislocation structure (or the associated structure of internal stress) is abruptly altered with a reversal of the applied stress, because previously immobilized dislocations are remobilized on their slip planes (ref. 18). Since the inelastic state variable α is taken as an averaged, phenomenological measure of the dislocation microstructure (or its associated internal stress state), it too should reflect a rapid change as the stress is reversed.

The specific functional form of the first of equations (2) is formulated in accordance with the experimental results of Mitra and McLean (ref. 19). The second of equations (2) can be considered an analytical continuation of the first equation, evaluated at α_0 (small α) in the first quadrant of the state space, into the second quadrant; or with symmetrical response in tension and compression, at $-\alpha_0$ in the third quadrant into the fourth quadrant.

This amounts to a highly idealized representation of the underlying physical process, but captures, nevertheless, the essential feature - that abrupt microstructural rearrangements occur with stress reversals.

The path of the state point in the fourth quadrant $\sigma\alpha < 0$ in figures 11 and 12, and, thus the extent of recovery, depend on the total strain rate and, critically, on the parameter α_0. Ideally, α_0, or, more comprehensively, a function of σ and α replacing it, should be determined from experiments in which the recovery of creep rate or flow stress under stress reversals is measured directly; and not inferred indirectly from available monotonic tensile, creep and/or relaxation data as was done here. The present representation, however, is believed to be adequate, and consistent with the objective of demonstrating the strong influence of state recovery in creep buckling. A more comprehensive description of dynamic recovery, in the same spirit as that described, and the relevant experimentation are topics of continuing research.

Thermal recovery, as depicted in figure 2 and in the state paths shown in figures 14 and 15, is manifest in the second (negative) term of the Bailey-Orowan evolutionary equations (2). In the applications considered, the state point recovers, in time, under constant (zero) reduced stress, giving rise to an increased creep rate on reapplication of stress (fig. 2). Physically, this macroscopic behavior is associated with thermally activated, diffusion controlled, microscopic processes such as climb of edge dislocations; which allow dislocations, in time, to bypass immobilizing obstacles, thus producing a softer state (smaller α). The important material parameters in equations (2) are R, m, and β. Ideally, these parameters are determined from both creep data and information obtained from stress or strain transient dip tests (ref. 6) that provide a direct measurement of thermal recovery. Again, as these data were not readily available for the alloy Narloy-Z, the pertinent parameters were inferred indirectly from available data. This approach although not optimal, is considered consistent with the present objectives.

CONCLUSIONS

We have examined the creep-buckling response of an idealized (Shanley) column under some special variable loadings. The two types of loading considered amount to superpositions of the following load sequences on a constant applied load: (1) rapid cyclic unloading/reloading sequences involving stress reversals, and (2) cyclic loading that includes intermittent reductions of load for extended periods of time (at elevated temperature).

Although the sandwich column model used is highly idealized, the constitutive model is quite comprehensive in that it incorporates a representation of dynamic and thermal (state) recovery. There is substantial experimental evidence that many structural alloys embody internal mechanisms at elevated temperature that allow inelastic strain rates to increase (recover) following periods of hardening. In particular, this is believed to be true for the representative copper alloy Narloy-Z characterized here.

The loading sequences examined are not intended to represent prototypical loading histories for any particular structural component; instead, they were chosen to best illustrate the generic influence of both dynamic and thermal recovery on structural behavior in the presence of a creep induced instability.

We expect that qualitatively similar behavior will accompany more realistic variable loading conditions (and more realistic structures), and that neglect of state recovery effects in such cases will lead, similarly, to nonconservative predictions of the critical time to creep buckling.

The following conclusions can be drawn from this study:

1. State recovery (dynamic and thermal) can have a significant effect on creep-buckling behavior, that is, on the critical time.

2. Failure to account for state recovery in the constitutive equations can lead to nonconservative predictions of the critical buckling time under variable loading.

3. A classical Norton-Bailey type creep law, commonly used in creep-buckling analyses, does not account for state recovery and, therefore, may significantly over predict the time to creep buckling under variable loading.

4. It is important that constitutive models (which are to be used in creep-buckling analyses involving variable loading) allow for recovery effects, and furthermore, that the characterization tests used for determining the pertinent material parameters include direct measurements of state recovery.

REFERENCES

1. Pugh, C.E.; and Robinson, D.N : Modified Auxiliary Procedures for Cyclic Creep and Relaxation. ORNL-5281, 1976, pp. 17-40.

2. Robinson, D.N.; Pugh, C.E.; and Corum, J.M.: Constitutive Equations for Describing High-Temperature Inelastic Behavior of Structural Alloys. Proceedings of Specialist Meeting on High-Temperature Structural Design Technology of LMFBRs, IAEA Report IWGFR/11, Apr. 1976, pp. 44-57. (CONF-760451-2).

3. Sartory, W.K.: Analysis of the ORNL Two-Bar Thermal Ratcheting Test SBRI. ORNL-5683, 1980, pp. 9-13.

4. Robinson, D.N.: Additions and Modifications to Constitutive Equations in RDT Standard F9-5T. ORNL-5622, 1979, pp. 2-11.

5. Kubo, S.: Effects of Creep Recovery and Hardening on the Stress and Strain-Rate Fields Near a Crack Tip in Creeping Materials. Elastic-Plastic Fracture: Second Symposium, Vol. 1 - Inelastic Crack Analysis, ASTM STP-803, ASTM, 1983, pp. I-594 to I-614.

6. Robinson, D.N.; and Swindeman, R.W.: Unified Creep/Plasticity Constitutive Equations for 2 1/4 Cr-1 Mo Steel at Elevated Temperature. ORNL TM-8444, 1982.

7. Hoff, N.J.: A Survey of the Theories of Creep Buckling. Proceedings of the Third U.S. National Congress of Applied Mechanics, R.M. Haythornthwaite, ed., ASME, 1958, pp. 29-49.

8. Hayman, B.: Some Observations on Creep Buckling Analysis. Preprints, 2nd International Conference on Structural Mechanics in Reactor Technology, T.A. Jaeger, ed., Vol. 5, Part. L, Berlin, 1973, pp. 1-12.

9. Hoff, N.J.: Rules and Methods of Stress and Stability Calculations in the Presence of Creep. J. Appl. Mech., vol. 45, no. 3, Sept. 1978, pp. 669-675.

10. Libove, C.: Creep Buckling of Columns. J. Aeronaut. Sci., vol. 19, no. 7, July 1952, pp. 459-467.

11. Jahsman, W.E.: Creep Stability of a Column with Coupled Geometric Imperfection and Material Behavior Effects. Creep in Structures, J. Hult, ed., Springer-Verlag, 1970, pp. 360-369.

12. Hoff, N.J.; and Levi, I.M.: Short Cuts in Creep Buckling Analysis. Int. J. Solids Struct., vol. 8, no. 9, 1972, pp. 1103-1114.

13. Shanley, F.R.: Weight-Strength Analysis of Aircraft Structures. Dover, 1960.

14. Esposito, J.J.; and Zabora, R.F.: Thrust Chamber Life Prediction, Vol. I - Mechanical and Physical Properties of High Performance Rocket Nozzle Materials. (D180-18673-1-VOL-1, Boeing Aerospace; NASA Contract NAS3-17838) NASA CR-134806, 1975.

15. Conway, J.B.; Stentz, R.H.; and Berling, J.T.: High-Temperature, Low-Cycle Fatigue of Copper-Base Alloys for Rocket Nozzles: Part I - Data Summary for Materials Tested in Prior Programs. (MTI-003-3-1-PT-1, Mar-Test Inc.; NASA Contract NAS3-19720) NASA CR-134908, 1975.

16. Kachanov, L.M. (Transl., E. Bishop): Theory of Creep (Teoriya Polzuchesti). Boston Spa, England, 1967.

17. Onat, E.T.: Representation of Inelastic Behavior. Creep and Fracture of Engineering Materials and Structures, B. Wilshire and D.R.J. Owen, eds., Pineridge Press, Swansea, U.K., 1981, pp. 587-602.

18. Orowan, E.: Causes and Effects of Internal Stresses. Internal Stresses and Fatigue in Metals, G.M. Rassweiler and W.L. Grube, eds., Elsevier, 1959, pp. 59-80.

19. Mitra, S.K.; and McLean D.: Work Hardening and Recovery in Creep. Proc. Roy. Soc. London Ser. A, vol. 295, no. 1442, Dec. 6, 1966, pp. 288-299.

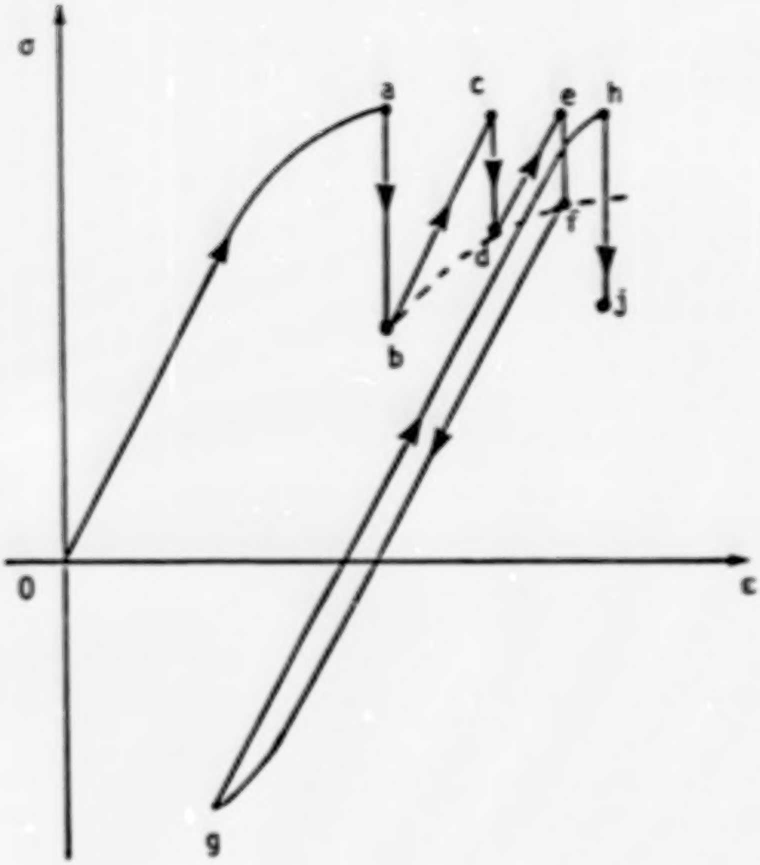

Figure 1. - Schematic representation of dynamic recovery. In the absence of stress reversals, the stress relaxations over a fixed time ab, cd, and ef show successive hardening. After the stress reversal fgh, stress relaxation hj shows evidence of (creep) softening, that is, evidence of recovery of state (ref. 1).

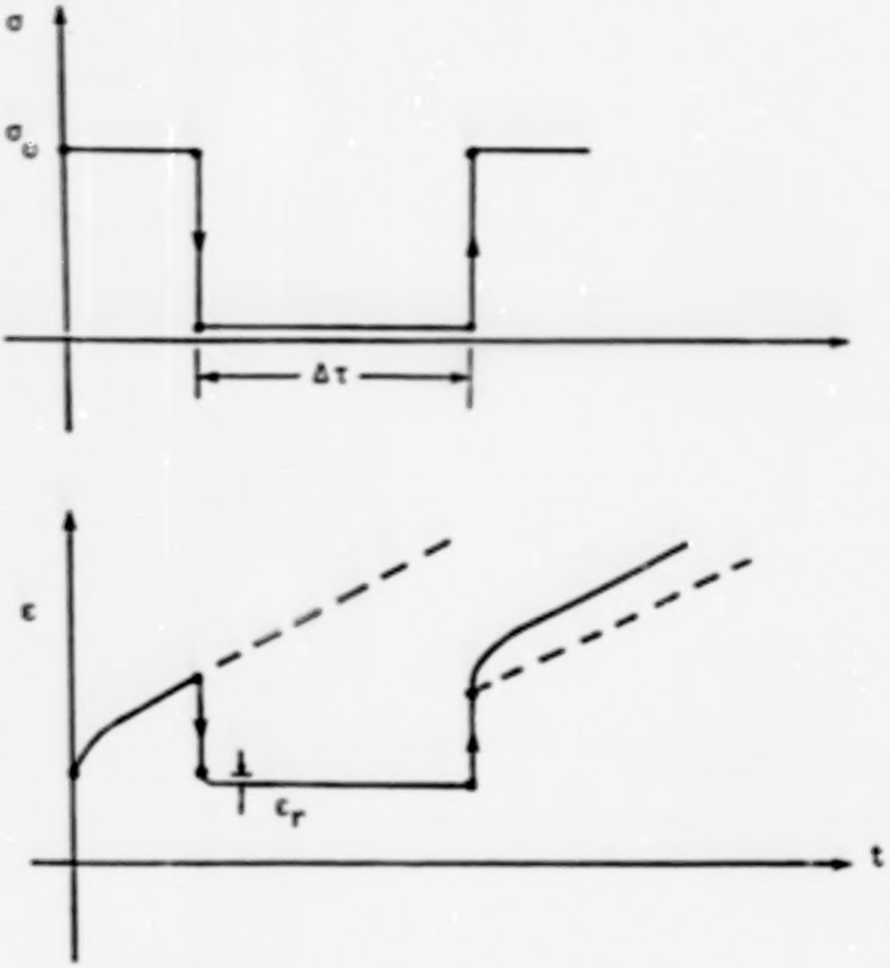

Figure 2. - Schematic representation of thermal recovery. Response in an interrupted creep test typically exhibits relatively small strain recovery ε_r but measurable softening (depending on the interval Δτ) following a stress reduction, that is, recovery of state (ref. 2).

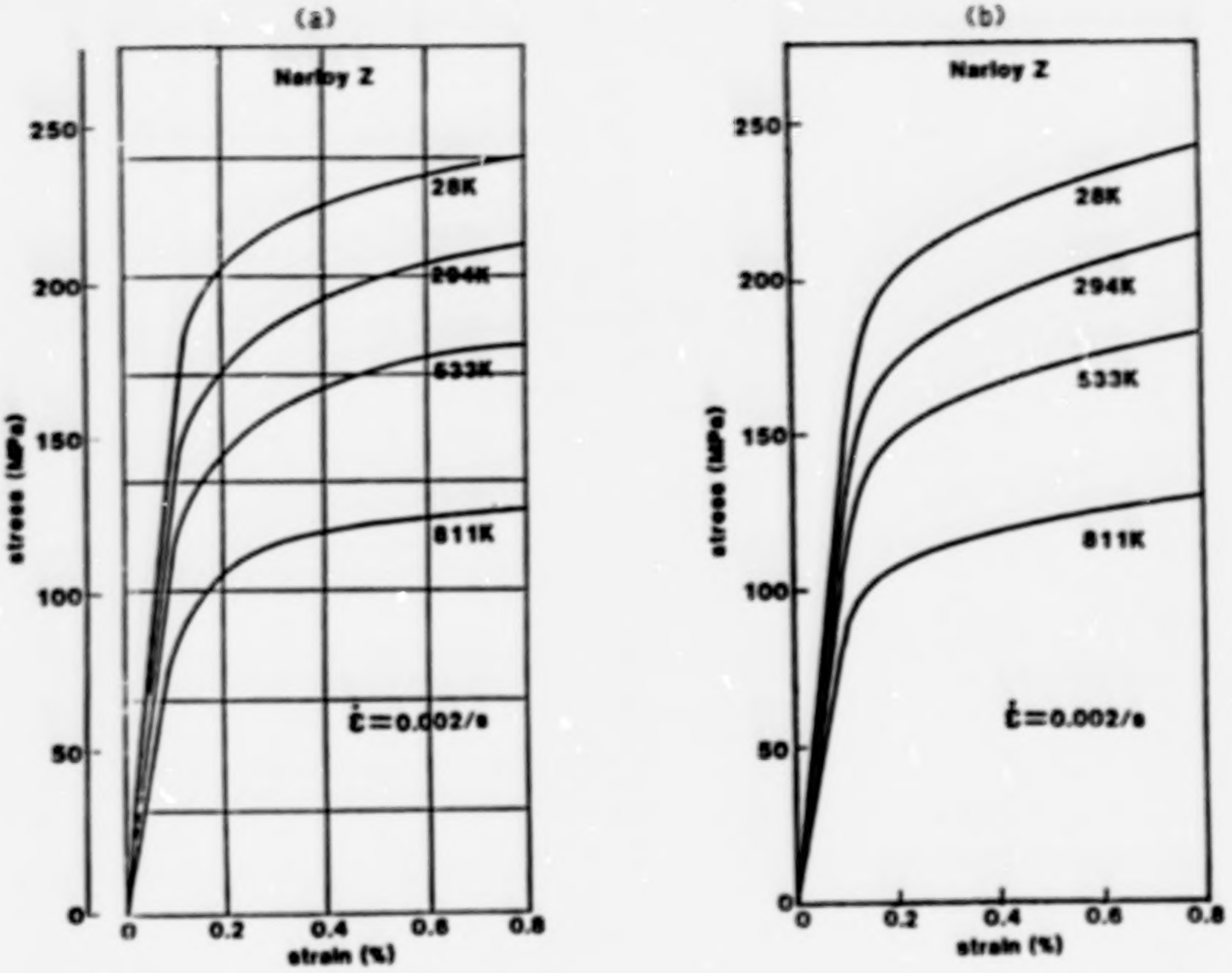

Figure 3. - Comparison of (a) tensile data (ref. 14) and (b) predictions for Narloy-Z at various temperatures. Strain rate is 0.002/sec.

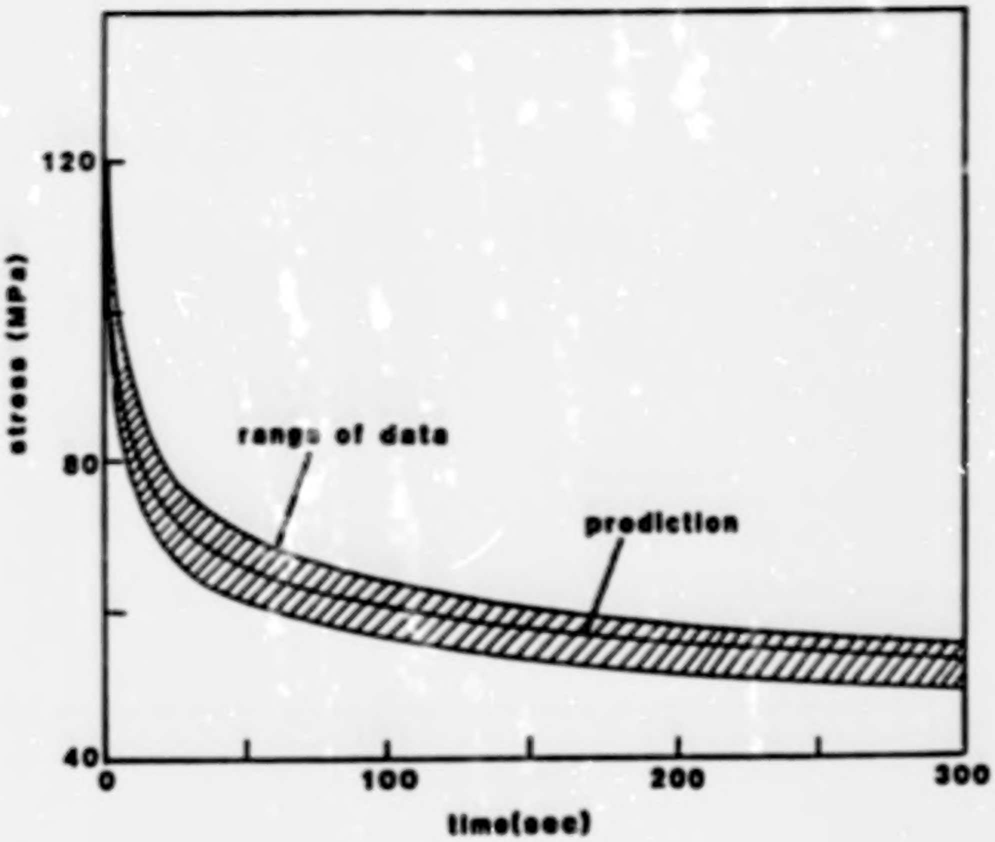

Figure 4. - Comparison of stress relaxation data (ref. 15) and a prediction for Narloy-Z at 811 K (1000 °F). Crosshatched region indicates range of three tests. Starting stress is 120 MPa.

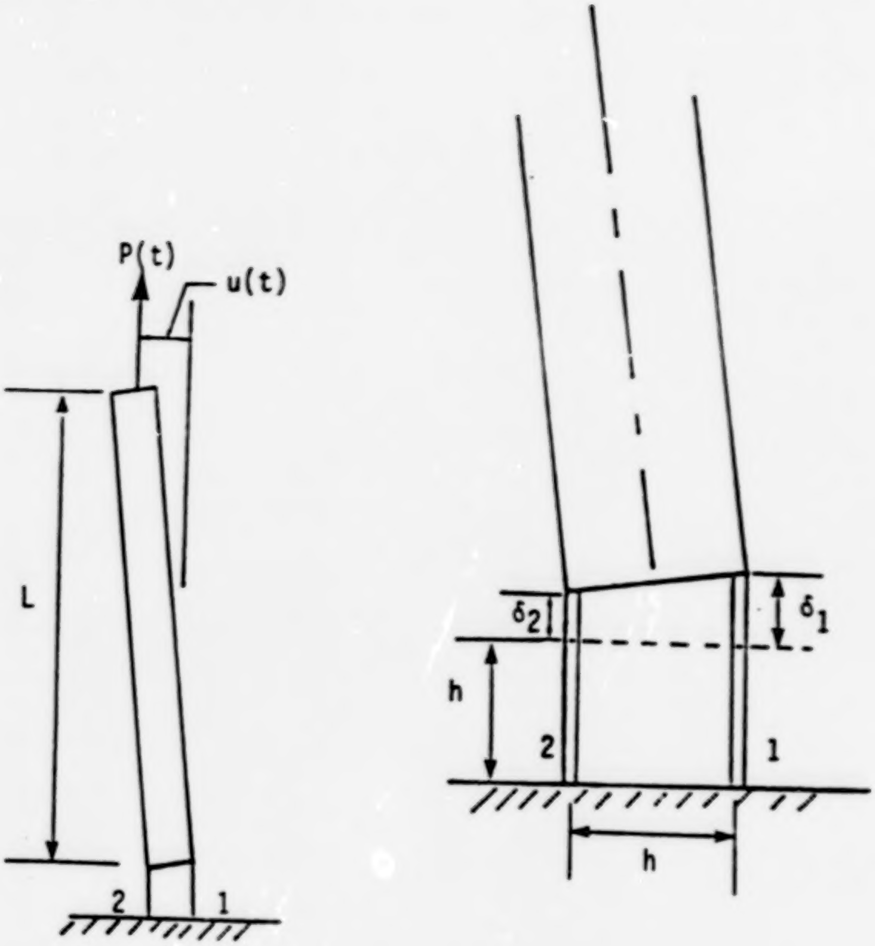
P(t)
u(t)
L
2
1
δ2
δ1
h
2
1
h

Figure 5. - Geometry of the Shanley sandwich column.

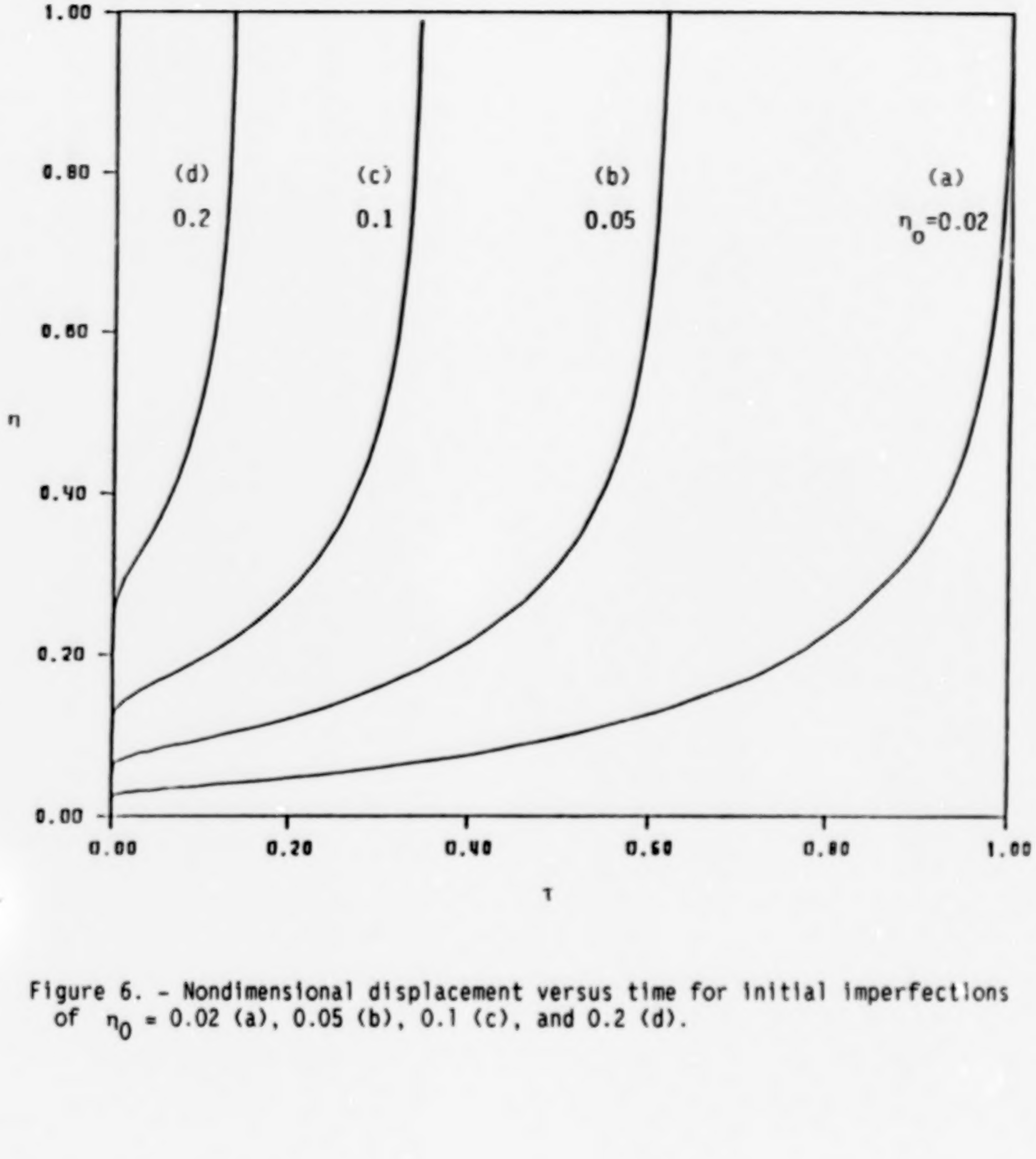

Figure 6. - Nondimensional displacement versus time for initial imperfections of η_0 = 0.02 (a), 0.05 (b), 0.1 (c), and 0.2 (d).

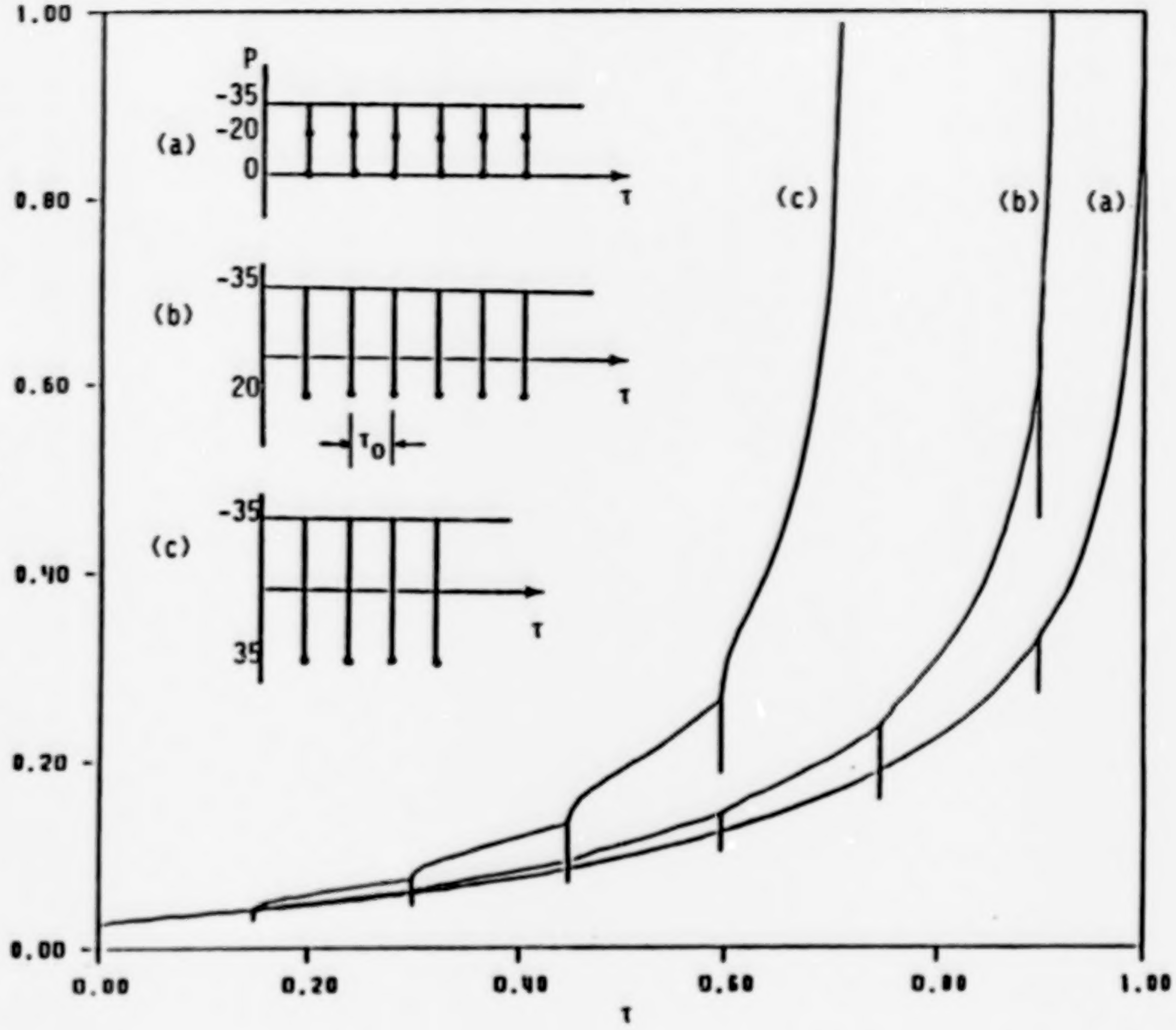

Figure 7. - Nondimensional displacement versus time for loading histories depicted in inserts (a), (b), and (c).

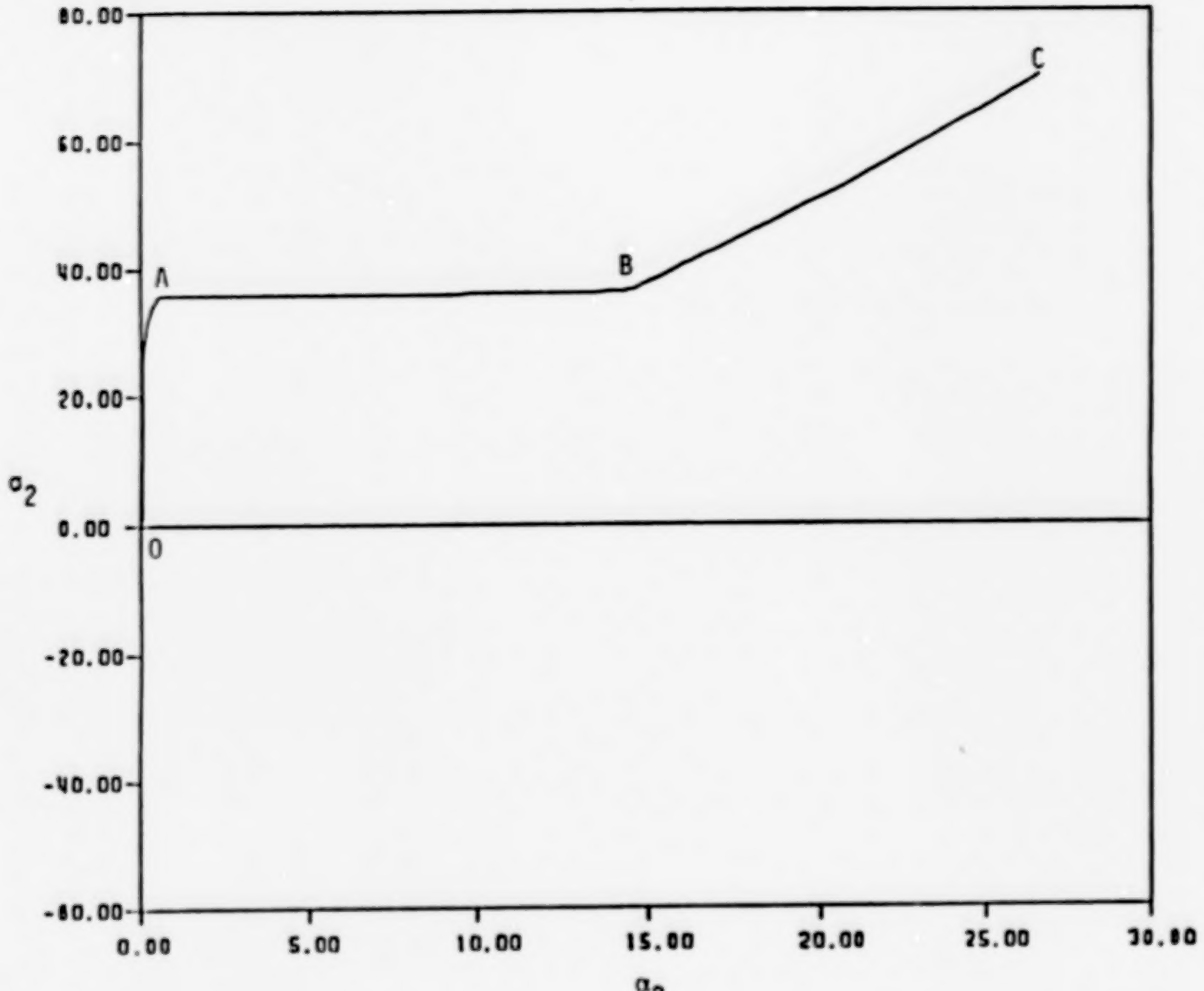

Figure 8. - State space for bar 2 showing state path for constant load (curve (a), fig. 6). Units MPa.

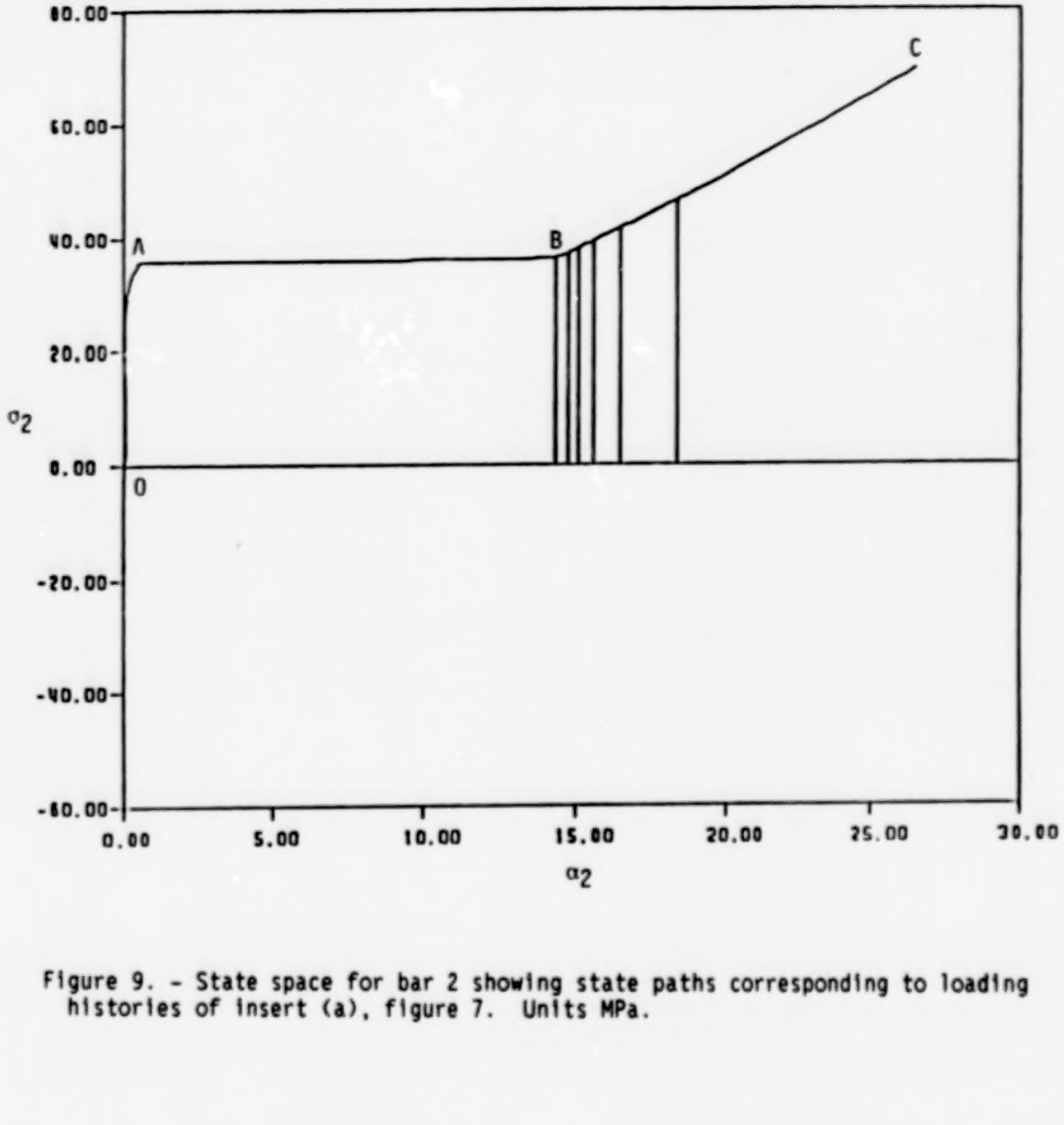

Figure 9. - State space for bar 2 showing state paths corresponding to loading histories of insert (a), figure 7. Units MPa.

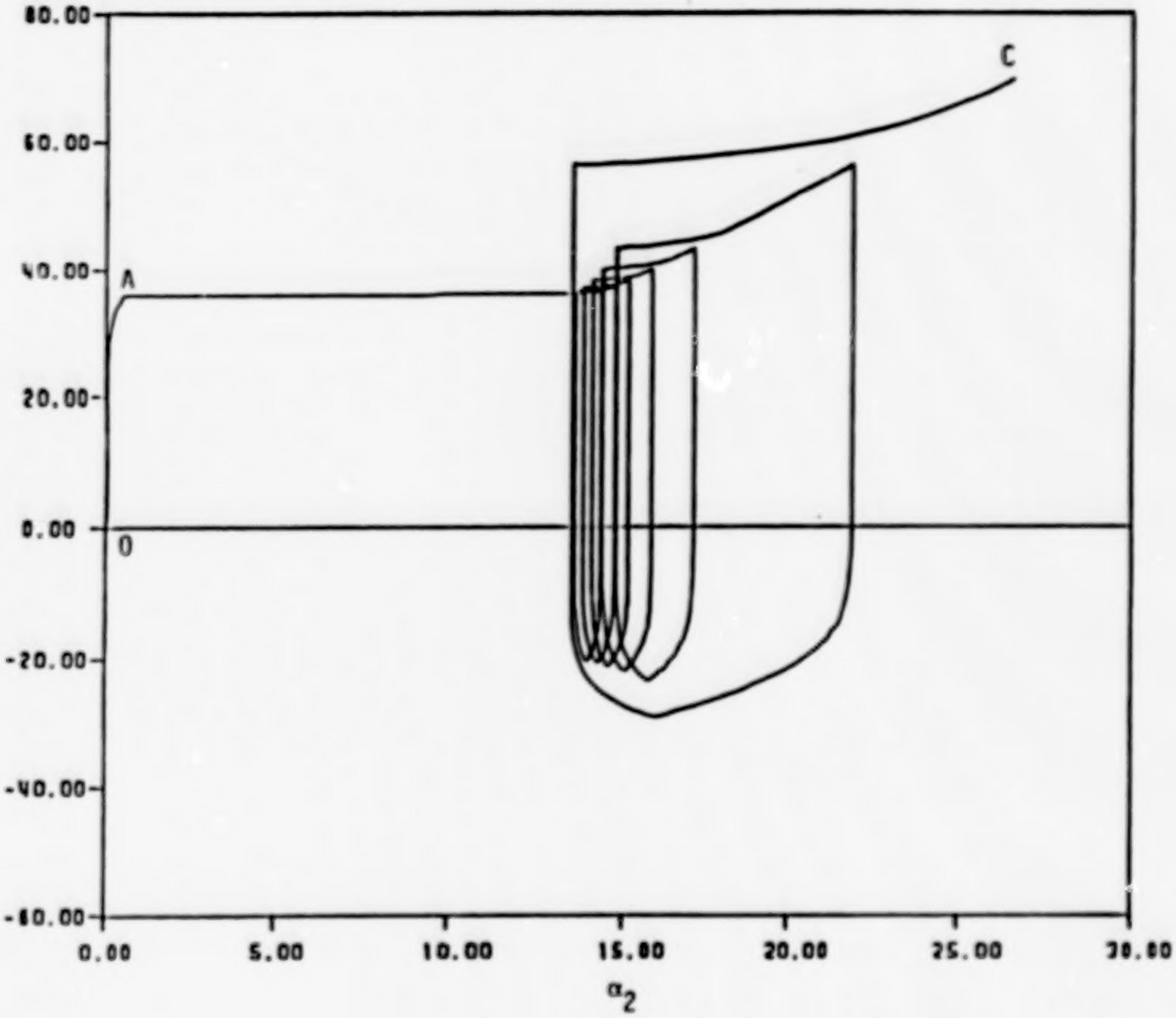

Figure 10. - State space for bar 2 showing state path corresponding to loading history of insert (b), figure 7. Units MPa.

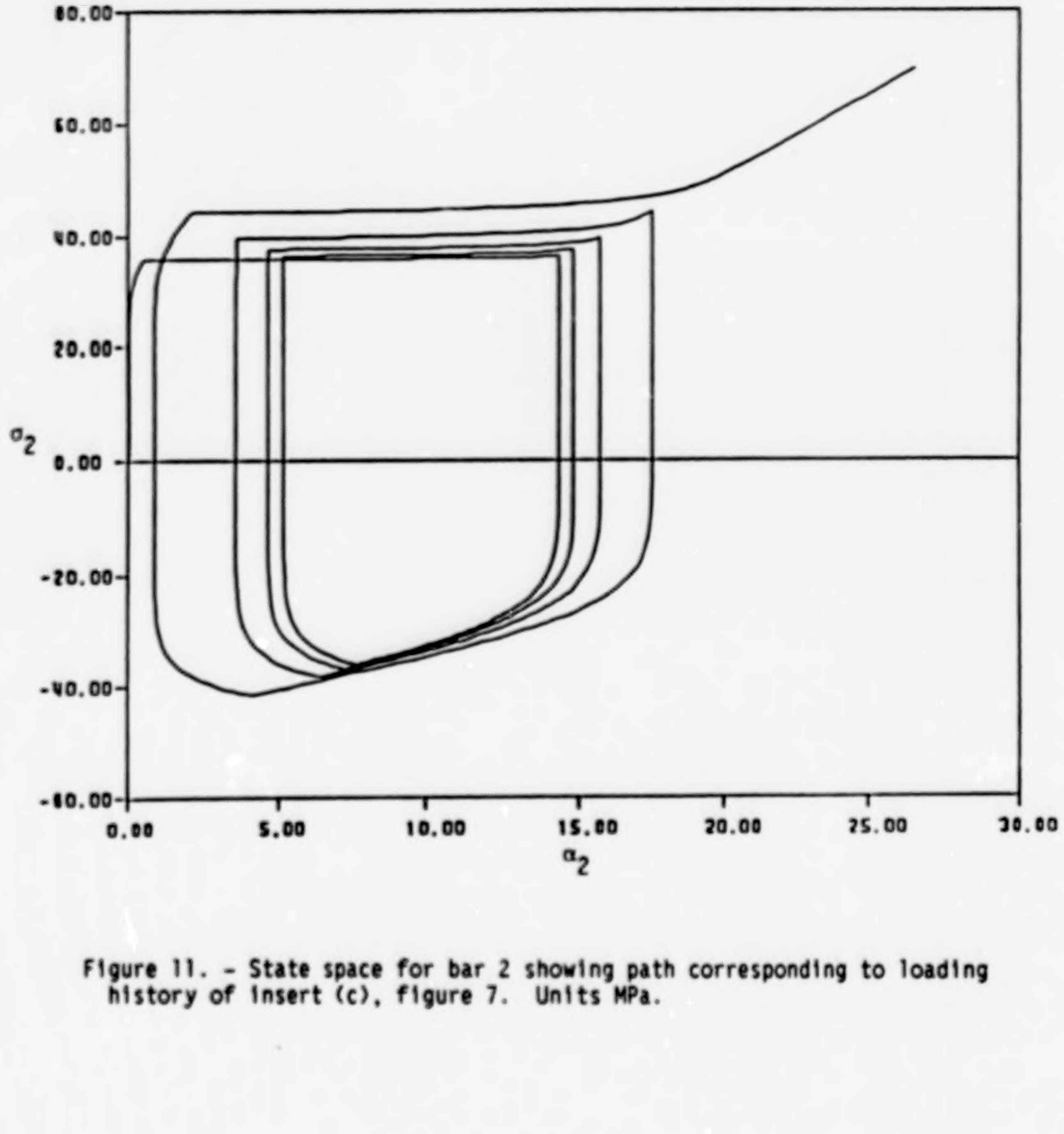

Figure 11. - State space for bar 2 showing path corresponding to loading history of insert (c), figure 7. Units MPa.

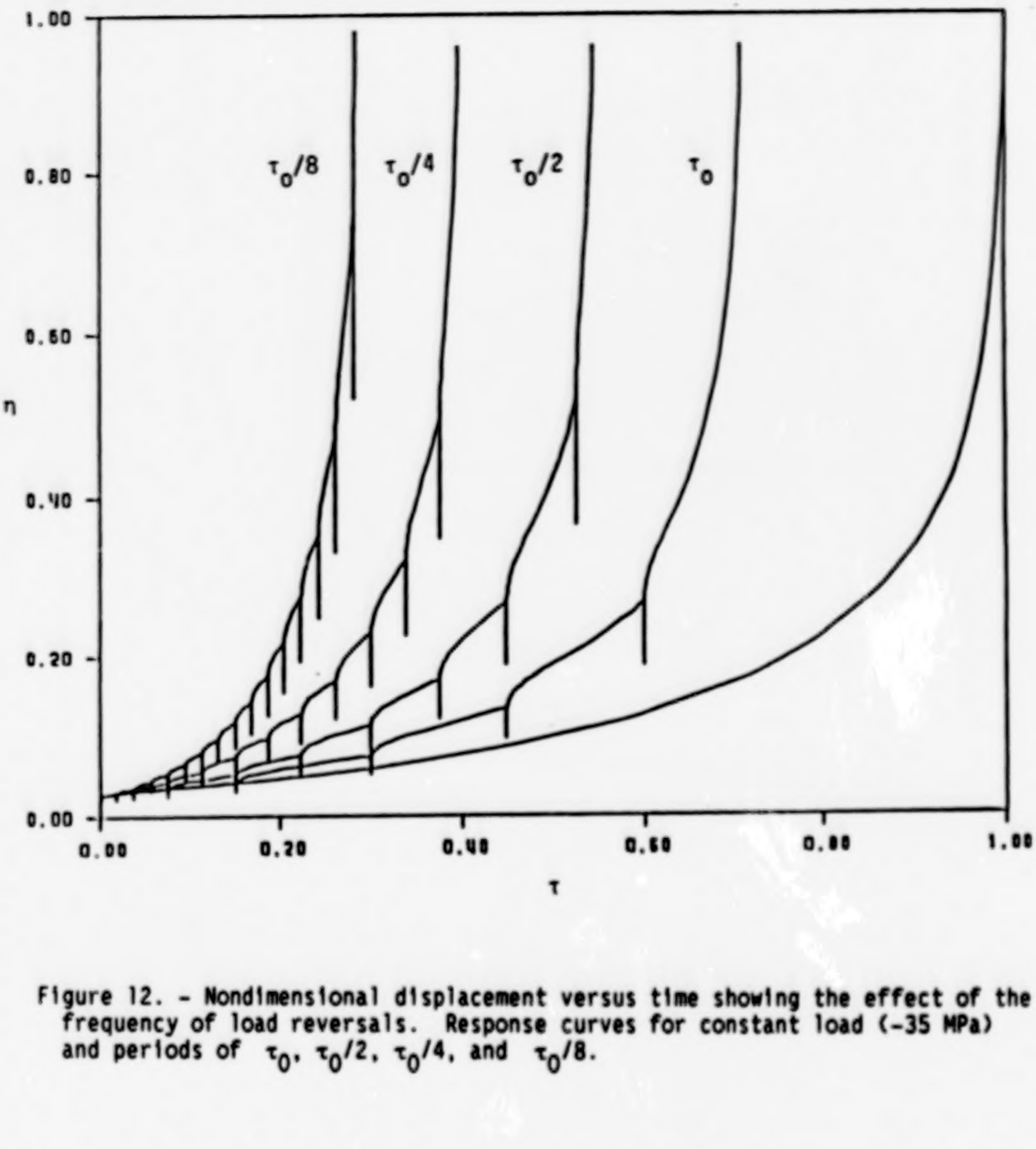

Figure 12. - Nondimensional displacement versus time showing the effect of the frequency of load reversals. Response curves for constant load (-35 MPa) and periods of τ_0, $\tau_0/2$, $\tau_0/4$, and $\tau_0/8$.

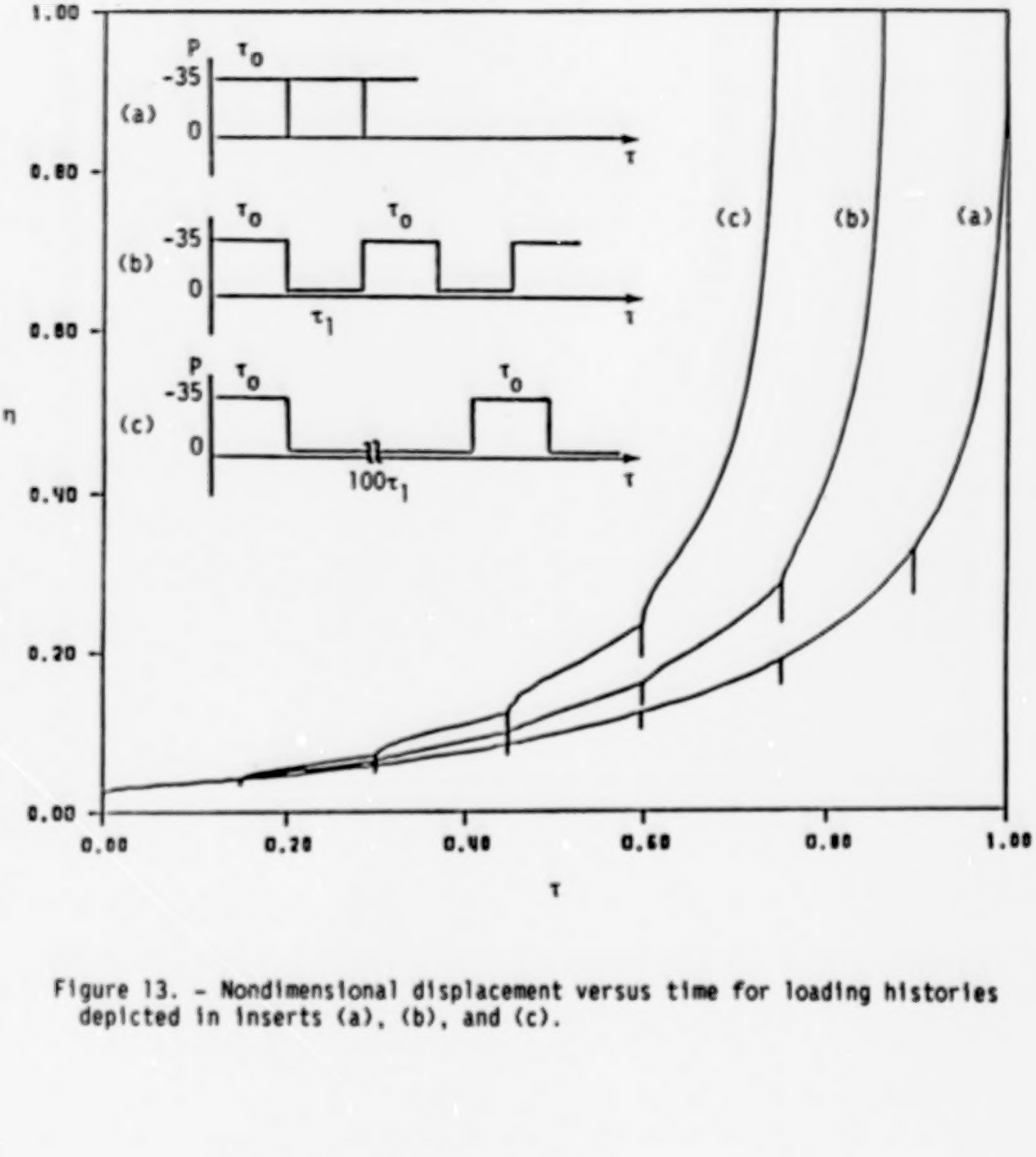

Figure 13. - Nondimensional displacement versus time for loading histories depicted in inserts (a), (b), and (c).

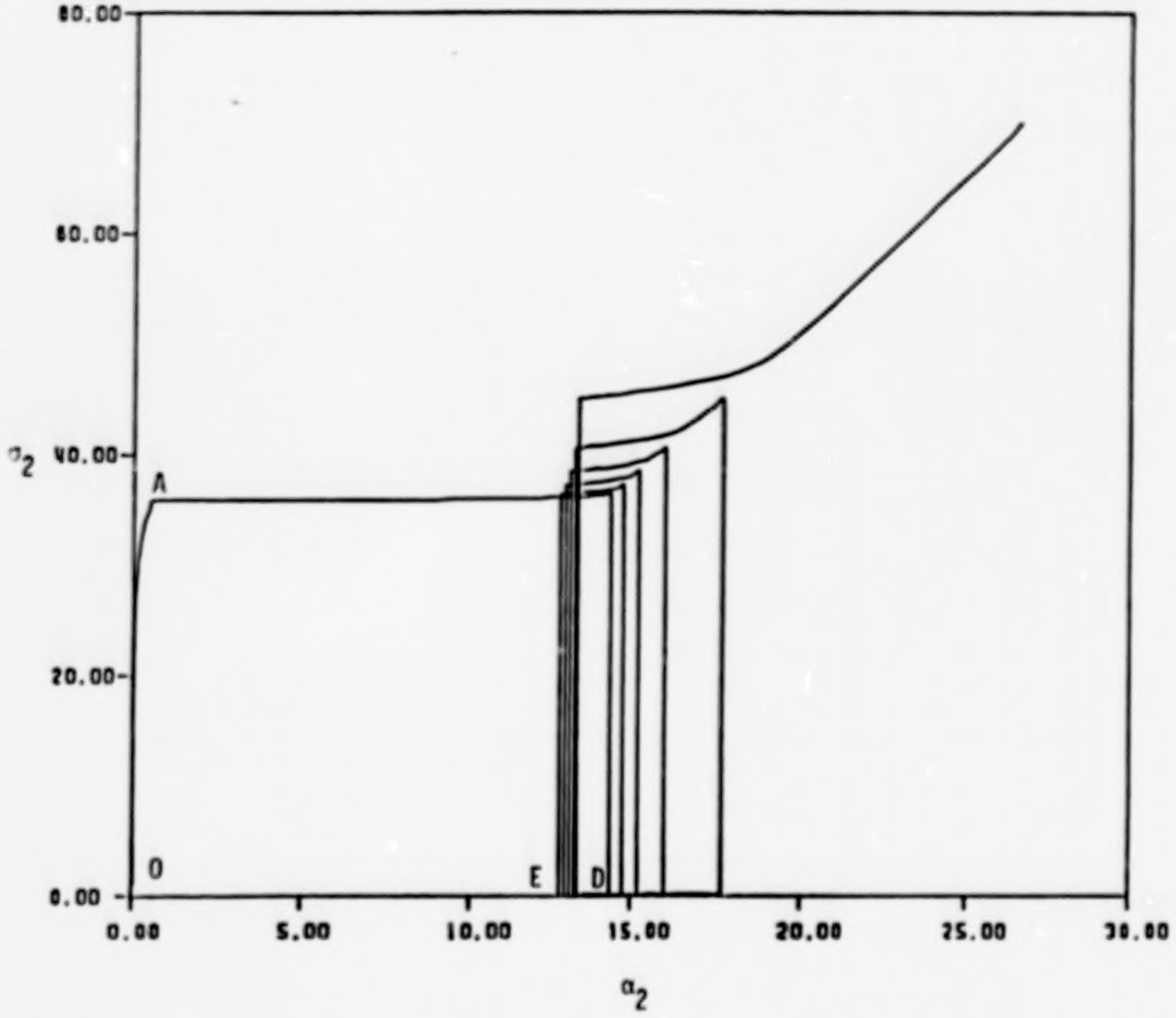

Figure 14. - State space for bar 2 showing state path corresponding to insert (b), figure 13. Units MPa.

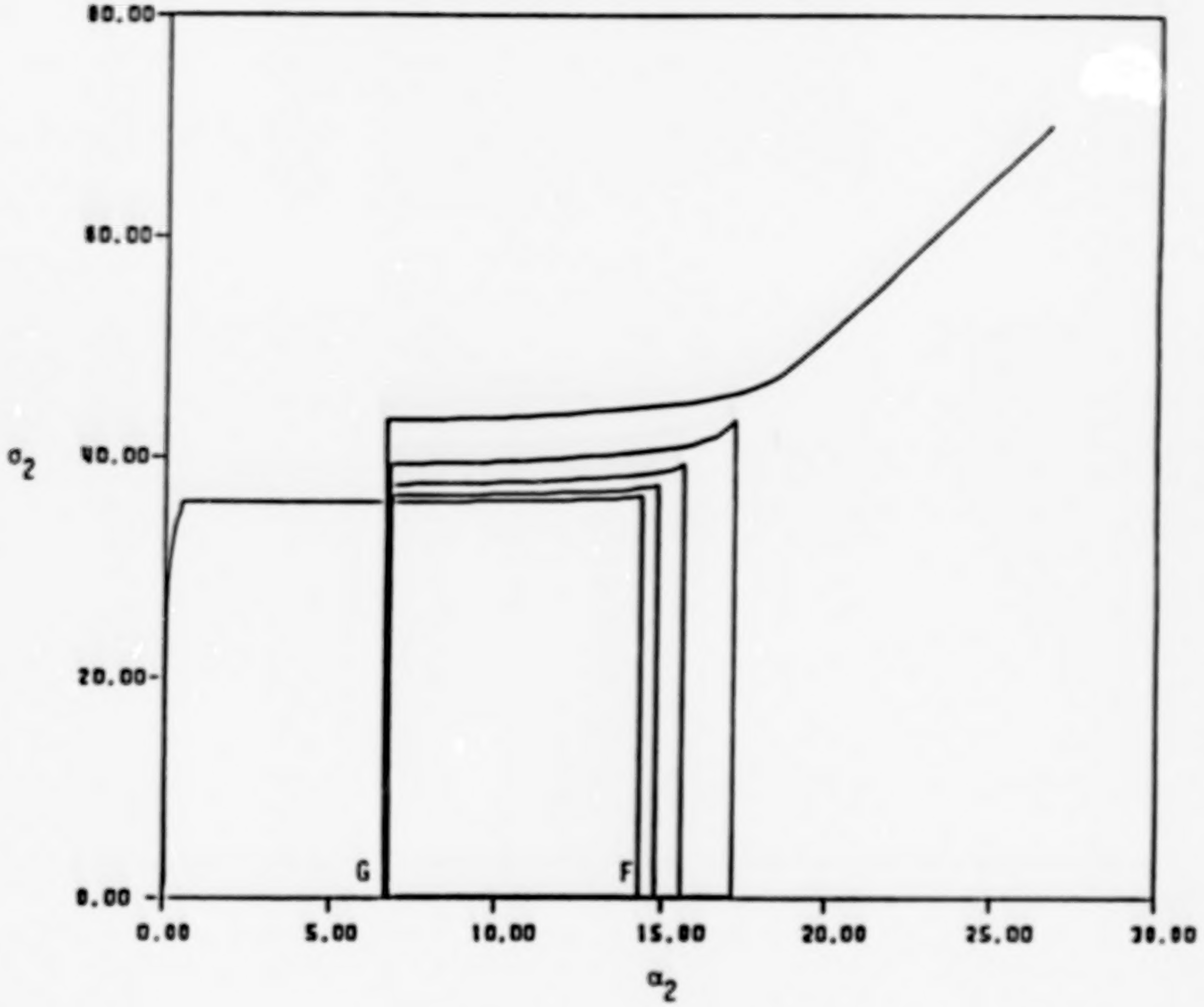

Figure 15. - State space for bar 2 showing state path corresponding to insert (c), figure 13. Units MPa.

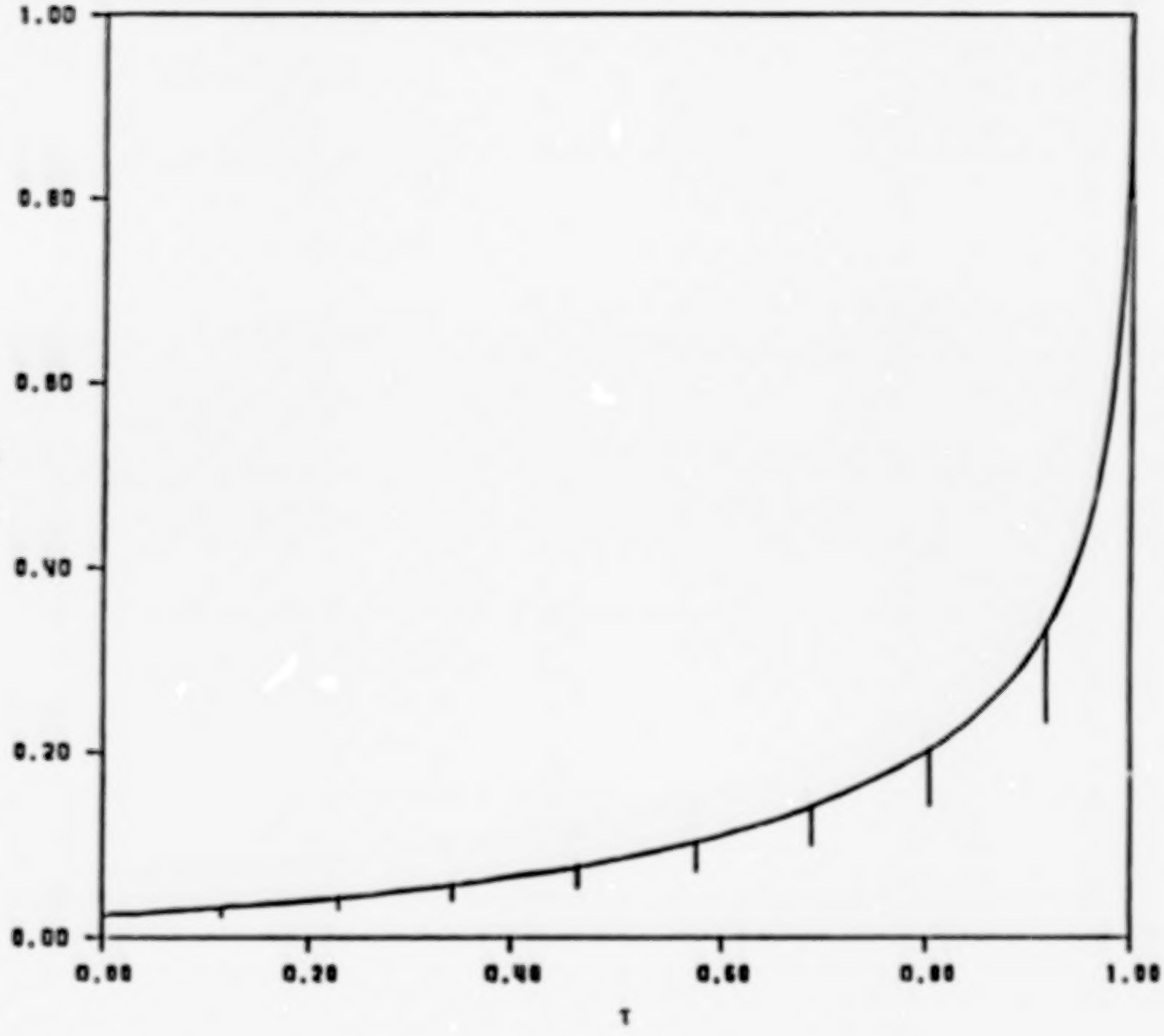

Figure 16. - Nondimensional displacement versus time for all loading histories using classical Norton type creep law.

★U.S. GOVERNMENT PRINTING OFFICE: 1988-548-157/82075

NASA
National Aeronautics and Space Administration

Report Documentation Page

1. Report No.
NASA CP-10010

2. Government Accession No.

3. Recipient's Catalog No.

4. Title and Subtitle
Nonlinear Constitutive Relations for High Temperature Applications - 1986

5. Report Date
April 1988

6. Performing Organization Code

7. Author(s)

8. Performing Organization Report No.
E-3956

10. Work Unit No.

9. Performing Organization Name and Address
National Aeronautics and Space Administration
Lewis Research Center
Cleveland, Ohio 44135-3191

11. Contract or Grant No.

13. Type of Report and Period Covered
Conference Publication

12. Sponsoring Agency Name and Address
National Aeronautics and Space Administration
Washington, D.C. 20546-0001

14. Sponsoring Agency Code

15. Supplementary Notes

16. Abstract

The Third Symposium on Nonlinear Constitutive Relations for High Temperature Applications, under the joint sponsorship of the NASA Lewis Research Center and the University of Akron, was held at the University of Akron on June 11-13, 1986. The purpose of this symposium was to review the state-of-the-art in nonlinear constitutive modeling of high temperature materials for aeronautics applications and to identify the need for future research and development efforts in this area. Through this symposium, it was recognized that considerable research efforts are urgently needed in the development of nonlinear constitutive relations for high temperature applications. In the aerospace industry this need is further prompted by recent advances in high temperature materials technology and new demands on material and component performance. Papers presented at this symposium are contained in the Conference Proceedings.

17. Key Words (Suggested by Author(s))
Constitutive models; Viscoplastic;
Nonlinear structural computations;
High-temperature experiments;
Stress/strain

18. Distribution Statement
Unclassified - Unlimited
Subject Category 39

19. Security Classif. (of this report)
Unclassified

20. Security Classif. (of this page)
Unclassified

21. No of pages
497

22. Price*
A21

NASA FORM 1626 OCT 86

*For sale by the National Technical Information Service, Springfield, Virginia 22161

END

DATE

FILMED

JUL 8 1988